The 55th Conference on Simulation and Modelling (SIMS 55)

Proceedings

21-22 October 2014

"Modelling, Simulation and Optimization"

Editors: Alireza Rezania Kolai, Kim Sørensen & Mads Pagh Nielsen

DEPARTMENT OF ENERGY TECHNOLOGY
AALBORG UNIVERSITY

Conference Organizing Committee

International Scientific Committee

Lars Eriksson, Linköping University, Sweden
Erik Dahlquist, Mälardalens Högskola, Sweden
Esko Juuso, University of Oulu, Finland
Brian Elmegaard, DTU, Denmark
Tommy Mølbak, Added Values P/S, Denmark
Axel Ohrt Johansen, Added Values P/S, Denmark
Kaj Juslin, VTT, Finland
Bernt Lie, Hogskolen i Telemark, Norway
Tiina Komulainen, Oslo University College, Norway
Magnus Jonsson, University of Iceland, Iceland
Jónas Ketilsson, National Energy Authority of Iceland, Iceland
Olav Nygaard, Cybernetic Drilling Technologies AS, Norway
Kim Sørensen, Aalborg University, Denmark
Mads Pagh Nielsen, Aalborg University, Denmark
Alireza Rezania Kolaei, Aalborg University, Denmark

National Organizing Committee at Aalborg University

Kim Sørensen, Associate Professor, Aalborg University, Denmark
Mads Pagh Nielsen, Associate Professor, Aalborg University, Denmark
Alireza Rezania Kolaei, Assistant Professor, Aalborg University, Denmark
Hanne M. Madsen, Information Officer, Aalborg University
Maria H. Friis, Information Officer, Aalborg University

Conference Contact Information

Dr. Alireza Rezania Kolaei, Aalborg University, +45 9940 9276, alr@et.aau.dk
Information Officer Hanne Madsen, Aalborg University, +45 9940 3313, hmm@et.aau.dk

Preface

The members of the Organizing Committee of SIMS 55 are pleased to present the Proceedings of the conference. The SIMS 55 conference is the 55th annual conference of the Scandinavian Simulation Society, SIMS.

It is our hope that you will enjoy the conference and the proceedings!

Alireza Rezania Kolai, Kim Sørensen & Mads Pagh Nielsen
(National Organizers and Conference Proceeding Editors, Dept. of Energy Tech., Aalborg University)

Papers

Modelling and control of energy systems 1

Modelling and control of energy systems 2

Simulation tools and applications 1

Process systems

Simulation tools and applications 2

Fluid dynamics

Buildings and offshore

Power systems and control 1

Mechanical modeling

Power systems and control 2

RETSCREEN MODELING FOR COMBINED ENERGY SYSTEMS: FERTILIZERS PLANT CASE

Iryna Kalinchyk*and Carlos F. Pfeiffer
Telemark University College
Kjølnes Ring 56, P.O. Box 203, N-3901
Porsgrunn, Norway

Evgenij Inshekov
NTUU "Kyiv Polytechnic Institute"
Borshchagivska 115, P.O. Box 311
Kyiv, Ukraine

ABSTRACT

Switching from traditional industrial systems to a modern way of organizing all processes (including energy supply) on the principles of 'green' economy is an up-to-date task, especially for countries under development. The article discusses the using of alternative energy sources to supply part of the energy demands of a chemical plant to produce fertilizers from natural gas in Ukraine. Fertilizers plants consume dozens of MW of power supplied from the grid. A plant pre-analysis showed that there was a high potential for using alternative energy sources. By using RETScreen 4 software it was possible to model systems with one or several alternative energy sources, calculate energy balances, and compare their performance. The results showed that hybrid electricity supply systems can perform beneficially for industry in terms of economy, diversification and environment.
*Keywords:*Combined Energy Supply, Hybrid Energy Systems, RETScreen Modeling, Ukraine Energy, Renewable Energy

NOMENCLATURE

b_{eq} specific cost for auxiliary equipment as a share from main

b_m specific maintenance cost from the main funds

C expenses for new technology implementation [\$]

CF capacity factor [%]

c_f cost of fuel unit [\$/m^3]

c_m maintenance cost [\$/kWh]

C_u cost of generating unit [\$]

g acceleration of gravity [9.81 m/s^2]

h falling height, head [m]

P installed capacity [kW]

P_n nominal capacity [kW]

P_{th} power theoretically available [W]

q fuel use per kWh of energy production [m^3/kWh]

T_{eq} exploitation term of auxiliary equipment [years]

T_u exploitation term of the unit [years]

v water flow [m^3/s]

v_0 initial water flow [m^3/s]

v_n nominal water flow [m^3/s]

W energy produced in average year [kWh/year]

ρ density [kg/m^3]

INTRODUCTION

Ukraine is an energy dependent country which imports 62% of natural gas, and 70.5% of consumed oil and oil products, and nuclear material[1, 2, 3, 4]. At the end of 2013 over 60% of electricity was generated from natural gas and coal on CHPs (combined

heat and power plants) and TPPs (thermal power stations), about 25% was generated from nuclear and about 10% from large-scale hydropower[5]. As energy price is steadily growing both individual consumers and industry are highly concerned on decreasing their grid energy dependence.

Energy carriers have a significant influence on the gross domestic product (GDP) level and economical development of the state[6, 7]. When analyzing the vulnerability of consumers to energy resources' price change, it appeared that the population's consumption is partially subsidized, while industry is highly vulnerable to any fluctuations of energy tariff. The most energy consuming industries are iron & steel, non-ferrous, chemical and petrochemical industries. In 2011 chemical and petrochemical industry consumed 6,248.5 millions kWh, which is 4.1% of the total electricity consumption[8].

According to the goals of the Energy Strategy of Ukraine the country is focusing on diversification of energy sources and wide implementation of renewable energy sources (RES), which should provide 10% of total electricity generation[9] by 2030. This goal will also meet the agreements Ukraine signed on mitigating climate change and pollution[10], since Ukraine has one of the highest levels of air pollution in Europe[11]. Producing green house gases (GHGs) emissions during both technological processes, and consuming energy industry has a significant carbon footprint, which is hardly regulated by governmental policies.

In this article the case of a fertilizer plant is considered as a typical example for a chemical industry in Ukraine. An ammonia plant mainly uses two types of energy carriers: natural gas and electricity[12]. Energy use, especially for ammonia production, has been growing since the 1960s due to expansion of production[13].

Energy price takes a large share in the prime cost formation of produced goods, thus affecting the market position and the ability to be internationally viable for the producers. Nowadays industrial plants in Ukraine obtain electricity from the Unified Electricity Grid of Ukraine (the UEG). Ammonia production has a high potential for energy saving via modernization of technological processes[14]; the article does not consider them because of high investment costs and region peculiarities. To raise the reliability and decrease the dependence on a single supplier the following actions are suggested:

- improving energy efficiency of local energy system (equipment modernization, energy saving measures);

- diversification of suppliers and tariff's change;

- modeling combined supply system.

Such energy systems are combined from renewable and alternative energy sources with or without connection to unified grid. They allow to use energy more fully and optimize energy flows via close interaction between different parts of energy complex. They are widely implemented for households and resorts in remote areas [15, 16, 17]; however, an explicit mechanism for modeling combined energy supply system for industrial plants is not yet developed.

DIVERSIFICATION OF POWER SUPPLY

In industry traditionally the supply from other sources has not been considered as it has not been proven to be profitable. Resources for implementation, accurate demand forecast, grid requirements and holistic benefit are hard for intrinsic estimation. However, diversification of energy sources for local energy systems, especially industrial plants, can lead to significant decrease of energy expenses. In its turn, it will decrease the energy intensity of production and energy expenses share in final goods price[18]. This will lead to higher competitiveness on the market. In fact, including "green energy" in energy supply can raise social acceptance and attract the "smart-consuming" customers[19]. Developed methodology includes analysis of eco-climatological conditions, possibility for connection to the secondary service and technological processes analysis. The considered renewable energy sources are wind, solar PV energy (which are intermittent sources) and hydro-power (which is more reliable). The plant is located in industrial region. Due to lack of available biomass such electricity plant was not considered in this case study. As an alternative energy source improving general efficiency of energy use a turbogenerator is considered.

The localization of energy suppliers can have positive influence on decreasing the number of current long distance electricity transmission. The con-

sumption was growing through years and the transmission capacity did not bringing the exhaustion of equipment. The distribution of energy sources can help to lessen the load on the transmission lines and decrease transmission losses. In this article a model for electricity supply is worked out for a fertilizers plant with potential ability for alternative sources connection. The following questions are discussed:

Which configuration of combined system is the most effective?

Can a combined system lead to economical benefits?

What environmental effect will be gained if a combined system is installed?

What is the payback period for such system?

The software used for modeling and analyzing the hybrid system is RETScreen 4 software[20]. RETScreen is a free tool for modeling, simulation and pre-feasibility study of energy effective and environmental-friendly systems. It provides eco-climatological and meteorological data for most regions of the world (from NASA data) and also uses an extensive database for equipment (solar panel collector, pumps, pipes etc), making it an excellent tool for pre-feasibility and environmental studies. The software was adapted to the case of the industrial plant, however, hand calculations can also be applied. Alternative software to RETScreen like HOMER or Hybrid2 can be also used[21].

THEORY AND CALCULATION

While modeling a local supply system, the following aspects should be considered: reliability and conditions of energy sources, transmission capacity and environmental impact. Considering intermittent availability of some sources it is necessary to provide accurate forecasting on both demand and supply sides. Establishing combined energy system requires simultaneous to power curve fluctuations demand-side management (DSM) for decreasing network risks[22, 23]. DSM is required for further optimization of combined system functioning via attribution an optimization target function. The majority of big enterprises operate with constant electricity demand with no peak or minimum load as they have normalized product output per hour. The energy supply should be constant and reliable, as it can lead to money loss.

When reviewing the energy system of the fertilizers plant in the Rivne region a possibility for connecting alternative sources was found. The analyzed fertilizers plant uses mostly two energy carriers: natural gas and electricity, which cannot be substituted. Combination of renewable and alternative energy sources with the UEG can create a stable and diverse energy system able to provide the cheapest available energy at every moment of time. The fertilizers plant does not produce bio-waste, thus potential for developing biogas utility is low. Eco-climatological conditions and available territory should be scrutinized to evaluate if they are potentially good for installing large wind or solar PV stations. In technological processes natural gas is used not only for energy, but as a raw material. During the ammonia production(fig.) natural gas, water and electricity are used; and, heat is produced. Ammonia is obtained from natural gas after carbon monoxide conversion and gas purification from CO_2. Ammonia synthesis in the fertilizers plant happens in reactors under pressure 280–330 bar. To compress syngas four-stage compressor with a nominal capacity of 32 MW and a productive capacity of 1360 t NH_3 per day is used. Its turbine consumes 350–370 t of vapor received after reforming with parameters 100 bar and 482°C per hour. This turbine produces and the compressor consumes the biggest amount of mechanical energy/work. Energy losses under exhaust steam condensation are about 1.465–1.675 GJ/t NH_3. Analyzing technological processes [13] of fertilizers plant the following conversion takes place:

$$N_2 + 3H_2 = 2NH_3 + heat \qquad (1)$$
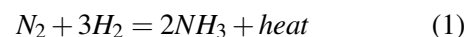
The compression energy during the process converts into heat, which is transferred further with the vapor. This vapor at 105 atm does not perform useful work. According to Ukrainian legislative framework the high-temperature vapor cannot be released into atmosphere. Thus, the enterprise should waste additional energy on compressors and pumps for cooling purposes. During the cooling processes water obtained from the nearby river is used. The river has a high energy potential according to its head and flow, besides, it is affluent enough to be used during all year.

The proposed cases for combined energy system for
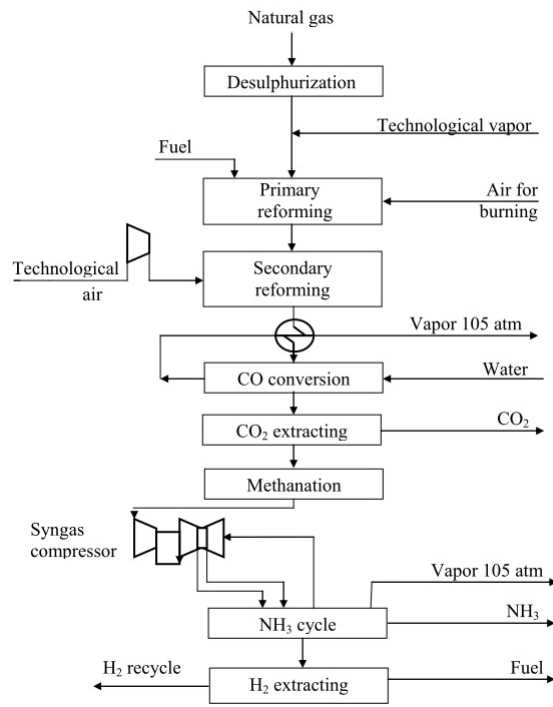
Figure 1: Technological scheme

the fertilizers plant operate on the UEG combined with 1) a turbogenerator on exhaust vapor; 2) a mini-hydropower plant; 3) a solar PV station and 4) a wind power station.

The following combinations can become more complex if interconnected and operating either in sequential or in parallel mode. To calculate the expenses from non-renewable energy sources eq. 2 can be used.

$$C = \frac{C_u}{T_u \cdot W} + c_m + c_f \cdot q \qquad (2)$$

where: C_u: cost of the turbogenerator unit, \$; T_u: exploitation term of the unit, years; W: energy produced in average year, kWh/year; c_m: maintenance cost, \$/kWh; c_f: cost of fuel unit, \$/m^3 (in the case of the turbo generator the price is already included as it has been used for ammonia production); q: fuel use per kWh, m^3/kWh. The expenses from renewable energy sources are obtained through eq. 3.

$$C = \left(\frac{C_u}{T_u} + \frac{C_u \cdot b_{eq}}{T_{eq}}\right) \times \frac{1 + b_m}{W} \qquad (3)$$

where C_u: cost of generating unit, \$; T_u: exploitation term of the unit, years; W: energy produced in average year, kWh/year; T_{eq}: exploitation term for aux-

iliary equipment, years; b_{eq}: specific cost for auxiliary equipment as a share from main; b_m: specific maintenance cost from the main funds.

Energy consumption

The energy model is typical for fertilizers plants in Ukraine. They have a constant energy consumption not much depending on day, season, year (fig.) with traditionally normalized production output. The average day load is 1656 MW, and the major consumers are compressors for NH$_3$–H$_2$ circulation, turbine, additional heater, filters, reformers etc.
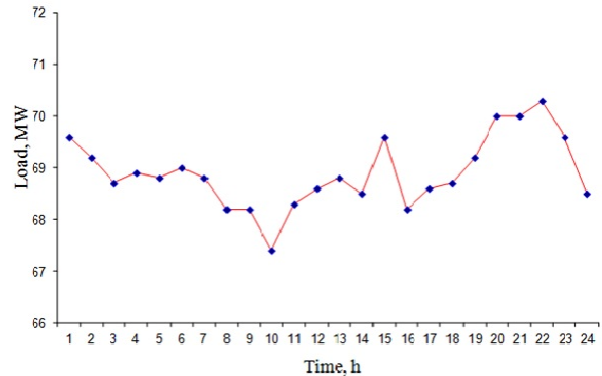
Figure 2: Load curve of the fertilizers plant

Turbogenerator

Cogeneration has proved itself cost-efficient in many industrial sectors [24, 25] with its short payback period and high energy potential. The input parameters for turbogenerator in table 1 are used to calculate energy saving from installation. A turbogenerator for the case perform work during all year (except for maintenance period) since waste vapor requires utilization. The theoretical capacity of the generator is 12,926 kW.

Hydropower

The plant uses water for technological processes from the nearest river. The characteristics of flow (5.2 m^3/s) and head (25 m) allow to calculate theoretical power capacity via eq. 4.

$$P_{th} = \rho \times v \times g \times h \qquad (4)$$

Table 1: Input data for the turbogenerator

Parameter	Value
Steam flow, kg/h	100,000
Operating pressure, bar	106
Superheated temperature, °C	500
Back pressure, kPa	7
Return temperature, °C	70
Steam turbine (ST) efficiency, %	35
Minimum capacity, %	98
Seasonal efficiency, %	90

where: P_{th}: power theoretically available, W; ρ: density, kg/m^3 (for water ~1000 kg/m^3); v: water flow, m^3/s; g: acceleration of gravity, 9.81 m/s^2; h: falling height, head, m.

This formula results in theoretical capacity of 1,200 kW and with efficiency of 93% the power capacity will be of 1,186 kW. To complete the calculations for the hydropower plant a capacity factor defined by eq. 5 is required:

$$CF(\%) = \frac{W}{P \times 8760} \cdot 100\% \qquad (5)$$

where: W: energy generated per year, kWh/year; P: installed capacity, kW with 8760 hours per year. Knowing the capacity factor and installed capacity from table 2, the produced energy can be calculated from eq. 5.

Table 2: Input data for renewable powerstations

Parameter	Hydrostation	Wind	Solar PV
Power capacity of one unit, kW	1,186	2,000	0.32
Number of units	1	3	3000
Total power capacity, kW	1,186	6,000	960
Capacity factor, %	66	46	16

The Canyon Hydro Cross-flow turbine was chosen for medium-head torrent. Electricity delivered to load will be W=6,857 MWh per year. The electricity generated from the hydro-power station depends on energy potential of the flow; the generation mode can be described by eq. 6:

$$W(v) = \begin{cases} 0 & \text{if } v \leq v_0 \\ W & \text{if } v_0 \leq v \leq v_n \\ W_n & \text{if } v_n \leq v \end{cases} \qquad (6)$$

where: v_0: initial water flow speed; v_n: nominal water flow when the hydro station generates P_n: nominal capacity.

Meteorological Data input for wind and solar energy estimations

Table 3 shows the meteorological parameters to calculate wind and solar energy use potential for the selected region (Rivne), which are available in NASA database in RETScreen.

Wind

RETScreen has a good database of wind turbines which can provide highly accurate data input. For the calculation a simplified method was applied using parameters from table 2. There is theoretical possibility for installing wind powerstation of 3 turbines of about 70 m high on the plant's territory, however, such factors as shadowing objects, wind speed and wind rose should be scrutinized. Such wind powerstation will require high capital investments.

Solar PV

The estimated solar potential of Ukraine is 718.4 $\cdot 10^9$ MWh per year (53.8·10^5 MWh per year are economically viable for extraction); the Rivne region in particular has a potential of 21.8·10^9 MWh per year (and 1.6·10^5 MWh per year respectively). While solar heaters can be applied in Rivne region only for 5 months in a year (since May till September), the PV station can provide energy output during all year. The combined system with solar PV uses the data in table 2. There is no big opportunity for developing a PV station by the plant since it would require a vast territory without shadowing objects, which is not available. However, the solar PV panels can reside on the roofs. For the calculation the mono-Si panels produced by Sunpower were considered. The frame area of such panel is 1.62 m^2 and efficiency is 19.62%. Total electricity delivered to the load will result in 1,346 MWh per year.

Hybrid system: hydropower station & turbogenerator

The possibility for interconnection several sources is considered via modeling hybrid supply system consisting of the grid, turbogenerator and a mini-hydro powerstation (fig.). Electricity from grid and turbogenerator is used to cover the base load, hydropower plant is used mostly in hours of semi-peak and peak

Table 3: Meteorological parameters for Rivne

Month	Air tempe-rature, °C	Relative humidity, %	Daily solar radiation, kWh/m^2/d	Atmospheric pressure, kPa	Wind speed, m/s	Earth tem-perature, °C	Heating "degree-days", °C-d	Cooling "degree-days", °C-d
January	-3.4	83.9	1.01	99.2	5.0	−5.0	663	0
February	-2.9	82.1	1.81	99.1	4.7	−4.1	585	0
March	1.1	77.6	2.83	99.1	4.6	1.0	524	0
April	8.4	69.3	3.87	98.8	4.2	9.9	288	0
May	14.3	68.0	5.08	98.9	3.9	16.5	115	133
June	16.6	73.5	5.17	98.8	3.7	18.9	42	198
July	18.7	74.5	4.98	98.8	3.3	20.7	0	270
August	18.0	73.8	4.58	98.9	3.3	20.5	0	248
September	13.1	78.7	3.02	99.0	3.8	15.0	147	93
October	7.9	80.7	1.87	99.3	4.2	8.5	313	0
November	1.8	85.3	1.04	99.2	4.5	1.0	486	0
December	-2.1	86.2	0.81	99.3	4.8	−4.1	623	0
Annual	7.7	77.8	3.01	99.0	4.2	8.3	3,786	942

Table 4: Plant implementation and maintenance cost

Parameter	Turbo-generator	Hydro-station	Wind turbines	Solar PV
Incremental initial costs, thousand $	5,000	2,000	12,000	2,100
Project life, years	20	25	25	20
Other initial costs, thousand $	3,000	200	1,500	400
O&M annual costs, thousand $	20	10	30	50

grid load. This configuration allows the plant to obtain energy from different sources during the day. The input parameters for calculation vide supra (tables 1, 2).
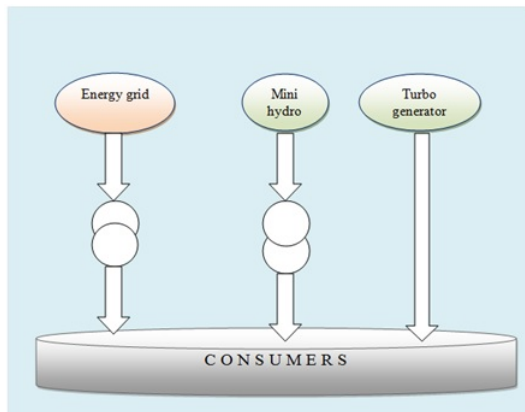
Figure 3: Electricity supply from grid, hydropower and turbogenerator

310

Financial data input

Table 4 reflects the input data for economic feasibility study. In the case if a loan is provided for the combined system implementation the financial pa-

Figure 4: Cashflow for a hybrid system case (grid, turbogenerator and mini-hydropower plant)

Station type	Maximum available capacity, kW	Simple payback period, years	Pre-tax IRR assets, %
Hydro	1,186	1.6	57
Turbogenerator	12,926	5.8	11
Wind	6,000	9.8	5.0
PV	960	1.8	47.7
Hybrid (hydro-, turbo, grid)	14,112	7.4	6.8

Table 5: Financial results

rameters were input as: inflation rate: 2%, debt ratio: 80 %, debt interest rate: 4.5%, debt term is considered to be: 10 years. It is possible to make hand calculations, however, in this article further economical analysis was conducted in RETScreen.

RESULTS

Economic analysis In the table 5 are shown obtained results for the systems to be compared. The combined systems were analyzed for the maximum available capacity, simple payback period and pre-tax IRR-assets.

To compare the economic performance of combined energy systems the cash flows are shown on fig.4,5 , .

(a) Hydrostation

(b) Turbogenerator

(c) Wind station
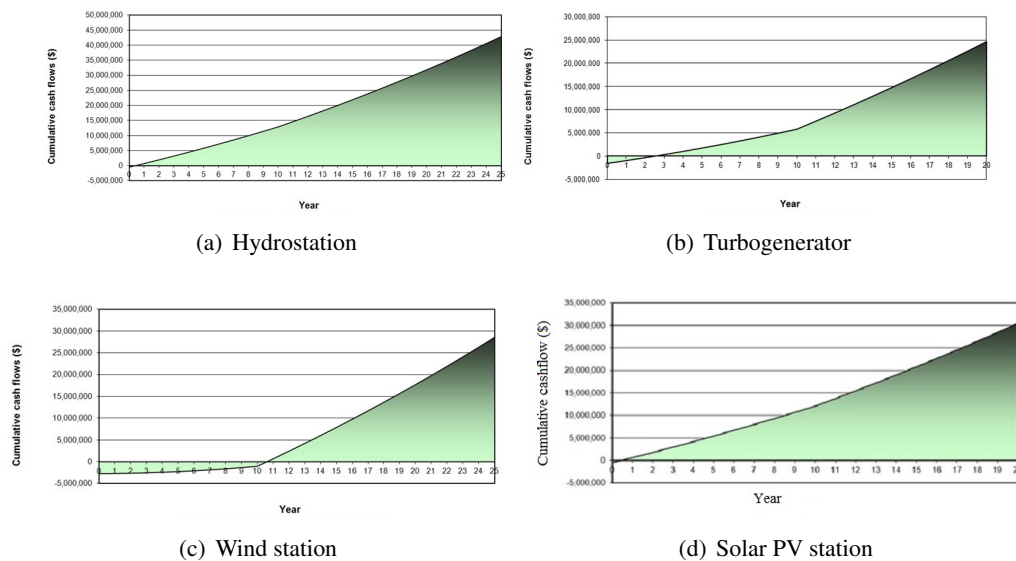
(d) Solar PV station

Figure 5: Comparison of cashflows: Hydrostation, Turbogenerator, Wind station and solar PV station

Energy source	Net annual GHG emission reduction tCO$_2$	
	Coal substitution	Natural gas substitution
Hydrostation	3,966.1	2,766.2
Turbogenerator	-76,636.0	-94,865.7
Wind powerstation	13,984.5	9,753.5
Solar PV panels	778.3	542.8

Table 6: Emissions analysis

Emissions analysis Introduction of combined energy system does not lead to direct GHGs emissions reduction. Conventional emissions reduction takes place as less of electricity is taken from the UEG. The potential not delivered GHGs can be estimated by the volume of emissions from the UEG generating units. As the biggest GHGs emitters are coal and gas CHPs, the analysis was provided for both cases (table 6).

erator has the highest potential for energy utilization via available capacity (almost 13,000 kW) and less than 6 years of payback period, which makes it optional for installation. The environmental analysis pointed out a significant reduction in GHGs emissions while implementing any of before-mentioned combinations. As the GHGs reduction depends a lot on stations' capacity it is shown (table 6) that wind powerstation has the highest environmental potential. In case of the turbogenerator installation there is no GHGs reduction as it operates on vapor received during natural gas processing. However, almost complete utilization of natural gas and wastes allows to say that conditional decrease in emissions is taking place.

DISCUSSION

From the tables 4, 5 it is shown that implementation of the wind powerstation is the most expensive project, which requires the longest payback period (almost 10 years) and a big territory. The hydropower plant and the solar PV station have the shortest payback period (less than 2 years). Maximum available capacity is in a close range, however, the hydropower plant can provide with flexible in time energy output and energy accumulation while the solar power is intermittent and requires precise radiation forecasting system. The turbogen-

CONCLUSION

At the recent level of renewable technologies development complete refill of industrial energy supply from the grid to the RES is impossible. However, the partial generation is proven to be beneficial. RETScreen provided pre-feasibility studies to find the most viable supply system, which is combined from mini-hydropower plant, turbogenerator and the unified grid. The system can work in sequential or in parallel mode. Solar PV station and wind powerstation have lower potential performance. Introducing renewable sources in supply chain will slightly re-

duce energy dependency from ultimate supplier — the grid; improve reliability of supply and decrease the UEG load. The model is of ultimate interest for industrial plants in remote areas and for those with intermittent electricity supply from grid. Optimization of energy supply of chemical industry can lead to significant energy and resource-saving and have a huge impact on all energy sector of Ukraine. Overall, it has a potential for decreasing GHGs emissions from power generating units (via carbon footprint), creating 'green' workplaces, and reduction of local air pollution. The study opens further questions, i.e. what other factors influence on combined energy systems, what will be the contribution of state's energy policies, how to make the system work in the optimal mode and if the real life benefit will be close to pre-feasibility study. Consideration of other RES (like biomass, biogas etc.) will make a complete picture for a future research.

GLOSSARY OF ACRONYMS

CHP: combined heat and power plant.

DSM: demand-side management.

GDP: gross domestic product.

GHG: green house gases.

IRR: internal rate of return.

NASA: the National Aeronautics and Space Administration.

O&M: operation and maintenance.

PV: photovoltaic.

RES: renewable energy source.

toe: tons oil equivalent.

TPP: thermal power plant.

UEG: the Unified Electricity Grid.

REFERENCES

[1] U.S.EIA *Ukraine overview*, Mar 2014,`http://www.eia.gov/countries/country-data.cfm?fips=up`

[2] Energy Delta Institute *Energy Delta Institute: Ukraine*, 2012, `http://www.energydelta.org/mainmenu/energy-knowledge/country-gas-profiles/ukraine`

[3] Balmaceda M.M. *Explaining the Management of Energy Dependency in Ukraine: Possibilities and Limits of a Domestic-Centered Perspective*, report no.79, Universität Mannheim, 2004.

[4] State Statistics Service of Ukraine, archive. *Energy balance of Ukraine for 2012*, report, State Statistics Service of Ukraine, Kyiv, Ukraine, Dec 2012.

[5] State enterprise NPC UKRENERGO *Installed capacity of generated capacity of Ukraine on December, the 31st 2013*, Dec 2013, `http://www.ukrenergo.energy.gov.ua/ukrenergo/control/uk/publish/article?art_id=149524&cat_id=35061`

[6] Apergis N., Payne J.E. *Energy consumption and economic growth: Evidence from the Commonwealth of Independent States*. Energy Economics 2009; 31(5):641–647.

[7] Cornillie J. *The energy intensity of transition countries*. Energy Economics 2004; 26(3): 283–295.

[8] State enterprise NPC UKRENERGO *Analysis of electricity consumption in Ukraine in 2013*, Feb 2014, `http://www.ukrenergo.energy.gov.ua/ukrenergo/control/uk/publish/article?art_id=148068&cat_id=35381`

[9] Ministry of Energy and Coal industry of Ukraine. *Revised Energy Strategy of Ukraine till 2030*, report, Ministry of Energy and Coal industry of Ukraine, Kyiv, Ukraine, Feb 2014.

[10] Grand M.C. *Is there a Future for Intensity Targets in the Durban Platform Climate Negotiations?*, discussion paper 13-59, Universidad del CEMA, Aug 2013.

[11] Central geophysical observatory. *Review on environmental pollution on territory of*

Ukraine according to hydrometeorological organizations data in 2013, report, Central geophysical observatory, Kyiv, Ukraine, 2009.

[12] Worrell E., Blok K.*Energy savings in the nitrogen fertilizer industry in the Netherlands*. Energy 1994; 19(2): 195–209.

[13] Ramírez C.A., Worrell E. *Feeding fossil fuels to the soil: An analysis of energy embedded and technological learning in the fertilizer industry*. Resources, Conservation and Recycling 2006; 46(1): 75-93.

[14] Rafiqul I., Weber C., Lehmann B., Voss A. *Energy efficiency improvements in ammonia production – perspectives and uncertainties*. Energy 2005; 30(13):2487–2504.

[15] Ashok S.*Optimised model for community-based hybrid energy system*. Renewable Energy 2007; 32(7): 1155–1164.

[16] Deshmukha M.K., Deshmukh S.S. *Modeling of hybrid renewable energy systems*. Renewable and Sustainable Energy Reviews 2008; 12(1): 235–249.

[17] Bekele G., Tadesse G.*Feasibility study of small Hydro/PV/Wind hybrid system for off-grid rural electrification in Ethiopia*. Applied Energy 2012; 97: 5–15.

[18] Jenne C.A., Cattell R.K. *Structural change and energy efficiency in industry*. Energy Economics 1983; 5(2): 114–123.

[19] Withanachchi S.S. *'Green Consumption' beyond mainstream economy: A discourse analysis*. Future of Food: Journal on Food, Agriculture and Society 2013; 1(1): 69–80.

[20] Natural Resources Canada *Natural Resources Canada. RETScreen official web-site*, May 2014, `http://www.retscreen.net/ang/home.php`.

[21] Georgilakis P.S. *State-of-the-art of decision support systems for the choice of renewable energy sources for energy supply in isolated regions*. Technology & science 2005; 2(2):129–150.

[22] Strbac G. Demand side management: Benefits and challenges. Energy Policy 2008; 36(12): 4419–4426.

[23] Paulus M., Borggrefe F. *The potential of demand-side management in energy-intensive industries for electricity markets in Germany*. Applied Energy 2009; 88(2): 432–441.

[24] Costa M.H.A, Balestieri J.A.P. *Comparative study of cogeneration systems in a chemical industry*. Applied Thermal Engineering 2001; 21(4): 523–533.

[25] Khurana S. Banerjee R., Gaitonde U. *Energy balance and cogeneration for a cement plant*. Applied Thermal Engineering 2002; 22 (5):485–494.

FEASIBILITY STUDY AND TECHNO-ECONOMIC OPTIMIZATION MODEL FOR BATTERY THERMAL MANAGEMENT SYSTEM

Mohammad Rezwan Khan[1], Mads Pagh Nielsen and Søren Knudsen Kær
Aalborg University
Department of Energy Technology
Denmark

ABSTRACT

The paper investigates the feasibility of employing a battery thermal management system (BTMS) in different applications based on a techno economic analysis considering the battery lifetime and application profile, i.e. current requirement. The preliminary objective is to set the decision criteria of employing a BTMS and if the outcome of the decision is positive, to determine the type of the employed BTMS. However, employing a BTMS needs to meet a number of application requirements and different BTMS associates a different amount of capital cost to ensure the battery performance over its lifetime. Hence, the objective of this paper is to develop and detail the method of the feasibility for commissioning BTMS called "The decision tool framework" (DTF) and to investigate its sensitivity to major factors (e.g. lifetime and application requirement) which are well-known to influence the battery pack thermal performance, battery pack performance and ultimately the performance as well as utility of the desired application. This DTF is designed to provide a common framework of a BTMS manufacturer and designer to evaluate the options of different BTMS applicable for different applications and operating conditions. The results provide insight into the feasibility and the required specification and configuration of a BTMS.

Keywords: Batteries, Economical Analysis, Cash Flow, Batteries; Battery Storage; Techno Economic Model and Analysis; Battery Thermal Management; Lifetime; Feasibility Procurement.

1   INTRODUCTION

Temperature excursions and non-uniformity of the temperature inside the battery systems are the main concern and drawback for any attempt to scale-up battery cells to the larger sizes as required for high power applications. The capacity of the battery pack increases as the operating temperature is raised for a battery pack. However, this is associated with a very high expense of accelerated capacity fade. Subsequently the lifetime of the battery system is reduced. Moreover poor performance (limited capacity availability) is observed at low operating temperature [1, 2]. In addition, excessive or uneven temperature rise in a system or pack reduces its cycle life significantly [3].

In general, temperature affects several aspects of a battery including operation of the electrochemical system such as round trip charge/discharge energy efficiency, charge acceptance, power and energy capability, reliability, lifetime, life cycle cost and so on [4].Thereof, temperature uniformity, within a cell and from cell to cell inside a pack (a collection of cells) and/or system (a collection of packs), is essential to achieve the maximum cycle life of battery system [5]. The battery thermal management system (BTMS) is an integral part of a battery management system (BMS) for this particular purpose. Basically, battery system design requires a trade-off between the risk of overheating individual cells of relatively large sizes and the cost of insulating or cooling a complex array of small cells. Usually, the BTMS is a combination of both hardware and software to preserve the temperature difference of battery cells in a pack in an optimal range to enhance the lifetime while ensuring safe and secure operation. Simulation results showed that thermal management systems might improve battery performance by 30–40% [6].

---

[1] Corresponding author, E-mail:rezwankhn@gmail.com; mrk@et.aau.dk

The BTMS designed on the basis of the given application requirements can be described in terms of its main characteristics. These form obviously the BTMS design specifications, which list the requirements rooted from the application and also the outputs from the design process that characterize the functions of the BTMS to have the long lasting life within restricted constraints.

The feasibility study of a BTMS means the appraisal of possibility and justification of employment of BTMS among possible alternative solutions. The economic feasibility of BTMS depends on several parameters: Thermal accessories' prices, battery prices, the corresponding lifetime, economic parameters e.g. real interest rate, inflation, financial stimulation structure etc. The preliminary target is to provide management with enough information to recommend BTMS is needed to be employed, if it is indeed needed to be employed what type is better among the alternatives so that a selection can be made in subsequent phases and the determination of a preferred alternative. A "go/nogo" decision is the consequence of the feasibility study by the management. Also the management needs to examine the problem in the context of broader business strategy [7]. However the design process of BTMS for the particular application design process is typically is complicated by the large number of variables involved for instance battery pack configuration, battery materials, mechanism of coolant flow etc. that require countless amount of demonstrations to find variability of parameters on different type of design. As a result of the various simplifications and approximations, the BTMS design problem is brought to a stage where it may be solved analytically or numerically. The next step in the BTMS design process is the evaluation of the various designs obtained for determining feasibility. This BTMS design effort would generally direct to a domain of acceptable or workable designs. From this domain, the best BTMS design is chosen based on different given criteria such as maximisation of return of investment (ROI).

Evaluating the feasibility of the design in terms of the results from the simulation and the given design

problem statement is an important step in the design process because it involves the decision to continue or stop the procurement of the BTMS for desired application. Optimization is of particular importance in choosing BTMS because of the strong dependence of cost and application profile on system design. Usually, the optimal design is not easily determined from either available simulation or acceptable design results. The optimization process is obviously applied to acceptable designs so that the given requirements and constraints are satisfied. Then the design finally obtained is an optimal one, not just an acceptable one. Optimization of a thermal system can be carried out in terms of the design hardware or the operating conditions. In these circumstances, modelling helps in obtaining and comparing alternative BTMS designs by predicting the performance of each feasible design ultimately leading to an optimal design. With optimization indicates the values at which the performance is optimal with respect to optimization criteria of the ROI.

In different literature battery systems are found to be in diverse applications. The applications may include electric power generating stations, substations, vehicles, telecommunications installations, large industrial and commercial installations, large uninterruptible power supply (UPS) installations and renewable energy plant installations etc. [8, 9]. Typically, the storage for PV panels is used in stand-alone applications [10, 11]. The potential profits of grid-connected storage are studied with help of a control mechanism but without dimensioning the storage size [12]. In Ref. [13] an empirical method is presented to determine the optimal battery size to cover most of the electricity needs using PV in a home. The financial aspects like battery costs were not taken into account while a similar analysis in a commercial building [14]. Ref. [15] presented an idea to use battery storage for district level autonomy for multifunctional application on transmission congestion and arbitrage application he profit potential without dimensioning the storage size based on a future peak pricing of electricity [16]. Ref. [17] performs an internal rate of return calculation over a range of battery sizes and prices of Real PV and consumption data and an economical evaluation for domestic batteries with

a cost range per kWh is explained [18]. Additionally, most assumptions did not account explicitly for the battery cost and life time. An economic analysis based on the feed-in tariffs and an inflation of 1.6%/annum is assumed [19]. Ref. [20] contains a multi-objective optimisation technique to determine the trade-off between the quality of ancillary services and its economic cost for a household with a PV installation.

The paper introduces with the proposed methodology on section 2, The decision framework on section 3, the application load profiles, and the design problem is formulated depicting requirements and specification (section 3.1), given quantities of technical and financial input (section 3.2), design variables (section 3.3), constraints (section 3.4) and relevant assumption (section 3.5). Within this a model (section 3.6) is built on governing equations (section 3.7). The results and discussions are elaborated on section 4. Unless stated specifically the methodology are valid for all battery chemistries.

2   METHODOLOGY

Fig. 1 illustrates the method used in the paper for the proposed feasibility study. A number of real life profiles originated from electric vehicle (EV) and photovoltaic (PV) application (specimen of the profile **Fig. 2**) have been selected so that they represent the best correspondence for the particular application. For a given battery chemistry with a given configuration, a thermal model is executed to find the temperature increase due to the current profile. However, practical BTMSs are largely very complex and must be simplified through idealizations and approximations to make the problem manageable to a solution with necessary accuracy. A mathematical model is employed. The mathematical modelling of BTMS generally involves modelling of the various components and subsystems that constitute the thermal components including the battery system, followed by a coupling of all these batteries and the relevant accessories' models to obtain the final, combined model for the system. The general procedure outlined in the preceding may be applied to a component and the governing equations derived based on various simplifications, approximations, and idealizations that

may be appropriate for the circumstance under particular application. The simplification is carried out largely to reduce the number of independent variables in the problem besides to generalize the results so that they may be used over wide ranges of conditions. The thermal model is executed for a given pack application. Using the result of the prospective increase of temperature range, the best suitable thermal system is chosen according to satisfy the application requirement. In this model, the economy based lifetime model is simulated to find the best optimum configuration that satisfies the maximum return of investment (ROI).
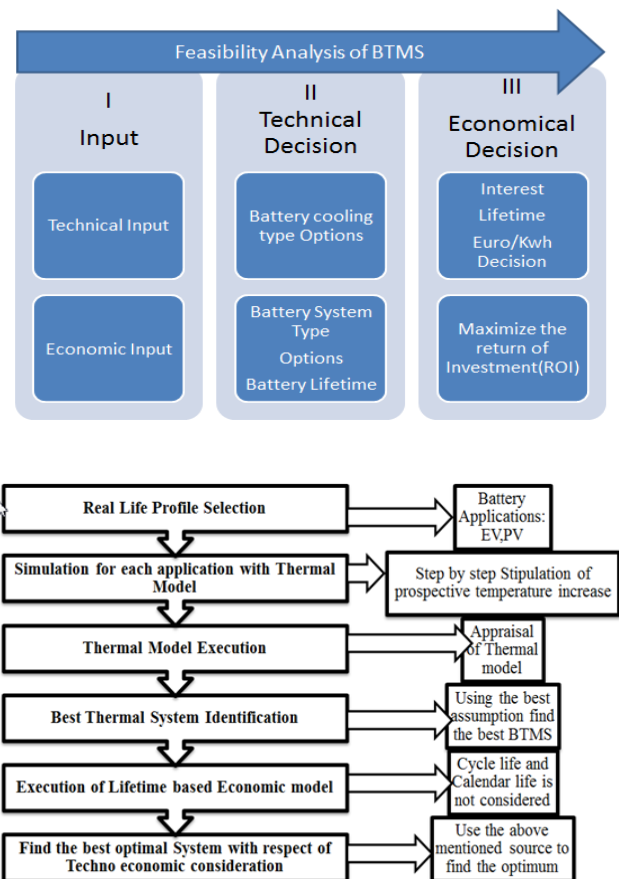
Fig. 1 Methodology used in feasibility study.
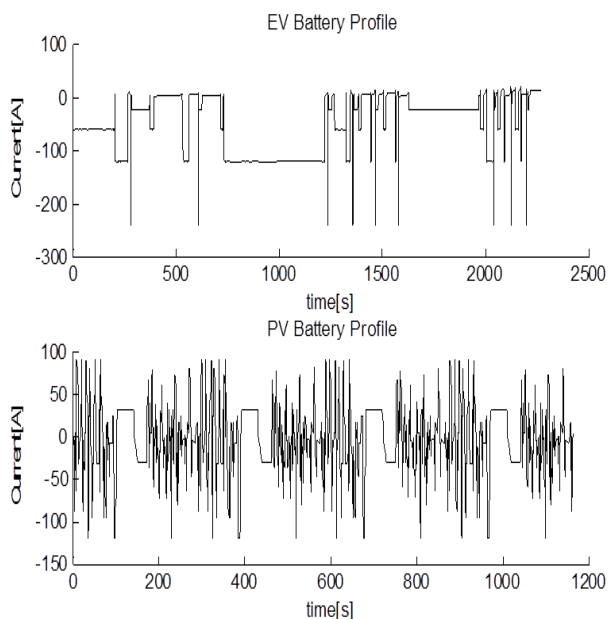
Fig. 2 Corresponding application profile [Top].Electrical Vehicle (EV) application. [Bottom] Photo Voltaic (PV) battery application load profile.

3 DECISION FRAMEWORK TOOL

The final design of the decision framework tool is obtained for the BTMS through the following steps elaborated in the subsequent sections.

3.1 Requirements and Specifications

Certainly the most important consideration in BTMS design is the requirements or the functional tasks to be performed by the specified system. A successful, feasible, or acceptable BTMS design must satisfy all the application requirements. The requirements form the basis for the design space of BTMS and for the establishment of evaluation of cost and consequently ROI of the different designs of BTMS.

The final specifications of the system include the performance characteristics; expected life of the system, cost associated, lifetime. An example for requirements for BTMS is shown in **Table 1**.

Table 1 A typical specification of BTMS [21, 22] Characteristic For EV application

Characteristic	For EV application
Cooling capability	800 W
Refrigerant type	R134a
Operation Temp of cells	$< 35\text{-}45°C$
Temperature difference from cell bottom to the top of the cell	$< 10°C$
Temperature difference from cell to cell	$< 5°C$
Max. pressure drop in the evaporator (stationary)	300 mbar
Additionals	No overheating at the outlet of the evaporator. Constant temperature in the evaporator. Heating for power and energy availability at low temperatures .

3.2 Given financial and technical input

The next step in the formulation of the BTMS design problem is to identify, determine and quantify of the entities that are given and are thus assumed to be fixed. In this paper, materials, dimensions, geometry, and the basic concept or method, particularly the type of energy source are given in the design of a thermal system considered as a lumped system. These include the components of the BTMS such as accessories, dimensions, materials, geometrical configuration, and other quantities that constitute the hardware of the system. In the paper, li-ion/ lead acid (PbAc) battery system and the corresponding cooling scheme air/liquid/refrigerant cooled BTMS are assumed to be fixed lumped parameter. In case of varying these parameters individually in general has several unwanted implications. For example physical size change of the battery that entails changes in the fabrication and assembly of the BTMS except the situations when these parameters are indeed available to change due to presence of the control over design. Furthermore, changes in the hardware are not easy to implement if existing systems are to be modified for a new design, for a new product even for optimization.

To complete the analysis the following battery and financial data are necessary as fixed parameters

costs and lifetime of the battery systems and required thermal accessories, their investment cost and operating cost, the discount rate (nominal interest rate) and the inflation as provided on Table 2.

Table 2 Different given model parameters used in the simulation.

Attribute / Technology	Lithium ion	Lead Acid
Price/KWhr(€)	1000	400
Efficiency(Full Cycle)	92-96%	80-82%
Calender Lifetime yrs	20	10
Cycle Lifetime	5000 @60% DOD	2500 @50% DOD
	5000@90% DOD	2500@60% DOD
Self-Discharge	3%/Month	5%/Month
Operating cost	1.5%	1%

Economic	
Project Period	1,3,5,10,15 year
Interest	4.8%
Inflation	2%

	Air BTMS(€)	Refrigerant	Liquid
Lithium ion	50	90	150
Lead Acid	30	70	120

Finally, the discount rate and inflation have to be considered. A discount rate of 4.5% is based on the yield of Danish loans on the secondary market. This was taken from 15 year maturity bond market between 4.2%-4.7 % [23]. The inflation is considered to be 2%, in line with the objective of the Central European Bank [24].

3.3 Design Variables

The design variables are the quantities that may be varied in a BTMS in order to satisfy the specified application requirements. In this paper for instance, the varying parameters are the choice of the battery system, i and associated accessories, j options of cooling systems (details in section 3.7) for thermal management. Therefore, during the BTMS design process attention is primarily focused on these varying parameters that determine the behaviour of the BTMS and are then chosen so that the system meets the given constraints of lifetime and financial aspects.

Three schemes are taken as the main factor to investigate in this study. Those are the air-cooling scheme; refrigerant cooling scheme and a liquid-cooling scheme. **Fig. 3** illustrates the basic schematics of the cooling options of the thermal management system while **Table 3** corresponds a comparison of the three schemes.
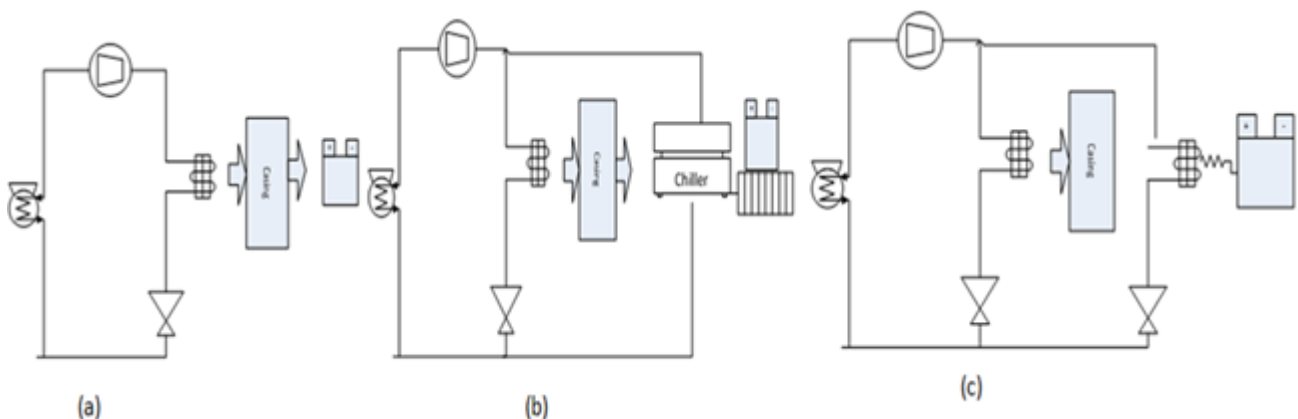
Fig. 3 Cooling options of a battery thermal management system generic diagram. (a)Air cooling, (b) liquid cooling, (c) Refrigerant cooling.

Table 3 Comparison between different cooling schemes in traditional BTMS.

Scheme	Description	Application	Temperature differntial allowed between the cells
Air cooling	-Both cooling and heating is feasible. -Good performance -Normally large space needed -Cheapest -Lower development effort is needed	-Application is limited but in most cases sufficient for HEV/48V/12V applications.	Temperature difference between air and cells can be > than 15°C limitation.
Liquid cooling	-Sufficient cooling capability. -Lowest temperature gradients. -Cooling and heating is feasible. -Best performance -Liquid cooling circuit is needed so moderate space is required. -Most expensive. -Most development effort is required	Liquid cooling can be found in EV, PHEV, HEV, 48V batteries.	Cooling plate 1-3°C
Refrigerant cooling	-"Aggressive" cooling due to very low cooler temperatures. Intelligent thermal management and specific pack design needed to avoid a too aggressive cooling and condensation of humidity -Heating can only be realized with extra devices. -Better performance -Low space requirement -Moderate expense -Moderate development effort is required	HEV,48V batteries	Cooling plate 3-8°C;

.

3.4 Constraints or Limitations

The BTMS design must also satisfy various constraints or limitations in order to be acceptable. These constraints generally arise due to the BTMS's material, weight, cost, availability, and space limitations. The maximum pressure and temperature to which a given BTMS's component may be subjected are limited by the properties of its material. The choice of the material itself may be limited by cost, availability, and environmental impact even if a particular material has the best characteristics for a given problem. Volume and weight restrictions also frequently limit the domain of acceptable design. In this paper, the constraints are project lifetime ($L_{i,j}$), expenditure caps (AC_{max})—more on section 3.7.

3.5 Assumptions and rational behind the assumptions

Knowledge of existing systems, characteristics of similar systems, governing mechanisms, and commonly made approximations and idealizations provides substantial help in BTMS techno economic model development. Material property data and empirical results, available on the characteristics of

devices and components that comprise the system, are also incorporated into the working model through lumped approximation of the battery system (i) and cooling system type (j)--more elaboration on section 3.7. In this paper, a predictive mathematical model for BTMS is of particular interest to the current problem and is employed because this can be used to predict the techno-economic performance of a given BTMS. However, thermal systems are often governed by sets of time-dependent, multidimensional, nonlinear partial differential equations with complicated domains and boundary conditions. Finding a solution to the full three-dimensional, time-dependent problem is usually an extremely time and cost consuming process that may not be existent while finding and choosing the feasibility for a BTMS over other alternatives and options. In addition, the interpretation of the feasibility results obtained and the particular application to the BTMS design process are typically complicated by the large number of variables involved for instance battery pack configuration, battery materials, mechanism of coolant flow etc. that require countless amount of experiments to find variability of parameters corresponding to different type of design. Even if the experiments are carried out to

obtain the relevant input data for feasibility study and design, the expense incurred in these experiments makes it pragmatic to develop a model applicable for BTMS and the battery system to emphasis on the dominant parameters e.g. lifetime, costs on different choices. Therefore, it is necessary to neglect relatively unimportant aspects, combine the effects of different variables in the problem, employ idealizations to simplify the BTMS design for the feasibility analysis, and consequently reducing the number of design parameters that govern the system for the specified application but emphasising more on the economic effect of the system for instance ROI and costs, since those may be the most important decision parameter to build and procure a battery system for desired application. Consequently, the first step is to consider the simulation results in terms of the physical nature of the system and to ascertain that the observed trends somewhat agree with the expected behaviour of the real BTMS in terms of the respective application load profile and corresponding lifetime. But the precaution is to be taken that all these measures are relatively approximate indicators, which generally suffice for the purpose of the feasibility study and evaluation of the different designs obtained. Since the design strategy, evaluation of the BTMS designs developed, and final design are all dependent on the problem statement, it is important to ensure that all of these aspects are considered in adequate detail and quantitative expressions are obtained to characterize those as explained in section 3.7.

Estimates of the relevant quantities are used to eliminate considerations that are of minor consequence. In this paper, negligible effects are heat removal rate, time to reach the required temperature and so on. Practical BTMS and associated processes are certainly not ideal. There are non-exhausting list for instance undesirable energy losses, friction forces, fluid leakages, operating conditions and so forth, that affects the system behaviour. However, in this paper a number of idealizations are usually made to simplify the problem and to obtain a solution that represents the best performance for proposed feasibility analysis. Actual systems may then be considered in terms of the ideal behav-

iour originating from this and the resulting performance given in terms of efficiency, coefficient of performance (COP), or effectiveness of this ideal system. The paper can be used to estimate how the specific BTMS perform against the representative ideal system functioning on the given application. Scaling laws are employed because they allow the modelling of complicated systems in terms of simpler, scaled-down versions. Using these laws, the results from the models can be scaled up to larger systems. All the results are shown in the paper consider the utilization of battery of 200 cycles per year is assumed as used in [1].

However in reality these refer to quantities of BTMS that can often be varied relatively easily over specified ranges with the holding the current structure of the hardware of the given BTMS, such as the operating settings for temperature, flow rate, pressure, speed, power input, etc. Therefore, several of these are generally kept fixed as stated section 3.2 in this paper and the ranges over which the others can be varied are determined from physical constraints, availability of parts, and information available from similar systems.

Even using the above mentioned simplifications and idealizations the techno economic model is said to have some level of precision due to inclusion of degrees of freedom than can be found in the literature [13, 15, 20, 25].

3.6   Modelling

The modelling of BTMS is an extremely important step in the feasibility study based on the design and optimization of the system. Modelling is generally first applied to the obvious components, parts, or subsystems related to its functionalities that make up the BTMS for current consideration of commissioning in battery system for the particular function. These models comprised of different type of battery systems in this article lead acid and lithium ion battery systems respectively as well as the corresponding accessories counterpart are assembled with necessary cost information in order to take into account the utility and interaction between the integrated battery systems cost and lifetime those

are worthwhile for the desired application. By executing these individual models, the actual utility of a battery system in term of costs with necessary adjustment inflation and real interest rate is calculated with each other for finding the overall model that satisfies the maximum ROI for the thermal system is obtained. The model is subjected to a range of project lifetime conditions due to various cost and performance options to choose the best of the system within the required constraints. A mathematical model that represents the performance and characteristics of BTMS in terms of mathematical equations is employed. The dominant considerations in the particular BTMS are to determine the important variables such as costs, lifetime costs etc. and the governing parameters (the battery system choice and the corresponding thermal system choice) because of their considerable versatility in obtaining quantitative results that are needed as inputs for the design. The price of different BTMS depends on the scale, volume of cost, quality and the lifetime as well as the financial aspects such as year of the investment, interest rate, inflation etc. Therefore it is imperative to take a financial cash flow with adjusted interest rate that ensures common ground base for the calculation that includes discount rate and inflation. Return on investment (ROI) measures the gain or loss generated on an investment relative to the amount of money invested. ROI is usually expressed as a percentage and is typically used for internal financial decisions, to compare an enterprise's profitability or to compare the efficiency of different investments.

In order to calculate the real present values of the battery systems with BTMS nominal interest rate is converted to real interest rate to accommodate inflation. The nominal interest rate (sometimes simply called the nominal rate) is the interest rate that is quoted by central banks. It is the rate that is used to discount actual, inflated future values. The real interest is the rate earned on a capital investment after accounting for inflation. The real interest rate should be used to discount future values that are expressed in current monetary values. In this article the real interest rates are considered than the nominal interest rate.
Let:

i = the nominal interest rate,
r = the real interest rate, and
k = the inflation rate.

Now, the formula for combining the real interest rate and the inflation rate to get the nominal interest rate is:

$$r = \frac{(1+i)}{(1+k)} - 1 \dots \dots (1)$$

Discount real future values with a real interest rate, and discount nominal future values with a nominal interest rate. Real future values are uninflated; nominal future values are inflated.

To discount real future values, a real interest rate is used. To discount nominal future values, a nominal interest rate is used. Compounding a present value with a nominal interest rate results in a nominal future value. Converting a real future value C_n^* to a nominal future values C_n is an example of inflating. In order to schematically represent the present values and future values with interest rate inflation and real interest rate with different cost of capital present capital apparent capital future value of present capital is described in the following **Fig. 4**.
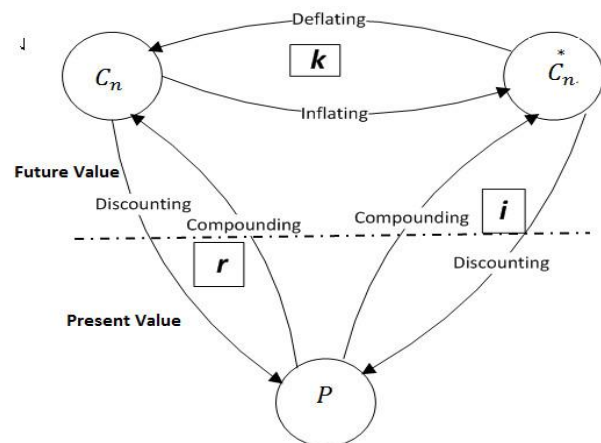
Fig. 4 Financial model schematics present and future values of capital using real and nominal interest rate.

All these considerations secure a permissible level of accuracy and credibility. A standard investment calculation is used. This calculates the net present value of cash flows under influence of inflation, discount rate (the given rate of return) and return of investment. This means that the real discount rate

is taken as reference instead of the nominal discount rate (i.e. without inflation) [24]. The investment in a combination of thermal accessories and battery system that leads to the highest ROI is the most attractive option, since it is the highest profit in absolute terms. In formula form this is expressed as:

$$ROI = \frac{\text{Lifetime Benefit} - Life\ time\ \text{Cost}}{\text{Cost}} \dots \dots (2)$$

Besides the net present value, also the internal rate of return (IRR) and the payback period (PB) are important financial indicators that can be incorporated into the calculation.

The payback period represents the operational year that the sum of the cash flows starting from the initiation of BTMS acquisition period is higher than the investment without taking the discount rate (or real interest) into account. It is also sometimes indicated as simple payback period to emphasise that no discounting is used. In the paper, the payback period is not shown. In this paper, the base cost for ROI calculation has been chosen as the choice when there is no BTMS for the two battery systems. So in calculation of ROI of these systems, this is worked like the lifetime cost. Since there is a lifetime increase in case of BTMS usage, the benefit is calculated. In all cases cost and benefits are calculated per annum basis to have a common scale for further comparison.

3.7 Governing equations

This section deals with mathematical modelling based on physical insight recourse and on a consideration of the governing principles that determine the behaviour of a given thermal system.

The governing equations are first written. After the governing equations are assembled, along with the various approximations and idealizations outlined here, further simplification can sometimes be obtained by a consideration of the various terms in the equations to determine if any of them are negligible. Table 4 provides the options for BTMS choices that are used in the simulation.

Table 4 Battery thermal management choice in the simulation.

Battery System	i	Thermal System	j
Lithium ion	1	No BTMS	0
Lead Acid	2	Air Cooled	1
		Refrigerant	2
		Liquid	3

Total battery system cost

$$TC_{i,j} = \sum_{i,j=1} KC_i + KC_j + K_{i,\text{j\_op}} \dots \dots (3)$$

$KC_i, KC_j, K_{i,\text{j\_op}}$ annotates battery system price, the cooling options and operation cost respectively.

Per Annum Cost $C_{i,j} = \frac{TC_{i,j}*CRF}{L_{i,j}} \dots \dots (4)$

Subject to

$$TC_{i,j} < \text{Maximum allotted cost}, AC_{max}$$

$$CRF = \left(\frac{1 - 1/(1+r)^{yr}}{r}\right)^{-1} \dots \dots (5)$$

ROI is calculated using Eqn.(2)

So the target is to determine the maximum ROI. Find best i, j for the best ROI.

$$\max_{i,j}(ROI)$$

4 RESULTS AND DISCUSSION

Ultimately, a satisfactory mathematical model of the feasibility analysis of BTMS is obtained and this can be used for design, optimization, and feasibility study of the battery system in the particular application, as well as for developing models for other similar systems in the future.

The following temperatures and temperature differences are ensured:

✓ Max. Temp. in the pack <40°C
✓ Max temperature difference between cells < 2°C

✓ Max temperature difference cell bottom – cell tap< 6°C

Two battery pack applications with cooling plates (**Fig. 3**) on the bottom of the cells but different cooling media have been introduced and validated on the test stand. Air cooling can be critical in matter of terms of cooling capability and temperature gradient within the battery pack. Besides that safety and comfort aspects have to be considered in real systems.

A sensitivity analysis is undertaken to determine how the choice of BTMS varies with the design variables and the operating conditions in order to choose the most appropriate, convenient, and cost-effective values at or near the extremum that would optimize the system or its operation.

In this paper the project horizons of 3 and 5 year (short term), 10 and 15 year (long term) are chosen. Also to show the results with a base project spanning 1 year is used. The system is simulated on same interest rate with inflation to compare each other's feasibility. Using the modelling methods and governing equations the model is simulated to find the maximum ROI. The short term result implicated that PbAc battery systems are more feasible and yield more ROI than its lithium ion counterpart. But if the project tenure is bigger than 5 years, Li-ion becomes the preferred technology. The reason is that Li ion has higher longevity and need to be replaced less times than PbAc counterpart.One of the further comment can be that the price of batteries are going down sharply for lithium ion batteries and in coming years the trend is going to persist. In that case again Li -ion batteries offer more prospects to change their PbAc counterpart.

The two applications EV and PV impose different type of thermal system requirement. The thermal system must adhere to the ever changing profile of the EV application cycle. Due to the restrictions that are needed to comply for EV application, the system is best suited to go with liquid and refrigerant type cooling mechanism as illustrated on **Fig. 5** So a cooling system is recommended to be em-

ployed while using the battery systems for EV systems. However, the choice among the liquid, refrigerant or air cooled may also be dictated by space constrains. Additionally, selected cooling layout can make use of battery's thermal capacity also participate on cost reduction of the whole vehicle.
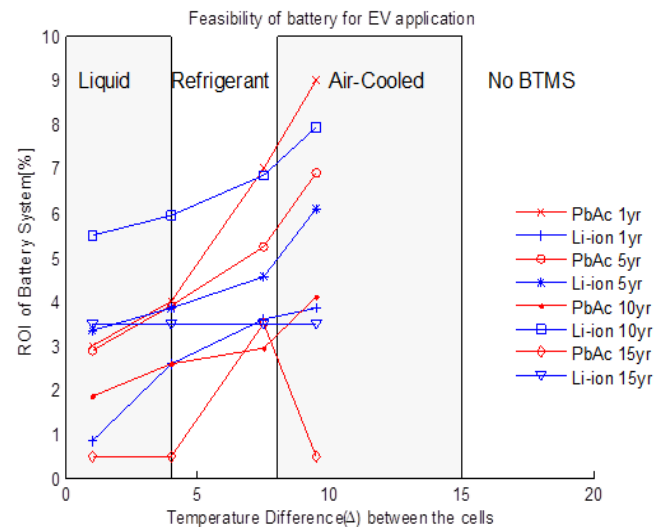
Fig. 5 Feasibility result for Electrical Vehicle application commissioned with different cooling BTMS with different PbAc and Li-on Battery system.

The result is congruent with real life project results. Especially for large size battery systems liquid cooling is the best compromise. Choice of cooling concept depends on battery pack requirements as well as on vehicle requirements and architecture.

But in case of PV application, the air and refrigerant type provide the optimized ROI criteria shown on **Fig. 6** . It is observed that PV profiles are not as much as varying as EV power requirement that results less temperature increase and consequently the stationary battery becomes more profitable by avoiding extra expenditures of the expensive BTMSs.
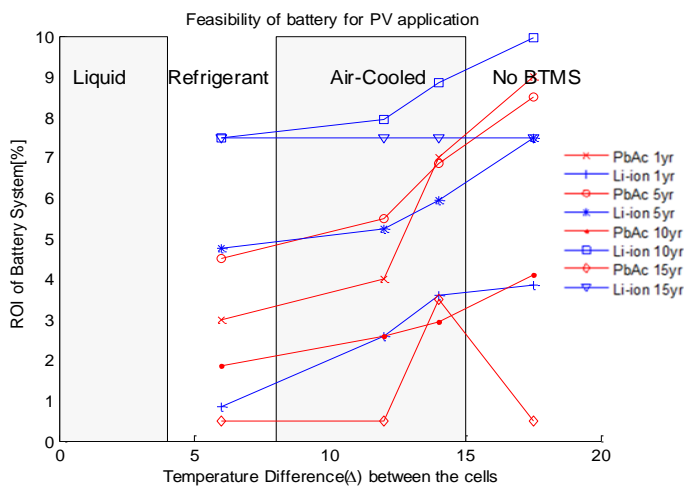
Fig. 6 Feasibility result for Photovoltaic application commissioned with different cooling BTMS with different PbAc and Li-ion Battery system.

This techno economic effort also generalizes the problem so that in future the results obtained from the analytical result originate from the techno-economic model can be compared to the experimental study that can be used without major modifications to other similar systems and circumstances covering all the scopes as detailed by this paper. Alternatively, if experimental data from a prototype are available, a comparison between these and the results from the simulation could be used to determine the validity and accuracy of the latter.

Since the basic concept introduced in the paper is not fixed, different concepts may be considered irrespective of battery chemistries resulting in considerable flexibility in the design. However, in many cases, different considerations may lead to different scaling parameters and the appropriate model may not be uniquely defined at least on the feasibility stage.

5   CONCLUSIONS

This paper provides a complete feasibility analysis of battery systems with necessary thermal management accessories functional in transport and photovoltaic applications based on a statistical significant amount of data, based on real system prices and technical lifetime expectations. The method takes into account technical parameters as battery lifetime and application requirement. Future work will be oriented towards applying the analysis to different types of profiles using taking more degrees of freedom into account for example impact of heating rate and method of cooling e.g. convection or forced based cooling and design of hybrid optimal system. Furthermore the method can be applied to determine the feasibility of the inclusion of any accessories that may be introduced over time corresponding to increased lifetime for different application criteria than PV-battery and EV-battery systems. The present paper aims to serve as decision-making support for researchers, practitioners and policy makers by reviewing costs and performance of battery before purchasing or acquiring a required BTMS. For most battery storage applications, the methodology can be used without major modifications.

REFERENCES

[1]   H. S. Kim, B. W. Cho, and W. I. Cho, "Cycling performance of LiFePO4 cathode material for lithium secondary batteries," *Journal of Power Sources,* vol. 132, pp. 235-239, May 2004.

[2]   C. K. Huang, J. S. Sakamoto, J. Wolfenstine, and S. Surampudi, "The Limits of Low-Temperature Performance of Li-Ion Cells," *Journal of The Electrochemical Society,* vol. 147, pp. 2893-2896, August 1, 2000 2000.

[3]   R. Sabbah, R. Kizilel, J. R. Selman, and S. Al-Hallaj, "Active (air-cooled) vs. passive (phase change material) thermal management of high power lithium-ion packs: Limitation of temperature rise and uniformity of temperature distribution," *Journal of Power Sources,* vol. 182, pp. 630-638, Aug 2008.

[4]   M. R. Khan, S. J. Andreasen, and S. K. Kær. (2014, 01.08.2014) Novel Battery Thermal Management System for Greater Lifetime Ratifying Current Quality and Safety Standard. *Battery Connections.* 6-10. Available: http://www.batteryconnections.net/summer2014issue/index.html

[5]   R. Kizilel, R. Sabbah, J. R. Selman, and S. Al-Hallaj, "An alternative cooling system to enhance the safety of Li-ion battery packs," *Journal of Power Sources,* vol. 194, pp. 1105-1112, Dec 2009.

[6] A. A. Pesaran, A. Vlahinos, and S. D. Burch, "Thermal Performance of EV and HEV Battery Modules and Packs," in *14th International Electric Vehicle Symposium*, Orlando, Florida, 1997.

[7] D. J. Bowen, M. Kreuter, B. Spring, L. Cofta-Woerpel, L. Linnan, D. Weiner*, et al.*, "How We Design Feasibility Studies," *American Journal of Preventive Medicine,* vol. 36, pp. 452-457, 5// 2009.

[8] B. Battke, T. S. Schmidt, D. Grosspietsch, and V. H. Hoffmann, "A review and probabilistic model of lifecycle costs of stationary batteries in multiple applications," *Renewable and Sustainable Energy Reviews,* vol. 25, pp. 240-250, 9// 2013.

[9] M. R. Khan, G. Mulder, and J. Van Mierlo, "An online framework for state of charge determination of battery systems using combined system identification approach," *Journal of Power Sources,* vol. 246, pp. 629-641, Jan 15 2014.

[10] D. U. Sauer and J. Garche, "Optimum battery design for applications in photovoltaic systems — theoretical considerations," *Journal of Power Sources,* vol. 95, pp. 130-134, 3/15/ 2001.

[11] M. R. Khan, J. V. Barreras, A. I. Stan, M. Swierczynski, S. J. Andreasen, and S. K. Kær, "Behavior Patterns, Origin of Problems and Solutions Regarding Hysteresis Phenomena in Complex Battery Systems," in *Hysteresis: Types, Applications and Behavior Patterns in Complex Systems*, J. C. Dias, Ed., First ed: Nova Science Publishers 2014, pp. 215-226.

[12] C. Clastres, T. T. Ha Pham, F. Wurtz, and S. Bacha, "Ancillary services and optimal household energy management with photovoltaic production," *Energy,* vol. 35, pp. 55-64, 1// 2010.

[13] G. Mulder, F. D. Ridder, and D. Six, "Electricity storage for grid-connected household dwellings with PV panels," *Solar Energy,* vol. 84, pp. 1284-1293, 2010.

[14] J. Kathan, "Increasing BIPV self-consumption through electrical storage –feasible demand-coverage and dimensioning the storage system," in *5th international renewable energy storage conference IRES*, Berlin, Germany, 2010.

[15] M. R. Khan, G. Mulder, J. Van Mierlo, and S. K. Kær, "The Integration and Control of Multifunctional Stationary PV-Battery Systems in Smart Distribution Grid," in *EU PVSEC The 28th European Photovoltaic Solar Energy Conference and Exhibition* Paris, France, 2013, pp. 3841 - 3851.

[16] K. Herter and S. Wayland, "Residential response to critical-peak pricing of electricity: California evidence," *Energy,* vol. 35, pp. 1561-1567, 4// 2010.

[17] G. Mulder and B. Claessens, "Insights in storage as a solution for local renewable electricity generation," *e & i Elektrotechnik und Informationstechnik,* vol. 128, pp. 116-121, 2011/04/01 2011.

[18] V. Wachenfeld, "Technical and economic aspects of storing electricity from PV to increase the share of self-consumption," in *5th international renewable energy storage conference(IRES)*, Berlin, Germany, 2010.

[19] M. Bost, "The impact of installation size, household size, storage dimensioning and consumer behaviour on the level of self-consumption, return on investment and feed-in tariff costs for private households," in *5th international renewable energy storage conference IRES*, Berlin, Germany, 2010.

[20] J. Tant, F. Geth, D. Six, P. Tant, and J. Driesen, "Multiobjective Battery Storage to Improve PV Integration in Residential Distribution Grids," *Sustainable Energy, IEEE Transactions on,* vol. 4, pp. 182-191, 2013.

[21] M. Jäger, J. Ogrzewalla, and T. Hülshorst, "Layout of a liquid-cooled highpower PHEV battery," presented at the Kraftwerk Batterie 2014 - Münster, Münster,Germany, 2014.

[22] P. Pichler, N. Hochgatterer, K. Grieshofer, and T. Hörmann, "Analysis of Cooling Requirements and Solutions for Low and High-Voltage Automotive Battery Packs," presented at the Kraftwerk Batterie 2014, Münster,Germany, 2014.

[23] K. M. Rasmussen, C. Madsen, and R. Poulsen, "Realkreditradgivning - Et studie af danskernes valg af realkreditlan og konverteringspraksis," ed. Boligøkonomisk Videncenter, 2011.

[24] *Monetary policy,* T. E. C. Bank.

[25] G. Mulder, D. Six, B. Claessens, T. Broes, N. Omar, and J. V. Mierlo, "The dimensioning of PV-battery systems depending on the incentive and selling price conditions," *Applied Energy,* vol. 111, pp. 1126-1135, 11// 2013.

MODELS FOR SOLAR HEATING OF BUILDINGS

Bernt.Lie@hit.no,[*] **Carlos Pfeiffer, Nils-Olav Skeie**
Telemark University College, Porsgrunn, Norway

Hans-Georg Beyer
University of Agder, Grimstad
Norway

ABSTRACT

The standard of living in a country is strongly correlated to the energy consumption, hence a considerable increase in the global energy use is expected. The effects of energy conversion on the climate, e.g. increased CO_2 level, is already observed. Thus it is imperative to base future energy conversion on resources that have negligible climate effects; solar energy is perhaps the most important of such resources.

The general structure of models for solar heating of buildings, with disturbances and relevant sensor technology is described. Simple models of the various parts of the system are developed, and the model is validated through simulation. Requirements for models for on-line control and optimization are discussed. It is noted that ventilation leads to an important energy loss if energy is not recovered by heat integration.

The main contribution in this paper is in putting together submodels from different fields and publications into a relatively complete model structure for control of a residential building. A second contribution is the discussion of key disturbances in the system.

Keywords: Solar heating, Building models, Model efficiency, Control.

INTRODUCTION

The observed increase of greenhouse gases in the atmosphere in tandem with an increase in global temperature, has led to a concern about the temperature development for the rest of the century with the possible consequence of increased ocean level, more violent weather, etc. To counter these predictions, there is an emphasis on reducing the use of fossil fuel and thus stop the increase in CO_2 level of the atmosphere.

Solar energy is a freely available alternative to fossil energy. One possible way to utilize solar energy is to capture the irradiance in a solar collector, and store the energy by heating up water in a storage tank. Such hot water can be used for heating, for showering, etc. The intermittent nature of irradiance is partially handled by such storage of energy, but it is usually necessary to combine solar energy with other energy forms such as electricity or fossil fuel to ensure sufficient availability of power. Because of fluctuations in energy prices (spot marked), it may be possible to take advantage of predictions of irradiance to reduce the energy bill: if we know that tomorrow will be sunny, we can reduce the heating by electricity or fossil fuel – or at least make sure that we use such co-energy forms when their cost is low.

The complexity level of models for solar heating of buildings range from simple models for energy planning over decades to detailed studies of the individual components in such systems. Of particular interest is the study of models suitable for on-line use. Such models should give sufficient information about the dynamics of the system, but should be simple enough to enable advanced on-line control and optimization. Even though detailed models may be necessary in detailed analysis of individual com-

---

[*]Corresponding author: Phone: +47 3557 5155 Fax: +47 3557 5401 E-mail:bernt.lie@hit.no

ponents, simpler unit models may suffice in a complete system model. This study thus aims at compiling models for the complete system of solar heating of buildings, with the long term goal of developing models that are sufficiently detailed yet sufficiently simple for on-line control and optimization.

For large scale solar collector plants, concentrated solar power systems are used [16], while for domestic heating, flat plate solar collectors or evacuated collectors are cheaper. Here, we focus on domestic heating. The fitting of an industry standard flat plate solar collector model to experimental data is discussed in [12], while [19] and [18] discuss more complex models for transient studies. Both [6] and [8] give useful background in solar radiation and design of such collectors. Models of storage tanks are discussed e.g. in [8], see also [9], [2], and [17]. Software libraries with detailed building models are available, but for control studies, the discussion in [13], [14] is particularly relevant. Disturbances are important in building models. Domestic hot water load profiles are treated in [11]; seasonal variations and optimization is important for design [7] and [3]. Variation in solar irradiance and ambient temperature are typically measured; see e.g. [8]. With respect to on-line use of models, [5] use a simple model of a building together with prediction of outdoor temperature and varying electric spot prices to study possibilities for cost savings through advanced control, with emphasis on efficient algorithms, while [10] and [15] discuss the use of Model Predictive Control of a system for thermal capturing of solar energy with auxiliary energy supply.

The paper is organized as follows. First, a description of the system with solar heating, storage tank and building is given, with some background information. Next, a simple mathematical model is presented. Then, operational conditions are given, and the model is verified through simulations. Finally, some conclusions are drawn.

SYSTEM DESCRIPTION
System elements

A system for mixed solar and electric (auxiliary) heating of a domestic building is depicted in Figure 1.

The reason for introducing heat exchangers to separate the fluids of the collector circuit and the heating
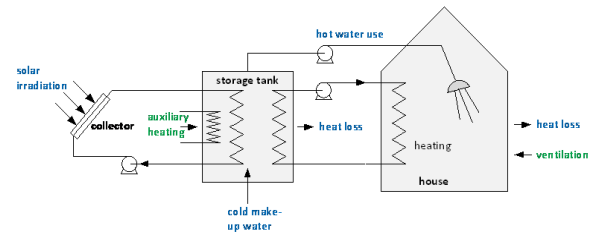
Figure 1: Blue font indicates disturbance variable, while green font indicates control variable. Heat losses are due to temperature differences to ambient temperatures. The storage tank is assumed to be instantly re-filled with cold make-up water, which may have a varying temperature.
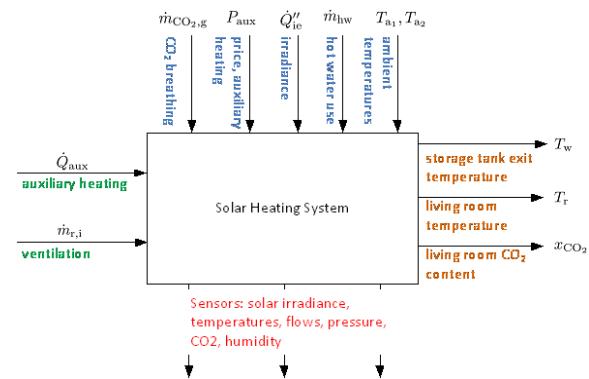
Figure 2: Functional description of the solar heating system with auxiliary heating input.

circuit from the utility hot water of the storage tank, is to allow for use of anti freeze and algae reducing components in these circuits.

Functional description

From a system theoretic point of view, it is useful to present the system as a block diagram with inputs and outputs — inputs and outputs will vary with time; Figure 2 illustrates this causal relationship with disturbances on the top of the block, control inputs (manipulating inputs) at the left side, while performance outputs (orange) are shown on the right side of the system block and available sensor signals (red) at the bottom of the block.

Sensors for buildings

A measurement system is needed to measure or estimate the sun irradiance and several parameters inside the house. In addition, the atmospheric pressure

should be measured.

Solar irradiance

The most common sensor device is the pyranometer. The pyranometer measures the solar irradiance flux density $(\mathrm{W/m^2})$ on a planar surface over a 180 degree field of view. The cost and size of pyranometers may be an disadvantage, other options for such a device can be solar cell, photo diode, photo transistor, or light dependent resistor (LDR).

The solar spectrum is dominated by the following wavelengths: ultraviolet $(300-400\,\mathrm{nm})$, visible $(400-700\,\mathrm{nm})$, and near infrared $(700-2500\,\mathrm{nm})$. A pyranometer is able to capture most of the solar spectrum, while the other sensor types capture the visible part.

The output from a solar cell is a voltage proportional to the light intensity. The output from a photo diode and photo transistor is a small variation in current; an electronic circuit is needed to convert this to an output voltage proportional to the light intensity. The output from an LDR is also current; an extra resistor suffices to have an output voltage proportional with the light intensity. These sensor devices are easy to integrate into a measurement system. A model must however be added to be able to estimate the sun irradiance from these sensor devices.

Other sensors

Other sensor devices needed for buildings include sensors for temperature, humidity, CO_2, flow, and pressure.

Several types of temperature sensor devices exist, both contact and non-contact types. Small, contact type sensor devices based on semiconductors are suitable for temperature measurement. The output is voltage, proportional to the temperature in the range $[-20\,\mathrm{^\circ C}, +60\,\mathrm{^\circ C}]$, and with an accuracy of ± 1 °C. These devices can be connected directly to a measurement system. If a higher accuracy is needed in a small sized sensor, then a resistance temperature detector (RTD) should be considered. The accuracy of these devices can be ± 0.2 °C. However, these sensor devices will require an additional electronic circuit for connection to a measurement system.

Humidity and CO_2 measures are needed to assess the quality of the air inside the house, depending on the ventilation system. These sensor devices can

also be of small size, however the cost may be a little higher then the other sensor devices in use. These sensor devices can normally be connected directly to a measurement system.

Flow of water can be measured by using a Coriolis mass flow meter or a magnetic flow meter. In principle, differential pressure sensors can also be used, but these require a relatively large pressure drop — which is unwanted. The most common flow meter is thus the magnetic flow meter, suitable for a wide range of pipe sizes. Flow meters normally use a digital connection with a standard protocol for connection to a measurement system. The cost of a Coriolis mass flow meter is higher than for a magnetic flow meter.

An absolute pressure sensor can be used to measure the atmospheric pressure. It may be useful to have pressure sensors inside the house as well; this will however require absolute pressure sensors of high accuracy.

Logging

The measurement system needs to include a preprocessing and a logging module, where the possibility of wireless connection between sensors and these modules is desirable. The preprocessing unit should take care of sensor errors and filtering (low pass filtering) of the measured values. The module may also include a check for outliers and early warnings. The logging module should be able to log the sensor value, the time stamp and the sensor status. The logging format can be either a set of text files such as a CSV format, or a database such as SQL or OPC.

On notation

In mathematical physics, *flux* is used to denote the flow of an *extensive* variable, while *flux density* is used to denote flux per unit area. In the field of *transport phenomena*, on the other hand, flux normally denotes the flow per unit area. Here, we will adopt the convention from transport phenomena.

It is relatively common to use a dot notation to indicate the flow of an extensive quantity, e.g. $\dot{m}$ implies mass flow where m is the extensive quantity *mass*; $\dot{Q}$ denotes heat flow where Q is the standard thermodynamics symbol for heat. Furthermore, we will use a prime notation do indicate per unit length, thus double prime denotes per unit area. It follows that $\dot{Q}''$
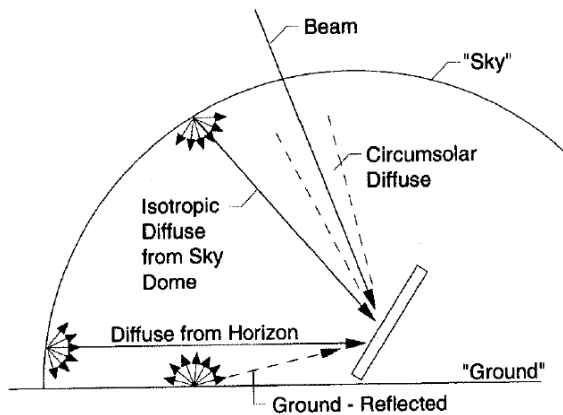
Figure 3: Beam, diffuse, and ground-reflected radiation on a tilted surface. From [6], fig. 1.16.1, p. 91.

denotes heat flux (e.g. unit W/m^2).

Fundamentals of radiation

Radiation emitted from a *black body* follows Planck's law with a *spectral heat flux* $\dot{Q}''_{b,\lambda}$ (monochromatic, at wavelength λ); integrated over all wavelengths the *extraterrestrial*[1] flux at the entrance to the atmosphere is $\dot{Q}''^{,\circ}_x = 1360\,W/m^2$ on average, varying slightly with the varying sun-earth distance. The atmosphere has a profound effect on solar radiation. The irradiance that hits a solar collector will thus consist of direct *beam* radiation, diffuse radiation from the "sky", but also of reflected radiation from the ground. In summary, the position on earth of the solar collector will reduce the local extraterrestrial irradiance from $\dot{Q}''^{,\circ}_x$, and because of the rotation of the earth, the irradiance will vary diurnally. Clouds, etc. will also reduce the available irradiance. Figure 3 illustrates how the various radiation components hit a tilted collector.

The glazing on solar collectors have a transmittance that varies with the wavelength (Planck's law): the radiation emitted from the sun with a surface temperature of $T_\sigma = 6000\,K$ will mainly pass through the glazing, while the radiation emitted from the collector surface at a temperature of perhaps $400\,K$ will have a shifted wavelength distribution and will be blocked. This effect is very important for the efficiency of solar collectors.

Figure 4: Atmospheric CO2 concentrations as observed at Mauna Loa from 1958 to 2008 (black dashed line) and projected under the 6 SRES marker and illustrative scenarios. Taken from www.ipcc-data.org/observ/ddc_co2.html.

Operational requirements

In general, the temperature comfort zone is around $20\,°C$, depending somewhat on humidity. In a working environment, $18–20\,°C$ seems to be common. During a summer day, higher temperatures are acceptable to avoid excessive cooling expenses. During night/sleep, lower temperatures are preferable.

Acceptable levels of CO_2 in populated rooms are[2] $x_{CO_2} \leq 600$ ppm. At levels in the range $x_{CO_2} \in [600, 1000]$ ppm, stiffness and odor will be observed.[3] Because breathing produces CO_2, ventilation is necessary; a typical requirement is to replace the air in a room 4 times per hour — the origin of this requirement is to satisfy the limit on x_{CO_2} level in the room. The CO_2 level of the atmosphere is currently[4] at a mole fraction of $x_{CO_2} = 401.3$ ppm $= 401.3 \times 10^{-6}$. Predictions of CO_2 levels are published by IPCC[5], and vary considerably depending on underlying assumptions and models, Figure 4. If the atmospheric CO_2 level increases as indicated in Figure 4, this may have a dramatic effect on the ventilation rate in the next few decades.

Hot water in storage tanks typically is required to have a temperature $\geq 55–60\,°C$ to avoid problems with Legionella bacteria, etc.; higher temperatures up to $90\,°C$ is relatively common. Such hot water

---

[1]Extraterrestrial implies just outside of the earth's atmosphere, with basically vacuum between the sun and the extraterrestrial surface.

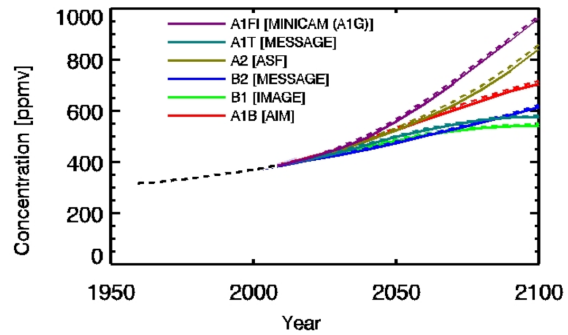[2]www.engineeringtoolbox.com/co2-comfort-level-d_1024.htmlwww.engineeringtoolbox.com/co2-comfort-level-d_1024.html

[3]ASHRAE and OSHAE standards are 1000 ppm.

[4]http://co2now.org/

[5]www.ipcc-data.org/observ/ddc_co2.html
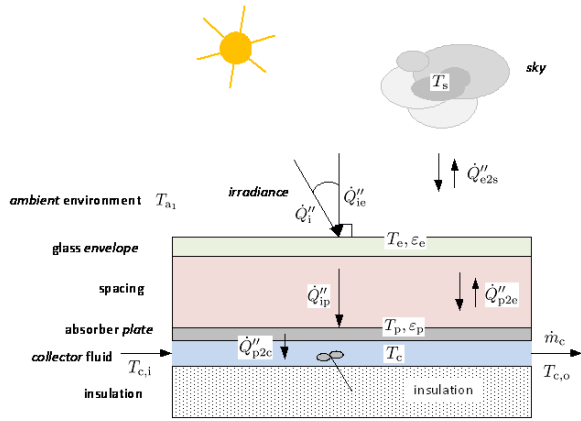
Figure 5: Sketch of collector system with some notation.

Figure 6: Sketch of storage tank.

is used for under floor heating (UFH), showering, etc. Mixing with cold water is common to reduce the temperature to usable levels. The liquid circulating in solar collectors may need anti-freeze components in Nordic countries, thus it is common to have a closed circuit for the solar collector fluid with heat exchange to the storage tank. Similarly, it is common to have closed circuits for UFH, with heat exchange to the storage tank.

MODEL DESCRIPTION
Collector system

The collector system with some notation is depicted in Figure 5. Models for the collector system ranges from full scale distributed CFD models to 1D and 0D models. As part of these models, it is necessary to describe the irradiance, and in particular how clouds, pollution, etc. reduces the theoretically available irradiance given by a *clearness index* $k_c < 1$. For design purposes, it is common to use a simplified model of the heat flow from the absorber plate to the collector fluid, $\dot{Q}_{p2c}$,

$$\dot{Q}_{p2c} = \eta_{e2c} A_e \dot{Q}''_{ie}$$

where A_e is the efficient surface of the glass envelope, $\dot{Q}''_{ie}$ is the solar irradiance entering perpendicular to the glass envelope, and η_{e2c} is the collector efficiency described as

$$\eta_{e2c} = \eta_{e2c,0} - a_1 \frac{\Delta T_c}{\dot{Q}''_{ie}} - a_2 \frac{\Delta T_c^2}{\dot{Q}''_{ie}},$$

with parameters defining the collector given by $\eta_{e2c,0}, a_1, a_2$. $\Delta T_c \triangleq \bar{T}_c - T_{a_1}$ is the difference be-

tween the temperature of the collector fluid and the ambient temperature; in Europe it is common to let $\bar{T}_c$ be the average of the influx and efflux temperatures of the collector fluid, $T_{c,i}$ and $T_{c,o}$. This model is combined with a steady state energy balance for the collector fluid, leading to

$$\dot{m}_c \hat{c}_{p,c} (T_{c,o} - T_{c,i}) = \dot{Q}_{p2c}$$

A problem which is sometimes not explicitly stated for this simple model is that the efficiency may go to $\pm\infty$ during the night ($\dot{Q}''_{ie} \to 0$); it is also possible that η_{e2c} becomes negative in some operating regimes. To make the model physically realistic, one may set $\dot{m}_c$ to zero when $\eta_{e2c} < 0$ or $\dot{Q}''_{ie} \to 0$.

Storage tank

A storage tank with heat exchangers is depicted in Figure 6. In reality, storage tanks are more or less stratified, i.e. the temperature varies from a low temperature at the bottom to a high temperature at the top, and it is thermodynamically beneficial to operate the system in such a way that water at different temperatures is not mixed: mixing leads to entropy increase. Stratification has been modeled in various ways, from fully distributed CFD models to 1D plug flow models to a sequence of 0D models.

Here we assume that the collector heat exchanger, the floor heat exchanger, and the water storage tank all are well mixed. The storage tank may have heat loss to the ambient temperature T_{a_2} of the room where the storage tank is placed.

An alternative could have been a main storage tank heated by the solar collector and used for under floor heating, followed by a secondary tank for hot water consumption operating at a higher temperature, with influx from the main storage tank and with auxiliary heating. However, here we use a 0d model of a single storage tank. Collector fluid in heat exchanger:

$$m_{cx}\hat{c}_{p,cx}\frac{dT_{cx}}{dt} = \dot{m}_c\hat{c}_{p,cx}\left(T_c - T_{cx}\right)$$
$$- UA|_{cx2w}\left(T_{cx} - T_w\right),$$

floor fluid in heat exchanger:

$$m_{fx}\hat{c}_{p,fx}\frac{dT_{fx}}{dt} = \dot{m}_f\hat{c}_{p,cfx}\left(T_f - T_{fx}\right) - UA|_{fx2w}\left(T_{fx} - T_w\right),$$

the storage tank itself:

$$m_w\hat{c}_{p,w}\frac{dT_w}{dt} = \dot{m}_{hw}\hat{c}_{p,w}\left(T_{w,i} - T_w\right)$$
$$+ UA|_{cx2w}\left(T_{cx} - T_w\right)$$
$$+ UA|_{fx2w}\left(T_{fx} - T_w\right)$$
$$- UA|_{w2a_2}\left(T_w - T_{a_2}\right) + \dot{Q}_{aux}.$$

Building model

We consider a building as proposed in [5], with slight modifications[6]. Their building is a single room with floor heating, with ventilation, and with occupants breathing CO_2 at a given rate. They have additional electric heating; here, this additional heating is added as auxiliary heat to the storage tank. Furthermore, they neglect the inertia of heating the floor; this inertia is added here. To this end, Figure 7 illustrates the parts of the domestic building. Assuming perfectly mixed volumes, we find for the floor fluid:

$$m_f\hat{c}_{p,f}\frac{dT_f}{dt} = \dot{m}_f\hat{c}_{p,f}\left(T_{fx} - T_f\right) - UA|_{f2m}\left(T_f - T_m\right),$$

floor mass:

$$m_m\hat{c}_{p,m}\frac{dT_m}{dt} = - UA|_{m2r}\left(T_m - T_r\right) + UA|_{f2m}\left(T_f - T_m\right)$$

air temperature:

$$m_r\hat{c}_{p,r}\frac{dT_r}{dt} = \dot{m}_{r,i}\hat{c}_{p,r}\left(T_{a_1} - T_r\right) + UA|_{m2r}\left(T_m - T_r\right)$$
$$- UA|_{r2a_1}\left(T_r - T_{a_1}\right),$$

---

[6]The notation is aligned with the notation in this document.
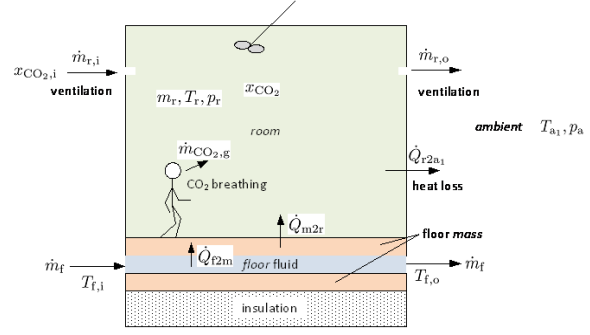
Figure 7: Sketch of domestic building; modification of description in [5].

air mass:

$$\frac{dm_r}{dt} = \dot{m}_{r,i} - k_r\left(\frac{m_r}{M_r}\frac{RT_r}{V_r} - p_a\right),$$

CO_2 fraction

$$\frac{dx_{CO_2}}{dt} = \frac{\dot{m}_{r,i}}{m_r}\left(x_{CO_2,i} - x_{CO_2}\right) + \frac{\dot{m}_{CO_2,g}}{m_r}.$$

Model parameters

The parameters of the model are given in Table 1.

SIMULATION OF MODEL
Disturbance description

The following disturbances are involved in the model, Figure 2.

Hot water load

In [8], it is suggested that the daily consumption of hot water is 30–60 liters per person. A coarse approximation of the domestic hot water consumption (DHWC) distribution of [4] is given in Table 2.
If measurements or better predictions are not available, this distribution can be repeated perpetually in simulations.

Ambient conditions

Ambient temperature T_{a_1} (out-door temperature) as measured in our case study, [1], is shown in Figure 8. A typical value for the ambient temperature for the hot water storage tank might be $T_{a_2} = 5\,°C$.

Table 1: Parameters for solar heating system.

Parameter	Value	Unit
a_1	3.83×10^{-3}	$\frac{\text{kW}}{\text{K}\,\text{m}^2}$
a_2	6.5×10^{-6}	$\frac{\text{kW}}{\text{K}^2\,\text{m}^2}$
A_e	$3 \times 1.5 \cdot N_{\text{pers}}$	m^2
A_r	25	m^2
A_{rx}	$4 \cdot h_r \sqrt{A_r} + A_r$	m^2
$\hat{c}_{pf}$	3.5	$\frac{\text{kJ}}{\text{kg}\,\text{K}}$
$\hat{c}_{pw}$	4.19	$\frac{\text{kJ}}{\text{kg}\,\text{K}}$
$\hat{c}_{pm}$	0.63	$\frac{\text{kJ}}{\text{kg}}$
$\hat{c}_{pr}$	1.005	$\frac{\text{kJ}}{\text{kg}\,\text{K}}$
h_r	2.5	m
k_r	$100 \cdot \frac{1}{1.01 \times 10^5}$	$\frac{\text{kg}}{\text{s}\,\text{Pa}}$
ℓ_{cx}	30	m
ℓ_f	100	m
ℓ_{fx}	30	m
m_{cx}	$\rho_w \cdot \pi r_p^2 \cdot \ell_{cx}$	kg
m_f	$\rho_w \cdot \pi r_p^2 \cdot \ell_f$	kg
m_{fx}	$\rho_w \cdot \pi r_p^2 \cdot \ell_{fx}$	kg
m_m	3000	kg
m_w	$60 \cdot N_{\text{pers}}$	kg
M_r	29	$\frac{\text{kg}}{\text{kmol}}$
N_{pers}	2	–
r_p	$\frac{13}{2} \times 10^{-3}$	m
R	8.31×10^3	$\frac{\text{J}}{\text{kmol}\,\text{K}}$
U_p	0.25	$\frac{\text{kW}}{\text{m}^2\,\text{K}}$
$UA|_{cx2w}$	$U_p \cdot 2\pi r_p \cdot \ell_{cx}$	$\frac{\text{kW}}{\text{K}}$
$UA|_{f2m}$	$U_p \cdot 2\pi r_p \cdot \ell_f$	$\frac{\text{kW}}{\text{K}}$
$UA|_{fx2w}$	$U_p \cdot 2\pi r_p \cdot \ell_{fx}$	$\frac{\text{kW}}{\text{K}}$
$UA|_{m2r}$	$10 \times 10^{-3} \cdot A_r$	$\frac{\text{kW}}{\text{K}}$
$UA|_{r2a_1}$	$0.4 \times 10^{-3} \cdot A_{rx}$	$\frac{\text{kW}}{\text{K}}$
$UA|_{w2a_2}$	$0.5 \times 10^{-3} \cdot 6 \cdot \left(\sqrt[3]{\frac{m_w}{\rho_w}} \right)^2$	$\frac{\text{kW}}{\text{K}}$
V_r	$25 \cdot 2.5$	m^3
$\eta_{e2c,0}$	$0.719, [0.75, 0.85]$	–
ρ_f	1060	kg/m^3
ρ_w	10^3	kg/m^3

Table 2: Typical DHWC (Domestic Hot Water Consumption) distribution over one day, in %.

Hour	DHWC	Hour	DHWC	Hour	DHWC
00–01	1.4	08–09	11.2	16–17	5.1
01–02	0.70	09–10	10.3	17–18	7.9
02–03	0.23	10–11	4.7	18–19	6.5
03–04	0.47	11–12	3.7	19–20	5.1
04–05	0.47	12–13	2.8	20–21	2.8
05–06	0.23	13–14	2.3	21–22	3.3
06–07	6.5	14–15	3.3	22–23	3.3
07–08	10.7	15–16	3.7	23–24	3.3
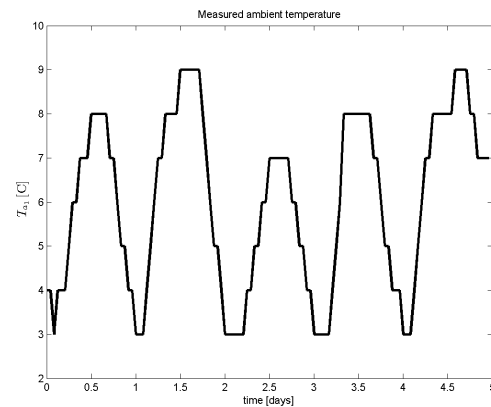
Figure 8: Measured ambient temperature T_{a_1} during five days.
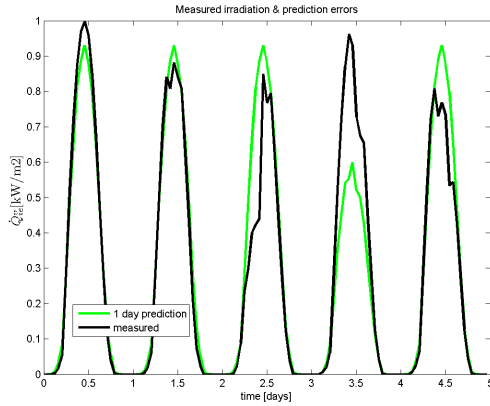
Figure 9: Measured irradiance $\dot{Q}''_{ie}$ over five days with one-day-ahead prediction.

Solar irradiance

Measured irradiance $\dot{Q}''_{ie}$ together with prediction error, [1], is displayed in Figure 9.

CO₂ production

In the literature, a typical breathing rate is $1\,\mathrm{kg/d}$ per person.

Operating conditions

Nominal operating conditions of the system are given in Table 3.

Implementation details

The differential equations are solved using MAT-LAB, with the `ode15s` ODE solver. The code is divided into a main script file that imports data, runs the simulations and presents results in figures, a script file defining model parameters and operating conditions, and a function file that describes the model/differential equations. Ambient temperature ($T_{a,1}$) and solar irradiance ($\dot{Q}''_{ie}$) recorded over a period of 30 days in Kristiansand, Southern Norway, are imported from a `.mat` file. The thermostat controller requires an initial value for its state.

Model verification

Using the disturbances from the previous section, the system temperatures for the first 5 days of simulation are depicted in Figure 10. Heat flows in the system are depicted in Figure 11. Collector effi-

Table 3: Nominal operating conditions of the solar heat collector system.

Quantity	Value	Unit
$\dot{Q}_{\mathrm{aux}}$	0	kW
$\dot{m}_{\mathrm{r,i}}$	$\frac{4 \cdot m_\mathrm{r}(0)}{3600}$	kg / s
T_{a_1}	10	°C
T_{a_2}	5	°C
$T_{\mathrm{w,i}}$	5	°C
$\dot{m}_{\mathrm{hw}}$	$\frac{50}{24 \cdot 3600} N_{\mathrm{pers}}$	kg / s
$\dot{m}_{\mathrm{c}}$	$\frac{2 \times 10^3}{3600}$	kg / s
$\dot{m}_{\mathrm{f}}$	$\frac{150}{3600}$	kg / s
$\dot{Q}''_{\mathrm{ie}}$	0.5	kW / m²
$\dot{m}_{\mathrm{CO_2,g}}$	$\frac{1}{24 \cdot 3600} N_{\mathrm{pers}}$	kg / s
$x_{\mathrm{CO_2,i}}$	400×10^{-6}	–
p_a	1.01×10^5	Pa
P_{aux}	1	$ / kWh
$T_{\mathrm{cx}}(0)$	44.326	°C
$T_{\mathrm{fx}}(0)$	41.508	°C
$T_{\mathrm{w}}(0)$	48.78	°C
$T_{\mathrm{f}}(0)$	26.3	°C
$T_{\mathrm{m}}(0)$	24.15	°C
$T_{\mathrm{r}}(0)$	18.563	°C
$m_{\mathrm{r}}(0)$	75.584	kg
$x_{\mathrm{CO_2}}(0)$	660.42×10^{-6}	–
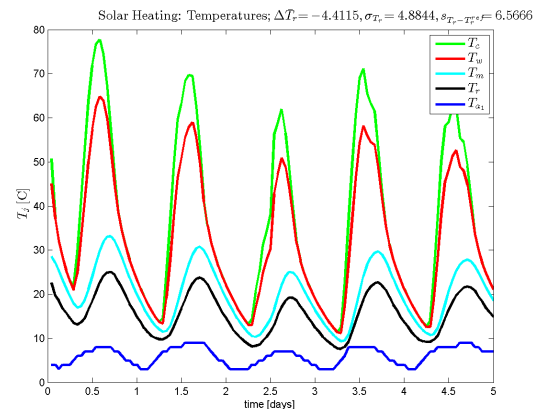
Figure 10: Temperatures at various positions in the system with realistic disturbance inputs.
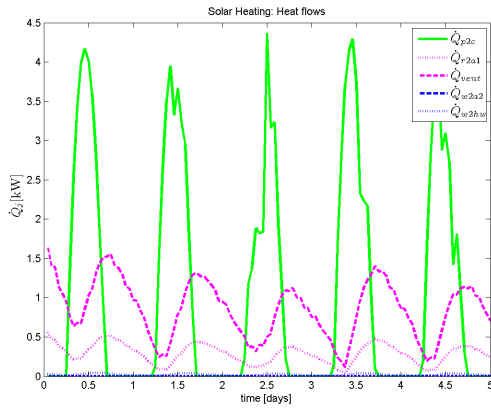
Figure 11: Heat flows at various positions in the system with realistic disturbance inputs.

Figure 12: Collector efficiency in the system with realistic disturbance inputs.

Figure 13: Temperatures at various positions in the system using thermostat controller.
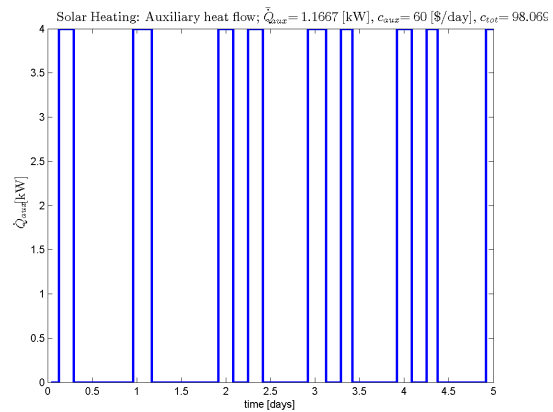
Figure 14: Auxiliary heat input to storage tank using thermostat controller.

Figure 15: Heat flows at various positions in the system using thermostat controller.

ciency in the system is depicted in Figure 12. The results of Figure 12 confirm the importance of modifying the collector model to avoid negative efficiency.

In a second simulation, a *thermostat controller* is used with room temperature setpoint of $T_r^{\mathrm{ref}} = 20\,^\circ\mathrm{C}$. The temperatures for the first 5 days of simulation (simulation time $\propto 10\,\mathrm{s}$) are depicted in Figure 13. The auxiliary heat flow is depicted in Figure 14. Heat flows in the system are depicted in Figure 15.

Discussion

The simulations, Figures 10–15, give results that seem to be reasonable from a physical perspective: Temperature levels decrease from that of the collector fluid to that of the ambient temperature (Figures

10, 13), the heat flows seem reasonable (Figures 11, 15), the collector efficiency is as expected (Figure 12), and the auxiliary heat input appears to come into use when the solar irradiance is reduced (Figure 14). These results verify that the model has a sound physical structure. In order to *validate* the model, it would be necessary to compare the model with experimental data, and possibly to tune the model and possibly change its complexity.

The model that has been used for the collector is relatively simple. The reason for this is that only the total forecast $\dot{Q}''_{ie}$ was available, and not beam irradiance, etc. (Figure 3). Also, the model for the water storage system is simple — too simple to be realistic, which is seen in that the temperature is lower than one would observe in reality. A model that better captures the stratification would improve the overall model; this could perhaps be achieved by using a 2–3 compartment description of the storage tank. Also, the model for the under floor heating (UFH) is somewhat simple, and should be improved. Other heating facilities should perhaps be introduced, e.g. a radiator. The model for the room/building itself is somewhat simple; it would be of interest to consider a building with more than one room, and somewhat more realistic heat transport through walls, etc. Finally, the description of the ventilation system is too simple: modern buildings normally have some sort of heat integration/heat recovery in the ventilation system. In the simulations here, no heat integration is used for the ventilation, and the result is that the heat loss through ventilation (e.g. Figure 15) is the dominating heat loss. This heat loss through ventilation is the reason for the relatively large amplitudes in the temperatures (e.g. Figure 13 except ambient temperature); heat integration would dampen these variations. Also, the IPCC forecasts of future atmospheric CO_2 concentrations indicates the importance of heat integration in the ventilation system.

The heat transfer coefficients that have been used are constants. In reality, heat transfer will vary with flow rates of liquid, etc. Correlations for heat transfer coefficients would also improve the model.

Finally, it is observed that although MATLAB is good for testing prototypes of models, it would be more efficient to build up a library of unit operations which is possible in e.g. Modelica: this would make it much easier to change the topology of the system. Building libraries exist for Modelica, but in this study the emphasis has been on testing models that are suitable for control studies.

CONCLUSIONS

This paper discusses the structure of models for solar heating of buildings applied for on-line control and optimization, with varying levels of detail. A simple model is developed and verified through simulations without and with auxiliary heating of the storage tank. Of particular interest is that the heat loss through ventilation is c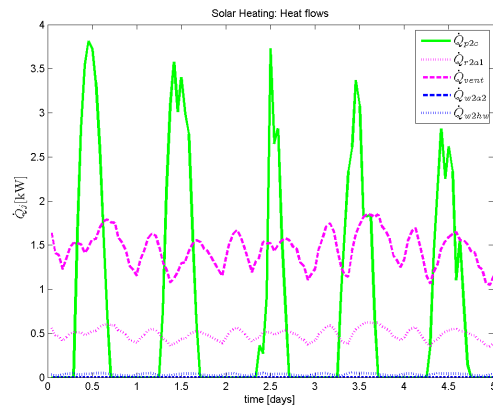onsiderable; this also leads to a relatively large variation in room temperature. The main contribution is in putting together submodels from different fields and publications into a relatively complete model structure for control of a residential building. A second contribution is the discussion of key disturbances in the system.

Future work will consider (i) the detail level of solar collector models, (ii) the detail level of storage tank models, (iii) the detail level of buildings with improved description of under floor heating, possibly with more rooms, and with energy recovery of the ventilated air. Such more complex models will benefit from the use of modern modeling languages, e.g. Modelica. It is of interest to validate the models further against measurements. The main application for the complete system model will be control and on-line optimization.

REFERENCES

[1] Arachchige, D.D.K. (2014). *An Approach to Day Ahead Forecasting of Solar Irradiance with an Application to Energy Gain in Solar Thermal Collectors*. M.Sc. thesis, University of Agder, Faculty of Engineering and Science, Grimstad.

[2] Bayón, R., and Rojas, E. (2013). "Simulation of thermocline storage for solar thermal power plants: From dimensionless results to prototypes and real-size tanks". *International Journal of Heat and Mass Transfer*, **Vol. 60**, pp. 713–721. http://dx.doi.org/10.1016/j.ijheatmasstransfer.2013.01.047

[3] Cheng Hin, J.N., and Zmeureanu, R. (2014). "Optimization of a residential solar combisystem for minimum life cycle cost, energy use and exergy destroyed". Solar Energy, **Vol. 100**, pp. 102–113.

[4] Defra (2008). *Measurement of Domestic Hot Water Consumption in Dwellings*. Department for Environment, Food and Rural Affairs (Defra), UK.

[5] de Oliveira , V., Jäschke, J., and Skogestad, S. (2013). "Dynamic online optimization of a house heating system in a fluctuating energy price scenario". Preprints of the 10th IFAC International Symposium on Dynamics and Control of Process Systems, The International Federation of Automatic Control, December 18-20, 2013, Mumbai, India, pp. 463—468.

[6] Duffie, J.A., and Beckman, W.A. (2013). *Solar Engineering of Thermal Processes, 4th edition.* John Wiley & Sons, Hoboken, NJ.

[7] Durão, B., Joyce, A., Farinha Mendes, J. (2014). "Optimization of a seasonal storage solar system using Genetic Algorithms". Solar Energy, **Vol. 101**, pp. 160–166.

[8] Eicker, U. (2014). *Energy Efficient Buildings with Solar and Geothermal Resources*. John Wiley & Sons Ltd., Chichester, UK. ISBN 9781118352243.

[9] Han, Y.M., Wang, R.Z., and Dai, Y.J. (2009). "Thermal stratification within the water tank". *Renewable and Sustainable Energy Reviews*, **Vol. 13**, pp. 1014–1026. doi:10.1016/j.rser.2008.03.001

[10] Holth, E. (2009). Model Predictive Control of mixed solar and electric heating. MSc thesis, NTNU, Norway.

[11] Jordan, U., and Vajen, K. (2000). "Influence of the DHW load profile on the fractional energy savings: a case study of a solar combisystem with trnsys simulations". Solar Energy, **Vol. 69**, Nos. 1–6, pp. 197-208.

[12] Kratzenberg, M.G., Beyer, H.G., and Colle, S. (2006). "Uncertainty calculation applied to different regression methods in the quasi-dynamic collector test". Solar Energy, **Vol. 80**, pp. 1453–1462

[13] Perera., D.W.U., Pfeiffer, C., and Skeie, N.-O. (2014). "Modelling the heat dynamics of a residential building unit: Application to Norwegian buildings". *Modeling, Identication and Control*, **Vol. 35**, No. 1, pp. 43–57, ISSN 1890-1328. doi:10.4173/mic.2014.1.4.

[14] Perera., D.W.U., Pfeiffer, C., and Skeie, N.-O. (2014). "Modeling and simulation of multi zone buildings for better control". *Proceedings, SIMS 2014, Aalborg, Denmark, October 21–22, 2014*.

[15] Pichler, M.F., Lerch, W., Heinz, A., Goertler, G., Schranzhofer, H., Rieberer, R. (2014). "A novel linear predictive control approach for auxiliary energy supply to a solar thermal combistorage". Solar Energy, **Vol. 101**, pp. 203–219.

[16] Powell , K.M., and Edgar, T.F. (2012). "Modeling and control of a solar thermal power plant with thermal energy storage". Chemical Engineering Science, **Vol. 71**, pp. 138–145.

[17] Powell , K.M., and Edgar, T.F. (2013). "An adaptive-grid model for dynamic simulation of thermocline thermal energy storage systems". *Energy Conversion and Management,* **Vol. 76**, pp. 865–873. http://dx.doi.org/10.1016/j.enconman.2013.08.043.

[18] Saleh, A.M. (2012). *Modeling of Flat-Plate Solar Collector Operation in Transient States*. M.Sc. thesis, Purdue University, Indiana.

[19] Zima, W., and Dziewa, P. (2010). "Mathematical modelling of heat transfer in liquid flat-plate solar collector tubes". Archives of Thermodynamics, **Vol. 31**, No. 2, pp. 45—62. doi: 10.2478/v10173-010-0008-7.

Implementation of Exhaust Gas Recirculation for Double Stage Waste Heat Recovery System on Large Container Vessel

Morten Andreasen[a,*], Matthieu Marissal[a,b,*], Kim Sørensen[a], Thomas Condra[a]

a Department of Energy Technology, Pontoppidanstræde 101, DK-9220 Aalborg, Denmark
b EPF Ecole d'Ingenieurs, 3 bis rue Lakanal, 92330 Sceaux, France

Abstract

Concerned to push ships to have a lower impact on the environment, the International Maritime Organization are implementing stricter regulation of NO_x and SO_x emissions, called Tier III, within emission control areas (ECAs). Waste Heat Recovery Systems (WHRS) on container ships consist of recovering some of the waste heat from the exhaust gas. This heat is converted into electrical energy used on-board instead of using auxiliary engines. Exhaust Gas Recirculation (EGR) systems, are recirculating a part of the exhaust gas through the engine combustion chamber to reduce emissions. WHRS combined with EGR is a potential way to improve system efficiency while reducing emissions. This paper investigates the feasibility of combining the two systems. EGR dilutes the fuel, lowering the combustion temperature and thereby the formation of NO_x, to reach Tier III limitation. A double stage WHRS is set up to reach the highest possible combination of pressure and temperature, and adapted to Tier III by introducing two alternative superheaters. The system design is optimized and found capable of producing from 400 to 1900 kW, with a weighted average power of 958 kW. The consumption profile is found to significantly impact the weighted average power, while the operation distribution between Tier III and Tier II (outside ECAs) has a much smaller influence. Furthermore, it is found that the low pressure should be kept near minimum, while the optimum high pressure increases from 7 to 12 bar with the load. By increasing the efficiency of the overall system, the CO_2 emissions can be reduced. The addition of a third cycle, used only in Tier III, is investigated. While increasing the total heat exchanger areas by approximately 40%, the cycle is found to increase the power production in Tier III operation by an average of 15%, and up to 50% at full load.

Keywords: Waste Heat Recovery, Exhaust Gas Recirculation, Tier III, Container Vessel, Steam Cycles, WHRS Model

1. IMO Regulations

Container ships are the most commonly used mean of intercontinental cargo freight. Due to the vast size of these ships, the amount of energy required for transport is similarly large. Increased focus on environmental issues, and the will to be part of a sustainable change have pushed the International Maritime Organization (IMO) to put regulations in place to lower the environmental impact of large container vessels.

*Corresponding author
**Project Supervisor
Email addresses: `mortenlandreasen@gmail.com` (Morten Andreasen), `matthieu.marissal@gmail.com` (Matthieu Marissal)

1.1. Challenges of ship transportation

Ship freight traffic has increased significantly for the last decades, corresponding to the demand and will likely continue to grow since the demand for transport capacities has increased by about 7% every year for the last 20 years [1]. Three main issues have pushed owners and designers to improve the ship performances:

- Transport costs: Even if a larger ship will consume more energy, increasing the capacity will reduce the specific costs ($/mile/ton) .

- Fuel cost increase: The increase of fuel prices and the large consumption of large container ships have made it important to optimize en-

ergy savings (i.e. minimizing the fuel consumption).

- Environmental impacts: The large consumption of those ships implies significant emissions of CO_x, SO_x and NO_x. International conventions and regulations make it mandatory for ships to reach certain levels of emission before they are allowed to travel. Some countries have limited the access to their national seas to ships complying with the strictest regulations.

1.2. CO_2 concern

CO_2 emissions have become a major focus point for most transportation related companies, since they have a large impact on global warming. To address it the IMO has established an index called EEDI that evaluates the amount of CO_2 emitted as function of the capacity and age of the ship [2]. It is required for any ship to comply with these limitation to sail. A Waste Heat Recovery System is often used to improve the overall efficiency of a ship. By generating on-board electricity, it reduces the fuel consumptions of the auxiliary engines, thereby reducing CO_2 emissions and reducing fuel costs [3].

1.3. NO_x and SO_x concern

NO_x and SO_x are not greenhouse gases. However, they are of importance since they have a large impact on the surrounding environment by leading to acid rain. To prevent such emissions, the IMO has set a number of emission limits with the MARPOL convention. Two of these are the Tier II and Tier III regulations. The condition Tier III is applied in ECAs, which are geographical areas located along the coasts of signatory countries. Soon the North Sea, North American coast, Mediterranean sea and part of Japan should be considered as ECAs. Going from Tier II to Tier III conditions implies a drastic reduction of NO_x and SO_x. NO_x emission limits are shown in Figure 1.[4][5]

While the SO_x concern can be addressed by the use of a higher quality fuel containing less Sulfur, or by the use of a scrubbing system, the NO_x emission reduction of around 70% will require the use of an additional system. Exhaust Gas Recirculation (EGR) can be used to lower the NO_x emissions by recirculating a part of the exhaust gas back into the combustion chamber.
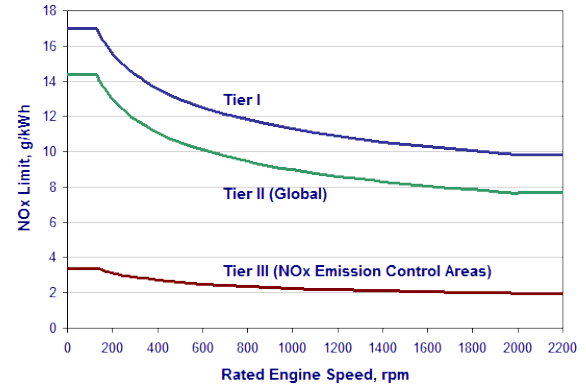
Figure 1: NO_x emissions limitation from MARPOL convention.[4]

2. Fuel and Combustion Model

The WHRS will recover energy from the exhaust gas. Knowing its composition is therefore required to evaluate its thermodynamic properties. Moreover, they are also required for they can demonstrate the impact of EGR and other parameters on the NO_x emissions. The combustion is modeled by using Cantera [6] software linked with MATLAB [7]. The exhaust gas properties are then determined by using REFPROP [8].

2.1. Fuel Model

The ships considered use Heavy Fuel Oil (HFO). According to the norm ISO 8217, HFO is: *A residual oil from distillation and/or the cracking system of natural gas processing and serves as fuel for marine diesel engines*[9]. The HFO category includes both finished products and the primary refinery streams from which they are blended. It is highly viscous and may contain some unwanted residuals. The chemical composition is therefore not exactly known and might differ from fuel to fuel.

HFO composition is complex to determine. However, using a statistical method [10], the mass fraction of chemical constituents can be calculated as follow:

$$\gamma_C = 0.64241 + 0.00505 \cdot LHV \qquad (1)$$
$$\gamma_H = -0.22426 + 0.00826 \cdot LHV \qquad (2)$$
$$\gamma_O = 0.27603 - 0.00628 \cdot LHV \qquad (3)$$
$$\gamma_S = 0.30582 - 0.00702 \cdot LHV \qquad (4)$$

Nitrogen, due to the low concentration in the fuel (lower than 0.34%) is neglected. Considering an

2

Lower Heating Value (LHV) of 42 $\frac{MJ}{kg}$ [3], the mass fraction of each components of the fuel can be determined. Relating the mass fraction to the number of atoms, the chemical composition of the HFO can be written as $C_1H_{1.54}O_{0.02}S_{0.01}$. It has to be noted here that the composition is evaluated per atom of carbon. The corresponding molar weight of fuel will be 14.18 kg/kmol.

The fuel will be mixed with air and then burned. The main stoichiometric chemical equation is shown in Equation 5 [11].

$$C_1H_{1.54}O_{0.02}S_{0.01} + 1.395 \cdot (O_2 + 3.76N_2) \rightarrow$$
$$CO_2 + 0.77 \cdot H_2O + 5.2452 \cdot N_2 + 0.01 \cdot SO_2 \tag{5}$$
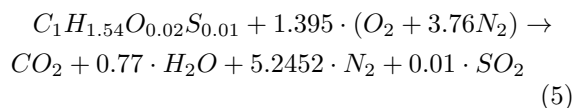
2.2. Combustion Model

The combustion is to be modeled in order to find accurate thermodynamic properties. Since no mechanism was found containing the exact fuel composition calculated, a combination of smaller known fuels is used to obtain a similar combustion. The selected mechanism would have to contain all of these smaller fuels. Additionally sulfur radicals are needed to evaluate the impact of various parameters on SO_x emissions. The Glassman mechanism [12] was found to comply with these two conditions. It was assumed that the HFO could be modeled with a combination of smaller fuels by fitting the LHV, the carbon/hydrogen and carbon/oxygen ratio. Moreover, it was assumed that the sulfur could be added as a fourth component.

Table 1 shows the fuel combination elected for the model.

Fuel	LHV	C/H	C/O	Mole Fraction
Methanol	19.92	1/4	1/1	0.2078
Acetylene	48.28	1/1	-	0.7489
Propane	46.34	3/8	-	0.0433
Average/Total	42.0	1/1.54	1/0.02	1

Table 1: Modeled fuel composition.

The resulting specific heat at constant pressure is found to be 1.68 kJ/kg·K, which is consistent with data on fuel properties for heavy diesel in gaseous phase (1.7 kJ/kg·K) [13].

The amount of excess air used during the combustion will depend on the load. Due to the occurrence of cross-over flow when the exhaust gas is pushed out of the combustion chamber, some of the air does not participate in the combustion. From MAN data

in Tier II conditions, an average excess air ratio of 3.75 has been chosen. The combustion was modeled at equilibrium conditions, considering a pressure of 140 bar and a temperature of 800 K. The exhaust gas composition found is shown in Table 2. This is without considering dissociation.

Molecule	Mass Fraction
Ar	0.0097
CO_2	0.0403
N_2	0.7700
O_2	0.1500
H_2O	0.0298
SO_2	0.0002
Total	1.0000

Table 2: Exhaust gas composition computed with Cantera.

3. EGR and NO_x emission

3.1. Exhaust Gas Recirculation

EGR consists in recycling a part of the exhaust back to the combustion chamber to lower the amount of NO_x emissions. The EGR is quantified by a percentage which can differ from source to source. Here, the EGR rate will correspond to the amount of exhaust recirculated over the total intake of the combustion chamber (i.e exhaust gas, air, fuel). The EGR rate is shown in Equation 6.

$$EGR(\%) = \left(\frac{\dot{m}_{EGR}}{\dot{m}_i}\right) \cdot 100 \tag{6}$$

The amount of EGR has been assumed as optimized and given by MAN Diesel&Turbo and is not constant, with lower percentage of exhaust being recirculated for higher load as shown in Figure 2.

3.2. NO_x kinetic and emissions

The main mechanisms of NO formation have been studied extensively in the literature. It is commonly accepted that in combustion of fuel involving Nitrogen, the *Zeldovich* mechanism shown in Equation 7 and 8 extended with the *Lavoie et al.* mechanism shown in Equation 9 can be used to describe NO formation [11].

$$O + N_2 \rightleftharpoons NO + N \tag{7}$$
$$N + O_2 \rightleftharpoons NO + O \tag{8}$$
$$N + OH \rightleftharpoons NO + H \tag{9}$$

3
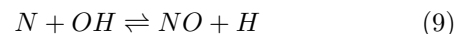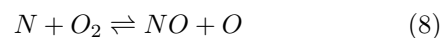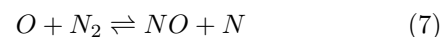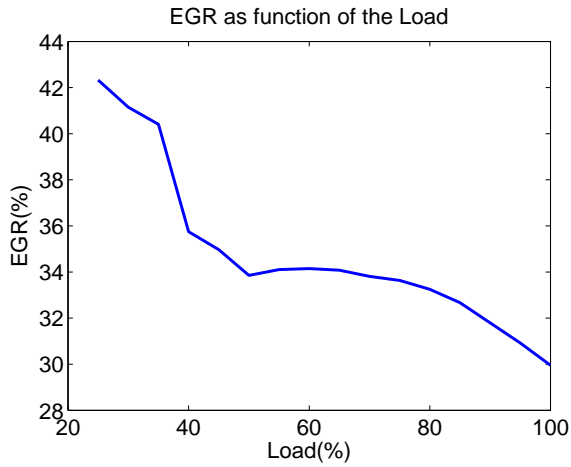
Figure 2: Recirculation percentage as function of the load.

Figure 3: NO formation rate for various adiabatic flame temperatures and excess air ratio.

By using these equations and the related kinetics of NO formation, Equation 10 can be found. Calculations are described more extensively in [13].

$$\frac{d\left[NO\right]}{dt} = \frac{6 \cdot 10^{16}}{T^{0.5}} exp\left(\frac{-69090}{T}\right)[O_2]_{eq}^{0.5}[N_2]_{eq} \tag{10}$$

From Equation 10 it can clearly be seen that the NO kinetic will be influenced by the amount of Oxygen and Nitrogen present during the combustion. However, it can also be seen that temperature will have a major impact on the NO formation, with lower temperature leading to slower NO production.

The influence of the temperature is illustrated in Figure 3, where the NO formation kinetic is shown as a function of the equivalence ratio and the adiabatic flame temperature. Lowering the equivalence ratio increases the quantity of air in the chamber, and thereby allows lower flame temperatures.

Recirculating exhaust gas will both increase the mass in the combustion chamber, and increase the c_p value of the mixture, thereby lowering the temperature. This will lead to lower NO_x emissions as illustrated in Figure 4, where the NO mole fraction is shown as function of the rate of EGR. It will also have an impact on NO_2 formation, but with the concentration being around 10 times lower than the NO, it has not been taken into account. Figure 4 shows that EGR has the capacity of lowering the NO emissions by a factor of 10, by going from 10 to 50 %.

Figure 4: NO mole fraction as function of the EGR(%).

4. Double-Stage Waste Heat Recovery

The Waste Heat Recovery System drains energy from the exhaust gas. Two steam cycles are preheated using the jacket water and scavenge air. The cycles are then evaporated and superheated in the stack before being sent through a steam turbine to generate electricity.

The process in demonstrated in a T-s diagram in Figure 5, where T is the temperature and s is the specific entropy.

4.1. Exergy

Exergy is a measure of potential work in a substance. This can principally include any kind of energy transfer. In thermodynamics, exergy can be

4
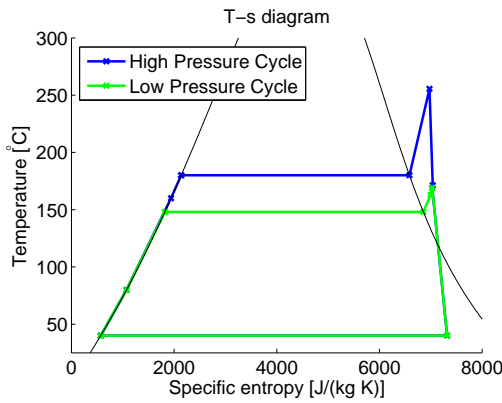
Figure 5: T-s diagram.

interpreted as a unit of steam quality. Equation 11
shows the expression used for the specific exergy ψ,
with the velocity term left out, since this becomes
negligible [14]. h and s are specific enthalpy and
specific entropy respectively, while T is the temperature. Subscript 0 denotes a reference state.

$$\psi = (h - h_0) - T_0(s - s_0) \qquad (11)$$

Figure 6 shows the development of specific exergy with temperature and pressure. It can be seen
that while increasing pressure does increase specific
exergy, this effect diminishes quickly. Specific exergy also increases with temperature, for which reason a fluid should be heated as high as possible in
a steam cycle. Consequently, a high temperature
heat source, such as the EGR string, should be used
as the final source of superheating.

Figure 6: Developement of Specific exergy with temperature.

4.2. Heat Sources

Figure 7 shows the available heat sources for the
WHRS during normal (Tier II) operation.
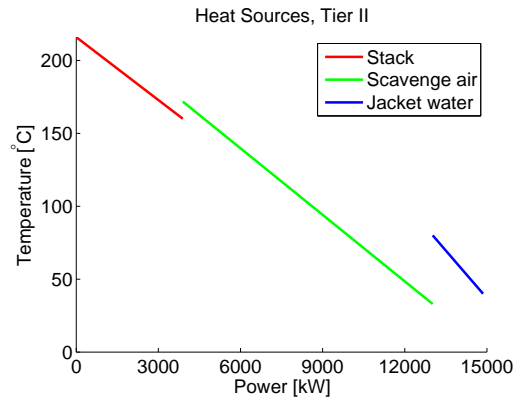
Figure 7: Tier II heat sources.

Notably, while the scavenge air represents the
largest quantity of energy available, the temperature of the stack is higher, making it more useful
and more worth extracting.

Figure 8 shows the available heat sources for the
WHRS during operation inside ECA's (Tier III) operation.
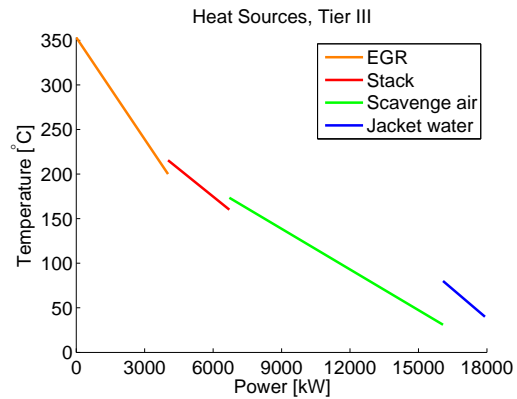
Figure 8: Tier III heat sources.

Not only does the recirculated exhaust gas represent a larger amount of available energy than the
stack, it is also of a higher temperature. Therefore, the EGR string should be the final sources of
heat used before the cycle fluid reaches the steam
turbine. The complete used system is shown in
Figure 9.

5
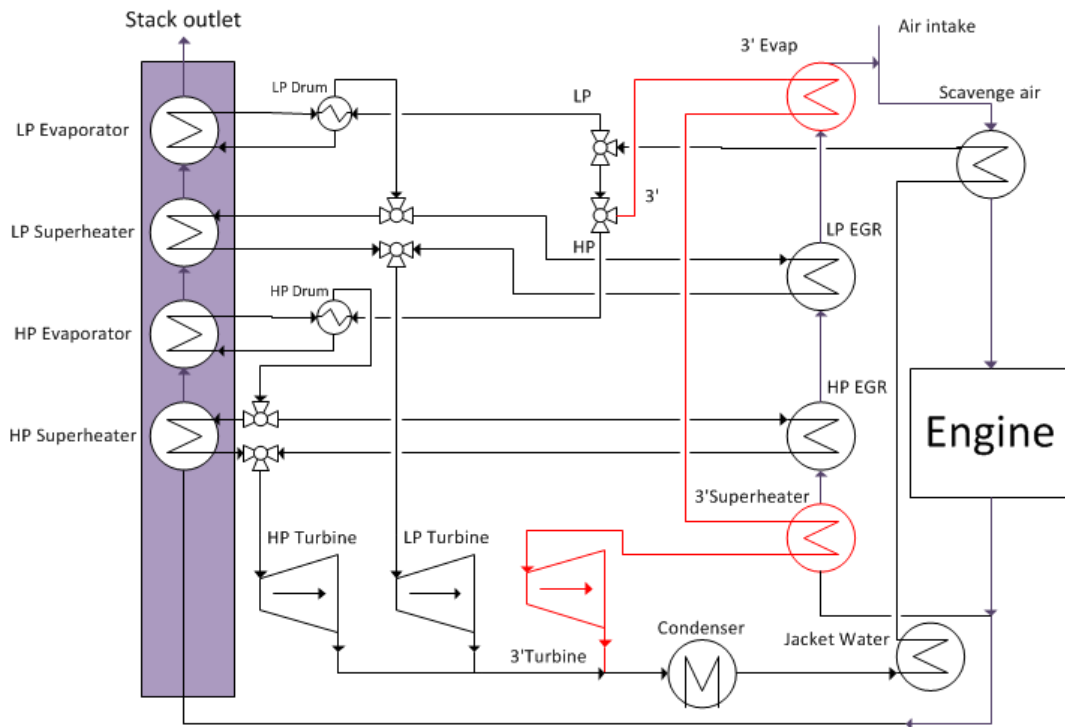
Figure 9: System schematic. The initially investigated 2-stage system is shown in black. For the later investigated 3rd cycle, the red components are added.

5. WHRS Model

To model the power production of the WHRS at all engine loads, two system characteristics must be established, One characteristic being the heat transfer capability of the heat exchangers in the system (here represented by an area and constant heat transfer coefficient) and the other being the turbine constant.

The turbine constant is found from Stodola's Law shown in Equation 12 [15].

$$C_T = \dot{m}\sqrt{\frac{p_{in}v_{in}}{p_{in}^2 - p_{out}^2}} \qquad (12)$$

The heat exchanger areas are approximated from desired temperatures and a reasonable overall heat transfer coefficient, using the log mean temperature difference method.

5.1. Design Model

The outline of the design model is shown in Figure 10. The model takes design pressures for the HP and LP cycle. The temperatures in the preheaters are defined by the heat sources. The high pressure

section of the stack is calculated first, and the low pressure section is then defined by the remaining energy in the exhaust gas. The cycle mass flows are then found, and used to calculate heat exchanger areas with the LMTD method. The mass flows are also used when the turbine constants are calculated with Stodola's law after having applied turbine efficiencies. The model is set up using MATLAB[7].
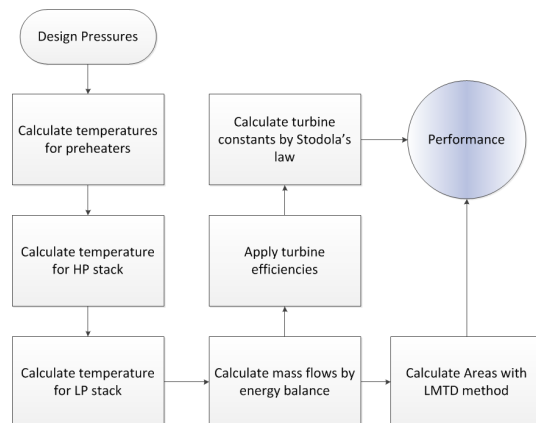
Figure 10: Design model flowchart.

6

5.2. Partload Performance Model

In the performance model, the outlet properties of the fluids are calculated with the NTU (Number of Transfer Units)- method, using the previously found heat exchanger areas. The mass flow of the system is further limited by Stodola's Law (Equation 12), which is now used with the found turbine constants to evaluate the turbine mass flow, given the operation pressure. The model now uses a partial engine load, the pressures of the HP and LP cycles, and the characteristics calculated in the design model. Here, the mass flows are initially guessed, and then re-evaluated when fluid properties have been calculated. Temperatures after each component are calculated with the NTU method. The process runs until the mass flows converge, before calculating the powers of the turbine at that particular load.
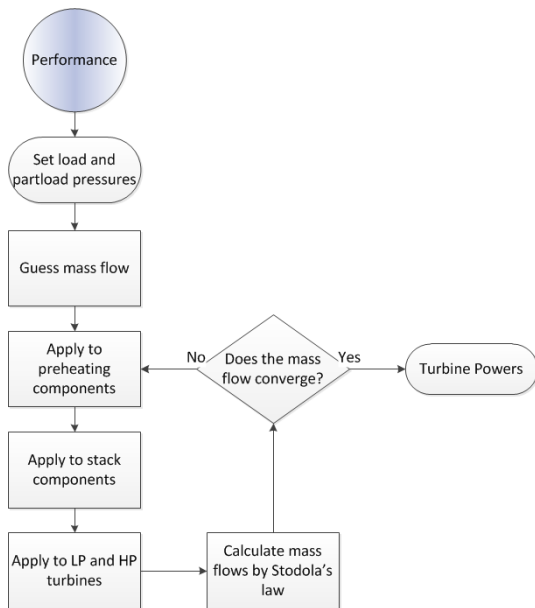
Figure 11: Partload performance model flowchart.

6. Optimization

To avoid extensive economic considerations, the heat exchangers are limited to be designed with a pinch of 10 K. The target variables of the optimization are therefore the input design pressures.

Since the heat exchanger areas and turbine constants are not the only variables in the performance model, the part-load pressures must be optimized for each load and for each configuration. This is done in an embedded performance optimization. The overall procedure is as follows:

1. Guess design pressures
2. Calculate aras and C_T
3. Optimize performance
   (a) Guess operation pressures
   (b) Calculate mass flows and turbine powers
   (c) Adjust operation pressures
   (d) Go to (b), repeat until convergence
4. Calculate objective function
5. Adjust design pressures
6. Go to (2), repeat until convergence

To account for both loads, and to account for the disparity between operation in Tier II and Tier III, the objective function in Equation 13 is used for the overall optimization. LR represents the load repartition, while the 0.7 and 0.3 are the repartition between Tier II and Tier III operation.

$$P_{WHRS} = \sum^{load}(0.7 \cdot LR_{T_{II}} \cdot P_{T_{II}} + 0.3 \cdot LR_{T_{II}} \cdot P_{T_{III}})$$
$$(13)$$

To avoid material concerns, maximum allowable pressure is set to 15 bar (at significantly higher pressures, reinforced components would be required [10]). The low pressure boundary is set to avoid the exhaust gas being cooled below condensation temperature, which would result in the formation of sulfuric acid in the chimney.

$$3.5 bar < p_{LP} < p_{HP} < 15 bar \qquad (14)$$

In addition to the limitation in Equation 14, the operation pressures cannot exceed the design pressure.

$$p_{HP\ operation} <= p_{HP\ design} \qquad (15)$$
$$p_{LP\ operation} <= p_{LP\ design} \qquad (16)$$

While the embedded performance optimization can be carried out with a Hessian-based solver, the overall design optimization is too unstable, and is optimized with a genetic algorithm. The optimal design pressures are 12.14 and 4.41 bar for the high- and low pressure cycles respectively. The optimal performance pressures are shown in Figure 12.

The power production at optimum pressures is shown in Figure 13. At higher loads, the exhaust gas contains more energy. To transfer the additional energy to the cycle, the cycle mass flows must

7
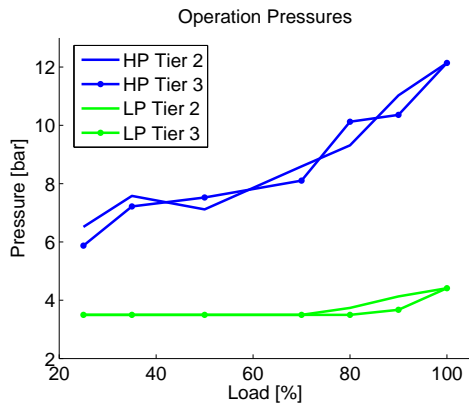
Figure 12: Optimal performance pressures.

increase, and the pressures must grow accordingly to respect Stodola's Law (Equation 12).
The optimum pressures therefore increase with the engine load until they reach the design pressures at full load.
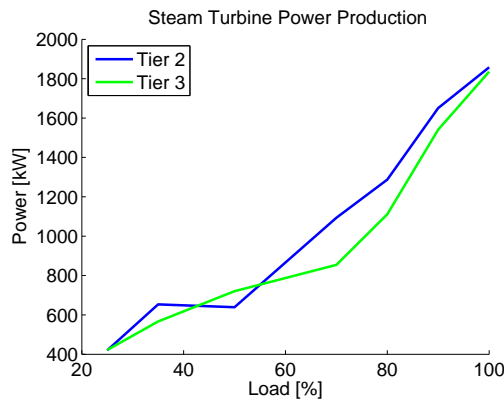
Figure 13: Power Production.

7. 3rd Cycle

7.1. Efficiency Analysis

To determine how much unrecovered energy is left in the stack, an exergy efficiency is defined as seen in Equation 17. Exergy efficiency represents the ratio of recovered energy to the recoverable energy, excluding preheating[16][17].

$$\eta_\psi = \frac{\eta_{WHRS}}{\eta_{\psi-max}} = \frac{P_{Turbines} - P_{pump}}{m_{eg}\psi_{eg}} \qquad (17)$$

The exergy efficiency is shown in Figure 14 for the optimized 2-cycle system for all loads. It can

be seen that while the Tier II operation ranged between 65% and 95%, Tier III stays just above 40%. This is because a large part of the energy in the exhaust gas recirculation string is not utilized.
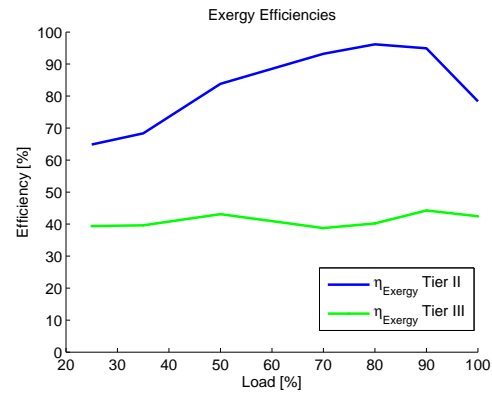
Figure 14: System efficiencies.

7.2. Additional Cycle

To fully utilize the remaining power in the exhaust gas recirculation string, an additional cycle, exclusive to Tier III operation, is introduced. This cycle will be set at 15 bar, and will superheat at the EGR inlet. The cycle fluid will evaporate in the EGR string after the superheaters of all three cycles, just before the EGR is re-introduced into the engine. The third cycle is shown in red on Figure 9.

The resulting optimized power production is shown in Figure 15. While the Tier II production remains unchanged, production in Tier III has increased to peak at almost 3000 kW. The system now operates more efficiently in Tier III operation than in Tier II.
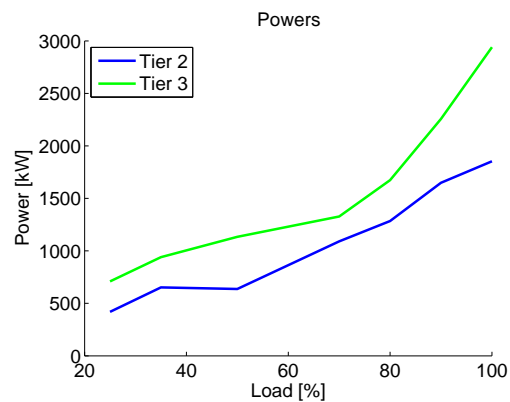
Figure 15: Third cycle power production.

8

Since an additional evaporator is a much larger component than an additional superheater, changes to the overall system size will be more prominent. Moreover, another turbine may be required for the third cycle, as well as another condenser, extra pipework, valves, etc.

No economic study has been made, but rough calculations estimate a total increase in heat exchanger areas of approximately 27% compared to the originally proposed 2-stage system. This does not include the potential need for an additional turbine, which would further increase the system cost. The maximum obtained steam turbine power production is increased by almost 1 MW, but the weighted average power production (Equation 13) is increased by 15-18%.

8. Conclusion

To evaluate the influence of exhaust gas recirculation on a waste heat recovery system, the chemical composition of the exhaust gas was studied. It was found that the composition of the fuel could be averaged to $CH_{1.54}O_{0.02}S_{0.01}$. Its combustion could be adequately modelled using the Glassman mechanism, and a mixture of three small known fuels, with the same average chemical composition and LHV as the evaluated HFO.

NO_x emissions have been shown to be highly dependent of the combustion temperature. It was found that re-introducing part of the exhaust gas to the combustion chamber would significantly reduce the combustion temperature due to the higher c_p value of the exhaust gas. This has been shown to reduce NO_x emissions sufficiently to comply with Tier III operation.

Even considering the massive reduction in NO_x particles after combustion, the thermodynamic properties of the exhaust gas were found to be nearly identical with or without EGR.

A double stage waste heat recovery system was used to regenerate heat from the exhaust gas. A brief exergy study revealed better theoretical results with higher temperatures rather than higher mass. Accordingly, the heat sources were arranged to maximize the the final temperature of each steam cycle. The WHRS model was split into a design and a partload performance model, with the main difference between them being a change from the LMTD to the NTU method for the heat exchangers, and a re-arrangement of Stodola's law for the steam turbines.

Operating a standard 2-stage WHRS with the EGR cycle, it was found that the system could produce up to 2 MW of electrical power, and that with the addition of two alternative superheaters in the EGR string, Tier III production could be kept near that of Tier II.

An exergy analysis revealed a large quantity of available power still present in the EGR string, and an additional steam cycle was proposed. Due to the vast size of the evaporator relative to the extra superheaters, as well as the possible need of a third turbine and additional condenser, this represents a much larger investment. However, it was found that the implementation of an additional high pressure cycle in the EGR string could increase steam turbine production in Tier III to almost 3 MW.

9. Acknowledgments

References

[1] A. S. G. . C. KG, Global Maritime Trade on Course, Esplanade 23, 20354 Hamburg, Germany.
URL http://www.auerbach-schifffahrt.de/en/knowledge/

[2] IMO, Guideline on the method of calculation of the attained energy efficiency design index (EEDI) for new ships (2012).

[3] MAN Diesel&Turbo, Waste Heat Recovery System (WHRS) for reduction of fuel consumption, emissions and EEDI (December 2012).

[4] IMO, Nitrogen Oxides - Regulation 13, International Maritime Organization (2013).

[5] IMO, Sulphur Oxides (SOx) - Regulation 14, International Maritime Organization (2013).

[6] Cantera, Cantera version 2.1.1 (2012).
URL http://cantera.googlecode.com

[7] Mathworks, Matlab is a product of the mathworks, inc., matLab is a product of The MathWorks, Inc. (2014).

[8] M. M. E.W Lemmon, M.L Huber, Refprop version 9.0, national Institute of Standards and Technology, U.S. Department of Commerce (2010).

[9] ISO, Iso 8217:2012 petroleum products – fuels (class f) – specifications of marine fuels (2012).
URL http://www.iso.org/iso/home/store/catalogue_tc/catalogue_detail.htm?csnumber=50613

[10] T. Condra, Conversations with Thomas Condra, AAU (2013).

9

[11] S. R. Turns, An Introduction to Combustion, Concepts and Applications, McGRAW-HILL, 2000, iSBN: 0-07-230096-5.

[12] I. Glassman, Combustion, 3rd ed. (Appendix B), Academic Press, 1996, iSBN: 978-0-12-285852-9.

[13] J. B. Heywood, Internal Combustion Engine Fundamentals, McGRAW-HILL, 1988, iSBN: 0-07-100499-8.

[14] M. A. Boles, Y. A. Cengel, Thermodynamics, An Engineering Approach, 7th Edition, McGraw-Hill, 2011, iSBN: 978-007-131111-4.

[15] M. P. Nielsen, Analysis Of Advanced Thermal Process Systems, notes and Slides from mm1, AAU (2013).

[16] K. Chen, J. Wang, Y. L. Yiping Dai, Thermodynamic analysis of a low-temperature waste heat recovery system based on the concept of solar chimney, Energy Conversion and Management 80.

[17] W. Fu, J. Zhu, W. Zhang, Z. Lu, Performance evaluation of kalina cycle subsystem on geothermal power generation in the oilfield, Applied Thermal Engineering 54.

10

MODELING FOR OPTIMAL CONTROL: A VALIDATED DIESEL-ELECTRIC POWERTRAIN MODEL

Martin Sivertsson[*] **and Lars Eriksson**
Vehicular Systems, Dept. of Electrical Engineering, Linköping
University, SE-581 83 Linköping, Sweden

ABSTRACT

An optimal control ready model of a diesel-electric powertrain is developed, validated and provided to the research community. The aim of the model is to facilitate studies of the transient control of diesel-electric powertrains and also to provide a model for developers of optimization tools. The resulting model is a four state three control mean value engine model that captures the significant nonlinearity of the diesel engine, while still being continuously differentiable.

Keywords: Modeling, Optimal Control, Diesel engine, Diesel-Electric

NOMENCLATURE

Symbol	Description	Unit
p	Pressure	Pa
T	Temperature	K
ω	Rotational speed	rad/s
N	Rotational speed	rpm
$\dot{m}$	Massflow	kg/s
P	Power	W
M	Torque	Nm
Π	Pressure ratio	-
V	Volume	m^3
η	Efficiency	-
A	Area	m^2
Ψ	Head parameter	-
Φ	Flow parameter	-
γ	Specific heat capacity ratio	-
c_p	Specific heat capacity constant pressure	J/(kg · K)
c_v	Specific heat capacity constant volume	J/(kg · K)
R	Gas Constant	J/(kg · K)
r_c	Compression ratio	-
n_{cyl}	Number if cylinders	-
$(A/F)_s$	Stoichiometric air/fuel-ratio	-
q_{HV}	Lower heating value of fuel	J/kg
u_f, u_{wg}, P_{gen}	Control signals	mg/cycle, -, W
J	Inertia	kg · m^2
BSR	Blade speed ratio	-
R	Radius	m
λ	Air/fuel equivalence ratio	-
ϕ	Fuel/air equivalence ratio	-

Table 1: Symbols used

Index	Description	Index	Description
amb	Ambient	*c*	Compressor
im	Intake manifold	*em*	Exhaust manifold
01	Compressor inlet	02	Compressor outlet
eo	Engine out	*a*	Air
e	Exhaust	*ac*	After Compressor
f	Fuel	*ice*	Engine
GenSet	Engine-Generator	*t*	Turbine
wg	Wastegate	*es*	Exhaust System
vol	Volumetric	*d*	Displaced
fric	Friction	*pump*	Pumping
ig	Indicated gross	*mech*	Mechanical
tc	Turbocharger	*ref*	Reference

Table 2: Subscripts used

INTRODUCTION

Optimal control can be an important tool to gain insight into how to control complex nonlinear multiple-input multiple-output systems. However for the model to be analyzable and also for the results to be relevant, higher demands are set on model quality. This relates both to differentiability of the model, for efficient solution processes of the optimal control problem, and also its extrapolation properties since the obtained solutions are often on the border to or outside the nominal operating region. This paper presents the modelling and final model of a diesel-electric powertrain to be used in the study of transient operation. This optimal control ready model will also be made available to the research community to further encourage optimal control studies.

The resulting model is a four state, three control, mean value engine model (MVEM) that consists of 10 submodels that are all continuously differentiable, and suitable for automatic differentiation, in the region of interest in order to enable the nonlinear program solvers to use higher order search methods.

---
[*]Corresponding author: Phone: +46 (0)13-284630 E-mail: marsi@isy.liu.se
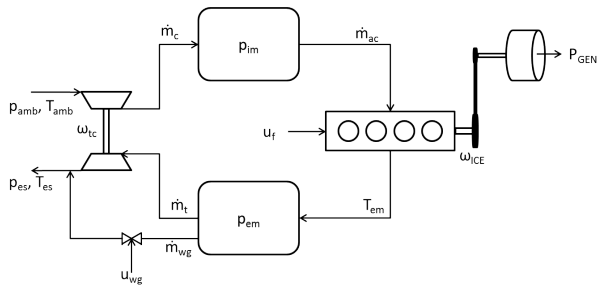
Figure 1: Structure of the model

In engine simulation the component efficiencies are often implemented as maps. In an optimal control framework such strategies are undesirable, instead the developed model includes analytically differentiable efficiency models for the compressor, turbine, cylinder massflow, engine torque and generator power. The efficiency map of the measured production engine is highly nonlinear, see Fig. 3-left, something that is well captured by the developed model, as seen in Fig. 2-left. The resulting mean relative model errors are less than 2.9% for the states and less than 5.4% for the component models.

A typical internal combustion engine normally has an efficiency "'island"' located near the maximum torque line where its peak efficiency is obtained, see [1, 2, 3]. Due to the special nature of the efficiency map of the measured engine the model is also provided with a second torque model, yielding a more typical efficiency map, see Fig. 2-right.
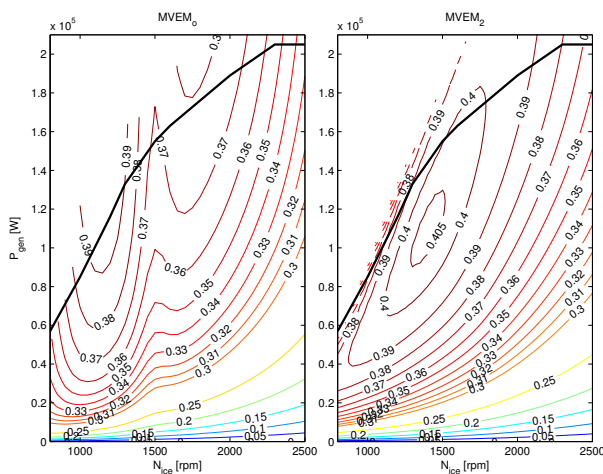
Figure 2: Efficiency of the two models, $MVEM_o$: a model trying to capture the characteristics of the modeled engine (left) and $MVEM_2$: a model representing a typical engine (right).

CONTRIBUTIONS

The contributions of the paper are three-fold: 1) A methodology how to model and parametrize a model of a diesel-electric powertrain is presented. The measurements are conducted without a dynamometer, the only requirements are a diesel-electric powertrain and sensors. 2) A model structure and modeling approach with provided equations, enabling researchers to adjust the parameters of the model to represent their own powertrain. 3) It also provides researchers without engine models or data a relevant and validated open source model on which control design or optimization can be performed.

MODEL STRUCTURE

The aim of the model is control systems design and optimization. This imposes the requirement that the model has to be detailed, but at the same time computationally fast. This leads to a 0-D or MVEM approach. Within MVEM there are two different approaches, one is black box modelling or standard system identification techniques, another is physical modelling where the engine is described using standard physical relations. Due to that one of the model aims is optimization and the solution of optimization problems often are on the border to or outside the nominal operating region the physical modeling approach is selected for its extrapolation properties. For more information about engine modelling as well as the state of the art of engine models the reader is referred to [1, 2].

MODELING

The measured and modeled engine-generator combination (GenSet) consists of a generator mounted on the output shaft of a medium-duty tier 3 diesel-engine. The engine is equipped with a charge air cooled wastegated turbocharger. The states of the developed MVEM are engine speed, ω_{ice}, inlet manifold pressure, p_{im}, exhaust manifold pressure, p_{em}, turbocharger speed, ω_{tc}. The controls are injected fuel mass, u_f, wastegate position, u_{wg}, and generator power, P_{gen}.

The submodels are models for compressor massflow and power, engine out and exhaust manifold temperatures, cylinder massflow, turbine massflow and power, wastegate massflow, engine torque and generator power, with connections between the compo-

Measured	Implemented	Measured	Implemented
ω_{ice}	State	T_{amb}	Constant
p_{im}	State	T_{01}	T_{amb}
p_{em}	State	T_{02}	not used
ω_{tc}	State	T_{im}	Constant
$\dot{m}_f$	Control (u_f)	T_{em}	Static model
u_{wg}	Control	p_{amb}	Constant
P_{gen}	Control	p_{01}	p_{amb}
$\dot{m}_c$	Static model	p_{02}	p_{im}
p_{es}	Constant	λ	Static model

Table 3: Measured variables and their implementation in the model.

nents as in Fig 1. The signals measured and also how they are implemented in the model are listed in Table 3. The data sets used are described in Appendix and listed in Table 5-7.

The tuning process is that first the component models are tuned to stationary measurements. Then the dynamic models are tuned using the results from the component tuning, and finally the whole model is tuned to both dynamic and stationary measurements. In the dynamic and full model tuning all measured signals except the states and $\dot{m}_f$ are used.

Error measure

In the modeling the following relative error is used:

$$e_{\text{rel}}(k) = \frac{y_{mod}(k) - y_{meas}(k)}{\frac{1}{M}\sum_{l=1}^{M}|y_{meas,stat}(l)|} \qquad (1)$$

i.e. regardless of whether it is dynamic or stationary measurements that are considered the error is normalized by the mean absolute value from the stationary measurements. In the tuning it is the euclidean norm of this relative error that is minimized.

Dynamic Models

There are four dynamic models, two rotational states and two manifolds. The rotational states, ω_{ice} and ω_{tc} are modelled using Newton's second law

$$J_{GenSet}\frac{d\omega_{ice}}{dt} = \frac{P_{ice} - P_{mech}}{\omega_{ice}} \qquad (2)$$

$$J_{tc}\frac{d\omega_{tc}}{dt} = \frac{P_t\eta_{tm} - P_c}{\omega_{tc}} \qquad (3)$$

and the manifolds are modelled using the standard isothermal model [4]

$$\frac{dp_{im}}{dt} = \frac{R_a T_{im}}{V_{im}}(\dot{m}_c - \dot{m}_{ac}) \qquad (4)$$

$$\frac{dp_{em}}{dt} = \frac{R_e T_{em}}{V_{em}}(\dot{m}_{ac} + \dot{m}_f - \dot{m}_t - \dot{m}_{wg}) \qquad (5)$$

where in the tuning the measured intake manifold temperature, T_{im} is used but in the final model the intercooler is assumed to be ideal, i.e. no pressure loss and T_{im} constant. The dynamic models have four tuning parameters, J_{GenSet}, J_{tc}, V_{im} and V_{em}.

Compressor

The compressor model consists of two sub-models, one for the massflow and one for efficiency. In order to avoid problems for low turbocharger speeds and transients with pressure ratios $\Pi_c < 1$ a variation of the physically motivated $\Psi \Phi$ model in [1] is used. The idea is that Ψ approaches a maximum at zero flow and that the maximum flow in the region of interest is quadratic in ω_{tc}.

Massflow model

The pressure quotient over the compressor:

$$\Pi_c = \frac{p_{02}}{p_{01}} \qquad (6)$$

Pressure ratio for zero flow:

$$\Pi_{c,max} = \left(\frac{\omega_{tc}^2 R_c^2 \Psi_{max}}{2c_{p,a}T_{01}} + 1\right)^{\frac{\gamma_a}{\gamma_a - 1}} \qquad (7)$$

Corrected and normalized turbocharger speed:

$$\omega_{tc,corr,norm} = \frac{\omega_{tc}}{15000\sqrt{T_{01}/T_{ref}}} \qquad (8)$$

Maximum corrected massflow:

$$\dot{m}_{c,corr,max} = $$
$$c_{\dot{m}_{c,1}}\omega_{tc,corr,norm}^2 + c_{\dot{m}_{c,2}}\omega_{tc,corr,norm} + c_{\dot{m}_{c,3}} \qquad (9)$$

Corrected massflow:

$$\dot{m}_{c,corr} = \dot{m}_{c,corr,max}\sqrt{1 - \left(\frac{\Pi_c}{\Pi_{c,max}}\right)^2} \qquad (10)$$

The massflow is then given by:

$$\dot{m}_c = \frac{\dot{m}_{c,corr}p_{01}/p_{ref}}{\sqrt{T_{01}/T_{ref}}} \qquad (11)$$

The surge-line is modeled using the lowest massflows for each speedline from the compressor map and is well described by the linear relationship:

$$\Pi_{c,surge} = c_{\dot{m}_{c,surge,1}}\dot{m}_{c,corr} + c_{\dot{m}_{c,surge,2}} \qquad (12)$$

In an optimization context surge is undesirable why this is implemented as a constraint according to:

$$\Pi_c \leq \Pi_{c,surge} \qquad (13)$$

Efficiency model

The efficiency of the compressor is modeled using a quadratic form in the flow parameter Φ and speed ω_{tc} following [1]. The dimensionless flow parameter is defined as:

$$\Phi = \frac{\dot{m}_c R_a T_{01}}{\omega_{tc} 8 R_c^3 p_{01}} \qquad (14)$$

Deviation from optimal flow and speed:

$$d\Phi = \Phi - \Phi_{opt} \qquad (15)$$
$$d\omega = \omega_{tc,corr,norm} - \omega_{opt} \qquad (16)$$

The compressor efficiency is given by:

$$\eta_c = \eta_{c,max} - \begin{bmatrix} d\Phi \\ d\omega \end{bmatrix}^T \begin{bmatrix} Q_1 & Q_3 \\ Q_3 & Q_2 \end{bmatrix} \begin{bmatrix} d\Phi \\ d\omega \end{bmatrix} \qquad (17)$$

The consumed power is calculated as the power from consumed in an isentropic process divided by the efficiency:

$$P_c = \frac{\dot{m}_c c_{p,a} T_{01} \left(\Pi_c^{\frac{\gamma_a - 1}{\gamma_a}} - 1 \right)}{\eta_c} \qquad (18)$$

Initialization

The compressor has 10 tuning parameters, Ψ_{max}, $c_{\dot{m}_c,1-3}$, Φ_{opt}, $\eta_{c,max}$ and ω_{opt}, Q_{1-3}. The model is first fitted to the compressor map then to the stationary measurements, using data set A, but then $\dot{m}_c$ is measured and η_c and P_c are calculated according to:

$$\eta_c = \frac{T_{01}(\Pi_c^{1-1/\gamma_a} - 1)}{T_{02} - T_{01}} \qquad (19)$$
$$P_c = \dot{m}_c c_{p,a}(T_{02} - T_{01}) \qquad (20)$$

The results are mean/max absolute errors of [2.4/8.2, 2.3/23.2, 1.4/7.8] % for [$\dot{m}_c$, η_c, P_c] respectively.

Cylinder Gas Flow

The cylinder gas flow models are models for the air and fuel flow in to the cylinder. The airflow model is

a model for the volumetric efficiency of the engine. The model used is the same as in [5] according to:

$$\eta_{vol} = c_{vol,1}\sqrt{p_{im}} + c_{vol,2}\sqrt{\omega_{ice}} + c_{vol,3} \qquad (21)$$
$$\dot{m}_{ac} = \frac{\eta_{vol} p_{im} \omega_{ice} V_d}{4\pi R_a T_{im}} \qquad (22)$$

The control signal u_f is injected fuel mass in mg per cycle and cylinder and the total fuel flow is thus given by:

$$\dot{m}_f = \frac{10^{-6}}{4\pi} u_f \omega_{ice} n_{cyl} \qquad (23)$$

The air-fuel equivalence ratio λ is computed using:

$$\lambda = \frac{\dot{m}_{ac}}{\dot{m}_f} \frac{1}{(A/F)_s} \qquad (24)$$

In diesel engines a lower limit on λ is usually used in order to reduce smoke. However in fuel cut, i.e. $u_f = 0$, $\lambda = \infty$ which is undesirable in optimization. Instead the fuel-air equivalence ratio ϕ is used and the lower limit on λ can be expressed as:

$$\phi = \frac{\dot{m}_f}{\dot{m}_{ac}}(A/F)_s \qquad (25)$$
$$0 \leq \phi \leq \frac{1}{\lambda_{min}} \qquad (26)$$

Initialization

The tuning parameters of the gas flow models are $c_{vol,1-3}$. The model is initialized using all stationary measurements, i.e. set A using that at stationary conditions $\dot{m}_{ac} = \dot{m}_c$. The volumetric efficiency model corresponds well to measurements with a mean/max absolute relative error of [0.9/3.7] %.

Engine torque and generator

The engine torque is not measured so the tuning of the torque models have to rely on the DC-power out from the power electronics. Then there are actually three efficiencies that should be modeled, the power electronics, the generator, and the engine efficiencies. In Fig. 3-left the total efficiency of the powertrain is shown, with the maximum power line.
First the engine torque model is tuned. In the tuning the engine torque is calculated using the stationary efficiency map of the generator, provided by the manufacturer. The efficiency of the power electronics is lumped with the generator efficiency and is here assumed to be 0.98. Then the generator model
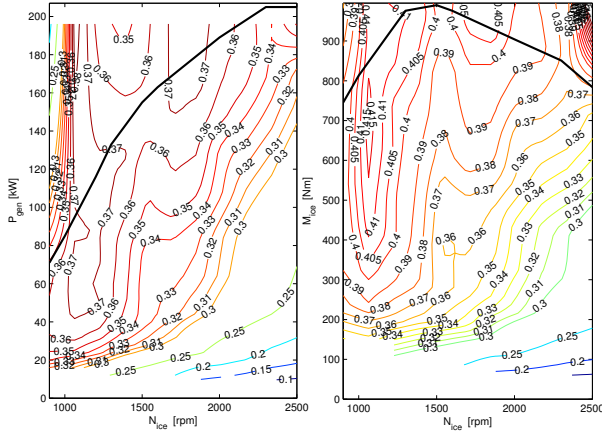
Figure 3: Efficiency of the powertrain (left) and efficiency of the engine (right)

is tuned, first using the stationary map and then measurements but with the torque calculated using the efficiency map.

Engine torque model

In Fig. 3-right the efficiency of the engine is shown, with M_{ice} calculated using the generators efficiency map and 2% losses in the power electronics assumed. The engine torque is modeled using three components, see [4], i.e. friction torque, M_{fric}, pumping torque M_{pump} and gross indicated torque, M_{ig}. The torque consumption of the high pressure pump is not modeled on it's own, but lumped in to the following models. The net torque of the engine can then be computed.

$$M_{ice} = M_{ig} - M_{fric} - M_{pump} \quad (27)$$

The pumping torque is proportional to the pressure quotient over the cylinder:

$$M_{pump} = \frac{V_d}{4\pi}(p_{em} - p_{im}) \quad (28)$$

The friction torque is modeled as a quadratic shape in engine speed:

$$M_{fric} = \frac{V_d}{4\pi}10^5\left(c_{fr1}\omega_{ice}^2 + c_{fr2}\omega_{ice} + c_{fr3}\right) \quad (29)$$

The indicated gross torque is proportional to the fuel energy:

$$M_{ig} = \frac{u_f 10^{-6} n_{cyl} q_{HV}\eta_{ig}}{4\pi} \quad (30)$$

Where the indicated gross efficiency is defined as:

$$\eta_{ig} = \eta_{ig,t}(1 - \frac{1}{r_c^{\gamma_{cyl}-1}}) \quad (31)$$

The torque model in (27)-(31) is fairly common, and if $\eta_{ig,t}$ is implemented as a constant maximum brake torque (MBT)-timing is assumed. A typical internal combustion engine normally has an efficiency "'island'" located near the maximum torque line where its peak efficiency is obtained, see [1, 2, 3]. However looking at Fig. 3-right this is clearly not the case. Therefore the model is provided with two different torque models, seen in Fig. 4.

Torque model 1 (TM1) is used in the model tuning and validation and is designed to capture the nonlinear nature seen in Fig. 3. TM1 consists of two second order polynomials and a switching function:

$$\eta_{ig,t} = M_{f,1} + g_f(M_{f,2} - M_{f,1}) \quad (32)$$

$$g_f = \frac{1 + tanh(0.1(\omega_{ice} - 1500\pi/30))}{2} \quad (33)$$

$$M_{f,1} = c_{M_{f,1},1}\omega_{ice}^2 + c_{M_{f,1},2}\omega_{ice} \quad (34)$$

$$M_{f,2} = c_{M_{f,2},1}\omega_{ice}^2 + c_{M_{f,2},2}\omega_{ice} + c_{M_{f,2},3} \quad (35)$$

Torque model 2 (TM2) is designed and provided to represent a "'typical'" engine with an efficiency island, to be used for optimal control studies, and is thus not used in the tuning or validation. TM2 is quadratic in $\frac{u_f}{\omega_{ice}}$ and expressed as

$$\eta_{ig,t} = \eta_{ig,ch} + c_{u_f,1}(\frac{u_f}{\omega_{ice}})^2 + c_{u_f,2}\frac{u_f}{\omega_{ice}} \quad (36)$$

The maximum power line is implemented as a limit on the net power of the engine, $P_{ice} = T_{ice}\omega_{ice}$, which is well approximated by two quadratic functions and a maximum value:

$$P_{ice} \leq P_{ice,max} \quad (37)$$

$$P_{ice} \leq c_{P_1}\omega_{ice}^2 + c_{P_2}\omega_{ice} + c_{P_3} \quad (38)$$

$$P_{ice} \leq c_{P_4}\omega_{ice}^2 + c_{P_5}\omega_{ice} + c_{P_6} \quad (39)$$

Initialization

The two torque models have eight and six tuning parameters respectively. The tuning parameters are c_{fr1-3}, and $c_{M_{f,1},1-2}$, $c_{M_{f,2},1-3}$, or $\eta_{ig,ch}$ and $c_{u_f,1-2}$ The models are fitted using set C. For (32) it is rather straight forward. For model (36) the "island" is not
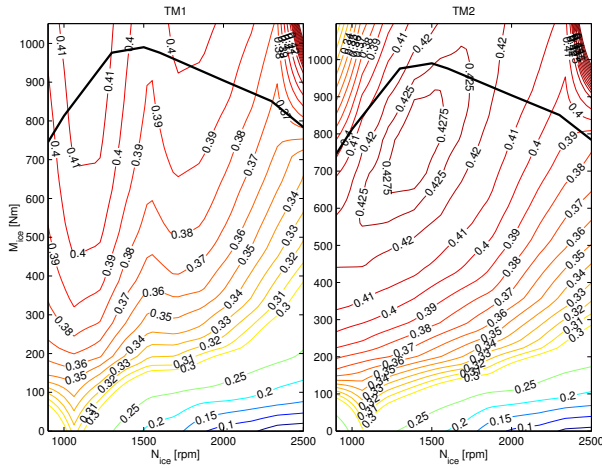
Figure 4: The two different torque models. Left: (32) certification speed . Right: (36) "'Typical'"

Figure 5: Mechanical generator power as a function of electrical power

generator map and secondly to measurement data, using set C. The mean/max absolute relative errors of the generator model are [0.7/2.5] %.

visible in the measured data, therefore the parameters of $\eta_{ig,ch}$ are manually tuned and the M_{fric} model is tuned assuming MBT-timing. The mean/max absolute relative errors of TM1 are [2.2/10.9] %.

Generator model

Looking at Fig. 5 a reasonable first approximation of the relationship between mechanical and electrical power of the generator is two affine functions, something normally denoted willans line, [6], where the slope of the line depends on whether the generator is in generator or motor mode.

$$P_{mech}^{+} = e_{gen,1}P_{gen} + P_{gen,0}, \quad \text{if } P_{gen} \geq 0 \quad (40)$$

$$P_{mech}^{-} = e_{gen,2}P_{gen} + P_{gen,0}, \quad \text{if } P_{gen} < 0 \quad (41)$$

This model is not continuously differentiable so therefore to smoothen it out a switching function is used. The model is then given by:

$$P_{mech} = P_{mech}^{-} + \frac{1 + \tanh(0.005P_{gen})}{2}(P_{mech}^{+} - P_{mech}^{-})$$
$$(42)$$

$e_{gen,1-2}$ are seen to have a quadratic dependency on ω_{ice}, a reasonable addition to the willans line is thus to model $e_{gen,1-2}$ as:

$$e_{gen,x} = e_{gen,x-1}\omega_{ice}^{2} + e_{gen,x-2}\omega_{ice} + e_{gen,x-3} \quad (43)$$

which constitutes the full model.

Initialization

The generator model has seven tuning parameters, $P_{gen,0}$ and $e_{gen,1/2,1-3}$. The model is first fitted to the

Exhaust temperature

The cylinder out temperature model is based on ideal the Seiliger cycle and is a version of the model found in [5]. The model consists of the pressure quotient over the cylinder:

$$\Pi_e = \frac{p_{em}}{p_{im}} \quad (44)$$

The specific charge:

$$q_{in} = \frac{\dot{m}_f q_{HV}}{\dot{m}_f + \dot{m}_{ac}}(1 - x_r) \quad (45)$$

The combustion pressure quotient:

$$x_p = \frac{p_3}{p_2} = 1 + \frac{q_{in}x_{cv}}{c_{v,a}T_1 r_c^{\gamma_a - 1}} \quad (46)$$

The combustion volume quotient:

$$x_v = \frac{v_3}{v_2} = 1 + \frac{q_{in}(1 - x_{cv})}{c_{p,a}\left(\frac{q_{in}x_{cv}}{c_{v,a}} + T_1 r_c^{\gamma_a - 1}\right)} \quad (47)$$

The residual gas fraction:

$$x_r = \frac{\Pi_e^{1/\gamma_a} x_p^{-1/\gamma_a}}{r_c x_v} \quad (48)$$

Temperature after intake stroke:

$$T_1 = x_r T_{eo} + (1 - x_r)T_{im} \quad (49)$$

The engine out temperature:

$$T_{eo} = \eta_{sc}\Pi_e^{1 - 1/\gamma_a} r_c^{1 - \gamma_a} x_p^{1/\gamma_a - 1}$$
$$\left(q_{in}\left(\frac{1 - x_{cv}}{c_{p,a}} + \frac{x_{cv}}{c_{v,a}}\right) + T_1 r_c^{\gamma_a - 1}\right) \quad (50)$$

To account for the cooling in the pipes the model from [7] is used, where V_{pipe} is the total pipe volume:

$$T_{em} = T_{amb} + (T_{eo} - T_{amb})e^{-\frac{h_{tot}V_{pipe}}{(\dot{m}_f + \dot{m}_{ac})c_{p,e}}} \qquad (51)$$

The model equations described in (45)-(50) are non-linear and depend on each other and need to be solved using fixed point iterations. In [5] it is shown that it suffices with one iteration to get good accuracy if the iterations are initialized using the solution from last time step. In an optimization context remembering the solution from last time step is difficult and also using a model that uses an unknown number of iterates is undesirable. However the loss in model precision of assuming no residual gas, i.e. $x_r = 0$, is negligible therefore this is assumed. Further, the addition of heat loss in the pipe through (51) drives x_{cv} to zero. The reduced model is then given by:

$$q_{in} = \frac{\dot{m}_f q_{HV}}{\dot{m}_f + \dot{m}_{ac}} \qquad (52)$$

$$T_{eo} = \eta_{sc}\Pi_e^{1-1/\gamma_a} r_c^{1-\gamma_a}\left(\frac{q_{in}}{c_{p,a}} + T_{im}r_c^{\gamma_a-1}\right) \qquad (53)$$

$$T_{em} = T_{amb} + (T_{eo} - T_{amb})e^{-\frac{h_{tot}V_{pipe}}{(\dot{m}_f + \dot{m}_{ac})c_{p,e}}} \qquad (54)$$

Initialization

The used temperature model has two tuning parameters, η_{sc} and h_{tot}. The first step of the initialization assumes that there is no heat loss in the manifold before the sensors. Then the complete model is fitted using the results from $T_{em} = T_{eo}$. The nominal set is used in the fitting. The mean/max absolute relative error of the temperature model is [1.9/5.4] % and the error increase from assuming $x_r = 0$ is [0.014/0.06] ‰.

Turbine and Wastegate

Since the massflow is not measured on the exhaust side, the models for wastegate and turbine have to be fitted together.

$$\Pi_t = \frac{p_{es}}{p_{em}} \qquad (55)$$

Turbine

The massflow is modeled with the standard restriction model, using that half the expansion occurs in
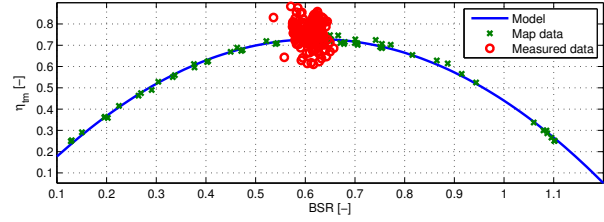
Figure 6: BSR model and its fit to map and measured data

the stator and half in the rotor, see [8]:

$$\Pi_t^* = \max\left(\sqrt{\Pi_t}, \left(\frac{2}{\gamma_e+1}\right)^{\frac{\gamma_e}{\gamma_e-1}}\right) \qquad (56)$$

$$\Psi_t(\Pi_t^*) = \sqrt{\frac{2\gamma_e}{\gamma_e-1}\left((\Pi_t^*)^{\frac{2}{\gamma_e}} - (\Pi_t^*)^{\frac{\gamma_e+1}{\gamma_e}}\right)} \qquad (57)$$

$$\dot{m}_t = \frac{p_{em}}{\sqrt{R_e T_{em}}}\Psi_t A_{t,eff} \qquad (58)$$

The turbine efficiency is modeled as a quadratic shape in blade-speed ratio (BSR), as used in [9, 8].

$$BSR = \frac{R_t \omega_{tc}}{\sqrt{2c_{p,e}T_{em}(1 - \Pi_t^{\frac{\gamma_e-1}{\gamma_e}})}} \qquad (59)$$

$$\eta_{tm} = \eta_{tm,max} - c_m(BSR - BSR_{opt})^2 \qquad (60)$$

The power to the turbocharger is then:

$$P_t \eta_m = \dot{m}_t c_{p,e} T_{em} \eta_{tm}\left(1 - \Pi_t^{\frac{\gamma_e-1}{\gamma_e}}\right) \qquad (61)$$

Due to uncertainty of the behaviour outside the mapped region, and to avoid problems with negative turbine efficiency, a reasonable constraint is to restrict BSR to the maximum and minimum values provided in the map, i.e. $BSR_{min} \leq BSR \leq BSR_{max}$.

Wastegate

The wastegate massflow is modeled with the standard restriction model and an effective area that changes linearly in u_{wg}.

$$\Pi_{wg}^* = \max\left(\Pi_t, \left(\frac{2}{\gamma_e+1}\right)^{\frac{\gamma_e}{\gamma_e-1}}\right) \qquad (62)$$

$$\Psi_{wg} = \sqrt{\frac{2\gamma_e}{\gamma_e-1}\left((\Pi_{wg}^*)^{\frac{2}{\gamma_e}} - (\Pi_{wg}^*)^{\frac{\gamma_e+1}{\gamma_e}}\right)} \qquad (63)$$

$$\dot{m}_{wg} = \frac{p_{em}}{\sqrt{R_e T_{em}}}\Psi_{wg} u_{wg} A_{wg,eff} \qquad (64)$$

Initialization

The initialization uses data set C. The massflow models need to be fitted together and the turbine efficiency cannot be calculated from measurements since none of the massflows are measured. Looking at the nominal data set the quadratic shape in BSR is not observed since the measurements are rather constant in BSR, see Fig. 6. Since this shape is nonexistent in the measurements the efficiency model of the turbine is locked to the map fit since otherwise it would converge to an arbitrary shape trying to capture as much as the cloud nature of the measured data as possible. One could consider adding pulse compensation factors for the massflow and efficiency but the resulting improvements are small. The massflow models are fitted together using $\dot{m}_{ac} + \dot{m}_f = \dot{m}_t + \dot{m}_{wg} = \dot{m}_{exh}$. Friction losses according to $P_c = P_t \eta_m - w_{fric} \omega_{tc}^2$ can be added, however the parameter w_{fric} becomes small in the optimization. The final turbine and wastegate models have three tuning parameters, $A_{t,eff}$, $\eta_{tm,max}$ and $A_{wg,eff}$. The results are mean/max relative errors of [2.3/5.4, 4.7/17.0] % for [$\dot{m}_{exh}$, $P_t \eta_{tm}$] respectively.

Exhaust flow models

Using the standard restriction model a max-expression is necessary under the square root to keep the flow real, representing choking which occurs at $\Pi_t^{-1} \approx [3.3, 1.8]$ for the turbine and wastegate. However such expressions are undesirable when using optimization tools. Instead the following expressions are used:

$$\Psi_t = c_{t,1} \sqrt{1 - \Pi_t^{c_{t,2}}} \qquad (65)$$

$$\Psi_{wg} = c_{wg,1} \sqrt{1 - \Pi_t^{c_{wg,2}}} \qquad (66)$$

The flow models are fitted to produce the same flow profile as the standard restriction models in (57), (63), where $c_{t,1-2}$ and $c_{wg,1-2}$ are tuning parameters.

Dynamic models

So far the models are tuned using stationary measurements. The next step is to tune the parameters of the dynamic models in (2)-(5). Since torque is not measured J_{GenSet} is fixed to it's real value and only V_{im}, V_{em} and J_{tc} are tuned. Since torque and eventual torque errors might lead to engine stalling the torque

model is inverted to track the real engine speed trajectory. This will lead to that there will be almost no errors in engine speed. To fit the dynamic models data set D-I are used but only the transients in the measurements, plus a couple of seconds before and after. As in [5] the transient is also normalized to 0-1 so that the stationary point has no effect on the dynamics.

Full models

The full models are tuned using both dynamic and stationary measurements, using a similar cost function as in [5]. If the same cost function is used the model will not be able to reach the same maximum torque as the real engine for low engine speeds without λ being excessively low. Therefore to ensure that the model is able to span the entire operating range of the engine an addition is made. The model is simulated with $\lambda = \lambda_{min}$ for $N_{ice} = 800$ rpm and the models maximum torque is added to the cost function according to:

$$V_{M_{max}} = w_{M_{max}} \left(\frac{M_{ice,max,mod}(800rpm)}{M_{ice,max,meas}(800rpm)} - 1 \right) \quad (67)$$

(67) assumes that the engine is smoke-limited at 800 rpm and maximum torque and thus tries to force the max torque of the model to coincide with that of the real engine, where $w_{M_{max}}$ is a weighting parameter.

To ensure reasonable behaviour also when the generator is in motoring mode this side is fitted using the efficiency map from the manufacturer with an assumed power electronics efficiency of 98%. For the stationary tuning set C is used and for the dynamics sets D-I are used. The full cost function is given by:

$$\begin{aligned}
V_{tot}(\theta) = & \frac{1}{y_{dyn}M_{dyn}} \sum_{k=1}^{M_{dyn}} \sum_{y_n=1}^{y_{dyn}} \sum_{l=1}^{N_{dyn}} \frac{(e_{rel,dyn}^{y_n}(l))^2}{N_{dyn}} \\
& + \frac{1}{y_{stat}} \sum_{y_s=1}^{y_{stat}} \sum_{m=1}^{N_{stat}} \frac{(e_{rel,stat}^{y_s}(m))^2}{N_{stat}} \\
& + V_{M_{max}}^2
\end{aligned} \qquad (68)$$

where y is the number of outputs, M the number of datasets and N the number of operating points in each dataset. The models are also, as in [5], validated using only dynamic measurements and in particular all load transients, i.e. set $J_{0.1, 1, 2}$-$N_{0.1, 1, 2}$.

Table 4: Mean relative errors of the complete model. Bold marks variables used in the tuning and T, V, are the errors relative tuning and validation sets respectively.

	ω_{ice}		$\boldsymbol{p_{im}}$		$\boldsymbol{p_{em}}$		$\boldsymbol{\omega_{tc}}$	
	T	V	T	V	T	V	T	V
Dyn.	0.0	0.0	2.8	2.2	2.8	2.9	2.9	2.9
	$\dot{\boldsymbol{m_c}}$	$\boldsymbol{P_c}$	$\dot{\boldsymbol{m}}_{ac}$	$\boldsymbol{T}_{em}$	$\dot{m}_{exh}$	$\boldsymbol{P_t}$	P_{mech}^+	P_{mech}^-
Stat.	2.5	1.8	2.5	2.4	3.3	5.4	3.4	1.4

RESULTS

The resulting fit to both tuning data and validation data is shown in Table 4. The variables used in the tuning are written in bold in the resulting tables. Table 4 shows that the model is a good mathematical repesentation of the measured system with state errors less than 3% and stationary errors in the same range. In Fig. 7 the state trajectories of the model are compared to measurements. There it is also seen that the agreement is good.

The pressure dynamics, and in particular the exhaust pressure, are faster than the speed dynamics therefore the resulting model is moderately stiff. This is also seen when selecting ode-solvers. In matlab ode23t and ode15s are twice as fast as the standard ode45 when simulating the model. When the states are normalized with their maximum values the relative and absolute tolerances [1e-4, 1e-7] are found to be good trade-offs between accuracy and performance.

CONCLUSION

In this paper a validated optimization ready model of a diesel-electric powertrain is presented. The resulting model is four state-three control mean value engine model, available for download in the **LiU-D-El**-package from [10]. The model is able to capture the highly nonlinear nature of the turbocharger diesel engine, and is at the same time continuously differentiable in the region of interest, to comply with optimal control software. The model is provided with two torque models to be used for optimal control studies. The first model, called $MVEM_o$ with a torque model representing the actual engine, as well as a model with a more general torque model aimed to represent a typical engine, called $MVEM_2$. Both $MVEM_o$ and $MVEM_2$ are included in the **LiU-D-El**-package together with a small example that

can be downloaded fully parametrized from [10] implemented in matlab.
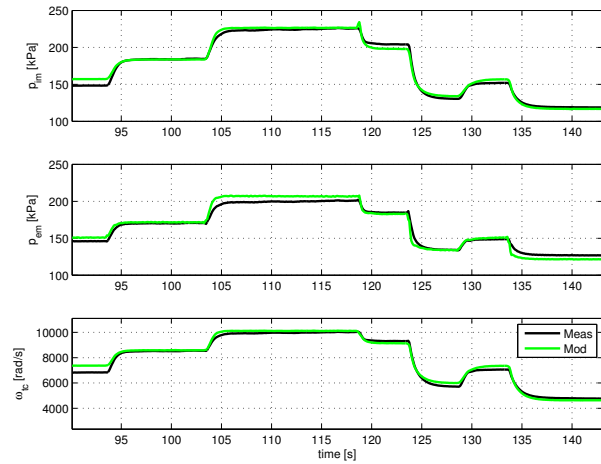
Figure 7: Model vs. measurements

REFERENCES

[1] Lars Eriksson and Lars Nielsen. *Modeling and Control of Engines and Drivelines*. John Wiley & Sons, 2014.

[2] L. Guzzella and C.H. Onder. *Introduction to Modeling and Control of Internal Combustion Engine Systems*. Springer, 1st edition, 2004.

[3] Michael Ben-Chaim, Efraim Shmerling, and Alon Kuperman. Analytic modeling of vehicle fuel consumption. *Energies*, 6(1):117–127, 2013.

[4] John B. Heywood. *Internal Combustion Engine Fundamentals*. McGraw-Hill Book Co., 1988.

[5] Johan Wahlström and Lars Eriksson. Modelling diesel engines with a variable-geometry turbocharger and exhaust gas recirculation by optimization of model parameters for capturing non-linear system dynamics. *Proceedings of the Institution of Mechanical Engineers, Part D, Journal of Automobile Engineering*, 225(7):960–986, 2011.

[6] Lino Guzzella and Antonio Sciarretta. *Vehicle Propulsion Systems - Introduction to Modeling and Optimization*. Springer, 2nd edition, 2007.

[7] Lars Eriksson. Mean value models for exhaust system temperatures. *SAE 2002 Transactions, Journal of Engines, 2002-01-0374*, 111(3), September 2003.

[8] Lars Eriksson. Modeling and control of turbocharged SI and DI engines. *Oil & Gas Science and Technology - Rev. IFP*, 62(4):523–538, 2007.

[9] N. Watson. Transient performance simulation and analysis of turbocharged diesel engines. In *SAE Technical Paper 810338*.

[10] Vehicular systems software. "http://www.fs.isy.liu.se/Software/", 2014.

Table 5: Stationary Data

Data Set	A	B	C
Delimiter	all	nominal	nominal & $P_{gen} > 0$
Nr. of points	192	139	127

APPENDIX
DATA USED

There are a total of 192 stationary points measured. Of those 192, 53 are with the wastegate locked in a fixed position. Since injection timing is not measured those points are only used when fitting the gas flow models since there are some questions about what the engine control unit does when the wastegate control is altered. Nominal refers to unaltered wastegate, see Table 5

The dynamic data set consists of 21 measurements. The first six, D-I, are engine speed transients with constant(as close as the generator control can track) generator power and a sequence of steps in reference speed that the engine speed controller tries to track, see Table 6.

The last 15 sets are with constant reference speed, and different load steps, see Table 7. As with the speed transients the ECU controls the engine speed and the generator acts as a disturbance. The load transients are conducted at different engine speeds and then a programmed sequence of 23 power steps is performed with varying rise time, or rate at which the power changes. The first five, $J_{0.1} - N_{0.1}$ are with a ramp duration of 0.1s and the other are with 1s and 2s respectively. The total length of each set is approximately 300s.

Table 6: Speed transients

Data Set	D	E	F	G	H	I
P_{gen} [kW]	30	60	90	130	160	180
Nr. of steps	22	22	22	22	21	21

Table 7: Load transients

Data Set	$J_{0.1, 1, 2}$	$K_{0.1, 1, 2}$	$L_{0.1, 1, 2}$	$M_{0.1, 1, 2}$	$N_{0.1, 1, 2}$
Speed [rpm]	1100	1500	1800	2000	2200
Nr. of steps	23	23	23	23	23

AN OPTIMAL CONTROL BENCHMARK: TRANSIENT OPTIMIZATION OF A DIESEL-ELECTRIC POWERTRAIN

Martin Sivertsson* and Lars Eriksson
Vehicular Systems, Dept. of Electrical Engineering, Linköping University, SE-581 83 Linköping, Sweden

ABSTRACT

An optimal control benchmark is presented and discussed. The benchmark is optimal transient control of a nonlinear four state three control model of a diesel-electric powertrain and constructed in such a manner that it is available in several versions to be of interest for developers of optimal control tools at different levels of development. This includes with and without time as a parameter as well as with and without time varying constraints.

Keywords: Optimal Control, Diesel engine, Diesel-Electric, Nonlinear optimization

NOMENCLATURE

Symbol	Description	Unit
p	Pressure	Pa
T	Temperature	K
ω	Rotational speed	rad/s
$\dot{m}$	Massflow	kg/s
P	Power	W
M	Torque	Nm
E	Energy	J
Π	Pressure ratio	-
V	Volume	m^3
R	Gas Constant	J/(kg · K)
u_f, u_{wg}, P_{gen}	Control signals	mg/cycle, -, W
J	Inertia	kg · m^2
BSR	Blade speed ratio	-
ϕ	Fuel-air equivalence ratio	-
λ_{min}	Air-fuel smoke-limit	-

Table 1: Symbols used

Index	Description	Index	Description
ice	Engine	*GenSet*	Engine-Generator
im	Intake manifold	*em*	Exhaust manifold
c	Compressor	*ac*	After compressor
t	Turbine	*wg*	Wastegate
f	Fuel	*tc*	Turbocharger
a	Air	*e*	Exhaust
gen	Generator-electrical	*mech*	Generator-mechanical
req	Requested	*c, surge*	Compressor surge-limit

Table 2: Subscripts used

This paper presents a benchmark on which to evaluate developed optimal control tools. The benchmark problem is the optimization of the control of a diesel-electric powertrain from idle to a target output power and energy. The benchmark relies on the validated model of a diesel-electric powertrain described in [1]. The model is a nonlinear four state, three controls mean value engine model (MVEM), that consists of 10 submodels that describe the individual components of the powertrain. Due to the complex and nonlinear nature of the modeled system the resulting optimization problem is non-convex and the optimization tools can therefore only guarantee local optima. The model is continuously differentiable in the desired operating region and is implemented using only analytical expressions. The motivation for this is to enable the solvers to use higher order search methods in the optimization. It also makes the model suitable for automatic differentiation (AD), enabling developers to also evaluate

INTRODUCTION

In this paper a benchmark for optimal control tools is suggested and presented. The current state of computer technology has enabled a rise in the development of optimal control packages that can handle models of complex systems. However to evaluate the performance of the tools developers often have to rely on relatively small problems that do not reflect the purpose for which the tools were developed.

---

*Corresponding author: Phone: +46 (0)13-284630 E-mail: marsi@isy.liu.se

AD routines versus computing gradients and hessians using finite differences.

In the paper the solutions to the problems using two different solvers, the ACADO Toolkit, see [2], TOMLAB/PROPT, see [3], is presented and discussed. The model and the resulting optimal trajectories, as well as the corresponding initial guesses, are available for research community. Two types of problems are considered, time and fuel minimization. To make the benchmark problem suitable for optimal control tools at different stages of development the problems are solved both with duration as a parameter to be optimized as well as for a fixed duration and also with and without path constraints.

CONTRIBUTIONS

The contribution of this paper is the formulation and solution of an optimal control problem to serve as a benchmark on which to evaluate optimal control. The intention of the benchmark is to provide the research community with a relevant problem of reasonable complexity on which to benchmark optimal control tools. The benchmark is provided together with a simultaneously developed model, both available for download. To ensure that the benchmark is relevant for tools at different stages of development the problem is provided both with and without path constraints as well as with and without time as a parameter.

MODEL

The model used can be downloaded from [4] and is described in detail as $MVEM_2$ in [1], and provided either on its own, in the **LiU-D-El**-package, or together with the benchmark in the **LiU-D-El+Benchmark**-package. The modeled diesel-electric powertrain consists of a 6-cylinder diesel engine with a fixed-geometry turbine and a wastegate for boost control, with a generator mounted on the output shaft. The states of the MVEM are engine speed, ω_{ice}, inlet manifold pressure, p_{im}, exhaust manifold pressure, p_{em}, and turbocharger speed, ω_{tc}. The controls are injected fuel mass, u_f, wastegate position, u_{wg}, and generator power, P_{gen}. The engine model consists of two control volumes, intake and exhaust manifold, and four restrictions, compressor, engine, turbine, and wastegate. The control volumes are modeled with the standard isothermal model, us-

ing the ideal gas law and mass conservation. The engine and turbocharger speeds are modeled using Newton's second law. The governing differential equations of the MVEM are:

$$\frac{d\omega_{ice}}{dt} = \frac{P_{ice} - P_{mech}}{\omega_{ice}J_{GenSet}} \tag{1}$$

$$\frac{dp_{im}}{dt} = \frac{R_a T_{im}}{V_{im}}(\dot{m}_c - \dot{m}_{ac}) \tag{2}$$

$$\frac{dp_{em}}{dt} = \frac{R_e T_{em}}{V_{em}}(\dot{m}_{ac} + \dot{m}_f - \dot{m}_t - \dot{m}_{wg}) \tag{3}$$

$$\frac{d\omega_{tc}}{dt} = \frac{P_t \eta_{tm} - P_c}{\omega_{tc}J_{tc}} \tag{4}$$

The MVEM is extended with two summation states to keep track on produced and consumed energy. The summation states are defined as:

$$\frac{dm_f}{dt} = \dot{m}_f \tag{5}$$

$$\frac{dE_{gen}}{dt} = P_{gen} \tag{6}$$

PROBLEM FORMULATION

The proposed benchmark problem is the same problem as is studied in [5, 6]. The problem is that the GenSet is at idle when the operator requests a step in output power, P_{gen}, that should be met either as fuel efficient or time efficient as possible. The requested power is also augmented with an energy requirement, E_{gen}, that has to be produced before the GenSet reaches stationary conditions. This problem is mathematically expressed as:

$$\begin{aligned}
&\min_{u(t)} \quad \int_0^T \dot{m}_f(x(t), u(t))\,dt \quad \text{or} \quad \min_{u(t)} T \\
&\text{s.t.} \quad \dot{x}(t) = f(x(t), u(t)) \\
&\qquad (x(t), u(t)) \in \Omega(t)
\end{aligned} \tag{7}$$

where x is the state vector of the MVEM, $\dot{x}$ is the state equations (1)-(4) together with the summation states in (5)-(6), and $u = [u_f, u_{wg}, P_{gen}]$.

The constraints of the optimization problems, $(x(t), u(t)) \in \Omega(t)$, can be divided into two categories, time independent and time varying constraints. The first category, time independent constraints, are bounds on states and controls as well as

initial and final conditions expressed as:

$$x(0) = x0, \qquad \dot{x}(T) = 0$$
$$u_{min} \leq u(t) \leq u_{max}, \qquad x_{min} \leq x(t) \leq x_{max}$$
$$0 \leq P_{gen}(t) \leq 100\ kW, \quad P_{gen}(T) = 100\ kW \qquad (8)$$
$$E_{gen}(T) \geq 100\ kJ$$

The time varying constraints are constraints imposed by the components, such as maximum power of the engine, surge-limit of the compressor, blade speed ratio-limit of the turbine, as well as environmental constraints, i.e. an upper limit on ϕ set by the smoke-limiter:

$$P_{ice}(x(t), u(t)) \leq P_{ice,max}(x(t))$$
$$\Pi_c \leq \Pi_{c,surge}$$
$$BSR_{min} \leq BSR(x(t), u(t)) \leq BSR_{max} \qquad (9)$$
$$0 \leq \phi(x(t), u(t)) \leq \frac{1}{\lambda_{min}}$$

To be relevant for software developers at different stages of development the benchmark problems defined in (7)-(9) are also available as a minimum fuel problem with fixed end time, as well as without the time varying constraints in (9).

SOLUTION ACCURACY

To ensure that the solutions are at least good local minima both benchmark problems, $\min T$ and $\min m_f$, are solved using PROPT and two different initial guesses, see Fig. 2-right. The first initial guess is a hard acceleration with $\phi = \frac{1}{\lambda_{min}}$ from idle followed by a step in load power to $P_{gen} = 100$ kW, and the second one is the GenSet at idle. Both initial guesses produce the same solution, although they are very different, indicating that the solutions are at least a good local minima. All solutions shown are with 125 control intervals/collocation points. In the following the initial guess from idle to 100kW is used.

WITH TIME VARYING CONSTRAINTS

The benchmark problems defined by (7)-(9) are solved using ACADO and PROPT, and the solutions from the two solvers are shown and compared in Fig. 1, where $\omega_{ice/tc}$ is engine speed and turbocharger speed, $p_{im/em}$ intake and exhaust manifold
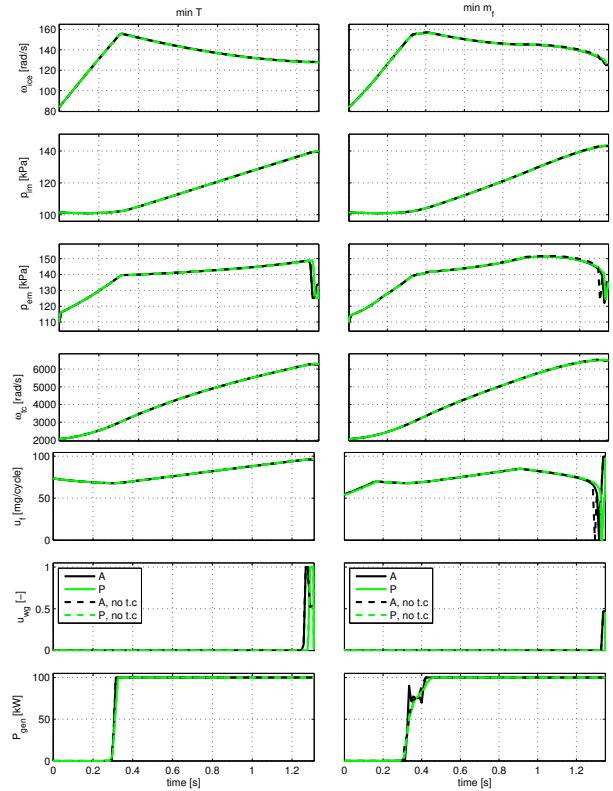
Figure 1: Minimum time (left) and minimum fuel (right) solutions to the benchmark problem using PROPT (P) and ACADO (A) with and without(no t.c) time varying constraints.
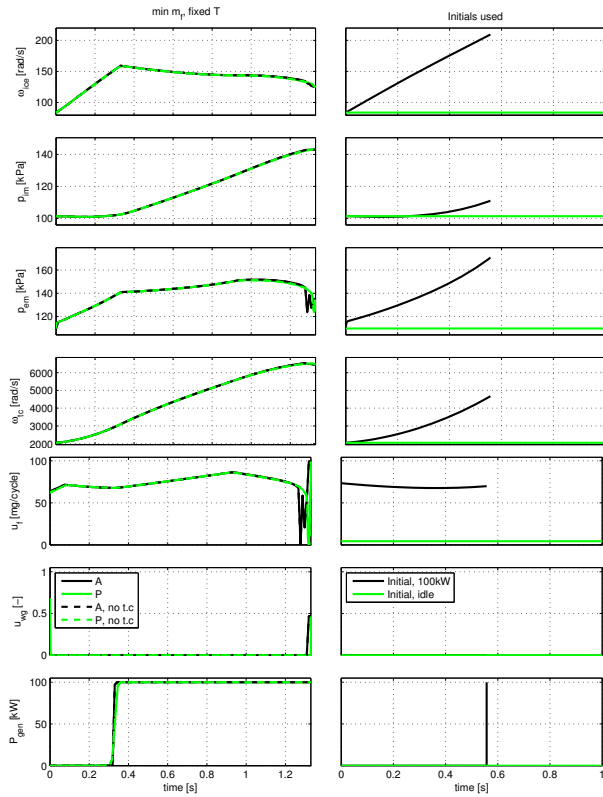
Figure 2: The fixed time solutions using PROPT (P) and ACADO (A) (left) with and without(no t.c) time varying constraints, as well as the different initial guesses used (right).

Criteria	Tool	m_f	T
min m_f	P	6.5917398e-03	1.3498815e+00
	A	6.5977572e-03	1.3497437e+00
min T	P	6.6392313e-03	1.3103439e+00
	A	6.6466370e-03	1.3110366e+00
min m_f, fixed T	P	6.5933240e-03	1.3300000e+00
	A	6.6005188e-03	1.3300000e+00

Table 3: Time and fuel consumption to the benchmark problems using both PROPT (P) and ACADO (A).
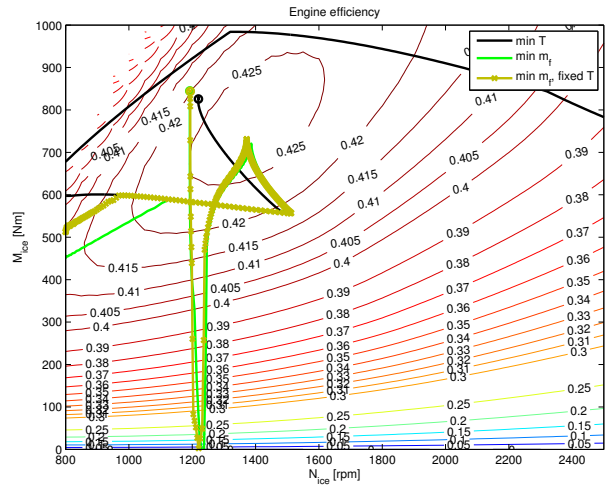
Figure 3: Torque-engine speed trajectories for the three benchmark problems.

pressure, $u_f/u_{wg}/P_{gen}$ are the controls, i.e. injected fuel mass per cycle, wastegate position, and output power from the generator. The min m_f problem is also solved with fixed end time, T. For this a duration between the time optimal and fuel optimal durations is selected, $T = 1.33$. The solution with fixed end time is shown in Fig. 2-left.

Both solvers produce qualitatively the same solutions, there are however some differences owing to discretization technique employed as well as solution method. The resulting consumptions are shown in Table. 3. For further comparison all three solutions using PROPT are shown in torque-engine speed domain in Fig. 3.

Looking at Fig. 1 the trajectories for min m_f and min T are a bit different. For min T u_f follows the smoke-limit, i.e. $\phi = \frac{1}{\lambda_{min}}$, during the entire transient, whereas for min m_f it is only smoke-limited $0.17 \leq t \leq 0.91$ and $t = T$. During the initial acceleration engine efficiency is instead maximized, clearly seen in Fig. 3. The min T solutions apply

a step in P_{gen} from $0 \rightarrow 100$ kW whereas the min m_f P_{gen} actuation is a slightly later and not in a step from $0 \rightarrow 100$ kW. At the end of the transient the min m_f use both u_f and u_{wg} to bring the states to stationarity whereas min T only uses u_{wg}. Noteworthy is that none of the solutions end in the peak efficiency operating point, neither of the GenSet nor of the ICE.

The min m_f, fixed time, solutions are as expected a mix between the min T/m_f solutions. The P_{gen} actuation follows that of min T but u_f and u_{wg} are more similar to min m_f. u_f during the initial acceleration does however not follow the maximum efficiency trajectory but instead follows a trajectory between this and the smoke-limit, see Fig.1.

WITHOUT TIME VARYING CONSTRAINTS

In the problems solved in Section the only time varying constraint that is active is the smoke-limiter,

Criteria	Tool	m_f	T
min m_f	P	6.5916926e-03	1.3497981e+00
	A	6.5985144e-03	1.3493627e+00
min T	P	6.6394831e-03	1.3103321e+00
	A	6.6468526e-03	1.3104947e+00
min m_f, fixed T	P	6.5930972e-03	1.3300000e+00
	A	6.6000832e-03	1.3300000e+00

Table 4: Time and fuel consumption to the benchmark problems without time varying constraints using both PROPT (P) and ACADO (A).

i.e. the constraint on ϕ. The others can therefore be removed without affecting the solution. For the problem without (9) to be relevant, i.e. the problem defined by (7)-(8), the smoke-limiter needs to be included. To achieve this without state-dependent time varying constraints the model is reformulated so that ϕ is a control signal and u_f calculated from it. Since $\phi = \frac{\dot{m}_f}{\dot{m}_{ac}}(A/F)_s$ and $\dot{m}_f = \frac{10^{-6}}{4\pi} u_f \omega_{ice} n_{cyl}$ the model can be reformulated to:

$$\dot{m}_f = \frac{\phi \dot{m}_{ac}}{(A/F)_s} \tag{10}$$

$$u_f = \frac{4\pi}{10^{-6}} \frac{\dot{m}_f}{\omega_{ice} n_{cyl}} \tag{11}$$

and with ϕ replacing u_f as control signal all the time varying constraints are removed. The solutions to the problem without time varying constraints follow, as expected, the same discussion as with time varying constraints. The results are also shown in Fig. 1-2 but the trajectories end up on top of eachother. The fuel and time consumptions are shown in Table 4. The reformulation leads to slightly different numerical values but the difference is negligible.

CONCLUSION

In this paper an optimal control benchmark is suggested and presented. The benchmark concerns transient optimization of a diesel-electric powertrain, from idle to a target power and energy. The benchmark makes use of a freely available four state-three control nonlinear model of a diesel-electric powertrain. Both the model and the initial guesses used are available for download in the **LiU-D-El+Benchmark**-package from [4]. The benchmark is available in several versions, both with and without time varying constraints, as well as with and without time as a parameter.

REFERENCES

[1] Martin Sivertsson and Lars Eriksson. Modeling for optimal control: A validated diesel-electric powertrain model. In *Abstract submitted to SIMS'14 - 55th International Conference on Simulation and Modelling*, Aalborg, Denmark, 2014.

[2] Boris Houska, Hans Joachim Ferreau, and Moritz Diehl. ACADO toolkit - an open source framework for automatic control and dynamic optimization. *Optimal Control Applications & Methods*, 32(3):298–312, 2011.

[3] TOMLAB. PROPT - Matlab Optimal Control Software, "http://www.tomdyn.com/", 2012.

[4] Vehicular systems software. "http://www.fs.isy.liu.se/Software/", 2014.

[5] Martin Sivertsson and Lars Eriksson. Optimal transient control trajectories in diesel-electric systems-part 1: Modeling, problem formulation and engine properties. *Journal of Engineering for Gas Turbines and Power*, Accepted for publication.

[6] Martin Sivertsson and Lars Eriksson. Optimal transient control trajectories in diesel-electric systems-part 2: Generator and energy storage effects. *Journal of Engineering for Gas Turbines and Power*, Accepted for publication.

A HOMOGENEOUS DYNAMIC TWO-PHASE FLOW MODEL OF A VERTICAL EVAPORATOR WITH VARYING FIRING PROFILES

Axel Ohrt Johansen[*]
Added Values P/S, Lysholt Allé 10
7100 Vejle
Denmark

Brian Elmegaard
Technical University of Denmark
Department of Mechanical Engineering
2800 Lyngby
Denmark

ABSTRACT

In this article we would like to demonstrate the ability to simulate the dynamic conditions in a homogeneous two-phase flow model of a power plant evaporator and thus complement the recent years, research efforts in areas related to flexibility of power production. On that basis we can contribute with new knowledge about the flow stability and dynamic effects in power plants, caused by both internal and external physical conditions, resulting in improved power plant flexibility. In this article is developed numerical model for solving a transient one dimensional compressible homogeneous two phase model, for predominantly one-dimensional flows in a vertical heated pipe element. The homogeneous model is based on the assumption of both hydraulic- and thermal equilibrium. The flow model consists of three hyperbolic fluid conservation equations; continuity, momentum and energy and the pipe wall is modelled as a one dimensional heat balance equation. The models is reformulated in the four in-dependent variables: pressure, enthalpy, velocity and wall temperature. We have implemented and tested a fifth-order WENO solver, with simplified weights functions and used it to simulate the dynamic response of evaporator tubes corresponding to SKV3, on the basis of a calibrated model, based on measurements from SKV3. The model is able to describe the entire evaporation process from sub-cooled water to super-heated steam at the outlet and verify the consequences of different firing profiles and evaporator presure for the boiler of SKV3 .

Keywords: Two-phase flow, evaporator, WENO scheme, heat flux bias, dynamic responce

NOMENCLATURE

A	Cross-sectional flow area of pipe	m^2
c	Volume fraction of layer	—
c_p	Specific heat capacity (fixed p)	$kJ/kg/^oC$
c_v	Specific heat capacity (fixed v)	$kJ/kg/^oC$
C	Virtual mass force coefficient	—
e	Specific energy	m^2/s^2
F	Force	N
f	Shear stress (friction force)	N/m^2
g	Acceleration due to gravity	m/s^2
G	Mass flux	kg/m^2s

---
[*]Corresponding author: Phone: +45 2447 9455 E-mail:aoj@addedvalues.dk

h	Enthalpy	$kJ/kg/^{o}C$
k	Thermal conductivity	$W/m/^{o}C$
l	Length of pipe/geometry/film	m
$\dot{M}$	Mass flux	$kg/m^{2}/s$
$\dot{m}$	Mass flow rate	kg/s
p	Pressure of fluid	Pa
q	heat flux	W/m^{2}
Q	heat uptake	W
R	Radius of pipe	m
S	Perimeter wetted	m
t	Time coordinate	s
T	Temperature (absolute)	^{o}C
u	Axial flow	m/s
v	Redial flow velocity	m/s
x	Dryness (steam quality)	$-$
z	Spatial coordinate	m

SUBSCRIPTS
d	Diffusion term
e	Evaporation
f	Flow / Fluid conditions
p	Constant pressure (p)
s	Source term
w	Wall conditions

ABBREVIATIONS
$AVV2$	Avedøreværket Unit 2
CFD	Computational Fluid Dynamics
CFL	Courant-Friedrichs-Levy
$DONG$	Danish Oil and Natural Gas
EOS	Equation of State
FEM	Finite Element Method
$IAPWS$	International Association for the Properties of Water and Steam
$IRBT$	Internally rifled boiler tubes
PDE	Partial Differential Equation
$SKV3$	Skærbækværket Unit 3, Denmark
TSO	Transmission system operator
VHP	Very High Pressure Turbine - Skærbækværket Unit 3, Denmark
$WENO$	Weighted Essentially Non-Oscillatory

INTRODUCTION

The deregulation of electricity markets and the massive investments in renewable energy in Europe have increased the request for flexibilization of large central power plants. Denmark was the first country re-

ally to experience the challenges that the stochastic nature of wind impose on the electricity systems. The challenges with renewable sources began in west Denmark as early as around the year 2000 and have ever since just increased as more wind farms have been commissioned. The average generation from renewables in Denmark is some 33.2 % by 2013, according to the annual energy statistics from the Danish TSO (Energinet.dk). In December 2013, wind power for the first time reached a level corresponding to more than half of the electricity consumption (54.8 per cent). The Danish politicians have set the objective of 50 per cent wind power in relation to the electricity consumption by 2020. Looking beyond Denmark's borders, Germany is about to impose even greater challenges up on themselves and their thermal power plants. They have invested massively in renewables, both wind and photovoltaic generation, and plan to have all nuclear generation phased out by 2023. Both Denmark and Germany already have massive challenges with the momentarly balancing of power consumption and generation which is a prerequisite for a stable power system. To balance consumption and generation it is necessary to operate the thermal power plants 'as the wind blows and the sun shines'. The flexibility requirements impose on thermal units are especially:

- The request for lower minimum load such that the units are ready to ramp up if the generation from renewables suddenly fails (e.g, forecast errors)

- The request for faster start-up (again typically forecast errors)

- The request for larger ramping rates (typically because fewer units are in operation but the total demanded load gradient remains the same)

All three flexibilization initiatives mentioned above are important for the inclusion of even more renewables. However, if one digs further into the technical challenges, it becomes clear that the lower stable minimum boiler load is one of the most important issues for the flexibility-optimisation and thus the integration of renewables.

MOTIVATION

Danish central power plants are all once-through boilers of the Benson type. The water walls are typically constructed of some 200 tubes connected in parallel, running from hopper to furnace outlet with an inclination angle of approximately 15 degrees. Each of these tubes must at any instant be sufficiently cooled at any location along the tube. Normally this corresponds to a tube mass flux rate of 700-800 [kg/s/m^2] at minimum stable generation and 2000-2500 [kg/s/m^2] at rated capacity (Effenberger, [1], p. 518). If cooling fails for a certain time, the tube in question will be damaged (material creep and cyclic hoop stress) and eventually burst. Consequently, each power plant has a minimum feed water flow rate, which must be respected in order to avoid trip of the plant. Typically, the boiler is tripped after only 10 seconds, if the flow rate is too low. This trip criterium is very problematic and imposes huge challenges for the control engineer at low load operation, for example, during start-up/shut-down of the second feed pump or during swelling.

LITERATURE REVIEW

Much effort has been put into modelling evaporators. Focus was especially on the dynamic regulatory technical features of the power plant boilers, but there is not much literature on dynamic modelling of the evaporation process in the power plant boiler and the consequent load limits. There are some references about experimental studies of evaporators, and much of this material is based on standards and is well documented in [7]. In [8] there is the modeling of a complete circuit distribution of a flow network system in a water wall of an ultra-supercritical boiler with vertical tubes. The model is steady, state and good agreement is achieved between the calculated mass flux distribution in the lower front wall and the plant data; the maximum relative difference is between 5.6 and 9.7 %. A dynamic evaporator model, which is able to simulate the entire vaporization process, including the sub-cooled liquid at the entrance and super-heated fluid at the outlet, has not been seen in published literature, due to the complexity around the saturation curve, which basically includes a singularity in the gradient of the density. With respect to internal rifled boiler tubes (IRBT),

Harald Griem, [9] wrote back in 1985 on the subject, and both KEMA, [10] and Siemens have performed considerable experimental work that is considered proprietary information, see [11] and [12]. Other authors have dealt with the experimental topic, with special focus on smooth and internal rifled boiler tubes; see [13], [14], [15] and [16]. Here consistent algebraic function terms are developed for the frictional pressure drop and heat transfer in smooth and IRBT. A thermo-hydraulic analysis of an ultra-supercritical boiler at full load is performed in [8], but no studies of part load conditions.

MODEL LAYOUT

The following section presents a mathematical model for both fluid and pipe wall of a circular evaporator.

1D - fluid model

A homogeneous model consists of three conservation equations given by (1), (2) and (4), which is formulated in the three non-dependent variables ρ(density), $\dot{m}$(mass flow) and E(internal energy), where the dependant variables z $\in$ [0 ,..., l_z] and t $\in$ [0 ,..., ∞[. For $\dot{m} = \bar{\rho}$uA we find:
Continuity equation:

$$\frac{\partial}{\partial t}(\bar{\rho}A) + \frac{\partial}{\partial z}(\dot{m}) = 0 \qquad (1)$$

Momentum equation:

$$\frac{1}{A}\frac{\partial}{\partial t}(\dot{m}) + \frac{1}{A}\frac{\partial}{\partial z}(\dot{m}u) = -\frac{\partial \bar{p}}{\partial z} - \bar{\rho}g\cos(\theta) - F_w \qquad (2)$$

where $F_w = \frac{S_w}{A}\tau_w$, and the wall shear stress (τ_w) is typically expressed as:

$$\tau_w = \frac{1}{2}f_w\rho|u|u. \qquad (3)$$

Energy equation:

$$\frac{\partial}{\partial t}\left(\bar{\rho}A\bar{h} + \frac{1}{2}\bar{\rho}Au^2 - pA\right) + \frac{\partial}{\partial z}\left(\dot{m}\bar{h} + \dot{m}\frac{1}{2}u^2\right) \qquad (4)$$
$$= \dot{q}_rS_w - \dot{m}g\cos(\theta).$$

Then equation (4) can be reformulated by using the definition of the total specific convected energy: $\bar{e} = \bar{h} + 1/2u^2 + gz\cos(\theta)$, and by using the continuity equation to eliminate the gravitational terms on the left side, we find:

$$\frac{\partial}{\partial t}\left(A(\bar{\rho}\bar{e} - \bar{p})\right) + \frac{\partial}{\partial z}\left(\dot{m}\bar{e}\right) = \dot{q}_r S_w - \dot{m}g\cos(\theta) \quad (5)$$

where $\dot{q}_r$ represents the heat flux per unit surface area through the outer wall of the tube. The internal energy E is given as: $E=(\bar{\rho}\bar{e} - \bar{p}) \cdot A$, which is measured in [J/m].

The independent variable t represents the time in [s], and z is the spatial coordinate referring to the flow direction of the fluid given in [m]. The dependent variables are $\bar{\rho}$, $\dot{m}$ and e, meaning the fluid density, mass flow and total energy of the conserved fluid, respectively. The pressure can be determined iteratively by water steam tables: $p = \mathrm{p}(e, \bar{\rho})$. A is the tube cross-section area, measured in [m^2]. The source term g_s consists of both source/sink terms related to gravity- and wall friction forces. The diffusion term g_d includes a contribution from the mixing length eddy viscosity (l^2=0.01 [m^2/s]), working as a damping term in the vicinity of the saturation line of water. A recommended size of attenuation area is found to be $x_e \in [-0.01, 0.01]$. The internal energy e is given as: $e = (\rho\bar{E} - p) \cdot A$, which is measured in [J/m]. Here the fluid temperature T_f is a function of $\bar{\rho}$ and h. The constitutive relations due to the thermodynamic properties are based on IAPWS 97, and are interpolated in a bilinear scheme, described in [5] for minimising the computational work. Note that the gravity is reduced according to the heat pipe inclination ($\sin(11.4^o)$) on the SKV3 boiler.

1D - pipe wall model

The solution of problems involving heat conduction in solids can, in principle, be reduced to the solution of a single differential equation, the heat conduction equation. As an alternative, we could use a two dimensional model to describe the spatial temperature resolution of the pipe material. The single-layer equation can be derived by making a thermal energy balance on a differential volume element in the solid. A volume element for the case of conduc-

tion only in the z-direction is illustrated in figure (1).
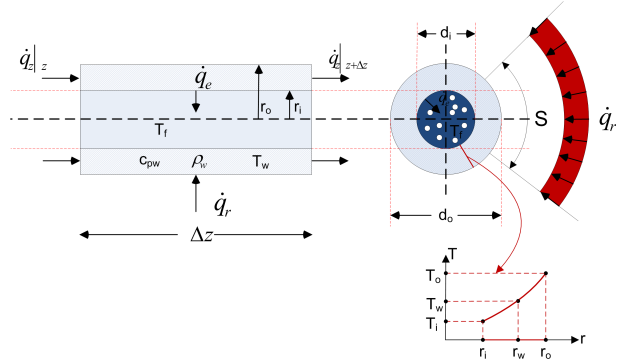
Figure 1: Energy transfer and heat flow terms on a slice of a pipe wall element.

The generation term is set to zero, but could be an electric current or the decay of a radioactive material. The rate at which thermal energy enters the volume element across the face at z is given by the product of the heat flux and the uniform cross-sectional area, $\dot{q}_z|_z A_c$, where $A_c = \pi(d_o^2 - d_i^2)/4$. Similarly, the rate at which thermal energy leaves the element across the face at z + Δz is $\dot{q}_z|_{z+\Delta z}A_c$. For a homogeneous heat source/sink of strength $\dot{q}_r$ per unit area, the net rate of generation is $\dot{q}_r$ S Δz, where S is the pipe perimeter of impact. Finally, the rate of accumulation is given by the time derivative of the thermal energy content of the volume element, which is $C_{pw}\rho_w(T - T_{ref})A_c$, where T_{ref} is an arbitrary reference temperature. Thus, the balance equation becomes:

$$\Delta z\, \rho_w\, C_{pw}A_c \frac{\partial T_w}{\partial t} = (\dot{q}_z|_z - \dot{q}_z|_{z+\Delta z})A_c$$
$$+ \dot{q}_r S\Delta z - \dot{q}_e d_i \pi \Delta z \quad (6)$$

where C_{pw} and ρ_w are the heat capacity and the density of the pipe wall, given by equation (9). By dividing (6) by Δz and letting $\Delta z \to 0$, we get a first-order PDE describing the energy balance in the pipe element as a function of t and z.

$$\rho_w\, C_{pw}A_c \frac{\partial T_w}{\partial t} = -A_c\frac{\partial \dot{q}}{\partial z} + \dot{q}_r S - \dot{q}_e d_i \pi \quad (7)$$

The heat flux $\dot{q}$ per unit area can be expressed via the Fourier formula: $\dot{q} = -k_w\frac{\partial T_w}{\partial z}$, where k_w is the thermal conductivity measured in [w/mK]. For isotropic

materials, we use the thermal diffusivity given by: $\alpha = \frac{k_w}{\rho_w C_{pw}}$ in $[m^2/s]$, which in a sense is a measure of thermal inertia and expresses how fast heat diffuses through a piece of solid. For a typical panel wall, the thermal diffusivity is approximately $1.98 \cdot 10^{-6}$ $[m^2/s]$ at $200°C$; see [25]. Hence the energy balance for the isotropic pipe wall can be described by:

$$\frac{\partial T_w}{\partial t} = \alpha \frac{\partial^2 T_w}{\partial z^2} + \frac{\dot{q}_r}{\rho_w\,C_{pw}}\frac{S}{A_c} - \frac{\dot{q}_e}{\rho_w\,C_{pw}}\frac{d_i\pi}{A_c}, \quad (8)$$
$$z \in [0, l_z] \wedge t \geq 0$$

where $\dot{q}_r$ is the radiation from the furnace and $\dot{q}_e$ is the convective heat transfer between the flowing fluid in the pipe and the pipe wall inner surface, $\dot{q}_e = h(T_w - T_f)$. The convective heat transfer coefficient is named h, and the driving temperature difference is given by the temperature difference between the wall mean temperature (T_w), outlined in equation (10), and the mixture fluid temperature (T_f). For isotropic materials, we have expressions of C_{pw}, k_w and ρ_w as a function of temperature in Kelvin from [25] and [26]:

$$C_{pw} = 6.683 + 0.04906 \cdot T + 80.74 \cdot \ln(T) \text{ [J/kgK]}$$
$$k_w = 9.705 + 0.00176 \cdot T - 1.60 \cdot 10^{-6} \cdot T^2 \text{ [w/mK]}$$
$$(9)$$
$$\rho_w = 7850 \text{ [kg/}m^3] \text{ at } 20°C \text{ for 13CrMo44}$$

and the wall mean temperature is estimated to:

$$T_w = \frac{1}{A_c} \int_{r_i}^{r_o} 2\pi r \cdot T(r) dr \quad (10)$$
$$= a_1 \cdot T_i + (1 - a_1) \cdot T_o$$

where $T(r)$ is given by (17) and a_1 is given by

$$a_1 = \frac{r_i^2}{r_i^2 - r_o^2} - \frac{1}{2 ln(r_i/r_o)} \quad (11)$$

The wall density is assumed constant in temperature T. A simple, fast and robust model of the heat transfer in film boiling is given by [27]. The heat transfer coefficient h_{fb} is given by equation (12). The single-phase laminar heat transfer coefficient is calculated from equation (14).

$$\alpha = c_1 \dot{q}^{0.673} \quad [W/m^2 K] \quad (12)$$

where the coefficient c_1 is given as

$$c_1 = \frac{0.06136}{\left[1 - \left(\frac{T_s}{378.64}\right)^{0.0025}\right]^{0.73}} \quad (13)$$

The single phase laminar heat transfer coefficients is calculated from

$$Nu_s = \frac{h_s d_i}{k_f}$$
$$= 4.36 \quad (14)$$

The total heat transfer coefficient is given by (15), and consists of two contributions: one from the convective heat transfer boundary layer associated to the flowing fluid inside the heat pipe and one that relates to conduction through the pipe wall material:

$$h = \frac{1}{\frac{1}{h_c} + \frac{r_i}{k_w} \cdot \ln(r_w/r_i)} \quad (15)$$

where h_c expresses the heat transfer coefficient due to the thermal boundary on the inner side of the pipe wall and r_w is defined by $T_w = T(r_w)_z$. h_c is smoothed in-between h_s and h_{fb} depending of the dryness (x) of the fluid.

$$h_c = \begin{cases} h_s & \text{for } x > 1 \vee x < 0 \\ \\ h_{fb} & \text{for } 0 \geq x \leq 1 \end{cases} \quad (16)$$

Additionally, h_c is adjusted on the basis of a smoothing between laminar and turbulent single-phase flow as well as for two-phase flow. The smoothing function is described in [2] and is of second-order. The associated slopes are determined numerically. Since we use the calculated average wall tube temperature as the driver in the calculation of the total heat transport to the fluid, we must know r_w. Due to the knowledge of radial conduction in the pipe, we use a simple analytical wall temperature profile for estimating the inner wall temperature, expressed by the averaged wall temperature (T_w), based on the heat transfer through the isotropic pipe wall to the flowing fluid given by equation (10). Let $T(r)_z$ represent the radial temperature distribution in the isotropic pipe wall by, which can be rewritten as

$$T(r)_z = a_0 \ln(\frac{r}{r_o}) + T_o \quad (17)$$

where $a_0 = \frac{T_i - T_o}{\ln(\frac{r_i}{r_o})}$ and r is the pipe radius with suffix (i=inner) and (o=outer). Hence, for small values of the thermal diffusivity, the averaged wall temperature can reasonably be estimated by equation (10). Hence the entire heat transfer can be estimated for the temperature range in-between the wall

mean temperature (T_w) and the fluid mixture temperature (T_f), which is assumed homogeneous and well mixed with a temperature boundary layer represented by h_c. The one dimensional pipe wall model only consists of the axial heat transfer term, and has no spatial resolution in the radial dimension.

The inner wall temperature (T_i) can be determined by use of the equation for pure conduction through the pipe:

$$\dot{q}_r S = \frac{2\pi k_w}{\ln(r_o/r_i)}(T_o - T_i) = \frac{2\pi k_w}{\ln(r_w/r_i)}(T_w - T_i) \ [w/m].$$
(18)

Hence we find T_i by insertion (17) in (18):

$$T_i = T_w - \frac{q_r S \ln(\frac{r_o}{r_i})(1 - a_1)}{2\pi k_w}$$
(19)

where a_1 is given by equation (11). Hence r_w in (15) can be determined from (17) and (19) and we find

$$h = \frac{1}{\frac{1}{h_c} + \frac{r_i(a_1 - 1)}{k_w} \cdot \ln(r_i/r_o)}$$
$$= \frac{1}{\frac{1}{h_c} + \frac{r_i}{k_w} \cdot \ln(r_w/r_i)}$$
(20)

Note that the heat flux is positive for $T_i > T_f$. Using the model parameters for the panel wall of SKV3 (from table (1)), we find a_1=0.423 and the temperature fall above the pipe wall is: T_o-T_i=27.9 [^oC], which gives a temperature gradient in the pipe wall of dT/dr= 3930 [$^oC/m$] for a heat flux of $\dot{q}_e$=100 [kW/m^2]. The heat conduction in the material is the most significant barrier for an effective cooling of the tube wall.

MODEL SETUP

A homogeneous model, is described in this article and is solved using the numerical algorithms based on a fifth-order WENO scheme, with corresponding diffusion and source term. The numerical method is briefly outlined in the Appendix and consists of 400 computational points with a CFL number of 0.8. A third-order TVD time integrator is used, for reasons of ensuring a high numerical stability as well as minimizing the time-consumption in the calculations. The numerical scheme is tested for consistency and stability with respect to both a scalar model and a system of hyperbolic equations

and both have been successfully compared to analytical results, from the literature as well as other published results. This work is outlined and published in [5]. Three Dirichlet boundary conditions are applied for the hydraulic case and two Neumann boundaries are applied for the thermal pipe wall model, given as zero gradients in the wall temperature at each pipe end (no heat loss).

The intention is to model an evaporator, that can induce pressure and density oscillations initiated by the compressibility, arising as a result of a phase shift in the lower part of the evaporator. Therefore, we apply a constant downstream Dirichlet pressure boundary condition that corresponds to a stiff system downstream the evaporator tube, meaning without any pressure absorption effects from compressibility in the downstream turbine system. A good analogy for this is a geyser, with a constant surface pressure and an intense heat absorption in the bottom region, whereby an oscillating pressure wave is initiated due to the compressibility and density reduction of the fluid, caused by intense heat from the underground. Additionally we force the model with both a constant enthalpy and mass flux located on the upstream boundary, supplied by a heat flux profile along the entire heat pipe.

The model is gently started (soft start) in two steps: at t=0 [s] the pure hydraulic model is gently started over 4 seconds, without heat flux. After ten seconds of simulation, the heat flux is built-up during four seconds to 100 [kW/m^2], in accordance with the operating observations obtained at SKV3. This is done to avoid heavy shock waves moving forward and back in the entire solution domain. The computational results are stored as line series for an equidistant time step and as time series at two stations, located at z_A=$\frac{l_z}{8}$ and z_B=$\frac{7l_z}{8}$, named stations A and B, respectively, where l_z is the total tube length.

The dynamic start-up process for a constant linear heat flux profile can be seen in figures (2) and (3), where the density is given in [kg/m^3], pressure in [bar], temperature in [^oC], enthalpy in [kJ/kg] and mixture velocity in [m/s].
Note that the temperature curves for the fluid and the pipe wall both refer to the same temperature

scale corresponding to the red fluid temperature scale on the right-hand side of the graph. This fact is applied in the whole paper. The soft start model is based on a third-order theory outlined in [2], which gives a C^2 continuous sequence, which means zero gradients of the first derivative at both ends of the soft start period. The *system of balance laws* (SBL) for the evaporator model is given in a compact vector notation:

$$\frac{\partial \Phi(z,t)}{\partial t} + \frac{\partial f(\Phi(z,t))}{\partial z} = g_s(\Phi(z,t)) \qquad (21)$$
$$+ g_d\left(\frac{\partial \Phi}{\partial z}, \Phi(z,t)\right),$$
$$\Phi \in R^m, m = 4, \quad t \geq 0 \wedge \ z \in \Omega$$

where the dependent variable Φ and the flux vector f are given as:

$$\Phi = \begin{pmatrix} \bar{\rho}A \\ \dot{m} \\ \bar{e} \\ T_w \end{pmatrix}, \quad f(\Phi) = \begin{pmatrix} \dot{m} \\ \frac{\dot{m}^2}{\bar{\rho}A} + \bar{p}A \\ \frac{(\bar{e}+\bar{p}A)\dot{m}}{\bar{\rho}A} \\ 0 \end{pmatrix}$$

and the source and diffusion vector are given as:

$$g_s(\Phi) = \begin{pmatrix} 0 \\ \bar{p}\frac{\partial A}{\partial z} - \bar{\rho}gA\cos\theta - \sqrt{\frac{\pi}{A}}f_w\frac{\dot{m}|\dot{m}|}{\bar{\rho}A} \\ S_w\dot{q}_e - \dot{m}g\cos(\theta) \\ \frac{\dot{q}_r}{\rho_w\,C_{pw}}\frac{S_w}{A} - \frac{\dot{q}_e}{\rho_w\,C_{pw}}\frac{d_i\pi}{A} \end{pmatrix} \quad \text{and}$$

$$g_d(\Phi) = \begin{pmatrix} 0 \\ \frac{l^2 S_w}{\bar{\rho}A^3}\frac{\partial \dot{m}^2}{\partial z^2} \\ 0 \\ \alpha\frac{\partial^2 T_w}{\partial^2 z} \end{pmatrix}$$

The independent variable t represents the time in [s], and z is the spatial coordinate referring to the flow direction of the fluid given in [m]. The dependent variables are $\bar{\rho}$, $\dot{m}$ and e, meaning the fluid density, mass flow and total energy of the conserved fluid, respectively. The pressure can be determined iteratively by water steam tables: $p = p(e, \bar{\rho})$. A is the tube cross-section area, measured in [m^2]. The source term g_s consists of both source/sink terms related to gravity- and wall friction forces. The diffusion term g_d includes a contribution from the mixing length eddy viscosity (l^2=0.01 [m^2/s]), working as a damping term in the vicinity of the saturation line of water. A recommended size of attenuation
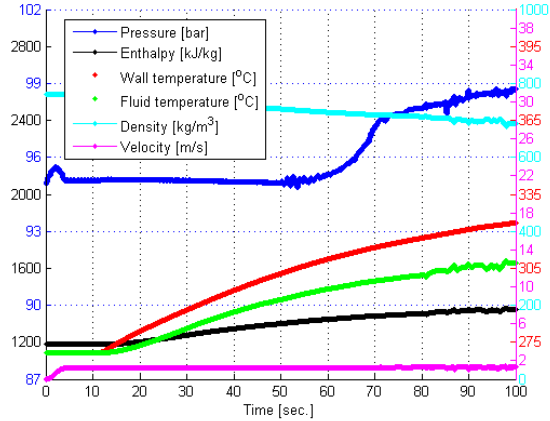

Figure 2: Soft start response of SKV3 evaporator model @ station A.
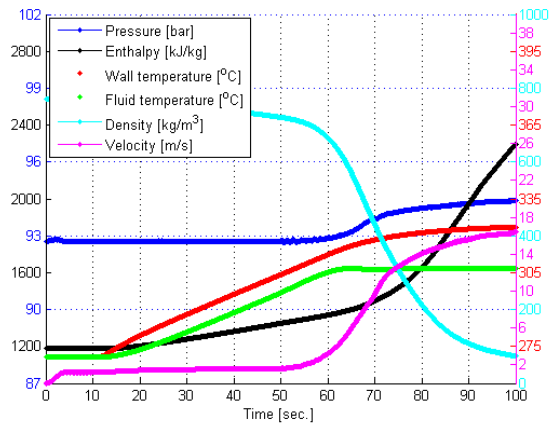
Figure 3: Soft start response of SKV3 evaporator model @ station B.

area is found to be $x_e \in [-0.01, 0.01]$. Here the fluid temperature T_f is a function of $\bar{\rho}$ and h. The constitutive relations due to the thermodynamic properties are based on IAPWS 97. To improve the computational speed it is recommended to use a bilinear interpolation; see [5], where we create a look-up table within approximately 160000 nodes, which ensures an accuracy below 4% as an absolute maximum, due to a smoothing of the interpolated properties in the vicinity of the saturation line. It is only in the vicinity of the saturation line of water, where we experience an significant error; otherwise the averaged relative error is below 0.3%.

Parameter	Value	Unit
Gravity (g) - projected	1.9399	[m/s^2]
Spatial start position	0.000	[m]
Spatial end position (L)	193.499	[m]
Inner diameter of pipe (d_i)	23.8	[mm]
Outer diameter of pipe (d_o)	38.0	[mm]
Heat conductivity in wall (k_w)	20.278	[w/mK]
Wall density (ρ_w)	7850.0	[kg/m^3]
Specific heat capacity of pipe wall (Cp_w)	527.21	[J/kg/K]
Heat flux ($\dot{q}_e$)	100.0	[kW/m^2]
Wall roughness (λ)	1.0E-6	[m]
Initial Enthalpy - left side	1187.6988	[kJ/kg]
Initial Enthalpy - right side	1187.6988	[kJ/kg]
Initial Pressure - left side	92.3762	[Bar]
Initial Pressure - right side	92.3762	[Bar]
Initial Velocity - left side	0.0	[m/s]
Initial Velocity - right side	0.0	[m/s]
Pressure BC (Dirichlet - right side)	92.3762	[Bar]
Enthalpy BC (Dirichlet - left side)	1187.6988	[kJ/kg]
Velocity BC (Dirichlet - left side)	1.1711	[m/s]
Simulation time	400.0	[s]
Output frequency	0.1	[s]
CFL number	0.80	[-]
Number of computational grids (N_p)	400	[-]
Slip Correction Factor	1.0	[-]

Table 1: Geometrical and numerical specifications for SKV3 heat pipe.

Model calibration

The hydraulic model is calibrated in relation to the static operating data, which are available from SKV3; see table (2).

Sample nr.	$\dot{m}$	h_{in}	h_{out}	$\dot{q}$	p_{in}	p_{out}	Δp	Load
Units	[kg/s]	[kJ/kg]	[kJ/kg]	[MW]	[bar]	[bar]	[bar]	[%]
1	195.46	1514.27	2894.32	269.75	244.20	230,05	14.15	80.5
2	258.11	1566.09	2835.05	335.27	325.20	306.29	18.91	100.0
3	89.54	1169.20	2819.71	140.48	110.89	105.58	5.31	41.9
4	90.04	1187.70	2720.25	137.99	96.87	92.38	4.49	41.2

Table 2: Mean values for heat and pressure balance for four samples at SKV3.

As a basis we focus on a model that works in part load, i.e., where we simulate the entire two-phase process in the evaporator, including sub-cooling and superheating. We aimed as a basis for the calibration simulation a heat flux value of approximately 83.8 [kW/m^2], according to the average flux received by the evaporator in sample 4. The only calibration parameter we are dealing with, is the wall friction, which is determined by a hydraulically smooth industrial boiler tube (The surface roughness is negligible.) The tube length is estimated to be a total of 193.5 m, including various bends and junction boxes. We calculate the upstream pressure in the steady state condition to approximately 97.5 [bar]$\pm$0.2 [bar], which approximately corresponds to the measured upstream pressure in sample 4, 96.87 [bar], - a deviation of approximately 0.5 [bar] for hydraulic smooth pipes. Note that the calculated pressure drop is very sensitive to the specified velocity boundary condition. There appears, however, minor pressure oscillations on the upstream boundary, initiated by a phase shift in the vicinity of the transition area to the two-phase region. Basically, the downstream condition should also reflect the measured static outlet enthalpy of 2764.38 [kJ/kg] and a corresponding steady state mass flow, even before the requirement of static energy balance is ful-filled. Here we are only slightly below the average measured static values, corresponding to an enthalpy of 2701 [kJ/kg] and a mass flow of 0.3807 [kg/s] at the very first computational cell versus 0.3816 [kg/s] at the very last computational cell. Based on the above considerations, we can conclude that the model meet our observations in table (2) (sample 4), although the model is not at completely steady state.

We can see from figure (11) that, e.g., the pressure signal contains oscillations, and the corresponding frequency components are difficult to identify. The signal can be analysed using FFT to find the frequency components of a signal in the time domain. The Matlab FFT spectral density analysis is carried out on a subset of the time series in station B, based on a close-up of the pressure time series measured from 150 [s] to 155 [s] of simulation. We can see that the pressure fluctuations primarily consists of a class of waves with frequencies of $f' \approx 0.25 \cdot n$ [Hz] and with decreasing intensity, where n is a positive integer. This very low frequency periodic process can be classified as pressure-drop oscillations due to

the dynamic interaction between channel and compressible specific volume in the fluid. The maximum wave-length is given by the length of the tube, l_z=193.5 [m] and the corresponding phase velocity $u_f = \lambda \cdot f' \cdot n = l_z \cdot 0.25 \cdot n = 48.4 \cdot n$ [m/s]. From figure (10) we can see that the pressure waves are initiated only 10% upstream the tube which corresponds to a standing wave with a phase velocity of 484·n [m/s]. It is interesting to see that the phase velocity can be identified within the orders of magnitude of the estimated speed of sound in a two-phase flow (250 m/s to 868 m/s @ 95 bar), based on the eigenvalue analysis of the two-layer fluid model developed in the Ph.D. thesis in [5].

Dynamic flow stability

The developed dynamic model is applicable for very different thermo-hydraulic problems, and we analyse four different heat flux distributions on the evaporator tube during the start-up phase, where we observe different dynamic pressure responses. The results that are presented in here, are not as clear as expected, but we can observe that start-up of the boiler, from zero flow to full combustion in part load [100 kW/m^2], can lead to slightly different dynamic response from the boiler, when changing firing profile at constant heat uptake as well as reduce the operation pressure of the evaporator. We see a higher degree of density fluctuations upstream the boiler, when low firing is applied, while top firing causes more heat-related fluctuations downstream the evaporator (temperature and enthalpy). The applied load gradients are larger than those we see in the real world; see figure (29) and (30). Also the restrictions with respect to reduced lifetime of thick-walled components, like junction boxes or valves, are not taken into account in this analysis.

Last, we touch upon a situation related to the major challenges that the traditional thermal power plants are facing, in connection with the introduction of renewable energy (sun and wind). With the close bond between district heating and electricity production, which is characterized by a so-called back-pressure plant, it is tempting to reduce the live steam pressure and bypass the high-pressure turbines and thus reduce both electricity production and the evaporator pressure. We see from the calculations that we obviously have a significant

pressure drop in the evaporator. The low-pressure evaporator simulation, with an exit pressure of 46 [bar] compared to a normal pressure of 90 [bar], shows a stable response, which after 180 [s] is in a steady state condition; see figures (23) to (25). The pressure loss is approximately 18 [bar]. It is interesting to see that the homogeneous model takes into account the load gradients of pressure and enthalpy, which can initiate the thermal slugs. It is also interesting to note the presence of thermo slugs in the homogeneous evaporator model. The model is able to resolve the sometimes steep gradients in the tubes, which demonstrates that violent slugs really exist at low operating pressures - even in a homogeneous model.

HEAT FLUX PROFILES

Here follow calculations for investigating how different heat flux profiles affect the dynamics of an evaporator during a start-up period. It is interesting to examine how the flux distribution in a boiler affects the start-up process in a power plant evaporator. Operational experience from SKV3 indicates major start-up problems, which is attempted to be reduced by firing with the top burner floor. We will investigate this in the following, where we examine the dynamic response from the evaporator by four different heat flux profiles. We use a moderate flux distribution coefficient, corresponding to a maximum redistribution of the heat flux of 10% (Δq = 0.1), meaning that the heat flux profile along the tube is altered a maximum of 20 %.

Constant heat flux profile

A constant heat flux profile indicates a constant heat flux on the panel wall, which results in a corresponding effective cooling of the pipe wall and can be used as a reference calculation for the study of different flux profiles. This scenario is of academic interest and reveals a more gentle impact of the evaporator. A constant heat flux profile in the evaporator string is illustrated in figure (4).

The numerical model is configured according to table (1), and the heat flux is specified to 100 [kW/m^2]. A close to static solution is obtained after approximately 400 seconds, and is depicted in figure (5), although a static solution is a truth with
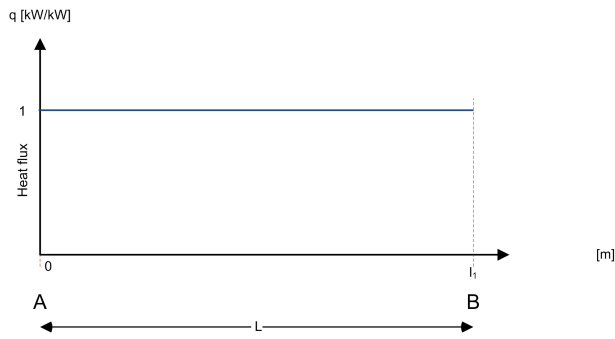
Figure 4: Constant heat flux to boiler.

Figure 5: Solutions of SKV3 evaporator model after (R) 400 [s].

modifications. Small perturbations in pressure and density are constantly induced, because the model is successively fed with the pressure oscillations created from the transition zone of the sub-cooled to the two-phase fluid, where the very large density gradients occur. These oscillations are controlled by artificial diffusion due to the local turbulence model in the area of transition from single to two-phase flow as well as a smoothing of the EOS along the saturation lines. The results show how the state of the fluid gradually moves from the inlet condition, in the form of sub-cooled water, to the two-phase zone, in which the boiling is starting, and finally reaches the super-heating zone, where the dry steam is superheated to about 385 ^oC. The pressure drop is fixed downstream in the form of a Dirichlet boundary condition, corresponding to measured pressure levels from (SKV3). The pressure distribution along the evaporator reflects different pressure loss models, the pressure gradient of single and two-phase regions, respectively. The two-phase region makes use of the two-phase multiplier outlined in [6], which multiplies the pressure gradient with up to 16 times relative to the pressure gradient for saturated water. The inlet velocity is specified as an upstream Dirichlet boundary condition, and is soft started by use of the before-mentioned smooth function, having a soft start period of four seconds. This ensures a smooth hydraulic flow condition of the cold evaporator. After wards, the heating is built up smoothly, applied by the same smoothing technique, so that undesirable thermal shock phenomena are avoided. The super-heated steam leaves the downstream boundary at a steady state flow condition with a speed of approximately 24 [m/s]. Pressure oscillations occur as a result of large upstream fluid compressibility in the flow boiling system; see [17],
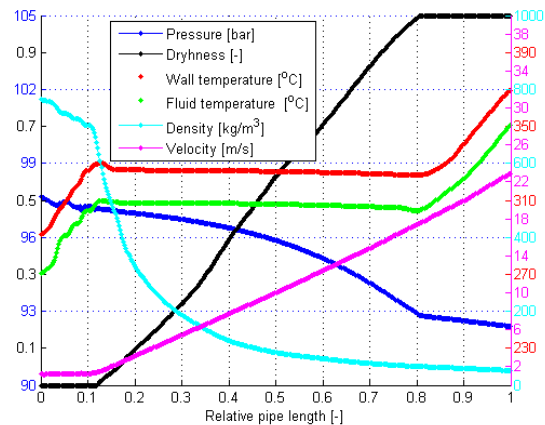
[18]. These pressure oscillations appear in the form of pressure fluctuations, arising from the singularity we experience in the gradient field of the fluid density, when saturation is approached and can be generated in the form of a standing wave in front of the boiling zone of the fluid. The dryness line in figure (5) expresses the mass based percentage of the steam flowing in the evaporator tube; not surprisingly, this process is linearly varying and corresponds to a constant heat flux along the tube.

By reducing the number of computational cells to, e.g., 50 elements, without adjusting the artificial diffusion, one would observe a more intensive standing wave at the entrance of the two-phase region, due to intensive heating of the differential cell in the vicinity of the boiling zone, where we have an intensive negative slope in the density as a function of the enthalpy; hence the density change becomes so violent that a pressure wave is established to ensure momentum balance.

Linear heat flux profile with bottom firing

Operating experience from the SKV3 says that there are inconveniences in the evaporator during start-up when firing low, i.e., when the lower burner roofs are in action during start-up. This enables us to model, by assuming a stylistic heat flux profile, and implement a dynamic thermal hydraulic calculation based on the homogeneous flow model. The profile is illustrated in figure (6), with $\Delta q = 0.1$.
Physically this can lead to massive slug formations

Figure 6: Bottom firing in boiler - linear heat flux to boiler with Δq=0.1.

(pressure and density). We have eyewitness reports from operational staff at SKV3 about how the high-pressure steam line from the evaporator during start-up has moved up to 1/2 meter and in this context has destroyed the insulation around the HP-pipe line and also damaged the associated thermocouples. It is violent forces that are at play, when provoked slugs in the form of density waves o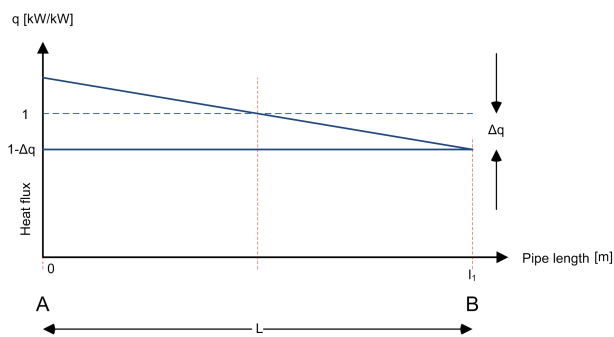r pressure surges act in the steam pipes. Figure (14) shows a dryness profile, which differs from the corresponding simulation with a constant heat flux profile. The difference reflects that the bottom firing case has not yet reached a steady-state condition, and thus is slower to settle into a stable plateau. This emphasizes that the two time series, as illustrated in figures (12 and 13), after 110 [s] from the start of simulation, show considerable density fluctuations in station A and both a strong temperature and a velocity fluctuation in station B. The temperature fluctuations in station B are damped towards the end of the simulation and become stable around 330 [^oC]. Note that both the tube wall temperature and the fluid temperature refer to the same temperature scale on the right axis of figures (12 and 13). Especially temperature fluctuations may be critical with respect to the fatigue of pipe material in general, especially when we draw attention to the material structures on the inner surface of the tube, which are extremely sensitive to temperature fluctuations, due to a short time constant in the evaporator tube. This is compensated to some extent by the thermal diffusion, which smooths the temperature distribution in the pipe wall, here illustrated as an averaged wall temperature. This phenomenon may be an early-stage cracking, particularly in the super-heaters, in which the steam temperature is considerably higher.

Linear heat flux profile with top firing

Operating experience from the SKV3 in particular indicates a greater stability in the evaporator, when the firing is intensified in the top of the boiler. We attempt to model this using a linear heating profile, with the highest heat flux at the top of the boiler. The profile is illustrated in figure (7) and the boiler specifications are similar to the previous setup, except for the reverse heat flux slope with Δq=0.1.
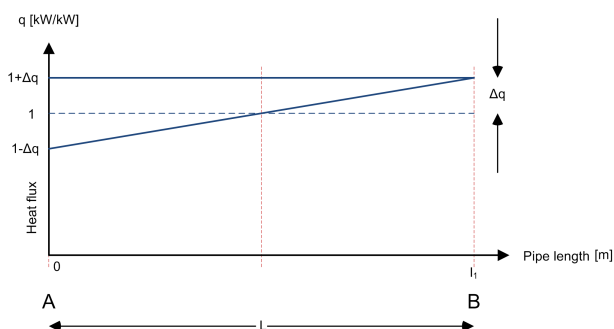
Figure 7: Top firing in boiler with linear heat flux to boiler.

Figure (15) shows an instant picture of the thermodynamic properties of the fluid in the pipe after 200 [s] of real time from the start of the boiler. It is noteworthy that the steam quality is progressing nearly linearly through the evaporator, but has not yet reached a steady state condition. The outlet temperature of the steam is slightly higher than the scenario with low firing. Similarly, we can see a significant difference in both the pressure and the velocity profile compared to the situation with low combustion in the boiler room. The inlet pressure is here approximately 1.5 bar lower, and the steam outlet velocity is only 21 [m/s] compared to 23 [m/s] for the scenario with low firing. Also in this scenario one can see violent fluid temperature fluctuations downstream at station B.

Parabolic heat flux profile with (parabolic firing)

In accordance with the CFD studies carried out in Chapter [5], we can correlate the flux distribution according to a parabolic profile, so that the flux intensity is greatest around the centre point of the burner zone, which for SKV3 consists of the four burner floors. It should be noted that the maximum value of

the flux intensity, is somewhat above the centre point of the burner system. A parabolic heat flux profile in an evaporator string is illustrated in figure (8) as a relative flux distribution profile and can be idealised
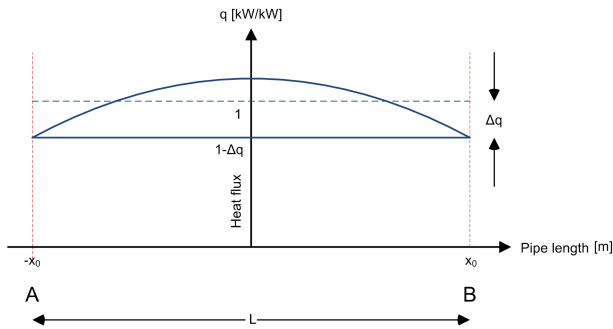
Figure 8: Normal firing in boiler with weak parabolic heat flux to boiler.

as a second-order symmetrical profile, given by

$$q^*(x) = a \cdot (x + x_0)(x - x_0) + b, \quad b = 1 - \Delta q. \quad (22)$$

A simple requirement for the distribution function is that the integral of the distribution function over the entire interval of definition must be of unity, so that we do not add more energy than expected for the evaporator tube. We can thus ensure that the distribution function has the desired functionality by requiring:

$$\int_{-x_0}^{x_0} q^*(x)dx = 2x_0 \cdot 1 \quad (23)$$

$$= \int_{-x_0}^{x_0} (a \cdot (x + x_0)(x - x_0) + b)dx$$

$$= -\frac{4a}{3}x_0^3 + 2bx_0$$

Hence the coefficient can be estimated to

$$a = -\frac{\Delta q}{x_0^2} \quad (24)$$

and for $x_0=1$, the equation (22) can be formulated as

$$q^*(x) = \frac{3\Delta q}{2} \cdot (1 - x^{*2}) + 1 - \Delta q, \quad x^* \in [-1, +1] \quad (25)$$

wherein x^* is a dimensionless position in the evaporator. We can see that the maximum flux occurs at $x^* = 0$, corresponding to $q^* = 1 + \Delta q /2$. Similarly, the minimum flux attached to the top and the bottom of the evaporator for $x^*=\pm x_0$, respectively. Here we find $q^*(\pm x_0) = 1-\Delta q$. We can again observe an almost linear relationship between steam quality and

pipe length, corresponding to a distinct stable heat absorption. The outlet temperature of the evaporator is the lowest of all scenarios, and the inlet pressure corresponds to the scenario with constant heat flux. This reflects that the models are not in dynamic equilibrium, since all scenarios receive the same effect and the heat flux profile is almost linear.

COMPARISON OF THE FLUX PROFILES IN HIGH PRESSURE EVAPORATOR

The start-up process with different heat flux profiles causes different dynamic pressure responses. As shown in the figure (31) for station A, one observes different pressure build-ups, where we clearly can see that the low combustion causes a faster and steeper pressure build-up than the other profiles, so that the top firing causes the smallest pressure build-up. Immediately thereafter, the response of the more or less homogeneous pressure build-up, is replaced by a more oscillating process, where the moving average gradually decreases over time. All four scenarios have an oscillating response; however, there is a trend to bottom firing have a more moderate exit amplitude. In station B we almost see identical pressure structures, but with varying timing. The bottom firing scenario flattens out soon and settles at a stable level, while the top firing scenario flattens out later and also attempts a second pressure build-up, but quickly falls back to the final level of the downstream pressure. When we look at the time series of enthalpy in station A, there is no significant difference observable among the four scenarios. Downstream station B, a time delay occurs of the enthalpy front, and not surprisingly, we see the fastest enthalpy front for low firing, while high firing has the slowest front; see figure (32). After 80 [s] of simulation we see a gradually more oscillating density-wave in station A, see figure (33), which dominates the rest of the simulation period. In station B we see a significantly higher density for the bottom firing scenario, but with a lower degree of oscillation compared to the other scenarios. Here we find surprisingly the greatest density oscillations in the top firing scenario. The fluid temperature is illustrated in figure (34). In station A there is a steeper increase in fluid temperature for the low firing scenario, which ends on the same level as for the other scenarios, due to the entrance to the two-phase region (almost identical saturation pressure).

In station B, we conversely see the largest temperature gradient before the two-phase region for top firing, and again, the temperature ends at the same level, as entering the two-phase region. In the superheated region, we again see drastic temperature fluctuations, surprisingly most notably for the high-fired scenarios. The observed momentary temperature fluctuations are above 20 degrees, for the top-firing scenario. The associated material temperature is dampened much, compared to the fluid temperature, and here we see the highest material temperature in the bottom firing scenario, with a difference of approximately 10 [^oC] compared to the top firing scenario. The material temperatures are illustrated in figure (35). At station A, we can see a significantly higher material temperature (+3 [^oC]) for the bottom-firing scenario, compared to the other scenarios.

LOW-PRESSURE EVAPORATORS

During the last decade, Danish utilities (Vattenfall AB and DONG Energy A/S) have invested much effort in the optimisation of thermal power plants in order to outbalance the fluctuations imposed by wind and sun. One could argue that we could phase out the existing thermal plants and switch to open pass gas turbines to solve the problem, but this is a rather expensive solution because we have a fleet of quite new super-critical power plants that still have a significant life time. Simultaneously, the power stations are committed to supply district heating to a large customer base. This means that there is a strong link between the production of district heating and electricity, which can result in a significant overproduction of electricity, when the weather is cold and windy. This can be accomplished by, for example, reducing the outlet pressure of the SKV3 evaporator, while bypassing the VHP turbine, so that the pressure of the evaporator is aligned with the HP turbine. Bypassing the VHP tubine at low load corresponds to an evaporator pressure decrease from approximately 90 [bar] to 46 [bar] at the evaporator outlet. This leads to less power output without compromising the district heating production, but the unit efficiency deteriorates.

In this part of the article, we examine how a power plant evaporator (SKV3) with smooth pipes behaves, when the boiler outlet pressure is reduced considerably below the normal circulation pressure for Benson boilers. Four simulations with different firing profiles are performed, so that the sensitivity to uneven heating can be assessed. Note that the applied input enthalpy (boundary condition) is unchanged relative to the previous calculations. This results in minimal sub-cooling, though sub-cooling still exists. In practice this can lead to mal-distribution problems.

Heat flux profiles

Here we carry out calculations with the aim of investigating how different heat flux profiles affect the dynamics of a low-pressure configuration of the SKV3 evaporator during a dynamic start-up period of 200 [s]. Again we use the four different profiles: a constant heat flux on the panel wall as illustrated by figure (4), a linear profile representing situations with bottom firing of the boiler as illustrated in figure (6), a parabolic heat flux profile in the evaporator string as illustrated in figure (8) and finally a linear profile representing situations with top firing of the boiler as illustrated in figure (7).

Constant heat flux profile

This scenario is again of academic interest and involves a more gentle impact of the evaporator. The outcome of the linear heat flux simulation shows a very stable evaporator, illustrated in figure (16), with a very high pressure drop (15.7 [bar]) and an outlet steam velocity of 48 [m/s], which is very high. The steam quality profile is perfectly linear along the pipe, indicating a constant and stable heat uptake. The corresponding time series at station A and B are illustrated in figures (17) and (18). There occur violent pressure oscillations in connection with the start-up of the model, and the model is first stabilized after approximately 140 [s]. The pressure oscillations achieve a size of up to 5.5 [bar] and thus may be critical in the supply of steam for each evaporator tube (mal-distribution). These oscillations occur in combination with enthalpy fluctuations and affect the flow velocity, which momentarily may rise 10 [m/s] within a period of less than one second. We can thus conclude that the start-up period in a low-pressure evaporator is a violent dynamical phenomenon for the first approximately 140 [s] of simulation.

Linear heat flux profile with bottom firing

Experience from earlier simulations has shown that bottom firing leads to higher dynamic instability in the evaporator, and is no exception in this situation with reduced evaporator pressure. After 200 [s] we see a steady state picture of the axial profile of the thermo-hydraulic properties; see figure (19). As shown in figure (20), the system reaches a steady state condition after more than 160 [s] from the start, whereas the scenario with linear heat flux uses 140 [s] to reach steady state. At the upstream station we see the same tendencies, but with less oscillations; see figure (21). The dynamic transients are also more violent here, where the fluid velocity fluctuates dramatically (up to 15 [m/s] in less than one second). The pressure fluctuates violently, too, but falls quickly into a plateau after only 100 [s] after start-up. The fluid velocity and enthalpy oscillations are dampened gradually, until a steady state situation is reached after 160 [s] from the start. This indicates that at a lower evaporator pressure, there is a greater compressibility in the evaporator, with a steeper negative gradient in the density, while entering the two-phase region. Operating experience from the SKV3 reveals that there are evaporator instabilities during start-up when firing low, i.e., when the lower burner rows are in action during start-up. This tendency is strengthened when the evaporator pressure is reduced.

Linear heat flux profile with top firing

Operating experience from the SKV3 in particular indicates a greater stability in the evaporator, when the firing is intensified in the top of the boiler. We attempt to model this using a linear heating profile, with the highest heat flux at the top of the furnace. The lower operation pressure leads to a high degree of stability after 200 [s].

Figure (22) shows how the thermodynamic properties of the fluid change along the pipe, for the top firing scenario. It is worth noting that the enthalpy increases linearly with the length of the tube, with no enthalpy slugs at all, which indicates a high level of stability in the production of the superheated steam. Similarly, we can see a significant difference in both the pressure and the velocity profile compared to the situation with low combustion in the furnace. The

pressure is here approximately 0.5 [bar] lower and the steam outlet velocity is here similar, 47 [m/s] against 48 [m/s] in the first scenario. The time series in stations A and B (figures 24 and 25) show an unstable start-up process of the evaporator, with stable conditions after 140 [s] from the start. This means that top firing appears more stable compared to bottom heating, which coincides with the results we found for the evaporation process at 90 bar pressure.

Parabolic heat flux profile with parabolic firing

In accordance with the high pressure studies, we continue the flux distribution studies for low pressure evaporator according to a parabolic profile. We see a couple of pressure/enthalpy slugs in figure (25) and after approximately 117 [s] simulation, the pressure rises rapidly. The fluid is here in a saturated condition in which the saturation temperature increases only slightly as function of the pressure rise. Subsequently, the pressure drops back to the original level, and the temperature follows back down to the original level as well, until the enthalpy suddenly rises rapidly above the level from before. Here we experience a kind of flashing, where the fluid is changing state from saturated steam to superheated steam, with significant temperature increases to follow (+15 [^{o}C]). In this context, the fluid velocity increases violently, locally up to 20 [m / s] within seconds. These slugs die gradually as time passes, and the flow stabilizes in a static situation after about 200 [s] of simulation.

Comparison of the flux profiles in low pressure evaporator

In general, we can see that reduced sub-cooling provides a more smooth solution over time, without the strong pressure oscillations initiated from the two-phase transition point. This is despite that the density jump is even more pronounced at lower pressure. But the degree of sub-cooling and thus the lower compressibility of water than steam is enough to change this. The start-up process with different heat flux profiles causes different pressure distribution. In figure (36) for station A, one can observe a different pressure build-up, in terms of both time and place. The greatest pressure wave build-up in the evaporator occurs in the bottom firing scenario, and

this occurs earlier compared to the other runs. The lowest pressure build-up occurs ultimately at top firing and arrives later. At station B, there is no significant difference in the pressure observations. At station B, we can also see that the enthalpy fluctuations occur earlier and more frequently at the bottom firing than the other scenarios; see figure (37). There are very significant differences in density for the bottom firing at station A. Here there is a lower density level created, significantly, earlier in the simulation, supplied with a clear pulsation, but without exceeding the density level of the other three flux configurations. The same trend is reflected in the fluid temperature, which is illustrated in figure (38). Here we also assume a higher value for the bottom firing, supplied with early pulsations to follow. This phenomenon can affect the delicate metal structures of the tubing, which are susceptible to fatigue fractures. The material temperature is illustrated in figure (39), here shown as an average temperature of the tube wall. At station A, we can see a significantly higher material temperature (+3 [^{o}C]) for the bottom-firing scenario, compared to the other scenarios. At station B, this is not applicable before we pass the two-phase region and move into the superheat region.

Comparison of high versus low-pressure evaporator

The evaporator at AVV2 is almost identical to that of SKV3. DONG Energy - Thermal Power has carried out experiments with reduced evaporator pressure at AVV2, where outlet pressure was reduced from 90 [bar] to 56 [bar] and minimum flow was 86 [kg/s]. This did not cause any major drama, even though the boiler manufacturer has assigned a minimum pressure of 90 [bar]. When we compare the two simulations carried out at 90 [bar] and 56 [bar], respectively, we notice that the high-pressure case has higher sub-cooling of the fluid (inlet enthalpy common for both cases). The homogeneous model considers the sub-cooled liquid as almost incompressible, which leads to rapid pressure oscillations in the sub-cooled sector of the evaporator, and when the fluid is transferred to the two-phase region, the density dramatically decreases with pressure oscillations to follow. In the case of low-pressure evaporation, we have a moderate sub-cooling of the fluid, but conversely an even more withdrawn reduction

of density, when passing the two-phase region. This initiates violent pressure oscillations, which die out after approximately 100 [s]; see figure (26). It is worth noting that shortly after the start of firing, a peak occurs in the mass flux. The peak is highest for high-pressure evaporation with approximately 4250 [kg/m^2s] after approximately 72 [s], while the low-pressure evaporation peaks earlier after only 25 [s] with a maximum mass flux of 2900 [kg/m^2s]; see figure (28). One can observe more violent pressure and enthalpy fluctuations for low-pressure evaporation; see figures (26) and (27). Pressure oscillations are more common downstream of the evaporator; while at upstream station A, more quiet pressure conditions appear, which apparently do not affect the mal-distribution to the panel walls.

CONCLUSION

In this paper, we use the fifth-order WENO solver to simulate the dynamic response of evaporator tubes corresponding to SKV3. Initially we describe the calibration process for the evaporator model, based on measurements from a steady state load case from SKV3 (sample 4) in table (2). The application is usable for various purposes, and initially we analyse four different heat flux distributions on the evaporator tube. We can observe several interesting dynamic phenomena that can be related to density-wave oscillations, we can see that bottom firing clearly reinforces the occurrence of density-waves, especially in the upstream section of the pipe (station A), where we can notice significant oscillations. There is a coupling between the density and the fluid velocity through the continuity equation. At certain periods, the fluid velocity is very low (read near-zero flow) and this can cause a significant temperature rise in the inner layer of the tube material. This again can increase the thermal load on the pipe wall, but we cannot trace any radial wall temperature increase in the simulation, because of the small time constants and because we are calculating an averaged tube wall temperature. The inner heat transfer will be weakened considerably when the flow rate approaches zero.

Another phenomenon which can be observed, is that the fluid temperature downstream is generally higher for the bottom firing scenario and there are temperature fluctuations of moderate strength.

Furthermore, the development of a pressure front occurs quickly in the bottom firing scenario, which gradually weakens, when the flow approaches a static state condition. During the transient period before steady state conditions are achieved, pressure oscillations occur. The remarkable thing is that the top firing scenario leads to surprising violent thermal fluctuations in fluid temperature, something that cannot be measured under operation of a plant. Conversely, we see that the top firing gives a more stable evaporator, in the sense that the evaporator has a lower degree of fluctuations in pressure and fluid velocity in the sub-cooled region, leading to a more safe operation of the evaporator during start-up. The applied load gradients are large, compared to the maximum allowable gradients on SKV3 ($+/-8$ MW/min.); see [5]. Further more, the restrictions compared to reduced lifetime of thick-walled components, like junction boxes or valves, are not taken into account in this analysis.

We have now developed a tool that can be used in further studies of the evaporator stability, and we must of course ensure compliance with the evaporator design rules, especially rules related to the flow distribution to panel walls via junction boxes. Here significant sub-cooling is usually used in order to ensure a satisfactory distribution of a single-phase fluid to the evaporator wall.

REFERENCES

[1] Helmut Effenberger. *Dampferzeugung*. ISBN 3-540-64175-o Springer-Verlage, Berlin 2000.

[2] Christoph C. Richter. *Proposal of New Object-Oriented Equation-Based Model Libraries for Thermodynamic Systems*. Von der Fakultät für Maschinenbau, der Technischen Universität Carolo-Wilhelmina zu Braunschweig.

[3] Anonymous. *Danmarks Energifremskrivning (October 2012)*. Edition, no.11, Energistyrelsen, ISBN: 978-87-7844-941-2, 2012.

[4] Rehman S. *Solar radiation over Saudi Arabia and comparisons with empirical models*. Energy 1998;23(12):1077-1082.

[5] Axel Ohrt Johansen. *Numerical study of evaporators in power plants for improved dynamic flexibility*. Ph.D thesis, Technical University Denmark, Department of Mechanical Engineering, 2013.

[6] S. M. Ghiaasiaan. *Two-Phase Flow, Boiling, and Condensation in Conventional and Miniature Systems*, 1st Edition, Cambridge University Press, Georgia Institute of Technology, 2008.

[7] H. Herman *VDI-Wärmeatlas* 9th Edition, Springer 2002, Berlin Heidelberg.

[8] Pan, J. and Dong, Y and Yu, H and Bi, Q. and Hua, H. and Gao, F. and Yang, Z. *Mathematical modeling and thermo-hydraulic analysis of vertical water wall in an ultra supercritical boiler*, Applied Thermal Engineering vol. 29, 2009, p. 2500-2507.

[9] Harald Griem *Untersuchung zur Thermohydraulik innenberippter Verdampferohre*, PhD thesis 1995, Technische Universität München, Lehrstuhl für Termische Kraftanlagen.

[10] Anonymous. *Guarantee test results of steam turbine SVS3 - 98550369-KPG/TCM 99-6907 Confidential*, KEMA, Arnhem The Netherlands, 25 January 1999.

[11] H. Schmidt, W. Köhler and W. Kastner. *"High-Pressure Test Facility - 25 Years of Operation, Framatome ANP GmbH"*. VGB Power Tech. 2001 p. 25-31.

[12] Joachim Franke. *Untersuchung der hydrodynamischen Stabilität*. Von fachbereich Maschinenbau an der Technischen Hochschule Darmstadt zur Erlangung des Grades eines Doktor-Ingenieurs (Dr.-Ing.) genehmigte Dissertation vorgelegt von Dipl.-Phys. Joachim Franke aus Breslau. 1986, vol.1.

[13] Pan, J. and Yang, D. and Dong, Z. and Zhu, T and Bi, Q, *Experimental investigation on heat transfer characteristics of low mass flux rifled tube upward flow*. International Journal of Heat and Mass Transfer 2011, vol. 54 p.2952-2961.

[14] Yang, D., Pan, J., Zhou, C., Zhu, X., Bi, Q. and Chen, T. *Experimental investigation on heat transfer and frictional characteristics of vertical upward rifled tube in supercritical CFB*

boiler. Experimental Thermal and Fluid Science. 2011, vol 11 p.291-300.

[15] Zhu, X. and Bi, Q. and Su, Q. and Yang, D. and Wang, J. and Wu, G. and Yu, S. *Self-compensating characteristic of steam-water mixture at low mass velocity in vertical upward parallel internally ribbed tubes*. Applied Thermal Engineering 2010 vol. 30, p. 2370-2377.

[16] Fan, X. and Wu, S. *Heat transfer and frictional characteristics of rifled tube in a 1000 MW supercritical lignite-fired boiler*. 2010, p. 1-5. School of Energy Science and Engineering, Harbin Institute of Technology, China.

[17] A.E. Bergles and J.H. Lienhard, et al. *Boiling and evaporation in small diameter channels*, Heat Transf. Eng.24 (2003) 18-40.

[18] S. Kakac, B. Bon. *A review of two-phase flow dynamic instabilities in tube boiling system*, Int. J. Heat Mass Transfer 51 (2008) 399-433.

[19] Capdeville,G.*A central WENO scheme for solving hyperbolic conservation laws on non-uniform meshes*, J. Comp. Phys., 2008, p. 2977-3014, vol. 4, num. 227.

[20] Castro, Marcos. and Costa, Bruno. and Don, Wai Sun *High order weighted essentially non-oscillatory WENO-Z schemes for hyperbolic conservation laws*, Journal of Computational Physics, 2010, p. 1766-1792, number230.

[21] Levy, D. and Pupo, G. and Russo, G. *Compact central WENO schemes for multidimensional conservation*, SIAM J. Sci. Comput. 2000, p. 656-672, vol.22.

[22] Kurganov, Alexander and Tadmor, Eitan *New high-resolution central schemes for nonlinear conservation laws and convection-diffusion equations*, J. Comput. Phys. 2000, p. 241-282, vol.160.

[23] Kurganov, A. and Levy, D. *A third-order semidiscrete central scheme for conservation laws and convection-diffusion equations*, SIAM J. Sci. Comp. 2000, p. 1461-1488, vol. 4, num. 22.

[24] Gotlieb, S and Shu, C.W. *Total variation diminishing Runge-Kutta schemes* Math. Comp. 1998, p. 73-85 num. 67.

[25] Bentz, P. Dale and Prasad, Kuldeep, R. *Thermal Performance of Fire Resistive Materials I. Characterization with Respect to Thermal performance Models*. NIST, Building and Fire research Laboratory, Gaithersburg, 2007, MD 20899-8615.

[26] Anonymous. *Rohre aus warmfesten und hochwarmfesten Stahlen Werkstoffblatter*, MannesMann Rohrenwerke, 1988, 1. ed.

[27] F. Brandt. *FDBR-FACHBUCHREIHE* Wärmeübertragung in Dampferzeugern und Wärmeaustauschern, Vulkan-Verlag, Essen. 1985, BAND 2, FDBR FACHVERBAND DAMPFKESSEL, BEHÄLTER UND ROHRLEITUNGSBAU E. V., ISBN 3-8027-2274-4.

APPENDIX
NUMERICAL SOLUTION OF HYPERBOLIC TRANSPORT EQUATION

Let us consider a hyperbolic *system of balance laws* (SBL) formulated on a compact vector notation, given by equation (21), where Φ is the unknown m-dimensional vector function, $\mathbf{f}(\Phi)$ the flux vector, $\mathbf{g}(\Phi)$ a continuous source vector function on the right hand side (RHS), with z as the single spatial coordinate and t the temporal coordinate, Ω is partitioned in n_z non-overlapping cells: $\Omega = \cup_{i=1}^{n_z} I_i \in [0, l_z]$, where l_z is a physically length scale in the spatial direction. This system covers the general transport and diffusion equations used in many physical aspects and gas dynamics as well. The SBL system is subjected to the initial condition:

$$\Phi(z, 0) = \Phi_0(z) \qquad (26)$$

and the below boundary conditions given by:

Dirichlet boundaries:

$$\Phi(z = 0, t) = \Phi_A(t) \text{ and} \qquad (27)$$
$$\Phi(z = l_z, t) = \Phi_B(t)$$

and

Neumann boundaries:

$$\frac{\partial \Phi(z = 0, t)}{\partial z} = \frac{\partial \Phi_A(t)}{\partial z} \text{ and} \qquad (28)$$
$$\frac{\partial \Phi(z = l_z, t)}{\partial z} = \frac{\partial \Phi_B(t)}{\partial z}$$

The above boundary conditions can be given by a combination of each type of boundaries. The Dirichlet condition is only specified, if we have ingoing flow conditions at the boundaries.

The development of a general numerical scheme for solving *PDE*'s may serve as universal finite-difference method, for solving non-linear convection-diffusion equations in the sense that they are not tied to the specific eigenstructure of a problem, and hence can be implemented in a straightforward manner as black-box solvers for general conservation laws and related equations, governing the spontaneous evolution of large gradient phenomena. The developed non-staggered grid is suitable for the modelling of transport of mass, momentum and energy and is illustrated in
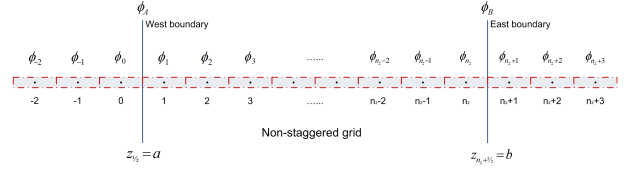

Figure 9: The computational grid $[0, l_z]$ is extended to a set of ghost points for specifying boundary conditions.

figure (9), where the cell $I_j = [z_{j-1/2}, z_{j+1/2}]$ has a cell width Δz and Δt the time step.

In this section, we review the central fifth order WENO schemes in one spatial dimension, developed by [19] with uses modified weight functions outlined by [20]. We recall the construction of the non-staggered central scheme for conservation laws. The starting point for the construction of the semi-discrete central-upwind scheme for equation (21) can be written in the following form:

$$\frac{d\Phi_j(t)}{dt} = -\frac{1}{\Delta z} \left[F_{j+1/2} - F_{j-1/2} \right] + S_j(\Phi). \quad (29)$$

where the numerical fluxes $F_{j+1/2}$ are given by

$$F_{j+1/2} = \frac{a_{j+1/2}^+ f(\Phi_{j+1/2}^-) - a_{j+1/2}^- f(\Phi_{j+1/2}^+)}{a_{j+1/2}^+ - a_{j+1/2}^-}$$

$$(30)$$

$$+ \frac{a_{j+1/2}^+ a_{j+1/2}^-}{a_{j+1/2}^+ - a_{j+1/2}^-} \left[\Phi_{j+1/2}^+ - \Phi_{j+1/2}^- \right].$$

Notice that the accuracy of this scheme is determined by the accuracy of the reconstruction of Φ and the ODE solver. In this paper the numerical solutions of (29) is advanced in time by mean of third order TVD Runge-Kutta method described by [24]. The local speeds of propagation can be estimated by

$$a_{j+1/2}^+ = \max \left\{ \lambda_N \left(\frac{\partial f(\Phi_{j+1/2}^-)}{\partial \Phi} \right), \lambda_N \left(\frac{\partial f(\Phi_{j+1/2}^+)}{\partial \Phi} \right), 0 \right\},$$

$$(31)$$

$$a_{j+1/2}^- = \min \left\{ \lambda_1 \left(\frac{\partial f(\Phi_{j+1/2}^-)}{\partial \Phi} \right), \lambda_1 \left(\frac{\partial f(\Phi_{j+1/2}^+)}{\partial \Phi} \right), 0 \right\}.$$

with $\lambda_1 < ... \lambda_N$ being the eigenvalues of the Jacobian given by $\mathbf{J} = \frac{\partial f(\Phi(z,t))}{\partial \Phi}$. Here, $\Phi_{j+1/2}^+ = p_{j+1}(z_{j+1/2})$, and $\Phi_{j+1/2}^- = p_j(z_{j+1/2})$ are the corresponding right and left values of the

piecewise polynomial interpolant $\{p_j(z)\}$ at the cell interface $z=z_{j+1/2}$.

To derive an **e**ssentially **n**on-**o**scillatory reconstruction (ENO), we need to define three supplementary polynomials $(\tilde{\Phi}_1, \tilde{\Phi}_2, \tilde{\Phi}_3)$, approximating $\Phi(z)$ with a lower accuracy on I_i. Thus, we define the polynomial of second-order accuracy, $\tilde{\Phi}_1(z)$, on the reduced stencil S_1: (I_{i-2}, I_{i-1}, I_i), $\tilde{\Phi}_2(z)$ is defined on the stencil S_2: (I_{i-1}, I_i, I_{i+1}), whereas $\tilde{\Phi}_3(z)$ is defined on the stencil S_3: (I_i, I_{i+1}, I_{i+2}). Now, we have to invert a 3×3 linear system for the unknown coefficients $\{a_j\}, j \in \{0, ..., 2\}$, defining $\tilde{\Phi}_1, \tilde{\Phi}_2, \tilde{\Phi}_3$. Once again, the constants determining the interpolation are pre-computed and stored before solving the PDEs. When the grid is uniform, the values of the coefficients for $\tilde{\Phi}_1, \tilde{\Phi}_2$ and $\tilde{\Phi}_3$ can be explicitly formulated. It is left to the reader to read [19] or [5] for further details about determining the coefficients in the reconstructed polynomials. To implement a specific solution technique, we extend the principle of the central WENO interpolation defined in [21]. First, we construct an ENO interpolant as a convex combination of polynomials that are based on different discrete stencils. Specifically, we define in the discrete cell I_i:

$$\tilde{\Phi}^i(z) \equiv \sum_j w_j \times \tilde{\Phi}_j(z), \qquad (32)$$

$$\sum_j w_j = 1 \quad \text{for} \quad w_j \geq 0 \ \text{for} j \in \{1, .., 4\},$$

and $\tilde{\Phi}_1$, $\tilde{\Phi}_2$ and $\tilde{\Phi}_3$ are the previously defined polynomials. $\tilde{\Phi}_4$ is the second-order polynomial defined on the central stencil S_5: $(I_{i-2}, I_{i-1}, I_i, I_{i+1}, I_{i+2})$ and is calculated such that the convex combination in (32), will be fifth-order accurate in smooth regions. Therefore, it must verify:

$$\tilde{\Phi}_{opt}(z) = \sum_j C_j \times \tilde{\Phi}_j(z) \ \forall z \in I_i, \qquad (33)$$

$$\sum_j C_j = 1 \quad \text{for} \quad C_j \geq 0 \ \text{for} \ j \in \{1, .., 4\},$$

The calculation of $\tilde{\Phi}^+_{i+1/2}, \tilde{\Phi}^-_{i+1/2}$ produces the following simplified result:

$$
\begin{aligned}
\tilde{\Phi}^+_{i+1/2} =& \left(-\frac{7}{120}w_4 - \frac{1}{6}w_1\right)\bar{\Phi}_{i-2} \\
&+ \left(\frac{1}{3}w_2 + \frac{5}{6}w_1 + \frac{21}{40}w_4\right)\bar{\Phi}_{i-1} \\
&+ \left(\frac{5}{6}w_2 + \frac{1}{3}w_1 + \frac{11}{6}w_3 + \frac{73}{120}w_4\right)\bar{\Phi}_i \qquad (34) \\
&+ \left(-\frac{1}{6}w_2 - \frac{7}{6}w_3 - \frac{7}{120}w_4\right)\bar{\Phi}_{i+1} \\
&+ \left(\frac{1}{3}w_3 - \frac{1}{60}w_4\right)\bar{\Phi}_{i+2}
\end{aligned}
$$

$$
\begin{aligned}
\tilde{\Phi}^-_{i+1/2} =& \left(-\frac{1}{60}w_4 + \frac{1}{3}w_1\right)\bar{\Phi}_{i-2} \\
&+ \left(-\frac{1}{6}w_2 - \frac{7}{6}w_1 - \frac{7}{120}w_4\right)\bar{\Phi}_{i-1} \\
&+ \left(\frac{5}{6}w_2 + \frac{1}{3}w_3 + \frac{11}{6}w_1 + \frac{73}{120}w_4\right)\bar{\Phi}_i \qquad (35) \\
&+ \left(\frac{1}{3}w_2 - \frac{5}{6}w_3 + \frac{21}{40}w_4\right)\bar{\Phi}_{i+1} \\
&+ \left(-\frac{1}{6}w_3 - \frac{7}{120}w_4\right)\bar{\Phi}_{i+2}
\end{aligned}
$$

To calculate the weights w_j, $j \in \{1, 2, 3, 4\}$, we review another technique to improve the classical smoothness indicators to obtain weights that satisfy the sufficient conditions for optimal order of accuracy. It is well known from [19], that the original WENO is fifth order accurate for smooth parts of the solution domain except near sharp fronts and shocks. The idea here is taken from [20] and uses the hole five point stencil S_5 to define a new smoothness indicator of higher order than the classical smoothness indicator IS_i. The general form of indicators of smoothness are defined in [21]:

$$IS_j^i = a_1^2 \Delta z^2 + \frac{13}{3} a_2^2 \Delta z^4 + O(\Delta z^6), \qquad (36)$$

$$j \in \{1, 2, 3\}.$$

and the form of IS_4^i is given by [19]:

$$IS_4^i = a_1^2 \Delta z^2 + \left[\frac{13}{3}a_2^2 + \frac{1}{2}a_1 a_3\right]\Delta z^4 + O(\Delta z^6). \quad (37)$$

where a_0 and a_1 can be determined by solving the coefficients to reconstructed polynomial $\tilde{\Phi}_4$ on S_5. For estimating the weights w_k, $k \in \{1, 2, 3, 4\}$, we proceed as follows: Define

$$IS_k^* = \frac{IS_k + \varepsilon}{IS_k + \varepsilon + \tau_5} \qquad (38)$$

where IS_k, $k \in \{1, 2, 3\}$ are given by (36), IS_4 given by (37) and $\tau_5 = |IS_1 - IS_3|$. The constant ε is a small number. In some articles $\varepsilon \approx$ from $1 \cdot 10^{-2}$ to $1 \cdot 10^{-6}$, see [21]. Here we use much smaller values of ε for the mapped and improved schemes in order to force this parameter to play only its original role of not allowing vanishing denominators at the weight definitions. The weights w_k are defined as:

$$w_k = \frac{\alpha_k^*}{\sum_{l=1}^4 \alpha_l^*}, \quad \alpha_k^* = \frac{C_k}{IS_k^*}, \quad k \in \{1, 2, 3, 4\} \quad (39)$$

The constants C_j represent ideal weights for (32). As already noted in [21], the freedom in selecting these constants has no influence on the properties of the numerical stencil; any symmetric choice in (33), provides the desired accuracy for $\tilde{\Phi}_{opt}$. In what follows, we make the choice as in [19]:

$$C_1 = C_3 = 1/8, C_2 = 1/4 \text{ and } C_4 = 1/2. \quad (40)$$

Convection-Diffusion equations

Let us again consider the general System of Conservation Laws (SCL), given by equation (21), where the source term g is replaced by a dissipative flux:

$$\frac{\partial \Phi(z,t)}{\partial t} + \frac{\partial f(\Phi(z,t))}{\partial z} = \frac{\partial}{\partial z}\left(g(\Phi(z,t), \frac{\partial \Phi}{\partial z})\right), \quad (41)$$

$$t \geq 0, \ z \in \Omega$$

The gradient of g is formulated on the compressed form: $g(\Phi, \frac{\partial \Phi}{\partial z})_z$ as a nonlinear function $\neq$ zero. This term can degenerate (41) to a strongly parabolic equation, admitting non smooth solutions. To solve it numerically is a highly challenging problem. Our fifth-order semi-discrete scheme, (29)-(30), can be applied to (21) in a straightforward manner, since we can treat the hyperbolic and the parabolic parts of (41) simultaneously. This results in the following conservative scheme:

$$\frac{d\Phi_j(t)}{dt} = -\frac{1}{\Delta z}\left[F_{j+1/2} - F_{j-1/2}\right] + G_j(\Phi, t). \quad (42)$$

Here $F_{j+1/2}$ is our numerical convection flux, given by equation (30) and G_j is a high-order approximation to the diffusion flux $g(\Phi, \frac{\partial \Phi}{\partial z})_z$. Similar to the case of the second-order semi-discrete scheme of

[22], operator splitting is not necessary for the diffusion term. By using a forth order central differencing scheme, outlined by [23], we can apply our fifth-order semi-discrete scheme, given by (29) and (30), to the parabolic equation (21), where $g(\Phi, \frac{\partial \Phi}{\partial z})_z$ is a function of ϕ and its derivative in space (diffusion). The diffusion term can be expressed by a high-order approximation:

$$G_j(t) = \frac{1}{12\Delta z}\left[-G(\Phi_{j+2}, (\Phi_z)_{j+2}) + 8 \cdot G(\Phi_{j+1}, (\Phi_z)_{j+1})\right]$$
(43)
$$-\frac{1}{12\Delta z}\left[8 \cdot G(\Phi_{j-1}, (\Phi_z)_{j-1}) + G(\Phi_{j-2}, (\Phi_z)_{j-2})\right]$$

where

$$(\Phi_z)_{j+2} = \frac{1}{12\Delta z}\left[25\Phi_{j+2} - 48\Phi_{j+1}\right]$$
$$+ \frac{1}{12\Delta z}\left[36\Phi_j - 16\Phi_{j-1} + 3\Phi_{j-2}\right], \quad (44)$$

$$(\Phi_z)_{j+1} = \frac{1}{12\Delta z}\left[3\Phi_{j+2} + 10\Phi_{j+1}\right]$$
$$- \frac{1}{12\Delta z}\left[18\Phi_j + 6\Phi_{j-1} - \Phi_{j-2}\right], \quad (45)$$

$$(\Phi_z)_{j-1} = \frac{1}{12\Delta z}\left[\Phi_{j+2} - 6\Phi_{j+1}\right]$$
$$+ \frac{1}{12\Delta z}\left[18\Phi_j - 10\Phi_{j-1} - 3\Phi_{j-2}\right] \quad \text{and} \quad (46)$$

$$(\Phi_z)_{j-2} = \frac{1}{12\Delta z}\left[-3\Phi_{j+2} + 16\Phi_{j+1}\right]$$
$$- \frac{1}{12\Delta z}\left[36\Phi_j + 48\Phi_{j-1} - 25\Phi_{j-2}\right] \quad (47)$$

and Φ_j are the point-values of the reconstructed polynomials.

Source Term

Next, let us consider the general SCL given by (21) and restrict our analysis to the source term of the form: $g(\Phi, t)$ as a continuous source vector function $\neq$ zero. By integrating system (21) over a finite space-time control volume $I_i, \Delta t$ one obtains a finite volume formulation for the system of balance laws, which usually takes the form

$$\Phi(z,t)_j^{n+1} = \Phi(z,t)_j^n - \frac{\Delta t}{\Delta z}\left(f_{j+1/2} - f_{j-1/2}\right) \quad (48)$$
$$+ \Delta t g(z,t)_j, \ t \geq 0, \ z \in \Omega$$

The integration of (21) in space and time gives rise to a temporal integral of the flux across the element

boundaries $f_{j+1/2}$ and to a space-time integral g_i of the source term inside I_i. In practice, one must replace the integrals of the flux and the source in (48) by some suitable approximations, that is to say one must choose a concrete numerical scheme. For SBL a numerical source must be chosen. Here, not only the three classical properties are required, but some additional properties are needed for the global numerical scheme: It should be well-balanced, i.e. able to preserve steady states numerically. It should be robust also on coarse grids if the source term is stiff.

Boundary conditions for Non-staggered grid

For a system of m equations we need a total of m boundary conditions. Typically some conditions must be prescribed at the inlet boundary ($z=a$) and some times at the outlet boundary ($z=b$). How many are required at each boundary depends on the number of eigenvalues of the Jacobian **A** that are positive and negative, respectively and whether the information is marching in or out for the boundaries.

By extending the computational domain to include a few additional cells on either end of the solution domain, called ghost cells, whose values are set at the beginning of each time step in some manner that depends on the boundary condition. In figure (9) is illustrated a grid with three ghost cells at each boundary. The idea behind the ghost point approach is to express the value of the solution at control points outside the computational domain in terms of the values inside the domain plus the specified boundary condition. This allows the boundary condition to be imposed by a simple modification of the internal coefficients using the coefficients of the fictitious external point. This can result in a weak imposition of the boundary condition, where the boundary flux not exactly agree with the boundary condition. By establishing a Taylor expansion around the boundary a or (b), we can express a relationship between the ghost points outside the solution domain and grid points inside the domain. For further details see [5].

Time discretization

The semi-discrete ODE given by (29) is a time dependent system, which can be solved by a TVD Runge-Kutta method presented by [24]. The optimal third order TVD Runge-Kutta method is given

by

$$\Phi_j^{(1)} = \Phi_j^n + \Delta t L(\Phi_j^n), \tag{49}$$

$$\Phi_j^{(2)} = \frac{3}{4}\Phi_j^n + \frac{1}{4}\Phi_j^{(1)} + \frac{1}{4}\Delta t L(\Phi_j^{(1)}),$$

$$\Phi_j^{n+1} = \frac{1}{3}\Phi_j^n + \frac{2}{3}\Phi_j^{(2)} + \frac{2}{3}\Delta t L(\Phi_j^{(2)}), \text{ for } j \in [1, n_z].$$

The stability condition for the above schemes is

$$CFL = \max\left(u_j^n \frac{\Delta t}{\Delta z}\right) \le 1, \tag{50}$$

where CFL stands for the *Courant-Friedrichs-Lewy* condition and u_j^n is the maximum propagation speed in cell I_j at time level n.

FIGURES
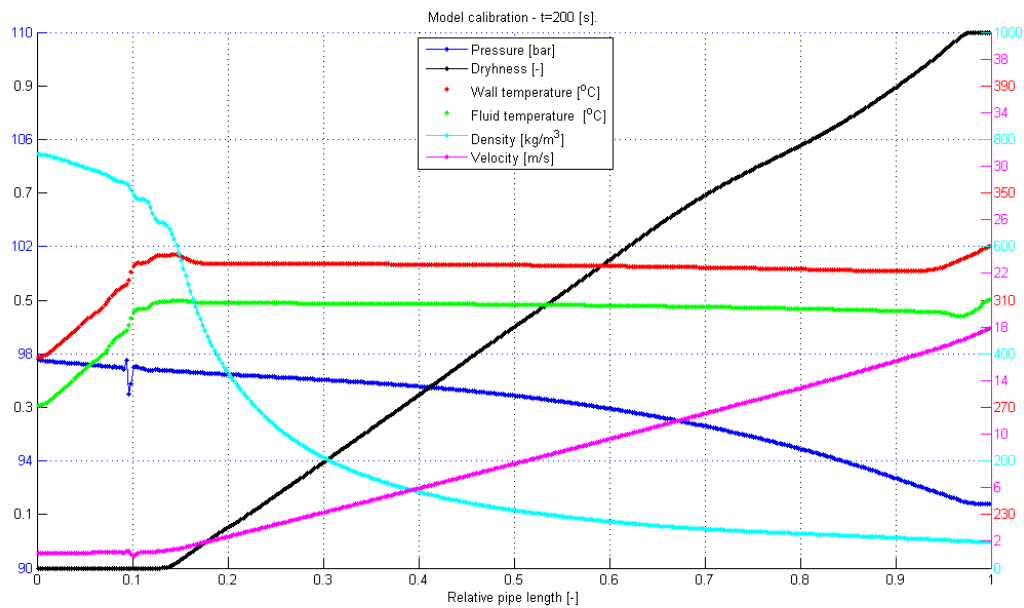
Figure 10: Line series of heat pipe calibration, t=200[s].
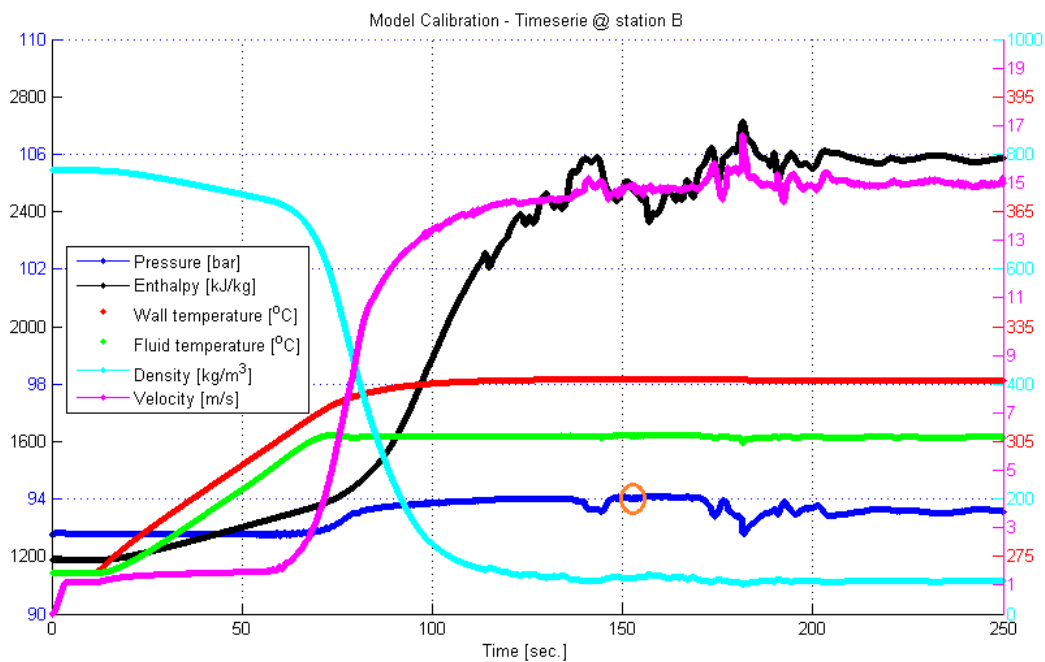
Figure 11: Time series of heat tube calibration, station B.

Figure 12: Time series of bottom firing in SKV3 evaporator model at station A.

Figure 13: Time series of bottom firing in SKV3 evaporator model at station B.
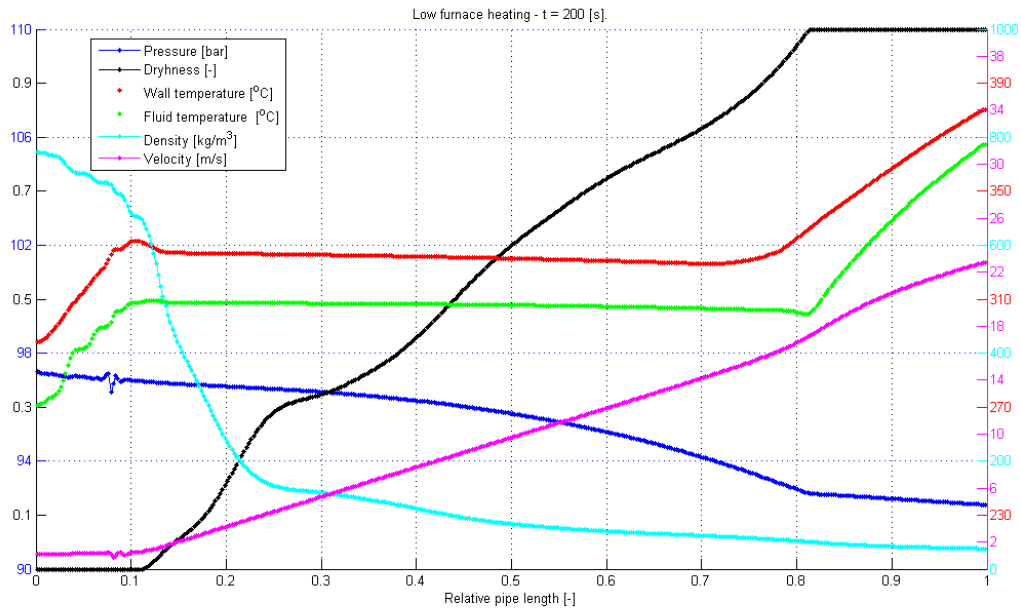
Figure 14: Bottom firing in SKV3 boiler, after 200 [s].
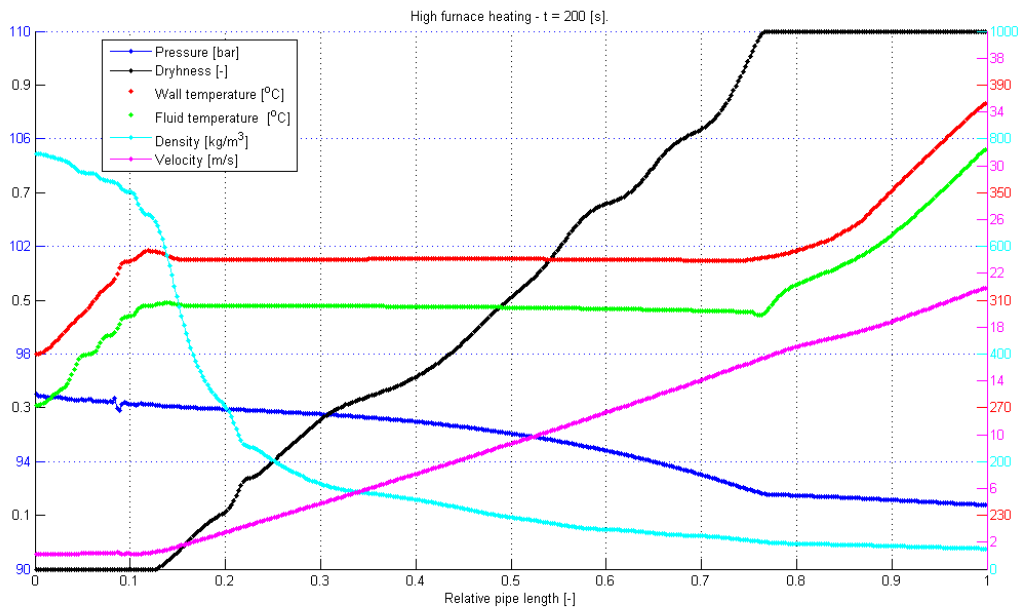
Figure 15: Top firing in SKV3 boiler, after 200 [s].
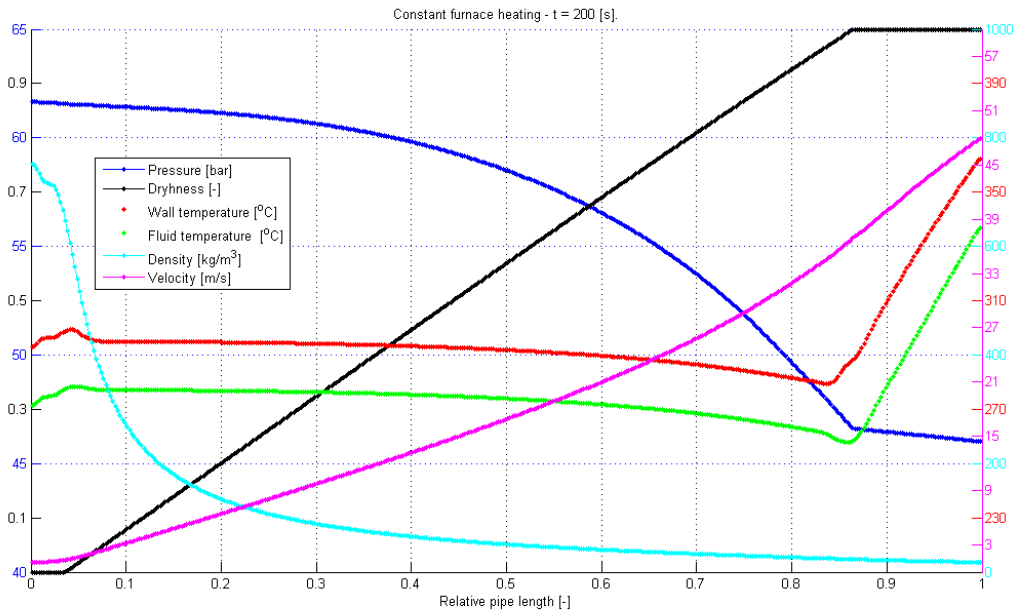
Figure 16: Constant heat flux to boiler, after 200 [s].
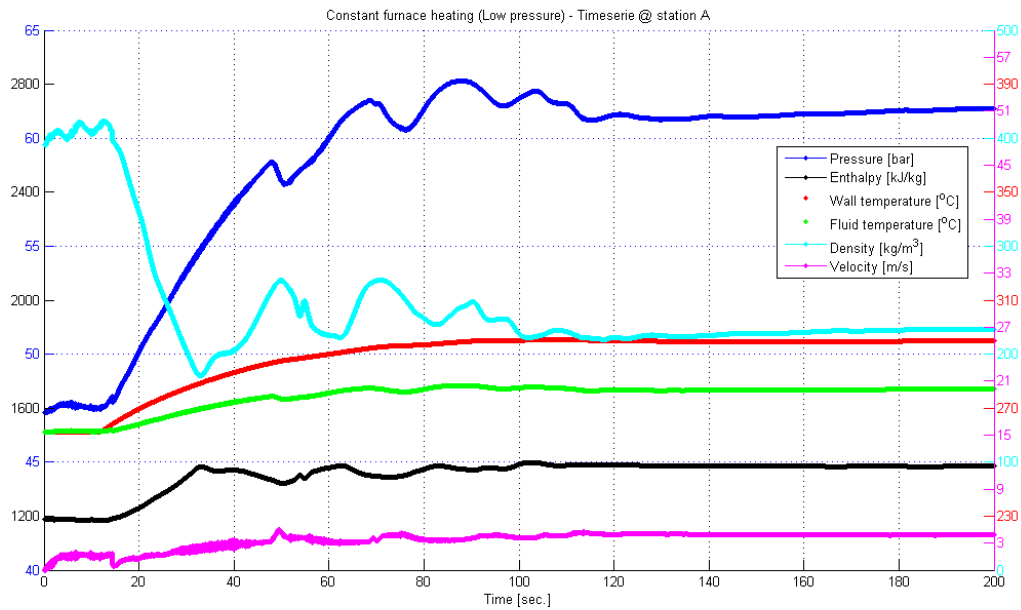
Figure 17: Time series of constant heat flux at the SKV3 evaporator model at station A.
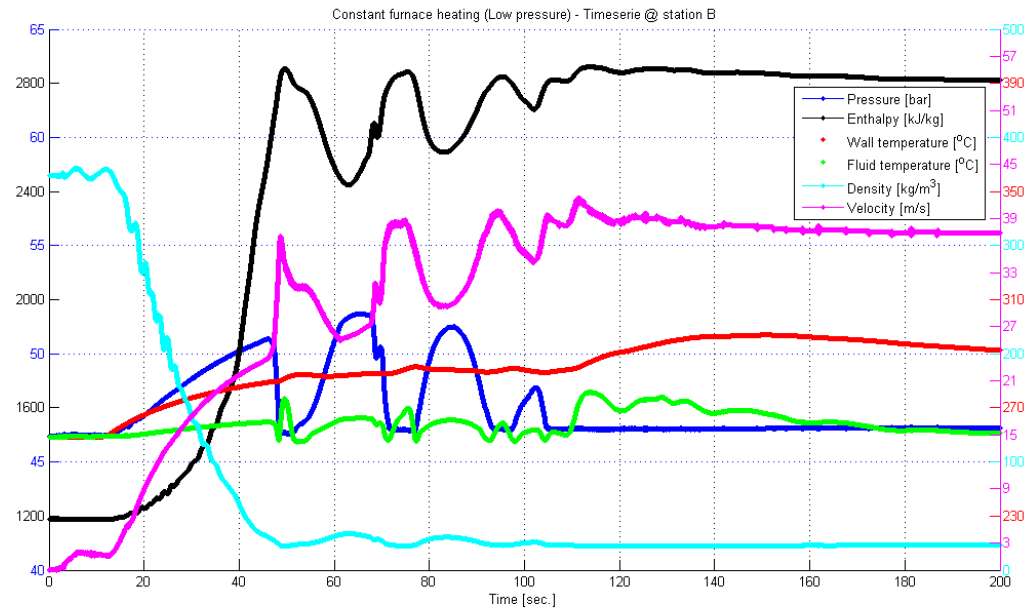
Figure 18: Time series of constant heat flux at the SKV3 evaporator model at station B.
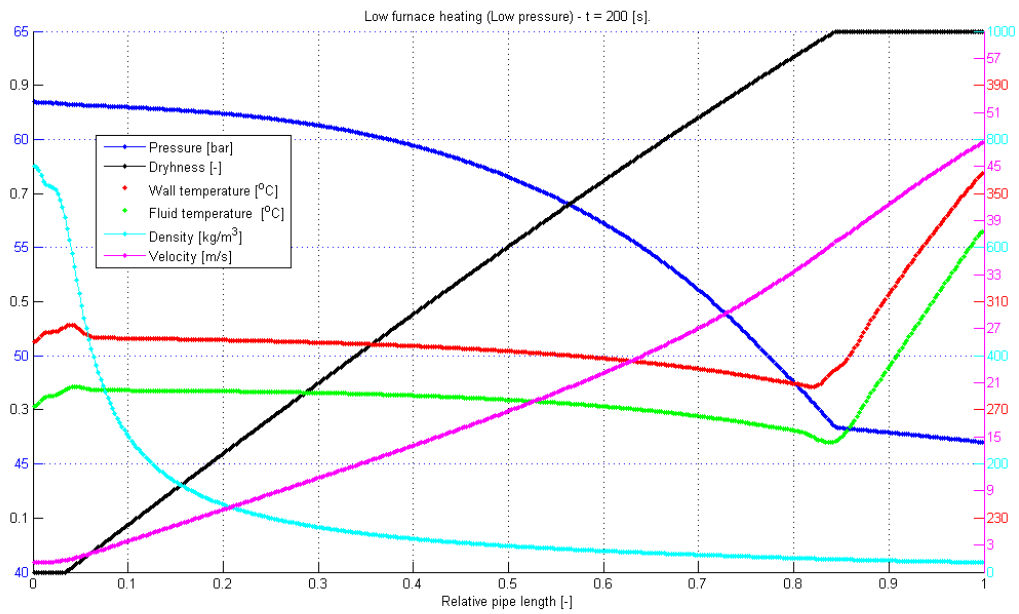
Figure 19: Bottom heating in the SKV3 boiler after 200 [s].
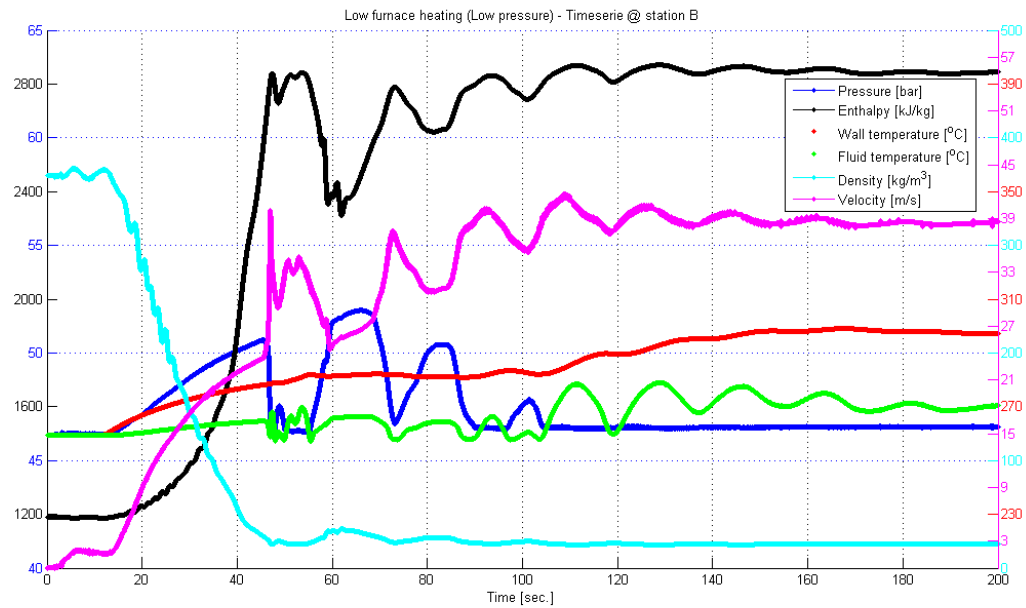
Figure 20: Time series of bottom heating in the SKV3 evaporator model at station B.
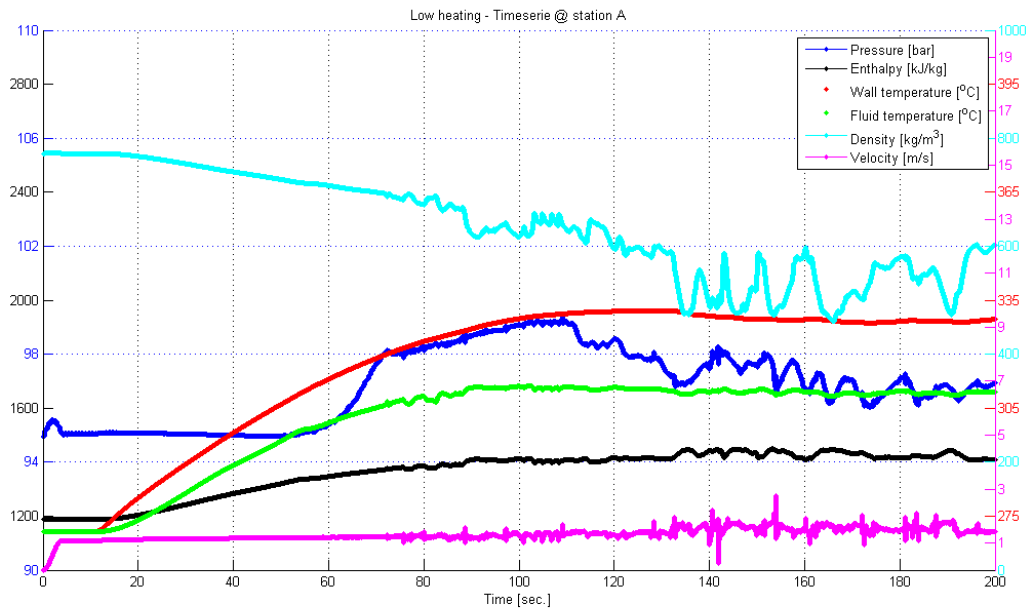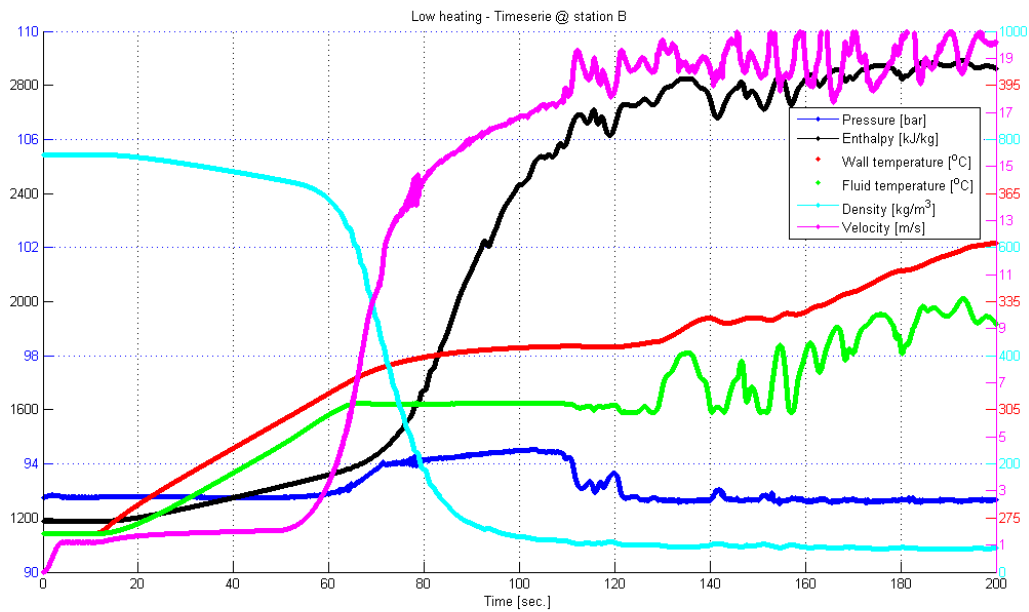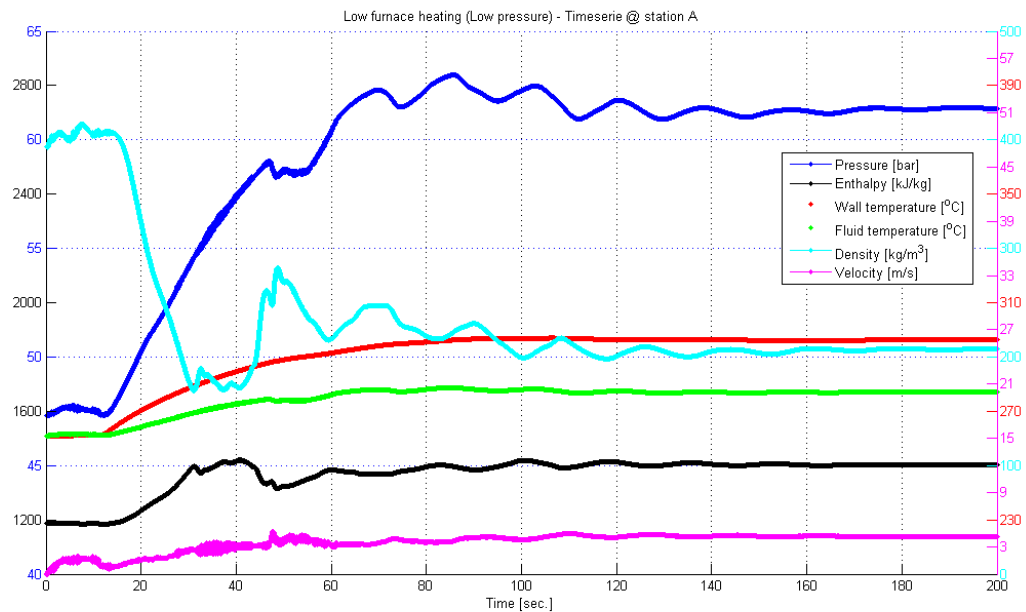

Figure 21: Time series of bottom heating in the SKV3 evaporator model at station A.
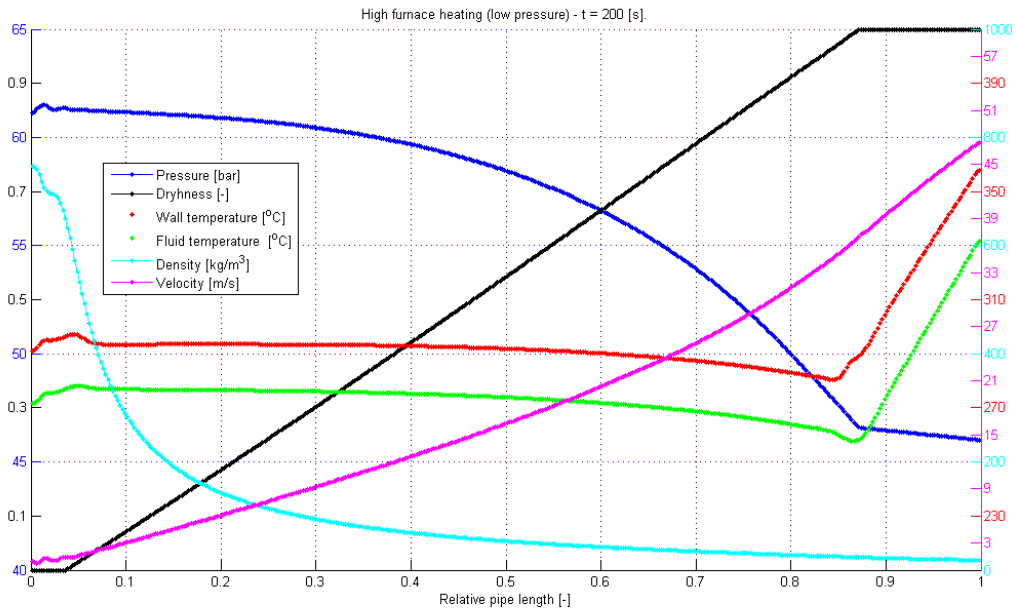
Figure 22: Top heating in the SKV3 boiler after 200 [s].
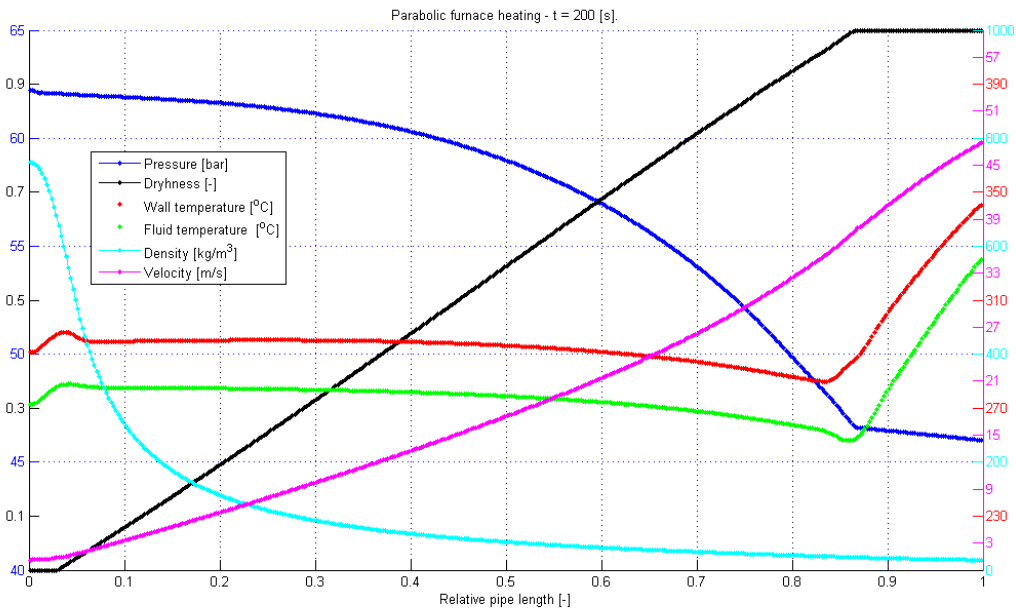
Figure 23: Parabolic heating in SKV3 boiler after 200 [s].
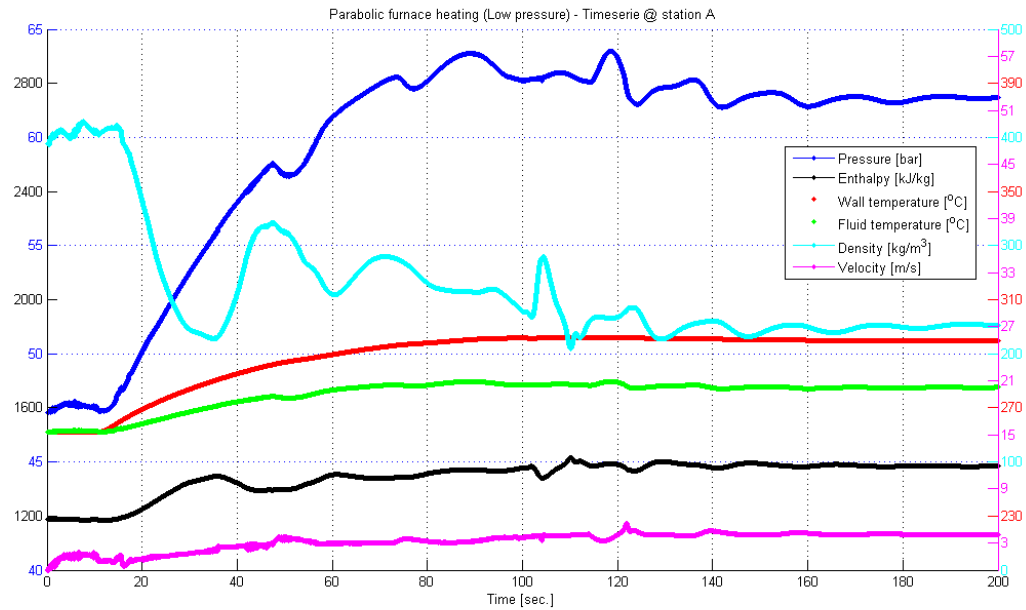
Figure 24: Time series of parabolic heating in SKV3 evaporator model at location A.
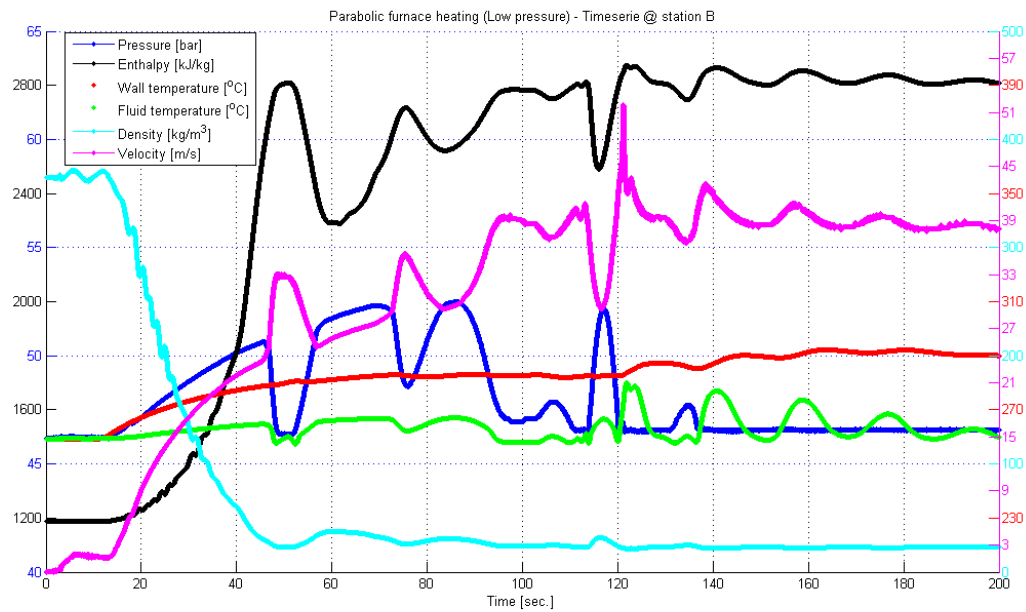
Figure 25: Time series of parabolic heating in SKV3 evaporator model at location B.
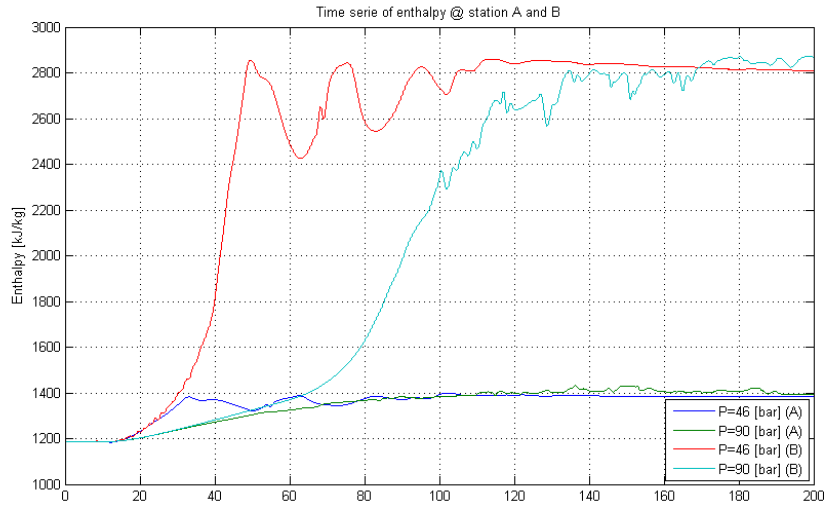
Figure 26: Comparison of enthalpy at different evaporation pressure at station A and B.
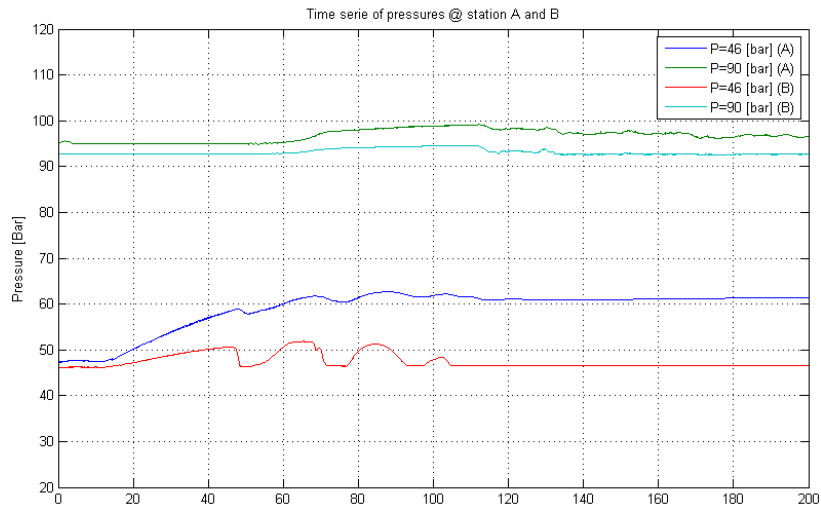
Figure 27: Comparison of pressure level at different evaporation pressure at station A and B.
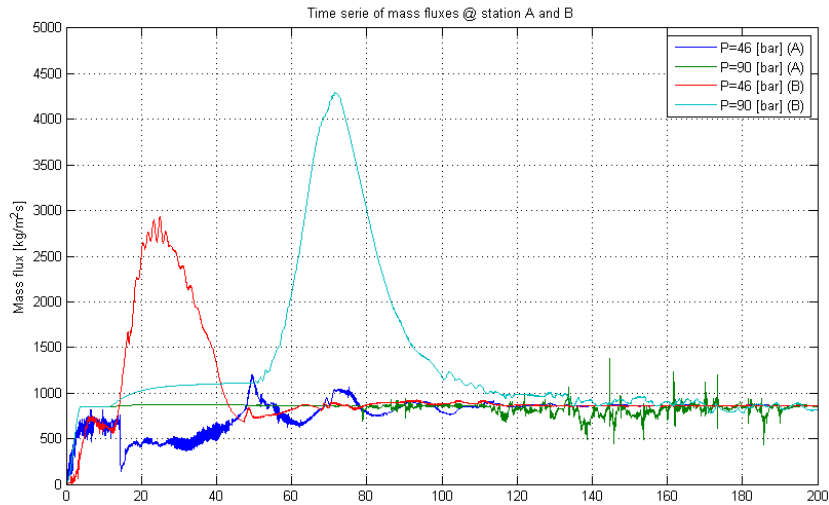
Figure 28: Comparison of mass flux at different evaporation pressure at station A and B.
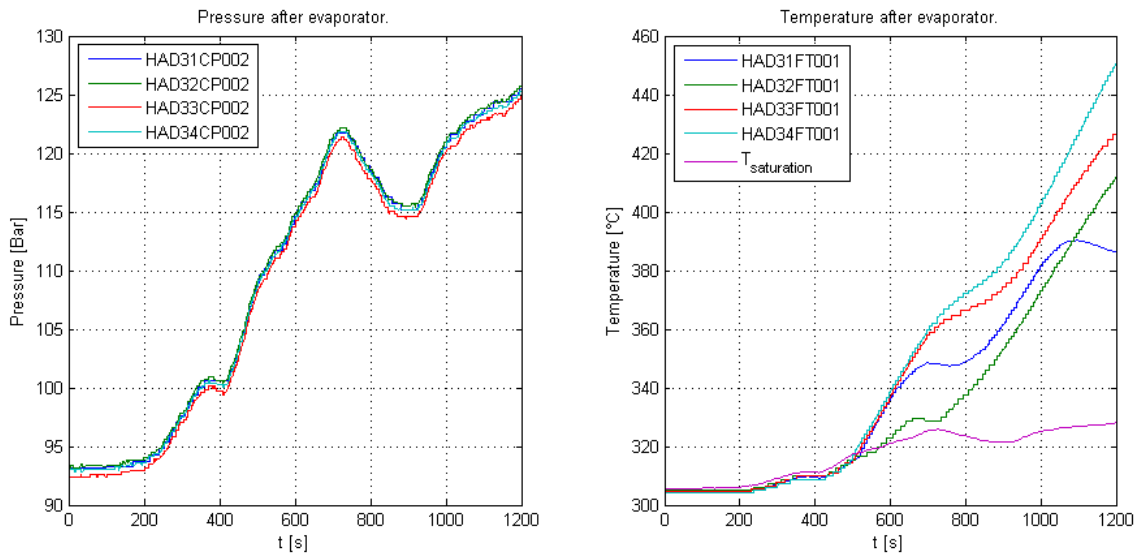
Figure 29: Pressure and temperature after boiler top section - sample 3.
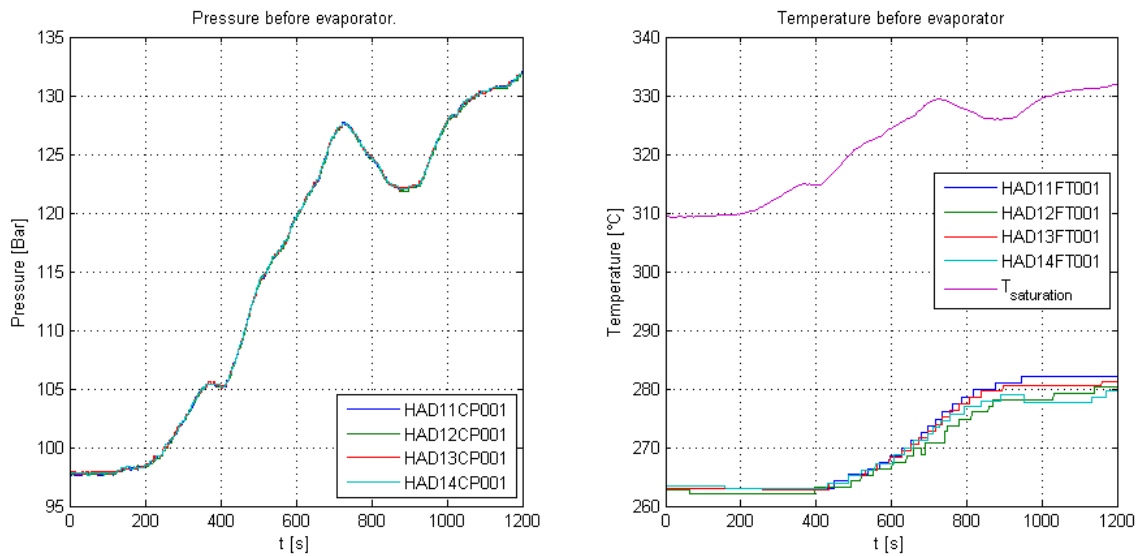
Figure 30: Pressure and temperature after ECO - sample 3.
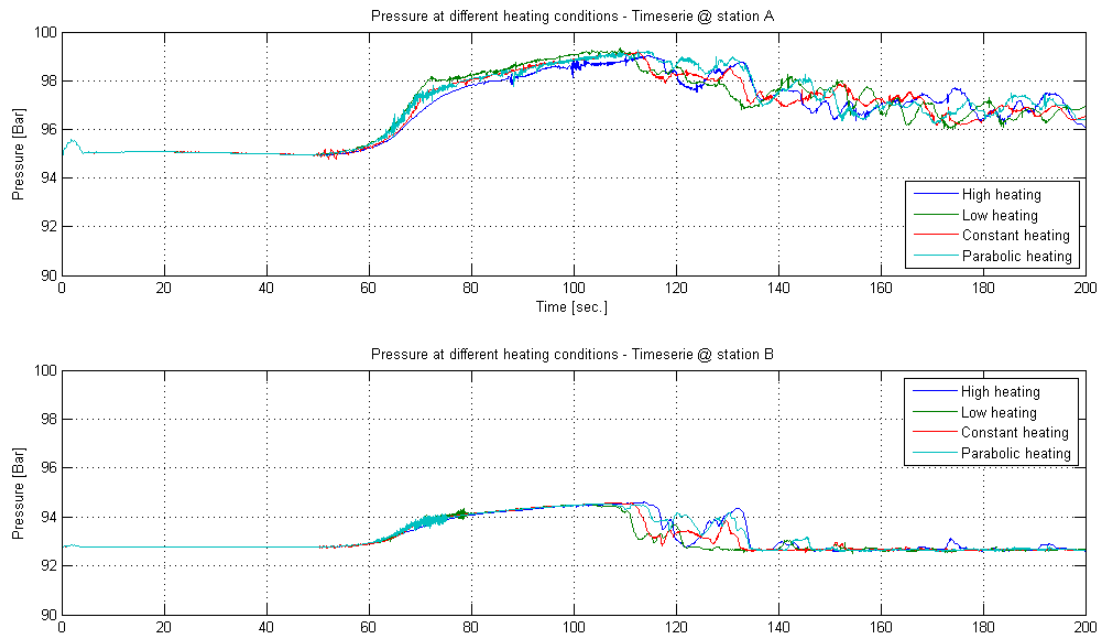
Figure 31: Comparison of the firing profiles on the SKV3 evaporator with respect to fluid pressure.
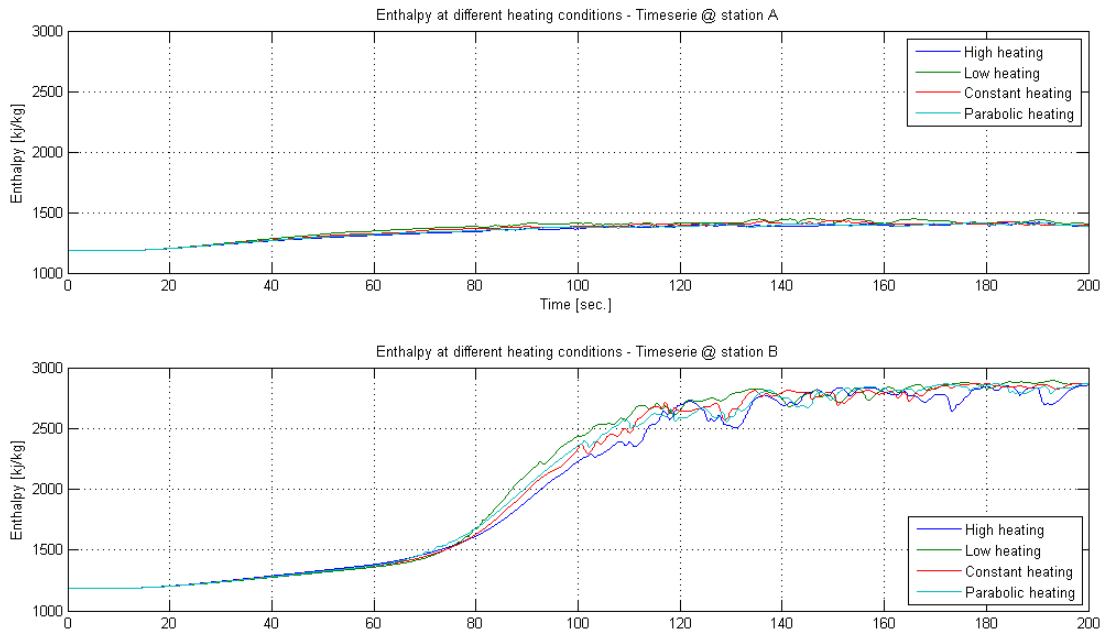
Figure 32: Comparison of the firing profiles on the SKV3 evaporator with respect to fluid enthalpy.
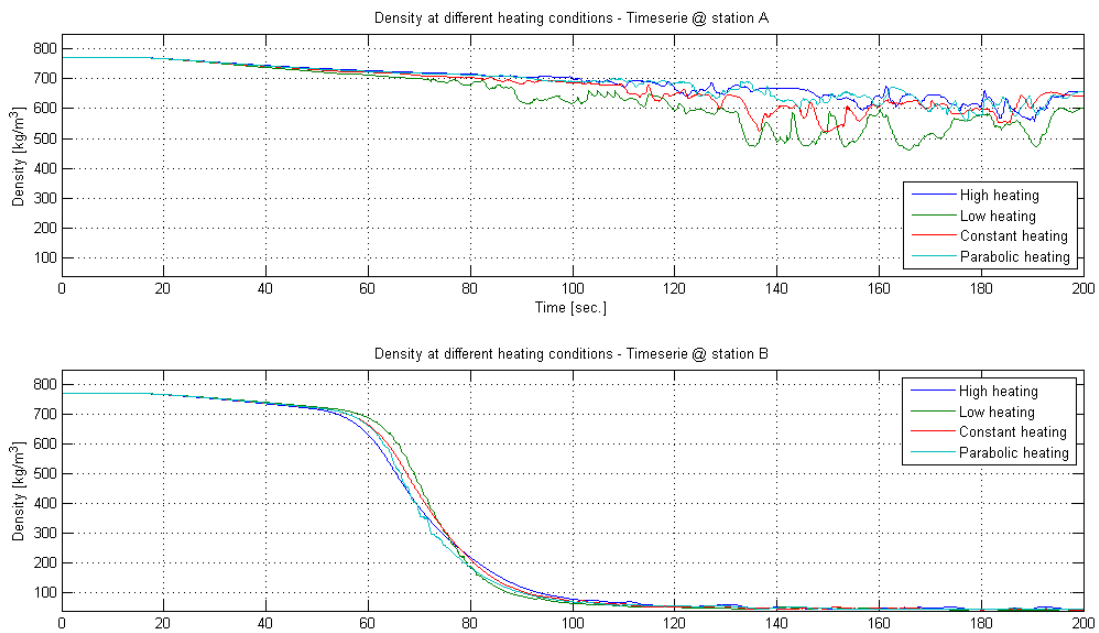
Figure 33: Comparison of the firing profiles on the SKV3 evaporator with respect to fluid density.
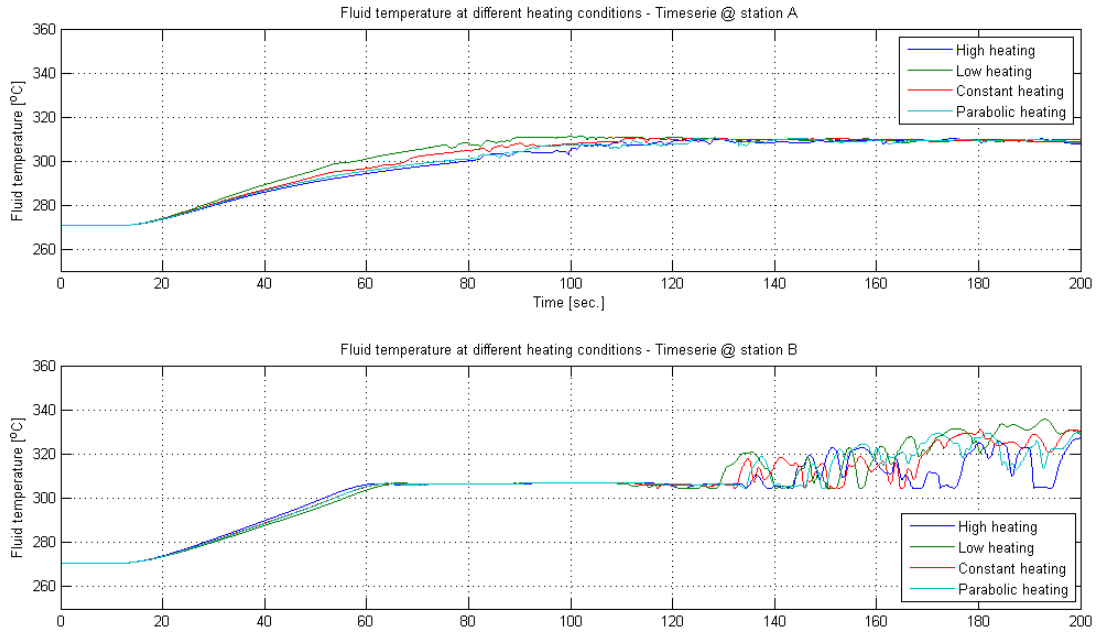
Figure 34: Comparison of the firing profiles on the SKV3 evaporator with respect to fluid temperature.
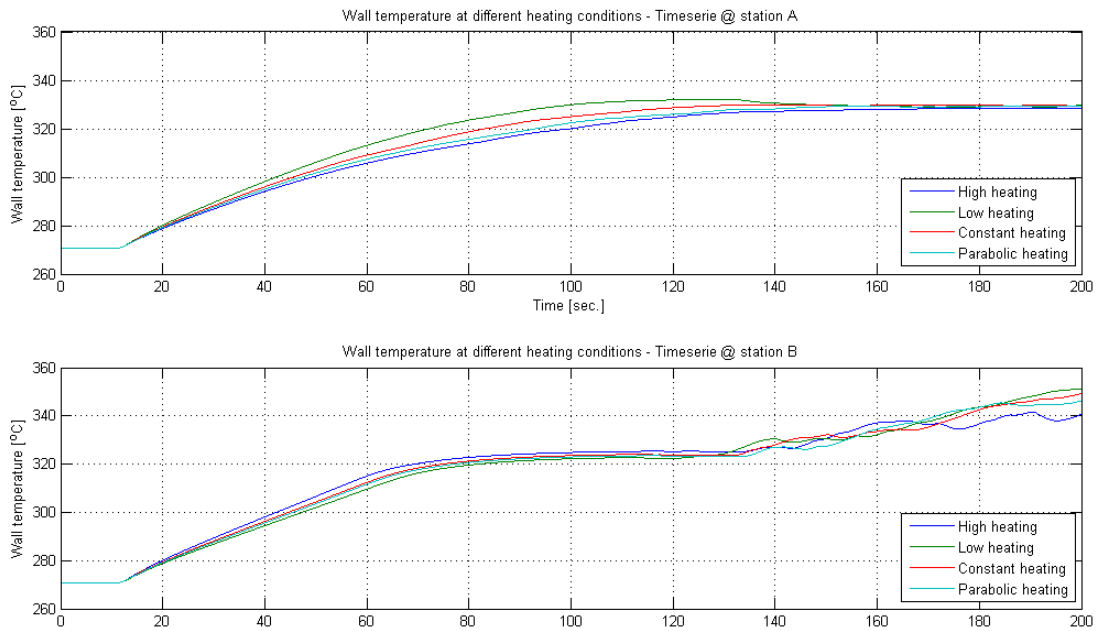
Figure 35: Comparison of the firing profiles on the SKV3 evaporator with respect to wall temperature.
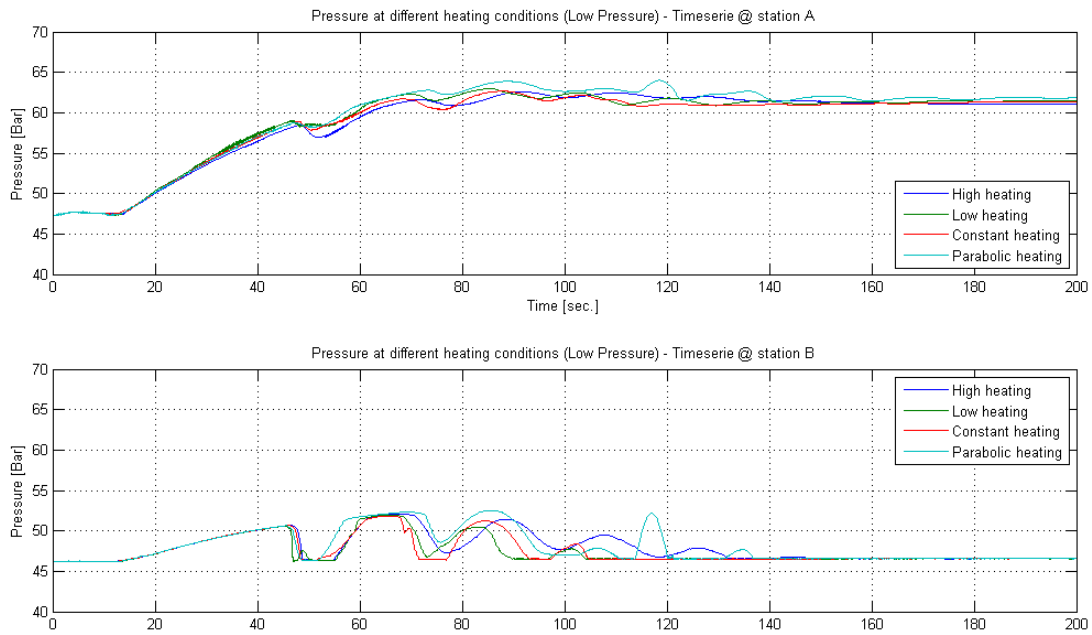
Figure 36: Comparison of the firing profiles on the SKV3 evaporator with respect to fluid pressure.
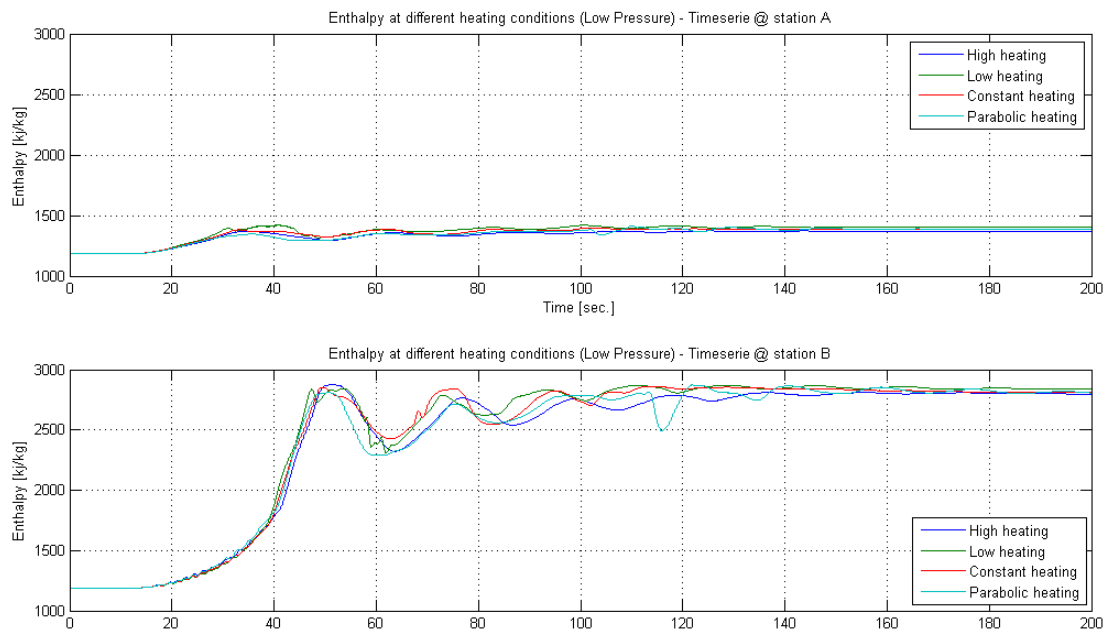
Figure 37: Comparison of the firing profiles on the SKV3 evaporator with respect to fluid enthalpy.
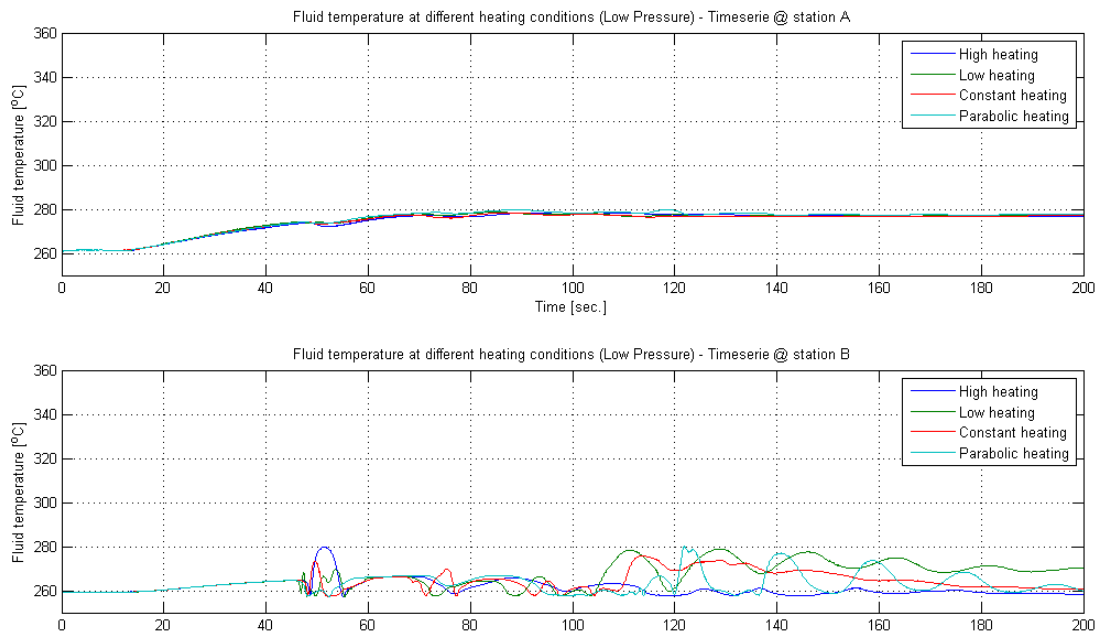
Figure 38: Comparison of the firing profiles on SKV3 evaporator with respect to fluid temperature at stations A and B.
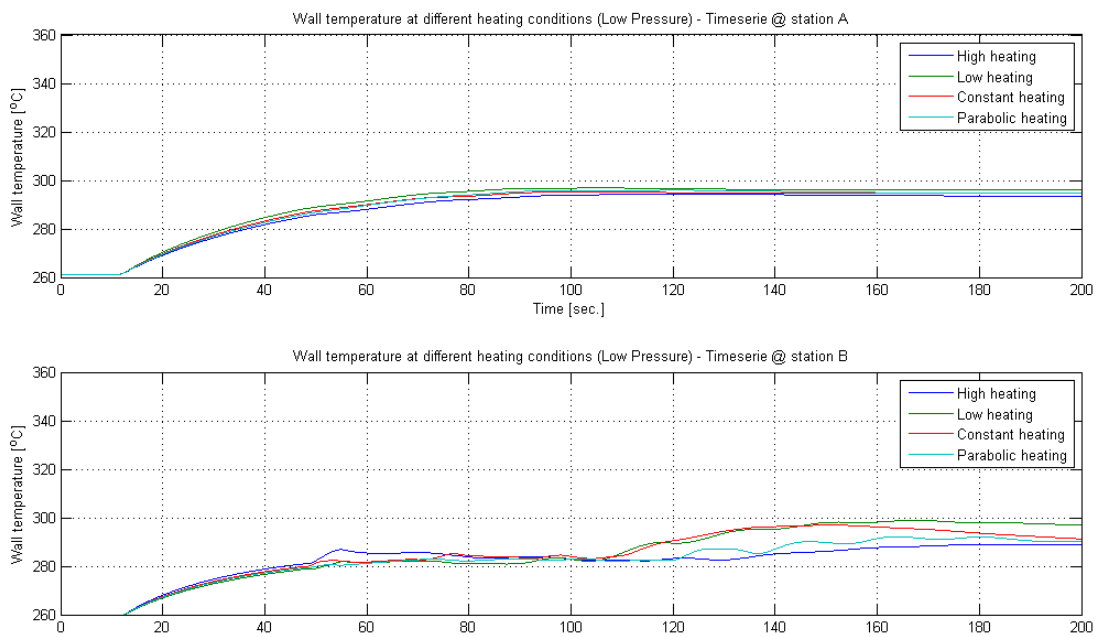
Figure 39: Comparison of the firing profiles on the SKV3 evaporator with respect to wall temperature.
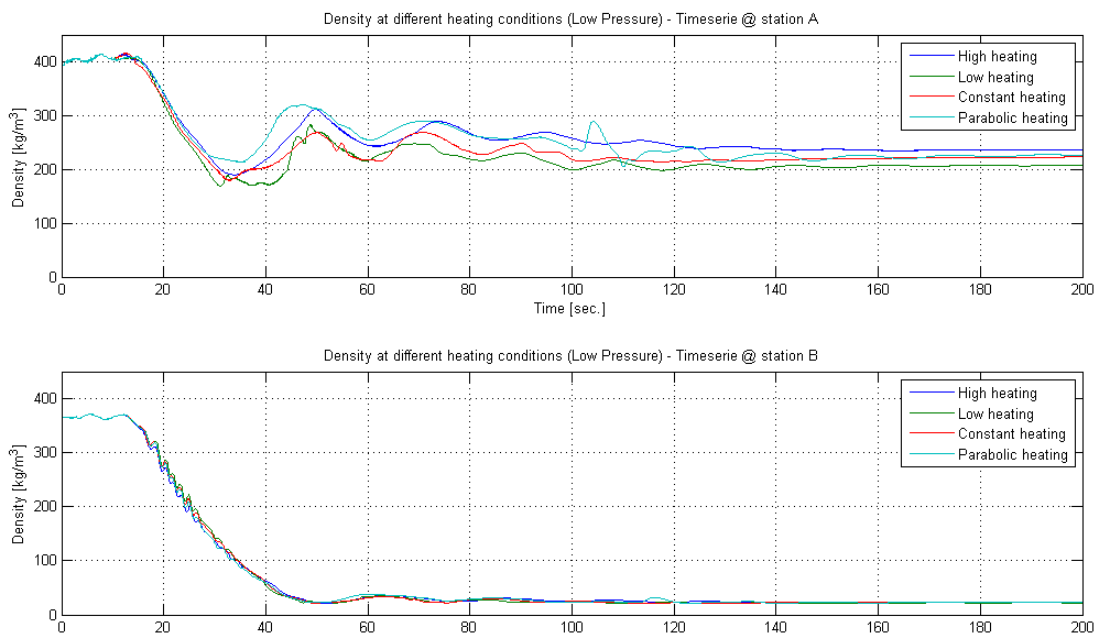
Figure 40: Comparison of the firing profiles on the SKV3 evaporator with respect to fluid density.

MODELING OF A MEMBRANE BASED HUMIDIFIER FOR FUEL CELL APPLICATIONS SUBJECT TO END-OF-LIFE CONDITIONS

Mads Pagh Nielsen[1] and Anders Christian Olesen
Aalborg University
Department of Energy Technology
9220 Aalborg, Denmark

Alan Menard
Dantherm Power A/S
9500 Hobro, Denmark

ABSTRACT

Proton Exchange Membrane (PEM) Fuel Cell Stacks efficiently convert the chemical energy in hydrogen to electricity through electrochemical reactions occurring on either side of a proton conducting electrolyte. This is a promising and very robust energy conversion process which can be used in many applications. For instance for automotive applications and various backup power systems substituting batteries. Humidification of the inlet air of PEM fuel cell stacks is essential to obtain optimum proton conductivity. Operational humidities of the anode and cathode streams having dew points close to the fuel cell operating temperature are required. These conditions must be met at the Beginning-Of-Life (BOL) as well as at the End-Of-Life (EOL) of the fuel cell system. This paper presents results of a numerical 1D model of the heat- and mass transport phenomena in a membrane humidifier with a Nafion-based water permeable membrane. Results are presented at nominal BOL-conditions and extreme EOL-conditions. A detailed sub-model incorporating the water absorption/desorption kinetics of Nafion and a novel and accurate representation of the diffusion coefficient of water in Nafion was implemented. The modeling explains why Nafion fails as a water permeable membrane at typical EOL-conditions.

Keywords: PEM fuel cell systems, Membrane Humidifiers, Nafion water diffusion, Numerical modeling.

NOMENCLATURE

|	
a	Water activity, [-]
c_p	Specific heat capacity [J/(kg·K)]
D	Diffusion coefficient [cm²/s]
f_v	Volumetric membrane H_2O content, [-]
h_L	Latent specific enthalpy, [J/kg]
M	Dry molar mass of Nafion [kg/kmol]
m	Number of discretization points [-]
$\dot{m}$	Mass flow [kg/s]
$\dot{n}$	Molar flux [mole/s·m²]
p	Total pressure [bar]
t	Thickness of Nafion membrane [m]
T	Temperature [K]
U	Total heat transfer coeff., [W/m²*K]
V	Partial molar volume, [kmol/m³]
$\dot{V}$	Volume flow [m³/s]
ΔA	Area element in humidifier [m²]

$\Delta\dot{m}$	Water mass flow exchanged [kg/s]
σ	Proton conductivity of Nafion [S/cm]
ρ	Density [kg/m³]
ϕ	Surface roughness parameter [m/m]
λ	Nafion H_2O content [$mol_{H_2O}/mol_{SO_3^-}$]
ω	Absolute humidity [kg H_2O/kg dry air]

Subscripts

Air	Properties related to humid air
Dry	Ref. to dry stream/dry Nafion
Equil	Equilibrium membrane water cont.
H_2O	Water
i	Index in space
in	Inlet
out	Outlet
Membrane/M	Referring to the Nafion Membrane
Water/W	Properties related to water
Wet	Referring to the wet stream

---

[1] Corresponding author: Phone +45 9940 9259 E-mail: mpn@et.aau.dk

INTRODUCTION

A Proton Exchange Membrane (PEM) fuel cell stack provides high efficient energy conversion. A typical PEM fuel cell assembly is illustrated in figure 1 (left). A fuel cell stack consists of a number of serially connected cells configured in this way. Hydrogen, air and cooling water are supplied through manifolds in the longitudinal dimension of the fuel cell stack. The proton exchange membrane fuel cell principle (the membrane assembly or MEA) is illustrated in figure 1 (right) along with the chemical reactions taking place in the catalyst layers at either side of the electrolyte. Please note that the figure to the right is not in scale but is stretched in the through-MEA axial direction (GDL=Gas Diffusion Layer).
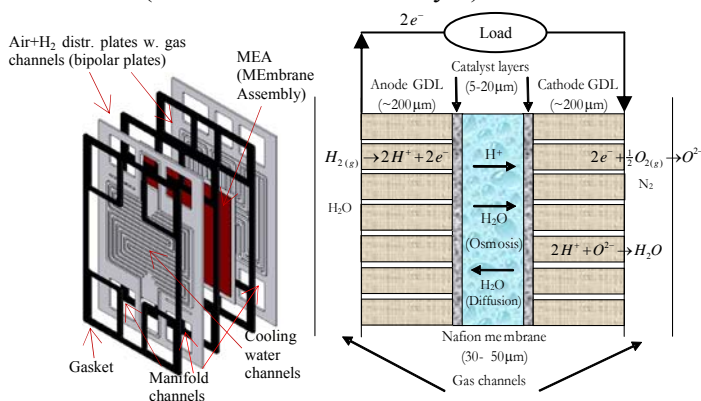
Figure 1: Typical PEM fuel cell assembly (left), PEM MEA topology and reactions (right).

The porous GDL assists the efficient distribution of reactants over the catalyst layers. Hydrogen is dissociated into protons and electrons at the anode. The electrons are passed through an electrical load. At the cathode, the electrons react with oxygen in the air and are reduced to O^{2-} ions which are combined with the protons passing the electrolyte membrane to produce water. A state-of-the-art single PEM fuel cell can operate at a potential of approximately 0.7 V at a current density of about 0.8 A/cm^2 MEA-area.

Humidifiers for PEM fuel cell stacks are essential components in order to reach acceptable performance and operational life. PEM fuel cells utilize Nafion membranes or polymers with similar properties. Nafion is a material which is a per-

fluorosulfonic acid PTFE (Poly-Tetra-Fluoro-Ethylene) copolymer. This PTFE, also known commercially as Teflon, is highly resistant to chemical reactions, due to the presence of strong carbon fluorine bonds. Thus, rugged polymer membranes can be manufactured thinner than 50 μm [1]. Hydrophilic sulfonic acid groups and their volume expanding nature absorbing water provides Nafion with the proton exchange properties.

However, the Nafion electrolyte membranes in PEM fuel cells must be fully hydrated with water in order to act as efficient proton conductors.
The specific proton conductivity in S pr. cm membrane thickness as function of water activity (i.e. partial pressure of water divided by saturation pressure of water at a given temperature) or relative humidity (as this is often referred to in the case of humid air up to activities of 1) of the fuel cell membrane is shown in figure 2.
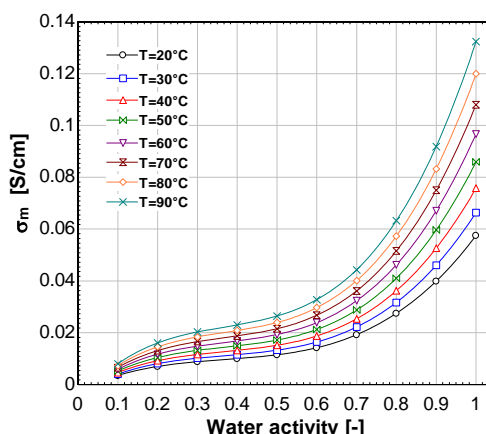
Figure 2: Nafion H$^+$ conductivity vs. activity & temperature.

It is thus essential, that the reactant gasses supplied to the PEM fuel cell stack (on both the anode and cathode) are humidified so that the membrane relative humidity is close to unity where optimum conductivity is achieved. At water activities exceeding 1, there is a risk of flooding the porous catalyst layers in the fuel cell stack.

Through the electrochemical conversion in a fuel cell, the reactants (hydrogen and oxygen) are converted to water. Membrane humidifiers offer the advantage of utilizing the product water in the depleted cathode exhaust air to humidify the dry inlet streams, simultaneously preheating the gas-

ses to the operational temperature of the fuel cell stack. Typically, the outlet air from the cathode is saturated with water at the operational temperature of the fuel cell stack (typically~60-70ºC). Either an air or a water cooling system makes sure that the stack temperature is maintained within a certain margin. The humidification is thus a balance of ensuring sufficient water to hydrate the electrolyte membrane, while simultaneously avoiding flooding of liquid water in the various parts of the fuel cell MEA [1].

A typical desired conditioning of the streams is to reach a dew point temperature of the dry air outlet (i.e. the humid air stream supplied to the fuel cell stack cathode inlet) from the humidifier close to the stack temperature. A schematic illustration of a typical fuel cell system configuration including a membrane humidifier is shown in figure 3.
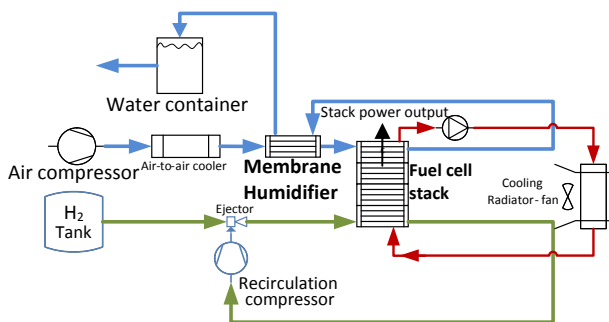
Figure 3: Humidifier integrated in a PEM-system.

At the fuel cell anode, hydrogen is supplied. The excess unreacted hydrogen leaving the anode is typically recirculated using an ejector often supplied by a small fan or compressor. The system is periodically purged to avoid problems with Nitrogen cross-over from the cathode side air [1]. Water is produced through the cathode half-reaction and typically, the higher water concentration here means that water migrates by back-diffusion from the cathode to the anode. By recirculating the anode output of hydrogen and water, active anode humidification is typically not necessary.

An air compressor supplies the air to the fuel cell stack cathode-side. Through the compression process, the temperature increases and thus the relative humidity and thus the water activity of the humid ambient air decrease significantly.

At EOL-conditions (normally after 10-20,000 hours of operation, depending on the application), the compressor efficiency has typically decreased meaning that the incoming air is further heated. Simultaneously, the fuel cell stack has also degraded affecting the operational conditions of the humidifier. An increased flow of both reactant gasses (air & H_2) to the fuel cell stack is necessary to maintain the required stack power output.

At very dry ambient conditions (for instance in a dessert with an ambient temperature of 50ºC) or conditions at higher altitudes at decreased pressures (for instance in the mountains), the temperature of the dry air inlet to the humidifier can be as high as 80ºC. A work-around to resolve this is to add an air-cooler after the air compression to cope with these EOL-extreme-conditions but this component adds to system cost and complexity.

In this paper, a nominal BOL-case and an EOL-case with realistic conditions are considered to model the humidifier behavior.

Membrane humidifiers have been utilized as the predominant means of humidification in commercial fuel cell stack systems during the past decade. The principle of utilizing the wet and warm depleted air exiting the cathode was first demonstrated in a 2kW stack setup developed by the Paul Scherrer Institute in 1999. Later membrane humidification has been adapted as the dominant method of humidification in PEM-systems by most system integrators [2-12]. Typically, membrane humidifiers are designed as shell and tube heat and mass exchangers (see figure 4) with a number of Nafion tubes (in the shell there are a bundle of fibers/tubes with inner-diameters of typically 0.4-0.8 mm).

Figure 4: Shell and tube membrane humidifier.

Recently, the trend has been going towards using circular tube shaped membranes based on Nafion

and polymers with similar properties due to their good mechanical, gas sealing properties and good water transport properties. Consequently, Nafion in fuel cell systems serves the different purposes as a water and proton conductor in PEM's and furthermore as water conductor in the humidifiers. This paper presents a 1D distributed parameter steady-state model of a membrane humidifier.

DIFFUSION OF WATER IN NAFION

The water transport in Nafion has been extensively researched [13-17]. The transport process is mainly governed by the water diffusivity D_w of the membrane subject to different conditions. Water diffusion coefficients in Nafion based on different sources are illustrated in figure 5 as function of the Nafion water content λ (a value of 14 corresponds to a fully hydrated membrane. Values > 14 indicate the presence of liquid water).

The different research groups determining these water diffusion coefficients measured the diffusion coefficient at very different conditions with varying methods. Some of the apparent deviations can be explained strictly mathematically as pointed out in [13]. The peaking diffusion coefficients around 3 from some references could very well be due to mathematical artifacts. If liquid water is present, the diffusion coefficient increases further.
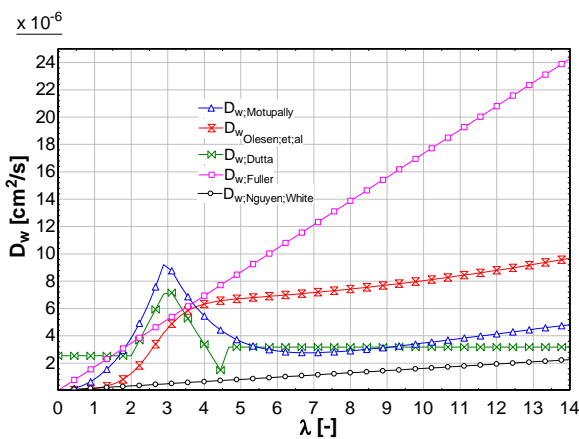
Figure 5: D_w as function of λ [13-17].

The recent relations proposed by Olesen et al. [13] are used for the calculation of the water diffusion through the membrane. These equations, account for the water uptake and release kinetics of Nafi-

on, while additionally also accounting for the swelling of the membrane. What is notable, using this model, is that a low λ results in virtually no water transport when kinetics is accounted for [13]. D_w's below 5 strongly limits water transport. To model the sorption/desorption kinetics of water in the Nafion membrane, the model suggested by Ge et al. [21] has been used. This paper suggests a non-equilibrium formulation of the water sorption/desorption phenomena. Equation (1) and (2) govern the kinetics of water sorption/desorption:

$$\dot{n}_{H_2O,membrane} = \phi k \frac{\rho_{membrane}}{M_{membrane}} \left(\lambda - \lambda_{equil} \right) \quad (1)$$

$$k = k^{T_0} f_v \exp \left(2416 \left(\frac{1}{303} - \frac{1}{T} \right) \right) \quad (2)$$

In (1) ϕ is a factor to account for the actual surface roughness. In [13] it is suggested to use a value of unity. The factor k^{T_0} is 1.14 m/s in case of absorption and to 4.59 m/s in case of desorption [21].

From [13], it can be found that the volumetric membrane water content is:

$$f_v = \frac{\lambda V_w}{\left(\dfrac{M_{membrane}}{\rho_{membrane}} + \lambda \cdot V_w \right)} \quad (3)$$

The partial molar volume of water V_w is found from (4) accounting for membrane water swelling:

$$1 + 0.0126 \cdot \lambda = 1 + \left(\frac{V_w}{\left[\dfrac{M_{membrane}}{\rho_{membrane}} \right]} \right) \cdot \lambda \quad (4)$$

The through-membrane molar flux of water is:

$$\dot{n}_{H2O;membrane} = \left(\frac{\rho_{Nafion;dry}}{M_{Nafion;dry} \cdot t_{membrane}} \right) \cdot \int_{\lambda_{dry}}^{\lambda_{wet}} D_w \ d\lambda \quad (5)$$

Equating equations (1) and (5), makes it possible to calculate the actual water content in the membrane based on the above kinetic model.
Based on the work presented in [13], following empirical fit for the diffusion coefficient of water in Nafion at different temperatures was found:

$$D_w = \left(5.39 \times 10^{-2} + 1.455 \times 10^{-5} \cdot \lambda^2 \right) \cdot$$
$$\left(1 + tanh \left(\frac{\lambda - 2.6225}{0.8758} \right) \right) \cdot exp \left(-\frac{3343}{T} \right) \quad (6)$$

Here λ as function of water activity is found from the references [13 & 14]:

$$\lambda = \begin{cases} 0.043 + 17.81a - 39.85a^2 + 36.0a^3 & ,0 \le a \le 1 \\ 14 + 1.4(a-1) & ,1 < a \le 3 \end{cases} \quad (7)$$

Multiplying the molar flux of water through the membrane by the Nafion membrane area and the molar mass of water enables us to find the water mass flow exchanged through the membrane, $\Delta\dot{m}$.

EXPERIENCES FROM FIELD TESTS

Several commercial Nafion-based membrane humidifiers were tested in fuel cell systems subject to real-life conditions by the Danish fuel cell system manufacturer Dantherm Power A/S.

Tests were conducted at different conditions on a commercial 3kW Ballard® PEM fuel cell stack system reflecting expected EOL stack conditions and extreme ambient conditions. The tests showed that the humidifiers would work at nominal conditions at BOL but would fail at high ambient temperatures at EOL due to limited water transport.

MODELING FORMULATION

A numerical model was developed to understand this phenomenon and to investigate how to optimize the system to be able to handle these extreme conditions at the lowest possible cost. The model was based on the same conditions as used in the abovementioned tests. The following inlet and outlet conditions were studied for the 2 cases:

Nominal BOL Case:
Humidifier Nafion tube total surface area: 0.5 m^2
Humidifier (dry side) inlet temperature: 45ºC
Humidifier (dry side) inlet pressure: 1.145 bar
Humidifier (wet side) inlet temperature: 70ºC
Humidifier (wet side) inlet pressure: 1.1 bar
Relative humidity at humidifier dry inlet: 14%
Relative humidity at humidifier wet inlet: 100%
Flow (on either side of humidifier) ~ 170 NLPM

Extreme EOL Case:
Humidifier Nafion tube total surface area: 0.5 m^2
Humidifier (dry side) inlet temperature: 80ºC
Humidifier (dry side) inlet pressure: 1.145 bar
Humidifier (wet side) inlet temperature: 70ºC
Humidifier (wet side) inlet pressure: 1.1 bar
Relative humidity at humidifier dry inlet: 0%
Relative humidity at humidifier wet inlet: 100%
Flow (on either side of humidifier) ~ 180 NLPM

The modeling was performed in the tool Engineering Equation Solver (EES) [22]. EES solves a set of non-linear equations using an efficient and accurate modified reduced step-size Newton-Raphson solver and has built-in thermo-physical property relations including psychrometric functions for the properties of humid air. In the modeling, it is assumed that the humid air will properly reflect the actual conditions with oxygen-depleted air due to the similarities of oxygen and nitrogen.
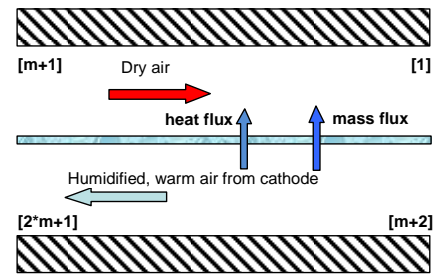
Figure 6: Modeling domain of the humidifier.

The steady power and mass flow balances in eqs. (8)-(11) were setup for the humidifier, using a discretized non-linear algebraic equation form where $i \in [1..m]$. It is modeled as a 1D heat and mass exchanger with *m* elements (here the wet stream power balance (8) is referring to the hot and wet stream exiting the cathode of the fuel cell stack and the dry stream energy balance (9) is the air stream entering counter current to be humidified. (10) and (11) give the mass flow balances).

$$\Delta\dot{m}_{water,m-i+1} \cdot h_l = \rho_{wet} \cdot c_{p,wet,air} \cdot \dot{V}_{wet} \cdot [T_{i+1} - T_i] + \quad (8)$$
$$U \cdot \Delta A \cdot [T_{i+m+1} - T_i]$$

$$\Delta\dot{m}_{water,i} \cdot h_l = U \cdot \Delta A \cdot [T_{i+m+2} - T_{i+1}] - \quad (9)$$
$$\rho_{dry} \cdot c_{p,dry} \cdot \dot{V}_{dry} \cdot [T_{i+m+1} - T_{i+m+2}]$$

$$\dot{m}_{dry,i} = \dot{m}_{dry,i+1} + \Delta\dot{m}_{water,i} \quad (10)$$

$$\dot{m}_{wet,i+m+2} = \dot{m}_{wet,i+m+1} - \Delta\dot{m}_{water,m-i+1} \quad (11)$$

The equidistant grid for the numerical calculations is arranged in a vector so that the inlet of the dry stream is at index [m+1], the inlet of the wet

stream at index [m+2], the outlet of the dry stream is [1] and the outlet of the wet stream is [2*m+1] (see figure 6).

Thermal and calorimetric properties were calculated in each element based on the thermophysical library in EES. Heat transfer-wise; there is laminar flow in all channels on both the shell and the tube side leading to constant Nusselt numbers. Appropriate values for circular tubes (tube side~3.66) and ~triangular tubes (shell side~2.47) were used to approximate the overall heat transfer coefficient [19].

The thermal conductivity of Nafion has been neglected. It depends on the water content in the Nafion and has been measured in several studies (for example in [23] & [24]). Even in cases of no hydration, the thermal conductivity is negligible.

It was furthermore assumed that the system is well-insulated, so surface heat losses are neglected. The flow distributions in tubes on either side were found to be quite even between the fibers in the shell-and-tube topologies under the given conditions [5]. Flow mal-distribution has thus been neglected on as well the shell as the tube side of the membrane humidifier.

The pressure losses in the humidifier channels were measured to be around 10-30 mbar at the earlier mentioned flow conditions. The pressure loss in the stack ranges from 10-20 mbar. An average pressure loss has been included as seen in the inlet and outlet conditions used in modeling.

Depending on the degree of condensing and surface evaporation at either side, the last term in the numerator with h_l (latent energy contribution) can be positive or negative. In general the transport through Nafion occurs via a so-called pervaporation process [20], which means that no direct latent energy is involved in the transport process through the membrane. However, surface evaporation will be present and in some cases condensation will occur (at water activities exceeding 1). These effects have been included in the calculation of the calorimetric properties in the membrane humidifier.

A grid consistency study showed that a discretization with 60 elements was sufficient to reach consistent results. Overall, this resulted in a non-linear equation set with approximately 3000 equations and 3000 unknowns. Energy and mass balances were calculated indicating energy and mass defects of far less than 1% in all calculated cases.

RESULTS AND DISCUSSION

Modeling results for the humidifier temperatures in counter-current operation mode are illustrated in figure 7.
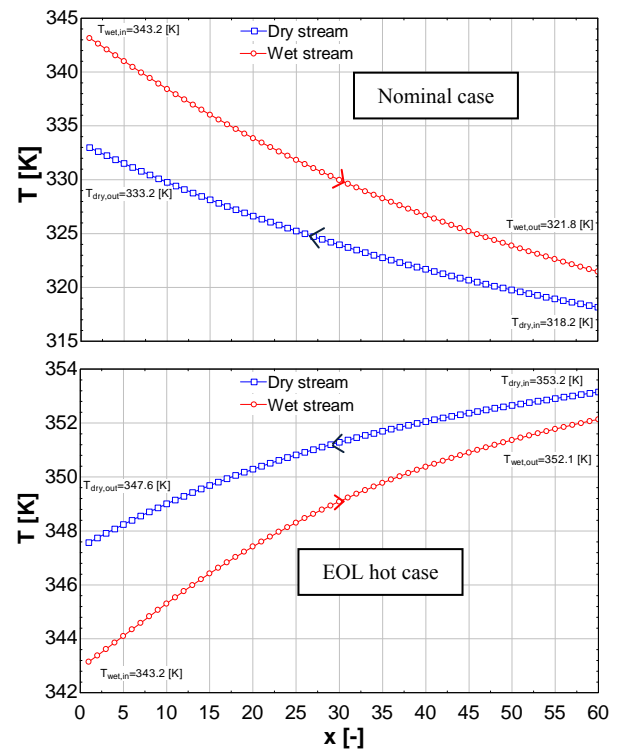
Figure 7: Temperature profiles in humidifier.

In the nominal BOL-case, there will be condensation at the wet stream outlet as the water activity exceeds 1.

The plots in figure 8 show the variation of the water activity (i.e. the ratio between the partial pressure of water in the humid air divided by the saturation pressure at the given temperature) along with the dry stream temperature in the 60 elements the two sides was discretized into through the humidifier (note the location of inlets and outlets).
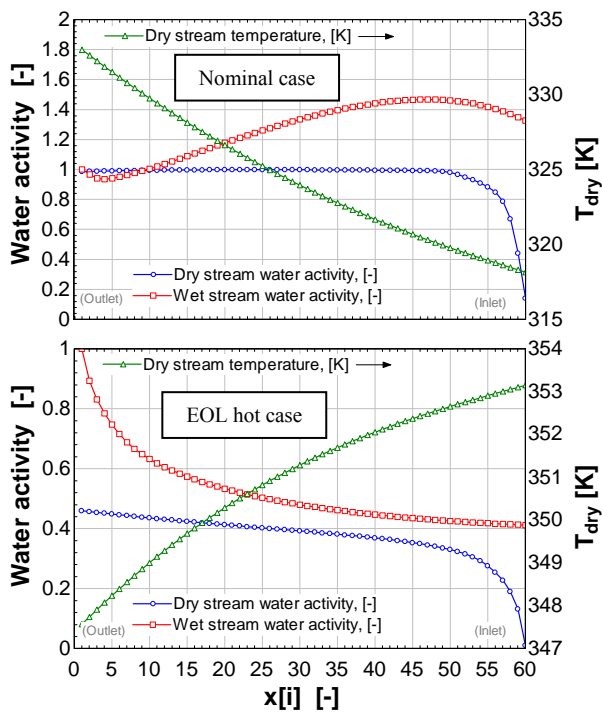
Figure 8: Water activities and dry stream temp.

The stack inlet temperature is desired to be 60ºC and the outlet temperature is ~70ºC. It follows from figure 8 that the membrane humidifier works properly at the nominal BOL-case where it saturates the cathode air with water ideally at a temperature close to the desired inlet temperature. At the extreme EOL conditions, the humidifier fails to reach the desired water transfer. This contradicts theoretical studies with other D_w-relations which indicate that the humidifier should work properly under such conditions. The present model agrees with the experiences from field tests.

The water contents in the two humidifier channels and the membrane are shown in figure 9. The reason for the bad water transport properties can be found considering these membrane water contents. In the nominal BOL-case, the membrane is nearly fully hydrated with water (i.e. λ~14). For the EOL extreme hot case, the water content is very low and when considering the sorption/desorption kinetics, there is only a very limited water transport through the membrane.
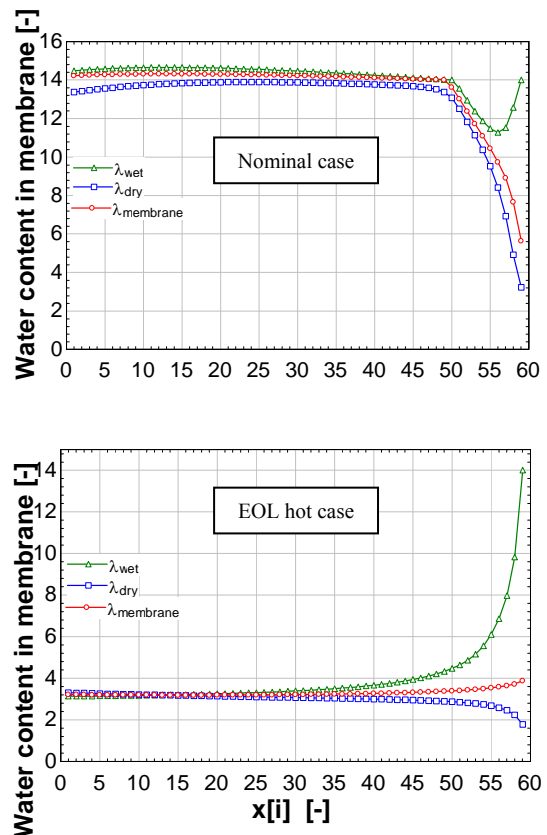
Figure 9: Membrane water contents.

Figure 10 and 11 are psychrometric charts illustrating the thermal processes occurring at respectively the dry and wet side of the humidifier. The psychrometric charts show the moist air (the property called "AirH$_2$O" in EES) absolute humidity or 'humidity ratio' as the ordinate in [kg water/kg dry air] and the abscissa is the temperature in [K]. The upper thicker black curve shows the saturation line of water in dry air subject to these properties (corresponding to a relative humidity of 100%~an activity of 1). The lines below from 0.2-0.8 illustrate iso-lines of relative humidity from 20-80%. Wet bulb temperatures and specific volumes are additionally given in the charts.

The two charts in figure 10 show the process in the nominal BOL-case. It is worth noting, that the nominal BOL-case reaches equilibrium at the saturation line (relative humidity of 100%).
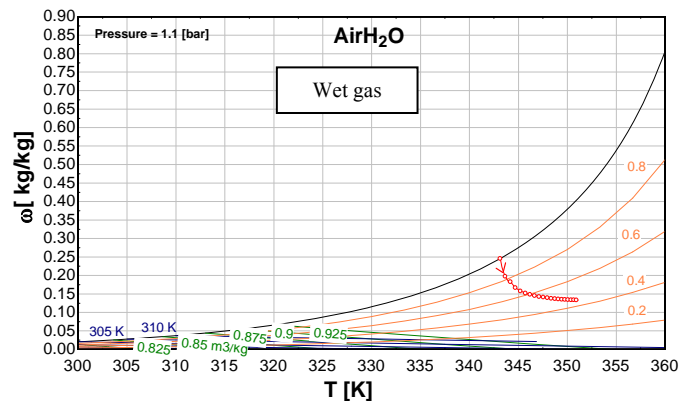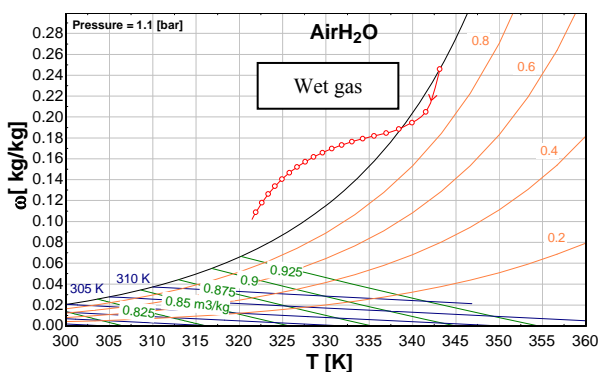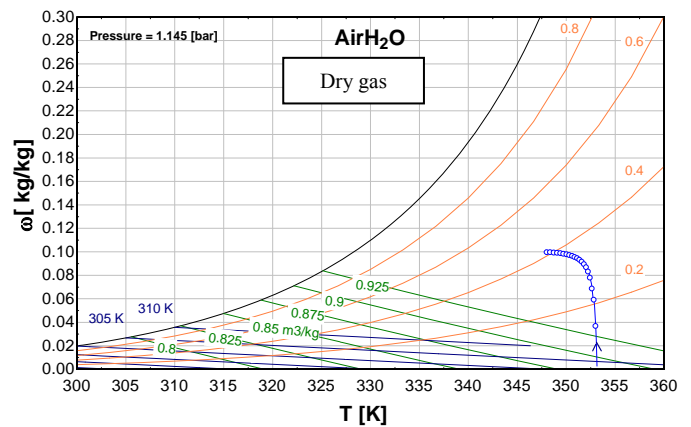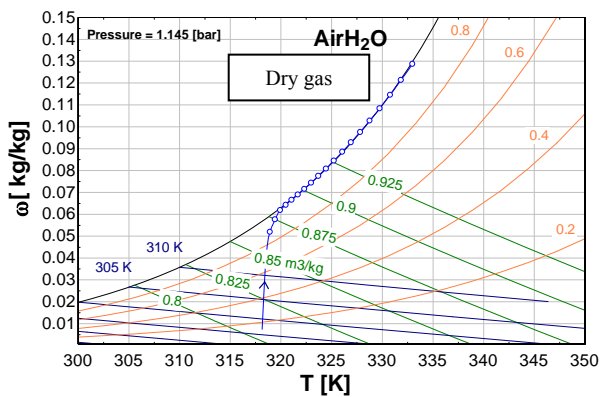
Figure 10: BOL case in psychrometric charts.

The plots in figure 11 illustrate the psychrometric charts for the extreme EOL case – i.e. operation with worn system components and extremely dry and warm conditions.

In this case, no equilibrium is reached but the absolute humidity keeps increasing slightly while the temperature decreases. Increasing the area of the humidifier will clearly not solve this problem. A certain degree of cooling will be required. In this case, the critical issue is not the dry ambient air but rather the high temperature resulting in a very low water activity at the dry air inlet to the humidifier limiting the mass transfer of water.

Figure 12 illustrates the transport of water through the membrane in two cases. The overall mass flow rate of water transported through the Nafion tubes of the humidifier are found by integrating the curves to yield respectively 0.47 g/s for the BOL nominal case and 0.35 g/s for the EOL extreme case. The difference may appear to be quite small but the fuel cell stack cannot operate at 0.35 g/s.

Figure 11: EOL case in psychrometric charts.

The membrane water transport from the wet to the dry side of the humidifier shows that the area of the membrane in many cases is less important in terms of water transfer as the majority of the mass transport will take place over a very limited area of the Nafion-membrane-tubes in the humidifier. This leaves a potential for constructing part of the tubes with a cheaper material having acceptable heat transfer properties. Nafion is a quite expensive material, so this is a quite relevant issue.

The streams must also be heated to the stack temperature so the heat transfer area is required.

In some cases, when operating the system at warm EOL conditions, it might be beneficial to bypass part of the insulated membrane humidifier area, since this leads to a better water transfer in this particular case if the humid air could be cooled in

an intelligent way not requiring additional components.
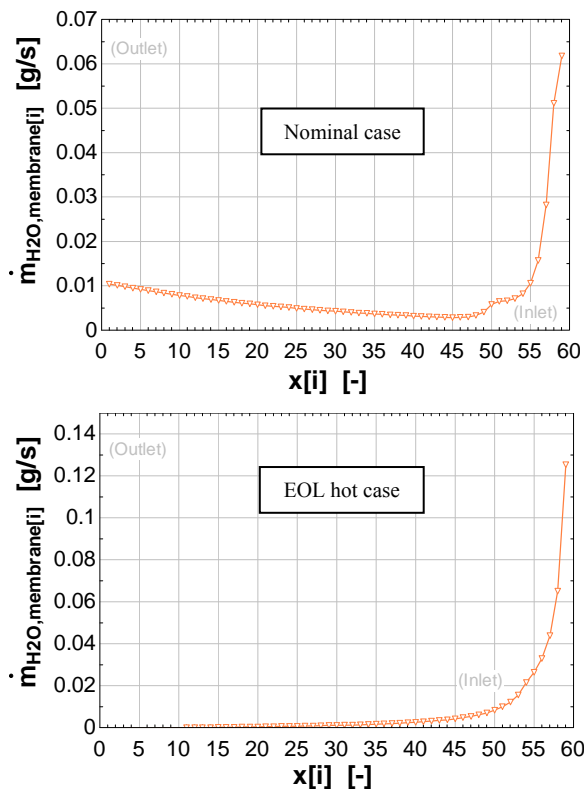
Figure 12: Nafion membrane water transport.

CONCLUSION

A steady-state distributed parameter model of a membrane humidifier has been developed. It has been found that the present simplified 1D-modeling approach has been able to replicate the physical phenomena and trends occurring during real life conditions in membrane humidifiers quite well. It is believed that the model with further improvements and comparison with more detailed experiments can be a very useful tool when designing and optimizing membrane based humidifiers for PEM fuel cell applications.

Future work will include the investigation of the influence of dynamic phenomena in the water transport process and a further study of the two-phase effects in membrane humidifiers.

REFERENCES

[1] Bernardi D. M., Verbrugge M. W, *A Mathematical Model of the Solid Polymer-Electrolyte Fuel Cell*, J. Electrochem. Soc. 1992 139(9).

[2] Choi K. H, Park D. J., Rho Y. W., Kho Y. T., T.H Lee, *A study of the internal humidification of an integrated PEMFC stack*, Journal of Power Sources, Volume 74, Issue 1, Jul. 1998, 146-150.

[3] Bhatia D., Sabharwal M., Duelk C., *Analytical model of a membrane humidifier for polymer electrolyte membrane fuel cell systems*, International Journal of Heat and Mass Transfer, Volume 58, Issues 1–2, March 2013, Pages 702-717.

[4] Huizing R., Fowler M., Mérida W., Dean J., *Design methodology for membrane-based plate-and-frame fuel cell humidifiers*, Journal of Power Sources, Volume 180, Issue 1, 15 May 2008, Pages 265-275, ISSN 0378-7753

[5] Gabelman A., Hwang S., *Hollow fiber membrane contactors*, Journal of Membrane Science, Volume 159, Issues 1–2, 1 July 1999, P. 61-106.

[6] Park S., Choe S., Choi S., *Dynamic modeling and analysis of a shell-and-tube type gas-to-gas membrane humidifier for PEM fuel cell applications*, International Journal of Hydrogen Energy, Volume 33, Issue 9, May 2008, Pages 2273-2282.

[7] Kang S., Min K., Yu S., *Two dimensional dynamic modeling of a shell-and-tube water-to-gas membrane humidifier for proton exchange membrane fuel cell*, International Journal of Hydrogen Energy, Volume 35, Issue 4, February 2010, Pages 1727-1741.

[8] Chen D., Li W., Peng H., *An experimental study and model validation of a membrane humidifier for PEM fuel cell humidification control*, Journal of Power Sources, Volume 180, Issue 1, 15 May 2008, Pages 461-467.

[9] Zhang H., Qian Z., Yang D., Ma J., *Design of an air humidifier for a 5 kW proton exchange membrane fuel cell stack operated at elevated temperatures*, International Journal of Hydrogen Energy, Volume 38, Issue 28, 19 September 2013.

[10] Zhang L., Huang S., *Coupled heat and mass transfer in a counter flow hollow fiber membrane module for air humidification*, International Journal of Heat and Mass Transfer, Volume 54, Issues 5–6, February 2011, Pages 1055-1063.

[11] Cave P., Mérida W., *Water flux in membrane fuel cell humidifiers: Flow rate and channel location effects*, Journal of Power Sources, Volume 175, Issue 1, 3 January 2008, Pages 408-418.

[12] Kadylak D., Mérida W., *Experimental verification of a membrane humidifier model based on the effectiveness method*, Journal of Power Sources, Volume 195, Issue 10, 15 May 2010, Pages 3166-3175.

[13] Olesen A. C, Berning T, Kær S. K. *On the diffusion coefficient of water in polymer electrolyte membranes.* ECS Transactions, 2012; 50 (2) 979-991.

[14] Thomas A., Zawodzinski Jr., T., Springer F. U., Gottesfeld S., *Characterization of polymer electrolytes for fuel cell applications*, Solid State Ionics, Volume 60, Issues 1–3, March 1993, Pages 199-211, ISSN 0167-2738

[15] Motupally S., Becker A. J., Weidner J. W., *Diffusion of Water in Nafion 115 Membranes*, J. Electrochem. Soc. 2000 147(9): 3171-3177.

[16] Fuller T. F., Newman J., *Water and Thermal Management in Solid‐Polymer‐Electrolyte Fuel Cellsm,* J. Electrochem. Soc. 1993 140(5): 1218-1225.

[17] Nguyen T. V., White R. E., *A Water and Heat Management Model for Proton‐Exchange‐Membrane Fuel Cells*, J. Electrochem. Soc. 1993 140(8): 2178-2186.

[18] Dutta S., Shimpalee S., Van Zee J. W., *Numerical prediction of mass-exchange between cathode and anode channels in a PEM fuel cell*, International Journal of Heat and Mass Transfer, Volume 44, Issue 11, June 2001, Pages 2029-2042.

[19] Mills A. F. *Heat And Mass Transfer.* Richard D. Irvin Inc., 1995

[20] Duan Q., Wang H., Benziger J., *Transport of liquid water through Nafion Membranes.* Journal of Membrane Science. 88-94, 2011.

[21] Ge S., Li X., Yi B., Hsing, I. M., *Absorption, desorption, and transport of water in polymer electrolyte membranes for fuel cells.* Journal of Electrochemical Society, 152, A1149, 2005.

[22] URL of F-Chart Software, which is the company developing and selling Engineering Equation Solver (EES) http://fchart.com.

[23] Burheim O., Vie P. J. S., Pharoah J. G., Kjelstrup S. *Ex Situ measurements of through-plane thermal conductivities in a polymer electrolyte fuel cell.* Journal of Power Sources, 195, 249-256, 2010.

[24] Khandelwal M, Mench M. M. *Direct measurement of through-plane thermal conductivity and contact resistance in fuel cell materials.* Journal of Power Sources, 161, 1106-1115, 2006.

SMART ADAPTIVE CONTROL OF A SOLAR THERMAL POWER PLANT IN VARYING OPERATING CONDITIONS

Esko K. Juuso[*]

Control Engineering Group, Faculty of Technology, FI-90014 University of Oulu, Finland
Luis J. Yebra
CIEMAT, Plataforma Solar de Almería, Automatic Control Group
Crta. de Senés s/n, 04200 Tabernas, Almería, Spain

ABSTRACT

Solar thermal power plants collect available solar energy in a usable form at a temperature range which is adapted to the irradiation levels and seasonal variations. Solar energy can be collected only when the irradiation is high enough to produce the required temperatures. During the operation, a trade-off of the temperature and the flow is needed to achieve a good level for the collected power. The storage is needed to keep the heat supply during the nights and heavy cloudy periods. Efficient operation requires a fast start-up and reliable operation in cloudy conditions without unnecessary shutdowns and start-ups. Fast and well damped linguistic equation (LE) controllers have been tested in Spain at a collector field, which uses parabolic-trough collectors to supply thermal energy in form of hot oil to an electricity generation system or a multi-effect desalination plant. Control is achieved by means of varying the flow pumped through the pipes in the field during the operation. The LE controllers extend the operation to varying cloudy conditions in a smart way. Varying irradiation and energy demand during the daytime can be smoothly handled in the LE control system with predefined model-based adaptation techniques. The system activates special features when needed to facilitate smooth operation. The intelligent state indicators react well to the changing operating conditions and can be used in smart working point control to further improve the operation in connection with the other energy sources.

Keywords: Solar energy, intelligent control, nonlinear systems, adaptation, optimisation, linguistic equations, modelling, simulation

INTRODUCTION

Solar power plants should collect any available thermal energy in a usable form at the desired temperature range, which improves the overall system efficiency and reduces the demands placed on auxiliary equipment. In addition to seasonal and daily cyclic variations, the intensity depends also on atmospheric conditions such as cloud cover, humidity, and air transparency. A fast start-up and efficient operation in varying cloudy conditions is important. A solar collector field is a good test platform for control methodologies [1, 2, 3]. Model-based approaches are useful since the operation depends strongly on weather conditions: the model structure is fairly clear but the properties of the oil depend on the temperature [4]. Lumped parameter models taking into account the sun position, the field geometry, the mirror reflectivity, the solar irradiation and the inlet oil temperature have been developed for a solar collector field [1]. A feedforward controller has been combined with different feedback controllers [5]. Local linearization has been used in feedback control [6]. Feedforward approaches based directly on the energy balance can use the measurements of solar irradiation and inlet temperature [7]. Energy collection is focused in [8]. Model-based predictive control [9, 10] is suitable for fairly smoothly changing conditions. The classical internal model control (IMC) can operate efficiently in varying time delay conditions [11]. Genetic algorithms have also been

---
[*]Corresponding author: Phone: +358 294 482463 E-mail:esko.juuso@oulu.fi

used for multiobjective tuning [12].

Linguistic equation (LE) controllers use model-based adaptation and feedforward features, which are aimed for preventing overheating, and the controller presented in [13] already took care of the actual setpoints of the temperature. The manual adjustment of the working point limit has improved the operation considerably. Parameters of the LE controllers were first defined manually, and later tuned with neural networks and genetic algorithms. Genetic algorithms combined with simulation and model-based predictive control have further reduced temperature differences between collector loops [14]. Data analysis methods are based on generalised norms [15] and extended to a recursive version of the scaling approach was introduced in [16]. New state indicators for detecting cloudy conditions and other oscillatory situations by analysing fluctuations of irradiation, temperature and oil flow [17]. The new indicators react well to the changing operating conditions and can be used in smart working point control. Recent developments include advanced model-based LE control are discussed in [18] and intelligent analysers [19].

This paper summarises and analyses the overall operation of the LE controller in changing operating conditions. The analysis is based on experiments carried out in the *Acurex Solar Collectors Field of the Plataforma Solar de Almeria (PSA)* in Spain.

SOLAR COLLECTOR FIELD

The aim of solar thermal power plants is to provide thermal energy for use in an industrial process such as seawater desalination or electricity generation. Unnecessary shutdowns and start-ups of the collector field are both wasteful and time consuming. With fast and well damped controllers, the plant can be operated close to the design limits thereby improving the productivity of the plant [4].

The *Acurex field* supplies thermal energy (1 MW_t) in form of hot oil to an electricity generation system or a multi–effect desalination plant. Parabolic–trough collectors are used for focusing the irradiation on the pipes and control is achieved by means of varying the flow pumped through the pipes (Fig. 1) during the operation. In addition to this, the collector field status must be monitored to prevent potentially hazardous situations, e.g. oil temperatures greater than 300 ^oC. The temperature increase in the field may
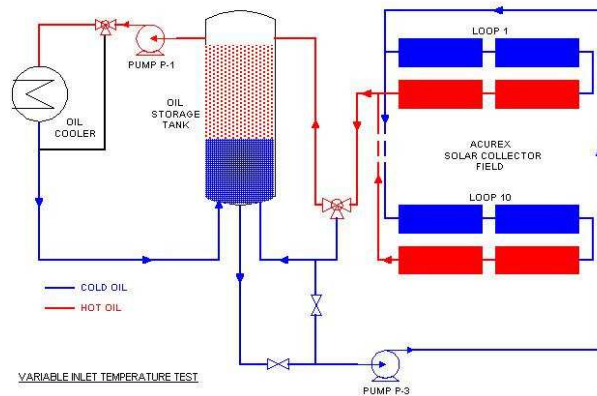
Figure 1: Layout of the Acurex solar collector field.

rise up to 110 degrees. At the beginning of the daily operation, the oil is circulated in the field, and the flow is turned to the storage system (Fig. 1) when an appropriate outlet temperature is achieved. The valves are used only for open-close operation: the overall flow F to the collector field is controlled by the pump. [20] The latest test campaigns focused on achieving a smooth operation in changing operating conditions to avoid unnecessary stress on the process equipment.

SMART ADAPTIVE CONTROL

The multilevel control system consists of a nonlinear PI-type LE controller with predefined adaptation models, some smart features for avoiding difficult operating conditions and a cascade controller for obtaining smooth operation (Fig. 2). Controller performance is used in the adaptation module. For the solar collector field, the goal is to reach the nominal operating temperature $180 - 295\ ^oC$ and keep it in changing operating conditions [16, 17]. The feedback controller is a PI-type LE controller with one manipulating variable, oil flow, and one controlled variable, the maximum outlet temperature of the loops. The controller provides a compact basis for advanced extensions. High-level control is aimed for manual activating, weighting and closing different actions.

Feedback LE controller

Feedback linguistic equation (LE) controllers use error $e_j(k)$ and derivative of the error $\Delta e_j(k)$. These real values are mapped to the linguistic range $[-2, 2]$
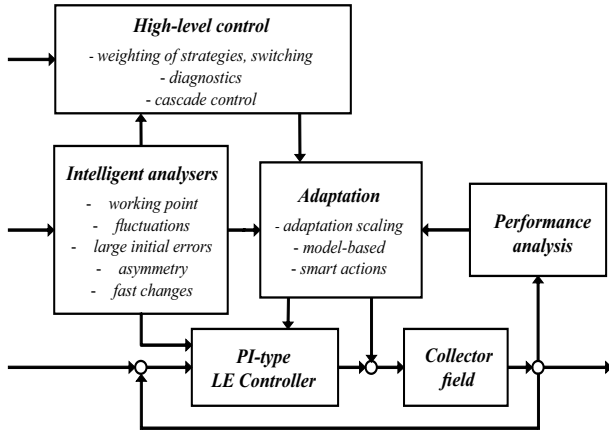
Figure 2: LE controller of the Acurex solar collector field.

by nonlinear scaling with variable specific membership definitions (f_e) and $f_{\Delta e}$), respectively. As all these functions consist of two second order polynomials, the corresponding inverse functions consist of square root functions. The linguistic values of the inputs, $\widetilde{e_j(k)}$ and $\widetilde{\Delta e_j(k)}$, are limited to the range $[-2,2]$ by using the functions only in the operating range: outside the scaled values are -2 and 2 for low and high values, respectively.

A *PI-type LE controller* is represented by

$$\widetilde{\Delta u_{ij}(k)} = K_P(i,j)\,\widetilde{\Delta e_j(k)} + K_I(i,j)\,\widetilde{e_j(k)}, \quad (1)$$

which contains coefficients $K_P(i,j)$ and $K_I(i,j)$. The effects of $\widetilde{e_j(k)}$ and $\widetilde{\Delta e_j(k)}$ can be tuned by membership definitions $(f_e)_j$ and $(f_{\Delta e})_j$, respectively. However, the direction of the control action is fixed in (1). Different directions and strengths can be handled with this controller.

The output i of a single input single output (SISO) controller is calculated by adding the effect of the controlled variable j to the manipulated variable i:

$$u_i(k) = u_i(k-1) + \Delta u_{ij}(k). \quad (2)$$

In the PI-type LE controller, the error variable is the deviation of the outlet temperature from the set point, and the control variable is oil flow.

Intelligent analysers

Intelligent analyzers are used for detecting changes in operating conditions to activate adaptation and

model-based control and to provide indirect measurements for the high-level control. The data analysis is based on the generalised norms

$$||^\tau M_j^p||_p = (^\tau M_j^p)^{1/p} = [\frac{1}{N}\sum_{i=1}^{N}(x_j)_i^p]^{1/p}, \quad (3)$$

where $p \neq 0$, is calculated from N values of a sample, τ is the sample time. These norms can be calculated recursively [16].

Working point On a clear day, the field could be operated by selecting a suitable a balance between the irradiation and the requested temperature increase. The *working point* is represented by

$$wp = \tilde{I}_{eff} - \tilde{T}_{diff}, \quad (4)$$

where $\tilde{I}_{eff}$ and $\tilde{T}_{diff}$ are obtained by the nonlinear scaling of variables: efficient irradiation I_{eff} and temperature difference between the inlet and outlet, $T_{diff} = T_{out} - T_{in}$. The outlet temperature T_{out} is the maximum outlet temperature of the loops. This model handles the nonlinear effects: the volumetric heat capacity increases very fast in the start-up stage but later remains almost constant because the normal operating temperature range is fairly narrow.

The working point variables already define the overall normal behaviour of the solar collector field, $wp = 0$, where the irradiation $\tilde{I}_{eff}$ and the temperature difference, $\tilde{T}_{diff}$, are on the same level. A high working point ($wp > 0$) means low $\tilde{T}_{diff}$ compared with the irradiation level $\tilde{I}_{eff}$. Correspondingly, a low working point ($wp < 0$) means high $\tilde{T}_{diff}$ compared to the irradiation level $\tilde{I}_{eff}$. The normal limit ($wp_{min} = 0$) reduces oscillations by using slightly lower setpoints during heavy cloudy periods. Higher limits, e.g. ($wp_{min} = 1$), shorten the oscillation periods after clouds more efficiently.

Fluctuations The *fluctuation indicators*, which were introduced to detecting cloudiness and oscillations, are important improvements aimed for practical use. The cloudy conditions are detected by calculating the difference of the high and the low values of the corrected irradiation as a difference of two moving generalised norms:

$$\Delta x_j^F(k) = ||^{K_s\tau}M_j^{p_h}||_{p_h} - ||^{K_s\tau}M_j^{p_l}||_{p_l}, \quad (5)$$

where the orders $p_h \in \Re$ and $p_l \in \Re$ are large positive and negative, respectively. The moments are

calculated from the latest $K_s + 1$ values, and an average of several latest values of $\Delta x_j^F(k)$ is used as an indicator of fluctuations. [17]

Large initial errors   Large steps and irradiation disturbances may cause very large initial errors which are detected by the *predictive braking indication*. The calculated braking coefficient, $bc_j(k)$ is used to emphasise the influence of the derivative of the error by means of the following equation:

$$K_P(i,j) = (1 + bc_j(k)) \, K_P(i,j) \qquad (6)$$

A new solution has been introduced to detecting the large error.

Asymmetry   The control surface should be asymmetric when the irradiation is strongly increasing or decreasing. The *asymmetry detection* is based on the changes of the corrected irradiation. The action is activated only close to the set point if there are no strong fluctuations of the controlled variable evaluated by e_j^- and e_j^+. The previous calculation based on the solar noon does not take into account actual irradiation changes.

Fast changes   Fast changes may occur in the temperatures (inlet, outlet and difference). Changes of the inlet temperature have a strong effect on the outlet temperature. The change is detected with the index

$$\Delta T_{in}^H(k) = T_{in}(k) - \frac{1}{n_L + 1} \sum_{i=k-n_L}^{k} T_{in}(i), \qquad (7)$$

where the average value is calculated from $n_L + 1$. A smooth increase is normal during the daily operation and strong effects are detected after load disturbances.

Fast changes of the outlet temperatures were considerably reduced when the fluctuation indicators were taken into use to adapt the setpoint. Too fast outlet temperature increase represented by the value range $\Delta T_{out}^R(k)$ obtained as the difference of maximum and minimum values of $T_{out}(i)$ in the range $i = k - n_L, \ldots, k$. This index is activated if T_{out} has increased during the period. An indicator of too high temperature differences is based on the detection of an overshoot

$$\Delta T_{out}^H(k) = \max\{0, T_{out}(k) - T_{out}^{sp}\}. \qquad (8)$$

Adaptive control

Adaptive LE control extends the operating area of the LE controller by using correction factors obtained from the working point (4) to reduce oscillations, when wp is low, and to speedup operation, when wp is high. This predefined adaptation is highly important since there are not time enough to adapt online when there are strong disturbances.

The predictive braking and asymmetrical actions are activated when needed. Intelligent indicators introduce additional changes of control if needed. The test campaigns have clarified the events, which activate the special actions. Each action has a clear task in the overall control system.

The additional intelligent features $\Delta T_{in}^H(k)$, $T_{out}^R(k)$ and $\Delta T_{out}^H(k)$, which detect anomalies, introduce an additional change of control:

$$\Delta \widetilde{u_j^{CH}}(k) = c_1 \widetilde{\Delta T_{in}^H}(k) + c_2 \widetilde{T_{out}^R}(k) + c_3 \widetilde{\Delta T_{out}^H}(k), \quad (9)$$

where the coefficients c_1, c_2 and c_3 are chosen from the range $[0, 1]$. The first two actions are predictive, and the third one is corrective. If T_{diff} is too high, also the set point is corrected correspondingly to avoid low working point $wp_i(k) \ll 0$.

Model-based control

Model-based control was earlier used for limiting the acceptable range of the temperature setpoint by setting a lower limit of the working point (4). The fluctuation indicators are used for modifying the lower working point limit to react better to cloudiness and other disturbances. This overrides the manual limits if the operation conditions require that.

The model-based extension is an essential part in moving towards reliable operation in cloudy conditions: the control system can operate without manual interventions. The high-level control moves towards control strategies to modify intelligent analysers and adaptation procedures (Fig. 2).

RESULTS

The control system was tested on a solar collector field at PSA in July 2012 to find a suitable solution for sustainable almost unattended operation. The results are used in developing optimisation solutions for the energy collection.

Normal operation

On clear days with high or fairly high irradiation, the setpoint tracking is acceptable: step changes from 15-25 degrees are achieved in 20-30 minutes with minimal oscillation. The working point adaptation operates efficiently and the temperature can be increased and decreased in spite of the irradiation changes (Fig. 3).

High setpoints can be used since the working point limit activates the setpoint correction when the temperature difference exceeds the limit corresponding to the irradiation level in the active working point level. There are three time periods of reduced setpoints in Figure 3 from 11:40 to 12:18, from 12:50 to 13:30 and from 14:48 to 15:40.

The oil flow changes smoothly: the fast changes are at the beginning of the step (Fig. 4). Working point corrections and limiting the fast changes are negligible. The predictive braking was activated in these situations, but the asymmerical action was not yet available. This causes positive offset, when the irradiation is increasing before the solar noon. Correspondingly, the offset is negative after the solar noon.

Figure 4: Operation of the LE controller on a fairly clear day: $x = [e, \Delta e]$, $xling = [\tilde{e}, \widetilde{\Delta e}]$, $yling = \widetilde{\Delta u}$ and $y = \Delta u$.

Figure 3: Test results of the LE controller on a fairly clear day [19].

Cloudy conditions

The setpoint correction operates throughout the cloudy periods to reduce oscillations and hazardous situations caused by the abrupt changes of irradiation (Fig. 5(b)).

Three cloudy periods occurred on the third day: a long period in the morning, a short light one close the solar noon and a short, but heavy, in the afternoon. The temporary setpoint correction operated well in these situations (Fig. 5(a)). During

the cloudy periods (Fig. 5(b)), the temperature went down with 20 degrees but rose back during the short sunny spells, and finally, after the irradiation disturbances, high temperatures were achieved almost without oscillations with the gradually changing setpoint defined by the working point limit although the inlet temperature was simultaneously rising. After these periods, the field reached the normal operation in half an hour.

The controller used high oil flow levels when the sky was clearing up. Also the change of control was reacting strongly (Fig. 6). The same approach operated well for the other two cloudy periods. The oil flow was changed smoothly also during these periods. The working point corrections were now very strong, but limiting the fast changes was hardly needed. Strong braking was used in the beginning and in the recovery from the first cloudy period. There were problems with some loops during that day.
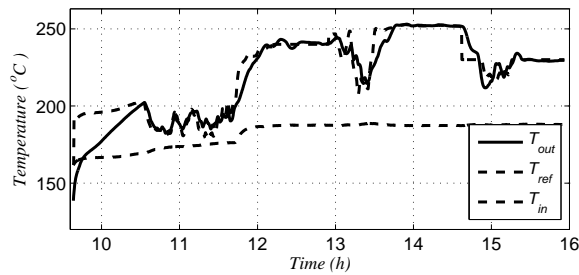
(a) Outlet temperature.
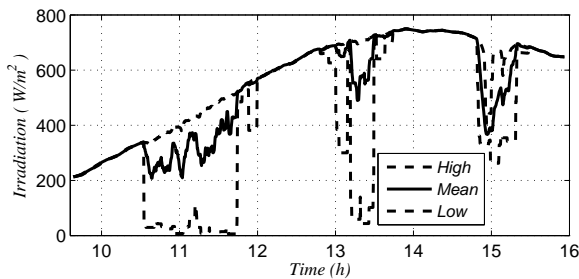
(b) Irradiation.

Figure 5: Test results of the LE controller on a cloudy day [19].

Figure 6: Operation of the LE controller on a cloudy day: $x = [e, \Delta e]$, $xling = [\tilde{e}, \widetilde{\Delta e}]$, $yling = \widetilde{\Delta u}$ and $y = \Delta u$.

The fourth day had two very different periods: the start was very bright and the irradiation was rising smoothly, but everything was changed just before the solar noon, and the heavy cloudy period continued the whole afternoon. The field was in temperatures 160 - 210 ^oC for more than two hours although the loops were not tracking the sun all the time. The working point corrections were during this period very strong, but limiting the fast changes was hardly needed [18].

Load disturbances

During a day, the temperature increases more or less smoothly in the storage tank (Fig. 1), but the use energy may cause fast disturbances. The controller should also handle these disturbances. On the fifth day, the start-up followed the setpoint defined by the working point limit. In addition, there was an unintentional drop of 16.9 degrees in the inlet temperature. The disturbance lasted 20 minutes. The controller reacted by introducing a setpoint decrease of 19.8 degrees. The normal operation was retained in 50 minutes with only an overshoot of two degrees, but with some oscillations.

This kind of disturbance was repeated on the sixth

day (Fig. 7(a)): the inlet temperature was dropped maximum 13.5 degrees during a period of 15 minutes. Now the setpoint was changed when the inlet temperature reached the minimum. The working point limit was changed to allow a higher setpoint in the recovery. The change of control is operating in a similar way as in the setpoint change (Fig. 8). The temperature drop was smaller (7.5 degrees) but the overshoot slightly higher (2.5 degrees). Also the recovery took less time (30 minutes).

Asymmetrical correction

The new asymmetrical correction was activated in several periods on the sixth day. There were good results on two previous days, but now the operation was better tuned for the afternoon as well. The setpoints were achieved in the range ± 0.5 degrees with hardly any offset (Fig. 7(a)). The change is considerable to the first days, when the outlet tempera-
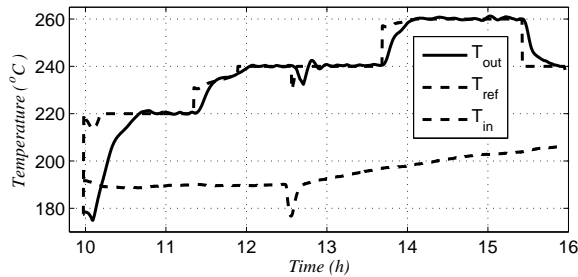
(a) Outlet temperature.
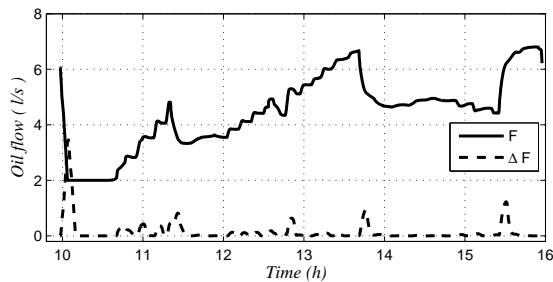
(b) Oil flow.

Figure 7: Test results of the LE controller on a clear day: asymmetral action [19,].

Figure 8: Operation of the LE controller on a clear day, including asymmetry action: $x = [e, \Delta e]$, $xling = [\tilde{e}, \widetilde{\Delta e}]$, $yling = \widetilde{\Delta u}$ and $y = \Delta u$.

ture exceeded the setpoint with 0.5-1 degrees, when the irradiation was increasing, and remained about 1.0 degrees lower when the irradiation decreased. Around the solar noon, the setpoint was achieved very accurately even for high temperatures corresponding negative working points. The increase of the inlet temperature is smoothly compensated with small changes of the oil flow and the setpoint is also accurately achieved after the load disturbance (Fig. 7(b)). In this case, the asymmetrical action increases the positive changes before the solar noon and the negative changes after that (Fig. 8).

Optimisation

The temperature increase in the collector field naturally depends on the irradiation, which is the highest close to the solar noon. As the inlet temperature often increases slightly during the day, there is a possibility to use even higher outlet temperatures. The temperatures increase with decreasing oil flow, which can be controlled smoothly in a wide range. A trade-off of the temperature and the flow is needed to achieve a good level for the collected power. The working point is chosen from the high power range

and used in the model-based control to choose or limit the setpoint. The power surface is highly nonlinear because of the properties of the oil. Disturbances of the inlet temperatures introduce fluctuation to the outlet temperature (Fig. 7(a)). The acceptable working point is limited by the oscillation risks and high viscosity of the oil during the start-up. In the latest tests, the inlet temperatures are high already in the start-up, since the oil flow was not first circulated in the field. During high irradiation periods, high outlet temperatures are avoided by keeping the working point high enough.

CONCLUSION

The intelligent LE control system, which is based on intelligent analysers and predefined model-based adaptation techniques, activates special features when needed. Fast start-up, smooth operation and efficient energy collection is achieved even in vary-

ing operating condition. The state indicators react well to the changing operating conditions and can be used in smart working point control to further improve the operation. The controller reacts efficiently on the setpoint changes, clouds and load disturbances. The setpoint is achieved accurately with the new asymmetrical action. The working point can be chosen in a way which improves the efficiency of the energy collection. A trade-off of the temperature and the flow is needed to achieve a good level for the collected power.

REFERENCES
[1] E. Camacho, M. Berenguel, F. R. Rubio, Adaptive Control of Solar Plants, Springer, London, 1997.

[2] E. K. Juuso, Fuzzy control in process industry: The linguistic equation approach, in: H. B. Verbruggen, H.-J. Zimmermann, R. Babuška (Eds.), Fuzzy Algorithms for Control, International Series in Intelligent Technologies, Vol. 14 of International Series in Intelligent Technologies, Kluwer, Boston, 1999, pp. 243–300, doi: 10.1007/978-94-011-4405-6_10.

[3] E. F. Camacho, M. Berenguel, F. R. Rubio, D. Martinez, Control of Solar Energy Systems, Advances in Industrial Control, Springer, London, 2012.

[4] E. K. Juuso, P. Balsa, L. Valenzuela, Multi-level linguistic equation controller applied to a 1 MW solar power plant, in: Proceedings of the ACC'98, Philadelphia, PA, June 24–26, 1998, Vol. 6, ACC, 1998, pp. 3891–3895.

[5] L. Valenzuela, P. Balsa, Series and parallel feedforward control schemes to regulate the operation of a solar collector field, in: Proceedings of the 2nd User Workshop Training and Mobility of Researchers Programme at Plataforma Solar de Almeria, November 10-11, 1998, Ciemat, 1998, pp. 19–24.

[6] C. M. Cirre, M. Berenguel, L. Valenzuela, E. Camacho, Feedback linearization control for a distributed solar collector field, Control engineering Practice 15 (2007) 1533–1544, doi: 10.1016/j.conengprac.2007.03.002.

[7] E. Camacho, F. Rubio, F. Hughes, Self-tuning control of a solar power plant with a distributed collector field, IEEE System Control Magazine 12 (2) (1992) 72–78.

[8] T. A. Johansen, C. Storaa, Energy-based control of a distributed solar collector field, Automatica 38 (2002) 1191–1199.

[9] D. Limon, I. Alvarado, T. Alamo, M. Ruiz, E. F. Camacho, Robust control of the distributed solar collector field ACUREX using MPC for tracking, in: Proceedings of 17th IFAC World Congress, Seoul, Korea, July 6-11, 2008, Vol. 17, IFAC, 2008, pp. 958–963, http://www.ifac-papersonline.net/.

[10] C. O. Ayala, L. Roca, J. L. Guzman, J. E. Normey-Rico, M. Berenguel, L. Yebra, Local model predictive controller in a solar desalination plant collector field, Renewable Energy 36 (2011) 3001–3012, doi: 10.1016/j.renene.2011.03.037.

[11] I. Farkas, I. Vajk, Internal model-based controller for a solar plant, in: L. Basanez, J. A. de la Puente (Eds.), Proceedings of the 15th Triennial World Congress, Barcelona, Spain, July 21-26, 2011, IFAC, 2002, pp. 49–54, http://www.ifac-papersonline.net/.

[12] J. Bonilla, , L. J. Yebra, S. Dormido, E. Zarza, Parabolic-trough solar thermal power plant simulation scheme, multi-objective genetic algorithm calibration and validation, Solar Energy 86 (2012) 531–540, doi: 10.1016/j.solener.2011.10.025.

[13] E. K. Juuso, L. Valenzuela, Adaptive intelligent control of a solar collector field, in: Pro-

ceedings of Eunite 2003 - European Symposium on Intelligent Technologies, Hybrid Systems and their implementation on Smart Adaptive Systems, July 10-11, 2003, Oulu, Finland, Wissenschaftsverlag Mainz, Aachen, 2003, pp. 26–35.

[14] E. K. Juuso, Modelling and simulation in development and tuning of intelligent controllers, in: I. Troch, F. Breitenecker (Eds.), Proceedings of 5th Vienna Symposium on Mathematical Modelling, February 8-10, 2006, Vienna, Austria, Argesim Report 30, Argesin Verlag, Vienna, 2006, pp. 6–1 – 10, iSBN 3-901608-30-3.

[15] E. Juuso, S. Lahdelma, Intelligent scaling of features in fault diagnosis, in: Proceedings of the 7th International Conference on Condition Monitoring and Machinery Failure Prevention Technologies, 22-24 June, 2010, Stratford-upon-Avon, UK, Vol. 2, Curran Associates, NY, USA, 2010, pp. 1358–1372, ISBN 978-1-61839-013-4.

[16] E. K. Juuso, Recursive tuning of intelligent controllers of solar collector fields in changing operating conditions, in: S. Bittani, A. Cenedese, S. Zampieri (Eds.), Proceedings of the 18th World Congress The International Federation of Automatic Control, Milano (Italy) August 28 - September 2, 2011, IFAC, 2011, pp. 12282–12288, doi: 10.3182/20110828-6-IT-1002.03621.

[17] E. K. Juuso, Model-based adaptation of intelligent controllers of solar collector fields, in: I. Troch, F. Breitenecker (Eds.), Proceedings of 7th Vienna Symposium on Mathematical Modelling, February 14-17, 2012, Vienna, Austria, Part 1, Vol. 7, IFAC, 2012, pp. 979–984, doi: 10.3182/20120215-3-AT-3016.00173.

[18] E. K. Juuso, L. Yebra, Model-based intelligent control of a solar energy collector field, in: Proceedings of 8h EUROSIM Congress on Modelling and Simulation, 10-13 September, 2013, Cardiff, UK, IEEE, 2013, pp. 513–518, doi:10.1109/EUROSIM.2013.92.

[19] E. K. Juuso, L. Yebra, Optimisation of solar energy collection with smart adaptive control, in: USB Proceedings of IECON 2013 - 39th Annual Conference of the IEEE Industrial Electronics Society, 10-14 November, 2013, Vienna, Austria, IEEE, 2013, pp. 7930–7935, doi: 10.1109/IECON.2013.6700459.

[20] E. K. Juuso, P. Balsa, K. Leiviskä, Linguistic Equation Controller Applied to a Solar Collectors Field, in: Proceedings of the European Control Conference -ECC'97, Brussels, July 1 - 4, 1997, Vol. Volume 5, TH-E I4, paper 267 (CD-ROM), 1997, p. 6 pp.

POWER SYSTEM STABILITY STUDY USING MODELICA

Thomas Oyvang, **Dietmar Winkler and Bernt Lie**
Telemark University College
Faculty of Technology
3901 Porsgrunn
Norway

Gunne John Hegglid
Skagerak Energi AS
Norway

ABSTRACT

This paper is concerned with power system modeling using the Modelica language in comparison to a traditional simulation tool. Though most common power system simulation tools are computationally efficient and reasonably user-friendly, they have a closed architecture. Thus, there is motivation to use an open-source modeling language to describe electric networks, such as Modelica. A well-established benchmark for power system studies was analyzed. Regarding the voltage as a function of time, a reasonable agreement was found between the simulation results of the used simulation tools for long-term voltage stability. However, a comparison of faster electromechanical mechanisms, such as rotor angle stability, demands more detailed models in the Modelica tool.

Keywords: Power system modeling and control, PSS®E, Modelica, Dymola, Voltage stability, Rotor angle stability, Frequency stability

NOMENCLATURE

P	Active power [W]
S	Apparent power [VA]
AVR	Automatic Voltage Regulator
GOV	Governor
δ	Load angle
$OLTC$	On-Load Tap-Changer
OXL	Over eXcitation Limiter
PSS	Power System Stabilizer
Q	Reactive power [VAr]
f	System frequency [Hz]
V	Voltage [V]

INTRODUCTION

The modeling of power system components and networks is important for planning and operating electric networks, as they provide insight into how the power system will respond to both changing power demand and to various types of disturbances. Traditional tools for power system modeling are usually tied to a certain time frame (e.g., 1 sec to 15 min) depending on the phenomenon being investigated. Different time frames often limit the applicability and/or validity of the models to a specific kind of study [1]. A broad range of time constants results in specific domain tools for simulations. Traditionally, simulation of stability in power systems has been constrained to tools developed specifically for this purpose, as PSS®E, EUROSTAG and PowerFactory [2]. Though most of these tools are computationally efficient and reasonably user-friendly, they have a closed architecture in which it is difficult to view or change most of the component models. The implementation of new network component models in PSS®E requires editing of the FORTRAN source code. PSS®E has the capability to export a linearized representation of the system for further analysis, but the full nonlinear representation

---

*Corresponding author: Phone: +47 3557 5155 Fax: +47 3557 5401 E-mail:thomas.oyvang@hit.no

remains hidden to the user. Thus, there is motivation to use an open-source modeling language, such as Modelica, to describe electric networks.

In this paper, power system modeling was performed using the Modelica language with the tool Dymola [3] as well as PSS®E, to analyze stability. PSS®E is one of the most widely used commercial programs of its type. Modelica effectively allows multi-domain modeling, including electrical, mechanical, and control systems. Thus, this paper presents power system stability simulations from an analysis of a simple power system to compare modeling tools.

The paper is organized as follows. Section 2 provides a brief overview of phenomena within power system stability. Section 3 introduces and describes the test system, and the simulation results are presented in Section 4. The results of the simulations are discussed in Section 5, and conclusions and future perspectives are presented in Section 6.

POWER SYSTEM STABILITY AND CONTROL

Two important highly nonlinear characteristics of power system stability are two pairs of strongly connected variables: reactive power Q and voltage V, and active power P and power angle δ. The power angle is often referred to as the load angle and associated with the system frequency f. These variables need to be monitored and controlled within certain limits to secure stable power system operation [1]. The TSO (Transmission System Operator) Statnett gives functional requirements in the power system [4] and has the overall supervision responsibility and physical control as regards Norway's power system. TSO ensures normally a power grid frequency of 50 Hz (or 314.16 rad/s) $\pm 2\%$ and a voltage interval of $\pm 10\%$ according too [5]. The system frequency of an interconnected power system has the same value everywhere in the system; in other words, it is independent of the location. A similar "'system voltage" does not exist the voltage amplitude depends strongly on the local situation in the system. Power system stability is understood as the ability to regain an equilibrium state after being subjected to a physical disturbance, and it can be divided into:

- Voltage stability

- Rotor angle stability

- Power imbalance (frequency stability)

Different types of disturbances are classified in the literature [1]. Only the large disturbances given in Table 1 will be addressed in this paper. Determination of large-disturbance stability requires examination of the nonlinear dynamic performance of a system over a period of time sufficient to capture interactions between the devices to be investigated. To manage these stability phenomena, synchronous generators in power systems are often protected or controlled by devices, such as an automatic voltage regulator (AVR), power system stabilizer (PSS), turbine governor (GOV) and over-excitation limiter (OXL). A simplified control structure for these different devices is illustrated in Figure 1 and will only be presented here briefly. The turbine governor controls either the speed or output power according to a preset active power-frequency characteristic (droop control). This control is achieved by opening/closing control valves to regulate the water-flow (e.g., hydropower) through the turbine, forcing the generator to rotate, converting mechanical energy into electricity. The excitation (or field) current required to produce the magnetic field inside the generator is provided by the exciter and controlled by an AVR. The AVR is designed to automatically maintain a constant voltage; it may be a simple "feedforward" design or may include negative feedback control loops and implemented as a PI or PID controller. The AVR, in cooperation with the PSS, regulates the generator terminal voltage by controlling the amount of current supplied to the generator field by the exciter.
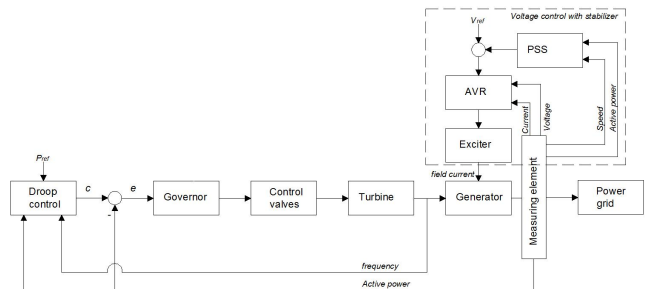
Figure 1: Single generator voltage and frequency control

10-BUS TEST SYSTEM

This paper presents the results from an analysis of a simple 10-bus[1] power system described in [1]. Typically nominal SI-voltage levels are used in simulations. The system is a well-established benchmark for exploring voltage stability issues [6]. This small system shares some of its characteristics with the Nordic system studied in [7]. In both systems, most generation occurs in a remote area that is connected to a main load area through five transmission lines. In addition to voltage stability, the frequency and rotor angle stability will also be visualized in this paper. The system has three synchronous hydro-power generators; one generator is connected to a slack-bus to represent inter-area power exchange. Both generators 1 and 2 are remote generators that supply power to the loads through five parallel feeders, and generator 3 is a local generator. A one-line diagram of the test system that will be used to illustrate some of the mechanisms of power system instability in a time simulation is shown in Figure 2.
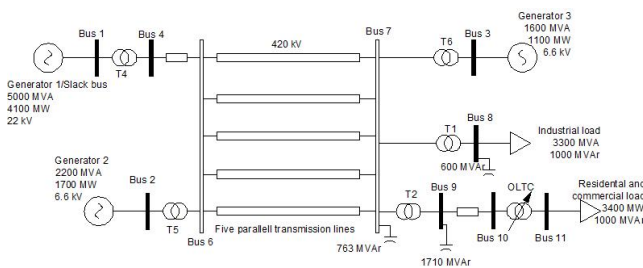
Figure 2: 10 bus case (BPA test system [1]).

The purpose of the simulations is to visualize how the generators in a power system respond when a momentary disturbance occurs in the power balance between the electrical power consumed in the system, the mechanical power delivered by the turbines, and the equivalent power from the slack-bus. The simulations were performed in Dymola [3] and compared with PSS⑧E Dynamic Simulation module [8]. An overview of simulations and counter-measures[2] carried out in this paper is shown in Table 1.

---

[1]In an electrical power system the bus is an electrical junction (node) where conductors terminate. It is usually made of copper bar.

[2]After an disturbance, measures are taken by different control components to stabilize voltage, frequency and rotor oscillations.

Test model constructed using PSS⑧E and Dymola

Power system parameters can be given in International System of measurement (SI) or per-unit system (pu). The pu system is used in power system modeling in which each parameter is expressed as a decimal fraction of its respective base. A minimum of two base quantities is required to completely define a pu system. For example, apparent power S and voltage V are fixed and then the current and impedance (or admittance) set arbitrarily. The pu bases used in the models developed in this paper were both "system base" (100 MVA) and a different "machine base".

PSS⑧E

The dynamic simulations of PSS⑧E are based on power-flow calculations in steady-state. The equipment used in dynamic simulations needs to be defined in power-flow. The main skeleton of PSS⑧E contains logic for data input, output, numerical integration, and electric network solutions but contains no logic related to differential equations for specific equipment [9]. The equipment used in this paper included standard PSS⑧E models and was defined in so-called subroutines in PSS⑧E. The model subroutines are called whenever the main skeleton logic needs numerical values of time derivatives. Dynamic models that are used for developing the test system are listed in Table 2. The models in PSS⑧E are restricted to block diagrams with input and outputs (casual), whereas in Modelica models can be acasual.

Dymola

Larsson [7, 10] created the freely available power system library ObjectStab, which is intended for power system stability simulations written in Modelica, a general-purpose object-oriented modeling language. The "Electric Power Library" (EPL) [10] in Dymola by Modelon AB was used to develop the test system in this paper. The EPL contains models of standard power system components, including the control of generators, exciters for synchronous machines (generators), and turbine GOVs. To investigate the stability phenomena in this paper, some additional components were made. An

Table 1: Simulations

Case	Stability	Countermeasures/Devices	Disturbance
A1	Voltage	Tap changer and OXL at G2 and G3	Loss of line
A2	Voltage	Tap changer and OXL at G3	Loss of line
B	Rotor angle	Power system stabilizer	3-phase fault and line trip
C	Frequency	Governor/Tie-line/load shedding	power imbalance

IEEE ST1A bus-fed thyristor excitation system with PSS and OXLs with inverse-time characteristics was built with logic blocks in Modelica. The ST1A has a PSS using only generator speed as the input signal. This stabilizer is simpler than the one used in PSS®E, which uses both speed and active power as the input. The ST1A was setup similar to a transient stability analysis of a power system in Kundur [1]. An On-Load Tap-Changer (OLTC) was also created as an state machine based on [11]. Generator G1 was modeled as an infinite bus (voltage with a constant amplitude and phase) and generators G2 and G3 using 6th-order models. The loads at bus 8 and bus 11 were modeled as constant impedance. The load at bus 11 was connected through the OLTC at T6. The GOVs were implemented as PI controllers (first-order transfer functions with limiter) using speed and power as reference values (set points).

For the comparison with PSS®E, some parameters needed to be correlated in EPL. This was done mainly at the transformer ratio and transmission line parameters (resistance, inductance, and capacitance).

SIMULATIONS

The simulations are designed to visualize the three main stability phenomena within power systems. Voltage instability/collapse is a major security concern for power system operation. This phenomenon is often preceded by a slow process of load restoration and limitation in generators reactive power supply, after some initial disturbances [12]. If each bus in a system elevating both the voltage (V) and reactive power (Q) after a disturbance the system is voltage-stable. On the other hand, if the voltage decreases and reactive power increases at one or more buses we have voltage instability. This phenomenon can be seen in case A1 in Figure 3 (only Dymola)

and case A2 in Figure 4 (Dymola and PSS®E). A disconnect between one of the five parallel lines occurred in the simulation at 100 s. At approximately 115 s, the short-term dynamics including the generator electromechanical and load recovery dynamics settled. As the voltage at bus 11 was below the OLTC deadband, its internal timer started. As seen from the figures, the OLTC reacted and slightly increased the voltage at bus 11 (secondary side) and decreased the voltage at bus 10 (primary side). In Figure 3, OXLs were implemented at G3 (at 140 seconds) and G2 (at 160 seconds). Bus 10 exhibited voltage instability until the OXL started to limit the reactive power after 140 seconds. In Figure 4, the OXL was only implemented at generator 3. The OXL limited the field voltage by ramping down the field voltage (or current), ensuring that G3 did not overheat. Consequently, the necessary voltage support was not dispatched locally and a power system "blackout" occurred. The use of a tap-changer as a countermeasure is often referred to as secondary voltage control. Another countermeasure for voltage instability is load shedding, but it is not presented in this case.

As seen in Figure 3, similar trend was observed for both PSS®E and Dymola. However, the voltage before disturbance was not the same due to how the power system was constructed in the different simulation tools. Also the OXL characteristic in PSS®E (MAXEX1) was slightly more complex than that implemented with EPL.

Rotor angle stability

In Figures 5 and Figure 6, the rotor angle stability phenomena and countermeasures are visualized by showing the speed deviation in pu from synchronous speed of generator G3 with and without stabilizer

Table 2: Test system in PSS®E and Dymola

Equipment	PSSE	Dymola
Governor G1 (Slack bus)	GENCLS	Infinite bus
Governor G2 and G3	GENROU	6-th order dq
Exciter G2 and G3	SEXS	IEEE ST1A
Overexcitation limiter at G3	MAXEX1	Inverse-time characteristic with ramping
Overexcitation limiter at G2	None	Constant maximum limit
Transformer tap changer at bus 11	OLTC1T	OLTC
Power system stabilizer at G2	PSS2A	Simplified PSS
Load at bus 8 and 11	Constant impedance	Impedance (Load at nominal voltage)
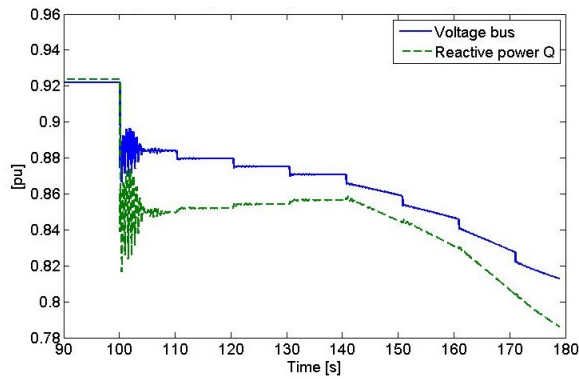
Figure 3: Case A1: Voltage instability at bus 10 with OXL implemented both at G2 and G3

Figure 4: Case A2: Voltage level due to tap-changer transformer T6 with results from both Dymola and PSS®E

during a large disturbance. Rotor angle [3] stability is the ability of interconnected synchronous machines of a power system to remain in synchronism. PSS provided supplemental damping to the oscillation of synchronous machine rotors through the generator excitation as shown in Figure 1. A fundamental factor in this problem is the manner in which the power outputs of synchronous machines vary as their rotors oscillates.

The effect of this positive damping after an large disturbance in the grid can be seen in figure 5, where PSS is applied to the excitation system at G3.

As mentioned, PSS®E is using the PSS2A stabilizer measuring both speed and active power as input. This gives a greater positive damping by the stabilizer compared to the one in EPL with only speed as input. Also the generator oscillation behavior

and amplitude are different due to different governor models. In both cases the stabilizer will lower the time for the system to settle in non oscillating state.

Frequency stability

If a large load is suddenly connected (disconnected) to the system, or if a generating unit is suddenly disconnected, a long-term distortion occurs in the power balance, changing the frequency in the system. In Figure 7 the frequency stability phenomena is visualized in Dymola by showing the rotor-dynamic oscillation at G2. In real-life applications, generators are protected against frequency instability by disconnecting equipment before a severe hazard. However, this protection was not implemented here and the simulations are only a theoretical approach for visualizing this phenomenon. When the

---

[3] the derivative of rotor angle is equal to the rotor angular velocity in [rad/s]
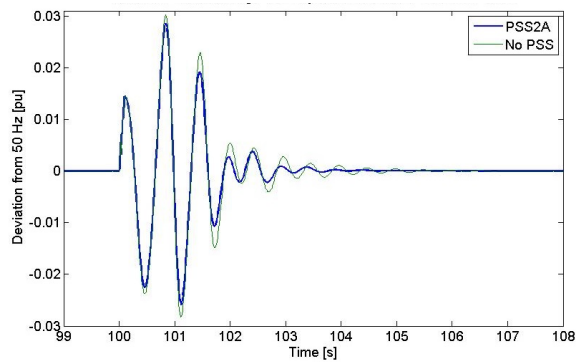
Figure 5: Rotor oscillations at G3 in PSS®E
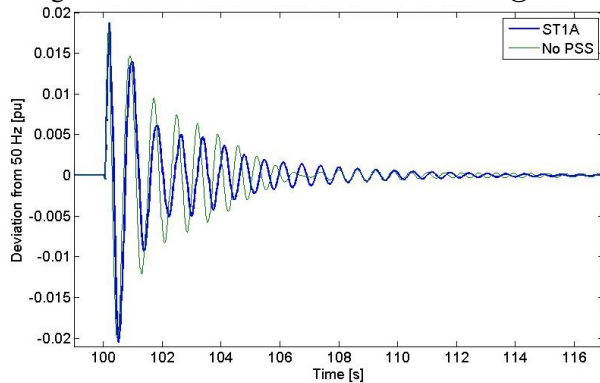
Figure 6: Rotor oscillations at G3 in Dymola

Figure 7: Case C in Dymola: Showing rotor-dynamic behavior at G2 influencing the grid frequency after an disturbance at time 103 seconds (oscillation starts) and countermeasure applied at 130 seconds.

turbine generators are equipped with governing systems following a change in total power demand (or loss of a generator), the system is not able to return to the initial frequency on its own without any additional action. In Figure 7, generator G3 was disconnected from the system at 103 seconds. The G2 is now oscillating due to the generator rotor-dynamics. This rotor oscillation is a good representation of the frequency instability that would occur in the 10-bus system. The 10-bus system is now in power imbalance transferring more power through the slack-bus trying to stabilize the system. This is often refered to tie-line power. After 130 seconds the load at bus 11 was disconnected (load shedding) making the frequency equilibrate after approximately 160 seconds. Simulation in this case is done only with Dymola. How the infinte bus are constructed in EPL and PSS®E are different causing the system to behave differently.

DISCUSSION

The simulations in Dymola were carried out with transient initialisation and simulations due to un-

certainty with the parameters of the power system and control components. There are two initialisation modes, transient (state variables with default-values) and steady-state. When choosing transient initialisation, no specific initial equations are defined. This type of transient simulation is only possible with feedback within the controllers. Periodically driven systems tend towards a periodic solution after some time. To get the periodic solution (after about 20 second simulation time in this paper) the initial limits of governor and AVR need to be greater than in balanced situations. Simulating transmission lines in steady-state was not possible in EPL due to some initializing problems.

The EPL's complexity (fully represents the actual physics of the components) demands the user to implement a huge amount of accurate parameters. Building a stable power system in the EPL with only limited knowledge of parameters is challenging, as some initial values need to be set explicitly to avoid guessing from the tool side. A real-life power system application with known parameters is recommended when comparing simulation tools with the EPL. When creating a large system model in Dymola, it is typically easier to build the system model through the composition of subsystem models that can be tested in isolation. However, connecting these well-posed subsystems together to create the full scale large power system may lead to instability and unwanted oscillations. A balanced power system, well posed initial equations, and accurate parameter values are of crucial importance to running

transient power system simulations in Dymola.

The main advantages of using Modelica as a modeling language is the readability and re-usability of the code. Models within this library are based on a clear set of equations rather than a set of diagrams as in the PSS®E tool. In this sense the library has a didactic intention. FORTRAN is considered a procedural language (i.e., you tell the computer what to do step-by-step), whereas Modelica is a declarative language. Thus, rather than developing source code that lists a set of steps to follow in order to solve a problem, you only have to describe the mathematical structure of your problem [13]. The disadvantage is longer execution times compared to the FORTRAN model. For example, in long term simulations as shown in case A2, PSS®E use less than 3 second computation time on the 180 second simulation, while Dymola uses about 20 seconds on the same calculation (without the transient initialization process). For example if you want to simulate a state utility network (where the number of buses will be in thousands) you will need a robust software such as PSS®E. But if you want to execute a system with less number of buses and do in depth analysis you can use EPL and Dymola.

The different complexity of models used in PSS®E and Dymola affect the results. For example, the GOV used in the EPL is a PI control done as a transfer function block, whereas in PSS®E the Hydro-Turbine Governor (HYGOV) models both the GOV and hydraulic systems. This HYGOV model is a more complex structure than the EPL model. However, visualizing the stability phenomena in this paper, the controllers made in EPL had promising results compared to PSS®E. As seen in the long-term voltage stability simulations, this difference has a limited impact. A detailed hydraulic system model like HYGOV and an infinite bus such as GENCLS in PSS®E should be created with the EPL.
However, the modeling detail required for any given study depends on the scope of the study and the system characteristics [1]. A Hydro Power Library (HPL) is also available [14]. The EPL could be combined with the HPL in Dymola to also include waterway components and droop control.

CONCLUSION
Regarding the voltage as a function of time, a reasonable agreement was found between the simulation results obtained using Dymola and PSS®E for long-term voltage stability. However, a comparison of faster electromechanical mechanisms, such as rotor angle demands, requires more detailed models in EPL. In this paper, PSS®E was clearly the fastest simulator. However, PSS®E has an closed architecture in which it is difficult to view or change most of the component models. Using an open-source model with didactic intention for describing electric networks, such as Modelica, could be preferable for in-depth power system studies.

REFERENCES
[1] Prabha Kundur. *Power System Stability and Control*. McGraw-Hill Professional, 1994. ISBN: 007035958X.

[2] Luigi Vanfretti, Tetiana Bogodorova, and Maxime Baudette. "A Modelica Power System Component Library for Model Validation and Parameter Identification". In: *Proceedings of the 10th International Modelica Conference, March 10-12, 2014, Lund, Sweden* (2014). DOI: 10.3384/ecp140961195.

[3] Dassault Systèms. *Dymola*. URL: http://www.dymola.com.

[4] Statnett. *FIKS Funksjonskrav i Kraftsystemet/Functional requirements in the power system*. Tech. rep. Statnett, 2012.

[5] Ministry of Petroleum and Energy (OED). *Forskrift om leveringskvalitet i kraftsystemet Norwegian Water Resources and Energy Directorate (NVE)*. 2004. URL: http://lovdata.no/dokument/SF/forskrift/2004-11-30-1557.

[6] Go Bong. "Voltage stability enhancement via model predictive control." ProQuest Dissertations and Theses, , 173. Dissertation. The University of Wisconsin, Madison, 2008.

[7] Mats Larsson. "Coordinated Voltage Control in Electric Power Systems". PhD thesis. Lund University, 2000.

[8] Siemens. *PSSE Dynamic Simulation module*. URL: `http : / / w3 . siemens . com / smartgrid / global / en / products – systems – solutions / software – solutions / planning – data – management – software / planning-simulation/pages/pss-e.aspx#`.

[9] Siemens. *Program Application Guide: Volume II PSSE 33.4 Siemens*.

[10] Larsson. "ObjectStab-an educational tool for power system stability studies". In: *IEEE Transactions On Power Systems* 19.1 (2004), pp. 56–63. DOI: `10.1109/TPWRS.2003.821001`.

[11] P.W. Sauer and M.A. Pai. "A comparison of discrete vs. continuous dynamic models of tap-changing-under-load transformers". In: *Proceedings of NSF/ECC Workshop on Bulk power System Voltage Phenomena - III: Voltage Stability, Security and Control, Davos, Switzerland* (1994).

[12] *A stable finite horizon model predictive control for power system voltage collapse prevention*. 2011, pp. 7105–7110. DOI: `10.1109/CDC.2011.6161396`.

[13] Michael M. Tiller. *Modelica by Example*. Xogency, Web. 2014. URL: `http://book.xogeny.com`.

[14] Modelon. *Hydro Power Library (HPL)*. URL: `http : / / www . modelon . com / products / modelica – libraries / hydro-power-library/`.

LARGE-SCALE TRAINING SIMULATORS FOR INDUSTRY AND ACADEMIA

Tiina M. Komulainen[1]
Oslo and Akershus University College of Applied Sciences, Oslo, Norway
Torgeir Løvmo[2]
Kongsberg Oil & Gas Technologies, Asker, Norway

ABSTRACT

How should industrial large-scale simulators be used in academia? Which aspects of industrial training can benefit engineering education? This article demonstrates the use of industrial large-scale simulators for educational and training purposes for both academia and industry. The didactic models of the simulator courses are described and the learning results are evaluated for two case examples using the same industrial oil and gas process simulator. The differences and similarities of the didactic models of the courses are explored and the further possibilities for collaboration between academia and industry are outlined.
Keywords: Dynamic process simulation, industrial simulator training, large-scale simulators, engineering education research

---

[1] Corresponding author, E-mail: tiina.komulainen@hioa.no
[2] , E-mail: torgeir.lovmo@kongsberg.com

INTRODUCTION

Simulator training in industry

High-fidelity operator training simulators (OTS) including the main process model and the control and safety system, have been used for more than twenty years in the oil and gas industry [1]. The high-fidelity OTS allows realistic, hands-on training of normal operations, startups and shutdowns, plant upsets and emergency situations without compromising the health and safety of the operators, the plant integrity and the surrounding environment [2, 3]. OTS are typically also used for operator training before initial start-up, major plant upgrades, training of procedures, and for regular refresher courses on emergency events [3]. There are numerous benefits related to the simulator utilization, including safety improvements, shorter startups through process and distributed control system testing, enhanced operator performance, trip and incidence avoidance, and knowledge transfer [4-6]. The development of the industrial simulators has traditionally focused on improving the technical quality and the additional functionalities, but during the past decade the educational framework of simulator training and training of team work skills have gained more and more interest [7, 8].

Simulator training in academia

In engineering education, e-labs are widely used as additional learning tools [9-12]. Virtual laboratories are an important addition to the traditional engineering curriculum due to their relevance for the industrial practice, positive learning effects, and time and cost effectiveness [9, 13, 14]. Rutten et al. [10] indicate that together with traditional teaching, the simulation exercises facilitate students' conceptual understanding of the theory, improve their ability to predict the experimental results, increase their interest in the course and improve overall learning outcomes. Important aspects enhancing learning are student-centered tasks that facilitate collaborative and active participation in groups [10, 11]. The virtual laboratories have become more sophisticated, providing more authentic experiences, for example by utilization of industrially relevant commercial simulation tools [9, 11, 15, 16].

The Norwegian Ministry of Education and Research [17] encourage the education institutions to implement industrially relevant, practical training into the engineering curricula. In the Norwegian petroleum industry all the plants are required to arrange simulator training for the process operators [18], and thus, high-fidelity process simulators are an important tool for process and automation engineers. Since many of the engineering students will be working in the petroleum-related industry after their graduation, industrially relevant simulators with small-scale models have been successfully used at Oslo and Akershus University College [16].

Aims of the article

The aim of this article is to explore the possibilities to use industrial large-scale simulators and assessment methods for engineering education.

In this paper the educational framework of simulator training in the petroleum industry and in academia are presented with two case examples. The case examples are given on a generic large-scale oil and gas process simulator model, using the K-Spice® dynamic process simulation software. The similarities and differences between the industrial and academic simulator training approaches are compared and the possibilities for collaboration are outlined. The didactic model is not software or process model specific, and thus the methods can be transferred to other industrial/academic simulation courses for other chemical processes using other dynamic simulation software.

MATERIALS AND METHODS

First, the simulation software and model are described, and then, the didactic models of the industrial and academic courses are presented in detail.

Software tools

K-Spice® is a high fidelity dynamic process simulation tool, based on over two decades of field testing, engineering studies and successful project deliveries by Kongsberg Oil & Gas Technologies. K-Spice® is used to provide a wide range of services and solutions to the oil and gas industry. These extend from early process design

studies to real-time production management systems, via engineering verification, control system check-out and process training. K-Spice® includes a module library that represents the vast majority of oil and gas unit operations. The equipment modules are all produced with a basis in first principles physics, chemistry and engineering.

Process design of the generic oil and gas production simulator model consists of a three-stage, three-phase separation train. The three-phase flow from the production wells is routed to the High Pressure (HP) Separator or Test Separator, for the initial separation into water, gas and hydrocarbon liquids. The hydrocarbon liquids are further degassed in the Medium Pressure (MP) Separator and then heated before the final degassing is done in the Low Pressure (LP) Separator. Stabilised crude from the Low Pressure separator is routed to an Electrostatic Coalescer for final dewatering prior to export. Water removed in the Coalescer is pumped back to the inlet of the HP Separator.

The associated gas from the Medium Pressure and Low Pressure stages are recompressed to High Pressure stage pressure, and mixed with gas from the HP and Test separators. This is done prior to the total gas stream being cooled for heavy hydrocarbon removal and then dehydrated by intimate contact with lean Tri Ethylene Glycol (TEG) in a Contactor in order to meet export specifications. The dried gas is compressed and then cooled for delivery into the Gas Export Pipeline. The rich TEG is returned to the Regeneration System.

Produced Water leaving the High Pressure Separator and Test Separator is routed to their respective Hydrocyclones for de-oiling before final degassing in the Degassing Drum and onward pumping to the Water Injection System or disposal to sea. A Test Separator, normally operating at the same pressure as the High Pressure Separator, caters for well testing. To support the process operations a number of utility systems are provided such as cooling medium, sea water and water injection. An overview of the plant is given in **Fig. 1**. Extensive and detailed documentation of the simulator, process-, automation, and safety system are included in the simulator package.
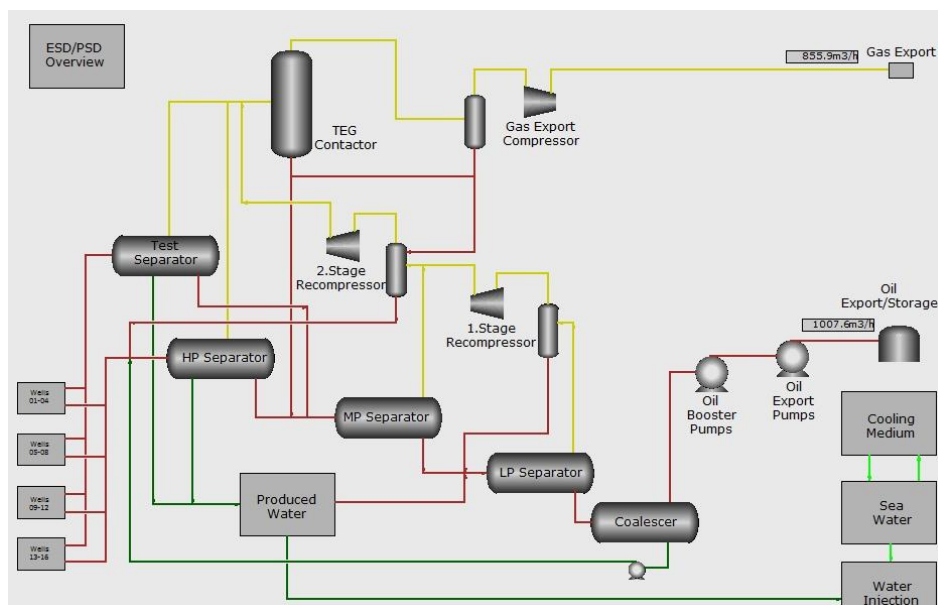
Fig. 1. Overview of the large-scale oil and gas production plant model.

Case1: industrial simulator training

Kongsberg Oil & Gas Technologies provides industrial simulator training for educational and operator training purposes. The generic oil and gas production simulator model is specially designed for teaching and learning different aspects of oil and gas production processes in a safe and informative environment. The simulator is an excellent visual aid to help enhance the learning experience and expand knowledge within process behavior, process equipment, process control and process safety systems.

Training is set up in three levels for varying degrees of difficulty, to target different prior knowledge. The first level is an introduction to oil and gas production processes and includes basic knowledge of process systems, equipment and control together with basic operations. The second level is training on normal process operations, and includes start-up and shut down of process equipment and systems from wells to oil and gas export and utilities. The third level is training on abnormal operations and troubleshooting. This level requires some prior knowledge on normal operations.

Each training level emphasizes practical exercises. The trainees are operating their own simulator process model and performing predefined exercises. For each level, at the last day of the training course, the trainees are evaluated by executing a set of predefined assessment scenarios. An assessment scenario comprises of triggers, actions and assessments and is combined in a way to evaluate trainee performance on training course content. A computer generated report, giving a score attained by the trainee when assessed, is issued. In addition an instructor observation report for each trainee is issued to supplement the computer generated score. An assessment Scenario Overview is presented in **Fig. 2**.

Framework.

Time: The simulator course length is 4 days at each level. An example on the time allocation is given in **Fig. 2**.

Room and group size: PC-classroom training in small groups of 4 – 10 participants.

Teaching materials: Generic simulator model and workbooks specific for the exercises are used as teaching materials.

Instructor prerequisites: The experienced course instructor has theoretical knowledge on chemical processes and practical skills on process dynamic simulation.
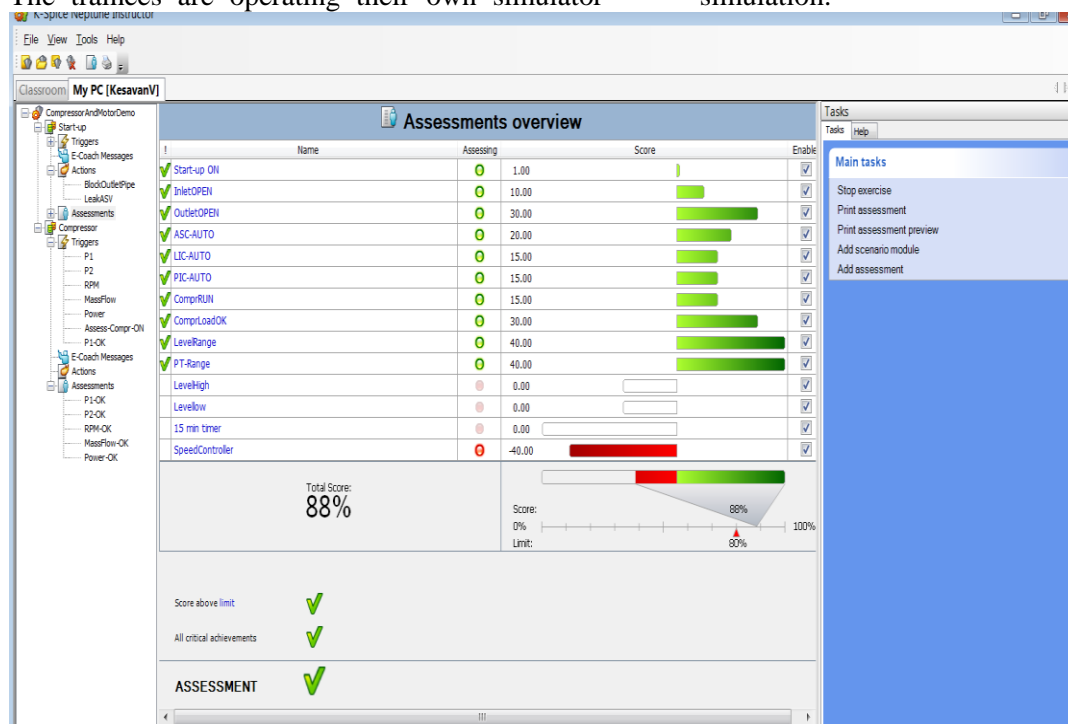
Fig. 2. K-Spice Exercise Manager, Assessment Scenario Overview.

Methods for teaching, learning and evaluation.
Teaching methods: Instructor leads classroom training with theory, practical examples before the simulation session. After the simulation session the instructor leads the debriefing of the practical simulation exercises.

Learning methods: Each of the course participants have a dedicated simulator PC, and operate the simulator model independently. The learning method is "learning by doing" during the simulation session, and by reflection/ peer-learning during the debriefing.

Evaluation: The learning outcome is evaluated using automatic Assessment Scenarios.

Learning goals, prerequisites, tasks.
General comments: No prior knowledge of dynamic simulator models is required. Training courses are suitable for all kinds of professionals that work or aim to work within the oil and gas industry.

Prerequisites: At level three, abnormal process operation and troubleshooting, some process knowledge and operational experience is advisable.

Learning goals: Increase knowledge and confidence within process behaviour and operations.

Examples on typical simulation tasks are given in **Table 2**.

Table 1. Industrial simulation module set-up.

Activity	Description	Time
Briefing	Instructor presents theory and simulation demos	Day 1 -Day 3
Simulation scenarios	Operators work through simulation scenarios	
Debriefing	Instructor gives feedback on completed scenarios	
Exam / assessment	Operators execute assessment scenarios, instructor observes	Day 4
Assessment report	Instructor and operator discusses results, instructor gives final assessment.	
Total time		4 days

Table 2. Examples on typical industrial simulation tasks.

Task A	Compressor Performance. Change: Increase temperature controller setpoint at inlet compressor system Consequence: Cooling medium supply will reduce. Response: Inlet temperature will increase. Hydrocarbon liquids from scrubber will decrease due to increased temperature. Massflow through compressor will increase since more water and heavy hydrocarbons are in gas phase.
Task B	Process Equipment Failure. Change: Machine failure at pump motor. Consequence: Machine will shut down. Response: Pump discharge pressure will reduce due to machine failure, pump is impossible to start and stand-by pump needs to be set in operation.
Task C	Process area start-up. Change: Process shut down (PSD) in gas export area. Consequence: The gas export area will shut down to safety position and all export gas routed to flare. Response: Restart of gas export area after PSD is required

Case2: simulator training for engineering students
In the following framework, teaching and learning methods and the learning goals are presented for the simulation module taught at the Oslo and Akershus University College for courses ELTS2300 Dynamic systems (Automation, 3rd semester, 10 ECTS). A similar simulation module with the same oil and gas process simulator is taught also for course KJTS2100 Introduction to Chemical Engineering (3rd semester, 10 ECTS).

Framework.
Time: The simulation module is implemented using the set-up given in **Table 3**. First, the teacher is presenting the simulator, the dynamic trends and the tasks in a classroom for all the students. Then the students are divided into larger groups that meet for the 4 hour long simulation sessions. The students will work on

familiarization tasks before the simulation scenarios. The students start writing a preliminary simulation report during the simulation session, and are to use approximately two hours afterwards to finish the report before the workshop. In the two-hour workshop, the students compare and discuss the simulation results in new groups of 4 students. At the end of the workshop the teacher facilitates the summarization of the simulation results and of overall experience on a whiteboard. Total time consumption of the module is 7-10 hours.

Room: The simulation module requires an auditorium with a PC and a whiteboard for the introduction lecture and the workshop, and 4 hours of PC classroom per simulation session. The minimum requirement for the PC classroom is one PC per student, and preferably an instructor station that can be connected to a projector for additional simulation demos.

Group size: The students are divided into groups of 10-20 students/session depending on the teaching resources and PC-classroom availability. Optimal group size is about 8 students per session if only one teacher/instructor is available. The students are working in pairs through the simulation tasks, and write the simulation report together.

Teaching materials: The user manual, prepared by the teacher, is specific for the simulation model. The user manual includes clear instructions on typical simulation commands; how to load the model, start and pause the simulation, open the relevant variable trends, make different process changes, save the simulation data and how to interpret the results. A detailed solutions manual, prepared by the teacher, is available for the teacher during the simulation sessions and during the workshop. The solutions manual is made available for the students after the grading of the simulation reports.

Instructor prerequisites: The teacher must have experience with dynamic simulation and the commercial process simulation software in order to be able to help the students with various process and software related questions. If the teacher is not familiar with the process simulation software, it could be advisable to invite an instructor from the software vendor. It is important that the instructor creates a positive learning environment inspiring the students to work together and to discuss the results during the simulation session.

Table 3. Academic simulation module set-up.

Activity	Description	Time
Introduction lecture/ briefing	Teacher introduces simulator, process, dynamic trends, tasks	1-2h
Familiarization software	Work through user manual: typical simulator commands, trend panels	45 min
Familiarization process	Browse through the process: fill in material balance-table	15-30 min
Simulation tasks/ scenarios	Dynamic simulation scenarios related to theory, calculations	2-3h
Reporting	Students write report and prepare workshop presentation	2h
Workshop/ debriefing	Students present the results	1-2h
Final exam	One exam task on simulation	15 min
Total time		7-10h

Methods for teaching, learning and evaluation.
Teaching methods: The teacher explains the basics of the simulation tasks and gives a simulation demonstration at the introduction lecture. During the simulation sessions the teacher has an instructor role, helping the students only if the student group cannot find the solution themselves. In the workshop the teacher is a facilitator, setting frames for the group discussions on the simulation results and guiding the final plenary presentation of the results. The teacher gives feedback to the students during the simulation sessions and the workshop, and grades the simulation reports.

Learning methods: The simulation tasks are to enhance social interaction in small groups while the main focus is for each student to learn by doing the simulation tasks and reporting at their own pace. Discussions on the simulation results are encouraged during the simulation sessions and

during the workshop, i.e. learning from peers and through reflection.

Evaluation: The students evaluate the simulation module as part of the compulsory report using a multiple-choice questionnaire. The learning outcome of the simulation module is measured using results of the formal final exam.

Learning goals, prerequisites, tasks.

The module is motivated by positive effects of good controller tuning in the process industry. Process parameter identification gives a good starting point for controller tuning, and good tuning gives more on-specification production, decreases amount of unplanned partial shut-downs (trips) and disturbances, thus more income for the operating company and less stress for the process operators. A trip is caused by HighHigh (HH) or LowLow (LL) alarm that leads to partial shut-down of the process (PSD) according to the cause&effect chart.

Prerequisites: The student can describe parametrization of simulated step responses for integrating processes and first order processes with time delay. The students are familiar with the basic elements of a control loop: transmitter, controller and control element.

Learning goals: The student gets familiar with the main unit operations and operating principles of typical industrial topsides oil and gas process, and its control and safety systems. The student is able to use an industrial process simulator to run step responses, can classify the process response (integrator, first order process with/without time delay) and calculate the model parameters.

Tasks: A short overview of the tasks is given in **Table 4**.

Table 4. Examples on academic simulation tasks.

Task1	Normal operation, no change Fill in steady-state process values for given 6 points in the process into the Heat & Material Balance
Task2	Level controller in manual mode Change: introduce ±5% change into the level controller output Consequence: Oil level decreases/ increases Response: Integrating process response

	with time delay, level alarm LL/HH causing a trip situation.
Task3	Pressure controller in manual mode Change: introduce ±5% change into the pressure controller output Consequence: Pressure in separator decreases/ increases Response: First order process response without time delay
Task4	Temperature controller in manual mode Change: Introduce ±1% change into the temperature controller output Consequence: Temperature of the export gas decreases/ increases Response: First order process response with time delay

RESULTS

In this section, the evaluations of the industrial and the academic simulator courses are presented.

Case1: Evaluation of the industrial course

In this section results from assessment scenarios after extensive simulator training are presented. A group of oil and gas production operators went through a training program including level 2 and 3 as described in section 2.2. After each level all operators were assessed by a set of 3 assessment scenarios. Average results from the group are presented in **Fig. 3**. Interestingly the results from the level 3 courses have a higher average; the level 3 assessments are more complex than level 2, so the trainees benefitted from the level 2 courses as a prerequisite for level 3.

Feedback from the majority of the operators participating in the training program is that they enjoyed the experience and gained a lot out of it. They found dynamic simulator training motivating, meaningful and enjoyable.

Experience from such training courses shows that assessment of operators is best in combination with computer generated score and instructor evaluation.
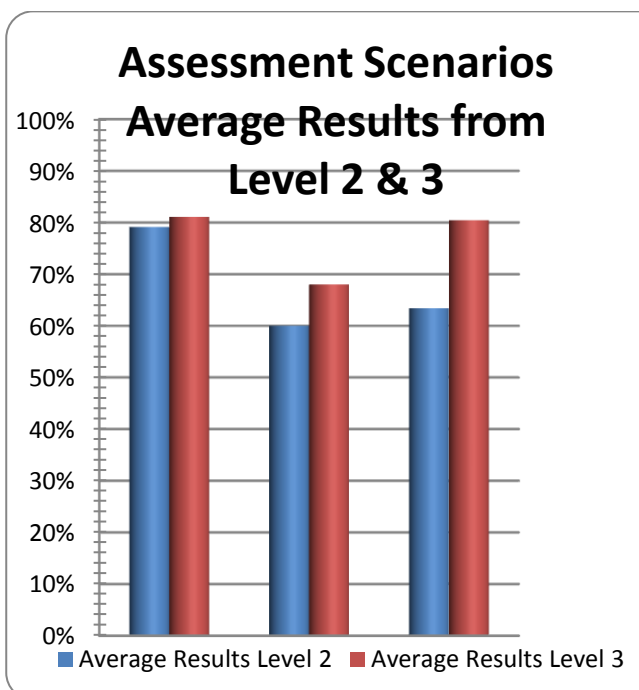
Fig. 3. Average results from assessment scenarios, industrial course, level 2 (blue) and level 3 (red).

Case2: Evaluation of the academic course

A total of 63 second year automation students evaluated the simulation module using an electronic multiple-choice questionnaire including 6 statements. A summary of the answers, given in **Fig. 4**, shows a very positive overall evaluation. All of the students agreed that the simulation exercises are useful for learning, and 97% agreed that simulation exercises increase understanding of process dynamics in fluid systems. The simulation tasks gave practical skills on identification of first order model parameters according to 89% of the students, and gave extra motivation for further studies in control for 80% of the students.

The use of the simulation tool was easy to learn according to 84% of the students, and 92% agree that K-Spice® is a suitable simulation tool for the course in dynamic systems. The average time consumption for the mandatory tasks including reporting was 5 hours.

The formal final exam included 5 sections of which one was about the simulation and model parameter estimation. The average score for the interpretation of the simulation chart was 48%, and the total average score for the exam was 59%.

The exam result is in sharp contrast to the students' and the teacher's positive evaluation of the simulation module. Possible explanations to the low exam score are confusion with the interpretation of the time axis of the simulation chart, something that many students wrote in the exam paper. Another explanation is students did not reach the learning goals because they did not work on the mandatory group tasks individually. However, the issue of interpretation of simulation charts must be addressed next fall semester, possibly with a mid-term test.
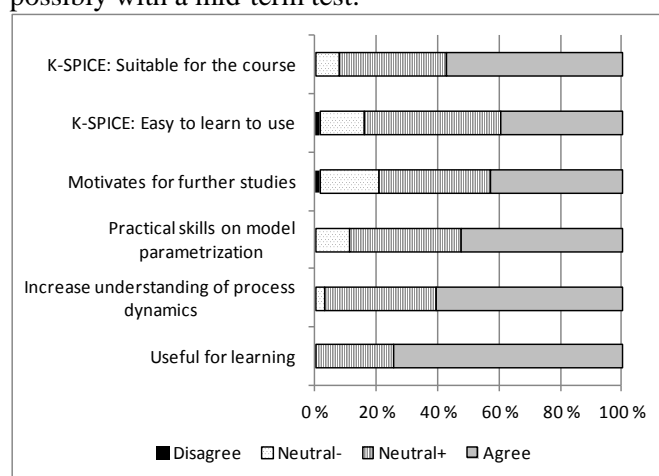
Fig. 4. Students' evaluation of the simulation module, academic course.

DISCUSSION – COMPARISON AND POSSIBILITIES FOR COLLABORATION

Simulator training is partly motivated by governmental requirements: The Petroleum safety authority Norway requires simulator training for all control room operators in the Norwegian petroleum industry, and the guidelines from the Ministry of education and research recommend more practical, industry-relevant content in the engineering education. Simulator training in the industry is motivated by more efficient and safer operation, and by higher revenues. In academia the industrial simulators can provide realistic examples on chemical processes and tools students will use after graduation. Relevant case examples from industry are motivating for the students, and have a great value for the academic courses.

Time spent on simulator training is much longer in the industry than in academia; typically an industrial course lasts from 2 days to 1 week, whereas in academia 1 day per semester is available.

The industrial simulation tools require dedicated simulator rooms or PC-labs; Simulators made available outside of the PC-lab, for example for student-activating classroom tasks during lectures, would be very beneficial for the briefing and debriefing sessions. A simulator-app would also increase the awareness of the simulators and chemical processes, and could be used for training of other working groups and disciplines.

The teaching materials specific for the simulation model and software can be used in academia and industry, but it is necessary to prepare exercise-specific user manuals and solution manuals for each course.

The success of a simulator training course is dependent on inspiring and competent instructors. If the academic staff is not familiar with industrial simulation tools, inviting simulator course instructors from industrial partners / simulator vendor could be a viable solution.

The course participants in the industry typically have a strong practical process background, whereas in academia the students have some theoretical knowledge, but lack practical skills and an overview of unit operations.

The learning goals and contents of the industrial and academic courses are very different. In industry, the purpose of simulator training is to qualify the operators for their daily work, whereas in academia the students learn to use industrial tools and get practical insight into industrial processes. Specification of the skills and knowledge the industry would like the engineering graduates to have is important feedback to the academic institutions.

The teaching methods for simulator training are similar, the structure on briefing/theory – simulation exercises – debriefing/workshop has been effectively used in many other application areas such as aviation, marine and medical simulation.

The learning methods are partly similar, the course participants are supposed to apply their theoretical and/or practical knowledge to solve the hands-on tasks, and to expand their knowledge during the exercises and the discussions in the debriefing sessions.

The assessment of the learning outcome using traditional exams is common both in academia and industry. In addition the industrial simulator courses rely on subjective evaluation from the instructor. New methods on automatic assessment, such as the K-Spice® Exercise Manager Assessment Scenario Tool, used for the industrial case example in this article, could be beneficial for academic courses with over a hundred participants. Methods to combine the valuable subjective instructor evaluations with automatic assessment could be one collaboration topic.

Further development of effective teaching, learning and assessment methods for process simulator training is an important collaboration area which requires multi-disciplinary research work between industry and academia, including other academic disciplines such as social sciences/pedagogy.

CONCLUSIONS AND FURTHER WORK

This article demonstrates the use of industrial large-scale simulator for academic and industrial simulator courses. The didactic set-up and simulation exercises are not software/ process specific, thus the methods can be transferred to other industrial/academic simulation courses for other chemical processes.

The didactic model for simulator training has provided successful learning results, and the generic oil and gas simulation model has proven to be suitable for academic and industrial courses. The engineering students can greatly benefit from practical case examples using industrial simulation tools, and industrially relevant topics for BSc/MSc/PhD thesis work.

The positive experiences in industry and academia encourage further research and development of didactic/pedagogical model for the simulator courses. Multi-disciplinary collaboration is necessary especially on research and development of the teaching, learning and assessment methods for simulator training.

REFERENCES

1. McArdle, S., D. Cameron, and K. Meyer, *The Life Cycle Simulator: From Concept to Commissioning... and Beyond*, in *SPE Intelligent Energy Conference and Exhibition* 2010, SPE: Utrecht.

2. Abel, J., *Aging HPI workforce drives need for operator training systems.* Hydrocarbon Processing, 2011. **90**(11): p. 11-11.

3. Cheltout, Z., R. Coupier, and M. Valleur, *Capture the long-term benefits of operator training simulators.* Hydrocarbon Processing, 2007. **86**(4): p. 111-116.

4. Fiske, T., *Benefits of dynamic simulation for operator training.* Hydrocarbon Processing, 2007. **86**(12): p. 17-17.

5. Lippin, J., *Preserving knowledge: Keys to effective lifecycle management.* Hydrocarbon Processing, 2011. **90**(12): p. 63-66.

6. Komulainen, T.M., et al., *Economic benefits of training simulators.* World oil, 2012(12): p. R61-R65

7. Glaser, D.C., *Put training back into operator training simulators.* Hydrocarbon Processing, 2011. **90**(6): p. 41-43.

8. Sneesby, M., *Operator training simulator: myths and misgivings.* Hydrocarbon Processing, 2008. **87**(10): p. 125-127.

9. Coble, A., et al. *Delivering authentic experiences for engineering students and professionals through e-labs.* in *Education Engineering (EDUCON), 2010 IEEE*. 2010.

10. Rutten, N., W.R. van Joolingen, and J.T. van der Veen, *The learning effects of computer simulations in science education.* Computers & Education, 2012. **58**(1): p. 136-153.

11. Corter, J.E., et al., *Process and learning outcomes from remotely-operated, simulated, and hands-on student laboratories.* Computers & Education, 2011. **57**(3): p. 2054-2067.

12. Edgar, T.F., Ogunnaike, B.A., Muske, K.R., *A global view of graduate process control education.* Comput. Chem. Eng., 2006. **30**(10-12): p. 1763-1774.

13. Martin-Villalba, C., Urquia, A., Dormido, S., *Object-oriented modelling of virtual-labs for education in chemical process control.* Comput. Chem. Eng., 2008. **32**: p. 3176-3186.

14. Rasteiro, M.G., Ferreira, L., Teixeira, J., Bernardo, F.P., Carvalho, M.G., Ferreira, A., Ferreira, R.Q., Garcia, F., Baptista, C.M.S.G., Oliveira, N., Quina, M., Santos, L., Saraiva, P.A., Mendes, A., Magalhaes, F., Almeida, A.S., Granjo, J., Ascenso, M., Bastos, R.M., Borges, R., *A virtual platform to teach chemical processes.* Educ. Chem. Eng., 2009. **4**: p. 9-19.

15. Wankat, P.C., *Integrating the Use of Commercial Simulators into Lecture Courses.* J. Eng. Ed., 2002. **91**(1): p. 19-23.

16. Komulainen, T.M., et al., *Experiences on dynamic simulation software in chemical engineering education.* Education for Chemical Engineers, 2012. **7**(4): p. e153-e162.

17. Norwegian Ministry of Education and Research, *National curriculum regulations for engineer education*. 2011. p. 5.

18. Petroleum Safety Authority Norway, *Veiledning til aktivitetsforskriften Til § 23 Trening og øvelser*. 2012.

MAKING MODELICA MODELS AVAILABLE FOR ANALYSIS IN PYTHON CONTROL SYSTEMS LIBRARY

Anushka Perera, Carlos Pfeiffer and Bernt Lie[*]
Telemark University College
Kjølnes ring 56, P.O. Box 203
N-3901 Porsgrunn
Norway

Tor Anders Hauge
Glencore Nikkelverk
Kristiansand
Norway

ABSTRACT

Modelica-based simulation environments are primarily targeted on model simulation, therefore they generally lack support for advanced analysis and synthesis needed for general control systems design and particularly for optimal control problems (OCPs), although a Modelica language extension (Optimica) exists to support general optimization problems. On the other hand, MATLAB has a rich set of control analysis and synthesis tools based on linear models. Similarly, Python has increasing support for such tools e.g. the "Python Control System Library" developed in Caltech. In this paper, we consider the possibility of automating the process of extracting linear approximations of Modelica models, and exporting these models to a tool with good support for linear analysis and design. The cost of software is an important aspect in our development. Two widly used free Modelica tools are OpenModelica and JModelica.org. Python is also freely available, and is thus a suitable tool for analysis and design in combination with the "Python Control System Library" package. In this work we choose to use JModelica.org as the Modelica tool because of its better integration with Python and CasADi, a CAS (Computer Algebra System) tool that can be used to linearize Modelica models. The methods that we discuss can in principle also be adapted for other Modelica tools. In this paper we present methods for automatically extracting a linear approximation of a dynamic model encoded in Modelica, evaluated at a given operating point, and making this linear approximation available in Python. The developed methods are illustrated by linearizing the dynamic model of a four tank level system, and showing examples of analysis and design based on the linear model. The industrial application of these methods to the Copper production plant at Glencore Nikkelverk AS, Kristiansand, Norway, is also discussed as current work.

Keywords: Modelica, JModelica.org, Python, CasADi, Symbolic/Numeric Linearization, Linear Analysis, python-control

1 INTRODUCTION

Modelica is becoming a de facto standard for modeling of large-scale complex physical systems. Since Modelica is object-oriented, declarative (acausal), and equation-based, it allows to create reusable components and to built efficient reconfigurable component-models. A Modelica-based simulation environment (a Modelica tool) is needed to simulate Modelica models.[1] Modelica tools mainly focus on model simulation. However, the model sim-

---

[*]Corresponding author: Phone: +47 41807744 E-mail: `bernt.lie@hit.no`

[1]A complete list of Modelica tools is available at `https://www.modelica.org/tools`.

ulation is not the only objective of mathematical modeling. Among others optimal control problems (OCPs), control analysis and synthesis, and state estimations are several aspects that require dynamic systems modeling. Optimica [1] extends Modelica language specifications to handle OCPs and JModelica.org provides Optimica compilers. OpenModelica partially support Optimica extension at the moment.

In order to exploit Modelica, either a simulation environment should be equipped with necessary tools for model analysis (e.g. good enough scripting facilities and/or GUI options) or Modelica should be interfaced with other existing tools. Some comercial Modelica tools provide interfaces to integrate toexternal software, such as Dymola integrating with MATLAB/Simulink. However, these tools are very expensive. A free tool, the JModelica.org platform, integrates completely with Python through two core Python packages: `pymodelica` for compilers and `pyfmi`/`pyjmi` for model import.[2]

Since we are mainly interested in free software tools that easily interface with other tools, we selected JModelica.org. The JModelica.org platform has also an interface with CasADi [2] and hence, it is possible to make Modelica/Optimica models available as symbolic model objects in Python. The `casadi` Python package is used to linearize Modelica models symbolically/numerically (see [3] for a detailed description.) and then the system matrices may be used in linear system analysis and in algorithms, in particular using the `python-control` package.[3] This paper demonstrates usefulness of interfacing Modelica with Python via CasADi. The method is explained with a simple example (a four tanks system). As a case study of a real process the Copper production plant [4] at Glencore Nikkelverk AS, Kristiansand, Norway is considered by showing how to design a LQR (Linear Quadratic Regulator) optimal state feedback controller using the `python-control` package.

2 STRUCTURE OF LINEARIZATION
2.1 MODELICA AND DAES

The execution of a Modelica model is started with a model flattening process that removes the hierarchical structure (i.e. expansion of inherited base classes, adding connector equations, etc.) of the Modelica model into a flat model [5]. A flattened model provides a set of acausal differential-algebraic-discrete equations, or so called hybrid DAEs form, which is given by

$$F(t,\dot{x},x,u,z,m,p) = \begin{bmatrix} F_1(t,\dot{x},x,u,z,m,p) \\ F_2(t,\dot{x},x,u,z,m,p) \\ \cdots \\ F_m(t,\dot{x},x,u,z,m,p) \end{bmatrix} = 0, \quad (1)$$

where x, u, z, m, p, and t are respectively, the dynamic state vector, the input vector, the algebraic state vector, the piece-wise constant vector, the parameter vector, and time. The keyword `input` is used to define input variables and `output`[4] for defining output variables. Output variables are also algebraic variables, hence they are included in z. An output vector, y, may be expressed as:

$$y = H(t,x,u,z,m,p). \quad (2)$$

For simplicity and notational convenience, m and p are neglected and thereby we have:

$$F(t,\dot{x},x,u,z) = \begin{bmatrix} F_1(t,\dot{x},x,u,z) \\ F_2(t,\dot{x},x,u,z) \\ \cdots \\ F_m(t,\dot{x},x,u,z) \end{bmatrix} = 0. \quad (3)$$

Where, $m = dim(x) + dim(y)$. A flattened Modelica model is not yet ready to be solved for $\dot{x}$ and z. A complicated set of manipulations are done on flattened models: sorting equations ($F_1, F_2, \ldots, F_m$), index reduction, common subexpression elimination, etc. prior to solving the equation 3 [5][7].

2.2 CONVERSION TO EXPLICIT STATE SPACE FORM

Consider the DAEs in the equation 3. Converting DAEs into explicit ODEs may be required in many

---

[2]See the JModelica.org user guide available at `http://www.jmodelica.org`.

[3]`http://www.cds.caltech.edu/~murray/wiki/Control_Systems_Library_for_Python`.

[4]The variables which are prefixed with `input`/`output` keywords within the Modelica components at the highest hierarchy of a component-model are appeared as input/output variables after flattening.

applications or to use most standard ODE solvers. If $\frac{\partial F}{\partial [\dot{x},z]^T}$ is not singular (a necessary condition for implicit to explicit transformation), then $[\dot{x},z]^T$ can be written as continuous functions of t, x, and u.[5] On the other hand, if $\frac{\partial F}{\partial [\dot{x},z]^T}$ is singular, then implicit to explicit transformation may not be possible. Algebraic constraint among t, x, z and u can make $\frac{\partial F}{\partial [\dot{x},z]^T}$ singular and in such situations, the constraint equations are differentiated with respect to time, t.

Theorem 1 *The index of a DAE, $F\left(t,\dot{x},x,u,z\right)=0$, is the minimum number of times that all or part of the DAE must be differentiated with respect to t in order to determine $[\dot{x},\dot{z}]^T$ as a continuous function of x, z, u, and t [8].*

The definition to the index of a system of DAEs is given in theorem 1. Higher index (i.e. index > 1) problems may be reduced into at most index 1 problems systematically using the Pantelides algorithm [9]. For simplicity, the DAEs

$$f\left(t,\dot{x},x,u,z\right)=0 \tag{4}$$

and

$$g\left(t,x,u,z\right)=0 \tag{5}$$

are considered in the following discussion (a special case of the equation 3). Sometimes, it may be possible to express algebraic state variables ($\in z$), explicitly in terms of t, x and u and in such cases the index of the problem is said to be 0. By differentiating the equation 5, we get:

$$\frac{\partial g}{\partial t} + \frac{\partial g}{\partial x} \cdot \dot{x} + \frac{\partial g}{\partial u} \cdot \dot{u} + \frac{\partial g}{\partial z} \cdot \dot{z} = 0. \tag{6}$$

If $\frac{\partial g}{\partial z}$ is not singular, then the equation 6 is used to find $\dot{z}$ and hence, the initial problem (equations 4 and 5) is said to be an index 1 problem and equations 4 and 6 gives an index 0 problem. The equation 4, in the general case, gives implicit ODEs, however often they appear as explicit ODEs (i.e. $\dot{x} = f\left(t,x,u,z\right)$). If $\frac{\partial g}{\partial z}$ is singular, it means there are algebraic dependencies among t, x, and u. In this case the algebraic constraints in equation 6 are differentiated once more and if this gives a possibility to find $\dot{z}$, then the initial system of DAEs is an index 2 problem. Constraint equations are differentiated, as many times as the index of the initial problem,

until an index 0 problem is obtained. Note that a reduced index 0 (or 1) problem may not necessarily give the solution to the initial high index problem, unless consistent initial conditions are given [10]. After reducing the index and BLT sorting[6], we have a causal system of DAEs,

$$\tilde{f}\left(t,\dot{\tilde{x}},\tilde{x},\tilde{u},\tilde{z}\right)=0, \tag{7}$$

and

$$\tilde{g}\left(t,\tilde{x},\tilde{u},\tilde{z}\right)=0 \tag{8}$$

with index 1. $\dot{\tilde{x}}$ is the new dynamic state vector of the reduced problem and $\tilde{u} = \left[u, \frac{du}{dt}, \frac{d^2u}{dt^2}, \dots\right]$. The index reduction process may result in adding additional variables and those variables are stacked in $\tilde{z}$. For examples, the dummy derivatives, the state variables which has become algebraic, etc [11]. As $\frac{\partial \tilde{g}}{\partial \tilde{z}}$ is not singular and thereby, it is thus possible to explicitly find $\dot{\tilde{z}}$ (if needed) by:

$$\dot{\tilde{z}} = -\left(\frac{\partial \tilde{g}}{\partial \tilde{z}}\right)^{-1} \cdot \left[\frac{\partial \tilde{g}}{\partial \tilde{t}} + \frac{\partial \tilde{g}}{\partial \tilde{x}} \cdot \dot{\tilde{x}} + \frac{\partial \tilde{g}}{\partial \tilde{u}} \cdot \dot{\tilde{u}}\right]. \tag{9}$$

Consistent initialization gives the solution to the equations 7 and 9 identical to the initial higher index problem in the equations 4 and 5.

2.3 LINEARIZATION

Suppose that $\left(t_0, \dot{\tilde{x}}_0, \tilde{x}_0, \tilde{u}_0, \tilde{z}_0\right)$ exists such that $\tilde{f}\left(t_0, \dot{\tilde{x}}_0, \tilde{x}_0, \tilde{u}_0, \tilde{z}_0\right) = 0$ and $\tilde{g}\left(t_0, \tilde{x}_0, \tilde{u}_0, \tilde{z}_0\right) = 0$, then $\left(t_0, \dot{\tilde{x}}_0, \tilde{x}_0, \tilde{u}_0, \tilde{z}_0\right)$ is an operating point. In many cases, it is required to find the linear approximation for given nonlinear model with respect to an operating point. The linear approximation to equations 7 and 8 are given by:

$$\frac{\partial \tilde{f}}{\partial \tilde{t}} + \frac{\partial \tilde{f}}{\partial \dot{\tilde{x}}} \cdot \delta \dot{\tilde{X}} + \frac{\partial \tilde{f}}{\partial \tilde{x}} \cdot \delta \tilde{X} + \frac{\partial \tilde{f}}{\partial \tilde{u}} \cdot \delta \dot{U} + \frac{\partial \tilde{f}}{\partial \tilde{z}} \cdot \delta \dot{Z} = 0 \tag{10}$$

and

$$\frac{\partial \tilde{g}}{\partial \tilde{t}} + \frac{\partial \tilde{g}}{\partial \tilde{x}} \cdot \delta \tilde{X} + \frac{\partial \tilde{g}}{\partial \tilde{u}} \cdot \delta \dot{U} + \frac{\partial \tilde{g}}{\partial \tilde{z}} \cdot \delta \dot{Z} = 0. \tag{11}$$

Jacobian matrices are evaluated at $\left(t_0, \dot{\tilde{x}}_0, \tilde{x}_0, \tilde{u}_0, \tilde{z}_0\right)$. $\frac{\partial \tilde{f}}{\partial \dot{\tilde{x}}}$ and $\frac{\partial \tilde{g}}{\partial \tilde{z}}$ are not singular and as a result equations 10 and 11 can be transformed into a state space form.

The usual procedure to obtain numerical Jacobian

---

[5]The implicit function theorem.

[6]BLT stands for Block-Lower-Triangular.

matrices is to use finite difference methods. For example, a finite difference approximation to $\frac{\partial \tilde{f}}{\partial \dot{\tilde{x}}}$ using the central difference method is

$$\frac{\tilde{f}\left(t, \dot{\tilde{x}} + I_{dim(x)} \cdot h, \tilde{x}, \tilde{u}, \tilde{z}\right) - \tilde{f}\left(t, \dot{\tilde{x}} - I_{dim(x)} \cdot h, \tilde{x}, \tilde{u}, \tilde{z}\right)}{2 \cdot h^2}.$$

(12)

Where h is a small-enough positive number and $I_{dim(x)}$ is a $dim(x)$-by-$dim(x)$ unit matrix. There are several drawbacks in finite difference methods: truncation errors, choosing h is harder, and the results depends on h. In order to avoid such problems, automatic/algorithmic differentiation (AD) techniques can be used, where derivatives are calculated as accurate as up to the working precision of a given computer. AD techniques are used to evaluate derivatives of functions defined by means of a high-level programming language such as Python/C++/etc.[7] The AD is implemented with the help of a computer algebra system (CAS) tool, which provides symbolic manipulations over mathematical expressions. A CAS tool is used to create symbolic variables, matrices, expressions, functions and do symbolic mathematical manipulations on them such as symbolic differentiation[8], integration, etc. There are many CAS tools available such as Maple, Mathematica, SymPy, CasADi, Maxima, etc.[9] A CAS tool may or many not support AD. For example the

---

[7]Consider a function $\bar{f}$ such that $\bar{y} = \bar{f}(\bar{x})$, where $\bar{x} = [\bar{x}_1, \bar{x}_2, \ldots, \bar{x}_n]$ and $\bar{y} = [\bar{y}_1, \bar{y}_2, \ldots, \bar{y}_m]$. $\bar{x}$ and $\bar{y}$ are the independent and the dependent variable vectors respectively. Often, it is possible to represent y_i-x_j relationships using elementary unary/binary operations (+, -, etc.) and elementary functions (sin, cos, etc.). Let $\bar{y}_1 = \bar{x}_1 \cdot e^{\bar{x}_1 \cdot \bar{x}_2}$. $\bar{y}_1$ can be expressed in terms of basic functions and unary/binary operators using a set of intermediate variables ($\bar{z}_k$'s): $\bar{z}_0 = \bar{x}_1$, $\bar{z}_{-1} = \bar{x}_2$, $\bar{z}_1 = \bar{z}_0 \cdot \bar{z}_{-1}$, $\bar{z}_2 = e^{\bar{z}_1}$, $\bar{z}_3 = \bar{z}_0 \cdot \bar{z}_2$, $\bar{z}_4 = \bar{z}_3$, and $\bar{y}_1 = \bar{z}_4$. $\bar{z}_k$ can be written as

$$\bar{z}_k = \bar{f}_e^k(\bar{z}_i),$$

(13)

where $i < k$ and $\bar{f}_e^k$ contains elementary functions and operations. Now, for example $\frac{\partial \bar{y}_1}{\partial \bar{x}_1} = \frac{\partial \bar{z}_4}{\partial \bar{z}_0} = \frac{\partial \bar{f}_e^4}{\partial \bar{z}_0}$ is given, by applying chain-rule, by

$$\frac{\partial \bar{z}_4}{\partial \bar{z}_0} = \Sigma_{i=1}^{4-1} \frac{\bar{f}_e^4(\bar{z}_i)}{\partial \bar{z}_i} \cdot \frac{\partial \bar{z}_i}{\partial \bar{z}_0}.$$

(14)

$\frac{\bar{f}_e^4(\bar{z}_i)}{\partial \bar{z}_i}$ is known as $\bar{f}_e^4$ contains known elementary functions. In order to find $\frac{\partial \bar{z}_i}{\partial \bar{z}_0}$, the equation 14 is applied again and so on. The derivative evaluation may be done in one of two modes: forward and reverse. The method just mentioned above is the forward mode. For further details, refer [12].

[8]Note that symbolic differentiation is not AD.

[9]http://www.autodiff.org/ gives a list of available AD tools.

---

sympy python package doesn't support AD while Maple does. If $\tilde{f}$ and $\tilde{g}$ in equations 7 and 8 can be symbolically expressed using a CAS tool which support AD, then the Jacobian matrices in equations 10 and 11 can be evaluated efficiently using AD techniques.

2.4 JMODELICA.ORG OPTIONS

There are several ways of creating Modelica/Optimica model objects, so called model export, in JModelica.org: FMU, JMU, and FMUX.[10] FMUs are based on FMI (Functional Mock-up Interface) standards[11] and all others are JModelica.org platform specific. The pymodelica package contains compilers for compiling Modelica/Optimica models into FMUs, JMUs, and FMUXes. But FMU-export doesn't support Optimica. FMUXes are crucial here because in order to work with symbolic DAEs, FMUX model units should be used and the relevant compiler is compile_fmux. A compiled model is stuffed in a zip file (with the file extension '.fmux') and the modelDescription.xml file is contained in it. modelDescription.xml file gives a flat model description of Modelica/Optimica models. JMUs closely follow FMI standards. zip files of both FMUs/JMUs provide a compiled C-codes and binaries besides modelDescription.xml files while in FMUXes only the modelDescription.xml file is given. The model import (loading FMU/JMU/FMUX model objects into Python) may be done via two Python packages: PyFMI and PyJMI. PyFMI is for FMUs while PyJMI for JMUs/FMUXes.

CasADi is a symbolic framework for AD and non-linear optimization as well as it is a CAS tool. CasADi can import Modelica/Optimica models, where those models have been transformed into compatible XML-files (modelDescription.xml) [13][14] and generates symbolic DAEs/OCPs. the parseFMI() method which is defined within the CasADi class SymbolicOCP is used to import XML-based Modelica/Optimica models. See [15] for more details. CasADi integra-

---

[10]The latest JModelica.org version 1.14 has introduced a new model class using the compiler transfer_-optimization_problem, which is available in pyjmi package. See the user guide for further details. In this paper JModelica.org version 1.12 is considered.

[11]https://www.fmi-standard.org/.

tion with JModelica.org [16] opens up a provision to use Modelica/Optimica models with complete flexibility within Python, and making it possible to exploit modeling power in Modelica as well as scripting power in Python.

3 A PYTHON IMPLEMENTATION WITH AN EXAMPLE

3.1 STRUCTURE OF PYTHON SCRIPT

A simple four-tank system is considered (taken from [17]). See Figure 1 for the schematic model of the system. The mathematical model is given by equations 15 - 20. The table 1 contains parameters. The Optimica model is stored in a text file named `TankSystems` with the file extension `.mop` (in this case, the file extension may have been used to be `.mo`). `TankSystems.mop` contains `TankSystems` package and this package contained two Modelica models: `FourTanks` for the dynamic model and `FourTanks_init` for the steady state model in order to find steady state. See appendix A for the Optimica code.
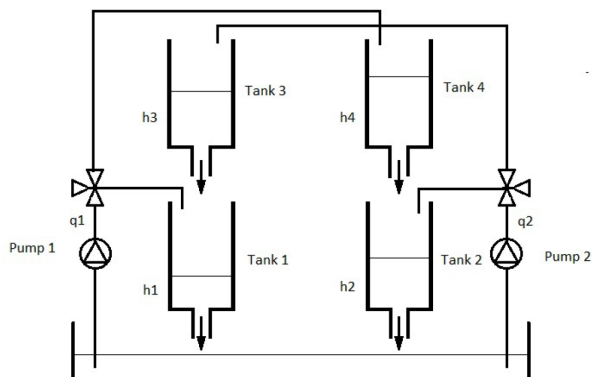
Figure 1: A schematic diagram for the four tank systems.

$$\frac{dh_1(t)}{dt} = -\frac{c_1 \cdot \sqrt{h_1(t)}}{A_1} + \frac{c_3 \cdot \sqrt{h_3(t)}}{A_1} + \frac{\gamma_1 \cdot q_1(t)}{A_1} \tag{15}$$

$$\frac{dh_2(t)}{dt} = -\frac{c_2 \cdot \sqrt{h_2(t)}}{A_2} + \frac{c_4 \cdot \sqrt{h_4(t)}}{A_2} + \frac{\gamma_2 \cdot q_2(t)}{A_2} \tag{16}$$

$$\frac{dh_3(t)}{dt} = -\frac{c_3 \cdot \sqrt{h_3(t)}}{A_3} + \frac{(1-\gamma_2) \cdot q_2(t)}{A_3} \tag{17}$$

$$\frac{dh_4(t)}{dt} = -\frac{c_4 \cdot \sqrt{h_4(t)}}{A_4} + \frac{(1-\gamma_1) \cdot q_1(t)}{A_4} \tag{18}$$

$$\frac{dq_2(t)}{dt} = -\frac{1}{\tau_2} \cdot q_2(t) + \frac{k_2}{\tau_2} \cdot v_2(t) \tag{19}$$

$$\frac{dq_1(t)}{dt} = -\frac{1}{\tau_1} \cdot q_1(t) + \frac{k_1}{\tau_1} \cdot v_1(t) \tag{20}$$

Variable	Value	Units
A_1	12.57	cm^2
A_2	12.57	cm^2
A_3	12.57	cm^2
A_4	12.57	cm^2
c_1	9.82	$c \cdot m^{5/2}/s$
c_2	5.76	$c \cdot m^{5/2}/s$
c_3	9.02	$c \cdot m^{5/2}/s$
c_4	8.71	$c \cdot m^{5/2}/s$
K_1	6.94	$c \cdot m^3/V$
K_2	8.72	$c \cdot m^3/V$
τ_1	6.15	s
τ_2	13.2	s

Table 1: Four-Tanks System Model Parameters.

The Python code used to compile the Modelica/Optimica Four Tanks is given below.

```
# Import compiler compile_fmux
from pymodelica import compile_fmux
# Compile Modelica/Optimica models
file_name = 'TankSystems.mop'
model_name = 'FourTanks'
compile_fmux(model_name,file_name)
# Note: name of the '.zip' file created is
\'FourTanks.fmux'
```

Now, the FMUX model object is imported as a `CasadiModel` object. See below:

```
from pyjmi import CasadiModel
casadiModelObject = CasadiModel('FourTanks.fmux')
# Get flat ocp representation
ocp = casadiModelObject.ocp
```

`ocp` gives a flat representation of Modelica/Optimica models based on the modelDescription.xml. `ocp.ode` and `ocp.alg` represent symbolic expressions for ordinary differential equations (ODEs) and algebraic equations respectively. Use Python commands `print ocp` and `help(ocp)` to get help. Now, the symbolic DAEs are available for general use in Python,[12] hence Modelica/Optimica models can be used in various

---

[12]For example, it is possible to implement Pantelides algorithm with symbolic DAEs.

algorithms and in analysis using CasADi functionalities, `numpy`[13], `matplotlib`[14], `scipy`[15] and `python-control` like Python packages. Use the following Python code to import CasADi and CasADi tools.

```
from casadi import *
from casadi.tools import *
```

If necessary, `ocp.makeExplicit()` method can be used to transform ODEs from implicit to explicit form.[16] Derivatives ($\in \dot{x}$), dynamic states ($\in x$), algebraic states ($\in z$), independent parameters ($\in p_i$), dependent parameters ($\in p_d$), free parameters ($\in p_f$), time (t), and control signals ($\in u$) are given by respectively `casadiModelObject.dx`, `ocp.x`, `ocp.z`, `ocp.pi`, `ocp.pd`, `ocp.pf`, `ocp.t`, and `ocp.u`. For example, `ocp.x[i]` gives x_{i+1} ($0 \leq i \leq dim(x) - 1$). `ocp.x[i]` is in `variable` data type, and it has to be converted into `SX` data type before creating `SXFunction` instances. This is done by `ocp.x[i].var()`[3]. Then all the states variables (in SX type) are stuffed in a Python `list`. The same procedure is applied to other variables as well. Using `ocp.eliminateDependent()`, dependent parameters are eliminated. `ocp.ode` can be taken as a function of t, $\dot{x}$, x, z, and u and let it be $0 = f(t, \dot{x}, x, u, z)$. Now, f is defined as an `SXFunction` class instance. Say, `ffun`. See below for the Python code to create it (see appendix B for the complete Python script):

```
# Define DAEs
f = ocp.ode
g = ocp.alg
# Create an SXFunction for f and g
ffun = SXFunction([t,vertcat(xDot),vertcat(x),\
vertcat(u),vertcat(z)],[f])
gfun= SXFunction([vertcat(x),vertcat(u),
vertcat(z)],[g])
ffun.init()
gfun.init()
```

Note that as explained in subsection 2.2, index reduction should be done on f and g, if the problem is higher index, to obtain lower index problems before creating `ffun` and `gfun`. Anyway, the four-tank system model has the index equal to 0. For an example, $\frac{\partial f}{\partial u}$ is given by `ffun.jac(2)`. See the result (by entering `ffun.jac(2)` in the command line) given below.

```
Matrix<SX>(
[[00,   00 ]
 [00,   00 ]
 [00,   00 ]
 [00,   00 ]
 [-1.12846,   00]
 [00,   -0.660606]]
)
```

Numerical Jacobian matrices are then found for given $(t_0, \dot{x}_0, x_0, u_0, z_0)$. See the code given below.

```
f_u_fun.setInput(t0,0)
f_u_fun.setInput(dx0,1)
f_u_fun.setInput(x0,2)
f_u_fun.setInput(u0,3)
f_u_fun.setInput(z0,4)
f_u_fun.evaluate()

f_u_num = f_u_fun.getOutput()
```

Operating points are usually choosen at steady states. A steady state, x_0 is calculated by: (1) compiling the static Modelica model TankSystems.FourTanks_Init into a JMU, (2) loading the JMU model, (3) setting the input vector u_0, and (4) finally, initializing the JMU model using `initialize()` method.[17] Hence, it is possible to find system matrices A, B, C, and D based on the Jacobian matrices just evaluated.

As the system matrices are available, the `python-control` package can be used in control analysis and synthesis. In order to import the `python-control` use:

```
import control
```

or

```
from control import *
```

As a summery to this section, the following points are made: (1) an Optimica package is created with two Modelica models (dynamic and static) in it, (2) use the static model to find the steady state using a JMU model object, (3) import the dynamic model as a CasadiModel object model and use `casadi` to linearization of symbolic DAEs (after reducing the index if needed), and (4) use the linearized model with the `python-control` package. See TankSystem.mop and TankSystem.py in the appendices A and B.

---

[13]http://www.numpy.org/.

[14]http://matplotlib.org/.

[15]http://www.scipy.org/.

[16]This is possible only if ODEs are linear w.r.t. $\dot{x}$.

[17]Initialization is done by formulating DAEs and equations given within `initial equation` clause in residual form and minimizing sum of square error using the `Ipopt` solver. See JModelica.org user guide.

4 INDUSTRIAL CASE STUDY

We consider the chlorine leaching and electro-winning process which is a part of the nickel refinery of Glencore Nikkelverk in Kristiansand, Norway. A mechanistic models is presented in [4] and it is a MIMO system with 3 inputs (u_1, u_2, u_3), 11 disturbances (w_1, w_2, ..., w_{11}), 3 outputs (y_1, y_2, y_3) and 39 states (x_1, x_2, ..., x_{39}). The process is in large-scale and it is complex (multi variable nature, non-linearities, etc.). Hence, Modelica and Optimica are ideal for the modeling and optimization. Also the process is a good candidate for model based control. In this section, what is explained in subsection 3.1 will be applied to the copper plant model.

The following demonstrations shows how to use the `python-control` tool to design a (infinite-horizon, continuous-time) LQR state feedback controller[18] for the linearized Copper plant model. The linearized model is given by

$$\dot{\delta x} = A \cdot \delta x + B \cdot \delta u, \qquad (21)$$

and

$$\delta y = C \cdot \delta x + D \cdot \delta u, \qquad (22)$$

where $\dot{\delta x}$, δx, δu, and δy are deviation variables with respect to a steady state point, x_0. Thus, $\dot{\delta x}_0 = 0$, $\delta x_0 = 0$, $\delta u_0 = 0$ and $\delta y_0 = 0$. The procedure to find A, B, C and D as well as x_0 is already given (see subsection 3.1). Use the following script to create a state space model (`sys`) object and optionally, the state space model may be transformed into transfer function form (`sys2`).

```
#Import python-control package
import control as ctrl
#Create state space model
sys = ctrl.ss(A,B,C,D)
#If needed, state space==>transfer function
sys2 = ctrl.ss2tf(sys)
```

The `ctrl.lqr()` method calculates the optimal feedback controller, $\delta u = -K \cdot \delta x$, such that minimizing the cost function J:

$$J = \int_0^\infty \left(\delta x^T \cdot Q \cdot \delta x + \delta u^T \cdot R \cdot \delta u + 2 \cdot \delta x^T \cdot N \cdot \delta u \right) \cdot dt. \qquad (23)$$

[18]This paper mainly focus on demonstrating the idea of making Modelica models available in Python in general and in particular using the `python-control` package. Therefore, a detailed theoretical discussion about LQR state feedback controllers is not given here. For more details about LQR state feedback controllers refer [6].

Let, N is a zero matrix. K is the state feedback gain matrix and it is given by $K = R^{-1} \cdot B^T \cdot S$. S is found by solving the algebraic Riccati equation (ARE)

$$A^T \cdot S + S \cdot A^T - S \cdot B \cdot R^{-1} \cdot B^T \cdot S + Q = 0. \qquad (24)$$

Use `K,S,E=ctrl.lqr(sys,Q,R,N)` finds K, S, and E. E gives Eigenvalues of the closed loop system. Now, the closed loop system is given by

$$\dot{\delta x} = (A - B \cdot K) \cdot \delta x, \qquad (25)$$

and

$$\delta y = (C - D \cdot K) \cdot \delta x. \qquad (26)$$

The closed loop system is simulated for a small perturbation in δx, say 0.01. Q and R are positive definite matrices and are used as the tunning parameters. A possibility is to set Q to be a unit matrix while R is a diagonal matrix and its elements are used in tunning. See the code given below and the results are given in figure 2.

```
Q = 1.0*np.eye(n_x,n_x)
R = 0.001*np.eye(n_u,n_u)
N = np.eye(n_x,n_u)
K,S,E=ctrl.lqr(sys,Q,R,N)

A1 = A - np.dot(B,K)
B1 = np.zeros((n_x,n_u))
C1 = C - np.dot(D,K)
D1 = np.zeros((n_y,n_u))
sys3 = ctrl.ss(A1,B1,C1,D1)

t0 = 0.
tf = 20.
X0 = 0.1*np.ones((n_x,1))
N = 500
T = np.linspace(t0,tf,N)

plt.figure(0)
plt.hold(False)
for i in range(n_y):
    Y,T=ctrl.step(sys3,T,x0,0,i)
    plt.plot(T,Y,label = 'y_{0}'.format(i+1))
    plt.hold(True)
    plt.xlabel('Time')
    plt.title('Outputs')
    plt.legend(loc='upper right', numpoints = 1)
    plt.grid(True)
    plt.show()
```

Note that both disturbances and control inputs are stacked in δu such that 12th, 6th and 5th elements are δu_1, δu_2, and δu_3 respectively.[19] When designing the LQR state feedback controller above, δu is considered to contain only control variables. However, this is not realistic. δu should have been decomposed as $\delta u := [\delta u, \delta w]^T$ and handled disturbances

[19]Check `print ocp.u`.
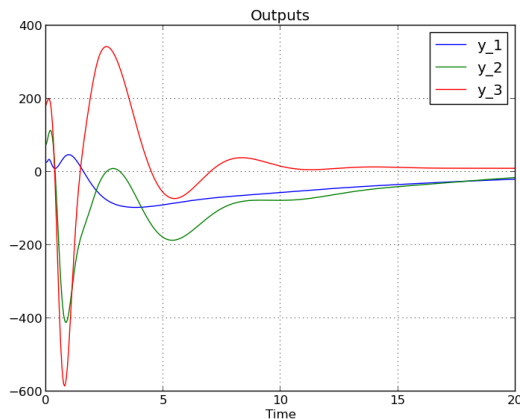
Figure 2: The $\delta y_1 - \delta y_2 - \delta y_3$ vs. t plot.

accordingly. Since, this paper is mainly concentrated on demonstrating the possibility of analyzing Modelica models in Python, in detail discussions on controller syntheis is not given here.

5 CONCLUSIONS

The features of Modelica language, in particular the notion of acausal modeling, have made it a powerful tool for modeling physical systems. However, the Modelica standards target primarily on model simulation, which is just one of the aspects of modeling. It is important that Modelica models are available for general use, but not just for the simulation. CasADi has an interface to Modelica/Optimica and JModelica.org is linked with CasADi. Therefore, Modelica-CasADi-JModelica.org combination provides a useful way to access Modelica/Optimica models in Python. Although, CasADi and JModelica.org has some limitations, they have provided a starting point. In this paper, it was explained the usefulness of interfacing Modelica models with Python. Special emphasis was given on the Python control system library as an up coming Python control tool, which could be an alternative to MATLAB control system toolbox.

Finally, couple of suggestions are made. CasADi-Modelica interface (via XML representation of Modelica models) may be further developed to support Modelica specification as much as possible. At the moment CasADi-Modelica interface is underdeveloped. The idea pointed out in this paper, in principal, for example may also be implemented within MATLAB environment. MathWorks pro-

vides the Simscape language and the Symbolic Math Toolbox (a CAS tool). The Simscape language is similar to Modelica. Therefore, Simscape-Symbolic Math Toolbox-MATLAB core may be designed to do the same as what Modelica-CasADi-Python does.

REFERENCES

[1] Åkesson J. *Optimica — An Extension of Modelica Supporting Dynamic Optimization*. 6th International Modelica Conference 2008.

[2] Andersson J. *A General-Purpose Software Framework for Dynamic Optimization*. PhD thesis. Arenberg Doctoral School, KU Leuven: Department of Electrical Engineering (ESAT/SCD) and Optimization in Engineering Center, Kasteelpark Arenberg 10, 3001-Heverlee, Belgium, 2013.

[3] Perera A. *Using CasADi for Optimization and Symbolic Linearization/Extraction of Causality Graphs of Modelica Models via JModelica.Org*. HiT Report No. 5. Porsgrunn: Telemark University College. https://teora.hit.no/handle/2282/2175. ISBN 978-82-7206-380-0. 2014.

[4] Lie B, Hauge TA. *Modeling of an industrial copper leaching and electrowinning process, with validation against experimental data*. Proceedings SIMS 2008, 49th Scandinavian Conference on Simulation and Modeling. Oslo University college. Oct 7-8, 2008.

[5] Fritzson P. *Introduction to Modeling and Simulation of Technical and Physical Systems with Modelica*. Wiley, 2011.

[6] Åström KJ, Murray RM. *Feedback Systems: An Introduction for Scientists and Engineers*. Princeton University Press, 2008.

[7] Cellier FE, Kofman E. *Continuous System Simulation*. Springer, 2006.

[8] Brenan KE, Campbell SL, Petzold LR. *Numerical Solution of Initial-Value Problems in Differential-Algebraic Equations*. SIAM, 1996.

[9] Pantelides CC. *The Consistent Initialization of Differential-Algebraic Systems*. SIAM Journal Scientific Statistical Computation, 1988.

[10] Bendtsen C., Thomsen PG. *Numerical Solution of Differential Algebraic Equations*. TECHNICAL Report No. 5. Porsgrunn: Department of Mathematical Modelling, Technical University of Denmark. http://www2.imm.dtu.dk/documents/ftp/tr99/tr08_99.pdf. 1999.

[11] Mattsson SE, Söderlind G. *Index Reduction in Differential-Algebraic Equations Using Dummy Derivatives*. SIAM Journal Scientific Statistical Computation, 1993.

[12] Griewank A, Walther A. *Evaluating Derivatives: Principles and Techniques of Algorithmic Differentiation*. SIAM, 2008.

[13] Pop A, Fritzson P. *ModelicaXML: A Modelica XML Representation with Applications*. Proceedings 3rd International Modelica Conference 2003.

[14] Casella F, Donida F., Åkesson J. *An XML Representation of DAE Systems Obtained from Modelica Models*. Proceedings 7th International Modelica Conference 2009.

[15] Andersson J, Gillis J, Diehl M. *User Documentation for CasADi*, 2014.

[16] Andersson J, Åkesson J, Casella F, Diehl M. *Integration of CasADi and JModelica.org*. 8th International Modelica Conference 2011.

[17] Pfeiffer CF. *Modeling, Simulation and Control for an Experimental Four Tanks Systems using ScicosLab*. 52nd Scandinavian Simulation and Modeling Society Conference 2011.

APPENDIX

A TANKSYSETEMS.MOP

```
package TankSystems
  //=====Dynamic model=====
  model FourTanks
  //Parameters
  parameter Real h1_init = 7.0;
  parameter Real h2_init = 7.0;
  parameter Real h3_init = 8.3;
  parameter Real h4_init = 3.1;
  parameter Real q1_init = 1;
  parameter Real q2_init = 1;
  parameter Real c1 = 9.82;
  parameter Real c2 = 5.76;
  parameter Real c3 = 9.02;
  parameter Real c4 = 8.71;
  parameter Real A1 = 12.57;
  parameter Real A2 = 12.57;
  parameter Real A3 = 12.57;
  parameter Real A4 = 12.57;
  parameter Real gama1 = 0;
  parameter Real gama2 = 0;
  parameter Real tau1 = 6.15;
  parameter Real tau2 = 13.2;
  parameter Real k1 = 6.94;
  parameter Real k2 = 8.72;
  //Dynamic variables
  Real h1(start=h1_init,fixed=true);
  Real h2(start=h2_init,fixed=true);
  Real h3(start=h3_init,fixed=true);
  Real h4(start=h4_init,fixed=true);
  Real q1(start=q1_init,fixed=true);
  Real q2(start=q2_init,fixed=true);
  //Output variables
  Real z1 = sqrt(h1)^2;
  Real z2 = sqrt(h2)^2;
  //Note: if we use z1 = h1, & z2 = h2 instead, then
  //z1 & z2 would not be+9 considered as algebraic
  //variables when the model is imported to CasADi.
  //The reason is that in the modelDescription.xml
  //file, both z1 & h1  would have  the same
  //valueReference. The same applied for z2. However,
  //there could be a better way of handling this!
  //Input variables
  input Real v1;
  input Real v2;
  equation
  der(h1) = ((-c1 * sqrt(h1)) +
  c3 * sqrt(h3) + gama1 * q1) / A1;
  der(h2) = ((-c2 * sqrt(h2)) +
  c4 * sqrt(h4) + gama2 * q2) / A2;
  der(h3) = ((-c3 * sqrt(h3)) +
  (1 - gama2) * q2) / A3;
  der(h4) = ((-c4 * sqrt(h4)) +
  (1 - gama1) * q1) / A4;
  der(q1) = ((-q1) + k1 * v1) / tau1;
  der(q2) = ((-q2) + k2 * v2) / tau2;
  end FourTanks;
  //=====Dynamic model=====
  //=====Static model=====
  model FourTanks_Init
  extends FourTanks(h1(fixed=false),
  h2(fixed=false),  h3(fixed=false),
  h4(fixed=false),q1(fixed=false),
  q2(fixed=false));
  initial equation
  der(h1) = 0;
  der(h2) = 0;
  der(h3) = 0;
  der(h4) = 0;
```

```
   der(q1) = 0;
   der(q2) = 0;
   end FourTanks_Init;
   //=====Static model=====
end TankSystems;
```

B TANKSYSTEMS.PY

Let, $0 = f(\dot{x}, x, u, z)$ and $0 = g(x, u, z)$. The linearized model is given by, $0 = \alpha \cdot \delta\dot{x} + \beta \cdot \delta x + \gamma \cdot \delta u + \delta \cdot \delta z$ and $0 = \zeta \cdot \delta x + \eta \cdot \delta u + \sigma \cdot \delta z$, where $\alpha = \frac{\partial f}{\partial \dot{x}}$, $\beta = \frac{\partial f}{\partial x}$,..., and $\sigma = \frac{\partial g}{\partial z}$. δy is taken as $\delta y = [\kappa_x \ \kappa_u \ \kappa_z] \cdot [\delta x \ \delta u \ \delta u]^T$, where κ_x, κ_u, and κ_z should be given.

```python
#Importing necessary packages.
import numpy as np
import matplotlib.pyplot as plt
import control as ctrl
from casadi import *
from casadi.tools import *
from pymodelica import compile_jmu
from pymodelica import compile_fmux
from pyjmi import JMUModel
from pyjmi import CasadiModel

#Compiling (to a JMU)/loading
#steady state model.
jmu_init = compile_jmu \
("TankSystems.FourTanks_Init", \
"TankSystems.mop")
init_model = JMUModel(jmu_init)

#Set inputs
v1_0 = 1.
v2_0 = 2.
u_0 = [v1_0, v2_0]
u = ['v1','v2']
init_model.set(u,u_0)

#DAE initialization with Ipopt
init_result = init_model.initialize()

#Store steady state
h1_0 = init_result['h1'][0]
h2_0 = init_result['h2'][0]
h3_0 = init_result['h3'][0]
h4_0 = init_result['h4'][0]
q1_0 = init_result['q1'][0]
q2_0 = init_result['q2'][0]

#Compiling (to a FMUX)/loading dynamic model
fmux_name = compile_fmux \
("TankSystems.FourTanks", \
"TankSystems.mop")
model = CasadiModel(fmux_name)

#Get access to OCP
ocp = model.ocp

# Get differential state
n_x = len(ocp.x)
x = list()
for i in range(n_x):
    x.append(ocp.x[i].var())

#Get derivatives
```

```python
xDot = list()
for i in range(n_x):
    xDot.append(model.dx[i])

# Get input
n_u = len(ocp.u)
u = list()
for i in range(n_u):
    u.append(ocp.u[i].var())

#Get algebraic states
n_z = len(ocp.z)
z = list()
for i in range(n_z):
    z.append(ocp.z[i].var())

#Eliminating dependent parameters
ocp.eliminateDependent()

#Define DAEs
f = ocp.ode
g = ocp.alg

#Create SXFunction instances for f and g
ffun = SXFunction([vertcat(xDot),vertcat(x), \
vertcat(u),vertcat(z)],[f])
gfun= SXFunction([vertcat(x),vertcat(u), \
vertcat(z)],[g])
ffun.init()
gfun.init()

#Define x0, u0, and z0
x0 = [h1_0,h2_0,h3_0,h4_0,q1_0,q2_0]
xDoto0 = [0.,0,0,0,0,0]
u0 = [v1_0,v2_0]
z0 = [h1_0,h2_0]

#Find symbolic/numeric Jacobian matrices
f_xDot = ffun.jac(0)
f_xDot_fun = SXFunction([vertcat(xDot),vertcat(x), \
vertcat(u),vertcat(z)],[f_xDot])
f_xDot_fun.init()

f_xDot_fun.setInput(xDoto0,0)
f_xDot_fun.setInput(x0,1)
f_xDot_fun.setInput(u0,2)
f_xDot_fun.setInput(z0,3)
f_xDot_fun.evaluate()

f_xDot_num = f_xDot_fun.getOutput()

alpha = np.array(f_xDot_num)
#
f_x = ffun.jac(1)
f_x_fun = SXFunction([vertcat(x),vertcat(u),\
vertcat(z)],[f_x])
f_x_fun.init()

f_x_fun.setInput(x0,0)
f_x_fun.setInput(u0,1)
f_x_fun.setInput(z0,2)
f_x_fun.evaluate()

f_x_num = f_x_fun.getOutput()

beta = np.array(f_x_num)
#
f_u = ffun.jac(2)
f_u_fun = SXFunction([vertcat(x),vertcat(u),\
vertcat(z)],[f_u])
```

```
    f_u_fun.init()

    f_u_fun.setInput(x0,0)
    f_u_fun.setInput(u0,1)
    f_u_fun.setInput(z0,2)
    f_u_fun.evaluate()

    f_u_num = f_u_fun.getOutput()

    gamma = np.array(f_u_num)
    #
    f_z = ffun.jac(3)
    f_z_fun = SXFunction([vertcat(x),vertcat(u), \
    vertcat(z)],[f_z])
    f_z_fun.init()

    f_z_fun.setInput(x0,0)
    f_z_fun.setInput(u0,1)
    f_z_fun.setInput(z0,2)
    f_z_fun.evaluate()

    f_z_num = f_z_fun.getOutput()

    delta = np.array(f_z_num)
    #
    g_x = gfun.jac(0)
    g_x_fun = SXFunction([vertcat(x),vertcat(u), \
    vertcat(z)],[g_x])
    g_x_fun.init()

    g_x_fun.setInput(x0,0)
    g_x_fun.setInput(u0,1)
    g_x_fun.setInput(z0,2)
    g_x_fun.evaluate()

    g_z_num = g_x_fun.getOutput()

    zeta = np.array(g_z_num)
    #
    g_u = gfun.jac(1)
    g_u_fun = SXFunction([vertcat(x),vertcat(u),\
    vertcat(z)],[g_u])
    g_u_fun.init()

    g_u_fun.setInput(x0,0)
    g_u_fun.setInput(u0,1)
    g_u_fun.setInput(z0,2)
    g_u_fun.evaluate()

    g_u_num = g_u_fun.getOutput()

    eta = np.array(g_u_num)
    #
    g_z = gfun.jac(2)
    g_z_fun = SXFunction([vertcat(x),vertcat(u), \
    vertcat(z)],[g_z])
    g_z_fun.init()

    g_z_fun.setInput(x0,0)
    g_z_fun.setInput(u0,1)
    g_z_fun.setInput(z0,2)
    g_z_fun.evaluate()

    g_z_num = g_z_fun.getOutput()

    sigma = np.array(g_z_num)

    # Define A, B, C, and D matrices
    n_y = 2
    kappa_x = np.eye(n_y,n_x)
```

```
kappa_u = np.zeros((n_y,n_u))
kappa_z = np.zeros((n_y,n_z))
if np.allclose(np.linalg.det(alpha),0.) != True:
    if np.allclose(np.linalg.det(sigma),0.) \
    != True:
        A = np.dot(np.linalg.inv(alpha),(-beta+\
        np.dot(delta,np.dot(np.linalg.inv(sigma),\
        zeta))))
        B = np.dot(np.linalg.inv(alpha),(-gamma+\
        np.dot(delta,np.dot(np.linalg.inv(sigma),\
        eta))))
        C = kappa_x - np.dot(kappa_z,\
        np.dot(np.linalg.inv(sigma),zeta))
        D = kappa_u - np.dot(kappa_z,\
        np.dot(np.linalg.inv(sigma),eta))
    #Use python-control
    #Create state space model object
        sys = ctrl.ss(A,B,C,D)
        print sys
    #State space to transfer function model object
        sys2 = ctrl.ss2tf(sys)
        print sys2
    # Simulate the system given input
        t0 = 0.
        tf = 120.
        N = 1000
        T = np.linspace(t0,tf,N)
        U = np.dot(np.diag([v1_0,v2_0]),np.ones((n_u,N)))
        t, yout, xout = ctrl.forced_response(sys,T,U,x0)

        plt.figure(0)
        plt.hold(False)
        for i in range(n_y):
            plt.plot(t,yout[i],'.',label = \
            'y_{0}'.format(i+1))
            plt.hold(True)
        plt.xlabel('Time')
        plt.title('Outputs')
        plt.legend(loc='upper right', numpoints = 1)
        plt.show()
        plt.figure(1)
        plt.hold(False)
        for i in range(n_x):
            plt.plot(t,xout[i],'.',label = \
            'x_{0}'.format(i+1))
            plt.hold(True)
        plt.xlabel('Time')
        plt.title('States')
        plt.legend(loc='upper right', numpoints = 1)
        plt.show()
        plt.figure(2)
        plt.hold(False)
        for i in range(n_u):
            plt.plot(t,U[i,:],'.',label = \
            'u_{0}'.format(i+1))
            plt.hold(True)
        plt.xlabel('Time')
        plt.title('Inputs')
        plt.legend(loc='upper right', numpoints = 1)
        plt.show()
    else:
        print 'sigma is singular. This case is \
        not considered.==>check Pantelides algorithm.'
else:
    print 'Alpha is singular. This case is \
    not considered.==>check Pantelides algorithm.'
```

Mechanical design principles and test results of a small scale airslide rig for alumina transport

Serena C. Valciu, Are Dyrøy[1], Richard J. Farnish[2], Cornelius E. Agu[3], Bernt Lie[3]

[1]Primary Metal Technology, Norsk Hydro, Porsgrunn Research Center, Norway

[2]The Wolfson Centre for Bulk Solids Handling Technology, the University of Greenwich, UK

[3]Faculty of Technology, Telemark University College, Norway

Abstract:

To enable online estimation and further modeling of full scale airslide capacity, a small scale rig with adjustable length was built at POSTEC in Porsgrunn. Airslide capacity (alumina flow rates) for different lengths of 3 m, 7 m and 15 m and inclination of 0 to 3.1 degrees of airslide were measured by using pressurized air in the range of 3 to 6.5 barg. It became clear that interfaces (feeding silo and standpipe) also have a great influence on the capacity of an airslide. The standpipe should be integrated into the mechanical design of an airslide, because if the material cannot be delivered (discharged) properly from the feeding unit, there is no conveying. There is a strong analogy with the flow of Newtonian or non – Newtonian fluids in an open channel which can be applied to the flow of fluidized alumina in an airslide. In this paper, the hydrological model used by Agu and Lie [2014] has been used to model alumina flow in an airslide. From the general Saint-Venant model of the open surface, a mechanistic model for non- Newtonian flow of powder in a rectangular channel has been developed. Such theoretical models based on the mass and momentum balance with bottom friction along the powder bed are numerically challenging to solve. An ODE solver in MATLAB seemed promising and showed similar trends compared to the results obtained from a small scale rig. Results so far indicated that a more detailed analysis needs to be conducted in order to find out how to tune the model parameters to further improve the model fit.

Keywords: Alumina transport, standpipe, fluidization, airslides, Saint Venant, non-Newtonian fluid.

Introduction

In the aluminium industry, as in other many industries, pressurised air at a certain velocity is introduced by nozzles through the bottom of airslides to effect a transportation of material. The air flows upwards, passes through a porous membrane and when in contact with the bed of alumina particles, it makes the bed flow. It is known that the transport capacity depends very much on the quality of alumina, size and size distribution of the powder and powder's flowability, the angle of inclination of the airside and the amount of pressurized air distributed through the system. In the fluidized bed, the mixing and the movement of air and powder will create a flow of high complexity. Approximately two tons of alumina are needed in order to produce one tone of aluminium. Thus the storage silos have to supply alumina at

a rate of almost twice (1.93 times) the aluminium production. Hydro Aluminium uses airslides for transport of alumina over short to long distances (kilometers), for the production of aluminium. Their length depends very much on the powder handling equipment they are connected to. One of the main goals is to make the end product, aluminium metal, at lowest possible costs energy wise, while satisfying and maintaining product quality performance when it comes to raw materials (e.g.: alumina). The bulk density and the supply air pressure drop influence the alumina transport conditions, thus the capacity of the kilometers long airslides. Capacity in this context is defined as tons per hour transported alumina powder through a fixed network of airslides at fixed air flow rate and layout geometry. Ideally in order to maintain a stable airslide capacity, parameters such as bulk density, particle size distribution and rheology of the fluidized alumina powder should be monitored continuously, on line. Results from previous measurement campaigns show how changes in alumina quality quickly affect the capacity of a feeding airslide and highlights the need for better understanding of the powders fluidized rheology and transport behavior. Ideally, changes in the alumina quality should immediately be picked up by the online measurement equipment and corrected for, based on a general powder model incorporated into the control system. Thus the control system should have the capability to make appropriate corrections for each quality of alumina encountered by the process. Such a general powder model does not currently exist. When a new alumina quality is to be distributed through the system, it is standard practice for operators to take manual measurements and alumina samples. The results are communicated to the control group who then makes the adjustments manually into the control system. Previous work at Hydro, POSTEC and at the Wolfson Centre for Bulk Solids Technology in UK with characterizing the flow behavior of fluidized alumina have shown that fluidized alumina typically has a non- Newtonian behavior and that methods of defining the rheology should be established and implemented. A complimentary piece of work considering off line rheology measurements of alumina have been performed in a small fluidized column by using a standard Brookfield rheometer – the results from which will form the basis of a separate paper.

Previous work

Stability and repeatability of gravitational flow rates from feeding silos and standpipes (addressed as interface) is crucial and needs to be achieved before one can further estimate and model the flow of alumina in an airslide. Capacity and powder quality go hand in hand with the mechanical design of the airslide and its interface. In the bulk solids community the work of Gu et al (1993) is well known. They provided experimental and theoretical evidence of the use of standpipes to increase gravity flow rates of both sand and alumina powders from mass flow bins. Their results on relatively small bore standpipes (D=44,5 mm) indicated that the effects of a standpipe attached under a bin/silo outlet would become more significant as the particle size of the bulk solid reduces and the length of the standpipe increased - provided that the standpipe would remain full of material during operation. The bulk solid discharging from the feeding silo under the effect of gravity has a self-limiting flow rate that is primarily attributed to the self-generated negative air pressure gradient within the inter-particle voids in the region of the outlet of the feeding silo.

Test equipment

Work to evaluate flow rates from a silo was initiated in 2012 as part of an industrial PhD project between Hydro, POSTEC and the University of Greenwich. The initial configuration (2012) of the rig is shown in Figure 1 a. It became clear that the mechanical design of the outlet from the feeding silo was the bottle-neck in trying to establish stable feed conditions s. Farnish and Bradley (2006) discussed the design faults present in this configuration in terms of discharge equipment and the overall system design commonly found in industrial applications, pointing out that consistency and repeatability of discharge from vessels was the keystone to the efficiency and profitability of many types of processes. Although techniques for design of storage vessels based on the flow characteristics of particulates have been in the public domain since the 1960's, they have been slow to gain acceptance in the industry (mainly through a lack of awareness of their existence amongst engineers). According to the authors, in terms of controlling discharge from gravity flow equipment, it was often the gravity discharge approach which generated the greatest degree of variability, in terms of both quantity and repeatability. The root of the problem of inconsistent discharge rates was identified to lie with the flow channel development within the feeding silo or the discharge head. The potential causes of flow irregularities were even more critical to be aware of, in the cases where mass flow principles were to be applied, especially in the case of easy to segregate materials. Thus on systems that operated on a discharge basis that uses an adjustable outlet aperture, the development of a flow channel subject to minimal shear at its boundaries is essential. In many cases the outlet aperture relied upon the insertion of devices such as iris valves or gate valves (acting perpendicular or nearly so) to the path of the flow channel. The authors pointed out that in such cases static material would be supported from the leading edge of the valve to the nearest wall of the discharge head or vessel outlet. This supported material could extend for some distance from the outlet and generate a major shear plane of powder on powder, which again, would induce inconsistent discharge rates from the outlet – mainly by imposing core flow discharge conditions (which are characterized by inconsistency in flow rate and exaggerated segregation effects).

In industry the strategy has been to increase the limiting flow rates without reducing the storage capacity of the feeding mass flow silos. Vertical standpipes often have limited application in industry due to headroom constraints commonly found in pot rooms (not enough room for cranes, rails and receiving silo/bin). Based on the previous work of Gu et al (1993), Farnish et al (2006-2012) and Dyrøy (2006), fresh measurements were carried out on a modified alumina rig at POSTEC during 2013 from which the iris valve was removed. Outlet diameter of the feeding silo was modified from 200 mm to 140 mm. A 140mm diameter standpipe (dispensing head) was installed at the outlet of the mass flow silo as shown in Figure 1 b. In order to be able to implement the mechanical changes, the upper ring of the feeding silo had to be removed due to headroom restrictions. A schematic view of the new rig is shown in Figure 2 a. The standpipe had a length to diameter ratio (L/D) of 7.5 and was connected to standard airslide segments of 3 m, 7 m and 15 m. The joint between the stand pipe and airslide was flexible to allow for testing at different downward inclinations of the airslide.
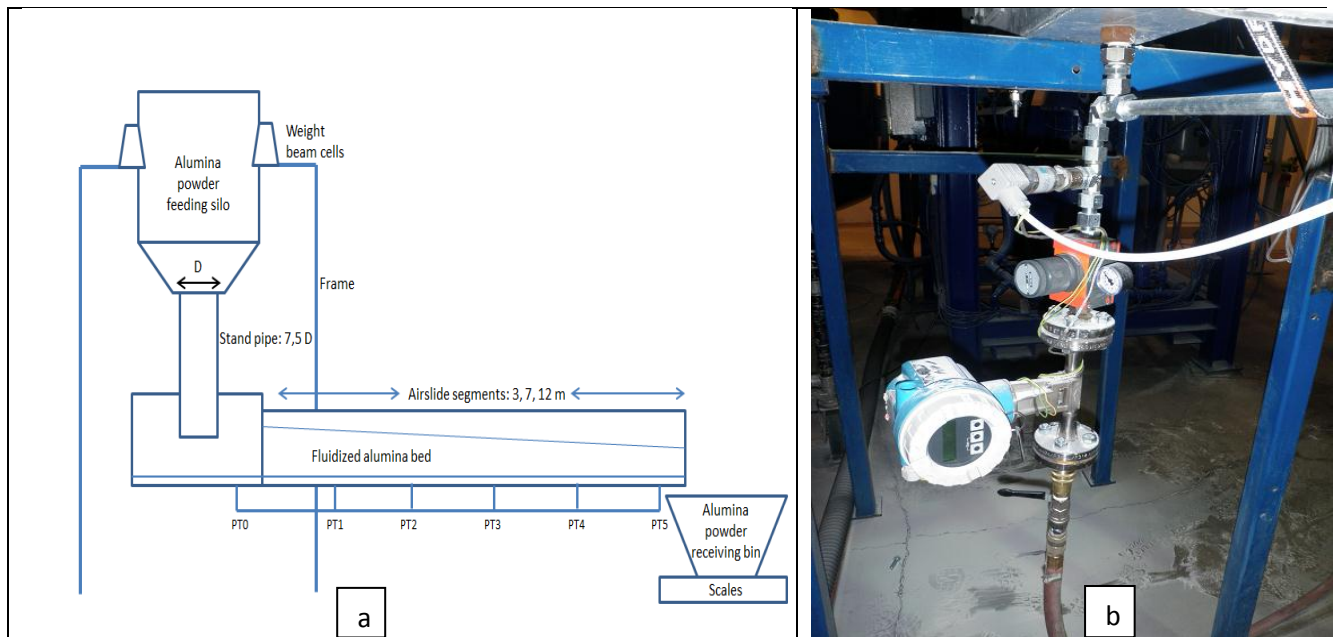
Figure 2 Schematic view of an instrumented alumina rig with: a) pressure transmitters PT0 –PT5 and b) flow meter and pressure regulator (0-6.5 barg) placed underneath PT0.

Airslide capacity for 0 to 3.1 degrees of downward inclination were measured for each segment by using pressurized air in the range of 3 to 6.5 barg. Air pressure was adjusted by using a small pressure controller as shown in Figure 2 b. Five tons alumina supplied by the Reference Centre in Årdal were used for conducting all the tests, around 500 kg being used per test round. Four consecutive tests were conducted for each operational condition (a given air pressure at a given airslide downward inclination). A hook crane was used to lift up and transport the receiving bin back and forth to the feeding silo for each test round. A butterfly valve had to manually be opened and closed for emptying alumina from the receiving bin into the feeding silo. LabView was used to record and display data from the flow meter,

pressure sensors, weight beam cells and scales. Beam cells and scales are simple weighing devices, thus the values of loss and gain in weight have been calculated by filtering the electrical signals from load cells. The loss in weight for the feeding silo mounted on a frame equipped with beam cells and gain in weight for the receiving bin placed on scales were recorded by measuring the mass variation in the feeding silo/stand pipe and receiving bin versus discharge time. The feeding silo and airslide (receiving bin) capacities calculated by differentiating the mass curves with respect to time were displayed online in LabView. It was known from previous work that the stand pipe had to remain full of product at any time during operation in order to achieve stability and good repeatability of test work. It was found that the weight of the powder in a full stand pipe was approximately 50-60 kg, thus each test was to be run until 60 kg of powder would remain in the system and then manually switch off the pressurized air and stop the test. The previous work of Gu (1993) played an important role in showing how the main parts: feeding silo, stand pipe and airslide of a transport system are integrated together. The standpipe is an important part of the system acting as interface between the feeding silo and the airslide. An example of on line measured and estimated capacities for a given set of specified parameters for a test round is shown in Figure 3.
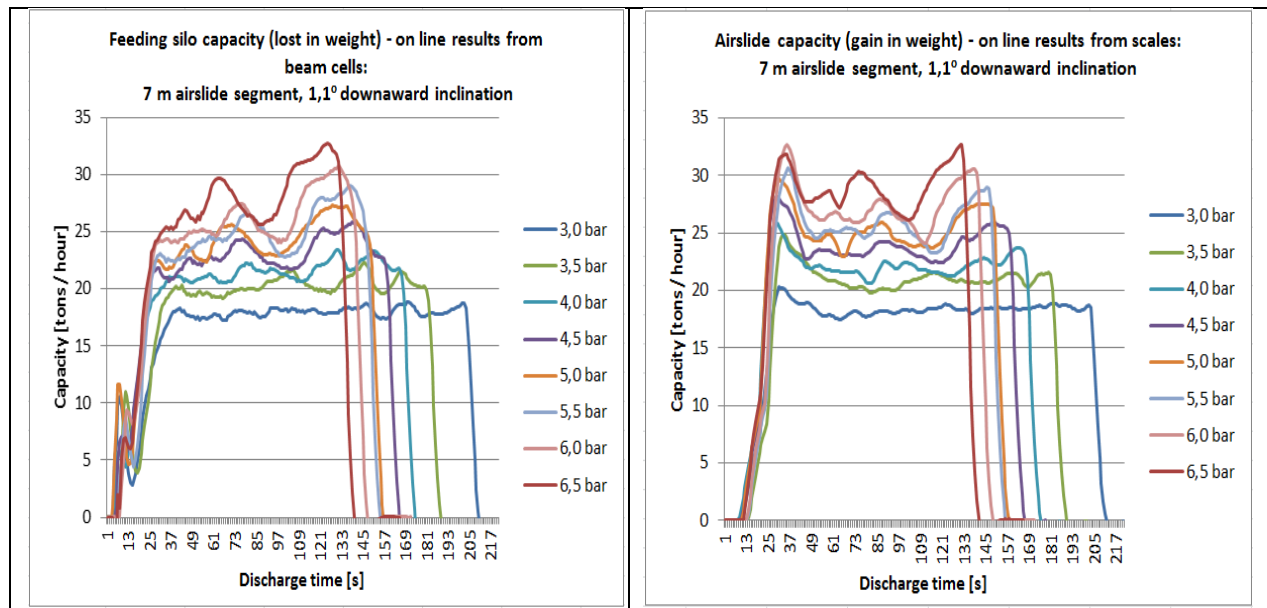
Figure 3 On line LabView results for a set of specified operational parameters.

Experimental test results

In this investigation the dimensionless air velocity factor U_0/U_{mf} has been varied from the start up value of 0.99, which corresponds to the minimum fluidization velocity of alumina powder, U_{mf} of 0.68 cm/s, up to an upper limit of 2.14. A comparison of capacity results from the initial rig and the modified rig is shown in Figure 4 a and b.
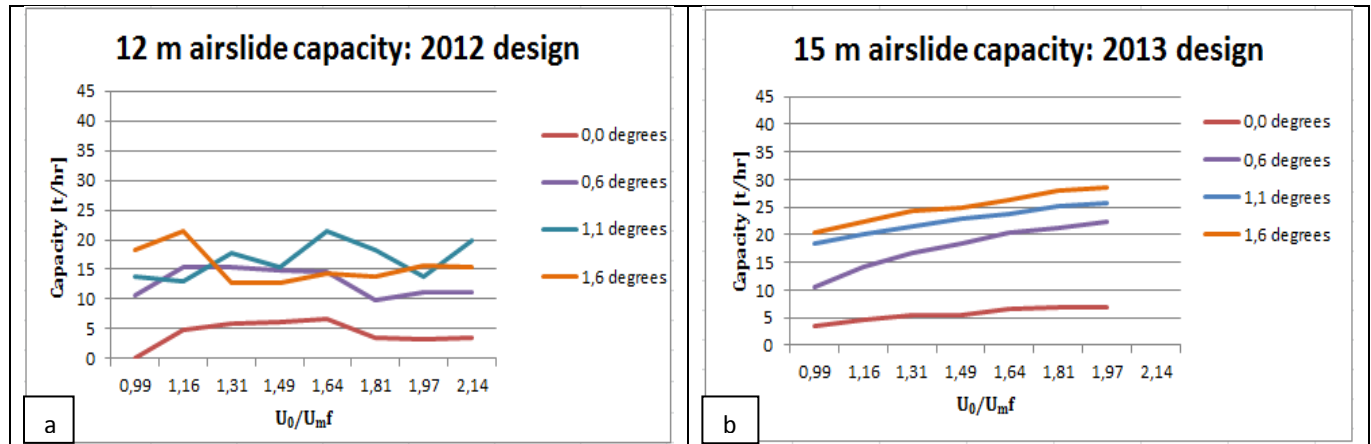
Figure 4 Capacity measurement results: a) 2012 design on 12 m airslide, b) 2013 design on 3 + 12 m airslide.

Improvements were immediately apparent on the modified rig. The flow rate of alumina increased when increasing the length of standpipe from 1D to 7.5 D by 190 % (similar to what had been reported by Gu et al (1993)), due to the positive air pressure gradient developed at the feeding silo outlet. Improved stability of flow was also achieved, results from an average of three consecutive tests for each operational condition, show a decrease of the coefficient of variation from 3 to 40 % down to ca. 1.2 % (Table 1). Stability increased by 90 % using a 7.5 D long pipe.
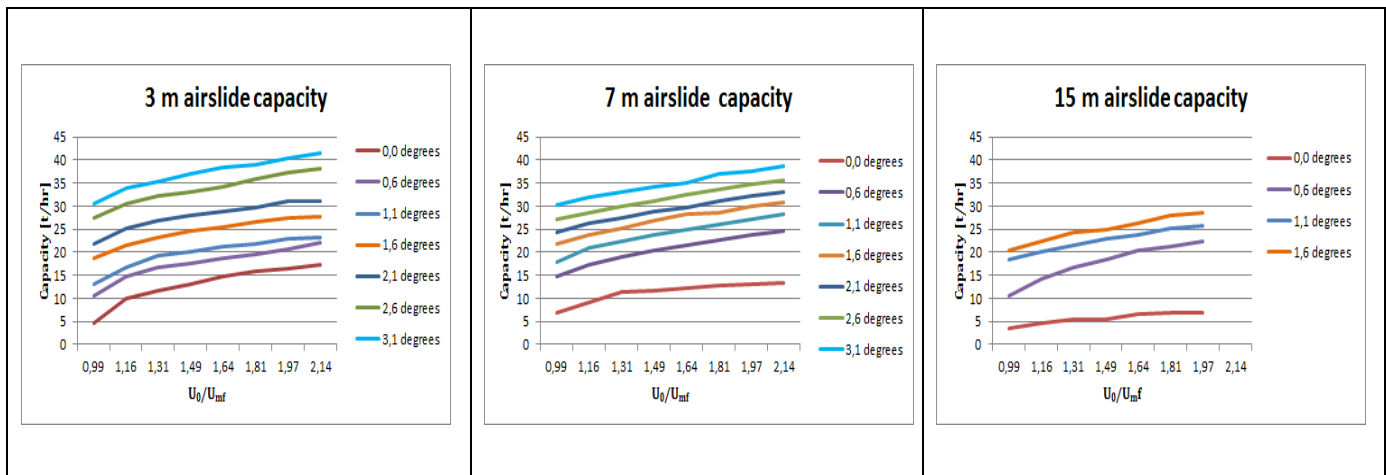
Figure 5 Airslide capacity results for a set of operational parameters in 3, 7 and 15 m long airslides.

Table 1 Coefficients of variation for the capacity of feeding silo/standpipe and airslide at 1.1 degrees downward inclination.

1,1 degrees												
	3 m				7 m				15 m			
U_o/U_{mf}	Capacity [t/hr]		Coefficient of variation [%]		Capacity [t/hr]		Coefficient of variation [%]		Capacity [t/hr]		Coefficient of variation [%]	
	Airslide	Feeding silo	Airslide	Feeding silo	Airslide	Feeding silo	Airslide	Feeding silo	Airslide	Feeding silo	Airslide	Feeding silo
0,99	13,1	13,2	2,1	2,1	17,9	17,7	3,1	1,6	18,4	17,0	5,0	0,6
1,16	16,8	16,9	1,1	1,1	20,9	20,4	0,1	0,5	20,0	19,3	5,6	0,7
1,31	19,3	19,5	1,5	1,7	22,3	21,7	1,3	1,0	21,5	20,6	3,1	1,3
1,49	20,2	20,3	1,6	1,8	23,8	23,1	0,5	0,8	22,9	21,4	1,3	1,6
1,64	21,3	21,4	2,8	2,8	24,9	24,3	0,4	0,1	23,9	22,7	1,1	1,1
1,81	21,8	21,9	0,4	0,2	26,1	25,2	1,6	0,9	25,1	23,6	0,5	0,1
1,97	22,9	22,9	1,0	0,9	27,0	26,2	0,6	0,7	25,8	24,2	0,5	0,6
2,14	23,1	23,2	2,1	1,2	28,4	27,6	0,6	0,7				

Steady State Saint Venant model

There is a strong analogy with the flow of Newtonian or non – Newtonian fluids in an open rectangular channel which can be applied to the flow of fluidized alumina in an inclined airslide. The flow of fluidized alumina in an open channel can be described by the one dimensional Saint Venant mass and momentum equations as presented in Agu and Lie (2014):

$$\frac{\partial A}{\partial t} + \frac{\partial Q}{\partial x} = 0$$

$$\frac{\partial Q}{\partial t} + \frac{\partial (\frac{\beta Q^2}{A})}{\partial x} = gAsin\theta - gAcos\theta \frac{\partial h}{\partial x} - gAS_f$$

where:

Q [m³/s] is the volume flow rate of alumina;

A [m²] is the alumina flow cross sectional area;

h [m] is the height of the alumina bed (free surface level) measured when the flow stopped;

θ [degree] is the angle of downward inclination of the airslide;

g [m/s²] gravitational acceleration;

β is the momentum correction coefficient;

R_h [m] is the hydraulic radius;

τ_y is the yield shear stress [Pa];

V=Q/A [m/s] is the calculated average flow velocity;

n is fluid consistency index, where $\varepsilon = \frac{1}{n}$;

K is flow behavior index [Pa.sⁿ];

S_f is the frictional slope given by:

$$S_f = \frac{\tau_y}{\rho g R_h}\left[1 + \left(\frac{(\varepsilon + 1)(\varepsilon + 2)|V|}{(0.74 + 0.656\varepsilon)\left(\frac{\tau_y}{K}\right)^\varepsilon R_h}\right)^{\frac{1}{\varepsilon + 0.15}}\right]$$

At steady state $\lim_{t \to \infty} \frac{\partial A}{\partial t} = 0$, $\lim_{t \to \infty} \frac{\partial Q}{\partial t} = 0$, Q is constant and $\frac{\partial h}{\partial x}$ becomes:

$$\frac{\partial h}{\partial x} = \frac{Ag(sin\theta - S_f) + \beta V^2 hC}{gA cos\theta - \beta BV^2}$$

where B is the width of the flow in the rectangular alumina airslide.

The denominator of $\frac{\partial h}{\partial x}$ characterizes the flow, the flow becomes critical when the denominator approaches zero value:

$$Agcos\theta - \beta u^2 b = 0$$

Multiplication by A^2 gives:

$$A^3 gcos\theta - \beta Q^2 b = 0$$

Thus the expression for alumina flow rate, Q becomes:

$$Q = \frac{(cos\theta)^{\frac{1}{2}} g^{\frac{1}{2}} b h^{\frac{3}{2}}}{\beta^{\frac{1}{2}}}$$

Preliminary results (Figures 3 and 6) and simulations with $K = 1.35$, $n = 0.51$, and $\tau_y = 1.76$ show good agreement between the model and the on line measurements of the alumina flow rate, Q for the steady state situation. Table 6 shows simulation results for a bulk density of $950 - 1000$ kg/m^3, where h_0 is the height of the bed and Q_0 is the capacity at the inlet.

The model needs further calibration and tuning.

| 1,1 degrees | | | | | | | |
| Operational parameters | | | | | Average capacity [t/hr] | | |
Pressure	U_0/U_{mf}	h_0 [m]	Q_0^{1000} [m^3/s]	Q_0^{950} [m^3/s]	Measured	Simulated[1000-950]	Error[1000-950]
3,0	0,99	0,126	0,00479	0,00504	17,9	17,2	3,7 %
3,5	1,16	0,119	0,00580	0,00611	20,9	20,9	-0,1 %
4,0	1,31	0,118	0,00611	0,00643	22,3	21,9	1,7 %
4,5	1,49	0,110	0,00658	0,00693	23,8	23,7	0,4 %
5,0	1,64	0,110	0,00695	0,00732	24,9	25,0	-0,2 %
5,5	1,81	0,102	0,00731	0,00769	26,1	26,3	-0,9 %
6,0	1,97	0,109	0,00747	0,00786	27,0	26,9	0,4 %
6,5	2,14	0,113	0,00785	0,00826	28,4	28,3	0,4 %

Figure 6 Simulated results for 7 m long airslide, 1,1 degrees downward inclination.

Conclusions

The use of the standpipe concept to increase flowrate during gravity discharge and to achieve stability of flow has been examined experimentally in a small rig at POSTEC by using similar concepts as what Gu et al (1993) had used in their work. The results of the measurements indicate that the concept, originally investigated for a standpipe of D = 44.5 mm, applied to a wider standpipe of D = 140 mm gave similar increase in flow rates and stability of flow. The standpipe is efficient only if it is kept full of powder, the feeding silo acting more as a buffer for the standpipe. This can be achieved by monitoring the weight of material in the standpipe and the flow rates of alumina on line. Thus the effect of interfaces, the feeding silo and the standpipe should be considered and included into further design of mechanical equipment, by balancing headroom availability in potrooms versus increase in transport capacity of bulk solids to optimize production. The concepts tested on the small scale rig are useful for further implementation on full scale equipment. The possibility of using non-Newtonian fluid flow behavior and Saint Venant equations was investigated. The analysis was based on the subcritical steady state flow conditions in the airslide. The model needs further calibration and tuning.

References

Z.H. Gu, P.C. Arnold and McLean, Permeability - A Principal Parameter for Predicting the Flowrate of Fine Powder from Mass Flow Bins, Powder handling and processing, Volume 4, Number 4, November 1992.

Z.H. Gu, P.C. Arnold and McLean, The Use of Standpipes for Increasing Limiting Gravitational Flowrate from Mass Flow Bins, KONA No.11 (1993)

R.J. Farnish, Effect of flow channel profiles on repeatability of discharge rates from dispensing heads used for flow control of materials in bulk. MPhil Thesis, The University of Greenwich, 2006.

R.J Farnish, M.S.A. Bradley (2006) Consistency and repeatability of gravity discharge of particulates in processes and packages.

R.J Farnish, R.J. Berry, E. Hernandez, (2012) The effect of segregation on handling characteristics.

A. Dyrøy, Dr.Ing. Thesis. Norwegian University of Science and Technolgy/Telemark University College.

C. E. Agu, B. Lie, Numerical solution of the Saint Venant equation for non-Newtonian fluid, SIMS 2014.

C. E. Agu, B. Lie, Smart sensors for measuring fluid flow using a Venturi channel, SIMS 2014.

STABILITY MAP FOR AMMONIA SYNTHESIS REACTORS

Kateryna Rabchuk, Bernt Lie and Are Mjaavatten
Telemark University College
Norway

Volker Siepmann[1]
Yara International ASA
Norway

ABSTRACT

Ammonia is one of the inorganic chemicals with the highest production rate in the world. This is explained by a wide range use of ammonia. Around 80 % of the produced ammonia is used for fertilizing agricultural crops. Aqueous ammonia solution is used in pharmaceuticals. Also, ammonia is used as a refrigerant and for the production of explosives. Safety and optimization of the ammonia synthesis process is an important industrial question, which was studied before and different approaches were used. Since most of the research on this topic is focused on a stability analysis of the process in the steady state, there was a need to develop a dynamic model. A simple dynamic model was developed by Morud and Skogestad and they showed the steady-state van Heerden analysis to be inadequate in their work [1]. In the work [2] the importance of the dynamic process simulation is shown on the example of the ammonia synthesis process. Going further in this topic, we develop the basis for a synthesis reactor monitoring tool that can be used to identify the "distance/margin to instability" with respect to current load, pressure and temperature. For this purpose, we develop a simple dynamic model of the synthesis process in the reactor using the equation of state for the ideal gas. A dynamic model is a convenient way to examine and analyze the process without the need for the actual testing in a real plant. In this paper, we discuss the stability of the ammonia synthesis process based on developed dynamic model.

Keywords: ammonia, synthesis, reactor, stability.

[1] Corresponding author, volker.siepmann@yara.com

NOMENCLATURE

A	Heat-exchanger area [m^2]
A_{H_2}	Activity of H$_2$
A_{N_2}	Activity of N$_2$
A_{NH_3}	Activity of NH$_3$
Ar	Argon
$\bar{\bar{c}}_{p\,gas}$	Average molar heat capacity of the gas mixture [J/(kmol·K)]
$C_{p\,cat}$	Total heat capacity of catalyst [J/K]
H$_2$	Hydrogen
k	Arrhenius term
K_{eq}	Temperature-dependent equilibrium parameter in Temkin-Pyzhev equation
N$_2$	Nitrogen
NH$_3$	Ammonia
N_{sl}	Number of elementary reactor volumes
n	State vector of species amounts [kmol]
n_{Ar}	Amount of Ar [kmol]
n_{H2}	Amount of H$_2$ [kmol]
n_{N2}	Amount of N$_2$ [kmol]
n_{NH3}	Amount of NH$_3$ [kmol]
N_{tot}	Sum of elements of n [kmol]
$\dot{n}^i$	Vector of input molar flows [kmol/s]
$\dot{n}^i_{Ar}$	Input molar flow of Ar [kmol/s]

1

$\dot{n}_{H2}^{i}$	Input molar flow of H_2 [kmol/s]
$\dot{n}_{N2}^{i}$	Input molar flow of N_2 [kmol/s]
$\dot{n}_{NH3}^{i}$	Input molar flow of NH_3 [kmol/s]
$\dot{N}^{i}$	Sum of elements of $\dot{n}^{i}$ [kmol/s]
$\dot{n}^{g}$	Vector of generated molar flows [kmol/s]
$\dot{n}_{Ar}^{g}$	Generated molar flow of Ar [kmol/s]
$\dot{n}_{H2}^{g}$	Generated molar flow of H_2 [kmol/s]
$\dot{n}_{N2}^{g}$	Generated molar flow of N_2 [kmol/s]
$\dot{n}_{NH3}^{g}$	Generated molar flow of NH_3 [kmol/s]
$\dot{N}^{g}$	Sum of elements of $\dot{n}^{g}$ [kmol/s]
$\dot{n}^{o}$	Vector of output molar flows [kmol/s]
$\dot{n}_{Ar}^{o}$	Output molar flow of Ar [kmol/s]
$\dot{n}_{H2}^{o}$	Output molar flow of H_2 [kmol/s]
$\dot{n}_{N2}^{o}$	Output molar flow of N_2 [kmol/s]
$\dot{n}_{NH3}^{o}$	Output molar flow of NH_3 [kmol/s]
$\dot{N}^{o}$	Sum of elements of $\dot{n}^{o}$ [kmol/s]
p	Pressure in the reactor [Pa]
$\dot{Q}$	Heat flow in the heat-exchanger [J/s]
$\dot{Q}_0$	Initial heat flow in the heat-exchanger [J/s]
$\dot{Q}_r$	Heat flow due to synthesis reaction [J/s]
r	Rate of the ammonia synthesis reaction [kmol/(m^3·s)]
R	Universal gas constant [J/(kmol·K)]
s	Stoichiometric vector of the ammonia synthesis reaction
t	Time [s]
T	Outlet temperature of a reactor slice [K]
T_i	Inlet temperature to a reactor slice [K]
T_C	Heat-exchanger time constant [s]
T_{in}^{hx}	Temperature of the fresh feed supplied to the heat-exchanger [K]
T_{out}^{hx}	Temperature of the gas at the heat-exchanger outlet (which was used to preheat the fresh feed) [K]
T_{in}^{r}	Temperature of the preheated feed out of the heat-exchanger supplied to the reactor inlet [K]
T_{out}^{r}	Temperature of the gas at the reactor outlet [K]
V_{sl}	Volume of the reactor slice [m^3]

U	Heat transfer coefficient of the heat-exchanger [W/(m^2·K)]
x_{NH3}	Mole fraction of ammonia
α	Parameter in Temkin-Pyzhev equation
$-\Delta\tilde{H}_r$	Heat of the ammonia synthesis reaction at 298 K [J/kmol]
ΔT_1	Temperature difference of the cold side of the heat-exchanger [K]
ΔT_2	Temperature difference of the hot side of the heat-exchanger [K]
ΔT_{lm}	Replacement for a logarithmic mean [K]

BACKGROUND

Ammonia is one of the inorganic chemicals with the highest production rate in the world. This is explained by the importance of ammonia in the production of fertilizers and hence the production of food. Around 85 % of the produced ammonia is used for fertilizing agricultural crops[2]. The other fields of the ammonia usages are: textile industry, production of explosives, pharmacy, water purification, food industry. Ammonia is produced in over 80 countries worldwide.

An ammonia synthesis reactor is the core of the ammonia plant. Ammonia is synthesized from hydrogen and nitrogen at high temperature and pressure in a catalyzed process.

The reaction rate of ammonia synthesis depends strongly on the temperature of the gas entering the reactor. The inlet gas is normally heated by the hot exit gas in a heat-exchanger, as illustrated in Figure 2. If the gas is not heated enough, the reaction rate will drop, leading to a lower exit gas temperature, which again lowers the inlet temperature further, eventually stopping the reaction completely. This situation is called a blow-out. The optimum operating point of the reactor (optimum inlet temperature of the feed to the ammonia synthesis reactor) is typically close to the blow-out limit for the synthesis loop.

Feedback control of the synthesis reactors can significantly reduce the risk of the reactor blow-out, but the operators and the plant management prefer manual operation [1]. To reduce the risk of a reactor blow-out during the manual control, the operation of the synthesis reactors is typically

---

[2] http://www.greener-industry.org.uk/index.htm

2

conservative (high inlet temperature) without knowing exactly the margin resulting in non-optimal operation and loss of conversion.

The objective of this paper is to discuss the basis for a synthesis reactor monitoring tool that can be used to identify the margin to instability/blow-out of the ammonia synthesis reactor. The work on this paper was carried out in cooperation with Department of Process Modeling and Control of R&D (Research and Development) and Innovation Centre, Yara International ASA, Porsgrunn.

PREVIOUS WORK

Stability of the processes in chemical reactors has been studied since the 1950s. Before that time, it was believed that all chemical reactions tended monotonically to equilibrium [3]. Hirsch, Smale and Devaney (2004) give some examples of the oscillating chemical reactions and a strategy to explore the reaction equations in their book [3].

The most of the available literature on the topic of chemical reaction stability is focused on steady state stability analysis. The ideas of the steady state analysis of the chemical reactions are well described in [4] with some insight to dynamic stability. However, a dynamic analysis of an ammonia synthesis plant proved that the system can become unstable even when the control setting of the system possesses a steady state solution [5]. Therefore, the maintenance of the system stability is also dependent on the dynamic state of the plant. The most recent works on the dynamic modelling of the ammonia synthesis process have the following content:

1. Master's thesis of Jon-Olav Li (1991) [6]. Jon-Olav Li performed a study on the optimization and control of the ammonia synthesis process. For the control and optimization purposes a dynamic model was developed based on the previous work of John Morud. The dynamic model of Jon-Olav Li corresponds to a particular reactor at the ammonia plant in Brunsbüttel, Germany. The model includes: a dynamic model of the synthesis process in the reactor with three beds and a model of an internal static heat exchange process; a model of a heat exchange process in an external heat-exchanger; a static compressor model; a model of a separator and valves. The developed model of the synthesis process has partial differ-ential equations and is discretized in space, e.g. each reactor bed is divided into 10 volume segments. The model is used to test different control structures for the ammonia synthesis process and it is concluded that a simple control strategy, such as a PI controller, can stabilize the system. Similar conclusions are made in [2].

2. Article of John Morud and Sigurd Skogestad (1998) [1]. This article emphasizes steady state stability analysis of the ammonia synthesis reactor being inadequate. Instability of the ammonia synthesis process is reproduced by the simulation of the dynamic model of the process in a synthesis reactor with three beds and a static model of a heat exchange process in an internal heat-exchanger. 30 temperatures along the reactor beds are selected as system states. Linear dynamic analysis is performed on the model. This analysis shows that instability of the ammonia synthesis process is caused by a positive heat feedback in the heat-exchanger combined with non-minimum phase behavior of the reactor temperature response. A simple feedback controller is believed to stabilize an unstable steady state.

3. Master's thesis of Erik Holter (2010) [7]. In this work, the model developed in [1] is fully reproduced with attempt to use a feed-forward control strategy to stabilize an ammonia synthesis process. Simulations are performed in Simulink software environment. However, the conclusion of this work is that the feed-forward controller cannot be used in the case of an ammonia synthesis reactor. The use of a PI controller is stated as inadequate for the ammonia synthesis reactor which contradicts [6] and [1]. The use of a PID controller is suggested.

The main differences of the work presented in this paper from the above mentioned works on dynamic modelling and stability analysis of the ammonia synthesis process are as follows:

1. A dynamic model in this paper includes only the process in ammonia synthesis reactor and internal heat-exchanger instead of the full synthesis process model [6]. The basis for this is the assumption that the possible temperature oscillations in the ammonia synthesis process are propagated from the reactor-heat-exchanger system, and this system requires the main attention.

3

2. The model is kept simple, but still represents the main dynamic effects of the real process. Only one reactor bed is modelled. The states of the model are the amounts of the species in the reactor segments and the heat flow through the heat-exchanger unlike [1], where the system states are the temperatures along the reactor beds. Also a model of the internal heat-exchanger includes simple dynamics unlike the static heat-exchanger models [6] and [1].

MODEL SUMMARY

The dynamic model of the synthesis process is a basis for a synthesis reactor monitoring tool that can be used to identify the "distance/margin to instability" with respect to current load, pressure and temperature. The dynamic model is developed for a synthesis process in the ammonia converter which includes one reactor bed with internal heat-exchanger. The model is based on the first principle laws of conservation of mass and energy. The simulations are performed in MATLAB.

Heat-exchanger model

The internal heat-exchanger is used for utilization of the heat produced during the ammonia synthesis reaction. The model of the heat-exchanger is sketched in Figure 1. The gas which comes out of the reactor passes the heat-exchanger and preheats the feed which is then supplied to the reactor inlet. The model of the heat exchange process is kept simple and is described by the equation (1):

$$\frac{d\dot{Q}}{dt} = \frac{1}{T_C} \cdot \left(UA \cdot \Delta T_{lm} - \dot{Q} \right), \tag{1}$$

where $\dot{Q}$ is the state of the heat-exchanger (heat flow). The initial state at the time instant $t = 0$ is assumed to be $\dot{Q}_0 = 0$ J/s. T_C, U and A are model parameters which are described in Table 1. ΔT_{lm} is an approximate logarithmic difference [8] of the heat-exchanger expressed by the system of equations (2).

$$\left.\begin{array}{l} \Delta T_{lm} = \frac{1}{2} \cdot \left(\Delta T_1 + \Delta T_2 \right) + \frac{2}{3} \cdot \sqrt{\Delta T_1 \cdot \Delta T_2}, \\ \Delta T_1 = T_{out}^{hx} - T_{in}^{hx}; \quad \Delta T_2 = T_{out}^{r} - T_{in}^{r}, \end{array}\right\} \tag{2}$$

where T_{in}^{hx} is a temperature of the fresh feed which comes into the heat-exchanger. T_{in}^{hx} corresponds to the cold side of the heat-exchanger. T_{out}^{hx} is a temperature of the gas which comes out of the heat-exchanger and was used to preheat the fresh feed. T_{out}^{hx} corresponds to the cold side of the heat-exchanger. T_{in}^{r} is a temperature of the preheated feed which comes out of the heat-exchanger and is supplied to the reactor inlet. T_{in}^{r} corresponds to the hot side of the heat-exchanger. T_{out}^{r} – temperature of the gas which comes out of the reactor. This temperature corresponds to the hot side of the heat-exchanger. See Figure 1 for the overview of the heat-exchanger temperatures.
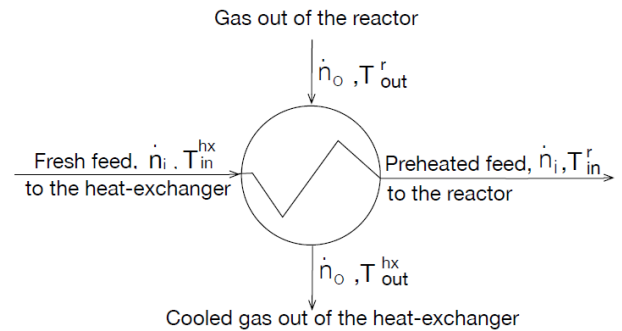
Figure 1: Sketch of the heat-exchanger model.

In expressions (2) temperature T_{in}^{hx} is known and listed in the Table 1. Temperature T_{out}^{r} is calculated using the ideal gas law and is described in the next subsection.

Temperatures T_{in}^{r} and T_{out}^{hx} are obtained from the expressions (3) and (4) respectively:

$$\dot{Q} = \dot{N}^i \cdot \overline{\overline{c}}_{p\,gas} \cdot \left(T_{in}^{r} - T_{in}^{hx} \right), \tag{3}$$

where $\overline{\overline{c}}_{p\,gas}$ is known parameter listed in Table 2. $\dot{N}^i$ is a sum of the inlet molar flows of ammonia,

4

hydrogen, nitrogen and argon, listed in Table 3. It should be also mentioned that $\dot{N}^i$ is a scalar number corresponding to the sum of the elements of the vector $\dot{n}^i$ (described in the next subsection).

Table 1: Parameters and known quantities for the heat-exchanger model.

Parameters and known quantities	Value	Unit	Comments
T_C	6	s	time constant
U	536	$\dfrac{W}{m^2 \cdot K}$	heat transfer coefficient of the heat-exchanger [1]
A	283	m^2	heat-exchanger area [1]
$T_{in}^{hx}(t)$	623.15	K	temperature of the fresh feed to the heat-exchanger

The equation, from which T_{out}^{hx} is found, is the following:

$$\dot{Q} = \dot{N}^o \cdot \overline{\overline{c}}_{p\,gas} \cdot \left(T_{out}^r - T_{out}^{hx} \right), \qquad (4)$$

where $\dot{N}^o$ is the sum of the outlet molar flows of ammonia, hydrogen, nitrogen and argon from the reactor. It should be also mentioned that $\dot{N}^o$ is a scalar number corresponding to the sum of the elements of the vector $\dot{n}^o$ (described in the next subsection).

Reactor model

The reactor system is assumed to be distributed (see Figure 2). Instead of partial differential equations a number of ODEs is developed assuming a discretized system with number of elementary volumes equal to $N_{sl} = 200$. A set of ODEs is obtained for each of 200 volume elements (slices). The number of volume elements was selected based on simulation experiments, when the further increasing of the number of elementary volumes

was not effecting simulation result. The output molar flow of each volume element is assumed to be an input to the next volume element. It is assumed to be no mixing between volume elements. Each elementary volume is assumed to be a continuous stirred-tank reactor. Modelling of a single slice of ammonia synthesis reactor was started with the following list of simplifying assumptions: 1. The volume element to be modelled is lumped. 2. All the feed to the reactor is assumed to be preheated by the heat-exchanger. No bypass is included. 3. Changes in potential energy and kinetic energy can be neglected, because they are small in comparison with changes in internal energy. 4. The net rate of work can be neglected, because it is small in comparison to the rates of heat transfer and convection. 5. Ideal gas, which also implies ideal solution. 6. Assumed average molar heat capacity of the gas mixture in the reactor $\overline{\overline{c}}_{p\,gas}$. The temperature and concentration dependency of $\overline{\overline{c}}_{p\,gas}$ is neglected. 7. The temperature and concentration dependency of the heat of the reaction is neglected. 8. Constant volume. Constant pressure. 9. Axial flow. 10. Gas temperature is equal to catalyst temperature. 11. Cross-sectional gas velocity is constant. 12. There is no variation in temperature, pressure, composition across the section.

The listed above assumptions are coarse assumptions and thus, the developed model is not intended to reproduce the accurate numerical values of the reactor parameters, but to reproduce the dynamics similar to the real system. Ideal gas law is used to simplify the simulation and one should use a more accurate thermodynamic model in order to get more accurate numerical values of the reactor parameters and variables.

The model of a single reactor slice is as follows:

$$\frac{dn}{dt} = \dot{n}^i - \dot{n}^o + \dot{n}^g, \qquad (5)$$

where $n = \begin{bmatrix} n_{NH3} & n_{H2} & n_{N2} & n_{Ar} \end{bmatrix}$ – state vector of amounts of ammonia, hydrogen, nitrogen and argon respectively.

$\dot{n}^i = \begin{bmatrix} \dot{n}_{NH3}^i & \dot{n}_{H2}^i & \dot{n}_{N2}^i & \dot{n}_{Ar}^i \end{bmatrix}$ – vector of input molar flows of ammonia, hydrogen, nitrogen and

5

argon respectively. Values of $n(t = 0)$ and $\dot{n}^i$ are listed in Table 3. $\dot{n}^o = \begin{bmatrix} \dot{n}^o_{NH3} & \dot{n}^o_{H2} & \dot{n}^o_{N2} & \dot{n}^o_{Ar} \end{bmatrix}$ – vector of output molar flows of ammonia, hydrogen, nitrogen and argon respectively. Output molar flows are calculated according to equation (6) based on energy balance and ideal gas law. $\dot{n}^g = \begin{bmatrix} \dot{n}^g_{NH3} & \dot{n}^g_{H2} & \dot{n}^g_{N2} & \dot{n}^g_{Ar} \end{bmatrix}$ – vector of generated molar flows of ammonia, hydrogen, nitrogen and argon respectively. Generated molar flows are calculated according to equation (9).
The expression for the output molar flow of the volume element follows below.

$$\dot{n}^o = \frac{n}{N_{tot}} \left[\frac{\bar{\bar{c}}_{p\,gas} \cdot \dot{N}^i \cdot (T_i - T) + \dot{Q}_r}{T \cdot (\bar{\bar{c}}_{p\,gas} \cdot \dot{N}^i + C_{p\,cat})} \times \right.$$
$$\left. \times N_{tot} + \dot{N}^i + \dot{N}^g \right] \qquad (6)$$

$$\dot{Q}_r = \left(-\Delta \tilde{H}_r \right) \cdot r \cdot V_{sl}$$

where $\bar{\bar{c}}_{p\,gas}$, $C_{p\,cat}$, $-\Delta \tilde{H}_r$ and V_{sl} are known model parameters described in Table 2. T_i – inlet temperature of the gas mixture and is equal to T^r_{in} mentioned in the previous subsection. T – temperature of the gas mixture inside the reactor volume element and is calculated using ideal gas law (8). The temperature of the last volume element corresponds to T^r_{out}. N_{tot} – sum of elements of the state vector n. r – the reaction rate of the synthesis process. The expression for the reaction rate was provided by Yara International ASA and is confidential. The rate expression is based on the Temkin-Pyzhev equation [9]:

$$r = k \left\{ \left(\frac{A^2_{NH_3}}{A^3_{H_2}} \right)^{1-\alpha} - K^2_{eq} A_{N_2} \left(\frac{A^3_{H_2}}{A^2_{NH_3}} \right)^\alpha \right\} \qquad (7)$$

where k is an Arrhenius term and A_i is the activity of species i. K_{eq} is a temperature-dependent equilibrium parameter. α is normally between 0.5 and 1. The effect of the Arrhenius term is that the reaction rate increases exponentially with temper-

ature, while the second term shows that the production rate of NH_3 decreases as the NH_3 concentration approaches equilibrium [9].
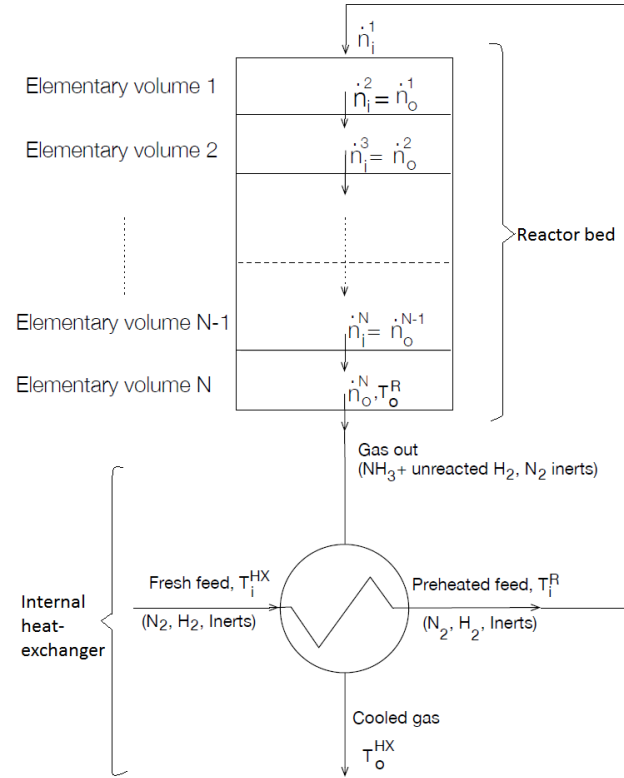
Figure 2: Sketch of the synthesis reactor with an internal heat-exchanger

To reproduce the result, the reaction rate expression for ammonia synthesis can be used from available literature [9], [1].
The temperature inside the volume element is found based on the ideal gas law:

$$T = \frac{p \cdot V_{sl}}{N_{tot} \cdot R}, \qquad (8)$$

where p – the pressure of the gas mixture inside the volume element and is listed in Table 3. R is the universal gas constant listed in Table 2.
The amount of generated quantity due to the synthesis reaction is given as (9).

$$\dot{n}^g = s \cdot r \cdot V_{sl}, \qquad (9)$$

6

where $s = \begin{bmatrix} 2 & -3 & -1 & 0 \end{bmatrix}$ is a stoichiometric vector of the reaction. The values in Table 2 and Table 3 can be changed using the data from a particular ammonia synthesis reactor (reactor bed). The developed model was verified based on theoretical knowledge about ammonia synthesis converters at Yara R&D and Innovation Centre.

Table 2: Model parameters.

Parameter	Value	Unit	Comments
$C_{p\,cat}$	$6.92 \cdot 10^5$	J/K	total heat capacity of the catalyst
$\widetilde{\bar{c}}_{p\,gas}$	$3.55 \cdot 10^4$	J/(kmol·K)	average molar heat capacity of gas mixture
$-\Delta \widetilde{H}_r$	$9.2 \cdot 10^7$	J/kmol	heat of reaction
V_{sl}	$57.2/N_{sl}$	m^3	elementary volume
R	$8.31 \cdot 10^3$	J/(kmol·K)	gas constant

Table 3: Operating conditions.

Quantity	Value	Unit	Comments
$n_{NH3}(t=0)$	0.0199	kmol	initial amount of NH$_3$
$n_{H2}(t=0)$	0.6545	kmol	initial amount of H$_2$
$n_{N2}(t=0)$	0.2254	kmol	initial amount of N$_2$
$n_{Ar}(t=0)$	0.0391	kmol	initial amount of Ar
$\dot{n}^i_{NH3}(t)$	0.141	kmol/s	inlet molar flow of NH$_3$
$\dot{n}^i_{H2}(t)$	4.641	kmol/s	inlet molar flow of H$_2$
$\dot{n}^i_{N2}(t)$	1.598	kmol/s	inlet molar flow of N$_2$
$\dot{n}^i_{Ar}(t)$	0.277	kmol/s	inlet molar flow of Ar
p	$1.78 \cdot 10^7$	Pa	pressure of gas in the reactor

SIMULATION RESULTS

Developed ODEs for 200 reactor volume elements were put together with the dynamic model of the internal heat exchange process (1) and simulated in MATLAB. Simulation results showed good performance with respect to system dynamics. Step tests were performed by changing the feed temperature to the heat-exchanger. Oscillations of temperature and concentration were obtained after the step was done in the feed temperature to the heat-exchanger from 250 to 200 °C. The following changes (compared to steady state) took place in the reactor according to Figure 3:

1. The outlet reactor temperature oscillates with approximate amplitude of 340 K: maximum level is 845 K, minimum is 505 K. The period of sustained oscillations is 700 s (around 12 minutes). 2. The inlet reactor temperature oscillates with approximate amplitude of 130 K: maximum level is 615 K, minimum is 485 K. The period of sustained oscillations is 700 s. 3. The yield of the produced ammonia oscillates with different amplitude for different reactor slices. In the middle of the reactor (81st slice) the oscillations have the largest amplitude: ammonia yield oscillates in the range from 0.2 to 14.4 %. At the reactor outlet (the last reactor slice) the yield of ammonia oscillates from 8.4 % to 15.7 %. The period of sustained oscillations is 700 seconds. Obtained oscillations show that the model is able to reproduce the dynamics of the real system.

CONCLUSION

As a result of the work a simple dynamic model of the ammonia synthesis process was developed. This model is combined with a simple dynamic model of the heat-exchanger for utilization of the heat of the reaction. It is shown by the simulation results that such a model can reproduce temperature oscillations which can be experienced in a real system. The temperature of the fresh feed to the heat exchanger has a significant effect on the oscillations. The dynamic model can be used as a basis for a synthesis reactor monitoring tool (stability map) in the following way:
 - check stability of the model when step test is made for different model parameters;
- evaluate stability of the simulated process based on the step response of temperature and concentration of ammonia in the reactor bed.
However, the developed model has features to be improved in order to be used for synthesis reactor

7

stability monitoring, i.e. more realistic thermodynamic model should be used and the reactor should be extended to the number of beds corresponding to the real ammonia converter at the plant.
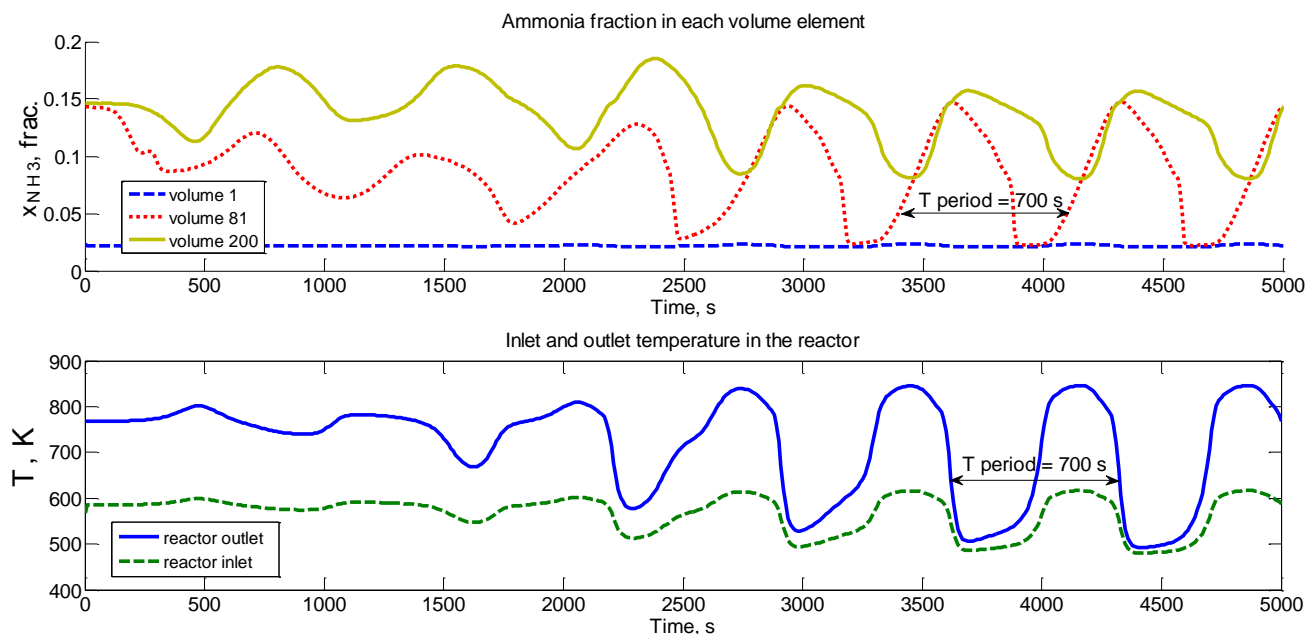

Figure 3: Step response of ammonia fraction and reactor inlet and outlet temperatures when changing temperature of the fresh feed to heat-exchanger from 250 to 200 °C.

REFERENCES

[1] J. Morud and S. Skogestad, "Analysis of instability in an industrial ammonia reactor," *AIChE Journal,* vol. 44, no. 4, p. 888–895, 1998.

[2] L. Naess, A. Mjaavatten and J.-O. Li, "Using dynamic process simulation from conception to normal operation of process plants," *Computers and Chemical Engineering,* vol. 17, p. 585–600, 1993.

[3] M. W. Hirsch, S. Smale and R. L. Devaney, Differential Equations, Dynamical Systems, And An Introduction to Chaos, 2nd ed., San Diego, California: Elsevier (USA), 2004.

[4] D. D. Perlmutter, Stability of chemical reactors, Englewood Cliffs: Prentice-Hall, 1972.

[5] A. D. Stephens and R. J. Richards, "Steady state and dynamic analysis of an ammonia synthesis plant," *Automatica,* vol. 9, no. 4, pp. 65-78, 1973.

[6] J.-O. Li, Regulering og optimalisering av en ammoniakksynteseprocess. Del A. Master's thesis, Universitetet i Trondheim. Norges Tekniske Høgskole. Avdeling for elektro- og, 1991.

[7] E. Holter, Feedforward for stabilization of an ammonia synthesis reactor, University of Trondheim. The Norwegian Institute of Technology, 2010.

[8] W. R. Paterson, "A replacement for the logarithmic mean," *Chemical Engineering Science,* vol. 39, no. 11, p. 1635–1636, 1984.

[9] M. Temkin and V. Pyzhev, "Kinetics of the Synthesis of Ammonia on Promoted Iron Catalysts," *Jour. Phys. Chem. (U.S.S.R.),* vol. 13, pp. 851-867, 1939.

8

GLYCOL DEHYDRATION OF CAPTURED CARBON DIOXIDE USING ASPEN HYSYS SIMULATION

Lars Erik Øi* and Mirela Fazlagic
Telemark University College
Department of Process, Energy and Environmental Technology
Norway

ABSTRACT

Water must be removed from carbon dioxide (CO_2) after capture because of risk for corrosion and hydrate formation. The level of accepted water content after dehydration depends on the next step for the captured CO_2, and can be in the range between 5 and 500 parts per million (ppm) on a volume basis. A water specification of 50 ppm is a traditional specification for pipeline transport. Absorption into triethylene glycol (TEG) followed by desorption is a traditional gas dehydration method, and can also be used for CO_2. For very low water content, use of solid adsorbents is expected to be the preferred method. There are very few references in the open literature on simulation of CO_2 dehydration. It is in this work demonstrated that it is possible to simulate both a traditional glycol dehydration process and more advanced CO_2 dehydration processes using different equilibrium models in the process simulation program Aspen HYSYS. Depending on the water content specification for the captured CO_2, different processes modifications have been suggested. It is simulated reasonable process alternatives for CO_2 dehydration down to water levels below 5 ppm.
Keywords: CO_2, glycol, dehydration, Aspen HYSYS, simulation

INTRODUCTION

Water specifications for CO_2 dehydration

CO_2 capture and storage has been extensively studied as a possible way to mitigate global warming. Removal of water (dehydration) from captured CO_2 is necessary to avoid corrosion and hydrate formation under transport and storage. The need for water removal from CO_2 and possible specifications are discussed in several references [1,2,3]. In some cases, a water level of 500 ppm (by volume) has been accepted. A specification of 50 ppm is a traditional specification for pipeline transport. CO_2 for enhanced oil recovery normally requires a stricter water specification.

_____
*Corresponding author, Phone: +47 3557 5141
E-mail: lars.oi@hit.no

Dehydration methods

There are several different gas dehydration methods available. The simplest dehydration method is by cooling, water condensing and gas/water separation. Other methods are dehydration by absorption, adsorption or by using membranes.
The most traditional method for large scale dehydration to moderate water levels is by absorption into triethylene glycol (TEG). For very low water levels, adsorption processes are necessary [4]. Membrane dehydration is economical only for low gas flow rates [5].

Process simulation programs

Process simulation programs solve material and energy balances and calculate vapour/liquid equilibrium in different unit operations like tanks,

heat exchangers, pumps and distillation columns. Most of the programs are sequential modular and solve the unit operations in the same sequence as in the real process. Commercial process simulation programs used for glycol dehydration are Aspen Plus, Aspen HYSYS, Pro/II and ProMax. Process simulation programs are useful for simulation of absorption processes because complex vapour/liquid equilibrium models are available in the programs, and because efficient stage to stage procedures are available.

Absorption and distillation columns are often simulated as a sequence of equilibrium stages. The stages can also be specified with a Murphree efficiency. Murphree efficiency can be defined as the change in concentration (in this case water content) from the stage below to a given stage, divided by the change if equilibrium was achieved on the given stage [4].

Vapour/Liquid data and equilibrium models

Equilibrium values in the TEG/water system from the work of Herskowitz and Gottlieb [6] and activity coefficients at infinite dilution measured by Bestani [7] are regarded as the most reliable data for this system [8].

To represent this vapour/liquid equilibrium either an equation of state can be used for the vapour phase and an activity model for the liquid phase or an equation of state for both phases. To describe the gas phase by an equation of state, the liquid phase by an activity model and the total pressure dependence by a Poynting correction is recommended for the TEG-natural gas-water system at high pressure [8].

The vapour/liquid equilibrium between CO_2 and water is reviewed by Cole [1]. This equilibrium must be included in a complete model of the TEG/water/CO_2 system. One special task is to calculate the correct solubility of CO_2 in a TEG/water solution.

In Aspen HYSYS, the equilibrium models Peng-Robinson (PR) [9] and Twu-Sim-Tassone (TST) [10] are available for glycol dehydration. The PR model is a standard cubic equation for general use with only one adjustable parameter for each component pair in the system. The TST model is a more advanced cubic equation of state with more adjustable parameters. The parameters are especially fitted for the glycol gas dehydration system. The TST model is recommended in the Aspen HYSYS program documentation as the most accurate. It is however not clear whether any of these models are especially suited for dehydration of CO_2.

In the Aspen Plus simulation program the SR-POLAR model is recommended for TEG dehydration simulation [11]. SR-POLAR is a property method based on the Schwartzentruber and Renon cubic equation of state [12]. The process simulation programs PRO/II and ProMax also have models available recommended for the TEG/water system.

Dehydration simulations in literature

Simulations of the natural gas dehydration process in Aspen HYSYS have been performed with emphasis on glycol regeneration by Øi and Selstø [13]. A traditional TEG dehydration process has been simulated using the Peng-Robinson equation of state [9]. A water content of 58 ppm was specified in the dehydrated gas. Different regeneration processes were simulated, e.g. addition of stripping gas to the reboiler, adding stripping gas to an extra stripping column and also some commercial processes. For the same inlet data, Emah [11] performed simulations of a natural gas dehydration process in Aspen HYSYS and Aspen Plus using different equilibrium models in order to investigate configurations suitable for achieving 37 ppm in the dehydrated gas.

Farhat [14] described TEG dehydration of a CO_2 stream with an additional stripping column below the reboiler for improving TEG regeneration. Dry CO_2 gas from the process was utilized as stripping gas. Bilsbak [15] used the simulation program Pro/II to simulate TEG dehydration of CO_2 using an equation of state.

Besides these references, there is very little information found in the open literature about simulation of CO_2 dehydration processes and particularly of CO_2 dehydration based on absorption in glycol.

Purpose of the paper

The main purpose of the paper is to give an overview over process simulation flow-sheet models for CO_2 dehydration by absorption in triethylene glycol. Especially, it is an aim to simulate different alternatives dependent on the water level specifications in dehydration gas. The results in this work are mainly from simulations performed in the Master Thesis work of Mirela Fazlagic [16].

PROCESS DESCRIPTION

Traditional TEG dehydration process

A traditional dehydration process for natural gas or CO_2 is shown in Figure 1. Wet gas is absorbed by a TEG solution in an absorption column (contactor). The liquid (rich glycol) is then depressurized to flash off some of the natural gas. Then the liquid is heated and sent to a desorber (regenerator). In this distillation column, water is removed from the top and regenerated TEG is removed from the bottom. Heat is added in the reboiler below the desorber. The regenerated TEG (lean glycol) is pumped through two heat exchangers back to the absorber.
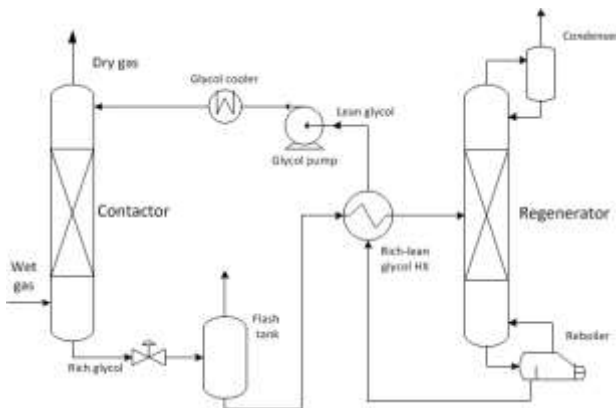

Figure 1: A traditional TEG dehydration process

Stripping gas to reboiler

It is possible to improve the removal of water in the regeneration by adding stripping gas to the reboiler or the bottom of the desorber column. The main effect of adding stripping gas is that the partial pressure of water in the gas phase is reduced so that more water will evaporate and then reduce the water content in the glycol. The stripping gas can come from the flash gas or from the dehydrated gas as indicated in Figure 2.

Stripping gas to extra stripping column

The regeneration of TEG can be improved further by adding an extra stripping column below the reboiler. This is shown in Figure 2. The extra stripping column results in more efficient water removal and reduced amount of stripping gas to achieve a specified TEG concentration [21].
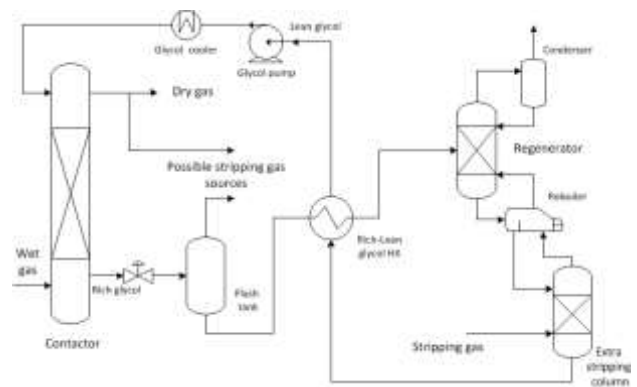

Figure 2: A TEG dehydration process with extra stripping column

PROCESS SIMULATION

Simulation of standard process

A traditional TEG dehydration process as in Figure 1 has been simulated in the simulation program Aspen HYSYS version 7.2 using the Peng-Robinson equation of state and the glycol property package (using the TST equilibrium model).
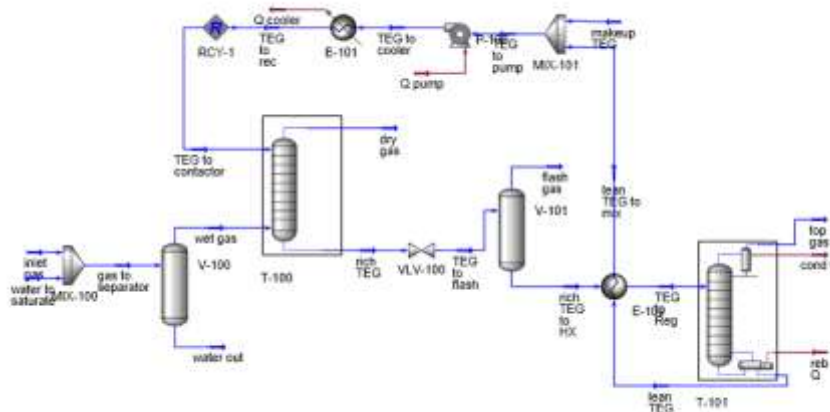
Figure 3: Aspen HYSYS flow-sheet model for traditional TEG dehydration process

Inlet gas temperature [^{0}C]	30
Inlet gas pressure [kPa]	3000
Inlet gas flow [kmol/h]	501.1
Water in inlet gas [mol-%]	0.23
Lean TEG temperature [^{0}C]	35
Lean TEG pressure [kPa]	3000
Lean TEG rate [kmol/h] (in first iteration)	3.583
Water in lean TEG [mass-%] (in first iteration)	1.04
Number of stages in absorber	10
Murphree efficiency in absorber	0.5
Pressure after the depressurization valve [kPa]	110
Heated rich TEG temperature [^{0}C]	153
Number of stages in stripper (+ condenser/reboiler)	4
Murphree efficiency in stripper	1.0
Reflux ratio in stripper	0.5
Reboiler temperature [^{0}C]	200
Pressure in stripper [kPa]	101
Lean TEG pump pressure [kPa]	3000

Table 1: Base-case specifications

The Aspen HYSYS flow-sheet model for the base case simulation is presented in Figure 3. The specifications for the base case process calculation are given in Table 1. The absorption column was simulated with 10 stages and with Murphree efficiency 0.5, which is assumed to be equivalent to approximately 10 actual plates or 5 meters of structured packing [17].

The calculation sequence of the process in the Aspen HYSYS flow-sheet is in practice following the real flow direction. The gas feed stream to the absorber is saturated with water and is calculated first. The liquid feed to the absorber is then guessed. Then the absorption column and the rest of the process is calculated step by step. The cold side of the main heat exchanger is calculated first based on a specified temperature on the stream to the desorber. The recycle block compares the stream returned from the TEG cooler with the guessed stream. Some iterations may be necessary to achieve convergence. In some simulations, Aspen HYSYS calculated unrealistic low temperatures. This indicates that it is something wrong with the enthalpy calculations. It is a traditional recommendation to be careful with calculations of enthalpies from an equation of state and rather replace the enthalpy calculation with a simpler and often more accurate method. This problem was solved by changing the enthalpy setting to the Cavett model instead of the default property package EOS (equation of state).

Using the base case specifications in Table 1, the water content in dehydrated gas was calculated to 153 ppm with the PR model and 206 ppm with the glycol package using the TST model.

The process was simulated also at other absorption pressures. The results are shown in Figure 4. Both the models give a minimum water content or maximum efficiency at a certain pressure. Minimum water content was 129 ppm at about 5000 kPa using the PR model and 205 ppm at about 3500 kPa using the TST model.

Because the glycol package using the TST model is probably the most accurate model, it is assumed that the optimum is between 3000 and 4000 kPa.
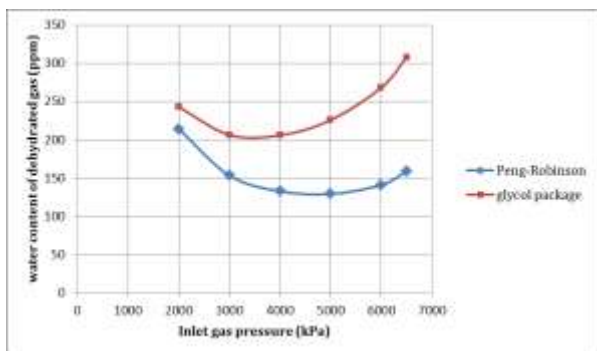

Figure 4: Water content in dehydrated gas as a function of absorption pressure

It was tried to improve the dehydration by increasing the TEG circulating rate and by increasing the number of absorption stages. This gave only minor improvements in achieved water content in the dehydrated gas.

Simulation of stripping gas to reboiler

A process with stripping gas added to the reboiler was simulated. Figure 5 shows the regeneration part of the flow-sheet of the Aspen HYSYS simulation.
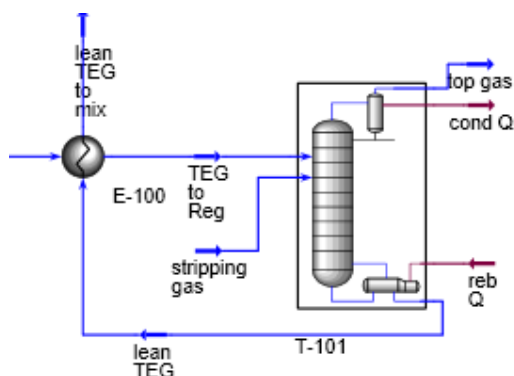

Figure 5: Aspen HYSYS flow-sheet of process with stripping gas to desorber

The stripping gas was specified with temperature 190 °C, pressure 101 kPa, 99.17 % CO_2 and 0.83 % water. The composition was similar to the flash gas composition from depressurization after the absorption column in the base-case calculation.

Calculations comparable to the base case simulations were performed with varying stripping gas flow and number of stages in the absorption column. Using the Peng-Robinson model, less than 50 ppm was achieved using 10 absorption stages and 1.8 kmole/h stripping gas. Using the glycol package, slightly more than 10 absorption stages was necessary. Using 20 stages, it was necessary to use 1.2 kmole/h to achieve less than 50 ppm in the dehydrated gas. Results from the calculations using the TST model is shown in Figure 6. It is seen that an increase to 30 absorber stages did not increase the efficiency significantly.
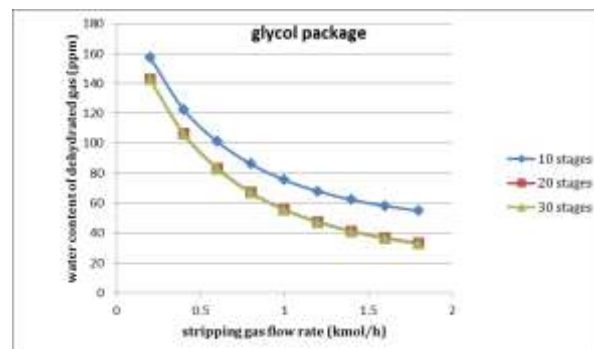
Figure 6: Water content as a function of stripping gas to reboiler and number of absorber stages

When the amount of stripping gas was limited to the amount of flash gas after the absorption column, the PR model calculated 42 ppm and the TST model 103 ppm. This large difference is mainly due to the large difference in calculated flash gas in the two cases, 0.9 kmole/h for PR and 0.4 for TST.

Increasing the number of stages and the amount of stripping gas made it possible to improve the dehydration down to about 30 ppm. This was achieved with both the PR and TST models.

Simulation of stripping gas to extra column

A simulation of the process in Figure 2 was performed with an extra stripping column. First, the process was simulated with two columns as in Figure 7. The calculation sequence is more complex than in the base case. To calculate the desorber, it is necessary to guess the stream from the extra stripping column. After that the extra stripper can be calculated, and the recycle stream from the extra stripping column is compared with the guessed stream in a second recycle block.

This process simulation approach is difficult to converge. The recycle blocks are normally solved using iteration by replacement. The water concentration in each recycle stream is normally the critical parameter. With only one recycle loop, the water content in the recycle stream normally stabilizes and the simulation converges. In case of more than one recycle loops, the water concentration in the recycle loops tend to be less stable, and the simulation does not converge.

Because of these problems it was tried to simplify the simulation flow-sheet model, and the desorption column and the extra stripping column were simulated as one column in Aspen HYSYS with heating at an intermediate stage. The resulting flow-sheet in Aspen HYSYS is shown in Figure 8. The same numerical results were achieved when using these two approaches.

Figure 7: Aspen HYSYS flow-sheet of desorber with extra stripping column

The extra stripping column was specified with 3 equilibrium stages. In the case of the extra stripping gas and the desorber simulated as one column, it was 3 stages between the stripping gas feed to the bottom and the reboiler heat addition.
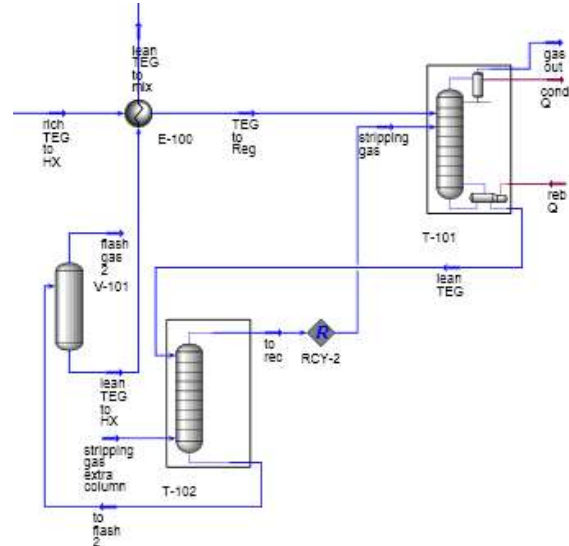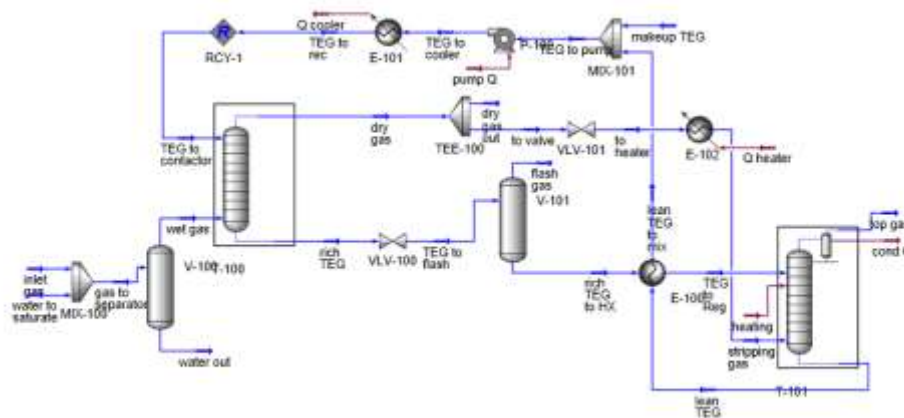

Figure 8: Aspen HYSYS simplified flow-sheet of process with extra stripping column
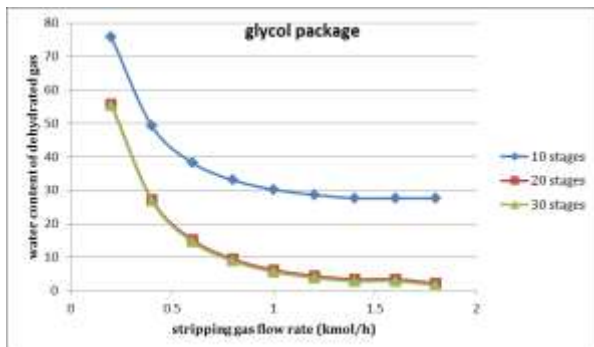
Figure 9: Water content as a function of stripping gas and number of absorber stages with extra stripping column

Figure 9 shows results from these calculations as a function of stripping gas and number of absorber stages for the process with an extra stripping column. Using 20 absorber stages and more than 1.2 kmole/h stripping gas gives less than 5 ppm in the dehydrated gas. These results were achived using the TST model. Using the PR equilibrium model gave even better dehydration results. As in earlier simulations, increasing to 30 absorber stages did not improve the dehydration efficiency significantly.

Influence of water content in stripping gas

The simulations were performed with different water levels in the stripping gas. For moderate water levels (50 ppm) there were no differences in the calculated results for different water levels of the stripping gas. To obtain very low levels (below 5 ppm) it is necessary to use almost pure stripping gas. Then it is reasonable to use stripping gas from the dehydrated CO_2.

DISCUSSION

Comparison of equilibrium models

Dehydration of CO_2 gas by absorption in TEG has been simulated in Aspen HYSYS using two different vapor/liquid equilibrium models. Both the PR and TST models give similar results for most of the simulated alternatives.

The calculated flash gas flow rate was significantly different between the two models. This indicates that the two models calculate the CO_2 solubility in TEG solution differently.

The glycol package in Aspen HYSYS using the TST model has been developed especially for TEG dehydration and is regarded as more accurate than the simpler PR model. The TST model gives slightly more conservative results than the PR model, and this is also an argument to recommend the glycol package using the TST model. It is assumed that the recommended equilibrium models in other process simulator programs also have satisfactory accuracy.

Optimum dehydration pressure

The calculated water content for different absorption pressures indicates that a maximum dehydration efficiency is achieved at a pressure between 3000 and 5000 kPa. According to the calculations using the model assumed most accurate, the optimum was between 3000 and 4000 kPa. Because captured CO_2 will normally be compressed to a higher pressure than 5000 kPa for further processing, it is reasonable to perform dehydration at an intermediate pressure between 3000 and 4000 kPa.

Process dependence on water specification

Water content requirement for dehydrated CO_2 influences the choice of dehydration process.
From calculations performed in Aspen HYSYS it can be concluded that a traditional TEG dehydration process is satisfactory to achieve a water content of about 200 ppm in dehydrated gas. Using stripping gas, a water specification of less than 50 ppm can be achieved. In a process including an extra stripping column and a high absorption column, it is possible to achieve less than 5 ppm. In that case, it is necessary to use dehydrated CO_2 gas as stripping gas.

CONCLUSION

It is demonstrated that it is possible to simulate both a traditional glycol dehydration process and more advanced CO_2 dehydration processes using Aspen HYSYS. Depending on the water content specification for the captured CO_2, different processes modifications have been suggested. It has been simulated reasonable process alternatives for CO_2 dehydration down to water levels below 5 ppm.

REFERENCES

[1] Cole IS, Corrigan P, Sim S, Birbilis N. *Corrosion of pipelines used for CO_2 transport in CCS: Is it a real problem*? International Journal of Greenhouse Gas Control 2011;5(7):749-756.

[2] Uilhoorn FE. *Evaluating the risk of hydrate formation in CO_2 pipelines under transient operation*. International Journal of Greenhouse Gas Control 2013;14(5):177-182.

[3] Buit L, Ahmad M, Mallon W, Hage F. *CO_2 EuroPipe study of the occurrence of free water in dense phase CO_2 transport*. Energy Procedia 2011;4:3056-3062.

[4] Kohl AL, Nielsen R. *Gas purification*. Houston, Tx: Gulf Publication, 1997.

[5] Kidnay AJ, Parrish WR. *Fundamentals of Natural Gas Processing.* Taylor&Francis, 2006.

[6] Herskowitz M, Gottlieb M. *Vapor-liquid equilibrium in aqueous solutions of various glycols and polyethylene glycols. 1. Triethylene glycol.* Journal of Chemical & Engineering Data 1984;29:173-175.

[7] Bestani B, Shing KS. *Infinite-dilution activity coefficients of water in TEG, PEG, glycerol and their mixtures in the temperature range 50 to 140 °C.* Fluid Phase Equilibria 1989;50:209-221.

[8] Øi LE. *Calculation of dehydration absorbers based on improved phase equilibrium data.* In Proceedings of the 78th Annual Convention of Gas Processors Association, 1999:32-37.

[9] Peng D, Robinson DB. *A New Two-Constant Equation of State.* Industrial & Engineering Chemistry Fundamentals 1976;55(1):59-64.

[10] Twu CH, Tassone V, Sim WD, Watanasiri S. *Advanced equation of state method for modeling TEG–water for glycol gas dehydration.* Fluid Phase Equilibria 2005;228-229:213-221.

[11] Emah E. *Process simulation of natural gas dehydration by absorption in triethylene glycol.* Master Thesis, Telemark University College, Porsgrunn, Norway, 2012.

[12] Schwartzentruber J, Renon H, Watanasiri S. *Development of a new cubic equation of state for phase equilibrium calculations.* Fluid Phase Equilibria. 1989;52(12):127-134.

[13] Øi LE, Selstø ET. *Process Simulation of Glycol Regeneration.* Presented at the GPA Europe's meeting Bergen, Norway, 2002.

[14] Farhat K. *CO_2 Interim Storage as a Tool for CO_2 Market Development: a Comprehensive Technical Assessment.* Master Thesis, Department of Energy Resources Engineering, Stanford University, Ca, 2011.

[15] Bilsbak V. *Conditioning of CO_2 coming from a CO_2 capture process for transport and storage purposes.* Master Thesis, NTNU, Trondheim, Norway, 2009.

[16] Fazlagic M. *CO_2 dehydration after CO_2 capture and compression.* Master Thesis, Telemark University College, Porsgrunn, Norway, 2014.

[17] Øi LE. *Estimation of tray efficiency in dehydration absorbers.* Chemical Engineering and Processing 2003;42(11)867-878.

Modelling of a Coil Steam Generator for CSP applications[☆]

Leonardo Pelagotti[a], Kim Sørensen[b,1], Thomas J. Condra[b], Alessandro Franco[a]

[a]*Energy Engineering Department, School of Engineering, Pisa University, Via Diotisalvi 2, 56126 Pisa, Italy*
[b]*Department of Energy Technology, Aalborg University, Pontopidanstræde 101, 9200 Aalborg, Denmark*

Abstract

The project investigates a new design for a CSP plant steam generation system, the Coil Steam Generator (CSG). This system allows faster start-ups and therefore higher daily energy production from the Sun. An analytical thermodynamic simulation model of the evaporator and a mechanical analysis are developed to optimize the behavior of the system in different start-up scenarios. The results improve the effective life time (ELT) of the CSG, the thermal flexibility of the overall CSP plant to have faster start-ups. Sensitivity analysis carried out to understand the importance of start-up time, oil circuit pressure in the CSP plant and header thickness, show that the these variables are important to determine the total state of stress in the headers, and therefore their effective life time. Applying the results of the optimization analysis means that, the oil headers are not critical anymore regarding the start-up process and can easily resist faster start-ups.

Keywords: CSP, Evaporator, Effective Life Time, Start-up, Solar Energy
2010 MSC: 00-01, 99-00

1. Introduction

Why is Solar Energy interesting?. There is a high potential of development of the use of (CSP) technology; the Sun is the renewable source on which there is the highest possibility to rely on in the future, in fact in one year the solar energy reaching the earth is about twice as much as will ever be obtained from all of the Earth's non-renewable resources.[1]

The CSP technology is complementary to the solar photovoltaic (PV) process. It uses concentrating collectors to provide high temperature heat, usually to a conventional steam power cycle. Efficient and low-cost thermal energy storage technologies can be integrated into CSP systems, allowing electricity production according to the demand profile. CSP systems can also avoid *shadow plant capacity* needed to secure generation capacity in periods without sunshine, can provide grid services, and if desired even black start capabilities. It thus supports the penetration of a high share of intermittent renewable sources like wind or PV and avoids a high share of expensive electric storage technology in the grid systems. CSP focuses on two technology options: *parabolic trough* technologies and *solar tower* technologies [2]. The CSG investigated in this paper is part of the parabolic trough technology, that is the most mature and economic solar thermal power generation technology today. Solar radiation is concentrated by parabolically curved, trough-shaped reflectors onto a receiver pipe running along the inside of the curved surface. Within the pipe, the solar energy heats up a heat transfer medium (*e.g.* oils, molten salt) to approximately 400°C. The medium transfers the heat to a power block, where steam is generated and electricity is produced in a conventional Rankine cycle.

By its unsteady nature, both within the day and the year, the capture and storage of solar energy is critical if a significant portion of the total energy demand needs to be met by this renewable form of energy. Fast start-ups and higher plant flexibility are necessary to extract as much power as possible from the Sun in CSP plants, in the limited amount of hours of solar radiation in a day. This is why a study on the thermal flexibility of CSP plants is of enormous importance to guarantee, in the near future, an increasing percentage of solar energy from

---

[☆]This document is a collaborative effort between Pisa University and Aalborg University with Aalborg CSP A/S.
[1]Corresponding Author, kso@et.aau.dk

CSP technology. The electricity grid requires the thermal plants to be as fast as possible to be able to supply the difference between power production and demand at any time. A system which is capable of providing flexibility to the grid could be a CSP power plant with a daily heat storage system based on molten salts or a steam generator unit where the steam is accumulated in the drum. [2]

2. Material and Methods

The coil-type evaporator analyzed in this project, see Figure 1 , has been specially developed for solar energy applications, where high steam capacity and high steam pressures are required due to frequent starts/stops and load changes, due to the intermittent nature of the Sun [3].
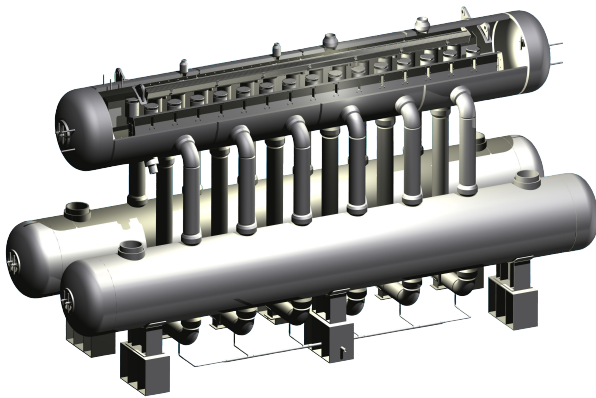

Figure 1: Steam generation system of the CSP plant,[3]

The coil-type evaporator does not have thick tube plates. The hot oil flows are distributed to the heat transfer tube bank via a circular manifold, or oil header as shown in Figure 2. The round shape of the header results in a relatively small material thickness and therefore low thermal stress as can be understood from Equations 11, 12 and 13 where the thermal stress is proportional to the square of the thickness. The new design of the oil collectors as cylindrical headers lowers the thermal stresses that were affecting seriously the life time. Moreover, by

splitting the evaporator unit in two heat exchangers and a steam drum, the diameters of the individual pressure vessels are smaller compared to a shell and tube evaporator, and the wall thickness required to sustain the pressure is smaller too. This means that the evaporator is less sensitive to fast temperature gradients and therefore is more flexible. That is exactly why the coil-type steam generator is especially interesting for solar applications that requires faster start-ups.
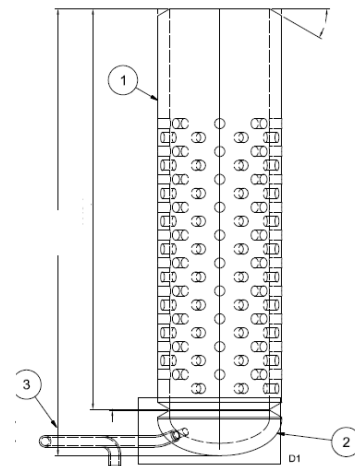
Figure 2: Circular oil header

Thermodynamic Model. The thermodynamic model includes energy balances and several heat transfer correlations, necessary to describe the cross flow evaporation process on the evaporator tube bundle. The data are based on heat balances and plant measurements provided by Aalborg CSP, and the model is solved analytically in MATLAB.

Figure 3 shows how the system has been conceptually described for the development of the Model.

The purpose of this model is to calculate the temperature distributions in the tube bundle of the evaporator, in every point of the 3-D space in the shell and thus determine the temperature in the oil headers. The model is based on the following assumptions: quasi-static conditions, no heat loss, the wall thermal resistance is uniform and negligible longitudinal heat transfer in both wall and fluid.

The model uses the $\epsilon - NTU$ method and solves an analytical system of partial-ordinary differential equations, as shown in Equation 1, from [4] . The system is derived from a 2-D energy balance of the heat exchange process in a cross flow evaporator, and is then made 3-D by the author, invoking the

---

[2]The author of this Paper have been in cooperation with the engineering company Aalborg CSP A/S, who manufactures heat exchangers for solar applications and develops and supplies steam generators for utility size CSP plants.

2

Figure 3: Cross sectional volume discretization principle of the entire tube bundle.

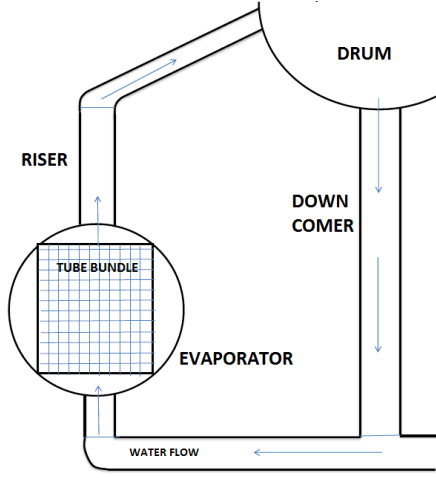assumption of axial symmetry for the tube in the tube bundle of the cross flow evaporator. The configuration for the cross flow heat exchanger is supposed to be unmixed on the water/steam side and mixed in the thermal oil side. This is due to the discretization used for the evaporator. This results in a 2D dimensional temperature field for the water/steam flow and a 1-D temperature field for the oil flow inside the tube. The model is based on Eq. 1, composed of differential equations, one partial and one ordinary.

$$\begin{cases} \dfrac{\partial \theta_2}{\partial \xi} + \theta_2 = \theta_1 \\ \dfrac{d\theta_1}{d\chi} + \theta_1 = \dfrac{1}{C^*NTU} \cdot \displaystyle\int_0^{C^*NTU} \theta_2 \, d\xi \end{cases} \quad (1)$$

The system above is made non dimensional and the symbols used are:

$$\theta_1 = \frac{T_1 - T_{2,i}}{T_{1,in} - T_{2,in}} \qquad \theta_2 = \frac{T_2 - T_{2,in}}{T_{1,in} - T_{2,in}} \quad (2)$$

$$\chi = \frac{z}{L1}NTU \qquad \xi = \frac{y}{L2}C^*NTU \quad (3)$$

The domain is $0 \leq \chi \leq NTU$ and $0 \leq \xi \leq C^*NTU$ and the boundary conditions $\theta_1(0) = 1$ and $\theta_2(\chi, 0) = 0$.

The solution of the above system of equations is carried out analytically implementing and solving in MATLAB. Applying the Laplace and Inverse

Laplace Transform technique and solving the integrals, the results is shown in Eq. 4.

$$\begin{cases} \theta_1(\chi) = e^{-K\chi} \\ \theta_2(\chi, \xi) = \left(1 - e^{-\xi}\right) \cdot e^{-(K\chi)} \end{cases} \quad (4)$$

Where K is a parameter related to the NTU method, and 1 refers to the oil and 2 to the water/steam.

$$K = \frac{\left(1 - \exp^{-C^*NTU}\right)}{C^*NTU} \quad (5)$$

The overall heat transfer coefficient value for UA is evaluated for every sections of the entire tube bundle with Eq. 6.

$$\frac{1}{UA} = \frac{1}{h_{oil}A_i} + \frac{\delta}{k_w A_{mean}} + \frac{1}{h_{w/s}A_o} \quad (6)$$

The heat transfer coefficient for the oil, h_{oil}, is evaluated with the *Second Petukhov equation*, [5]. Instead for calculating the heat transfer coefficient on the water/steam side, it is necessary to use correlations developed for a tube bundle in a horizontal cross flow evaporator, such as the Palen and Yang (1983) correlation or the Thome & Robinson (2006), see [6] . These correlations gives mean bundle boiling heat transfer coefficients and use the h_{NcB}, the *nucleate* boiling heat transfer coefficient and the h_{nc}, the natural convection coefficient of heat transfer around a tube bundle. Several different nucleate boiling correlations have been implemented, such as the Stephan & Abdelsalam [7] and the Ribatski et al. [8] correlation. Additionally a sensitivity analysis on the effect of using different correlations has been also investigated. The h_{nc}, has been calculated using the Zukauskas correlation, see [5].

In order to calculate the enthalpy distribution in the tube bundle from the temperature distribution for every section in the entire evaporator, Eq. 7 has been used to compute the heat flux received by the water/steam on the outside of the tube.

$$\dot{q}(i) = C_{min}\left(T_{oil}(i+1) - T_{oil}(i)\right) \qquad [W] \ (7)$$

Assuming that all the heat flux from the oil goes to the water/steam, in order to calculate the enthalpy for every section along the tube diameter, Eq. 8 has been implemented:

3

$$h_{ws}(i, j+1) = h_{ws}(i, j) + \left(\frac{nz}{ny}\right)\frac{q(i)}{\dot{m}_{w/s}} \quad \left[\frac{kJ}{kg}\right] \tag{8}$$

Where the i index denotes the tube length coordinate along z and the j index the section on the vertical y coordinate on the tube outside diameter. Also nz and ny is the number of discretization in z and y coordinate. Knowing the value of the enthalpy as a 3D function inside the cross flow evaporator tube bundle, the quality as a 3D space function, assuming thermodynamic equilibrium, is calculated.

It is relevant to understand how the system adapts to different load conditions, and therefore pressure and heat flux ranges. This reflects how the cross flow evaporator works under transient conditions, and that is relevant for a CSP plant. Figure 4 shows the evolution of the exchanged heat flux in the evaporator, during a normal warm start-up of 28 minutes.
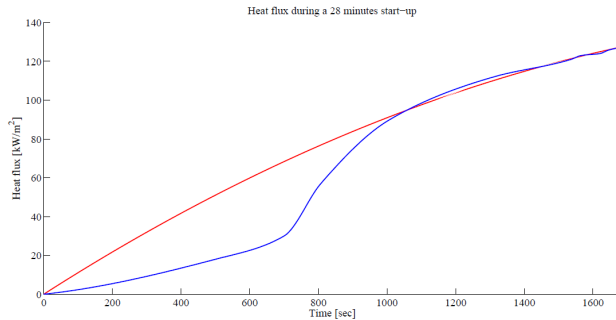

Figure 4: Evolution of the heat flux exchange in the evaporator during a warm start-up of 28 minutes

As it can be seen from Figure 4, the two curves are in good accordance at the end of the start-up phase, when the load is approaching the design value, while instead, the two curves differ significantly at low and medium load cases at the beginning of the start-up. The red curve, with a quadratic shape, represents an interpolate profile based only on the heat flux calculated for high load cases, in a range of 70-100 % of the design load case. The blue curve is the profile based on data from the plant. The fact that the profile at high load cases is different from the profile at lower load cases, means that the evaporator behaves differently according to the load, and that the heat transfer correlations used to describe the system at high loads have to

be different than the ones to use for the lower load cases [9].

3. Theory and Calculations

Thermal-Pressure Stress Analysis. The thermal stresses in the thick walled oil headers are calculated based on the temperature profile, found by solving the heat conduction equation in the wall of the headers. An analytical approach is used for the formulation of the entire problem, involving basic assumptions and the calculation of the temperature in an hollow cylinder in transient conditions, with the Fourier equation of Thermal Conduction applied to the oil header. It is assumed that the problem is symmetrical in the θ coordinate and the final heat equation to be solved is :

$$\frac{1}{r}\frac{\partial}{\partial r}\left(r\frac{\partial T}{\partial r}\right) - \alpha\frac{\partial T}{\partial t} = 0 \tag{9}$$

where α is the thermal diffusivity of the header wall. Eq. 9 is a parabolic partial differential transient equation (PDE). The initial-boundary value problem of parabolic equation in 1-D space and time is given in Eq. 10.

$$\begin{cases} \dfrac{1}{r}\dfrac{\partial}{\partial r}\left(r\dfrac{\partial T}{\partial r}\right) - \alpha\dfrac{\partial T}{\partial t} = 0 & \\ T(r,0) = T_0 & I.V. \\ T(R_{in}, t) = T_{oil}(t) & B.C. \\ T(R_{out}, t) = T_{w/s}(t) & B.C. \end{cases} \tag{10}$$

Once the temperature in the thickness of the headers is calculated it is possible to calculate the thermal stresses deriving from that profile. The *plane strain state* equations are used in order to compute the thermal stresses, Equations 11 and 12 and 13, as explained in [10] and [11].

$$\sigma_{\theta,th} = \frac{E\alpha}{1-\nu}\frac{1}{r^2}\left[\frac{r^2+R_i^2}{R_e^2-R_i^2}\int_{R_i}^{R_e} T(r)\,r\,dr + \int_{R_i}^{r} T(r)\,r\,dr - T(r)\,r^2\right] \tag{11}$$

$$\sigma_{r,th} = \frac{E\alpha}{1-\nu}\frac{1}{r^2}\left[\frac{r^2-R_i^2}{R_e^2-R_i^2}\int_{R_i}^{R_e} T(r)\,r\,dr - \int_{R_i}^{r} T(r)\,r\,dr\right] \tag{12}$$

4

$$\sigma_{z,th} = \frac{E\alpha}{1-\nu} \left[\frac{2}{R_e^2 - R_i^2} \int_{R_i}^{R_e} T(r)\,r\,dr - T(r) \right] \tag{13}$$

At the end of the start-up the thermal stresses are shown in Figure 5
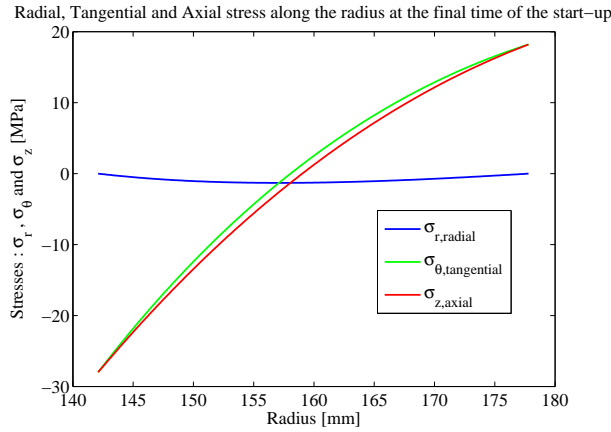

Figure 5: Thermal stresses in the radius at the end of the start-up

Once the thermal stresses are evaluated also the stresses due to the pressure field are considered in Eq. 14 , 15 and 16 . For a thick walled cylinder the pressure stresses are evaluated with the *Lame Equations*, explained in [12] and [13].

$$\sigma_{r,p}(r) = \frac{P_{in}R_{in}^2 - P_{out}R_{out}^2}{R_{out}^2 - R_{in}^2} + \frac{(P_{out} - P_{in})\,R_{out}^2 R_{in}^2}{r^2\,(R_{out}^2 - R_{in}^2)} \tag{14}$$

$$\sigma_{\theta,p}(r) = \frac{P_{in}R_{in}^2 - P_{out}R_{out}^2}{R_{out}^2 - R_{in}^2} - \frac{(P_{out} - P_{in})\,R_{out}^2 R_{in}^2}{r^2\,(R_{out}^2 - R_{in}^2)} \tag{15}$$

$$\sigma_{z,p} = 2\nu \left(\frac{P_{in}R_{in}^2 - P_{out}R_{out}^2}{R_{out}^2 - R_{in}^2} \right) \tag{16}$$

The stresses are functions of time and radius and for the design load case at the end of the start-up Figure 6 shows them.

When the stresses are function of time, the failure criteria that has to be applied is the theory of *Fatigue of Material.*
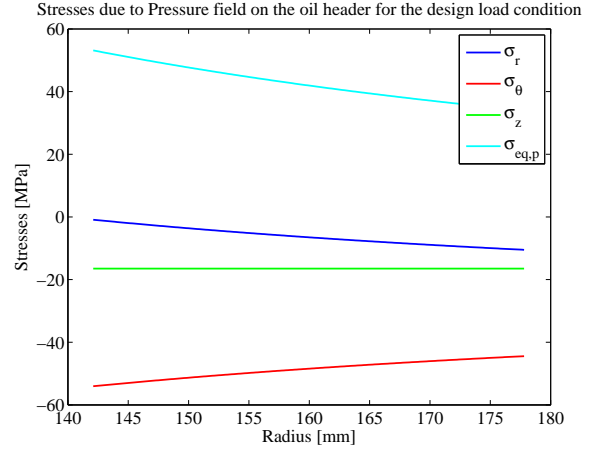

Figure 6: Stresses due to the Pressure field at the design load

Fatigue Analysis. Empirical curves of fatigue endurance have to be applied, but these curves are rarely available, due to the long time required for their estimation. In this project, the *Fatigue Life Evaluation* is carried out using the S-N curves, Basquin law, Goodman diagram and Sines equivalent stress criteria for ductile materials, as explained in [13], [14], [15] and [16].

The first step is to calculate the total transient stress state, caused by the pressure and temperature effect in the header thick-wall. The total stress state is simply the linear superposition of the temperature and pressure derived tension state, as they are independent. Therefore the total radial, tangential and axial stress are calculated as in Equation 17, where j=r,θ,z.

$$\sigma_{j,tot} = \sigma_{j,p} + \sigma_{j,th} \tag{17}$$

At a fixed time, the tension state is expressed in the header by Figure 7.

At the internal radius, where there is the most critical tension state, Figure 8 shows how is the evolution during the time of the total principal stresses. When assuming the start-up as a daily process, followed by the plant shut-down, repeated every day, a repeated alternating stress cycle in the time occurs.

This stress cycle is an alternating cycle with a maximum and minimum stress and a trapezoidal wave form. An holding time between the cycling part of the stress, corresponding to the daily design load at steady state and the night closing down time of the plant is present. The triaxial total state of
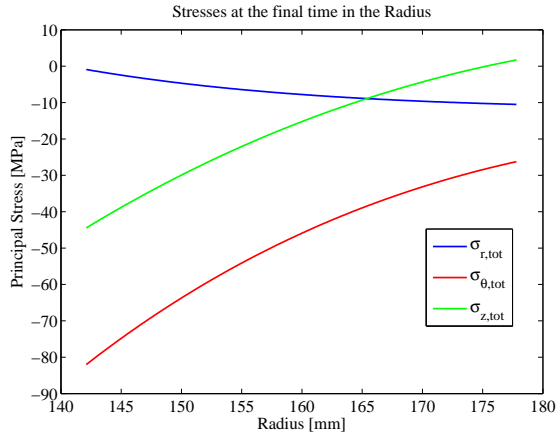
5

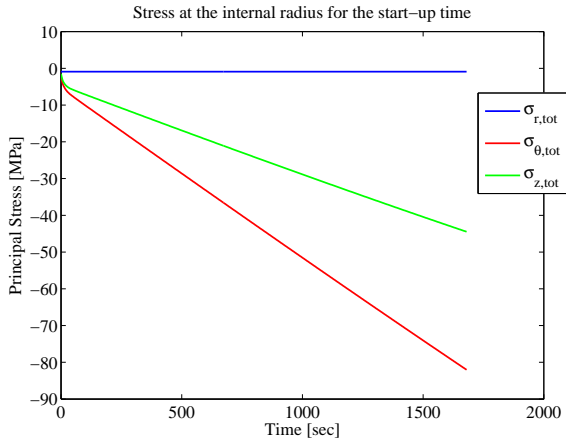Figure 7: Principal stresses at the design load in the outlet header

Figure 8: Principal stresses at the internal radius for the start-up time

stress in the time has an alternating component and a mean component of all the three principal stresses as calculated in Eq. 18 and 19 where j=r,θ,z.

$$\sigma_{a,j} = \frac{\sigma_{max,j} - \sigma_{min,j}}{2} \qquad (18)$$

$$\sigma_{m,j} = \frac{\sigma_{max,j} + \sigma_{min,j}}{2} \qquad (19)$$

Moreover it is important to consider that the applied stresses and fatigue happens at high temperature where it has been proven that there is an interaction between *Creep* and *Fatigue* [3].

—————————
[3]But the ASME code [17] suggests to consider creep in

When the nominal *alternating* stresses and nominal *mean* stresses are computed from the alternating cycle, the presence of several holes in the oil header is taken into consideration for calculating the effective stresses. The holes contribute to generate a peak of stress on the surface of the header in the proximity of the hole, that can be calculated using the stress concentration factor K [18]. In fatigue conditions the concentration factor does not apply totally to the intensification of the stress, and the fatigue concentration factor is calculated with the Peterson equation [18].

When the effective stresses are known, an equivalent stress from the triaxial state of stress has to be obtained in order to be able to use the S-N curves necessary for estimating the fatigue life. For cylindrical vessel under triaxial stress state the Sines criteria is used for calculating an equivalent stress, from the three principal effective stresses, [18].

A point corresponding to $\sigma_{a,eq}$ and $\sigma_{m,eq}$ as an equivalent uni-dimensional state of stress in the Goodman diagram is found. The Goodman diagram represents a way of computing an effective pure alternate stress that can be used in the S-N curve (also known as Wöhler curve) , from the total state of stress, and is expressed in the Goodman relationship, Eq. 20.

$$\sigma_a = S_N \cdot \left(1 - \frac{\sigma_m}{\sigma_{yield}}\right) \qquad (20)$$

S_N is then used in the Wöhler curve to calculate N, the number of cycle before rupture. In order to calculate the S-N curve for the oil header, the Basquin law it is used combined with the Marin formulation, [16].

4. Results

For the specific case of this project, assuming a start-up procedure that follows the maximum allowable thermal gradient in the drum of the CSP plant of 5 K/min from the morning conditions, the warm start-up takes approximately 28 min. For this procedure for the case of the outlet oil header the number of cycles to rupture was calculated to be approx. N = 5700, that corresponds to approx.

—————————
SA 106 B, the steel of the oil header, only above 370°C, that is actually the maximum temperature at the design load case for the oil. Therefore creep is not considered.

6

16 years (if a warm start-up is considered every day of the year). If a faster start-up procedure is followed, the same analysis can be carried out. New temperature profiles during time are calculated and different thermal stresses occurs. This results in a different fatigue damage that can be calculated related to how fast the start-up is. Thus a number of cycle to rupture, following the faster start-up is calculated for the outlet oil header as showed in Table 4. It can be seen how having faster a start-up is more critical for the component.

Table 1: Start-up time and corresponding fatigue life

Gradient followed	Start-up time [min]	Fatigue life [years]
3 K/min	*47*	*6800 cycles ≈ 19*
5 K/min	*28*	*5700 cycles ≈ 16*
7 K/min	*20*	*4600 cycles ≈ 13*

5. Discussion and Optimization

A sensitivity analysis on the influence of the oil circuit pressure was carried out. The oil pressure was varied in a feasible range, compared to the CSP plant operational parameters, and Figure 9 summarizes the results. It can be seen from Figure 9 that the life time of the header is highly influenced by the oil circuit pressure. An increasing oil pressure leads to longer fatigue lives. For example if the oil pressure is changed from 10 bar to 100 bar there is an improvement of the fatigue life by a factor of five. This is due to the pressure state of stress that is opposite to the temperature state of stress, and therefore the resultant state of stress is lower, and induces a smaller fatigue damage. [4]

The thickness of the oil header is also a key parameter and highly affects the value of the pressure and thermal stresses. It is easy to understand analyzing Equations 11, 12 and 13 for the thermal stresses in plane strain and Equations 14, 15 and 16 for the pressure stresses. Once a range of feasible values in which varying the thickness is found, the

---

[4] Of course the oil circuit pressure modification from 10 bar to 100 bar, has to be thoroughly investigated when applied to all the components of the oil circuit. It has to be a value that does not exceed other limits for other part of the plant. The value of 100 bar is an tentative value that expresses the high influence of the oil circuit pressure on the effective life of the oil headers.
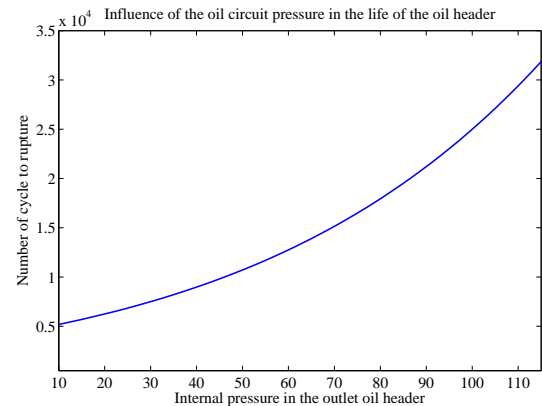
Figure 9: Influence of the oil pressure in the fatigue life of the Outlet Header for a start-up of 20 min

sensitivity analysis can be carried out for what concerns the thickness. Varying the thickness value for the outlet header and repeating the fatigue life calculation for each value, Figure 10 was found. There is an optimum in the value of the thickness at fixed R_{in} that gives a maximum fatigue life of the component with the right thickness value. The optimum depends on the thermal and pressure stresses and therefore on the start-up time and scenarios. It is therefore interesting at the design phase to take into account the thickness value as a parameter affecting the effective life of the header. The faster is the start-up and the lower is the thickness optimum value as shown in Table 2.
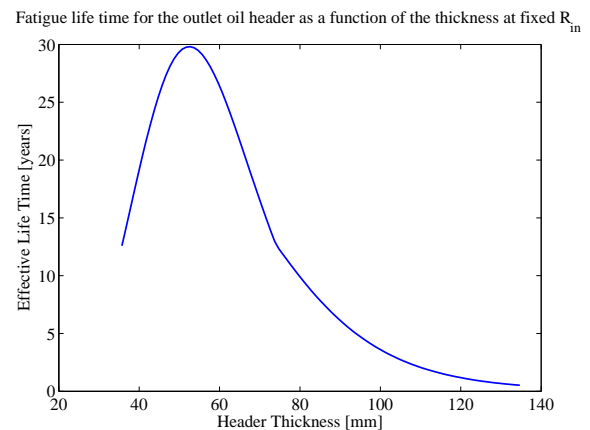
Figure 10: Fatigue Life for the Outlet Header as a function of the header thickness

This is because the thickness value is influenced with an upper limit from the thermal stresses. The higher the thermal stresses are and the lower is

Table 2: Optimized outlet header thickness

Start-up time	Optimum thickness
15 minutes	*47 mm*
20 minutes	*53 mm*
28 minutes	*58 mm*

the upper limit value on the header thickness. So faster start-up, means higher thermal stresses and lower optimum thickness of the header. Table 5 summarizes the main results and the optimizations. WSU20 stands for a warm start-up that takes 20 minutes. WSU20OHT is the WSU20 scenario with the optimum header thickness value.

Table 3: Main results of the Analysis on the Effective Life Time of the Outlet Oil Header

Scenarios	ELT [years]
WSU20	13
WSU28	16
WSU47	19
WSU20 & 100 bar oil pressure	68
WSU20OHT	29
WSU20OHT & 100 bar oil pressure	90
WSU20 & oil pressure ≡ drum pressure	≥ 100
WSU10 & overall optimization	25

Another way to optimize the oil circuit pressure is finding the best oil pressure profile as a function of time during the start-up. It was found that a oil pressure profile that follows the drum pressure building-up during the start-up is a very good strategy in order to drastically reduce the pressure stresses in the header and therefore the total state of tension. Since the pressure in the system is high, also the stresses related are significant. Reducing them, means reduce an high component of the state of tension. In fact the outlet header for a start-up of 20 minutes, that has a calculated ELT of approximately 13 years, reaches a calculated ELT of more than 100 years if the oil pressure follows exactly the drum pressure at any time during the start-up. See Table 5 .

6. Conclusions

Using the thermodynamic model developed for the tube bundle in the evaporator it was possible to predict the behavior of the evaporation process inside the tube bundle for different load conditions, and also the behavior of several variables with accuracy in the 3D space inside the shell of the evaporator. Knowing the temperature in the evaporator, and using a quasi-static stress analysis it was possible to investigate the oil headers and understand how they react to different loads and scenarios. Results show that not only the thermal stresses are significant but also the pressure stresses have to be considered.

When the stresses are calculated for different load cases, using a fatigue life calculation method it was possible to study the effect on the life of the oil headers for different start-up procedures. Several sensitivity analysis were carried out on the importance of start-up time, oil circuit pressure and header thickness.

It was found that the value of the oil circuit pressure is extremely important on determining the total state of stress in the headers, and therefore their effective life time. If the right value of the pressure is used in the CSP plant, the effective fatigue life can be increased significantly. This means that the headers would not be a critical component for the plant anymore, regarding the start-up procedure, and this would make a faster start-up possible. Also the value of the thickness of the header is very important and can lead to significant improvement of the effective life time. If the thickness is increased from 36 mm to the optimum value the life is increased up to more than double.

Having a 10 minutes faster start-up in the morning of one CSP plants of 75 MW, leads to an energy production higher of 12.5 MWh every day and more than 4500 MWh_{el} a year. This means that, if there are 6 CSP plants of 75 MW each run by a Company, the annual income would be approximately 1 Million dollars higher [5]. With the study developed it was indeed possible to find the right design value for several parameters in order to increase the effective life of the system and therefore be able to have a several minutes faster start-up.

A Analysis of the same kind can be applied to similar systems in thermal power plants of different kinds, in order to improve their flexibility regarding transient conditions. This means moving towards the possibility to increase the share of renewable and unpredictable energy sources in the electricity grid.

---

[5]Considering 40$/$MWh$ as the price of the produced electricity.

8

Nomenclature

Symbol	Name	Unit
α	Thermal diffusivity	m^2/s
α	Coefficient of linear thermal expansion	K^{-1}
A	Area	m^2
C	Flow Stream Heat Capacity	$W/K, \%$
χ	A-dimensional length along z	$-$
E	Young Module	GPa
h	Heat transfer coefficient	W/m^2K
k	Thermal conductivity	W/mK
K	NTU constant	$-$
$L1$	Longitudinal dimension along z	m
$L2$	Vertical Dimension along y	m
m	Mass flow	kg/s
NTU	Number of transfer unit	$-$
ν	Poisson Module	$-$
P	Pressure	bar
q	Heat flux	W/m^2
r	radius	mm
R	radius	mm
S	Stress	MPa
σ	Stress	MPa
t	Time	sec
T	Temperature	C, K
U	Overall heat transfer coefficient	W/m^2K
θ	A-dimensional Temperature	$-$
ξ	A-dimensional length along y	$-$
y	Vertical coordinate	m
z	Longitudinal coordinate	m

Subscript

1	Oil
1	Water
a	Alternate
e	External
i	Internal
in	Inlet
m	Mean
max	Max
$mean$	Mean
min	Min
N	Number of cycle
o	External
oil	Oil
out	Outlet
p	Pressure
r	Radial
th	Thermal
θ	Tangential
w	Wall
w/s	Water/steam
$yield$	Yield
z	Axial
$*$	Min/Max Ratio

References

[1] Joint-Research-Centre, Solar radiation, Website, last checked: 5.06.2014 (2014).
URL http://re.jrc.ec.europa.eu

[2] SBC, Economic opportunities resulting from a global deployment of concentrated solar power (csp) technologies, Energy Police.

[3] AalborgCSP, Aalborg csp, Website, last checked: 5.06.2014 (2014).
URL http://www.aalborgcsp.com/

[4] R. K. Shah, D. Sekulic, Fundamentals of heat exchanger design, 1st Edition, Wiley India, 2003, iSBN-10: 0471321710.

[5] Y. A. Cengel, J. Ghajar, Heat and Mass Transfer, 4th Edition, Mc Graw Hill, 2011.

[6] J. G. Collier, J. R. Thome, Covective boiling and condensation, 3rd Edition, Oxford University Press, 1994, iSBN: 0191591262.

[7] K. Stephan, M. Abdelsalam, Heattransfer correlations for natural convection boiling., International Journal of Heat and Mass Transfer, 23(1):7387.

[8] R. G., S. J. J. M., , da Silva E. F., Modeling and experimental study of nucleate boiling on a vertical array of horizontal plain tubes., Experimental Thermal and Fluid Science, 32(8):15301537.

[9] A. Franco, Conversations and courses material, Conversation at Pisa University.

[10] R. F. Barron, B. R. Barron, Design for Thermal Stresses, 1st Edition, Wiley, 2011, iSBN: 978-0-470-62769-3.

[11] A.Kandil, A. El-Kady, A. El-Kafrawy, Transient thermal stress analysis for thick-walled cylinder, Int. J. Mech. Sci. Vol. 37, No. 7, pp. 721-732, 1995.

[12] J. M. Gere, S. P. Timoshenko, Mechanics of Materials, 5th Edition, PWS Kent Publishing, 1970.

[13] P. Forte, Conversation and courses material and lectures, Master in Energy Engineering at Pisa University.

[14] R. C. Juvinall, K. M. Marsheck, Fondamenti della progettazione dei componenti nelle macchine, 1st Edition, Edizioni ETS, 2001, iSBN :88-7741-730-7.

[15] R. Hetnarski, M. Eslami, Thermal Stresses- Advanced Theory and Applications, 1st Edition, Springer, 2009, iSBN 978-1-4020-9246-6.

[16] R. Budynas, J. Nisbett, Shigley's Mechanical Engineering Design, 9th Edition, Mc Graw Hill, 2010, iSBN-10: 0077942906.

[17] ASME, ASME Boiler and Pressure Vessel Code (BPVC) — 2013 (2013).

[18] A. D. Paulis, E. Manfredi, Costruzione di Macchine, 1st Edition, Pearson, 2012, iSBN : 978-88-7192-783-1.

9

PDE MODELING WITH MODELICA VIA FMI IMPORT OF HIFLOW3 C++ COMPONENTS WITH PARALLEL MULTI-CORE SIMULATIONS

Kristian Stavåker, and Peter Fritzson
{ Kristian.Stavaker, Peter.Fritzson }@liu.se
Programming Environments Laboratory
Department of Computer and Information Science
Linköping University
Sweden

Chen Song, Martin Wlotzka, and Vincent Heuveline
{ Chen.Song, Martin.Wlotzka, Vincent.Heuveline }@iwr.uni-heidelberg.de
Engineering Mathematics and Computing Laboratory
Interdisciplinary Center for Scientific Computing
University of Heidelberg
Germany

ABSTRACT

The Modelica modeling and simulation language is widely used in academia and industry to model complex, coupled dynamic systems which can be described by systems of ordinary differential equations (ODE) or differential algebraic equations (DAE). Recent work by the authors showed a way to enable partial differential equation (PDE) modeling with Modelica via functional mock-up interface (FMI) import of C++ components based on the multi-purpose finite element library HiFlow3. The finite element method (FEM) is largely used in both research and industry as a reliable technique for solving PDE problems. In contrast to methods based on language extensions or automatic semi-discretizations in space, the approach with FMI import of HiFlow3 components into Modelica requires no change to the Modelica language, enables the use of specialized PDE solvers, and it allows for full flexibility in the choice of geometry, model parameters, and space discretization between simulation runs without recompilation. However, the computationally intensive PDE solving part in this approach can form a bottleneck in the simulations. In this work, we enhance the PDE solver by using a distributed memory parallelization based on a domain decomposition. As an example application, we consider a mechanical linear elasticity problem consisting of physical forces applied on a beam. Beams, plates and shells are common elements of solid structures with a sizable quantity of application in engineering design, appearing in fuselage, ship hulls, concrete roof structure, etc. The derivation of elastic stress strain relations is a crucial point for mechanical analysis and validation, as the bending properties of the structure effects greatly the stability properties. In this work the actual beam is modeled and solved in parallel using a C++ HiFlow3 component whereas the physical force acting on the beam is modeled using Modelica. We use the OpenModelica development environment but the same approach can be adapted to other Modelica environments.

Keywords: Modelica, HiFlow3, OpenModelica, Partial Differential Equations, Finite Element Method, Functional Mock-Up Interface, Multi-Core, Parallel Computing

INTRODUCTION

This paper is a continuation of the work in [20]. We discuss numerical simulation of models that couple partial differential equations (PDEs) and differential-algebraic equations (DAEs) in the context of the Modelica modeling and simulation language [14, 5, 6]. Modelica originated around the idea of solving complex coupled dynamic systems, which can be described by systems of ordinary differential equations (ODE) or DAE. Up to now, there is only limited support for working with PDEs, despite the fact that the number of Modelica users in academia and in industry has lately grown significantly.

Some attempts of incorporating PDE support into Modelica are described in [11], [12] and in Chapter 8 of [5]. In [18] and [17] two different approaches are investigated: (1) expressing the PDEs using a combination of new language constructs and a supporting Modelica PDE library using the method-of-lines; (2) exporting the PDE part to an external PDE FEM C++ tool which solves the PDE part of the total problem. Based on this work, an experimental implementation of PDE support was added to the OpenModelica [3] compiler. However, this implementation has not been maintained, even though there have recently been discussions in the Open-Modelica community about re-activating these features. Only one simple PDE operator is currently in the official Modelica language specification: spatial distribution for 1D PDEs. In [10] a Modelica library with basic building blocks for solving one-dimensional PDE with spatial discretizations based on the method of lines or finite volumes is described. Although this approach is attractive due to its simplicity, it is not clear how it could be extended to higher dimensions, without increasing the complexity significantly.

In this work, we propose a way to allow for PDE modeling with Modelica by importing C++ components, written with the HiFlow3 multi-purpose finite element software [19], into Modelica using the Functional Mock-Up Interface (FMI) [15] import. FMI is a standard for model exchange and co-simulation between different tools. FMI supports only C but with correct linking it is possible to execute with C++ code. We use the OpenModelica [3] development environment but the same approach can be adapted to other Modelica environments. As noted earlier, this paper is a continuation of the work in [20]. In that paper the heat distribution was computed for a copper beam. The heat source was controlled by a PID-controller. In this paper we continue to explore the Modelica-HiFlow3 coupling with parallel computations on multi-core architectures. We use a model of a steal beam with a force acting on it to demonstrate our implementation. We measure the elasticity deformation of the beam. In this work the actual membrane plate is modelled and solved in parallel using a C++ HiFlow3[13, 16] component whereas the physical force acting on the beam is modeled using Modelica.

The method described in this paper and in [20] has several advantages:

- HiFlow3 is well maintained and has strong support and capabilities for PDE modeling and solving;

- HiFlow3 and OpenModelica are free to download and use;

- The PDE structure is not lost but is maintained throughout the actual run-time simulation process. This allows for mesh refinement, solver run-time adjustments, etc.;

- It is possible to mix PDE and DAE systems in the same system setting. This is also possible in [10].

SIMULATION SCENARIO

We consider the deformation of a rectangular building element under a load. Fig.1 shows the setup of
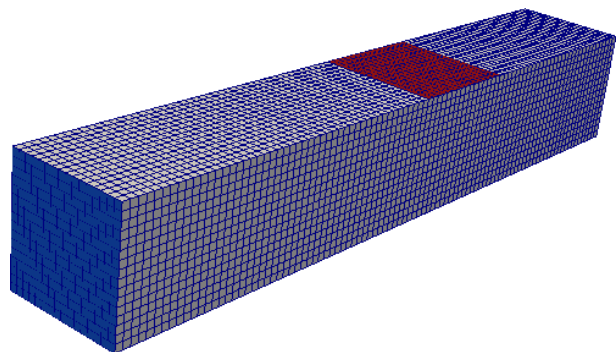

Figure 1: Geometry and computational mesh for the concrete element. The fixed front end is colored in blue, a force is acting on the red part.

the configuration. The element is fixed at both ends, and the load is modeled by an external force acting on a part of the upper boundary.

Linear Elasticity Model

The element occupies a domain $\Omega \subset \mathbb{R}^3$ with boundary $\Gamma := \partial\Omega$. The behaviour of the object subject to a force is described by means of the displacement $\boldsymbol{u}$ and the stress tensor σ. Conservation of momentum leads to the equilibrium equation

$$-\nabla \cdot \left([I + \nabla u]\sigma\right) = \rho \boldsymbol{f} \quad \text{in } \Omega, \qquad (1)$$

where ρ is the density of the material, $\boldsymbol{f}$ is a volumetric force, and I denotes the identity matrix. In our scenario, gravity is the only volumetric force, therefore $\boldsymbol{f} = -g\boldsymbol{e}_z$.

According to Hooke's law for isotropic materials the stress tensor is related to the deformation tensor ε as

$$\sigma = 2\mu\varepsilon + \lambda \operatorname{tr}(\varepsilon)I,$$

with material parameters μ and λ, known as the Lamé elasticity constants. Assuming small deformations, we neglect nonlinear terms in the deformation tensor resulting in the linearised form [2]

$$\varepsilon \approx \frac{1}{2}(\nabla u + \nabla u^\top),$$

and also the deformation gradient is simplified as

$$I + \nabla u \approx I.$$

This leads to the following problem formulation:

Find a function $\boldsymbol{u} : \Omega \to \mathbb{R}^3$ as the solution of

$$-\mu\nabla \cdot (\nabla u + \nabla u^\top) - \lambda\nabla(\nabla \cdot u) = \rho \boldsymbol{f} \quad \text{in } \Omega, \quad (2a)$$

$$u = 0 \quad \text{on } \Gamma_0, \tag{2b}$$

$$\left[\mu(\nabla u + \nabla u^\top) + \lambda(\nabla \cdot u)I\right] \cdot \boldsymbol{n} = p \quad \text{on } \Gamma_1, \tag{2c}$$

$$\left[\mu(\nabla u + \nabla u^\top) + \lambda(\nabla \cdot u)I\right] \cdot \boldsymbol{n} = 0 \quad \text{on } \Gamma_f. \tag{2d}$$

The homogeneous Dirichlet boundary condition (2b) fixes the beam at its ends. The load on the beam acts as a pressure p through the Neumann boundary condition (2c), and the homogeneous Neumann condition (2d) is imposed on the free part of the boundary.

Variational Formulation

A well-established method for numerically solving PDEs is the finite element method, which is based on a variational formulation of the system (2).

Assuming that there is a classical solution $u \in C^2(\Omega, \mathbb{R}^3)$ of problem (2), equation (2a) is multiplied by a test function $v \in C_0^\infty(\Omega)$ and integrated over Ω:

$$-\mu \int_\Omega \left[\nabla \cdot (\nabla u + \nabla u^\top)\right] \cdot v \, dx$$

$$-\lambda \int_\Omega \left[\nabla(\nabla \cdot u)\right] \cdot v \, dx = \int_\Omega \rho f \cdot v \, dx$$

The divergence theorem yields (note that $\nabla v = \nabla v^\top$)

$$-\mu \int_\Omega \left[\nabla \cdot (\nabla u + \nabla u^\top)\right] \cdot v \, dx$$

$$= \frac{\mu}{2} \int_\Omega (\nabla u + \nabla u^\top) : (\nabla v + \nabla v^\top) \, dx$$

and

$$-\lambda \int_\Omega \left[\nabla(\nabla \cdot u)\right] \cdot v \, dx = \lambda \int_\Omega (\nabla \cdot u)(\nabla \cdot v) \, dx,$$

where the boundary integrals are omitted since they vanish as $v = 0$ on $\partial\Omega$. This leads to

$$\int_\Omega \frac{\mu}{2}(\nabla u + \nabla u^\top) : (\nabla v + \nabla v^\top)$$

$$+ \lambda(\nabla \cdot u)(\nabla \cdot v) \, dx = \int_\Omega \rho f \cdot v \, dx. \quad (3)$$

For equation (3) to be well-defined, weaker regularity properties of u and v than in the classical context are sufficient. The problem can be formulated in terms of the Lebesgue space $[L^2(\Omega)]^3$ of square-integrable functions defined on Ω and with image in $\mathbb{R}^3$, and the Sobolev space $[H^1(\Omega)]^3$ of functions in $[L^2(\Omega)]^3$ with square-integrable weak derivatives. We define the weak solution space

$$V := \{u \in [H^1(\Omega)]^3 : u = 0 \text{ on } \Gamma_0\},$$

the bilinear form

$$a : [H^1(\Omega)]^3 \times [H^1(\Omega)]^3 \to \mathbb{R},$$

$$a(u,v) := \int_\Omega \frac{\mu}{2}(\nabla u + \nabla u^\top) : (\nabla v + \nabla v^\top)$$

$$+ \lambda(\nabla \cdot u)(\nabla \cdot v) \, dx,$$

and the linear form

$$l : [H^1(\Omega)]^3 \to \mathbb{R},$$

$$l(v) := \int_\Omega \rho f \cdot v \, dx + \int_{\Gamma_0} p \cdot v \, ds.$$

Note that the bilinear form a is symmetric, continuous and V-elliptic. Now we can state the variational formulation of problem (2):

Find $u \in V$ as the solution of

$$a(u, v) = l(v) \quad \forall v \in V. \tag{4}$$

This variational formulation admits a unique solution, which is called the weak solution of the elasticity problem.

Finite Element Discretization

Let $T_h := \{K_1, ..., K_N\}$ be a triangulation of Ω with N tetrahedron cells $K_i \, (i = 1, ..., N)$. We define the finite element space of piecewise linear functions

$$V_h := \{v \in V : v|_K \text{ is linear } (K \in T_h)\}.$$

V_h has the finite dimension $n := \dim(V_h)$. We give the problem formulation for a conforming finite element approximation of (4):
Find $u_h \in V_h$ as the solution of

$$a(u_h, v_h) = l(v_h) \quad \forall v_h \in V_h. \tag{5}$$

Let $\{\varphi_1, ..., \varphi_n\}$ be a basis of V_h. We define the ansatz function as :

$$u_h(x) := \sum_{i=1}^n x_i \varphi_i(x)$$

with coefficients $x_i \in \mathbb{R}$ and insert it into (5), yielding

$$\sum_{i=1}^n x_i a(\varphi_i, \varphi_j) = b(\varphi_j) \quad (j = 1, ..., n).$$

This can be written as the linear system

$$Ax = b, \tag{6}$$

where

$$A := \left(a(\varphi_j, \varphi_i) \right)_{i,j=1,...,n} \in \mathbb{R}^{n \times n}$$

is the stiffness matrix and

$$b := \left(l(\varphi_i) \right)_{i=1,...,n} \in \mathbb{R}^n$$

is the load vector. As the stiffness matrix is symmetric and positive definite [2], we employ the Conjugate Gradient (CG) method [7] for solving (6).

COUPLED IMPLEMENTATION
More details of the coupled simulation setup can be found in [20].

The Modelica Modeling and Simulation Language

Modelica is a language for equation-based object-oriented mathematical modeling which is being developed and standardized through an international effort in the Modelica Association [14]. The equation parts of Modelica requires a lot of the compiler developer: knowledge in compiler construction, symbolic manipulation of equations and associated mathematics, as well as knowledge of numerical mathematics. The simulation run-time system is also an important part and can be complex; various solver techniques for solving the differential equations can be applied. Modelica allows high-level concepts such as object-oriented modeling and component composition. Multi-domain modeling is also possible in Modelica with the possibility of combining model components from a variety of domains within the same application. There exist several mature and well-maintained Modelica development environments, such as Dymola, OpenModelica, MapleSim, Wolfram SystemModeler, Simulation X, and JModelica.org. See [5] and [6] for more information on the Modelica language.

The OpenModelica Environment

OpenModelica is a modeling and simulation environment, which is developed and supported by an international consortium, the Open Source Modelica Consortium (OSMC) [3]. This effort includes an open-source implementation of a Modelica compiler, a simulator and a development environment for research, education and industrial purposes.

The HiFlow3 Finite Element Library

HiFlow3 [19, 1] is a multi-purpose finite element software providing powerful tools for efficient and accurate solution of a wide range of problems modeled by partial differential equations (PDEs). Based on object-oriented concepts and the full capabilities of C++ the HiFlow3 project follows a modular and generic approach for building efficient parallel numerical solvers. It provides highly capable modules

dealing with mesh setup, finite element spaces, degrees of freedom, linear algebra routines, numerical solvers, and output data for visualization. Parallelism - as the basis for high performance simulations on modern computing systems - is introduced at two levels: coarse-grained parallelism by means of distributed grids and distributed data structures, and fine-grained parallelism by means of platform-optimized linear algebra back-ends.

HiFlow3-based PDE Component

HiFlow3 is a multi-purpose finite element method orientated mathematical library, it is well designed for modular and generic approach. Considering our application, HiFlow3's modules provide us an efficient computing platform [1] for things such as mesh setting, finite element function spaces, linear algebra structure, numerical solvers, etc. HiFlow3 also provides a well-defined parallel environment which allows to build up our elasticity solver as a robust component that we can execute on large scale machines with respect to high performance computing (HPC).

Modelica Model

Our (relatively simple) Modelica model is shown in Listing 1. It contains the PDE component and the force variable. The variables $hfBlock.stateVar$ and $hfBlock.der_stateVar$ don't do anything useful but are in the model because the OpenModelica runtime system needs at least one state variable to operate.

Listing 1: Modelica model.

```
// _____
//   ElasticitySolver
// FMI application  with
// HiFlow^3 block  for  PDE solving.
//
// Authors:
// Chen Song, Martin Wlotzka,
//  Kristian  Stavaker
//
// Main class
model  ElasticitySolver
   // HiFlow^3 component
   ElasticitySolver_me_FMU hfBlock;
```

```
 // Source  for  signals  that
 // should  be  constantly  0
 Modelica.Blocks.Sources.Constant
    zeroSource(k=0.0);

 Real  u_center( start =0.0);
 Real  force( start =10.0);
equation
 connect(hfBlock.u_center,  u_center );
 connect( force ,hfBlock.force );
  force  =  10.0;
 connect(hfBlock. der_stateVar ,
    zeroSource.y );
 connect(hfBlock. stateVar ,
    zeroSource.y );
end  ElasticitySolver ;
```

PARALLELIZATION CONCEPT

The parallelization concept of HiFlow3 is based on a decomposition of the spatial domain into a number of subdomains. For distributed memory systems, the message passing interface (MPI) [4] is used for data transfer. Each MPI process is dedicated to the computation for one of the subdomains. Hereby, work is distributed among the processes. After creating the mesh, that our finite element discretization is based on, the METIS graph partitioner [9] is used to determine a balanced partitioning of the mesh according to the number of MPI processes. Each process then only stores one part of the global mesh. Couplings between neighbouring parts are taken into account by means of a layer of ghost cells. Figure 2 shows an example of a domain decomposition into 8 parts. The matrix and vector data structures in HiFlow3 are
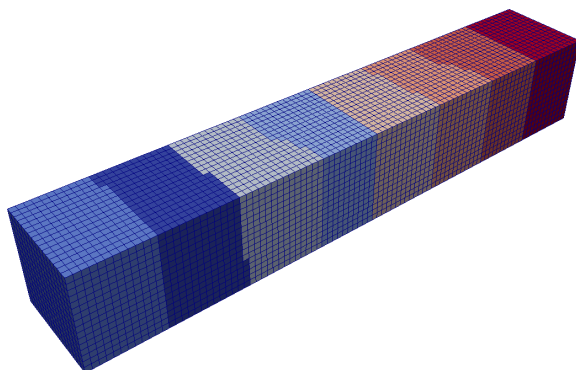

Figure 2: Partitioning of the mesh into 8 subdomains, indicated by different color.

distributed data structures which fit the partitioning imposed by the domain decomposition. Each process holds exactly those degrees of freedom of the finite element space which belong to its part of the domain. Couplings between different partitions are achieved by using ghost degrees of freedom. Only these have to be exchanged during parallel matrix-vector-product execution.

Assembly of the system matrix and right-hand-side vector, i.e. the computation of the entries, is done independently on each process for the corresponding subdomain. Hereby, the assembling process is designed in two levels: The global assembler iterates concurrently on each subdomain over the cells, while the local assembler computes the contributions for any single cell. Once the matrix and vector are assembled, the Conjugate Gradient linear solver takes advantage of the parallel implementation of the matrix-vector-operations when computing the solution.

Parallel Execution of the Model

The Modelica compiled model code is executed on a number of processes. The Modelica compiled model code is hereby replicated on each process. Whenever the HiFlow3 PDE component is called, it performs distributed parallel computations for solving the elasticity problem, hereby taking advantage of its parallelization concept based on the domain decomposition.
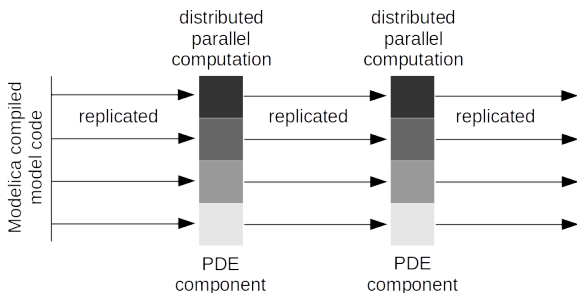
Figure 3: Replicated parallel execution of the Modelica compiled model code and distributed parallel computation in the HiFlow3 PDE component, sketched for 4 processes.

NUMERICAL EXPERIMENTS

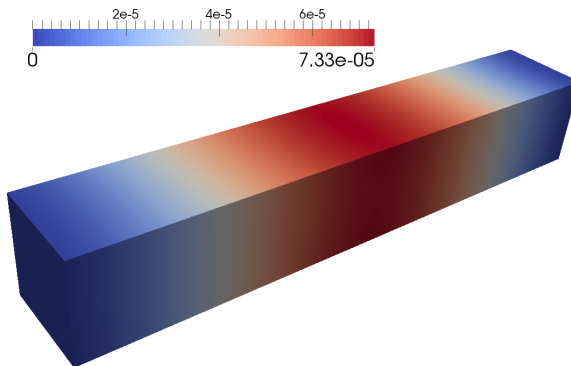We carried out a series of test runs with number of processes $n \in \{1, 2, 4, 8, 16\}$. We measured the run-

Figure 4: Visualization of the displacement in vertical direction.

time T_n for the PDE component when running on n processes. To asses the parallel performance of the solver, we computed the speedup

$$S_n := \frac{T_n}{T_1}$$

and the efficiency

$$E_n := \frac{S_n}{n},$$

where T_n is the run-time of the solver when executed on n MPI processes. Results are given in Table 1.

n	run-time T_n [sec]	speedup S_n	efficiency E_n
1	8.830	1.0	1.0
2	4.736	1.864	0.932
4	2.948	2.995	0.749
8	1.968	4.487	0.561
16	1.741	5.072	0.317

Table 1: Run-times for the PDE component with varying number of MPI processes.

Figure 5 shows a plot of the speedup and efficiency. The results show a parallel performance of the HiFlow3 PDE component within the Modelica context which is much poorer than the performance obtained for pure HiFlow3 applications. This is due to a technical reason: We needed to install a custom Open-MPI library, where we disabled the plugin architecture of the OpenMPI implementation on the machine while still using shared libraries. This was necessary for compiling the HiFlow3 PDE component into a dynamic shared object which can be loaded by the Modelica compiled model code during runtime. The diminished parallel efficiency is clearly due to the
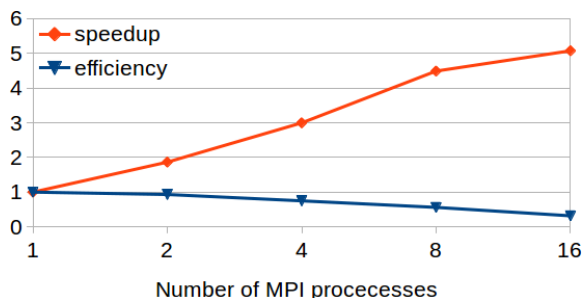
Figure 5: Parallel speedup and efficiency plot for $n = 1, 2, 4, 8, 16$ MPI processes.

use of such non-optimized MPI installation, since HiFlow3 shows good scalability on other machines with a high-performance MPI installation [8].

Nevertheless, we were able to leverage the parallel computing capabilities of HiFlow3 in the PDE component to introduce distributed memory parallelization for Modelica simulations. The performance tests show that even if parallel efficiency may not be optimal, our approach allows for solving large scale 3D PDE problems in high resolution on distributed memory machines. This is especially advantageous with respect to the amount of memory available, as the problem data can be split and distributed to several compute nodes, as opposed to a shared memory parallelization.

CONCLUSIONS

In this paper we have investigated a method of incorporating PDEs in the context of a Modelica model, by using FMI to import a PDE solver from the finite element library HiFlow3. Numerical results obtained using a simple coupled model that invoke a force and measures the elasticity deformation of a beam demoefficient and with already validated software. This paper is a continuation of a paper from the SIMS 2013 workshop [20]. In that paper the distribution of heat was measured in a piece of copper. The heat source was controlled by a PID-controller. A novelty in this paper is that we make use of parallel computations. The main advantages of this type of coupling include its simplicity and the possibility to reuse existing solver technology on multi-core and distributed memory architectures. In the results section we provided some run-time measurements of these parallel computations and compared to single-core computations. In-

duced by the needs for compiling the PDE component into a dynamic shared object and loading it by the Modelica compiled model code, limitations in the MPI library influenced the parallel performance. However, the speedup obtained is considerable in simulation practice, and the use of distributed memory architectures is a clear advantage with respect to memory, especially for large scale problems. In combination with our previous work reported in [20], this opens opportunities to address even more compute- and memory-intensive applications like instationary fluid dynamics problems. The parallelization approach with replication might seem somewhat clumsy. A better method would perhaps be to let the OpenModelica run-time system drive the parallel distribution. This is future work and it should be noted that the FMI places limits on parallel communication.

REFERENCES

[1] Hartwig Anzt, Werner Augustin, Martin Baumann, Thomas Gengenbach, Tobias Hahn, Andreas Helfrich-Schkarbanenko, Vincent Heuveline, Eva Ketelaer, Dimitar Lukarski, Andrea Nestler, Sebastian Ritterbusch, Bjoern Rocker, Staffan Ronnås, Michael Schick, Mareieke Schmidtobreick, Chandramowli Subramanian, Jan-Philipp Weiss, Florian Wilhelm, and Martin Wlotzka. Hiflow3 a multi-purpose and flexible parallel finite element package. pages 1–15, 2011.

[2] C.L. Dym and I.H. Shames. *Solid Mechanics: A Variational Approach, Augmented Edition*. Springer New York, 2013.

[3] The Open-Source OpenModelica Development Environment. http://www.openmodelica.org.

[4] Message Passing Interface Forum. *MPI: A Message-Passing Interface Standard, Version 3.0*. High-Performance Computing Center

Stuttgart (HLRS), 2012. http://www.mpi-forum.org.

[5] Peter Fritzson. *Principles of Object-Oriented Modeling and Simulation with Modelica 2.1.* Wiley-IEEE Press, 2004.

[6] Peter Fritzson. *Principles of Object-Oriented Modeling and Simulation with Modelica 3.3: A Cyber-Physical Approach. (to appear).* Wiley-IEEE Press, 2014.

[7] M. R. Hestenes and E. Stiefel. Methods of conjugate gradients for solving linear systems. *Journal of research of the National Bureau of Standards*, 49:409–436, 1952.

[8] Vincent Heuveline, Eva Ketelaer, Staffan Ronnas, Mareike Schmidtobreick, and Martin Wlotzka. Scalability study of hiflow3 based on a fluid flow channel benchmark. *8th BFG/bw-GRID Workshop Proceedings*, 2012.

[9] George Karypis and Vipin Kumar. A fast and high quality multilevel scheme for partitioning irregular graphs. *SIAM J. Sci. Comput.*, 20(1):359–392, December 1998.

[10] Zhihua Li, Ling Zheng, and Huili Zhang. Solving pde models in modelica. *2008 International Symposium on Information Science and Engieering. ISISE 08*, 1:53–57, 2008.

[11] Manuel Ljubijankić and Christoph Nytsch-Geusen. 3d/1d co-simulation von raumlufströmungen und einer luftheizung am beispiel eines thermischen modellhauses. *Fourth German-Austrian IBPSA Conference, BauSIM 2012, Berlin University of the Arts*, 2012.

[12] Manuel Ljubijankić, Christoph Nytsch-Geusen, Jörg Rädler, and Martin Löffler. Numerical coupling of modelica and cfd for building energy supply systems. *8th International Modelica Conference 2011*, 2011.

[13] Engineering Mathematics and Computing Lab (EMCL) publication database., 2014. http://emcl.iwr.uni-heidelberg.de/79.html.

[14] Modelica and the Modelica Association. http://www.modelica.org.

[15] Modelica Association. *Functional Mockup Interface for Model Exchange and Co-Simulation*, v. 2.0 beta 4 edition, 2012. https://www.fmi-standard.org/downloads [Accessed 2013-08-06].

[16] Preprint Series of Engineering Mathematics and Computing Lab (EMCL)., 2014. https://journals.ub.uni-heidelberg.de/index.php/emcl-pp/issue/archive.

[17] Levon Saldamli. *PDEModelica - A High-Level Language for Modeling with Partial Differential Equations.* Dissertation 1016, Department of Computer and Information Science, Linköping University, 2006. http://urn.kb.se/resolve?urn=urn:nbn:se:liu:diva-7281.

[18] Levon Saldamli, Bernhard Bachmann, Hans-Jürg Wiesmann, and Peter Fritzson. A framework for describing and solving pde models in modelica. *In Proceedings of the 4th International Modelica Conference, Hamburg, Germany, March 7-8*, 2005.

[19] The HiFlow3 Multi-Purpose Finite Element Software. http://www.hiflow3.org.

[20] Kristian Stavåker, Staffan Ronnås, Martin Wlotzka, Vincent Heuveline, and Peter Fritzson. Pde modeling with modelica via fmi import of hiflow3 c++ components. *Proceedings of SIMS 54th Conference, Bergen, Norway*, 2013.

EXPRESSING REQUIREMENTS IN MODELICA

Lena Buffoni[*] **and Peter Fritzson**
Linköping University
SE-581 83 Linköping
Sweden

ABSTRACT

As cyber-physical systems grow increasingly complex, the need for methodologies and tool support for an automated requirement verification process becomes evident. Expressing requirements in a computable form becomes a crucial step in defining such a process. The equation based declarative nature of the Modelica language makes it an ideal candidate for modeling a large subset of system requirements. Moreover, modeling both the requirements and the system itself in the same language presents numerous advantages. However, a certain semantic gap subsists between the notions used in requirement modeling and the concepts of cyber-physical modeling that Modelica relies on. To bridge this gap, in this paper, we illustrate through the use of dedicated types, pseudo function calls and function block libraries, how the Modelica language can be tailored to fit the needs of requirement modeling engineers.

Keywords: Requirements, Equation-based modeling

INTRODUCTION

Functional safety is a key concern in all industry sectors, be it nuclear plants, medical appliance manufactures or the automotive industry. The functional correctness of a component is the guarantee that the component behaves the way it should and fulfils all the functional requirements of the system. As the complexity of cyber-physical systems increases, maintaining coherent requirement specifications and using them to verify models of physical systems requires the formalisation of the requirements in a computable manner [2, 4]. In this paper, we propose an approach to formalising the requirements in the same language as the model of the physical system. For this purpose we choose Modelica, an object-oriented equation-based language for modeling multi-domain physical systems [5, 1].

Expressing requirements in the same language as the physical model has numerous advantages. It improves the maintainability of the overall model, ensures that the requirements stay coherent as the model changes and simplifies the verification process, as the requirements can be simulated together with the system model. However, engineers expressing requirements use domain specific terms and concepts [6]. Although requirement-specific notions can be expressed directly in Modelica, writing them from scrach every time manually can be complicated, and the resulting requirements can be harder to understand at first glance.

To bridge the gap between the requirement designer vision and the Modelica world, we define a set of types and pseudo functions, presented in the following section. A pseudo function is not a real function, since it allows side-effects and the use of time-dependent operators and equations in its body, which are disallowed in normal declarative Modelica functions. We extend Modelica with a mechanism for calling these pseudo functions, to simplify the readability of requirements. We illustrate these concepts on a simple example of a backup power system.

The paper is organized as follows. Section 2 introduces the notions used to map the requirements, Section 3 illustrates how the requirement verification is done, Section 4 discusses related works and finally

---

[*]Corresponding author: E-mail: lena.buffoni@liu.se

Section 5 summarizes the article and discusses future works.

MODELING REQUIREMENTS

In order to make the expression of requirements in Modelica as intuitive as possible in this section we introduce an approach of mapping concepts from the requirement modeling domain, such as those defined in [6] to the Modelica language.

Requirement Type

To treat requirements in a systematic manner, we need to define a dedicated requirement type. A requirement model should not influence the execution of the physical model, but only access the information from the physical model necessary for the requirement verification. Requirements are defined as special types of blocks: they have several inputs and a single output that represents the status of the requirement. A status can take the following values[11, 8]:

violated when the conditions of the requirement are not fulfilled by the design model;

not violated when the conditions of the requirement are fulfilled by the design model;

undefined when the requirement does not apply, for instance a requirement that describes the behaviour of a power system when it is switched on, cannot be verified when the system is off.

If we take the example of a simple backup power system, which consists of several blocks connected in parallel and operates when the main power supply is lost, we can model a simple requirement *"When the power is on, the backup power-supply must not be activated"*, as follows in standard Modelica:

```
block R1
   extends Requirement;
   input Boolean powerOn;
   input Boolean bPSOn;
 equation
   status = if powerOn then
               if bPSOn then
                  violated
               else not_violated
            else undefined;
 end R1;
```

In the case of such a simple requirement, no additional construct are necessary.

"Pseudo Function" Library

To bridge the semantic gap between the concepts used in requirement modeling and Modelica, we propose to define a set of Modelica function blocks to represent basic requirement modeling constructs. As mentioned, function blocks are a modified version of standard Modelica blocks, with a single output that can be called using a function syntax.

In particular, the time locator properties as defined in [6], such as `after`, `WithinAfter`, `until`, `everyFor` can be defined as Modelica function blocks. These constructs are used to which define a period in time when a requirement should be verified.

For instance `everyFor(duration1, duration2)`, is a time locator that is used to define a requirement that must hold every duration1 seconds, for duration2 seconds.

Such constructs cannot be modeled as simple functions, as they are not context free and rely on time. Therefore to represent this `everyFor`, we can define the following Modelica function block:

```
function block everyAfter
  parameter Real everyT;
  parameter Real forT;
  output Boolean out;
protected
  Real tmp(start = 0);
equation
  when sample(0, everyT) then
    tmp = time;
  end when;
  if time > tmp + forT then
    out = false;
  else
    out = true;
  end if;
end everyAfter;
```

Requirements can then be expressed in terms of these basic building blocks in a more readable fashion. A set of predefined time locators based on the FORM-L specification is available, but the user can also define his own components.

Anonymous Function Blocks Through Function Calls

If we take another simple requirement for a backup power unit, *"Within 40 seconds of the power being lost, at least two sets must be powered"* and attempt to express it in Modelica, we will need to use the function block `withinAfter`, which is defined as follows:

```
function block withinAfter
  parameter Real withinT;
  input Boolean event(start = false)
    ;
  output Boolean out;
  protected
  Real time_event(start = -1);
equation
  when event then
    time_event = time;
  end when;
  if time_event > (-1) and
     time_event + withinT < time
     then
    out = true;
  else
    out = false;
  end if;
end withinAfter;
```

If we use standard Modelica blocks, then we need to explicitly create an instance of an withinAfter block and connect it to the corresponding inputs and outputs, which reduces the readability of the model. Therefore we propose to define a syntax for pseudo functions, where a function block can be called like a function by it's name and with parameters and input variables as arguments. We have implemented an extension in OpenModelica[7], that will automatically generate an instance of the required function block and the corresponding connection equations.

With this syntax, we can define the above requirement in Modelica as follows:

```
block R2
    extends Requirement;
    input Boolean[5] isOn;
    input Boolean powerLoss;
    output Integer status(start = 0)
        ;
    Boolean wA;
  equation
    wA = withinAfter(40, powerLoss);
    when wA then
```

```
    status = if countTrue(isOn) >=
        2 then
      not_violated else violated;
    elsewhen not wA then
      status = undefined;
    end when;
  end R2;
```

In this example, the function block withinAfter, is called as a function, and the arguments of the call represent the values that the function block should be instantiated with. The parameter withinT should take the value 40, and the signal powerLoss should be connected with the input event.

To generate this transformation we call the function `rewriteFunctionBlockCalls(modelToRewrite, libraryPackage)` in the OpenModelica API. This function will take two arguments, the model that needs to be rewritten and a package containing the function block definitions. It will then parse all the function calls, and replace all the calls to functions with the same names as the function blocks in the package passed in parameters with instantiations of the corresponding function blocks in the declaration section, and the result of pseudo function call will be the single output of the function block. The updated model is then reloaded into memory and can be simulated.

The argument passing works in the same way as for normal function calls, the positional instantiation will bind the values passed to the function call to the parameters and input variables of the function block in the order in which they are defined. Arguments can also be named explicitly, in which case the corresponding input value or parameter will be instantiated with the expression passed to the function.

Saving a model after `rewriteBlockCalls` was called on it will generate standard Modelica code, for instance for the example above:

```
block R2
    extends Requirement;
    input Boolean[5] isOn;
    input Boolean powerLoss;
    output Integer status(start = 0)
        ;
    Boolean wA;
    withinAfter _agen_withinAfter1(
        withinT = 40);
  equation
    _agen_withinAfter1.event =
      powerLoss;
    wA = withinAfter(40, powerLoss);
```

```
  when wA then
    status = if countTrue(isOn) >=
        2 then 1 else -1;
  elsewhen not wA then
    status = 0;
  end when;
end R2;
```

The extra step of generating standard Modelica code is important, as it allows to export the resulting models in standard Modelica, compatible with any Modelica tools, therefore function blocks are mapped to standard Modelica blocks.

It is improtant to destinguish between a requirement and a function block. The requirement maps to a system requirement, such as the one defined by R2 (*"Within 40 seconds of the power being lost, at least two sets must be powered"*) and can contain one or more function blocks to represent time locators. As illustrated in the previous section, a requirement can also be time independent of time and should then hold continuously.

REQUIREMENT VERIFICATION

Once the the requirement model and the system model are combined, they can be simulated together in order to verify the requirements. Each requirement has a status value which can subsequently be plotted to see at which times the requirement is violated.

The advantage of having the requirements in the same language as the system model is that no additional work is necessary to simulate the system.

In the verification scenario in our example, the power is lost at time 20, and the back-up units 1 and 2 are turned on at time 40 (Figure 1). Therefore the requirement is not violated. The units 1 and 2 are turned off again at time 80, however since this behaviour does not affect the requirement, it remains not violated (Figure 2).

If we modify the verification scenario so that unit 2 is turned on at time 70, the requirement will be violated as illustrated in Figure 3.

RELATED WORK

In this paper we have shown how textual requirements can be formalised in Modelica, however when dealing with large numbers of requirements and simulation scenarios, there is a need for an automated
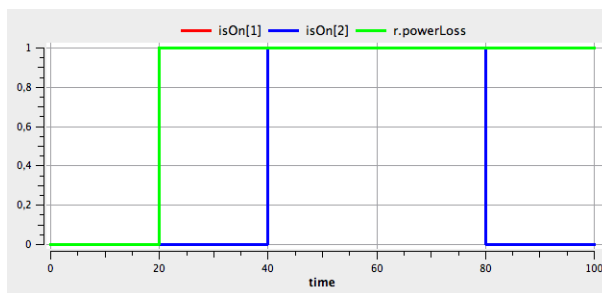

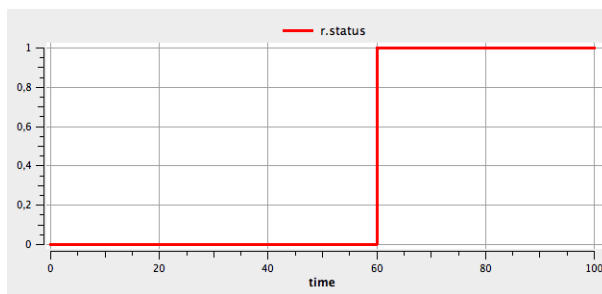Figure 1: The power loss of the main power system and the switching on/off of backup units 1 and 2

Figure 2: The requirement status, where 0 represents undefined, -1 violated and 1 not_violated
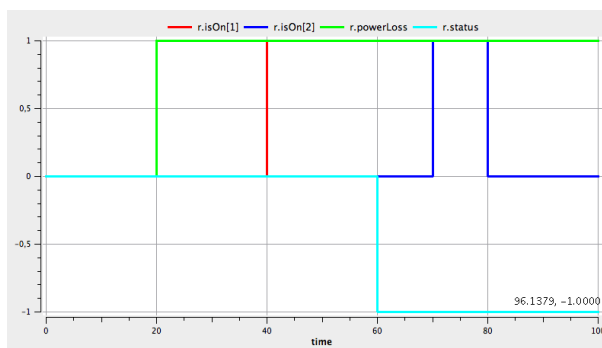

Figure 3: The requirement is violated because the power block 2 is not turned on time.

approach for composing the requirements with a given system design for the purpose of verification. In [10, 9] an approach for automating this process through the use of binding is proposed with an implementation in ModelicaML, a Modelica profile for UML. In [8] the requirement verification methodology is adapted to Modelica syntax. This work complements the work on formalising requirements in Modelica presented in this paper.

FORM-L language (FOrmal Requirements Modelling Language) is a language specification developed by EDF dedicated to expressing requirements and properties in a clear and concise manner [6]. In the work presented in this paper, concepts from FORM-L were mapped to Modelica function blocks in order to use them when modeling requirements in Modelica.

CONCLUSION

In this paper we have illustrated how through a minimal set of extensions, we can use Modelica to formalise requirements and then verify them with respect to a specific system design.

Expressing requirements in the same language as the physical model brings the advantages of a modular, object-oriented language for system design to the process of requirement formalisation, and allows for a runtime verification of requirements. This work is part of a larger ongoing research project aiming to develop tool and methods [3] for model-driven, integrated system verification and fault analysis. Moreover, expressing the requirements in Modelica allows to formalise them and remove the ambiguity present in a verbal description.

The next step in this work is the integration with the work in [8] for an automatic generation of verification scenarios as well as tool support for batch processing of requirements.

ACKNOWLEDGEMENT

REFERENCES

[1] Peter Fritzson. *Principles of Object-Oriented Modeling and Simulation with Modelica 2.1.* Wiley IEEE Press, 2004.

[2] E. Hull, K. Jackson, and J. Dick. *Requirements Engineering.* Springer, 2005.

[3] ITEA 2 Projects. MODRIO. http://www.itea2.org/.

[4] Martin Leucker and Christian Schallhart. A brief account of runtime verification. *The Journal of Logic and Algebraic Programming*, 78(5):293 – 303, 2009.

[5] Modelica Association. Modelica 3.2 revision 2 specification, 2013. www.modelica.org.

[6] Thuy Nguyen. FORM-L: A MODELICA Extension for Properties Modelling Illustrated on a Practical Example. In *Proceedings of The 10th International Modelica Conference*, 2014.

[7] Open Source Modelica Consortium. Openmodelica project, 2013. www.openmodelica.org.

[8] Wladimir Schamai. *Model-Based Verification of Dynamic System Behavior against Requirements.* PhD thesis, Method, Language, and Tool Linköping: Linköping University Electronic, PressDissertations, 1547, 2013.

[9] Wladimir Schamai, Lena Buffoni, and Peter Fritzson. An Approach to Automated Model Composition Illustrated in the Context of Design Verification. *Modeling, Identification and Control*, 35(2):79–91, 2014.

[10] Wladimir Schamai, Peter Fritzson, and Chris Jj Paredis. Translation of UML State Machines to Modelica: Handling Semantic Issues. *Simulation*, 89(4):498–512, April 2013.

[11] Andrea Tundis, Lena Rogovchenko-Buffoni, Peter Fritzson, Alfredo Garro, and Mattias Nyberg. Requirement verification and dependency tracing during simulation in modelica. In *Proceedings of EUROSIM Congress on Modelling and Simulation*, September 2013.

DNA - AN INTEGRATED OPEN-SOURCE OPTIMIZATION PLATFORM FOR THERMO-FLUID SYSTEMS

Leonardo Pierobon,[*] **Jorrit Wronski, Brian Elmegaard and Fredrik Haglind**
Technical University of Denmark
Department of Mechanical Engineering
2800 Kongens Lyngby
Denmark

Ian H. Bell
University of Liège
Thermodynamics Laboratory
4000 Liège
Belgium

ABSTRACT

This paper presents developments and new features added to the simulation tool Dynamic Network Analysis. This open-source software is the result of ongoing development at the Department of Mechanical Engineering, Technical University of Denmark since 1988. Ever since, it has been employed to model dynamic and steady-state energy systems and is now available for the most common operating systems (Windows, Mac OS and Linux). Emerging interest in novel plant technologies, high-temperature heat pumps, refrigeration absorption modules, and in energy system optimization has stressed the necessity to extend the capabilities of the software, while at the same time decreasing computational time. Dynamic Network Analysis can now solve non-convex optimization problems by virtue of the fully-embedded genetic algorithm. Moreover, the thermophysical fluid property library has been extended with more than 110 fluids by interfacing CoolProp, a high-accuracy open-source property package for pure and pseudo-pure fluids, as well as humid air. The new features are unveiled in one case study where the optimization of an air bottoming cycle unit recuperating the exhaust heat from an offshore power system is performed by taking advantage of CoolProp's table-based property interpolation scheme.
Keywords: DNA, CoolProp, Evolutionary algorithm, Thermophysical properties

NOMENCLATURE

a	Constants in Eq. 2 or air
F_h	Fin height [mm]
F_l	Fin length [mm]
h	Specific enthalpy [kJ$\cdot$kg^{-1}]
l_{exh}	Length gas side [m]
p	Pressure [bar]
T	Temperature [K]
v	Specific volume [m$^3\cdot$kg^{-1}]
$\bar{X},\bar{Y}$	Arrays of optimization variables
x,y	Tabulated and normalized fluid properties
Δ	Difference
ρ	Density [kg$\cdot$m^{-3}]

---
[*]Corresponding author: Phone: +45 254129 Fax: +45 884325 E-mail:`lpier@mek.dtu.dk`

INTRODUCTION

Simulation of thermodynamic systems has become one of the main pillars of engineering work, university education as well as public and private research. Many software products are deeply integrated into existing workflows and increasing simulation quality has led to decreasing experimental efforts while accelerating the pace of implementation and development of new and optimised thermodynamic pro-

cesses. Such processes involve a number of non-linear phenomena, e.g. the phase change of a working fluid or transitions between laminar and turbulent flow regimes, calling for robust solution strategies and integrators.

Software for modelling thermo-fluid systems typically involves an ecosystem of at least three interacting software components. First, a system interpreter (a) converts the users' input and creates a modified system of equations along with bindings to external libraries. These equations are then processed by a numerics component (b) containing solvers and integrators, which typically consist of custom-made special-purpose algorithms and modified versions of popular mathematics libraries like the Basic Linear Algebra Subprograms (BLAS) [1], its high-level companion the Linear Algebra Package (LAPACK) [2] and the Harwell Subroutine Library (HSL) [3]. The third component is the fluid property package (c) whose calculations are the bottleneck of the entire solving procedure while discontinuities in the thermophysical properties and their derivatives challenge the solvers' stability. For dynamic simulations, a fourth functional (d) unit can be introduced to provide access to data for varying operating conditions including controller inputs. Common software packages in the field of thermo-fluid simulations implement one or more of the four aspects, (a) through (d), mentioned above. If needed, missing features are often supplemented by accessing an independent library.

There are a number of software for steady-state simulation. Many customised solutions are based on the general purpose computing packages SciPy [4] and Matlab [5] exploiting their powerful solvers and data treatment facilities. A popular equation-based application for static modelling is the Engineering Equation Solver (EES) [6]. Another package for similar purposes is CycleTempo [7], which also comes with its own fluid property database, representing the component-based modelling environments. Dynamic problems formulated in systems of differential equations require other approaches such as the ones implemented in Ascend [8], AspenONE [9], Dynamic Network Analysis (DNA) [10] and the different implementations of the Modelica language, e.g. Dymola [11] and OpenModelica [12].

Fluid property calculations are usually delegated to external libraries that are accessed on a per-call ba-

sis extending a small group of built-in fluid property correlations. A commonly used library for this purpose is REFPROP [13] developed by the U.S. National Institute of Standards and Technology (NIST). It can handle pure and pseudo-pure fluids as well as a large amount of mixtures of common working fluids. Another commercial software for a similar purpose is FluidProp [14], the property calculation engine behind CycleTempo. Furthermore, the TIL Media Suite [15] provides access to optimised routines tailored for dynamic simulations.

The only freely-available high-accuracy property library for mixtures, known to the authors is TREND [16]. Both, TREND and CoolProp [17] are competitive free fluid property libraries for pure and pseudo-pure fluids since they contain a large selection of relevant working fluids with CoolProp offering the unique features of tabulated property interpolation. The other open-source alternatives FPROPS [18] from the Ascend project and the Modelica-based packages ModelicaMedia [19] and HelmholtzMedia [20] only have a limited number of working fluids. Currently, DNA includes its own routines for a number of fluids like water/steam by Wagner and Pruss [21] with LiBr-Water solutions added by Pátek and Klomfar [22], some real gases and mixtures of ideal gases [23], refrigerants [24]. It also contains functions for calculating properties of solid fuels such as biomass and coal. In particular, functions for thermal radiation properties of combustion products and exergy may be mentioned as uncommon features.

Looking at the above, integrating DNA with CoolProp combines a mature steady-state solver and integrator with a computationally efficient fluid property database. Due to the enhanced simulation speed, DNA can now be used to perform optimisation and control development tasks as described below.

DYNAMIC NETWORK ANALYSIS

The present section discloses new features and capabilities of the simulation tool Dynamic Network Analysis. Particular emphasis is dedicated to the newly implemented capabilities of solving multivariable optimization problems and of utilizing advanced techniques for rapid computation of thermophysical and transport properties for a large variety of pure fluids.

New features

Dynamic Network Analysis is the present result of ongoing development at the Department of Mechanical Engineering, Technical University of Denmark, which began with a Master's Thesis work in 1988 [25]. DNA may be described as a modelling language for describing thermo-fluid systems and as the compiler that interprets this language and makes it accessible for the numerical solver. It can also provide some fluid property data and therefore covers the aforementioned components (a) and (c), while partly fulfilling tasks done by the numerics component (b). In DNA, the physical model is formulated analogously to electrical networks by connecting the relevant component models through nodes and by including operating conditions for the complete system. The physical model is converted into a set of equations to be solved numerically. The mathematical problem can include both dynamic and steady-state mass and energy conservation balances for all components and nodes, as well as relations for thermodynamic properties of the fluids involved. The program includes a component library with models for a large number of different components existing within energy systems.

DNA is an open source tool written in FORTRAN. It is integrated with the open source editor Emacs and the open source compiler suite GCC both distributed by the Free software Foundation [26].

DNA solves both steady state and dynamic problems. For steady state problems algebraic loops due to mass balances in thermodynamic cycles are detected and removed by the compiler. The solver is a modified Newton method.

Dynamics occur in mass and energy balances as well as in control algorithms and in inertia of rotating shafts. This results in differential-algebraic equations which are solved by a backward differentiation formulae (BDF) implemented for variable step size by use of the Nordsieck formulation. The solver handles discontinuities by restarting at the point of crossing.

The software capabilities are improved by linking DNA with the open-source genetic algorithm implemented by Carroll [27]. The code, readily available in Fortran language, is compiled together with DNA to form a unique software capable of solving non-convex optimization problems, to be set directly through the user interface. The genetic algorithm is preferred to gradient-based methods since it is less prone to end its search in local minima of the problem, usually converging towards global optima. This comes at the cost of an increased computational effort, due to the large number of evaluations of the objective functions [28]. For a more in-depth description of the key features of the genetic algorithm employed in this work the reader can refer to Goldberg and Holland [29].

Additionally, the fluid library is extended with over 110 compressible fluids given as Helmholtz-free-energy-based equations of state (EOS) and over 50 incompressible liquids and solutions by using a custom-built C-interface to pass property calls to the open-source thermophysical property library Cool-Prop [17]. Furthermore, an integration with Cool-Prop also enables the usage of all fluids and mixtures available in REFPROP [13].

Matlab interface

Matlab is an important tool in many technical applications. It is used in control applications, often in combination with the Simulink tool. DNA has been demonstrated integrated with Matlab as a function that Matlab can call when needed to obtain data from the plant that the DNA model is emulating. This means that the complete DNA application more or less will be considered as a Simulink block with inputs and outputs. The inputs are control signals and the outputs are measurements one sampling time ahead, when DNA has calculated the new state. Matlab then may change to the control signals and run DNA again. The integration is implemented via the Matlab external interface (Mex) [30, 31]. One feature which has been wanted for the development of DNA as a Mex routine has been that it should run on both Microsoft Windows and Linux. For this reason GCC is used as compiler [32].

The algorithm used is:

Call Mexdna from Matlab with the DNA input file as argument. The call is done via a Mex gateway file.

Read the input file and initialize the DNA model Return to Matlab

while Simulating **do**

Change boundary conditions for control signals, load requirements and disturbances for the model.

Call Mexdna with sampling time step as input
Simulate until sampling time is reached
Return measurements (simulation results) to Matlab
end while

To pass variables between Matlab and the external program, a gateway routine is required. This routine handles conversion between Matlab array pointers and the external types. In order to keep all variables in memory while the execution control is in Matlab, the persistent arrays feature is used.

Fluid properties

Nowadays, many engineering applications make heavy use of advanced mathematics to solve design and control problems. Especially iterative methods and differential equations involve numerous calls to the connected fluid property library. Hence, computational efficiency is of the utmost importance.

Helmholtz-free-energy-based equations of state (EOS) provide the most accurate source of thermodynamic data for many relevant working fluids [33] . However, evaluating state points to provide properties based on random inputs is a computationally expensive task. The EOS is usually provided in a temperature-density-explicit form and those two are not very common iteration variables for a simulation software. Interpolation methods can improve the speed of evaluation drastically. The described software uses two different interpolation methods: a) Tabular Taylor Series Expansion (TTSE) as described by Miyagawa and Hill [34] and Watanabe and Dooley [35] and b) bicubic interpolation published in the work of Keys [36]. To work efficiently, both methods require a regularly spaced grid of state points and a couple of derivatives with respect to the two independent variables.

The following examples illustrate the procedures employed to obtain the property values using the interpolation methods. Using TTSE, the temperature can be obtained from the often used inputs pressure

and enthalpy with the expansion

$$
\begin{aligned}
T = & \Delta h \left(\frac{\partial T}{\partial h} \right)_p + \frac{\Delta h^2}{2} \left(\frac{\partial^2 T}{\partial h^2} \right)_p \\
& + \Delta p \left(\frac{\partial T}{\partial p} \right)_h + \frac{\Delta p^2}{2} \left(\frac{\partial^2 T}{\partial p^2} \right)_h \\
& + \Delta h \Delta p \left(\frac{\partial^2 T}{\partial p \partial h} \right) + T_{i,j}
\end{aligned}
\tag{1}
$$

where the derivatives are evaluated at the point i, j, and the differences are given by $\Delta p = p - p_j$ and $\Delta h = h - h_i$. The nearest state point can be found directly due to the regular spacing of the grid of points. For an improved representation of the p-v-T surface, bicubic interpolation can be used. In the bicubic interpolation method, the state variable and its derivatives are known at each grid point. This information is used to generate a bicubic representation for the property in the cell, which could be expressed as

$$
T(x,y) = \sum_{i=0}^{3} \sum_{j=0}^{3} a_{ij} x^i y^j
\tag{2}
$$

where a_{ij} are constants based on the cell boundary values and x and y are normalized values for the enthalpy and pressure, for instance. The constants a_{ij} in each cell are cached for additional computational speed.

The increase in computational speed depends on the complexity of the EOS. Using IAPWS 1995[21] as an example for the properties of subcooled water at 10 MPa, both methods yield an acceleration by a factor of more than 120 for one of the most involved equations of state when calculating density from p and h based on the current implementation in Cool-Prop. The measured computational time of approximately 1 µs per $\rho(p,h)$-call is in good agreement with figures reported by Johansen [37] for the same fluid, which also provides an in-depth comparison of numerous interpolation schemes.

As another example of the accuracy of these interpolation methods, the density of air is evaluated at 40 000 random data points covering the entire fluid surface. Figure 1 presents the results of this analysis. These data show that the accuracy of the bicubic interpolation method is generally several orders of magnitude better than that of the TTSE method, though both yield acceptable accuracy for most technical needs.
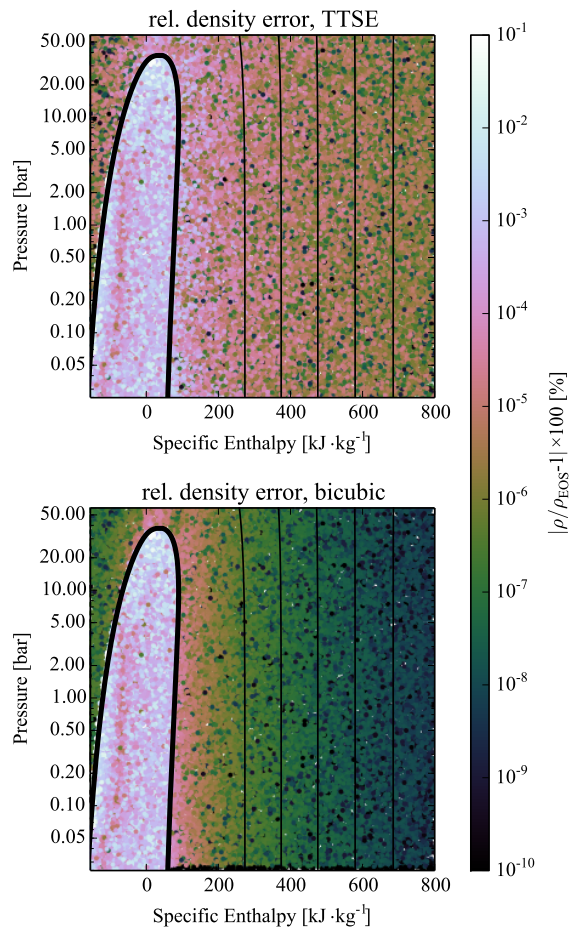
Figure 1: Interpolation errors for air from slightly above the triple point to 500 °C and 60 bar with isolines shown for 0 °C, 100 °C, 200 °C, 300 °C and 400 °C.
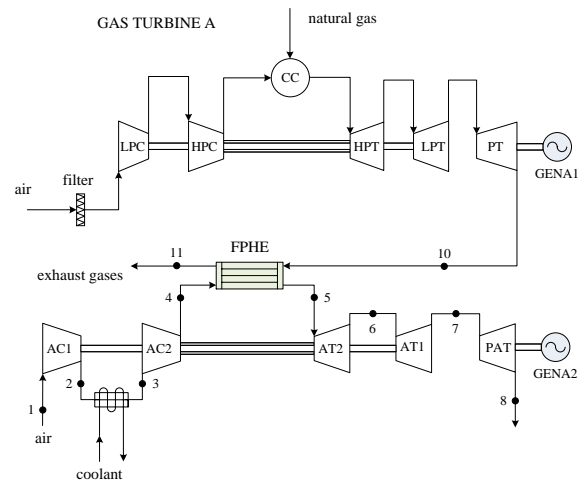

Figure 2: Simplified layout of the power system on the Draugen offshore oil and gas platform. Gas turbine B and C are not shown. The air bottoming cycle module recuperates part of the thermal power released with the exhaust gases of one engine, in the case gas turbine A.

serve power for peak loads, and the safe operation of the engines.

The system layout

Figure 2 shows the layout of the power system with the additional air bottoming cycle (ABC) module which recuperates the exhaust heat produced by gas turbine A. The engines B and C are not reported. Note that the bottoming cycle unit should have the capability to harvest the waste heat alternatively from the other two engines, thus ensuring high performances when switching the gas turbines on operation. The twin-spool engine employs two coaxial shafts coupling the low pressure compressor (LPC) with the low pressure turbine (LPT) and the high pressure compressor (HPC) with the high pressure turbine (HPT). The power turbine (PT) transfers mechanical power through a dedicated shaft to the electric generator (GEN). Natural gas is the fuel utilized in the combustion chamber (CC).

As regarding the ABC part, the first compressor (AC1) intakes ambient ($1 \rightarrow 2$) air which then cools down in the intercooler ($2 \rightarrow 3$), in this way diminishing the specific work during the compression process. The second compressor (AC2) increases further the pressure of the working fluid ($3 \rightarrow 4$) which then harvests the exhaust energy from the gas turbine in the finned-plate heat exchanger ($4 \rightarrow 5$). As reported in Kays and London [38], this device offers
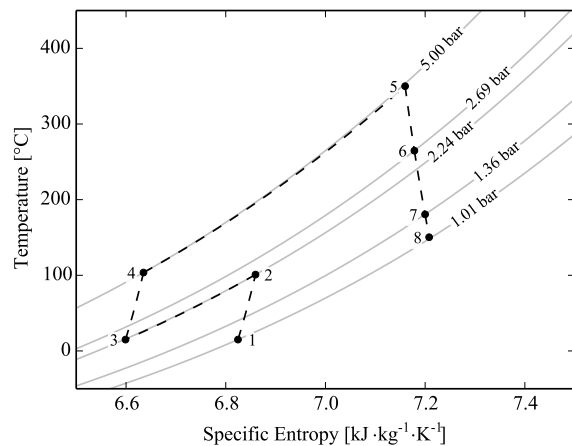
CASE STUDY

The work considers as exemplary application the power plant installed on the Draugen oil and gas offshore platform, located 150 km from Kristiansund, in the Norwegian Sea. The reservoir was discovered in 1984 and started operation in 1993. The platform, operated by A/S Norske Shell, produces gas exported via Åsgard gas pipeline to Kårstø (Norway) and oil, which is first stored in tanks at the bottom of the sea and then exported via a shuttle tanker (once every 1-2 weeks). The normal power demand is around 19 MW and it can increase up to 25 MW during oil export. To enhance the reliability and to diminish the risk of failure of the power system, two turbines run at a time covering 50 % of the load each, while the third one is kept on standby, allowing for maintenance work. Despite the low performance, this strategy ensures the necessary re-

Figure 3: *T-s* diagram for the ABC unit (triple spool arrangement with one intercooler).
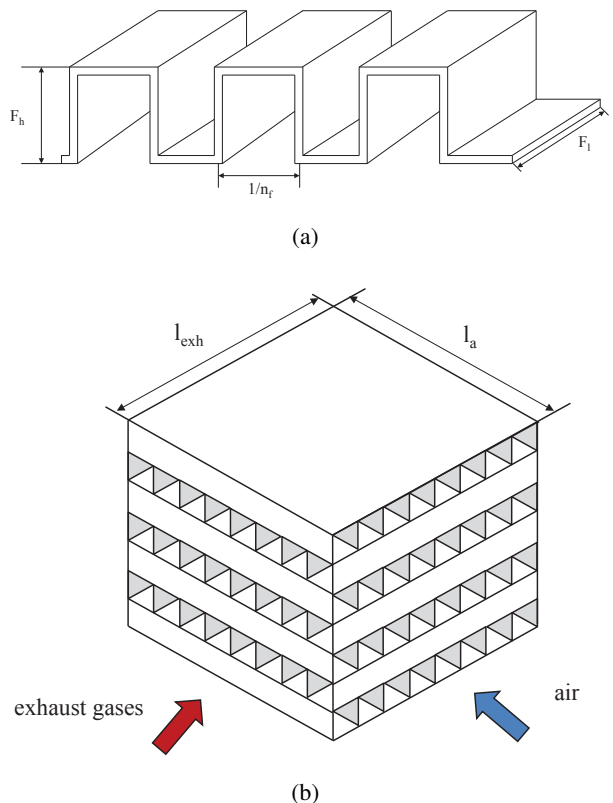

Figure 4: Layout of the finned-plate heat exchanger serving the air bottoming cycle power unit. 4(a) Exhaust gas and air flow pattern. 4(b) Detail of the fin pattern.

higher performances and compactness for gas-to-gas heat transfer processes compared to shell-and-tube and flat-plate heat exchangers. The air then expands through the air turbine AT2 (5 → 6) which drives the second compressor, and afterwards through the air turbine AT1 (6 → 7) which is mechanically connected to AC1. Finally, the power air turbine (PAT) produces useful power by driving the electric generator (7 → 8).

Heat transfer equipment

The finned-plate heat exchanger serving the ABC power system consists of a stack of plates where the hot and cold fluids flow in the free space between the plates, typically in a cross flow arrangement, see Figure 4(a). The plates are equipped with a number of fins with the purpose of augmenting the surface area and of attaining larger heat transfer area-to-volume ratios, i.e. high compactness. The fins may have different shapes, e.g. wavy fins, offset fins and offset strip fins. The latter configuration (see Figure 4(b)) is the most widely adopted and it is thus the one selected in the current work. It is worth mentioning that FPHEs have to operate at lower temperatures (840 °C) and pressures (8.3 bar) [39] compared to shell-and-tube heat exchangers, depending on the process utilized to bond the metal plates. Given the boundary conditions for the ABC unit (see Table 2), these limitations are fulfilled in the present analysis.

The design approach to size the heat transfer equip-

ment is the *effectiveness – NTU method* implemented as reported in Yousefi et al. [40]. The heat transfer coefficient and the pressure drop on each side of the finned-plate heat exchanger (see Figures 4(a) and 4(b)) are calculated in accordance to Manglik and Bergles [41]. The design model of the FPHE was verified by comparison with the geometrical data reported in Yousefi et al. [40]. The differences between the model results and the values reported in the references are within 4.0% in terms of both overall heat transfer coefficient and pressure drop.

The optimization problem

A feasible implementation of bottoming cycle units offshore requires to design compact and light modules, while at the same time exploiting the entire waste heat recovery potential. For this case study, the optimization problem is formulated in two main steps: i) find the cycle parameters maximizing the net power output of the ABC unit, and ii) define the

Table 1: Lower and upper bound for the variables involved in the optimization of the air bottoming cycle unit depicted in Figure 2.

Variable	Lower - upper bound
Outlet pressure p_2/p_1 [-]	1.2 - 3.2
Outlet pressure p_4/p_3 [-]	1.2 - 3.2
Fin height [mm]	50 - 200
Fin length [mm]	20 - 100
Gas side length [m]	1.0 - 3.0

Table 2: Parameters assumed for the two-step optimization.

Parameter	Value
Generator efficiency [%]	98
Ambient temperature [°C]	15
Ambient pressure [bar]	1.013
Gas turbine	
Electric power output [MW]	16.524
Thermal efficiency [%]	31.3
Exhaust gas temperature [°C]	379.2
Exhaust gas mass flow [kg$\cdot$ s^{-1}]	91.5
Air bottoming cycle unit	
Water inlet temperature [°C]	5
Water outlet temperature [°C]	40
Pressure drops air side [bar]	0.03
Outlet temperature t_5 [°C]	330
Exhaust temperature t_{11} [°C]	160
Compressor mechanic efficiency [%]	99.8
Compressor isentropic efficiency [%]	86
Turbine isentropic efficiency [%]	90
Finned-plate heat exchanger	
Fins per meter air side [m^{-1}]	500
Fins per meter gas side [m^{-1}]	500
Number of plates [-]	60
Fin thickness [µm]	200
Plate thickness [µm]	200

geometry of the finned-plate heat exchanger which minimizes its weight given the optimal cycle variables.

The genetic algorithm carries out the two tasks by acquiring the array of the parameters and the upper and lower bounds limiting the possible values for the vectors of the optimization variables $\bar{X}$ and $\bar{Y}$, which read

$$\bar{X} = \left[\frac{p_2}{p_1}, \frac{p_4}{p_3} \right] \text{ and } \quad (3)$$

$$\bar{Y} = [F_{h,a}, F_{l,a}, F_{h,exh}, F_{l,exh}, l_{exh}] . \quad (4)$$

In Equation 3, p_2/p_1 and p_4/p_3 are the pressure ratios of the two air compressors, see Figure 2. The variables F_h, F_l and l_{exh} are the fin height, the fin length and the length of the exhaust gas side. The subscripts "a" and "exh" refer to the air and the exhaust stream side.

The objective functions for steps i) and ii) are the electric power output of the generator serving the ABC unit and the weight of the finned-plate heat exchanger calculated from the design analysis. Table 1 lists the upper and lower bounds of the optimization variables. Note that the values related to the geometry of the heat exchanger are set accordingly with the figures reported in Shah and Sekulić [39] and Yousefi et al. [40].

Table 2 lists the parameters which are maintained constant during the two successive optimizations. As the use of integer variables in the optimization routine is beyond the capabilities of the algorithm, the fin per meter and the number of plates are kept constant. The thickness of the finned-plate heat exchanger and the construction material (stainless steel) are retrieved from Bolland et al. [42].

As the gas turbine can operate on a wide range of both liquid and gaseous fuels, the terminal temper-

ature of the exhaust gases exiting the FPHE is set to 160 °C. This precaution prevents condensation of corrosive compounds when fuels such as crude oil, heavy fuel oil and naphtha are combusted. In the geometric optimization of the finned-plate heat exchanger it is verified that the velocity on the hot and cold side of the heat exchangers is within 1 m$\cdot$s^{-1} and 40 m$\cdot$s^{-1}, while an upper limit of 3 kPa is selected for the pressure drops. If such test is not passed the objective function is set to a large number, i.e. 10^6.

The parameters of the genetic algorithm are specified according to De Jong and Spears [43]: generation size 1000, crossover rate 0.6, and mutation rate 0.001. As for the population number in the first optimization and in the weight minimization, the specified values are 5 and 50, respectively. These numerical quantities are selected so as to ensure the repeatability of the solution when different simulations are performed. The process terminates when the average change in the objective function of two succes-

sive iterations is lower than the specified tolerance (10^{-4}) or when the number of generation reaches the maximum value.

RESULTS

Figure 5 shows the optimal value of the objective function, i.e. the net power output of the ABC module, at each generation for the optimization of the thermodynamic cycle. The electric power remains between 2730 kW and 2750 kW for the first 180 generations. The largest improvement is attained at generation 179 where the objective function reaches a value of 2756 kW. Considering the first generation as a reference, the total gain in power across the optimization process is around 30 kW which corresponds to a relative improvement of 1.1 %.

Figure 6 reports the value of the optimization variables, i.e. the pressure ratios of the two air compressors, as a function of the generation number. Accordingly with the trend of the objective function, the pressure ratios reach the best values, i.e. 1.685 and 2.543, after 340 generations. The final quantities differ from the ones of the first generation by 8.1 % and 3.7 %, respectively.

Figure 7 reports the evolutionary trend of the weight of the finned-plate heat exchanger for the second optimization. It is underlined that the pressure ratios of the compressors are now fixed to the optimal values. It can be noted that the algorithm employs all the available generations to abate the value of the objective function. The largest improvements occur during the first ten generations where the target parameter decreases from 40 $10^3 \cdot$ kg to 35 $10^3 \cdot$ kg.

Figure 6: Best values of the optimization variables (see Equation 3) for each generation number of the air bottoming cycle optimization.

Smaller weight decrements can be found during iteration number 210 and 870. The final value of the objective function is 33.8 $10^3 \cdot$ kg.

Figure 8 shows the evolutionary trend of one optimization variable, i.e. the fin height on the exhaust gas side, involved in the routine. The largest variations occur during the very first evolutions where the fin height of the exhaust gas side diminishes from 75.5 to 84.7 mm. The last variation (≈ 1.0 mm) occurs at iteration number 846.

Table 3 lists the results of the two-steps optimization of the ABC power system. The thermal efficiency of the ABC unit (12.6 %) is calculated as the ratio between the electric power output and the heat rate exchanged by the FPHE.
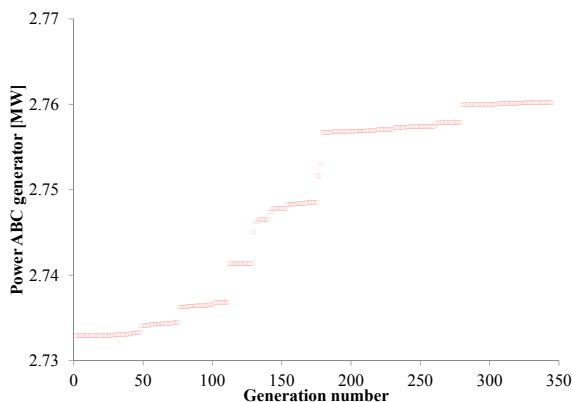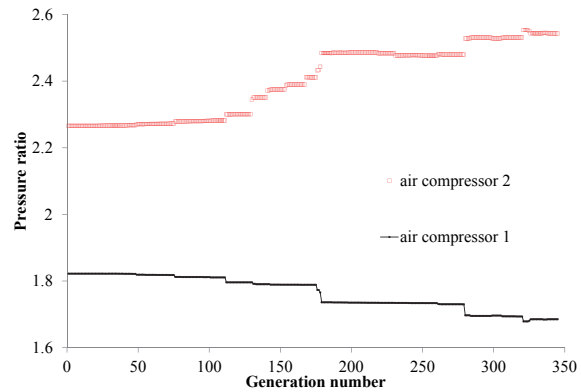

Figure 5: Maximum value of the object function (net power output) for each generation number of the air bottoming cycle optimization.
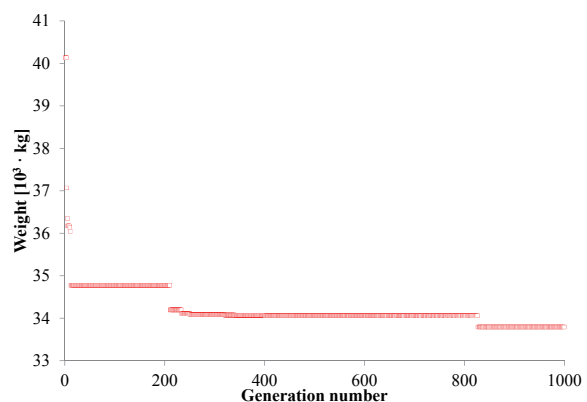

Figure 7: Maximum value of the object function (weight) for each generation number of the finned-plate heat exchanger optimization.
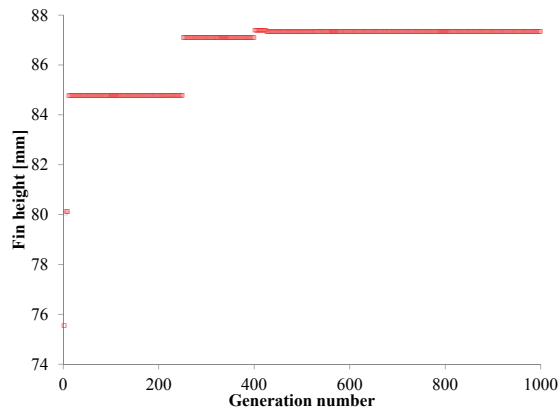
Figure 8: Best value of the fin height on exhaust gas side (see Equation 4) for each generation number of the weight optimization.

Table 3: Results of the two-step optimization. Air bottoming cycle unit and finned-plate heat exchanger design.

Parameter	Value
Air bottoming cycle	
Pressure ratio p_2/p_1 [-]	1.685
Pressure ratio p_4/p_3 [-]	2.543
Net power output [MW]	2.76
Thermal efficiency [%]	12.6
Finned-plate heat exchanger	
Fin height air side [mm]	80.5
Fin length air side [mm]	30.8
Fin height gas side [mm]	87.3
Fin length gas side [mm]	66.5
Gas side length [m]	1.43
Effectiveness [%]	86.9
Heat transfer area [m^2]	20463
UA-value [kW $\cdot$ m^{-2} $\cdot$ K^{-1}]	90.3
Core volume [m^3]	42.0
Total weight [$10^3 \cdot$ kg]	33.8

DISCUSSION

As for the optimization of the ABC system, the power output and the thermal efficiency of the plant illustrated in Figure 2 increase from 16.5 MW to 19.3 MW and from 31.3 % to 36.5 %, respectively. Hence, for the thermal efficiency an increment of 5.2 %-points is attained. The improvement appears to be smaller than the values reported in the open literature. For example, Tveitaskog and Haglind [44] report an increment of around 10.5 %-points for the LM2500 gas turbine, and Poullikkas [45] estimates an improvement of the net power output of the Al-

lison 571-K engine from 5.9 MW to 7.5 MW, corresponding to an increment of 27.0 %. The lower gains obtained here are due to two reasons. Firstly, the SGT-500 machine exhibits a colder exhaust gas temperature (379.2 °C) compared to the gas turbines investigated in the aforementioned works. Thus, smaller increments are to be expected due to the lower attainable efficiency of the bottoming cycle. Furthermore, this work assumes conservative values for the temperature of the exhaust gases and at the inlet of the first air turbine so as to account for a reasonable size of the primary heat exchanger and to preserve the fuel flexibility of the topping unit. Operating gas turbines at lower temperatures effectively reduces corrosion caused by impurities in the fuel as well as the deposition of ashes [46].

As for the heat exchanger calculations, the values listed in Table 3 are in accordance, considering the different size of the plants, with the values obtained by Bolland et al. [42] for the design of a finned-plate heat exchanger of a ABC module recuperating the exhaust heat from the LM2500 gas turbine.

As reported in the previous section, the genetic algorithm computes the optimal pressure ratios of the two air compressors in 345 generations, given the boundary conditions listed in Table 2. Figure 9 shows a contour plot which highlights the impact of the two optimization variables on the net power output of the air bottoming cycle unit. The dark-red zones are characterized by low net power outputs, while the white ones define the regions of high values for the target function. The outcomes of the first optimization step are in-line with the results of such sensitivity analysis since the optimal pressure ratios lay in the white area of Figure 9.

To be noted that the first optimization handles a convex quadratic function with positive definite Hessian, see Figure 9. Under these hypothesis gradient-based approaches such as the steepest descent method are ensured to detect the exact solution with high rates of convergence and with a fixed number of iterations. These properties are expected to be poorer for the genetic algorithm due to the stochastic approach and depending on the input parameters, e.g. populations size, mutation rate.

The benefits of evolutionary approaches are instead fully exploited when minimizing the weight of the finned-plate heat exchanger. In fact, the second optimization process has to deal with numerous discon-
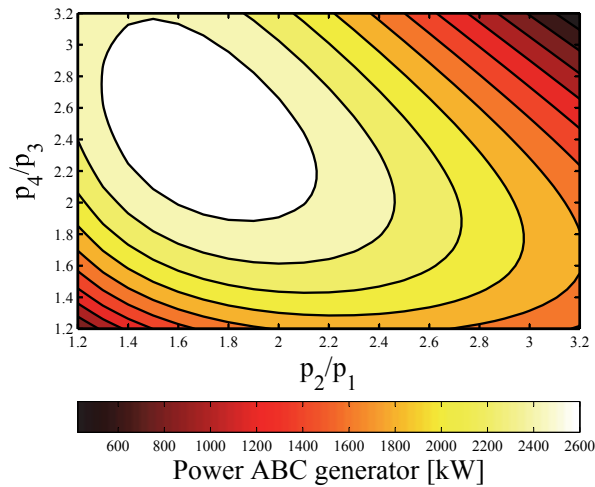
Figure 9: Contour plot showing the impact of the pressure ratios of the air compressors on the net power output of the air bottoming cycle unit.
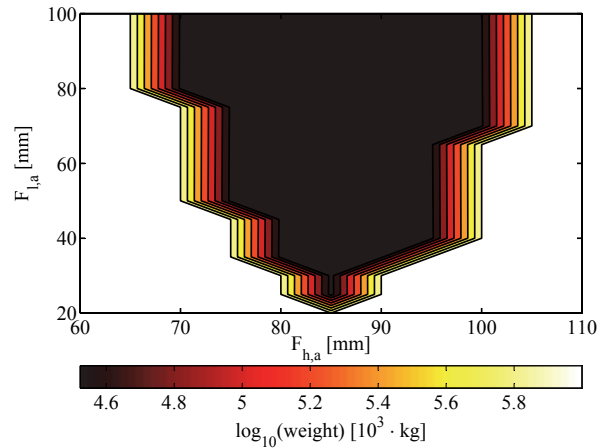

Figure 10: Contour plot showing the impact of the height and length of the fins installed on the air side on the weight of the finned-plate heat exchanger.

tinuities in the objective function, which arise when the solver hits the limitations of the velocity and of the pressure drops in the FPHE. Figure 10 shows the effect of variations in the height and length of the fins installed on the air side. The figures for the remaining three variables are kept at the optimal values listed in Table 3.

In this case the white zones indicate regions where infeasible designs are attained as the pressure drops or fluid velocities exceed the predefined limits. Since in these cases the objective function is set to an arbitrary value (10^6), the bounds create discontinuities which can be promptly handled by the genetic algorithm. Moreover, stochastic methods are in this case preferable by virtue of the non-convexity of the target function, making gradient-based methods largely dependent on the starting point and more prone to convergence issues.

OUTLOOK AND CONCLUSIONS
Fluid Properties

In order to employ the interpolation techniques discussed above, tabulated data has to be generated from the EOS. The current implementation uses gridded data sets in terms of enthalpy h and logarithmic pressure $\log p$ and logarithmic specific volume $\log v$ and temperature T, respectively. The minimum enthalpy $h_{\min}$ is the enthalpy of the saturated liquid state at the minimum temperature defined by

the employed EOS $T_{\min}$. The enthalpy difference between saturated liquid and saturated vapour at $T_{\min}$ is added twice to $h_{\min}$ yielding $h_{\max}$. The minimum pressure $p_{\min}$ is defined by the saturated vapour state at $T_{\min}$. $p_{\max}$ is obtained from multiplying the reducing pressure of the EOS (often the critical pressure) with two. $T_{\max}$ is defined in the same way, while minimum and maximum specific are extracted from the previously generated tables in h and $\log p$. The regularly spaced grids are shown in Figure 11.

It is obvious from Figure 11, that the two ranges of tabulated data do not cover the same regions. Therefore, additional calculation steps are required to assure that the calculation stays within the bounds of both data sets.

Due to the high accuracy of the interpolation methods shown in Figure 1, the next version of CoolProp will cover the whole T, p and h, p space for an EOS with the same amount of data points. Maximum enthalpy is obtained from $T_{\max}$ in the low pressure limit. Besides the obvious boundaries given by T, p and h, p, a melting curve based on the Simon-Glatzel equation can be used to further reduce the application of the interpolation schemes. Special cases like with a negative inclination of the melting curve in h, p coordinates, like water, still require the evaluation of the EOS in some cases. With those two data sets, a one-dimensional search in the tables allows for twelve different input pairs. Only the combinations s, u and s, v and u, v will not be covered. Transport properties will be tabulated in T, p with numerical derivatives instead of T, v to play well together
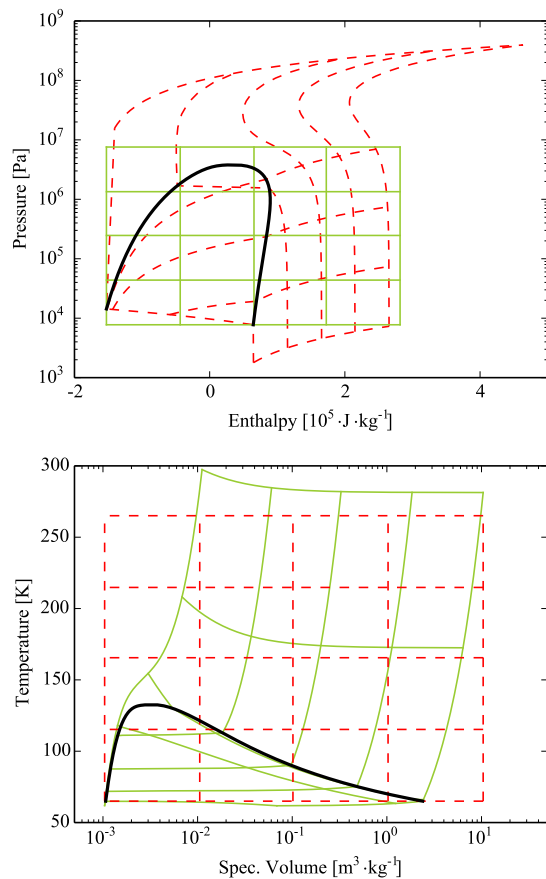
Figure 11: Interpolation tables in h, p (solid) and v, T (dashed) as generated by CoolProp v4.

with the other tabulated data.

Modelling and Optimisation

This paper discloses new features and capabilities of the open-source simulation program Dynamic Network Analysis developed at the Technical University of Denmark.

The tool has been interfaced to the open-source thermophysical property library Coolprop. The user can now model novel energy system technologies by leveraging the extended fluid library which includes more than a hundred compressible and incompressible fluids. Rapid and accurate calculations of thermodynamic and transport properties are delivered by virtue of advanced interpolation methods, i.e. tabular Taylor series expansion and bicubic interpolation. Moreover, Dynamic Network Analysis can deal with non-convex multi-variable optimization problem utilizing the fully embedded genetic

algorithm.

The new features are here exploited to design an air bottoming cycle module to recuperate the exhaust heat from the gas turbine-based power system installed on an oil and gas facility in the Norwegian Sea. Optimizing the pressure ratios of the two air compressors evidences opportunities for improvements in efficiency and installed power capacity of 5.2 %-points and 2.76 MW, respectively. Furthermore, the application of the genetic algorithm enables to minimize the compactness and the weight of the heat transfer equipment of around 6.2 $10^3 \cdot$ kg. The full potential of the evolutionary algorithm is exploited in the latter optimization owing to the large discontinuities in the objective function.

Closing Remarks

From a broader perspective, the implemented routines, returning the physical properties of real fluids and optimal plant designs delivered in an open-source environment, constitute essential features to tackle the modelling challenges posed by future energy system in a computationally efficient and accurate way.

REFERENCES

[1] C L Lawson, R J Hanson, D R Kincaid, and F T Krogh. Basic linear algebra subprograms for fortran usage. *ACM Transactions on Mathematical Software*, 5(3):308–323, September 1979.

[2] E Anderson, Z Bai, C Bischof, S Blackford, J Demmel, J Dongarra, J Du Croz, A Greenbaum, S Hammarling, A McKenney, and D Sorensen. *LAPACK Users' Guide*. Society for Industrial and Applied Mathematics, Philadelphia, PA, third edition, 1999. ISBN 0-89871-447-8.

[3] Scientific Computing Department and UK Science and Technology Facilities Council. HSL – A collection of Fortran codes for large scale scientific computation, 2013. URL http://www.hsl.rl.ac.uk.

[4] E Jones, T Oliphant, P Peterson, et al. SciPy: Open source scientific tools for Python, 2001.

URL http://www.scipy.org/. [Online; accessed 2014-08-04].

[5] The MathWorks. Matlab R2013b, 2013.

[6] Sanford Klein and F L Alvarado. *EES – Engineering Equation Solver v9.616*. F-Chart Software, Madison, Wisconsin, USA.

[7] Asimptote bv and Propulsion and Power group at Delft University of Technology. Cycle-Tempo, 2014. URL http://www.asimptote.nl/ software/cycle-tempo.

[8] B Allan, K Chittur, L Cisternas, J Pye, V Rico-Ramirez, J Shao, J St Clair, M Thomas, A Westerberg, and D Coffey. ASCEND modelling environment v4, 2014. URL http://ascend4.org.

[9] Aspen Plus. Release AspenONE, Aspen Technology. *Inc., Cambridge, MA, USA*, 2004.

[10] B Elmegaard and N Houbak. DNA–a general energy system simulation tool. In *Proceedings of SIMS 2005*, pages 1–10, Trondheim, Norway, October 2005.

[11] Dassault Systèmes AB. Dymola 2014. Lund, Sweden, 2013.

[12] Open Source Modelica Consortium. OpenModelica, 2014. URL https://openmodelica.org.

[13] E W Lemmon, M L Huber, and M O McLinden. NIST Standard Reference Database 23: Reference Fluid Thermodynamic and Transport Properties-REFPROP, Version 9.0, 2010.

[14] Asimptote bv and Propulsion and Power group at Delft University of Technology. FluidProp v3.0, 2014. URL http://www.fluidprop.com.

[15] TLK Thermo GmbH. TIL Media Suite, 2014. URL http://www.tlk-thermo.com.

[16] R Span, T Eckermann, J Gernert, S Herrig, A Jäger, and M Thol. TREND – Thermodynamic Reference and Engineering Data v1.1, 2014. URL http://www.thermo.rub.de. Lehrstuhl für Thermodynamik, Ruhr-Universität Bochum.

[17] I H Bell, J Wronski, S Quoilin, and V Lemort. Pure and pseudo-pure fluid thermophysical property evaluation and the open-source thermophysical property library CoolProp. *Industrial & Engineering Chemistry Research*, 53 (6):2498–2508, 2014.

[18] J Pye, S Muratet, K Chittur, H Ke, R Towers, S Ranganadham, and A Mittal. FPROPS, 2014. URL http://ascend4.org/ FPROPS.

[19] H Tummescheit, J Eborn, F J Wagner, M Otter, M Tiller, H Elmqvist, H Olsson, S E Mattsson, and K Pröß. Modelica.Media v3.1, 2013. URL http://modelica.github.io/Modelica/ om/Modelica.Media.html. Modelica Association.

[20] M Thorade. HelmholtzMedia – A fluid properties library, 2014. URL https://github.com/thorade/HelmholtzMedia.

[21] W Wagner and A Pruss. The IAPWS Formulation 1995 for the Thermodynamic Properties of Ordinary Water Substance for General and Scientific Use. *Journal of Physical and Chemical Reference Data*, 31:387–535, 2002.

[22] J Pátek and J Klomfar. A computationally effective formulation of the thermodynamic properties of LiBr-H2O solutions from 273 to 500 K over full composition range. *International Journal of Refrigeration*, 29(4):566–578, June 2006.

[23] B Lorentzen. *Power Plant Simulation*. PhD thesis, Technical University of Denmark, Laboratory for Energetics, 1995.

[24] M J Skovrup. Thermodynamic and thermophysical properties of refrigerants – package in borland delphi for the refrigerants. Technical Report Version 3.10, Technical University of Denmark, October 2001.

[25] C Perstrup. Analysis of power plant installation based on network theory. Master's thesis, Technical University of Denmark, Laboratory of Energetics, 1991.

[26] "Free Software Foundation". The free software directory, 2014. URL http://www.fsf.org/.

[27] D L Carroll. D.L. Carroll's FORTRAN Genetic Algorithm Driver, November 1998. URL http://read.pudn.com/downloads47/sourcecode/others/158036/ga170.f___.htm.

[28] K Deb. *Multi-objective optimization using evolutionary algorithms*, volume k. John Wiley & Sons, Inc., West Sussex, Great Britain, 2001.

[29] D E Goldberg and J H Holland. Genetic algorithms and machine learning. *Machine learning*, 3(2):95–99, 1988.

[30] MathWorks. *External Interfaces – version 6*. The MathWorks, http://www.mathworks.com, . Introduction of mex, downloaded May 27, 2004.

[31] MathWorks. *External Interfaces Reference – version 6*. The MathWorks, http://www.mathworks.com, . Reference of mex and mx functions, downloaded May 27, 2004.

[32] M Brett. *Compiling Matlab mex files with gcc for Windows*. http://gnumex.sourceforge.net/, wed dec 3 18:42:22 pst 2003 edition, 2003. Documentation of gnumex, downloaded May 28, 2004.

[33] R Span, W Wagner, E W Lemmon, and R T Jacobsen. Multiparameter equations of state— recent trends and future challenges. *Fluid Phase Equilibria*, 183:1–20, 2001.

[34] K Miyagawa and P G Hill. Rapid and accurate calculation of water and steam properties using the tabular taylor series expansion method. *Journal of Engineering for Gas Turbines and Power*, 123(3):707–712, 2001.

[35] K Watanabe and R B Dooley. Guideline on the Tabular Taylor Series Expansion (TTSE) Method for Calculation of Thermodynamic Properties of Water and Steam Applied to IAPWS-95 as an Example. Technical report, The International Association for the Properties of Water and Steam, Vejle, Denmark, August 2003.

[36] R G Keys. Cubic convolution interpolation for digital image processing. *Ieee Transactions On Acoustics, Speech, And Signal Processing*, 29 (6):1153–1160, 1981.

[37] A O Johansen. *Numerical study of evaporators in power plants for improved dynamic flexibility*. Phd thesis, Technical University of Denmark, 2013.

[38] W M Kays and A L London. *Compact heat exchangers*. McGraw-Hill, New York, United States of America, 1984.

[39] R K Shah and D P Sekulić. *Fundamentals of Heat Exchanger Design*. John Wiley & Sons, Inc., Hoboken, United States of America, 2003.

[40] M Yousefi, R Enayatifar, and A N Darus. Optimal design of plate-fin heat exchangers by a hybrid evolutionary algorithm. *International Communications in Heat and Mass Transfer*, 39(2):258–263, 2012.

[41] R M Manglik and A E Bergles. Heat transfer and pressure drop correlations for the rectangular offset strip fin compact heat exchanger. *Experimental Thermal and Fluid Science*, 10 (2):171–180, 1995.

[42] O Bolland, M Forde, and B Hånde. Air bottoming cycle: use of gas turbine waste heat for power generation. *Journal of engineering for gas turbines and power*, 118:359–368, 1996.

[43] K A De Jong and W M Spears. An analysis of the interacting roles of population size and crossover in genetic algorithms. In *Parallel Problem Solving from Nature*, volume 496 of *Lecture Notes in Computer Science*, pages 38–47. Springer Berlin Heidelberg, 1991.

[44] K A Tveitaskog and F Haglind. Optimization of advanced liquid natural gas-fuelled combined cycle machinery systems for a high-speed ferry. In *Proceedings of ASME Turbo Expo 2012*, pages 329–338, Copenhagen, Denmark, June 2012.

[45] A Poullikkas. An overview of current and future sustainable gas turbine technologies. *Renewable and Sustainable Energy Reviews*, 9 (5):409–443, 2005.

[46] F Haglind. A review on the use of gas and steam turbine combined cycles as prime movers for large ships. part iii: Fuels and emissions. *Energy Conversion and Management*, 49(12):3476–3482, 2008.

EFFECTS OF CHANNEL GEOMETRY AND COOLANT FLUID ON THERMOELECTRIC NET POWER

A. Rezania[1], L.A. Rosendahl, K. Sørensen

Department of Energy Technology, Aalborg University, DK-9220 Aalborg, Denmark

[1]Corresponding author, E-mail:alr@et.aau.dk

ABSTRACT

Channel geometry has a strong influence on the heat transfer coefficient and cooling energy input in a heat sink. The net power output in a thermoelectric generator (TEG) can be defined as power generation minus the required cooling energy in TEG. This study aims to evaluate the net power generation in TEG for different size of hydraulic diameter of plate-fin heat sink and over a wide range of Reynolds number. The particular focus of this study is to find optimal Reynolds number in each considered channel hydraulic diameter and to explore optimal channel hydraulic diameter for maximum TEG net power output. Three-dimensional governing equations for the flow and the heat transfer and thermal-electrics are solved using the computational fluid dynamics (CFD) simulation environment. The results show that there is an optimal Reynolds number that provides maximum net power output in the TEG, and the maximum net power output occurs at smaller Reynolds number when the channel hydraulic diameter reduces.

KEYWORDS: Thermoelectric generator, plate-fin heat sink, geometry effect, net power.

1. INTRODUCTION

Micro-structured heat sinks provide compact and low weight energy system and can enhance modularity of power systems. This type of heat sink has been interesting for researchers in field of waste heat recovery applications such as thermoelectric generators (TEGs) [1, 2]. TEGs convert heat energy to electrical power by means of semiconductor charge carriers due to temperature difference between a heat source and a heat sink. A key factor in TEG application is to design an optimal heat sink to enhance the power generation in the TEG. Heat transfer coefficient provided by the heat sink critically affects temperature distribution in the thermoelements and their optimum dimensions design for maximum power generation by the TEG [3]. Thermoelements with different temperature distribution generate different electric voltage. Therefore, the impact of the heat sink geometry on flow and temperature distribution needs to be carefully considered to create high heat transfer coefficient in the heat sink [4, 5].

NOMENCLATURE

A	area, m^2
D_h	hydraulic diameter, m
c	specific heat capacity, J/kg. K
H	channel height , m
J	electric current density, A/m^2
k	thermal conductivity, W/m. K
N	number of channels in heat sink
Nu	Nusselt number
P	power, W
p	pressure, Pa
q	heat flux across TEG, W/m^2
$\dot{q}$	heat generation rate per unit volume, W/m^3
R	internal electrical resistance, Ω
Re	Reynolds number
T	temperature, K
ΔT	temperature difference, K
$\vec{V}$	velocity vector, m/s
v	velocity, m/s
W	volumetric flow rate, m^3/s
w	channel width, m

Greek symbols

α	Seebeck coefficient, V/K
μ	dynamic viscosity, N. s/m^2
Π	Peltier coefficient, V
ρ	fluid density, kg/m^3
σ	electrical conductivity, S/m
φ	electric scalar potential, V

Subscripts

c	cooling energy
cr	ceramic
f	coolant fluid
n	n-type thermoelement
net	net
max	maximum
p	p-type thermoelement
ce	cooling energy
w	wall

The voltage generation due to temperature difference of the hot and cold junctions of TEG can be improved by reduction of thermal resistance in heat sink. Because the performance of TEG system also depends on required cooling energy [6, 7], pressure drop is an important factor beside the thermal resistance consideration for optimization of heat sink design. One way to reduce the thermal resistance is to increase mass flow rate in channels of heat sink. However, a higher cooling energy input is required for a given channel hydraulic diameter because of rapidly increase of the pressure drop in the channels. Depending to TEG operating temperature, this cooling energy input can be higher than the power generation by TEG module and cause to negative net power (power generation by the TEG minus required cooling energy input in the heat sink) by the module [8]. Moreover, heat transfer in the heat sink enhances when the channel hydraulic diameter decreases at constant Reynolds number and channels ratio. Smaller channel hydraulic diameter causes lower heat sink thermal resistance. The channel ratio is defined as ration of the channel height to the channel width. Smaller hydraulic diameter also causes higher pressure drop in the channels that increases the coolant energy input in the heat sink.

Rectangular cross-section shaped channels have highest heat transfer coefficient amongst trapezoidal and triangular shaped microchannels [9]. In addition, it gives minimum thermal resistance when the channel width and the fin thickness are equal [10]. Jang et al. [11] explored optimal fin height and number of fins in rectangular channel heat sink to maximize the net power density in TEGs. The results that provide useful information for waste heat recovery applications, suggest proper flue gas velocity for maximum net power output of TEG per the heat sink base area.

In this study, the effectiveness of compact micro-structured heat sink on the power generation and cooling energy input is considered to maximize net power output in TEG. The optimal range of channel hydraulic diameter is explored over practical range of Reynold number to find maximum net power output. In order to reduce thermal resistance of the heat sink and to provide compact heat sinks, the microchannels are designed on the cold side

ceramic layers of TEG module. There are four types of heat sinks in this study. The fluid and thermal characteristics in the heat sinks are considered in laminar regime.

2. GOVERNING EQUATIONS

The coupled thermoelectric constitutive equations (heat flow and the continuity of electric charge) under steady-state condition are defined as follow [12]:

$$\nabla.([\Pi].J) - \nabla.([k_{\text{teg}}].\nabla T) = \dot{q}, \tag{1}$$

$$\nabla.([\sigma].[\alpha].\nabla T) + \nabla.([\sigma].\nabla \varphi) = 0. \tag{2}$$

The maximum power generation in the TEG, where the internal electrical resistance of the uni-couple is equal to the imposed electrical load resistance, is:

$$P_{\text{max}} = \frac{(\alpha \Delta T)^2}{4R}. \tag{3}$$

where the internal resistance of TEG module is total electrical resistance of the n-type and p-type thermocouples [13]:

$$R = n \times (R_{\text{n}} + R_{\text{p}}) =$$

$$n \times \left[\left(\sigma_{\text{n}} \frac{A_{\text{n}}}{H_{\text{n}}} \right)^{-1} + \left(\sigma_{\text{p}} \frac{A_{\text{p}}}{H_{\text{p}}} \right)^{-1} \right]. \tag{4}$$

The length and width of the TEG module are 7.2 mm, and the height of thermoelements in this studied is 1.4 mm with squared footprint area equal to 1 mm^2. The distance between the thermoelements is 0.8 mm. The interconnectors that connect the thermoelements to each other are silver with thermal conductivity of 429 W/K.m, and its electric resistivity varies with $0.0038T + 1.52 \times 10^{-8}$ Ω.m [14]. The applied thermoelectric material is Bismuth Telluride (Bi_2Te_3) with thermal conductivity, electrical resistivity and Seebeck coefficient equal to 1.2 W/m.K, 9.09 Ω.m and ± 0.2 mV/K, respectively.

Equations (5), (6) and (7) represent continuity, momentum and energy in the heat sink under laminar and incompressible flow conditions [15]:

$$\nabla.\vec{V} = 0, \tag{5}$$

$$\rho_{\text{f}}(\vec{V}\nabla.\vec{V}) = -\nabla p + \mu_{\text{f}}\nabla^2\vec{V}, \tag{6}$$

$$\rho_{\text{f}}c_{\text{f}}(\vec{V}.\nabla T) = k_{\text{f}}\nabla^2 T. \tag{7}$$

As mentioned, pressure drop in heat sink is an important factor that influences net power of the TEG module. Required cooling energy is related to the pressure drop and the volumetric flow rate in the heat sink:

$$P_{\text{ce}} = \Delta p W. \tag{8}$$

The net power output of the TEG is defined as follows:

$$P_{\text{net}} = P_{\text{teg}} - P_{\text{ce}}. \tag{9}$$

Water is used as the coolant fluid in this study with inlet temperature of 290 K. Range of the Reynolds number in the microchannels is $2 - 2000$, and the hot junction temperature of TEG is fixed at 400 K. Table 1 presents properties of the coolant fluid and the heat sink used in the simulation. Hydraulic diameter of the designed channels in heat sinks N4, N8, N24 and N72 are 900 µm, 450 µm, 150 µm and 50 µm, respectively, where N represents number of microchannels in heat sink. The channels dimensions (width and height) and the fin thickness are considered equal. Fig. 1 shows configuration of the heat sinks with the TEG. The thermoelectrical characteristics of the thermoelements are

implemented in a three dimensional simulation environment and are solved by the finite element method, Mechanical, in conjunction with the computational fluid dynamics (CFD) simulation environment, CFX, that solve the coupled thermal and fluid equations in the heat sinks and coolant fluid.

Table 1 Properties of the coolant fluid and the heat sink.

Dimension	k_{cr}(W/m K)	k_f(W/m K)	ρ_f(kg/m^3)
Value	30	0.6	998.2
Dimension	μ_f(kg/m. s)	c_f(J/kg. K)	
Value	0.001	4182	
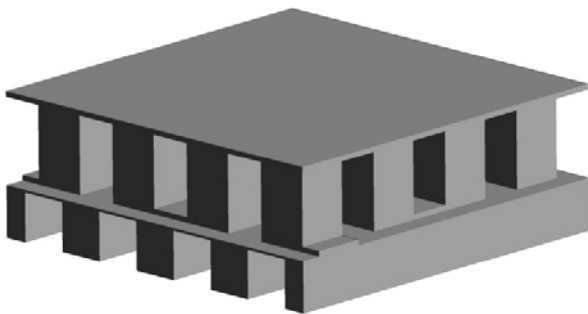
a.
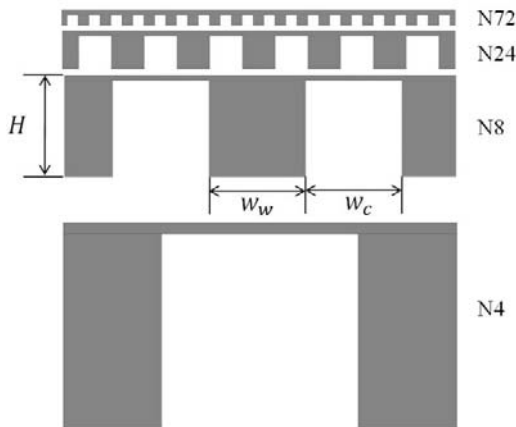
b.

Fig. 1 **a.** Configuration of the studied TEG **b.** front view of symmetric domain of studied heat sinks (A quarter of heat sink geometry is shown here for better resolution).

3. RESULTS

Thermal characteristic of the microchannels in this study is validated with [16] with the same geometrical details. Fig. 2 shows variation of the circumferential Nusselt number along the channel with the same boundary conditions that are is in good agreement with previous study.
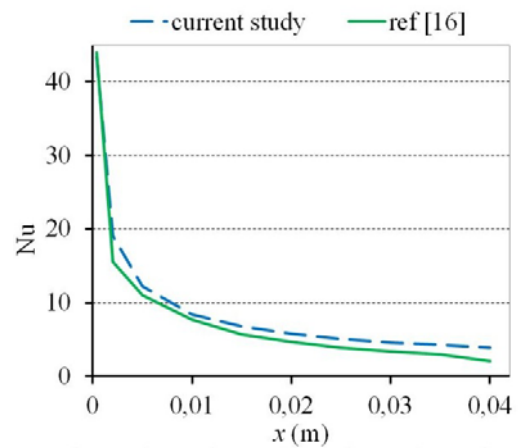

Fig. 2 Comparison of Nusselt number in the microchannel with ref [31] ($H_c = 500$ μm, $w_c = 300$ μm $v_i = 3$ m/s $T_i = 293.15$ K, $q = 30$ W/cm^2).

The computational model used in this study is able to demonstrate 3D results of temperature distribution and voltage generation in the TEG affected by the flow in the micro-structured heat sinks. As Fig. 3 shows, temperature of the flow rises along the channels because of heat absorbed from the TEG. Therefore, temperature on the cold junction of the thermoelements is not constant, and each thermoelement generates different electric voltage. Fig. 4 illustrates how electrical potential increases in the series design of n and p-type thermoelement.
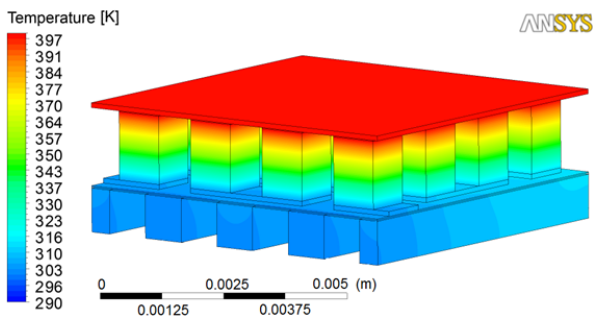
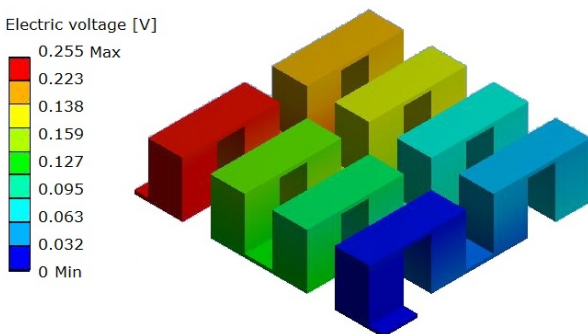Fig. 3 Temperature distribution in the TEG and fins of heat sink. Re = 10.

Fig. 4 Generation of the electric voltage in TEG. R = 10.

The results show that, when the hydraulic diameter of channels decreases, the maximum net power output happens at lower Reynolds number. For a given Reynolds number in the channels and constant hot junction temperature on the TEG, the thermal resistance of the heat sink decreases with the channel hydraulic diameter. The smaller thermal resistance provides lower temperature at the cold junction of the TEG module and increases voltage generation in the TEG. On the other hand, pressure drop in the channel increases at smaller channel and causes higher cooling energy input. This elevation of pressure drop is rapid at high Reynolds number condition, and creates significant cooling energy required in the heat sink, as shown in Fig. 5.

To avoid of evaporation of water due to absorbing of heat in the channels, the minimum Reynolds number considered in this study is Re = 2. However, since water has high specific heat capacity, suitable temperature can be achieved on the TEG cold junction at low Reynolds numbers. The cold junction of TEG remains at close temperature to the flow inlet temperature and thermal resistance of the heat sink is small under high Reynolds number conditions. Therefore, power generation in the TEG increase slightly with the Reynolds number compared to the low Reynolds number conditions. In this case, specifically when the channels have small hydraulic diameter, the net power of the system can be negative because of high cooling energy in the heat sink. Depending to the hydraulic diameter of the micro-channels, the limitation of Reynolds number needs to be carefully considered to avoid negative net power output. There is an optimal value for the Reynolds number for each design of heat sink that the net power output is at maximum value. This optimal Reynolds number is lower when the hydraulic diameter of channels is smaller. For example, the optimal Reynolds number for studied heat sinks N72, N24, N8 and N4 are Re = 50, Re = 200, Re = 500 and Re = 100, respectively.

For a given TEG design and its hot junction temperature and for constant thermoelectric material properties, a higher heat flux across the TEG means a higher temperature different between the cold and hot junctions of the TEG. Since the power generation depends to this temperature difference according to (3), if the heat flux enhances the voltage generation in the TEG increases. Fig. 6 shows how the maximum power generation in TEG follows the heat flux across the TEGs.
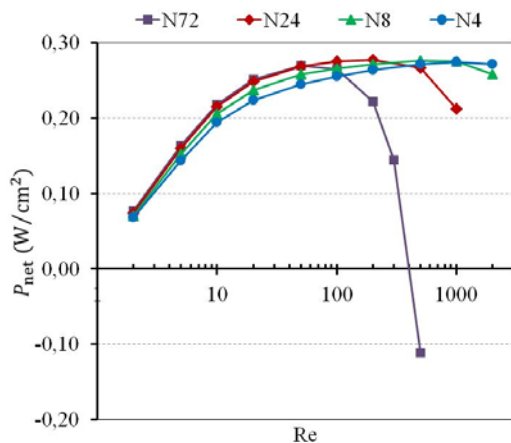
Fig. 5 Variation of TEG net power output with variation of Reynolds number in channels.
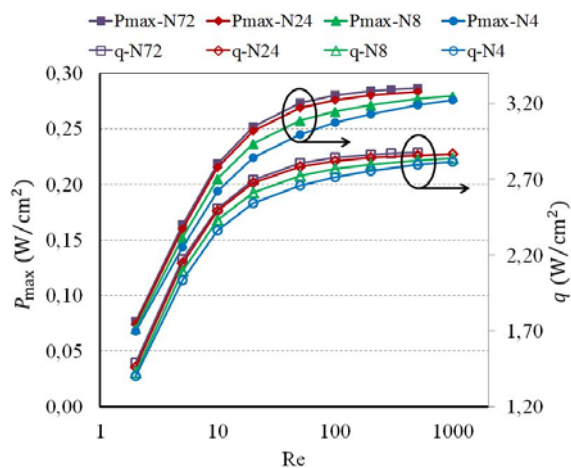

Fig. 6 Variation of thermoelectric maximum power generation and heat flux across the TEG with variation of Reynolds number.

4. CONCLUSIONS

In this study, effect of hydraulic diameter of microchannels on the power generation and net power output in TEGs and cooling energy input in heat sink is considered over a wide range of Reynolds number. The 3D governing equations of thermoelectricity and flow are solved, and analysis of the model generated detailed description of the temperature distribution and voltage generation in the TEGs and heat sinks. The results of this study

show that there is an optimal Reynolds number of flow in each heat sink that provides maximum net power output in the TEG. The maximum net power output occurs at smaller Reynolds number when the channel hydraulic diameter reduces. As future work, the results will be developed with consideration of other channel cross section shapes and air as coolant fluid in the heat sinks.

REFERENCES

[1] A. Rezania, K. Yazawa, L.A. Rosendahl, A. Shakouri, Co-optimized design of microchannel heat exchangers and thermoelectric generators, International Journal of Thermal Sciences 72 (2013) 73-81.

[2] N. Wojtas, L. Rüthemann, W. Glatz, C. Hierold, Optimized thermal coupling of micro thermoelectric generators for improved output performance, Renewable Energy 60 (2013) 746-753.

[3] A. Rezania, L.A. Rosendahl, H. Yin, Parametric optimization of thermoelectric elements footprint for maximum power generation, Journal of Power Sources 255 (2014) 151-156.

[4] T.J. Hendricks, Thermal system interactions in optimizing advanced thermoelectric energy recovery systems, Journal of Energy Resources Technology 129 (2007) 223-231.

[5] X.F. Zheng, C.X. Liu, R. Boukhanouf, Y.Y. Yan, W.Z. Li, Experimental study of a domestic thermoelectric cogeneration system, Applied Thermal Engineering 62 (2014) 69-79.

[6] Ercan M. Dede, Yan Liu, Experimental and numerical investigation of a multi-pass branching microchannel heat sink, Applied Thermal Engineering 55 (2013) 51-60.

[7] M. Reyes, J.R. Arias, A. Velazquez, J.M. Vega, Experimental study of heat transfer and pressure drop in micro-channel based heat sinks with tip clearance, Applied Thermal Engineering 31 (2011) 887-893.

[8] A. Rezania, L.A. Rosendahl, S.J. Andreasen, Experimental investigation of thermoelectric power generation versus coolant pumping power in a microchannel heat sink, International Communications in Heat and Mass Transfer 39 (2012) 1054-1058.

[9] P. Gunnasegaran, H.A. Mohammed, N.H. Shuaib, R. Saidur, The effect of geometrical parameters on heat transfer characteristics of microchannels heat sink with different shapes, Int. J. Heat and Mass Transfer 37 (2010) 1078–1086

[10] D.B. Tuckerman, R.F.W. Pease, High-performance heat sinking for VLSI, IEEE Electron Device Letters 2 (1981) 126–129.

[11] J.Y. Jang, Y.C. Tsai, C.W. Wu, A study of 3-D numerical simulation and comparison with experimental results on turbulent flow of venting flue gas using thermoelectric generator modules and plate fin heat sink, Energy 53 (2013) 270-281.

[12] E.E. Antonova, D.C. Looman, Finite elements for thermoelectric device analysis in ANSYS, 24th International Conference on Thermoelectrics (2005) 215- 218.

[13] M. Chen, L.A. Rosendahl, T. Condra, A three-dimensional numerical model of thermoelectric generators in fluid power systems, International Journal of Heat Mass Transfer 54 (2011) 345-355.

[14] R.A. Serway, Principles of Physics, 2nd ed., Fort Worth, Texas; London: Saunders College Publishing (1998) 602.

[15] M.I. Hasan, Investigation of flow and heat transfer characteristics in micro pin fin heat sink with nanofluid, Applied Thermal Engineering 63 (2014) 598-607.

[16] Y. Chen, C. Zhang, M. Shi, J. Wu, Three-dimensional numerical simulation of heat and fluid flow in noncircular microchannel heat sinks, International Communications in Heat and Mass Transfer 36 (2009) 917-920.

NUMERICAL SOLUTION OF THE SAINT VENANT EQUATION FOR NON-NEWTONIAN FLUID

Cornelius E. Agu and Bernt Lie[1]
Faculty of Technology, Telemark University College
Norway

ABSTRACT

Non-Newtonian fluid flow through a Venturi channel is studied using the Saint Venant equation. The nonlinear hyperbolic equation is numerically tricky to solve, therefore in this study, we consider the finite volume method with staggered grids which we find suitable for control applications. Both steady state and dynamic solutions of the fluids with different rheological properties are simulated and analyzed. The purpose of this study is to develop a numerical algorithm for estimation of flow rate of a non-Newtonian fluid in an open channel. Because a non-Newtonian fluid flow is often associated with supercritical flow upstream, the standard subcritical flume may not be suitable for estimating the flow rate. This study reveals that when a sufficient contraction is introduced in a channel, the supercritical flow jumps to subcritical flow level and then passes through the critical depth at the throat while accelerating towards the channel end. With this flow transition, the study shows that in steady states a unique relationship can be established between the flow rate and the free surface level at the gauging point. The dynamic solution also shows that the system responds positively for a step change in the flow rate, reaching the steady state solution within the simulation run time.

Keywords: Venturi channel, Saint Venant equation, non-Newtonian fluid, Rheological properties, Finite volume method.

---

[1] Corresponding author, E-mail:bernt.lie@hit.no

NOMENCLATURE

A Cross sectional area [m^2]
$\bar{A}$ Average cross sectional area [m^2]
B Free surface top width [m]
b Channel width [m]
Fr Froude number
g Gravitational acceleration [m/s^2]
h Free surface level [m]
K Flow behaviour index [Pa.s^n]
L Length [m]
N Spatial grid size
n Fluid consistency index
P_{wet} Wetted perimeter [m]
Q Flow rate [m^3/s]
R_h Hydraulic radius [m]
S Slope
V Average velocity [m/s]
x Distance
α Kinetic energy correction coefficient
β Momentum correction coefficient
ρ Density [kg/m^3]
θ Inclination of the channel bottom [degree]
τ_y Yield shear stress [Pa]

Subscripts

0   Bottom origin; initial condition
c Critical
i Index in space
in Inlet
out Outlet

INTRODUCTION

Fluid flow in an open channel has wide industrial applicability. It is used in transportation of slurries, water supply for irrigation and river flow [1]. Due to severe operating conditions, use of common flow meters may be considered very expensive or unsafe to measure the flow rate of slurries (non-Newtonian fluids). One common and simple method is to use an open channel hydraulic structure such as a "weir" (Notch) or a "control flume" which introduces a restriction in the flow direction that results in flow variations (that is change in approach velocity and level) along the

channel [2]. Flumes are commonly used in the industry. In homogeneous slurry transport, particle settling is not desired, and this requires that the flume used for the transport and flow measurement must be designed for supercritical flow conditions [3, 4]. The current flume design based on ISO 4359 standard is applied to subcritical upstream conditions [5], and this brings about this study. There has been some research on the requirements for supercritical flume design. A procedure for designing and using a supercritical flume where it is assumed that critical flow conditions occur at the entrance of the channel throat is outlined in [4].

The main purpose of this study is to develop a numerical scheme for estimating the flow rate of a non-Newtonian fluid in an open channel. To complete this task, one-dimensional Saint Venant equation is solved in both steady and unsteady states. One major drawback in the use of the model is that the unsteady 1-D Saint Venant equation is numerical difficult to solve [6]. Several techniques for solving the non-linear partial differential equations have been documented in recent research. One such scheme is based on finite volume method with a switch to energy head conservation model to ensure accuracy, especially in a rapid change in the channel width [7, 3]. Most of the schemes are based on finite different methods with or without staggered grids, and majority is suitable for subcritical flow conditions. Some methods used in supercritical conditions are based on shock-capturing approach or a classical scheme for solving compressible Euler equations [6]. The schemes especially those for supercritical and transition state are significantly computational demanding [6].

The present work focuses on the steady state solution of 1-D Saint Venant equation for a supercritical flow in a Venturi channel. In steady

state conditions, determining a model which uses only the free surface level measured at a specific point in the flow to estimate the flow rate is the main objective. A scheme for obtaining a solution for unsteady state model will also be covered. For unsteady state solution, the main idea is to ascertain the dynamic response of the system for a slight deviation in a steady state value. The scheme which will be based on the finite volume method is expected to be simple and suitable for control purposes.

In the following sections, the governing equations are presented, and the numerical scheme for steady state and unsteady state analyses are derived. The numerical solution is compared with a known solution from literature, and the model for flow rate estimation is then derived. Different results from the scheme are presented and discussed.

GOVERNING EQUATIONS

The unsteady state flow of fluid in an open channel can be described by the one-dimensional Saint Venant equations [6]:

$$\frac{\partial A}{\partial t} + \frac{\partial Q}{\partial x} = 0 \qquad (1)$$

$$\frac{\partial Q}{\partial t} + \frac{\partial \left(\frac{\beta Q^2}{A}\right)}{\partial x} = gA \sin\theta - gA\cos\theta \frac{\partial h}{\partial x} - gAS_f \quad (2)$$

Eq. (1) and (2) are based on mass conservation and momentum conservation principles respectively; Q is the volume flow rate, and A and h are the flow cross sectional area and the free surface level respectively. θ is the angle of inclination of the channel, and g is the acceleration due to gravity. β is the momentum correction coefficient with a value between 1.03 and 1.07. In a non-Newtonian fluid flow, the internal frictional shearing stresses dominate; the frictional slope S_f is then given by [8]:

$$S_f = \frac{\tau_y}{\rho g R_h} \left[1 + \left(\frac{(\epsilon+1)(\epsilon+2)|V|}{(0.74+0.656\epsilon)\left(\frac{\tau_y}{K}\right)^\epsilon R_h} \right)^{\frac{1}{\epsilon+0.15}} \right] \quad (3)$$

where $V = Q/A$ is the average flow velocity. $\epsilon = \frac{1}{n}$; ρ, τ_y, K and n are the fluid properties denoting the density, yield shear stress, fluid behaviour index and fluid constituency index respectively. When the wall frictional stresses are significant, the frictional slope is obtained by [8]:

$$S_f = \frac{n_T V}{R_h^{2/3}} \qquad (4)$$

where n_T is the total roughness coefficient and $R_h = \frac{A}{P_{wet}}$ is the hydraulic radius at each cross section. When the fluid is Newtonian, $n_T = n_M$; n_M is Manning roughness coefficient.

Steady state scheme-ODE form

At steady state, $\frac{\partial A}{\partial t} = 0$, $\frac{\partial Q}{\partial t} = 0$ and then $Q = constant$. Simplifying eq. (2) yields

$$V\beta \frac{dV}{dx} + g\cos\theta \frac{dh}{dx} = g(\sin\theta - S_f) \qquad (5)$$

Differentiating the continuity equation $Q = AV$ with respect to x gives

$$V\frac{dA}{dx} + \frac{AdV}{dx} = 0 \qquad (6)$$

Assuming a trapezoidal channel with side slope m, $A = (mh + b)h$, and

$$\frac{dA}{dx} = B\frac{dh}{dx} + ch \qquad (7)$$

where $c = \frac{db}{dx}$; $B = 2hm + b$ is the top width of the flow, and b is the bottom width at a given section of the flow. Combining eq. (5), (6) and (7) yields:

$$\frac{dh}{dx} = \frac{gAS + \beta chV^2}{gA\cos\theta - \beta BV^2} \qquad (8)$$

where $S = \sin\theta - S_f$. The denominator of eq. (8) determines the condition and behaviour of the flow. The critical flow occurs when:

$$gA\cos\theta - \beta BV^2 = 0 \qquad (9)$$

The depth of the flow which satisfies eq. (9) is the critical depth. The open channel flow is generally characterized by the Froude number which is expressed as the ratio of flow velocity to the gravity wave celerity, i.e. $Fr = \dfrac{V}{\sqrt{\left(\frac{gA}{B}\right)}}$ [3]. When $Fr < 1$, the flow is subcritical and when $Fr > 1$, the flow is supercritical. The flow condition is near critical when $Fr \approx 1$. This suggests that eq. (8) can be used to simulate both subcritical and supercritical flow conditions, and also the transition between the two extremes.

Unsteady state scheme

In this paper, we base the numerical scheme for the unsteady state equations (1) and (2) on the finite volume method with staggered grids. With the staggered grid arrangement, the varying slope of the liquid surface is captured [9]. Figure 1 shows the grid arrangement. The node of control volume for momentum conservation is indicated by the line **P** where the velocity is stored. The boundaries of the velocity control volume indicated by the lines **w** and **e** correspond to the nodes of the control volumes for mass conservation, where the depths of the liquid surface are stored. The grid is uniform with spatial spacing, Δx.

Scheme for volume conservation

Spatial integration of eq. (1) over the mass conservation control volume gives

$$\frac{dA_i}{dt} = -\frac{Q_{i+1/2} - Q_{i-1/2}}{\Delta x} \qquad (10)$$

To ensure there is no negative depth in the flow, the depths at the boundaries are obtained according to the first order upwind rule [7, 10]:

$$h_{i+1/2} = \begin{cases} h_i,; & Q_{i+1/2} \geq 0 \\ h_{i+1}; & Q_{i+1/2} < 0 \end{cases} \qquad (11)$$
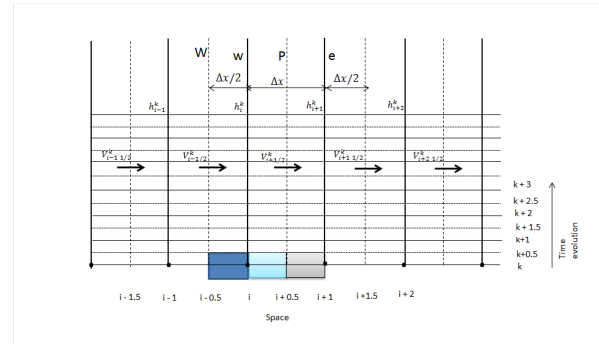

Figure 1: Staggered grid arrangement for V and h control volumes.

Scheme for momentum conservation

Here, the spatial integration of the free surface depth gradient is approximated by the central differencing method, and the flux term is approximated by first order upwind [9]. Over the velocity control volume, the integration of eq. (2) gives

$$\frac{dQ_{i+1/2}}{dt} =$$
$$-\beta\frac{(QV)_{i+1} - (QV)_i}{\Delta x} - g\bar{A}_{i+1/2}\cos\theta\frac{h_{i+1} - h_i}{\Delta x} + g\bar{A}_{i+1/2}S_{i+1/2} \qquad (12)$$

The boundary discharge, Q_i of each cell can be computed as the average value of the neighboring nodes values. The areas at the nodes $\bar{A}_{i+1/2}$ are computed with the average depth measured at the boundaries of the cell [7]:

$$Q_i = \frac{Q_{i+1/2} + Q_{i-1/2}}{2} \qquad (13)$$

$$\bar{A}_{i+1/2} = f\left(\frac{h_{i+1} + h_i}{2}\right) \qquad (14)$$

The value of flux, $(QV)_i$ can be estimated by the following upwind conditions:

$$(QV)_i = \frac{Q_{i+1/2}+Q_{i-1/2}}{2} \begin{cases} V_{i-1/2}; & \frac{Q_{i+1/2}+Q_{i-1/2}}{2} \geq 0 \\ V_{i+1/2}; & \frac{Q_{i+1/2}+Q_{i-1/2}}{2} < 0 \end{cases}$$

$$(15)$$

The stability of the scheme described by eq. (10) through eq. (15) depends on the ODE solver for its implementation. The accuracy is only of first order since the scheme is based on first order upwind conditions.

Steady state scheme-discretized form

Considering a positive flow in a trapezoidal channel, from eq. (12) the steady state solution is derived.

$$-\beta \frac{(QV)_{i+1}-(QV)_i}{\Delta x} - g\bar{A}_{i+1/2}\cos\theta\frac{h_{i+1}-h_i}{\Delta x} + g\bar{A}_{i+1/2}S_{i+1/2} = 0$$

$$h_{i+1} = h_i + \frac{1}{\cos\theta}\left(\frac{\beta Q^2}{g(\bar{A}_{i+1/2}*\bar{A}_{i-1/2})} - \frac{\beta Q^2}{g\bar{A}_{i+1/2}^2} + \Delta x S_{i+1/2}\right)$$

$$(16)$$

where

$$\bar{A}_{i+1/2} = \frac{1}{4}(h_{i+1}+h_i)^2\cot\alpha + \frac{1}{2}(h_{i+1}+h_i)b$$

$$\bar{A}_{i-1/2} = \frac{1}{4}(h_{i-1}+h_i)^2\cot\alpha + \frac{1}{2}(h_{i-1}+h_i)b$$

$$(17)$$

for $i = 1,2,3,\dots,N+1$

Boundary and initial conditions

In the numerical scheme governed by eq. (10), (12) and (16), we consider only subcritical flow conditions. With the use of staggered grids, physical boundaries coincide with scalar control volume (mass conservation) boundaries, and then additional nodes surrounding the domain boundaries are required to store the scalar boundary values [9]. As shown in figure 2, the inlet flow rate Q_{in} is stored at the domain boundary located at $i = 1/2$, and the inlet depth h_{in} is stored at $i = 0$. The outlet values, Q_{out} and

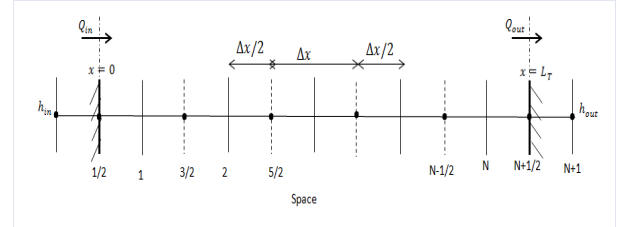h_{out}, are also located accordingly as given in the figure.

Figure 2: Position of h and Q cells at the domain boundaries.

The values of h at the physical boundaries are obtained by the upwind method, that is $h_{1/2} = h_{in}$ $h_{N+1/2} = h_{out}$. With $Fr < 1$, both boundaries must be specified (Q_{in} and Q_{out} or h_{in} and h_{out}). The numerical solution is based on the so-called backwater curve, implying that the scheme is solved backwards along the domain as indicated in figure 3.
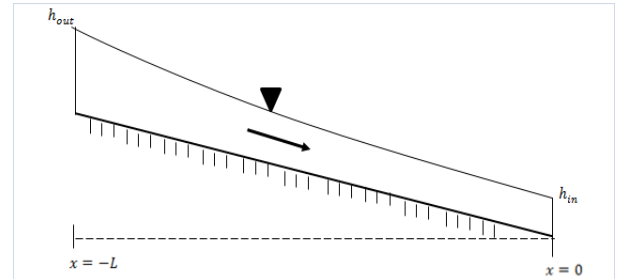

Figure 3: Boundary conditions for computing subcritical flow.

The initial conditions are the values of h and Q at time zero over the entire domain, $i = 1,2,3,\dots,N$. Initial values are often used to initialize the iterations for a system with fully defined boundary conditions, and it depends on specific flows. A steady state solution, h^0 and Q^0, can be assumed as the initial values.

VERIFYING THE NUMERICAL SCHEME

The results obtained from the numerical scheme developed here are in good agreement with the results documented in the literature [6]. Water flow with a steady state flow rate, $Q = 4\ m^3/s$ through a trapezoidal channel: bottom width, $b = 3.5\ m$, side slope $m = 1.5$, length, $L = 1000\ m$, bottom slope, $\theta = 0.05730\ deg$ and Manning's roughness coefficient, $n_M = 0.015$, was simulated for three different levels at the downstream boundary (initial conditions): $h_0 = 1.0,\ 0.664\ and\ 0.4$ m. Figure 4(b) shows the result obtained for the described channel using the steady state eq. (16). Comparing with figure 4(a), it shows that the numerical scheme presented here yields results which are in good agreement with those accepted in literature. Both results are typical of flow profiles for subcritical flow conditions in a uniform channel. It can be seen in the figures that the flow approaches the normal depth $h_n = 0.664$m provided that the flow depth at the inlet is greater than or equal to the critical depth, $h_c = 0.4$m.

FLOW PROFILE IN A RECTANGULAR VENTURI CHANNEL

The Venturi flume simulated here is taken from [11]. The flume geometry is given in figure 5. The data used are the experimental data contained in [12] for studying behaviour of non-Newtonian fluids in open channel flow using a straight rectangular channel of width 300mm. The extracted data are those of kaolin- and bentonite-based fluids with properties and channel bottom slopes shown in table 1. Each pair of the experimental data (Q and h) are only used to establish the initial conditions for simulating the steady state model described by eq. (6), (7) and (8). Figure 6 shows the flow profile for fluids III and IV shown in table 1. The scheme was simulated in MATLAB using ode23. The upper plots in figure 6 give the variation of the level, and the lower plots are the profile of the Froude

number associated with the flow along the channel. Figure 6(a) shows that hydraulic jump occurs at the contraction, transiting the flow from supercritical to subcritical conditions. It can also be seen in figure 6(a) that the flow passes through a critical depth in the throat. Figure 6(b) shows that fluid IV with high flow rate accelerates steadily in the channel, and as it can also be seen the channel contraction is not large enough to
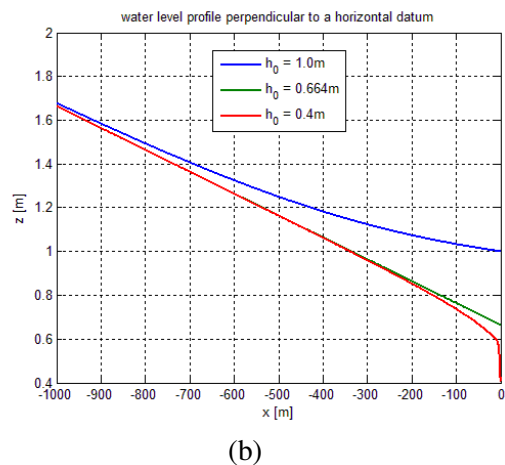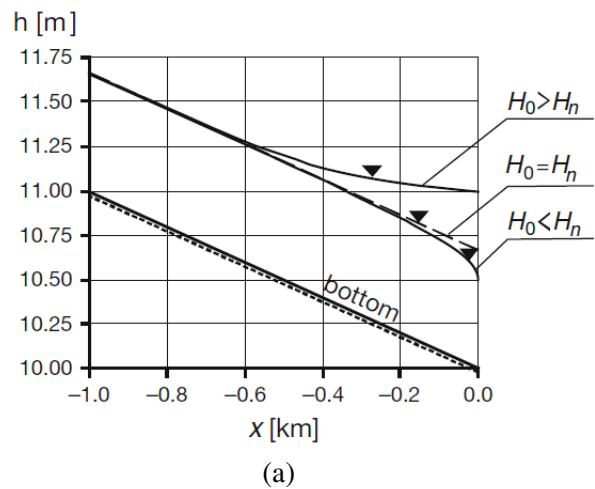

(a)

(b)

Figure 4: Steady gradually varied flow level profile in a uniform trapezoidal channel; (a) Result presented in [6]. (b) Result obtained with eq. (16).
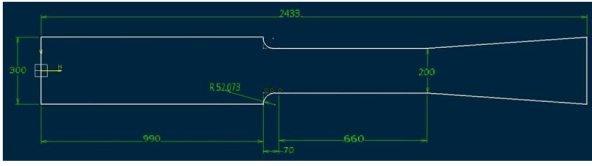
Figure 5: Flume dimension [11].

| Properties	Fluids			
	Bentonite-based	Kaolin-based		
	I	II	III	IV
ρ (kg/m^3)	1025	1118.5	1087.1	1098.5
τ_y (Pa)	5.410	10.551	4.985	6.84
K (Pa.s^n)	0.004	0.834	0.03	0.148
n	1.000	0.387	0.717	0.517
channel slope (degree)	2	4	2	3

Table 1: Properties of non-Newtonian fluids for flow simulation [12].

cause a hydraulic jump in the flow. Figure 7 shows the flow profiles of fluids III and IV in the channel when the throat width is reduced to $b = 0.085m$. The result in figure 7(b) shows that increasing the contraction of the channel, the high viscous fluid can transit from supercritical to subcritical flow conditions as expected within the channel. Figure 7(a) shows also that as the contraction is increased the height of the hydraulic jump at the channel contraction increases and the position of the critical depth at the throat is extended.

FLOW RATE MODEL

As can be seen in figure 7, when a sufficient contraction is introduced in a channel, a supercritical flow transits to subcritical flow condition over a relatively large area of the throat. If the flow passes through a critical depth within the throat, a unique relationship between the steady state flow rate and the level measured at a

point where the flow is subcritical is established. As given in [5], the flow rate can then be estimated using the same model applicable to subcritical flume.
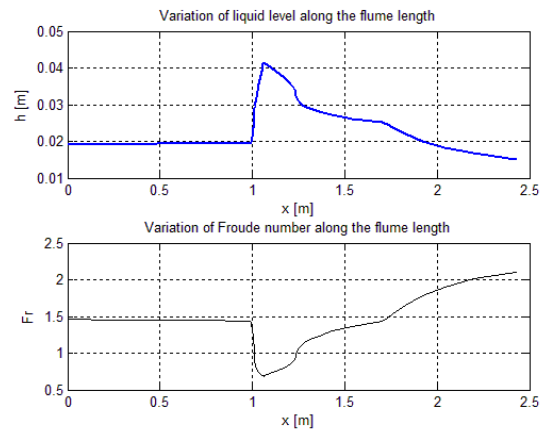
(a) Fluid III: $Q = 3.644 l/s$.
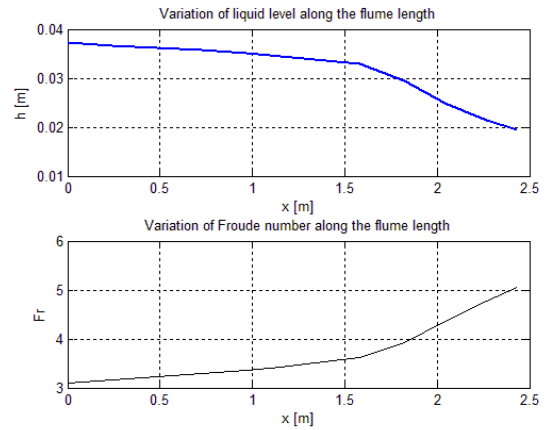
(b) Fluid IV: $Q = 20.821 l/s$.

Figure 6: Steady gradually varied flow profiles with a supercritical upstream flow in a rectangular flume: $b = 0.2m$.

For a rectangular flume, the model is described as follow:

$$Q = \left(\frac{2}{3}\right)^{1.5} C_d \, C_v \sqrt{\frac{g}{\alpha}} \, b h_m^{1.5} \qquad (18)$$
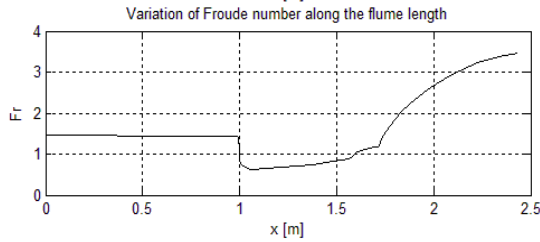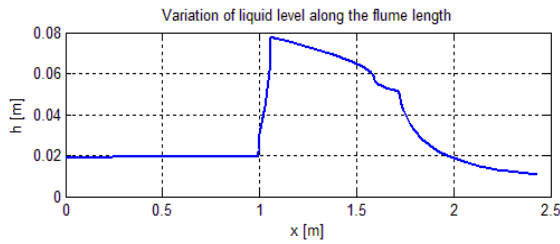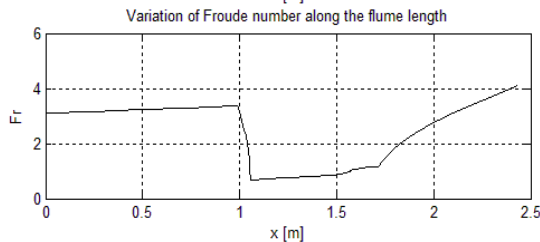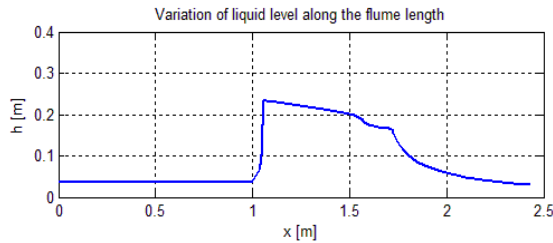
(a) Fluid III: $Q = 3.644 l/s$.

(b) Fluid IV: $Q = 20.821 l/s$.

Figure 7: Steady gradually varied flow profiles with a supercritical upstream flow in a rectangular flume: $b = 0.085 m$.

where C_d is the coefficient of discharge accounting for losses, and C_v is the coefficient correcting the replacement of the specific energy at the measuring point with the measured depth, h_m. b is the width of the throat, and α is the average kinetic energy correction factor. C_d and C_v are given by:

$$C_d = (1 - 0.006 L/b)(1 - 0.003 L/h_m)^{3/2} \quad (19)$$

$$C_v = \left(1 + \frac{\alpha}{2gh_m^3}\left(\frac{Q}{b}\right)^2\right)^{1.5} \quad (20)$$

where L is the length of the throat. Since the width of the throat is uniform and the flow within the throat before critical depth is subcritical, the level can be measured in the throat.

RESULTS AND DISUSSION

The model described by eq. (18) was used to estimate the steady state flow rate, and the response of the system to any slight deviation from a steady state was studied using the unsteady state numerical scheme given by eq. (10) and (12).

Estimation of flow rate

Figure 8 shows the simulated flow rate compared with the real flow rate at different measured levels in each of the fluid conditions I and II given in table 1. The values of level used were simulated from the steady state scheme, eq. (8) at the position 1/4th of the throat length from the throat entrance. It can be seen that the simulated flow rates in both fluids show very good agreement with the real flow rate. The results were obtained with some calibration of the model using α as the only tuning parameter. The value shown against each plot of figure 8 shows that α depends on the fluid and on the channel contraction. α also corrects the simulated flow rate for deviations due to inaccurate estimation of the discharge coefficient.

Dynamic behaviour

Since the expected flow condition within the throat of the testing channel is subcritical, the algorithm for unsteady state solution presented here can be performed between the entrance of the throat and the downstream where the flow is critical. The flow rate at the inlet and the
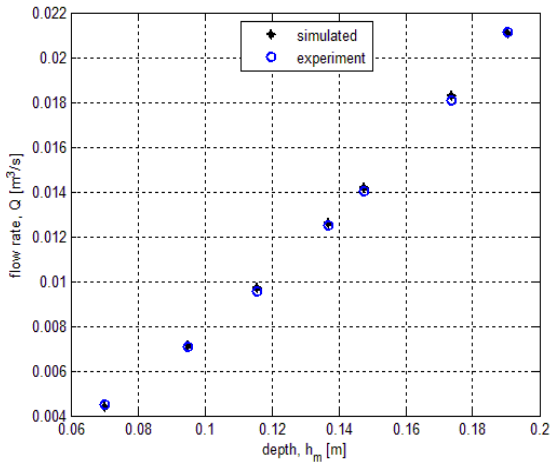
(a) Fluid I: $b = 0.11m$; $\alpha = 1.03$.
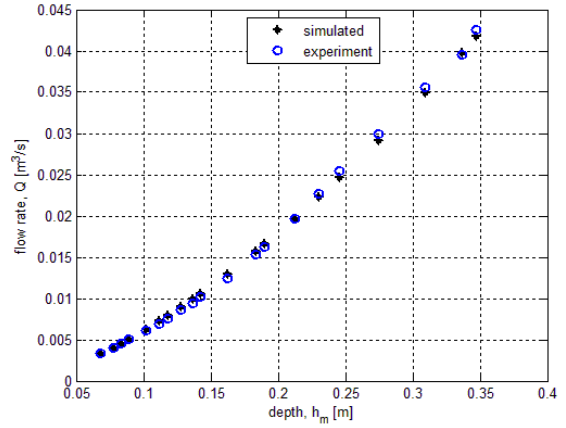
(b) Fluid II: $b = 0.087m$; $\alpha = 0.98$.

Figure 8: Comparing the simulated flow rate with the real flow rate in a Venturi channel.
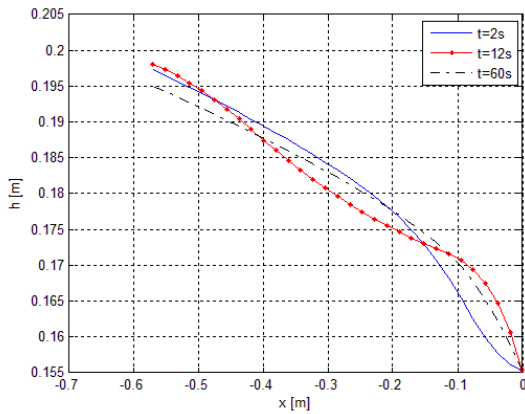
(a) Fluid I: Flow profiles at different time.
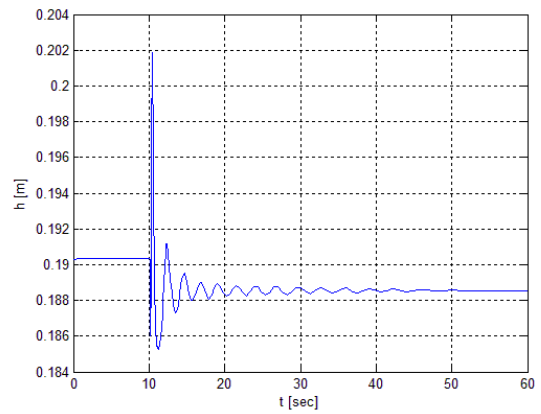
(b) Fluid I: Time evolution of measured depth, 22nd cell.
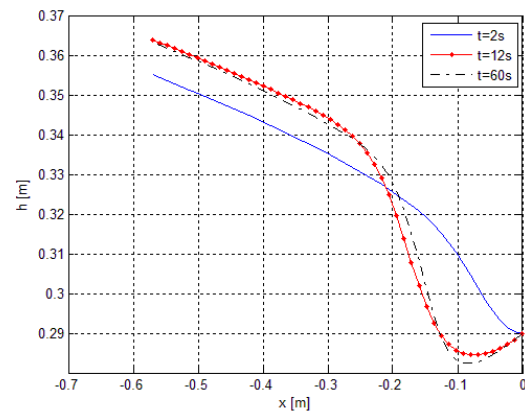
(c) Fluid II: Flow profiles at different time.
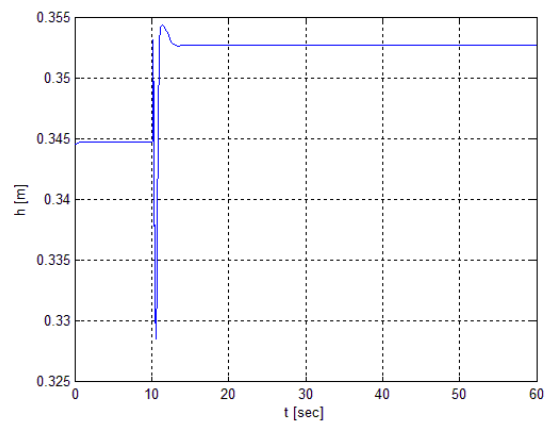
(d) Fluid II: Time evolution of measured depth, 37th cell.

Figure 9: Unsteady state solution for a step change in the flow rate.

corresponding critical depth were the two boundary conditions. The steady state solution based on the boundary flow rate was used as the initial condition. The results shown in figure 9 gives the dynamic response of the flows for fluids I and II with steady state flow rates $Q = 21.137\,l/s$ and $Q = 42.539\,l/s$, and a step change in the flow rate -1.0 and 2.0 l/s respectively. The step change was applied after 10 seconds in each case. The left side plots of figure 9 show the free surface level profile at three time instances, and the right plots show the corresponding time evolution of the level at the measured position for the two cases. As can be seen in figure 9(a and c), the solution of the unsteady state lies within the point of level measurement. The levels before 10 seconds correspond to the steady state values as can be seen by comparing figures 8(a) with 9(b), and 8(b) with 9(d). The values shown in figure 9(d) is slightly lower, and this is due to the size of the grid used. Using the levels in each flow at the end of the simulation run time where the flow is steady, the corresponding simulated flow rates are $20.08\,l/s$ and $42.80\,l/s$ representing accuracy of 0.28% and 3.9% respectively in using the unsteady state scheme for flow rate estimation in a dynamic system. As can be seen in figure 9(d), the system reaches a new steady state corresponding to the new flow rate in less than 5 seconds after the step change is applied with few oscillations. However, with a sudden decrease in the flow rate (fluid I), the system oscillates quite long before reaching a steady state. The systems were simulated in MATLAB using ode15s with spatial grid sizes 30 and 50 respectively. The major challenge in achieving the results was locating the critical depth in the throat.

CONCLUSION

In this paper we investigated the possibility of using a Venturi channel to estimate the flow rate of a non-Newtonian fluid in an open channel. Non-Newtonian fluid flow behavior was studied using the one-dimensional Saint Venant equation. The analysis was based on the supercritical upstream flow condition in the channel. We found that both channel contraction and the fluid apparent viscosity are critical parameters that determine the fluid flow behavior in the channel, and when there is a sufficient contraction to cause flow jump to subcritical levels within the throat, the standard specific energy model can be used to simulate a steady state flow rate. The results showed that the simulated flow rate is in a good agreement with the real flow rate when the model is properly tuned. Also, the dynamic response of the system for a slight deviation of steady state values was studied, and the results showed that the scheme we presented here is stable within some degree of accuracy, and capable of predicting the system response, reaching the steady state solution within the simulation run time. We will investigate the optimum channel contraction and throat length for a supercritical Venturi flume in our future work.

ACKNOWLEDGEMENT

REFERENCES

[1] Balmforth NJ, Craster RV. *Geophysical aspects of non-Newtonian fluid mechanics*. Geomorphological Fluid Mechanics 2001; LNP 582: 34 - 51.

[2] Ministere du Developpment durable, de L'environment et Desparcs du Que'bec (2007). *Sampling guide for environmental anlysis: booklet 7 - flow measurement methods in open channels*. May 2007, Centre d'expertiseen analyse environmentale du Que'bec, 223p.

[3] Wilson KC. *Flume design for homogeneous slurry flow*. Particulate Science and Technology 1991; 9: 149-159.

[4] Smith RE, Chery DL, Renard Jr KG, Gwinn WR. *Supercritical flow flumes for measuring sediment-laden flow,* Bulletin No. 1655, 72 p. Illus: U.S. Department of Agriculture Technical, 1981.

[5] ISO 4359: 2013(E). *Flow measurement structures-rectangular, trapezoidal and U-shaped flumes*. Switzerland: International Standard, 2013.

[6] Szymkiewicz R. *Numerical modeling in open channel hydraulics (Vol.83),* Springer, ISBN 978-90-481-3673-5, 2010.

[7] Aldrighetti E. *Computational hydraulic techniques for the Saint Venant equations in arbitrarily shaped geometry*, PhD thesis. Trento, Italy: Universit`a degli Studi di Trento, 2007.

[8] Jin M, Fread DL. *One-dimensional routing of mud/debris flows using NWS FLDWAV model, in Debris-Flow Hazards Mitigation: Mechanics, Prediction, and Assessment*, Edited by Chen-lung Chen, ASCE, New York, 1997: 687–696.

[9] Versteeg HK, Malalasekera W. *An introduction to computational fluid dynamics: finite volume method*, 2nd ed. England: Pearson Education Limited, Edinburgh Gate Harlow Essex CM20 2JE, 2007.

[10] Stelling GS, Duinmeijer SPA. *A staggered conservative scheme for every Froude number in rapidly varied shallow water flows*. International Journal for Numerical Methods in Fluids 2003; 43: 1329 - 1354.

[11] BAMO Measure. *Flow rate measurement in open channel: DF 2500 Instructions manual*. Argenteuil: BAMO Control Ltd., 2009.

[12] Haldenwang R. *Flow of Non-Newtonian Fluids in Open Channels*, PhD thesis. Cape Town, South Africa: Cape Technikon, 2003.

SMART SENSORS FOR MEASURING FLUID FLOW USING A VENTURI CHANNEL

Cornelius E. Agu and Bernt Lie[1]
Faculty of Technology, Telemark University College
Norway

ABSTRACT

In certain applications, the use of a direct flow meter to measure flow rates could be very expensive due to size, and may give inaccurate results due to adverse operating conditions. One alternative is to use an open channel flow measurement technique. The use of a hydraulic structure such as Venturi flume with one point level measurement is robust enough to estimate the flow rate. However, flow rates estimated by using the flow-depth relationship established in the channel are only accurate in steady state conditions. For conditions where the free surface flow is influenced by waves such as flows in oil platform, river flow in hydropower, fluidized powder transport, etc., steady state free surface level is barely reached within the required control time. This study presents a smart system for continuous measurement of fluid flow rate in a Venturi channel, which is required for control purposes. The method developed and presented here is based on merging the level measurements with the one-dimensional Saint Venant equation through a Kalman filter to provide real-time estimation of flow rate for both Newtonian and non-Newtonian fluids.
Keywords: Smart Sensor, Venturi channel, Saint-Venant Equation, Real-time estimation, Kalman filter.

---

[1] Corresponding author, E-mail: bernt.lie@hit.no

NOMENCLATURE

A Cross sectional area [m^2]
$\bar{A}$ Average cross sectional area [m^2]
f Coefficient
b Channel width [m]
C Observation matrix
E Innovation covariance matrix
e Error
Fr Froude number
g Gravitational acceleration [m/s^2]
h Free surface level [m]
K Flow behaviour index [Pa.s^n]
K Kalman gain
N Spatial grid size
N_r Ensemble size
n Fluid consistency index
P_{wet} Wetted perimeter [m]
Q Flow rate [m^3/s]
R_h Hydraulic radius [m]
S Slope
u Model input
V Average velocity [m/s]
V Measurement noise covariance matrix
v Measurement noise vector
w Process noise vector
W Process noise covariance matrix
X Estimated state covariance matrix
x Distance
x State vector
$\hat{x}$ Estimated state vector
$\bar{x}$ Mean value
y Measurement signal vector
$\hat{y}$ Estimated measurement signal vector
Z Cross covariance matrix
β Momentum correction coefficient
$\mathcal{E}$ Error matrix
$\boldsymbol{\rho}$ Density [kg/m^3]
θ Inclination of the channel bottom [degree]
θ Model parameter vector
$\hat{\theta}$ Estimated model parameter
$\boldsymbol{\tau_y}$ Yield shear stress [Pa]

Subscripts

x State
0 Bottom origin; initial condition
c Critical

i Index in space
in Inlet
out Outlet
θ Parameter

Superscripts

0 Initial condition
a Assimilated
f Forecast
j Index in size
k Index in time
T Transpose

INTRODUCTION

Fluid flow in an open channel has wide industrial applicability. It is used in transportation of slurries, water supply for irrigation and river flow [1]. Due to severe operating conditions, use of common flow meters may be considered very expensive or unsafe to measure the flow rate of slurries (non-Newtonian fluids). One common and simple method is to use an open channel hydraulic structure such as a "weir" (Notch) or a "control flume" which introduces a restriction in the flow direction that results in flow variations (that is, changes in approach velocity and level) along the channel [2]. Flumes are commonly used in the industry. The flow-depth relationship established in control flumes is only applicable in steady state [3]. For conditions such as flows in oil platform, river flow in hydropower, fluidized powder transport, etc., where the free surface flow is influenced by waves, a steady state free surface level is barely reached within the required control time. In this situation, estimating any flow rate in the channel will require a real-time estimation technique.

A real-time estimation technique requires knowledge about a model which accurately describes the system, and that the system must be observable. For an observable system, it follows

that from an output of the system the behavior of the entire system can be determined. For simplicity, one-dimensional Saint Venant equation is commonly used to model an open channel flow [4]. Several techniques have been used to incorporate a measurement from the physical system into the Saint Venant equation for state estimation in an open channel flow. Most of these methods are based on Kalman filter algorithms applied to linear models [5, 6, 7]. The use of the standard Kalman filter will require linearizing the Saint Venant model, and this may mean not capturing some important detail of the system, especially when there is rapid variation of the system boundary conditions [7]. In [8], the Extended Kalman filter was applied to estimate uncertain parameters in two-dimensional shallow water models. The Extended Kalman filter (EKF) involves computation of the Jacobian at every time step which increases the computation burden [9]. The Ensemble Kalman filter (EnKF) is an alternative to the Extended Kalman filter, and is based on Monte Carlo simulation of the nonlinear system [9]. The Ensemble Kalman filter was originally developed for data assimilations in weather prediction and other areas involving large use of data [10]. In [9], the author used EnKF to incorporate Lagrangian measurements into a two-dimensional shallow water model with poorly known boundary conditions.

The main purpose of this study is to investigate a smart system for continuous measurement of fluid flow rate in an open channel. In the present work, we apply the Ensemble Kalman filter scheme to estimate the real-time flow rate of fluid in a Venturi channel. The main idea about the use of EnKF is to ensure that the nonlinear unsteady state system is used directly without any form of linearization. Since it is numerical tricky to solve the Saint Venant equation, we consider a scheme based on the finite volume method with staggered grid for obtaining solutions of the unsteady state

model in this work. With the staggered grid arrangement, the varying slope of the liquid surface is captured [11]. As the numerical scheme is only suitable for subcritical flow conditions, we consider using a Venturi channel to make the method presented here applicable to supercritical upstream flow condition as well. With this, the method can be applied to non-Newtonian fluid flow where the upstream flow conditions are often supercritical.

In the following sections, the mathematical models describing the system are presented. The algorithm for state estimation of the flow is described. Different results from the algorithm are presented and discussed.

MATHEMATICAL MODEL

The unsteady state flow of fluid in an open channel can be described by the one-dimensional Saint Venant equations [4]:

$$\frac{\partial A}{\partial t} + \frac{\partial Q}{\partial x} = 0 \tag{1}$$

$$\frac{\partial Q}{\partial t} + \frac{\partial \left(\frac{\beta Q^2}{A}\right)}{\partial x} = gA\sin\theta - gA\cos\theta\frac{\partial h}{\partial x} - gAS_f \tag{2}$$

Eq. (1) and (2) are based on mass conservation and momentum conservation principles respectively; Q is the volume flow rate, and A and h are the flow cross sectional area and the free surface level respectively. θ is the angle of inclination of the channel, and g is the acceleration due to gravity. β is the momentum correction coefficient with a value between 1.03 and 1.07. S_f is the frictional slope, and is given by [12,13]:

$$S_f = \frac{n_m V}{R_h^{2/3}} \tag{3}$$

where $V = Q/A$ is the average flow velocity, n_m is Manning's roughness coefficient and

$R_h = \frac{A}{P_{wet}}$ is the hydraulic radius at each cross section. In a non-Newtonian fluid flow, the internal frictional shearing stresses dominate; the frictional slope S_f is then given by [12]:

$$S_f = \frac{\tau_y}{\rho g R_h}\left[1 + \left(\frac{(\epsilon+1)(\epsilon+2)|V|}{(0.74+0.656\epsilon)\left(\frac{\tau_y}{K}\right)^\epsilon R_h}\right)^{\frac{1}{\epsilon+0.15}}\right] \quad (4)$$

where $\epsilon = \frac{1}{n}$; ρ, τ_y, K and n are the fluid properties denoting the density, yield shear stress, fluid behaviour index and fluid constituency index respectively.

Steady state scheme-ODE form

Considering a rectangular channel: $A = bh$ where $b(x)$ is the width at a given section of the flow, the steady state solution is obtained by solving the following set of ODE's:

$$\frac{dV}{dx} = -\frac{V}{A}\frac{dA}{dx} \quad (5)$$

$$\frac{dA}{dx} = b\frac{dh}{dx} + ch \quad (6)$$

$$\frac{dh}{dx} = \frac{gAS + \beta chV^2}{gA\cos\theta - \beta BV^2} \quad (7)$$

where $c = \frac{db}{dx}$ and $S = \sin\theta - S_f$. From eq. (7), the critical flow occurs when:

$$gA\cos\theta - \beta BV^2 = 0 \quad (8)$$

The depth of the flow which satisfies eq. (8) is the critical depth. The open channel flow is generally characterized by the Froude number, $Fr = \frac{V}{\sqrt{(gh)}}$ [14]. When $Fr < 1$, the flow is subcritical and when $Fr > 1$, the flow is supercritical. The condition is near critical when $Fr \approx 1$.

Unsteady state scheme

Figure 1 shows the grid arrangement. The node of control volume for momentum conservation is indicated by the line **P** where the velocity is stored. The boundaries of the velocity control volume indicated by the lines **w** and **e** correspond to the nodes of the control volumes for mass conservation, where the depths of the liquid surface are stored. The grid is uniform with spatial spacing, Δx. In eq. (2), the spatial integration of the free surface depth gradient is approximated by the central differencing method, and the flux term is approximated by first order upwind [11], and this leads to:

Scheme for volume conservation

$$\frac{dA_i}{dt} = -\frac{Q_{i+1/2} - Q_{i-1/2}}{\Delta x} \quad (9)$$

Scheme for momentum conservation

$$\frac{dQ_{i+1/2}}{dt} = -\beta\frac{(QV)_{i+1} - (QV)_i}{\Delta x} - g\bar{A}_{i+1/2}\cos\theta\frac{h_{i+1} - h_i}{\Delta x} + g\bar{A}_{i+1/2}S_{i+1/2} \quad (10)$$

The boundary discharge, Q_i of each cell can be computed as the average value of the neighboring nodes values. The areas at the nodes $\bar{A}_{i+1/2}$ can be computed with the average depth measured at the boundaries [15].

$$Q_i = \frac{Q_{i+1/2} + Q_{i-1/2}}{2} \quad (11)$$

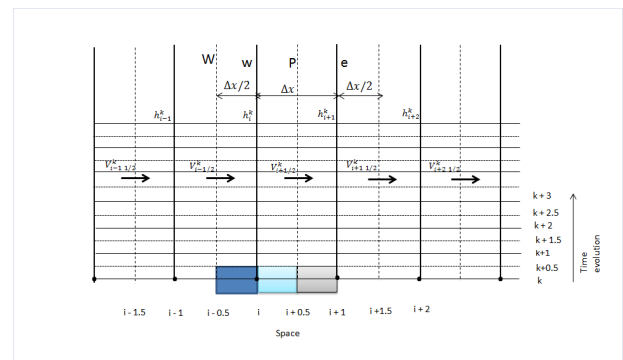$$\bar{A}_{i+1/2} = f\left(\frac{h_{i+1} + h_i}{2}\right) \quad (12)$$

Figure 1: Staggered grid arrangement for V and h control volumes.

Considering only the positive flows, the depths at the boundaries of the mass conservation control

volume and the value of flux, $(QV)_i$ from the momentum equation can be estimated by the following upwind conditions [15, 16]:

$$h_{i+1/2} = h_i \tag{13}$$

$$(QV)_i = \frac{Q_{i+1/2} + Q_{i-1/2}}{2} V_{i-1/2} \tag{14}$$

The stability of the scheme described by eq. (9) through eq. (14) depends on the ODE solver for its implementation. The accuracy is only of first order since the scheme is based on first order upwind conditions.

Boundary conditions

As shown in figure 2, the inlet flow rate Q_{in} is stored at the domain boundary located at $i = 1/2$, and the inlet depth h_{in} is stored at $i = 0$. The outlet values, Q_{out} and h_{out}, are also located accordingly as given in the figure. The values of h at the physical boundaries are obtained by the upwind method, that is $h_{1/2} = h_{in}$ $h_{N+1/2} = h_{out}$ [11]. With $Fr < 1$, both boundaries must be specified (Q_{in} and Q_{out} or h_{in} and h_{out}).
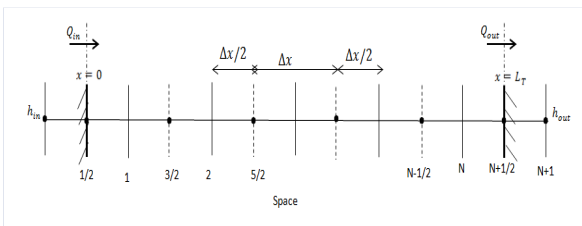

Figure 2: Position of h and Q cells at the domain boundaries.

The solution is based on the so-called backwater curve, implying that the scheme is solved backwards along the domain.

REAL-TIME ESTIMATION ALGORITHM

The algorithm we present here is based on the Ensemble Kalman filter (EnKF) which is based on Monte Carlo simulation of the nonlinear system.

State estimation

Consider a discrete time nonlinear dynamic system given by

$$x_{k+1} = f(x_k, u_k, w_k) \tag{15}$$

$$y_k = g(x_k, u_k, v_k) \tag{16}$$

where x_k and u_k are the state and deterministic input respectively, at time step k, and y_k is the measurement sensor signal at time step k, assumed to be related to system states. $w_k \sim \mathrm{N}(\bar{w}_k, W_k)$ and $v_k \sim \mathrm{N}(\bar{v}_k, V_k)$ are stochastic white noise disturbances in the process and in the measurement respectively at time step k. Both w_k and v_k are assumed normally distributed with respective mean $\bar{w}_k$ and $\bar{v}_k$, and covariance W_k and V_k. The objective is to obtain the estimate, $\hat{x}_k$ of the real state x_k using signal from the level measurement, y_k, so that the covariance $\varepsilon[(e_k)(e_k)^T]$ of the estimate is minimized, where $e_k = \hat{x}_k - x_k$, and superscript T implies transposition.

Given the initial condition of the state $x_0 \sim \mathrm{N}(\bar{x}_0, X_0)$, in which $\bar{x}_0$ is the mean value and X_0 is the covariance; assuming there are N_r realizations (ensembles) of x_0 drawn at random such that $x_0^j \sim \mathrm{N}(\bar{x}_0, X_0)$ with $j = 1,2,3, \dots, N_r$, the forecast of the state estimate and measurement signal for each ensemble point are given by [10]:

$$x_k^{fj} = f(x_{k-1}^{aj}, u_{k-1}, w_k^j) \tag{17}$$

$$y_k^{fj} = g(x_k^{fj}, u_k, v_k^j) \tag{18}$$

When the forecasted state estimate, x_k^{fj} for each ensemble point is updated, it gives the analyzed state estimate, x_k^{aj}:

$$x_k^{aj} = x_k^{fj} + K_{xk}(y_k + v_k^j - y_k^{fj}) \tag{19}$$

where v_k^j is a random variable drawn from a normal distribution of data with zero mean and covariance, V_k. K_k is the Kalman gain at time step k, given by:

$$K_{xk} = Z_{xk}E_k^{-1} \tag{20}$$

Z_k and E_k are the cross and innovation covariance matrices respectively given by:

$$Z_{xk} = \frac{1}{N_r-1}\sum_{j=1}^{N_r}(x_k^{fj} - \hat{x}_k^f)(y_k^{fj} - \hat{y}_k^f)^T \tag{21}$$

$$E_k = \frac{1}{N_r-1}\sum_{j=1}^{N_r}(y_k^{fj} - \hat{y}_k^f)(y_k^{fj} - \hat{y}_k^f)^T \tag{22}$$

where $\hat{x}_k^f = \frac{1}{N_r}\sum_{j=1}^{N_r}x_k^{fj}$ and $\hat{y}_k^f = \frac{1}{N_r}\sum_{j=1}^{N_r}y_k^{fj}$.

The best possible estimate given by this algorithm is the ensemble mean $\hat{x}_k$ of the analysed state estimate, with covariance X_k which measures the uncertainty in the estimated state, $\hat{x}_k$:

$$\hat{x}_k = \frac{1}{N_r}\sum_{j=1}^{N_r}x_k^{aj} \tag{23}$$

$$X_k = \frac{1}{N_r-1}\sum_{j=1}^{N_r}(x_k^{aj} - \hat{x}_k)(x_k^{aj} - \hat{x}_k)^T \tag{24}$$

Because the ensemble spread may be too small to draw the model states to the observations [17], a coefficient f_x having value within $0 < f_x < 1$ is introduced to minimize the forecast error variance.

$$K_{xk} = f_x Z_{xk}E_k^{-1} \tag{25}$$

Performance of the estimation

The performance of the algorithm over the computation domain (cells $1 = 1,2,3,\dots,N$) is analyzed based on the relative error given by:

$$e_{rk} = \sqrt{\frac{\sum_{1=1}^{N}(\hat{x}_{i,k}-x_{i,k})^2}{\sum_{i=1}^{N}(x_{i,k})^2}} \tag{26}$$

where $x_{i,k}$ and $\hat{x}_{i,k}$ are the true state and estimated state respectively at cell i and time step k.

Parameter estimation

Effective application of the EnKF algorithm assumes that the system model is perfect. It implies that the algorithm does not account for any deficiency such as model parameter uncertainty. In real-time state estimation, the model time invariant parameters need to be estimated and then augmented into the state vector. As given in [18], the parameter estimation algorithm has the same structure as that of the state.

Let θ be any parameter of the model, and let θ_0 be the measured parameter. Supposing there are N_r realization of θ_0 such that $\theta_0^j \sim \mathbb{N}(\overline{\theta}_0, P_0)$ with $j = 1,2,3,\dots,N_r$, and $\overline{\theta}_0$ and P_0 the mean and covariance of the distribution respectively, the propagation of the parameter in time is given below.

Forecast: $\theta_k^{fj} = \theta_{k-1}^{aj}$ (27)

Corrected: $\theta_k^{aj} = \theta_k^{fj} + K_{\theta k}(y_k + v_k^j - y_k^{fj})$ (28)

where
$$K_{\theta k} = \alpha_\theta Z_{\theta k}E_k^{-1} \tag{29}$$
$$Z_{\theta k} = \frac{1}{N_r-1}\sum_{j=1}^{N_r}(\theta_k^{fj} - \hat{\theta}_k^f)(y_k^{fj} - \hat{y}_k^f)^T \tag{30}$$
and $\hat{\theta}_k^f = \frac{1}{N_r}\sum_{j=1}^{N_r}\theta_k^{fj}$. The ensemble mean of the corrected forecast parameter gives the best possible estimate of the parameter.

$$\hat{\theta}_k = \frac{1}{N_r}\sum_{j=1}^{N_r}\theta_k^{aj} \tag{31}$$

The coefficient $\alpha_\theta > 0$ is used to correct the small spread of the ensemble so that the variance between the estimated parameter and the true value is minimized.

RESULTS AND DISUSSION

The model described by eq. (5), (6) and (7) was used to simulate a fluid flow in a Venturi channel to ascertain the flow conditions. The results obtained by applying the real-time estimation algorithm described in this paper are presented here. All the simulations were done in MATLAB with ode23 for the steady state and ode15s for the unsteady state scheme.

Venturi channel and the Real system

The Venturi channel used in this work is taken from [19]. In this paper, we modified the channel throat width from 0.2m to 0.06m so as to ensure that the supercritical upstream flow jumps to subcritical flow level and then passes through the critical depth at the throat while accelerating towards the channel end.

The "real system" was obtained by simulating the model detailed under the unsteady state scheme section with arbitrary initial conditions. The measurement signal was related to the flow depth taken at the middle of the computation domain with number of cells $N = 50$. The sampling interval for the measurement is 0.25 second. The properties of the real system are given below [20]:
Fluid properties: $\rho = 1034 kg/m^3$, $K = 0.006 Pa.s^n$, $\tau_y = 12.698 Pa$, $n = 1.00$
Channel width: $b = 0.06m$
Channel slope: $\theta = 5\ deg$
Boundary flow rate: $Q = 21.017\ l/s$

The process noise, W and measurement noise, V covariance are each set to 1×10^{-8}. The fitted

covariance for the estimated states are 5×10^{-7} for the level and 3×10^{-7} for the flow rate. The covariance for the measurement noise in the estimated states was fitted to 1.5×10^{-4}.

Steady state flow profile

Figure 3 shows the flow profile of the non-Newtonian fluid (bentonite-based) simulated in the Venturi channel. The upper plot gives the variation of the fluid level, and the lower plot the profile of Froude number associated with the flow along the channel. The figure shows that hydraulic jump occurs at the contraction, transiting the flow from supercritical upstream condition to subcritical condition. It can also be
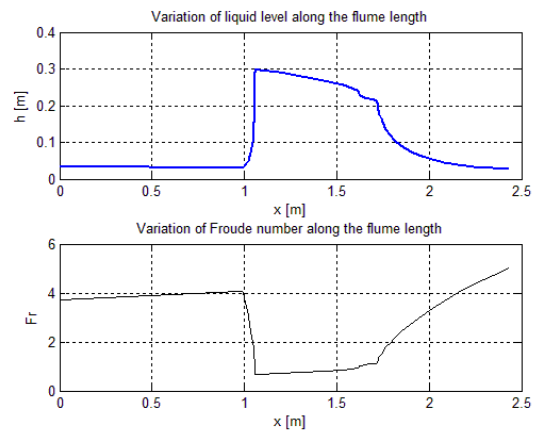
Figure 3: Steady state gradually varied flow profiles with a supercritical upstream flow in a rectangular flume.

seen that the flow passes through a critical depth in the throat where $Fr = 1$. The result shows that measurement of the fluid states ($h\ or\ Q$) can be taken at the throat where $Fr < 1$, and the unsteady state scheme described in this paper can be applied only within the throat section since the numerical scheme only considers subcritical flow conditions.

State estimation

Both the estimated states and model parameter are compared with those of the real system. In all cases, the simulation was carried out for 85 time steps. We also assumed that the boundary conditions of the system are known and fixed.

Ensemble size

Figure 4 shows variation of the mean square error (MSE) of the estimated states at the middle cell (26th cell) over 85 time steps against the ensemble size, N_r with $f_x = 1.0$ (upper plot), and the MSE against the spread coefficient (gain factor), f_x with $N_r = 60$ (lower plot). The result shows that MSE of both flow rate and level decrease as the N_r increases. When $N_r > 50$, it shows that there is no much significant different in the error. With $N_r = 60$, the result shows that MSE of the flow level is minimum at $f_x \approx 0.75$. The MSE of flow rate slightly decreases with decreasing f_x.

In the subsequent results shown in this section, we use the values $N_r = 60$ and $f_x = 0.75$ in the simulations.

Perturbed system with correct model parameters

Figure 5 compares the estimated states with the true states of the system when there is no uncertainty in the model parameters. The upper plots are the flow profiles over the computation domain simulated after 20 seconds ($k = 81$), and the results show that estimation of both the flow rate and the fluid level are good within a tolerable limit. Figure 6 shows the time evolution of the relative error of the estimates for both level (upper plot) and flow rate (lower plot). In both plots, the errors rapidly drop after 2 time steps from the initial value to a value relatively constant over time. It can be seen that the average relative error is about 1.0% for the level and 0.7% for the flow rate. The relative error measures the spread of the

estimated states around the real state over all the cells in the domain, and the time evolution shows that the error is approximately the same as the time elapses.
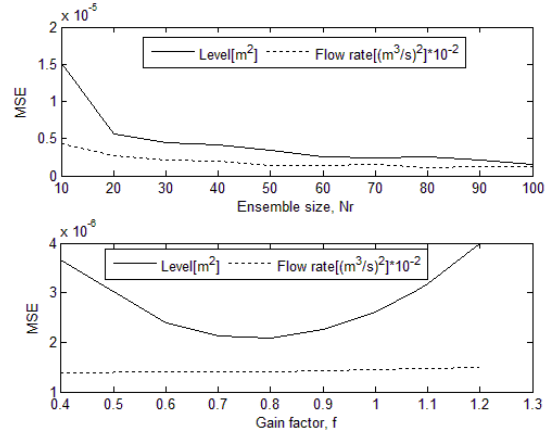
Figure 4: Variation of mean square error at the measured point with ensemble size (upper plot) and with ensemble spread coefficient (lower plot).

System with uncertain model parameters

The results of using uncertain model parameters are presented here. The results compare the estimated states with the true state when the channel width used in the model is 0.059m as against 0.06m used in the real system. Figure 7 (a) shows that the estimated flow level is very poor when the model parameter estimation algorithm is not incorporated in the state estimation algorithm, and the variance in the result is due to uncertainty in the measurement of the channel width. Comparing figure 7 (a) (lower plot) with figure 5(b) (lower plot), it shows that within the width measurement uncertainty the estimated flow rate is not significantly affected; this is also shown by the evolution of the relative error of the flow rate estimate, figure 7(b) (lower plot). The relative error of the estimated level, figure 7(b) relatively increases after time step 2, showing that the estimation yields poor results with time. The uncertainty in the channel width affects the estimation of the flow level possibly because both
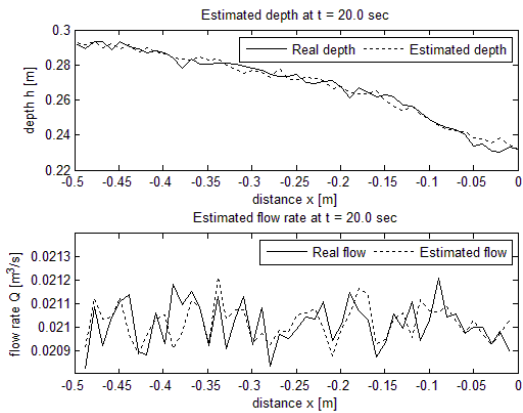
(a)
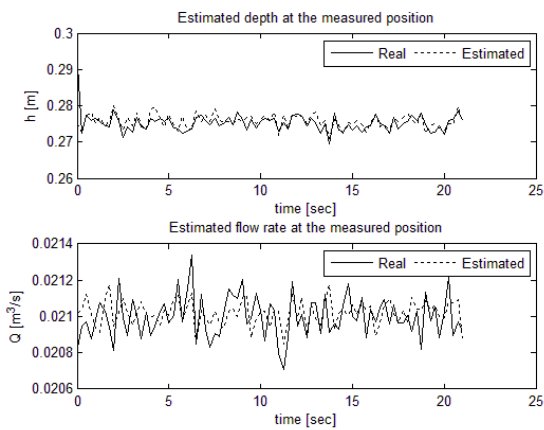
(b)

Figure 5: Comparison of the estimated state with the real state: (a) flow Profile along the domain at time step 81 (b) time evolution of the states at the middle cell.

Figure 6: Time evolution of the relative error of the estimated states: flow level (upper plot); flow rate (lower plot).

quantities have the same dimension and because the flow level directly depends on the channel width for a given flow area.

Figure 8 shows the results when the parameter estimation model is incorporated into the state estimation algorithm. Comparing figures 5(b) and 8(a), it shows that the states estimation is relatively the same. Figure 9 s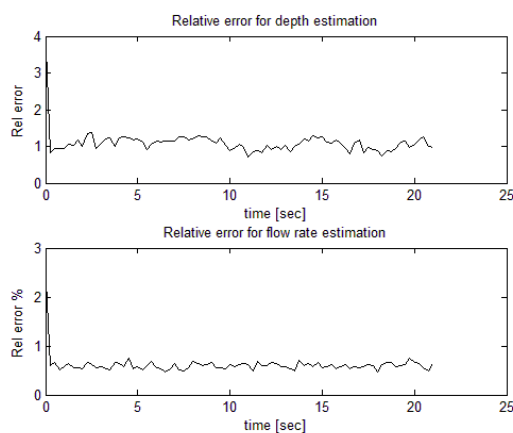hows the evolution of the estimated channel width with time. It can be seen that the width (curve line) rapidly increases reaching the real system width (straight line) after about 7.0 sec. The result shows that after 7.0 sec, the estimated width has a mean value of about 0.06m with mean error of $\pm 0.042\%$ over the simulation time.

CONCLUSION

In this paper we investigated the possibility of estimating the flow rate of a non-Newtonian fluid in an open channel by using the ensemble Kalman filter (EnKF) algorithm. Due to possible uncertainties in the model parameters, we incorporated estimation of the parameters into the state estimation algorithm. Although the numerical scheme for solving the unsteady state of the system considers only subcritical flow conditions, we found that by using a Venturi channel with adequate contraction, the scheme can also be applied to a non-Newtonian fluid flow with supercritical upstream conditions within the throat where the flow is subcritical. The results for assimilating one measurement of the free surface level taken at the middle of the throat into the state forecast showed that the real-time estimation algorithms we presented here are capable of estimating the wavy nature of the states due to process disturbances and measurement noise within $\pm 0.7\%$ accuracy for the flow rate and $\pm 1.0\%$ accuracy for the free surface level. The main challenge in applying the scheme to the flow
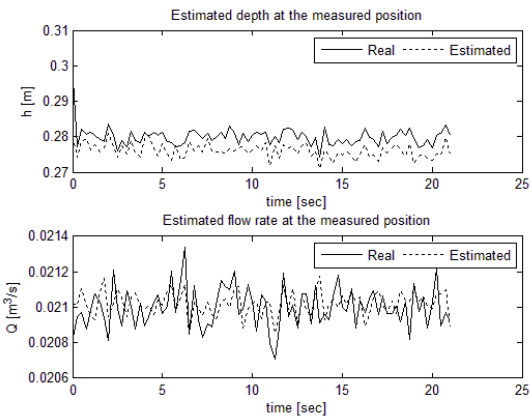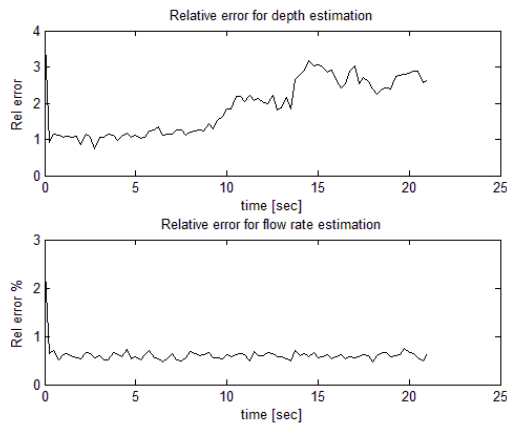
Figure 7: Comparison of the estimated state (without parameter model) with the real state: (a) time evolution of the states at the middle cell. (b) time evolution of the relative error of the estimated states.

in a Venturi channel is locating the position of the critical depth used as the downstream boundary condition in the throat. Since it is possible that the flow rate at the boundary can change in real time, we will investigate the method for estimating the boundary flow rate and how it can be incorporated into the state estimation algorithm in future work.
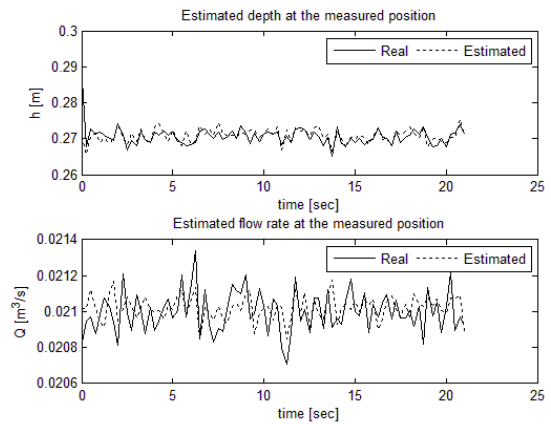
ACKNOWLEDGEMENT

Figure 8: Comparison of the estimated state (with parameter model) with the real state: (a) time evolution of the states at the middle cell. (b) time evolution of the relative error of the estimated states.
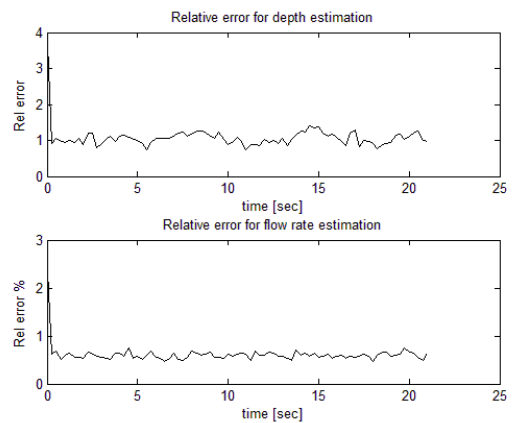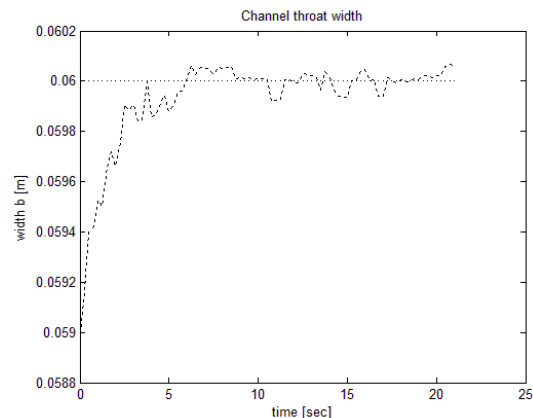

Figure 9: Estimated time-invariant channel width.

REFERENCES

[1] Balmforth NJ, Craster RV. *Geophysical aspects of non-Newtonian fluid mechanics*. Geomorphological Fluid Mechanics 2001; LNP 582: 34 - 51.

[2] Ministere du Developpment durable, de L'environment et Desparcs du Que'bec (2007). *Sampling guide for environmental anlysis: booklet 7 - flow measurement methods in open channels*. May 2007, Centre d'expertiseen analyse environmentale du Que'bec, 223p.

[3] Clemens AJ, Wahl, TL, Bos, MG, Replogle JA. *Water measurement with flumes and weirs*, Publication 58. The Netherlands: International Institute for Land Reclamation and Improvement, 2001.

[4] Szymkiewicz R. *Numerical modeling in open channel hydraulics (Vol.83),* Springer, ISBN 978-90-481-3673-5, 2010.

[5] Reddy JM. *Kalman filtering in the control of irrigation canals*. Applied Mathematical Modelling 1995; 19.

[6] Durdu ÖF. *A comparison of recursive least squares estimation and Kalman filtering for flow in open channels*. Turkish Journal of Engineering and Environmental Sciences 2005; 29: 171-183.

[7] Rafiee M, Wu Q, Bayen AM. *Kalman filter based estimation of flow states in open channels using Lagrangian sensing*. In: 48th IEEE Conference on Decision & Control, Shanghai, 2009.

[8] Wu Q, Litrico X, Bayen AM. *Data reconciliation of an open channel flow network using modal decomposition.* Advances in Water Resources 2009; 32: 193-204.

[9] Tossavainen O-P, Percelay J, Tinka A, Wu, Q, Bayen AM. *Ensemble Kalman filter based estimation in 2-D shallow water equations using Lagrangian Sensing and state augmentation*. In: Proceedings of the 47th IEEE Conference on Decision and Control, Cancun, 2008.

[10] Gillijns S, Mendoza OB, Chandrasekar J, De-Moor BLR, Bernstein DS, Ridley A. *What is the ensemble Kalman filter and how well does it work?* In: Proceedings of the 2006 American Control Conference, Minneapolis, 2006.

[11] Versteeg HK, Malalasekera W. *An introduction to computational fluid dynamics: finite volume method*, 2nd ed. England: Pearson Education Limited, Edinburgh Gate Harlow Essex CM20 2JE, 2007.

[12] Jin M, Fread DL. *One-dimensional routing of mud/debris flows using NWS FLDWAV model, in debris-flow hazards mitigation: mechanics, prediction, and assessment*, Edited by Chen-lung Chen, ASCE, New York, 1997: 687-696.

[13] Jeppson R. *Open Channel Flow: Numerical Methods and Computer Applications*. Boca Raton: Taylor and Francis Group, 2011.

[14] Wilson KC. *Flume design for homogeneous slurry flow*. Particulate Science and Technology 1991; 9: 149 – 159.

[15] Aldrighetti E. *Computational hydraulic techniques for the Saint Venant equations in arbitrarily shaped geometry*, PhD thesis. Trento, Italy: Universit`a degli Studi di Trento, 2007.

[16] Stelling GS, Duinmeijer, SPA. *A staggered conservative scheme for every Froude number in rapidly varied shallow water flows*. International Journal for Numerical Methods in Fluids 2003; 43: 1329 - 1354.

[17] Lin C, Wang Z, Zhu J. *An ensemble Kalman filter for severe dust storm data assimilation over China*. Atmospheric Chemistry and Physics 2008*;* 8: 2975 - 2983.

[18] Yang X, Delsole T. *Using the ensemble Kalman filter to estimate multiplicative model parameters.* The International Meteorological Institute 2009; 61A: 601 – 609.

[19] BAMO Measure. *Flow rate measurement in open channel: DF 2500 Instructions manual.* Argenteuil: BAMO Control Ltd., 2009.

[20] Haldenwang R. *Flow of non-Newtonian Fluids in Open Channels*, PhD thesis. Cape Town, South Africa: Cape Technikon, 2003.

FLOW MALDISTRIBUTION IN THE ANODE OF A POLYMER ELECTROLYTE MEMBRANE WATER ELECTROLYSIS CELL EMPLOYING INTERDIGITATED CHANNELS

Anders Christian Olesen∗ and Søren Knudsen Kær
Aalborg University
Department of Energy Technology
9220 Aaborg East
Denmark

ABSTRACT

In this work a macroscopic, steady-state, three-dimensional, computational fluid dynamics model of the anode of a high-pressure polymer electrolyte membrane electrolysis cell (PEMEC) is presented. The developed model is used for studying the effect of employing an interdigitated, planar-circular cell design on the distribution of water in the anode. In the electrolysis of water using PEMEC the anode is fed by demineralized water. Throughout the anode, oxygen is produced and a two-phase flow develops. Interdigitated channels assist in avoiding that gaseous oxygen obstructs the transport of liquid water towards the catalytic layer of the electrode. As opposed to the more common serpentine and parallel channels, interdigitated channels force liquid water through the porous gas diffusion layer (GDL) of the electrode. This improves the supply of water, however it increases pressure losses. While interdigitated channels have been examined for planar-square cells in detail, less is known for planar-circular cells. To examine the extent of flow maldistribution, a base case is defined and a parameter variation is conducted relative to it. In the study, the following parameters are examined: water stoichiometry, temperature, GDL permeability and thickness. In conclusion, it is found that the interdigitated flow field results in an uneven distribution across the cell and that the extent depends strongly on the permeability and weaker on the remaining parameters.

Keywords: Flow maldistribution, PEMEC, Electrolysis, Modeling

NOMENCLATURE

$\mathbf{U}$	Velocity	[m/s]
K	Permeability	[m]
p	Pressure	[Pa]
N	Number of channels	[m]
A	Area	[m^2]
S	Source term	[kg / (m^3 s)]
L	Channel length	[m]
T	Temperature	[K]
J	Current density	[A/cm^2]
$\dot{m}$	Mass flow	[kg/s]
ε	Volume porosity	[-]
ρ	Density	[kg/m^3]
σ	Standard deviation	[-]
F	Faradays constant	[C/mol]
L_T	Gas diffusion layer thickness	[m]
λ	Stoichiometric factor	[-]
μ	Mean	[-]
μ	Dynamic viscosity	[Pa s]
$\mathbf{M}$	Interfacial forces	[kg/(m^{3}s)]
$\mathbf{n}$	Normal vector	[-]
r_p	Fiber radius	[m]
ε_p	Percolation threshold	[m]
n_r	Moles of reactant required	[mol]
n_s	Moles of reactant supplied	[mol]
α	Directional dependent parameter	[-]
M_W	Molecular weight	[kg/kmol]
$\mathbf{i}$	Identity matrix	[-]

∗Corresponding author: Phone: +45 2139 9153 E-mail:aco@et.aau.dk

INTRODUCTION

The production of hydrogen through water electrolysis has received growing attention in recent years [2, 1]. This interest has partially been sparked by the growing demand for sustainable produced hydrogen in fuel cell applications and partially by the demand for energy storage during peak production periods especially associated with the increasing use of sustainable power sources like wind turbines and solar power [4, 6, 3]. As a technology water electrolysis has been commercially available for nearly a century. These systems have typically been alkaline based, very bulky, inefficient and suffered from poor dynamic response to load changes. With the recent developments of polymer electrolyte membrane electrolysis cells (HP PEMEC), a technology has been developed that offers significant higher energy densities, current densities, efficiency as well as a good dynamic response. [1]

In the electrolysis of water using PEMEC the overall reaction is split into two half-cell reactions occuring at the anode and cathode, respectively:

$$2H_2O \rightarrow 4H^+ + 4e^- + O_2 \qquad (1)$$

$$2H^+ + 2e^- \rightarrow H_2 \qquad (2)$$
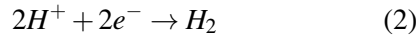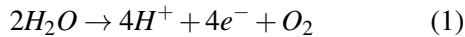
While electricity is supplied to the PEMEC, the anode is fed with demineralized water. Throughout the anode, oxygen is produced and a two-phase gas-liquid flow develops. Similarly in the cathode, hydrogen is produced along the channel length. Since water can permeate the polymer membrane, two-phase gas-liquid flow can also occur at the cathode. Although PEMEC are competitive on many levels, durability and lifetime still need to be improved. One way is by optimizing the flow distribution across the cell. Because the incoming liquid water both serves as a fuel and coolant, an even distribution not only ensures good mass transport characteristics, it also allows for an even heat removal. If either of these issues cannot be ensured, the risk of hotspots and catalyst degradation increases. As opposed to PEM fuel cells (PEMFC), which are typically operated at low pressures (e.g. 1 bar), it is an advantage to operate PEMEC at elevated pressures of up to 200 bars and thereby decreasing the need for subsequent compression of the hydrogen to store it.

(a) Parallel   (b) Serpentine

(c) Interdigitated
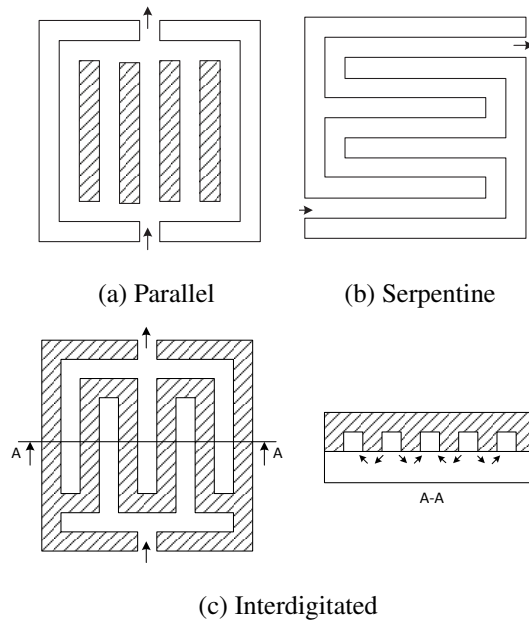
Figure 1: Three archetype channel configurations for square-planar cells

To improve mechanical stability at elevated pressuresm circular-planar cells are used instead of square-planar cells. Evidently, this difference in outer geometry affects the channel design. Another difference that affects channel design is the difference in two-phase morphology. In PEMFC the two-phase flow consists of a continuous gaseous phase and a dispersed liquid water droplets phase. However, in PEMEC this is only true for the cathode; in the anode the continuous phase consists of liquid water and dispersed oxygen bubbles.

For square-planar cells three archetype channel configurations are traditionally considered [5], although more types exist [10]. These are parallel, serpentine and interdigitated channels. A schematic drawing of each type is shown in Figure 1. While parallel and serpentine channels distribute reactants over a porous gas diffusion layer (GDL), through which species mainly diffuse, interdigitated channels forces convective flow through the GDL. Interdigitated flow fields therefore offer better mass transport, whereas parallel and serpentine offer a significant lower pressure loss. For systems subject to two-phase flow, parallel channels suffer from a high extent of flow maldistribution, since a single channel might become blocked by a gas bubble or liquid droplet. To circumvent this blocking or at least reduce it, combinations of parallel and serpen-

tine channels are often used. In interdigitated flow fields the reactant phase in the two-phase flow is much less prone to becoming blocked, since the reactant phase is convectively transported through the GDL. Nevertheless, it should be noted that the exact characteristics of each archetype depends on channel length, channel height, channel width and number of channels.

In the literature, various experimental and modeling studies have been conducted for square-planar cells in PEMFC comparing interdigitated flow fields with parallel or serpentine fields. Among others, Wang and Liu 2004 [8], Wang et al. [9] and Berning et al. 2014 [7] have demonstrated the improved reactant mass transport in the presence of two-phase gas-liquid flow by switching to an interdigitated flow field. Furthermore, the study by Berning et al. 2014 [7] underlined that an improved waste heat removal could be seen.

For PEMEC the available number of publications is scarcer. A few studies have investigated the effect of two-phase gas-liquid flow in the anode using parallel and serpentine flow fields in PEMEC at low pressures. Ito et al. 2010 [11] found in their experimental study that these flow fields are sensitive to the two-phase flow regime. At high current densities when a high amount of oxygen is produced slug or annular two-phase flow develops and obstructs the liquid reactant phase flow towards the catalyst layer. In the numerical modeling study by Nie and Chen 2010 [12] it was further shown that a high extent of flow maldistribution could occur. Even reversed flow was observed in some channels.

Although the use of an interdigitated, square-planar flow field in PEMFC has been shown to offer particular benefits in avoiding mass transport limitations induced by two-phase gas-liquid flow, no studies are available for interdigitated, circular-planar flow fields of PEMEC. In particular, the benefit of interdigitated flow fields for the anode is unknown. The main objective of this work is therefore the investigation of flow maldistribution in an interdigitated PEMEC anode flow field. As a first attempt, two-phase gas-liquid flow phenomena are disregarded, and only single-phase flow is considered. This is done in order to get a clear effect of the circular-planar cell design, rather than a mixed effect from both.

In the following, a parametric study of a macro-

scopic, steady-state, three-dimensional, single phase model is presented. The model accounts for mass and momentum transport in channels and the porous GDL. Initially, a short description of the geometry, mathematical model, numerical solver and data treatment will be given, followed by a grid independency study. Then, results from a base case and parametric study are analyzed and discussed.

METHODOLOGY
In this work the interdigitated, circular-planar flow field shown in Figure 2 is used. It consists of one inlet, one outlet, an interdigitated channel structure and a porous medium. There are 8 incoming and 9 outgoing channels in the interdigitated channel structure. Each channel has a width of 1 mm and height of 0.5 mm. The inlet manifold has a height of 1 mm and width of 5 mm. The diameter of the circular GDL is 10 cm.
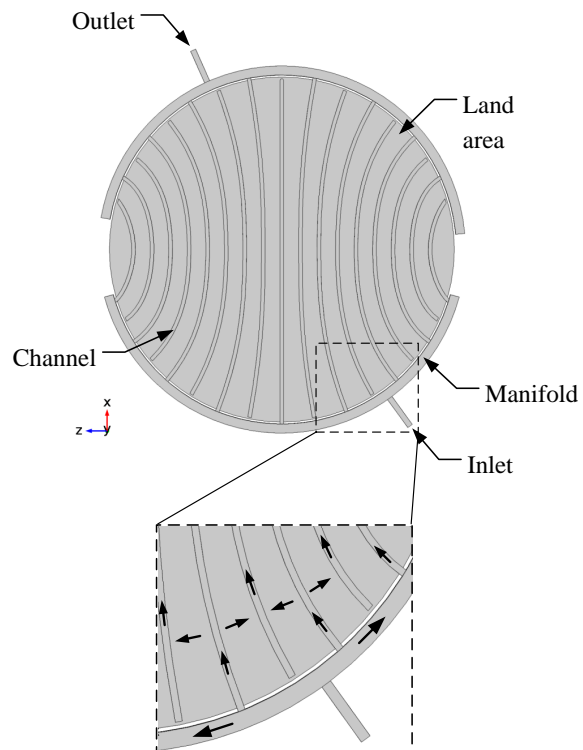

Figure 2: Interdigitated flow field geometry

The channels are fairly thin compared to the land width, however this is to avoid that the porous medium intrudes into the channels. Moreover, the channels are curved to minimize the difference in length between them; however this comes at the expense of an uneven land width.

The zoomed area in Figure 2 highlights the flow direction in the geometry. Flow from the inlet, the liquid is distributed in the inlet manifold and hereafter in the inlet channels. Then, the flow is forced underneath, through the GDL, and out through each outlet channel. The flow from the outlet channels then merge in the manifold and flow out of the geometry.

Mathematical Equations

To obtain the velocity and pressure field distribution inside channels and porous media the macroscopic, volume-averaged, steady-state continuity and momentum conservation equations are solved in eqn. 3 and 4, respectively:

$$\nabla \cdot (\varepsilon \rho \mathbf{U}) = \varepsilon S \tag{3}$$

$$\nabla \cdot (\varepsilon \rho \mathbf{U} \mathbf{U} - \varepsilon \tau) = \varepsilon (\mathbf{S} - \nabla p) + \varepsilon \rho \mathbf{g} + \varepsilon \mathbf{M} \tag{4}$$

$$\tau = \mu \left(\nabla \mathbf{U} + (\nabla \mathbf{U})^T - \frac{2}{3} (\nabla \mathbf{U}) \mathbf{I} \right) \tag{5}$$

Here $\mathbf{U}$ is the true velocity, ρ is density, ε is the volume porosity, which is 1 outside the GDL, τ is the stress tensor, $\mathbf{I}$ is the identity matrix, $\mathbf{g}$ is the gravity vector, S is a mass source, p is pressure, $\mathbf{S}$ is a momentum source term, μ is the dynamic viscosity and $\mathbf{M}$ covers the interfacial forces acting on phase in the porus medium, else it is zero.

For laminar flow in porous media the interfacial force is given by Darcy's law:

$$\mathbf{M} = \frac{\mu \varepsilon}{K} \mathbf{U} \tag{6}$$

Here K is the viscous permeability. The viscous permeability of a fibrous porous medium, which is typically used, can be estimated via the following empirical correlations as a function of porosity [15]:

$$K = \frac{\varepsilon}{8 \left(\ln \varepsilon \right)^2} \frac{(\varepsilon - \varepsilon_p)^{\alpha+2} r_f^2}{(1 - \varepsilon_p)^{\alpha} ((\alpha+1) \varepsilon - \varepsilon_p)^2} \tag{7}$$

Here ε_p is the percolation threshold porosity, which for two-dimensional fibrous structures is 0.11, r_f is the carbon fiber radius and α is a directional dependent parameter, which in the through-plane and in-plane direction is 0.521 and 0.785, respectively.

The framework for modeling macroscopic single-phase flow in porous media was originally developed by Slattery [14] and Whitaker [13], and later extended by numerous authors. For a general introduction to the topic of macroscopic modeling of porous media and the application of volume averaging, interested readers are referred to Jakobsen [16].

Boundary condition

The inlet mass flow of liquid water is calculated as follows:

$$\dot{m}_{in} = \frac{M_w \lambda j A_c}{2F} \tag{8}$$

Here M_w is the molecular weight, λ is the stoichiometric factor, j is current density, A_c is the cross-sectional area and F is Faradays constant.

In the context of fuel cell and electrolysis modeling the stoichiometric factor λ is defined as the number of moles of reactant supplied n_s relative to the number of moles required for a stoichiometric reaction n_r:

$$\lambda = \frac{n_s}{n_r} \tag{9}$$

Thus, a stoichiometric factor of 1 corresponds to the exact amount needed for a given current density, whereas a stoichiometric factor of 5 corresponds to 5 times the required amount for a given current density supplied.

Numerical Solver

The presented mathematical model was solved using the commercial software, COMSOL Multiphysics. In this software the partial differential equations are solved using the finite element approach. For laminar flow the default discretization scheme is the so-called P1+P1, where both the pressure and velocity are discretized using linear elements. The resulting non-linear algebraic matrix systems were solved using a coupled, multigrid solver.

Data Treatment

To be able to evaluate the extent of mass flow maldistribution in a systematic fashion a channel mass flow standard deviation is defined as follows:

$$\sigma = \sqrt{\frac{1}{N}\sum_{i=1}^{N}\left(\frac{\dot{m}_i}{L_i} - \mu\right)^2} \qquad (10)$$

$$\mu = \frac{1}{N}\sum_{i=1}^{N}\frac{\dot{m}_i}{L_i} \qquad (11)$$

Here σ is the channel mass flow standard deviation, μ is the average channel mass flow, N is the number of channels, $\dot{m}_i$ is the mass flow rate of each channel, and L is the channel length. The reason why the mass flow is devided by channel length is to account for the difference in channel length, and thus the difference in surface area and the need for water and cooling. The channel mass flow is calculated by integrating over the cross-sectional area of the channel outlet:

$$\dot{m}_i = \int_{A_i} \rho \mathbf{U} \cdot \mathbf{n} dA \qquad (12)$$

Here $\mathbf{n}$ is the normal vector of the cross-sectional area. The advantage of defining a channel mass flow standard deviation is the quantification of the flow maldistribution. However, to enable a direct comparion between the individual simulation cases in the parameter variation, the standard deviation needs to be normalised by the mean channel mass flow.

RESULTS AND DISCUSSION

In the parameter variation three different parameters are varied. In order to minimize the test matrix a base case reflecting nominal operation conditions is defined. From this point each parameter is then varied. The values of the base case are shown in Table 1.

Parameter	Symbol	Value	Unit
Temperature	T	343	K
Permeability	K	$1.0 \cdot 10^{-11}$	m^2
Porosity	ε	0.7	-
GDL thickness	L_T	200	μm
Stoichiometry	λ	100	-
Current density	J	1.0	A/cm^2

Table 1: Base case modeling properties

Before commencing with the results from the base case and parameter variation, a grid independency study is presented.

Grid Independency

The mesh required for the presented interdigitated geometry has to resolve large differences in length scales across the flow field; hence the number of cells is bound to be in the order of millions.
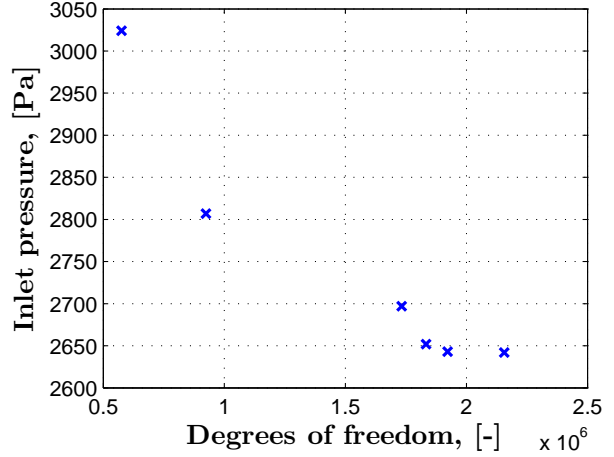
Figure 3: Grid independency study at 298 K

A grid independency study is carried out to ensure that only the minimum required number of cells, which guarantees a grid independent solution, is solved. In this study, the back pressure is monitored as the number of cells is gradually increased towards the maximum number of degrees of freedom that the computer can handle. As shown in Figure 3, a stable solution is reached around 2 million degrees of freedom. Thus, all simulation results presented in the following where obtained using a grid consisting of 1.95 million cells.

Base Case

To quantify the extent of flow maldistribution between channels, the obtained results from the base case are depicted in two ways: 2D contour plots in Figure 4 and bar plots in Figure 5. While 2D contour plots depict the velocity and pressure fields, the bar plots show the mass flow rate out of the channels with and without channel length normalization.

The velocity distribution within the GDL depicted in Figure 4a can be used as an indicator of how well cooling and mass transport occurs. The higher the velocity, the better the effect is, and vice versa. The highest velocities are found near the outer interdigitated channels. Velocities then appear to gradually

(a) Velocity distribution in the gas diffusion layer $(y/t_{GDL} = 0.5)$

(b) Velocity distribution in channels and manifold $(y/t_{channel} = 0.5)$

(c) Surface pressure distribution
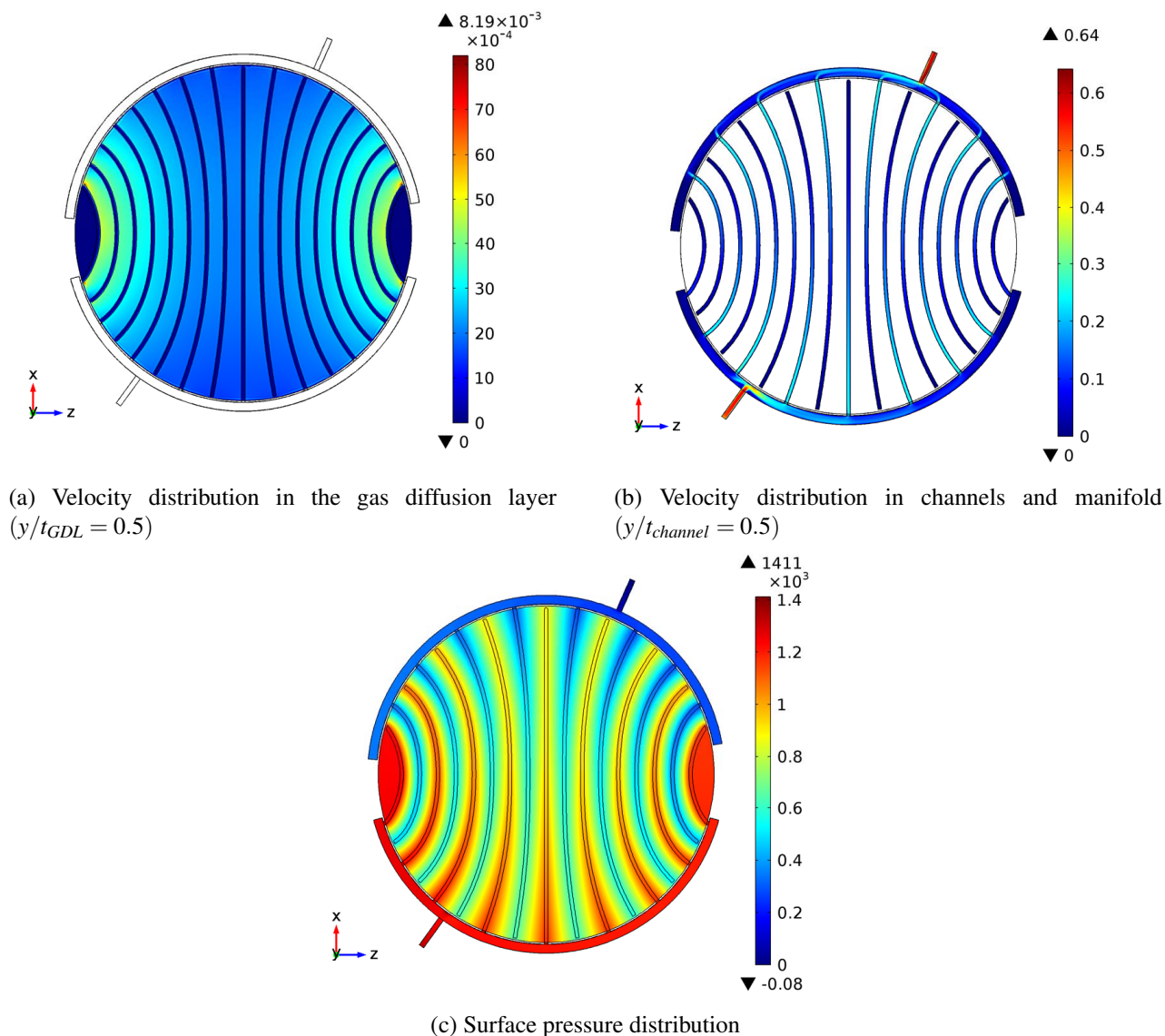
Figure 4: Crosssectional contour plots

decrease from the outer channels and towards the center of the plate. Two low velocity zones can further be identified. These occur because fluid flow is not forced through the GDL here.

In Figure 4b the velocity distribution within the interdigitated channels and manifold can be seen. The velocity distribution reveals large differences throughout the geometry. At the inlet, a high velocity jet is formed, which creates a high dynamic pressure zone as seen in Figure 4c. Similarly high velocities can be observed into and out of each interdigitated channel due to a reduced cross sectional channel area. Interestingly, these large velocity differences between each channel and the manifold make it possible to clearly observe how the fluid flow out

of each channel mixes into the manifold flow.

From the pressure distribution in Figure 4c it should be noted that the pressure loss through the system is 1411 Pa under the prescribed conditions. It is clearly visible that the majority of the pressure loss originates from the convective flow through the GDL. However, some extent of uneven pressure distribution within the manifold is visible. It can further be observed that the land area width is larger for channels near the center of the plate. Hence, pressure losses are bound to be higher here, which in turn corresponds to a lower mass flow

When comparing the mass flows through each interdigitated channel in Figure 5a, it appears that a fairly even distribution is obtained with the excep-
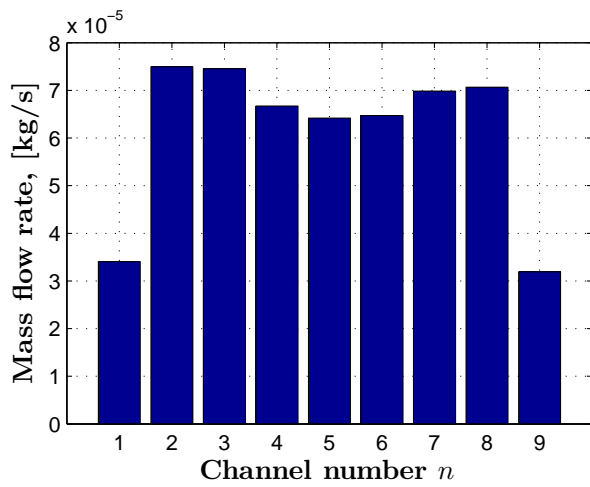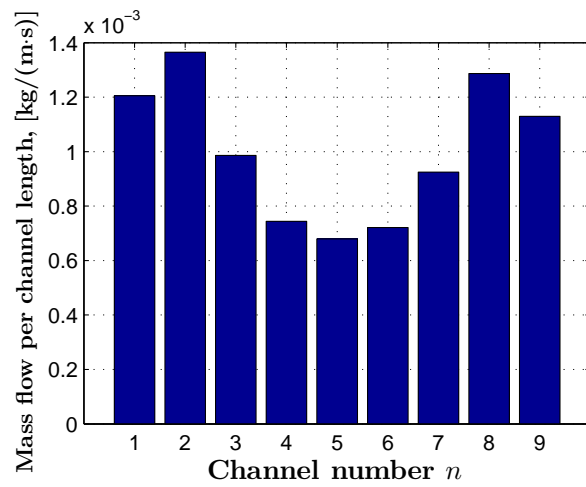
Figure 5: Channel mass flow with (a) and without (b) channel lenght correction, respectively.

tion of channel 1 and 9. Meanwhile, when accounting for the difference in channel length, this picture changes dramatically, as can be seen from Figure 5b. It now becomes evident that especially channel 4 to 6 suffer from a lower mass flow rate relative to the cross-sectional area they need to supply with water and coolant. For these channels the local water stoichiometry would be roughly half compared to the outer channels. The observation that the mass transport gradually improves towards the outer channels is in good agreement with the velocity distribution in the GDL shown in Figure 4a. Moreover, it further emphasizes that merely studying mass flows rather than mass flows per channel length does not reveal the extent of flow maldistribution.

A further comparison between the individual channels reveals a non-symmetric mass flow distribution. This indicates that the position of the inlet and outlet to some extent is significant. If the inlet and outlet where positioned in the middle, a symmetric distribution would be expected.

Parameter Variation

The obtained results from each parameter variation are depicted as x-y plots in Figure 6. In each subfigure, the standard deviation is shown on the y-axis and the parameter in question on the x-axis.

It can be observed in Figure 6a that the normalized standard deviation increases as a function water stoichiometry. This means that the extent of flow maldistribution increases proportionally to the water stoichiometry. Hence, when higher flows are needed, in order to cool the cell, an inherent more non-uniform cooling is enforced.

From Figure 6b, it can be observed that the normalized standard deviation shows a strong dependence on viscous permeability. As the permeability gradually decreases, the normalized standard deviation rapidly follows. However, ones the permeability reaches a value around $1.0 \cdot 10^{-11}$ m^2, the change in the normalized standard deviation begins to decrease significantly. In fact, it appears that the standard deviation asymptotically approaches a constant value. The identified threshold seems to indicate a transition towards a porous medium dominated maldistribution. Above this point, the flow between the channels is important, whereas below primarily the flow through the porous medium is.

Decreasing the permeability is equivalent to increasing the flow resistance; this can likewise be achieved by decreasing the GDL thickness while keeping the permeability constant. However, as seen from Figure 6c, the change in normalized standard deviation only shows a weak dependence on GDL thickness compared to the viscous permeability. Evidently, the possible benefit is rather limited in comparison.

In Figure 6d, a weak temperature dependence of the normalized standard deviation can be observed. The temperature affects fluid density and viscosity. The higher the temperature is, the lower both become. Since the viscous shear stress in the channel and porous medium both linearly dependent on viscos-
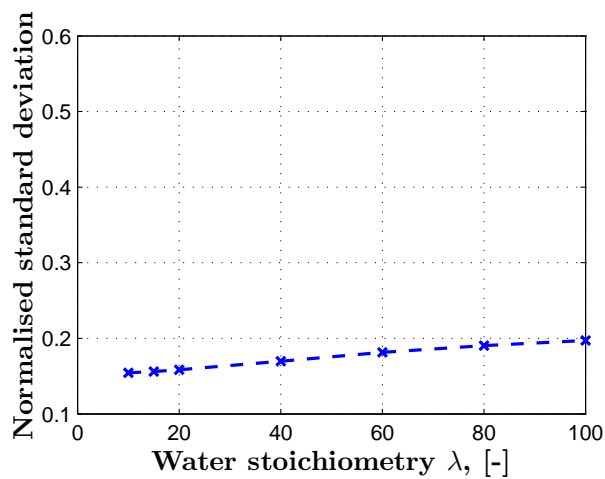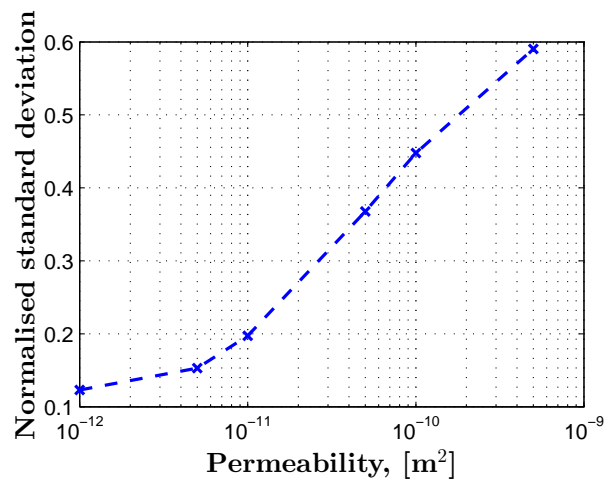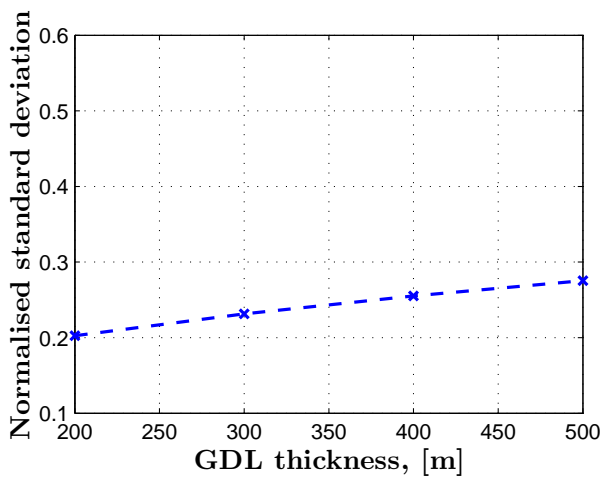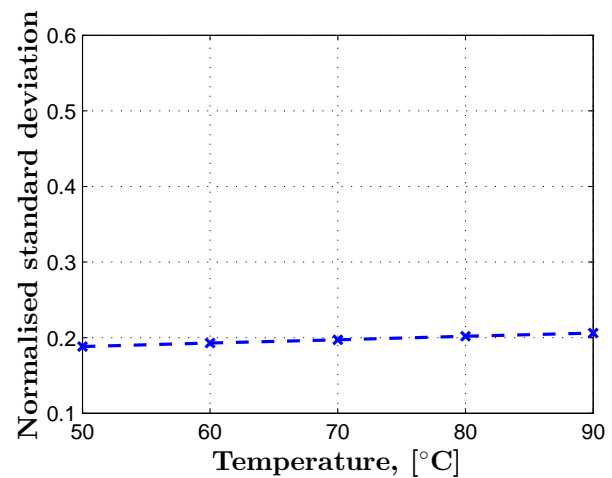
Figure 6: Channel mass flow standard deviation as a function of water stoichiometry (a), permeability (b), GDL thickness (c) and fluid temperature (d), respectively.

ity, a significant difference would not be expected as function of temperature. However, the increase that does occur with temperature may reflect some small inertial, or viscous affects due to the slightly increase volume flow in the channels.

CONCLUSION

In this work, the extent of flow maldistribution in an interdigitated, circular-planar anode flow field of a PEMEC was investigated using a macroscopic, steady-state, three-dimensional, single-phase, computational fluid dynamics model. It was found that an uneven mass flow distribution could be observed within the GDL. Moreover, a parametric study underlined that the extent of flow maldistribution,

shows a strong dependence on viscous permeability and weaker dependence on water stoichiometry, GDL thickness and temperature. Furthermore, it appears that the dependence on viscous permeability exhibits a threshold around $1.0 \cdot 10^{-11}$ m^2. Below this point, the dependence reduces rapidly and the porous domain dominates the flow maldistribution.

ACKNOWLEDGEMENT

REFERENCES

[1] Carmo M, Fritz DL, Mergel J, Stolten D. *A comprehensive review on PEM water electrolysis*. International Journal of Hydrogen Energy, 38 (2013) 4901-4934.

[2] Zeng K, Zhang D. *Recent progress in alkaline water electrolysis for hydrogen production and applications*. Progress in Energy and Combustion Science 36 (2010) 307-326

[3] Pickard WF, Shen AQ, Hansing NJ. *Parking the power: strategies and physical limitations for bulk energy storage in supply-demand matching on a grid whose input power is provided by intermittent sources*. Renewable & Sustainable Energy Reviews, Oct 2009;13(8):1934-45

[4] Hedegaard K, Meibom P. *Wind power impacts and electricity storage e a time scale perspective*. Renewable Energy Jan 2012;37(1):318-24

[5] O'Hayre R, Cha SW, Whitney C, Fritz PB. *Fuel Cell Fundamentals*. John Wiley & Sons, Inc., ISBN 978-0-470-25843-9, 2009

[6] Gutierrez-Martin F, Guerrero-Hernandez I. *Balancing the grid loads by large scale integration of hydrogen technologies: the case of the Spanish power system*. International Journal of Hydrogen Energy, Jan 2012;37(2):1151-61.

[7] Berning T, Kær SK. 2012. *Low stoichiometry operation of a proton exchange membrane fuel cell employing the interdigitated flow field: A modeling study*. International Journal of Hydrogen Energy. 37(10):8477-8489

[8] Wang L, Liu H. *Performance studies of PEM fuel cells with interdigitated flow fields*. Journal of Power Sources 134 (2004) 185-196

[9] Wang XD, Duan YY, Yan WM, Weng FB. *Effect of humidity of reactants on the cell performance of PEM fuel cells with parallel and interdigitated flow field designs*. Journal of Power Sources 176 (2008) 247-258

[10] Li X, Sabir I. *Reviewof bipolar plates in PEM fuel cells: Flow-field designs*. International Journal of Hydrogen Energy 30 (2005) 359 - 371

[11] Ito H, Maeda T, Nakano A, Hasegawa Y, YokoiNb, Hwang CM, Ishida M, Kato A, Yoshida T. *Effect of flow regime of circulating water on a proton exchange membrane electrolyzer*. International Journal of Hydrogen Energy 35 (2010) 9550 - 9560

[12] Nie J, Chen Y. *Numerical modeling of three-dimensional two-phase gas-liquid flow in the flow field plate of a PEM electrolysis cell*. International Journal of Hydrogen Energy 35 (2010) 3183 - 3197

[13] Whitaker, S. *ADVANCES IN THEORY OF FLUID MOTION IN POROUS MEDIA*. Industrial & Engineering Chemistry 61 (1969) 14-28

[14] Slattery, JC. *Single-phase flow through porous media*. AIChE Journal 15 (1969) 866-872 year = 1969

[15] Tomadakis MM, Robertson TJ. *Viscous Permeability of Random Fiber Structures: Comparison of Electrical and Diffusional Estimates with Experimental and Analytical Results*. Journal of Composite Materials, 39(2), pp. 163-188. 2005

[16] Jakobsen, HA. *Chemical Reactor Modeling*. Springer Berlin Heidelberg, 2008, p. 335-501

Dynamic modeling of seasonal thermal energy storage systems in existing buildings

Carol Pascual*, Asier Martinez and Maider Epelde
Tecnalia, Energy and Environment Division
20730 Azpeitia
Spain

Roman Marx and Dan Bauer
University of Stuttgart
Institute of Thermodynamics and Thermal Engineering (ITW)
Research and Testing Centre for Thermal Solar Systems (TZS)
70550 Stuttgart
Germany

1. ABSTRACT

This paper presents a system simulation and parametric study of the most standard Seasonal Thermal Energy Storage System (STES) configuration, hot water tank STES system for district heating. This configuration is detailed is modeled in detail in TRNSYS, a dynamic simulation program, in order to integrate the different sub-systems (storage, generation and consumption) and optimize the overall performance of the whole system for four different climate zones Southern (Madrid), Northern (Stockholm), Central (Amsterdam) and Eastern Europe (Warsaw). These locations have been selected as reference locations in order to realize simulations and get throughout results. The aim of the chosen configuration is to cover the required space heating demand and domestic hot water preparation (DHW) of 50 retrofitted dwellings (district heating network) for each location and analyze the different alternatives concerning economic and technical aspects.

Keywords: Seasonal thermal energy storage system (STES); Dynamic modeling; TRNSYS; Heat pumps (HP); Solar thermal.

2. NOMENCLATURE

A	Collector area [m^2]
ATES	Aquifer Thermal Energy Storage
BTES	Borehole Thermal Energy Storage
C	Thermal Capacity of the heat pump [kW$_{th}$]
CSHPSS	Central Solar Heating Plants with Seasonal Storage
DHW	Domestic Hot Water
E	Electricity consumption
FPC	Flat Plate Collectors
F	Primary energy savings / CO2 emissions reduction [%]
f	Primary energy or CO_2 eq. emission factors
HP	Heat Pump
Inv	Investment cost [€]
PTES	Pit Thermal Energy Storage systems
Q	Energy delivered or consumed [kWh]

---

* Corresponding author at: TECNALIA, Phone: +34 667119581, e-mail: carol.pascual@tecnalia.com

STES	Seasonal Thermal Energy Storage System		*Col*	Collector

STES   Seasonal Thermal Energy Storage System

TTES   Tank Thermal Energy Storage

V   Storage volume [m^3]

Z   Annual cost [€]

η   efficiency

Subscripts:

Aux   Auxiliary

Col   Collector

Eq   Equivalent

Hp   Heat Pump

PE   Primary Energy

Ref   Reference

Th   Thermal

3. INTRODUCTION

Energy use in buildings accounts for approximately 40% of EU energy consumption. Energy efficiency in new buildings is important, but existing building stock is the main target. Existing buildings, however, are characterized by particular requirements and constraints that are not present in new buildings and that require new developments and adaptation of existing technologies. In order to fulfil the most recent EU directives, solutions for a drastic reduction in primary energy consumption are required. Space heating and domestic hot water preparation (DHW) represent the largest part of energy use in buildings nowadays, thus solar thermal energy seems to be one of the most promising heat source.

The technology of large scale seasonal thermal energy storage has been investigated in Europe (only north of Europe) since the middle of the 1970´s. The first demonstration plants were realized in Sweden in 1978/79. Besides Sweden also Switzerland, Denmark and Germany investigated STES and built demonstration plants.

In Germany, eleven large scale Central Solar Heating Plants with Seasonal Storage (CSHPSS) demonstration plants have been built since 1996. They are designed for solar fractions of between 35 and 60% of the total annual heat demand for DHW and space heating of the connected consumers.

During the past fifteen years of research on thermal seasonal storage technologies four different types of different types of storages turned out as main focus for the ongoing engineering research (Figure 1).

- Tank thermal energy storage (TTES): consists of underground reinforced concrete tank filled with water, connected to charging and discharging loops.

- PIT thermal energy storage (PTES): is made of an artificial pool filled with storage material closed by a lid.
- Borehole thermal energy storage (BTES): In this kind of storage, the heat is directly stored in the underground. Ducts are inserted into vertical boreholes to build a huge heat exchanger.
- Aquifer thermal energy storage (ATES): Naturally occurring self-contained layers of ground water are used for heat storage.
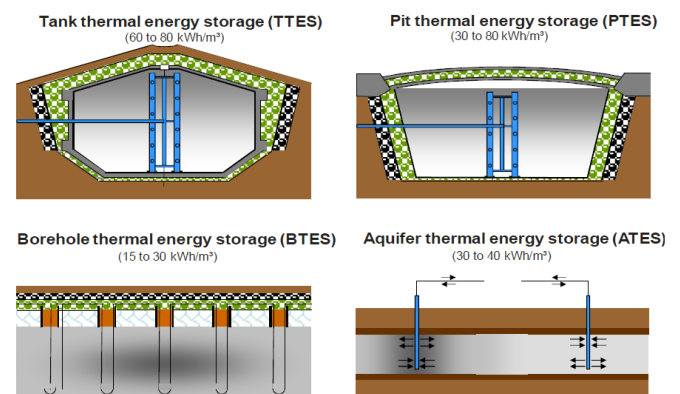
Figure 1: The four sensible thermal energy storage technologies (source: Solites).

The overall objective of EINSTEIN (Effective integration of seasonal thermal energy storage systems in existing buildings) project is the development, evaluation and demonstration of a low energy heating system based on Seasonal Thermal Energy Storage (STES) concept in combination with heat pumps (HP) for space heating and DHW requirements for existing buildings to drastically reduce the energy consumption.

This paper presents the detailed modeling and parametric study of STES system.
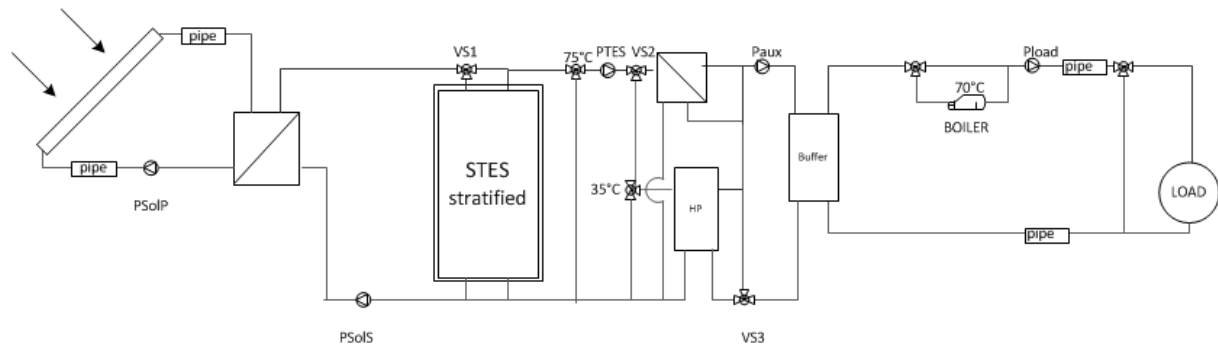
Figure 2: Studied STES system configuration.

4. SYSTEM DESCRIPTION

The model of the system will be divided into four subsystems: Heat generation, heat storage, distribution and heat consumption. Figure 2 shows the system concept for the simulations of the STES system.

Solar collectors deliver heat to the system either by a direct heat supply to the short buffer tank or by charging the STES. If there is not solar energy available to cover the demand, heat can be discharged from the STES either by an external heat exchanger or by a heat pump. However, if there is no solar energy available and the STES is completely discharged, the energy demand of the district net will be covered by the auxiliary backup boiler.

Heat generation:

In this configuration there are three heat generation sources, flat plate solar thermal collectors, water-to-water heat pump and the auxiliary boiler.

The solar system consist of a flat plate solar thermal collector field facing south with a slope of 40° and a water-glycol circuit connected to an external heat exchanger with a pump to control the temperature in the loop.

The heat pump is connected directly to STES as heat source and short term buffer tank as heat sink. The heat pump is switched on when there is no solar energy available to discharge the STES. The electric driven compression heat pump design is based on a modified performance map from the data of the heat pump WRL400X from Airlan [1]. A Gas boiler is integrated as auxiliary heating system.

Heat storage:

The choice for a certain type of seasonal storage mainly depends on the local prerequisites like the

geological and hydro-geological situation in the underground of the respective construction site. Above all an economical rating of possible storages according to the costs per GJ of thermal energy that can be used from the storage allows the choice of the best storage technology for every single project. In this paper TTES is modelled as STES and simulated because this kind of seasonal storage can be built at early any place. TTES is connected to solar loop by an external heat exchanger to be charged and to another heat exchanger or heat pump to discharge and provide the required energy to the system.

A short term water tank is also included in the system in order to facilitate the operation of the heat pump and decouple the energy production and consumption.

Heat distribution and consumption:

Distribution system refers to water circuits to cover DHW and space heating of the district heating network.

A district of 50 retrofitted residential buildings is defined for four locations, Amsterdam, Madrid, Warsaw and Stockholm. The table below shows the annual demand of each location.

	N° of buildings	DH demand / MWh per year
Amsterdam	50	552.40
Stockholm	50	855.91
Madrid	50	370.29
Warszawa	50	692.01

Table 1: Yearly demand of four locations.

The base for the profile is the profile of the IEA Task 26 building [2]. The load for space heating and hot water preparation is temporarily distributed by standardized normal distribution taking the simultaneity factor for district heating networks [2] into account. Figure 3 shows the load profile for one

family house in a small district heating network in Amsterdam. The supply temperature of the district heating is 70°C.
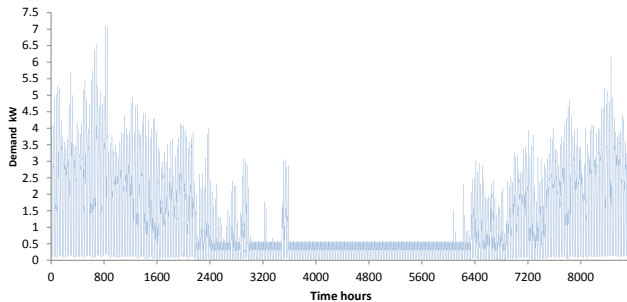

Figure 3: Hourly demand for one family house in Amsterdam.

5. IMPLEMENTATION IN TRNSYS

The system described before was modeled using TRNSYS Version 17, transient thermal energy modeling software developed at the University of Wisconsin-Madison [3].

Heat generation:

The flat plate collectors (FPC) are modelled by the standard type 1a. The FPC is integrated into a solar primary loop consisting of a pump (type 114) and a heat exchanger (type 91). And the solar heat is transferred to other modules at the heat exchanger (HX solar loop).

The heat pump is based on a modified performance map from the data of the heat pump WRL400X from Airlan [1]. To use the data in TRNSYS, type 42b is selected. The type can interpolate the performance figures for given outlet respectively input temperatures of the heat pump on the brine/water side of evaporator and condenser. In this case the inlet temperature of evaporator and condenser are the independent variables and the thermal power of the condenser and the electrical power of the compressor are the depending variables. The modifications of the data have been made in order to suit the requirements to a heat pump used in a STES system.

As an auxiliary heating system a boiler is integrated. Therefore the auxiliary heater model (type 6) is used. If the temperature is lower than the set point temperature the heater modulates from 0-100 % of the maximum heating power to reach the set point temperature. The efficiency is set to 100 % so that the energy consumption of the boiler equals the heating power.

Heat storage:

The multi-port store model (non-standard type 340 [4]) is used for modelling the TTES. For the simulation direct charging and discharging units are used called double-ports. The solar yield is charged into the top of the store using a stratification device. The return flow for the solar collectors is taken from the bottom of the store. A temperature sensor at ¼ of height from the bottom is used as lower input value for the hysteresis controller of the secondary collector loop pump. Hence a buffer volume for solar heat of ¾ of the buffer store is generated leaving ¼ of the volume for the return flow of the district heating net at the bottom which is also connected to a stratification device. The supply flow for the district heating net respectively the heat pump (evaporator side) is taken from the top of the store.

The short term buffer storage is also simulated by the type 340 multiport store model. The system is charged on top of the store by the heat pump or TTES and the return will take from the bottom. The buffer provides the energy to the distribution loop from the top of the buffer and the return to the bottom. The buffer storage is modelled as stratified and insulated water tank.

Heat distribution and consumption:

The district heating network is modelled by the type 31 either for the supply and return pipe.

A load module is developed to simulate the load side of the district heating net on building level. The type 9e is used as data reader. The data files used have an hourly resolution of the thermal heat consumption (in kWh).

6. RESULTS

For the comparison of the efficiency of different concepts and parameter sets different characteristic numbers have been calculated. A definition is presented in the following.

6.1 Environmental analysis

Described system is environmentally evaluated. Primary energy saving and CO_2 equivalent emission reduction are taken into account for analyzing system and calculated using equations (1-2).

$$F_{save,PE} = 1 - \frac{\sum_i \frac{Q_{aux,i}}{\eta_{aux,i}} f_{PE,aux,i} + \sum_i E_{elec,i} \cdot f_{PE,aux,i}}{\sum_i \frac{Q_{aux,ref,i}}{\eta_{aux,ref,i}} f_{PE,aux,ref,i} + \sum_i E_{elec,ref,i} \cdot f_{PE,aux,i}} \tag{1}$$

$$F_{CO2,eq} = \sum_i \frac{Q_{ref,i}}{\eta_{ref,i}} \cdot f_{CO2-eq,ref,i} - \sum_i \frac{Q_{aux,i}}{\eta_{aux,i}} \cdot f_{CO2-eq,aux,i} \tag{2}$$

Reference system consists on a gas boiler with an efficiency of 0.9. Primary energy factors are 1.3 and 2.3 for gas and electricity respectively and CO_2 equivalent emissions 294 and 415 $g \cdot kWh^{-1}$.

6.2 Economic analysis

Main equipment's investment costs are considered for calculating the initial system installation investment cost. Collector field and STES costs were estimated as [5]. It has been estimated that average investment costs for a heat pump were on average 500 € per kW_{th} [6].

$$Inv_{col} = 740 \cdot A^{0.860} \tag{3}$$

$$Inv_{STES} = 4660 \cdot V^{0.615} \tag{4}$$

$$Inv_{HP} = 500 \cdot C_{HP} \tag{5}$$

The rest of the existing equipment's costs (pumps, heat exchangers, valves, etc.) are considered 25% of total investment and engineering indirect cost (engineering project, project management, assurances, etc.) are estimated as 12%.

The annual operation and maintenance cost are estimated in 1.5% of the investment cost according to criteria proposed by IEA [7]. Annual costs are calculated with the next equation for each element:

$$Z_i = Inv_i \cdot \left(f_{ope} + i \cdot (1 + i)^{ni} / ((1 + i)^{ni} - 1) \right) \tag{6}$$

Where:

- i: annual interest rate (3.0%)
- ni: equipment lifetime (25, 50 and 20 years for collectors, STES and Heat pump respectively.)
- f_{ope}: annual operation and maintenance cost (0.015 y^{-1})

System heat costs are the ratio between annual cost and system load.

These indicators will be used for considering best system configuration depending on collector field area, STES volume and heat pump capacity.

6.3 Simulation Results

For each location one reference system has been defined. The objective of the reference systems is to

	Amsterdam		Stockholm		Madrid		Warszawa	
A) Total Generation / MWh	613.90		912.11		431.86		751.68	
a.1) System Generation / MWh	359.03		567.48		268.47		427.54	
a.1.1) Solar direct / MWh	10.80	1.76%	11.02	1.21%	12.05	2.79%	10.28	1.37%
a.1.2) STES + HP / MWh	348.24		556.46		256.41		417.27	
a.1.2.1) Directly STES / MWh	230.04	37.47%	371.66	40.75%	181.33	41.99%	287.30	38.22%
a.1.2.2) HP / MWh	118.20	19.25%	184.80	20.26%	75.08	17.39%	129.96	17.29%
a.2) Auxiliary Boiler / MWh	254.86	41.52%	344.63	37.78%	163.40	37.84%	324.14	43.12%
B) District demand / MWh	552.40		855.91		370.29		692.01	
C) System looses / MWh	61.50	10.02%	56.20	6.16%	61.57	14.26%	59.67	7.94%
D) Environmental factors								
d.1) Primary Energy Saving / %	55.53		59.05		59.63		54.19	
d.2) CO_2-equivalent Savings / tons/ y	108.74		171.53		82.25		139.02	
E) Economic factors								
e.1) Initial Investment / k€	1093.15		1670.75		493.17		1414.06	
e.2) Equipment Anual Costs / k€	76.77		104.23		39.97		94.69	
e.3) System Heat Costs / €·MWh-1	213.83		183.76		149.24		221.60	

Table 2: Reference cases TRNSYS results and indicator values for 4 locations.

Amsterdam	Solar Col. Area / m^2	STES Volume / m^3	HP Power Factor
Reference Case	1000	2000	2.00
Case 1, 2, 3, 4	600 - 800 - 1200 - 1400	2000	2.00
Case 1', 2', 3', 4'	1000	1200 - 1600 - 2400 - 2800	2.00
Case 1", 2", 3", 4"	1000	2000	1.5-2.5-3.0-3.5
Stockholm	Solar Col. Area / m^2	STES Volume / m^3	HP Power Factor
Reference Case	1500	3500	2.00
Case 1, 2, 3, 4	900 - 1200 - 1800 - 2100	3500	2.00
Case 1', 2', 3', 4'	1500	2100 - 2800 - 4200 - 5600	2.00
Case 1", 2", 3", 4"	1500	3500	1.5-2.5-3.0-3.5
Madrid	Solar Col. Area / m^2	STES Volume / m^3	HP Power Factor
Reference Case	350	600	2.00
Case 1, 2, 3, 4	210 - 280 - 420 - 490	600	2.00
Case 1', 2', 3', 4'	350	360 - 480 - 720 - 840	2.00
Case 1", 2", 3", 4"	350	600	1.0-1.5-2.5-3.0
Warszawa	Solar Col. Area / m^2	STES Volume / m^3	HP Power Factor
Reference Case	1100	3500	2.00
Case 1, 2, 3, 4	660 - 880 - 1320 - 1540	3500	2.00
Case 1', 2', 3', 4'	1100	2100 - 2800 - 4200 - 5600	2.00
Case 1", 2", 3", 4"	1100	3500	1.5-2.5-3.0-3.5

Table 3: Values for reference systems and studied parameters (Collector area, STES volume and HP capacity scaled by a linear scaling factor- HP Power Factor).

cover 40% of the demand by solar thermal energy, 20% by the heat pump and the rest by the auxiliary heater.

Table 2 shows the results of simulations and the values of described indicators for the reference cases in Amsterdam, Madrid, Warsaw and Stockholm.

The simulations have been run for two years of operation but the values given represent results for the 2nd year.
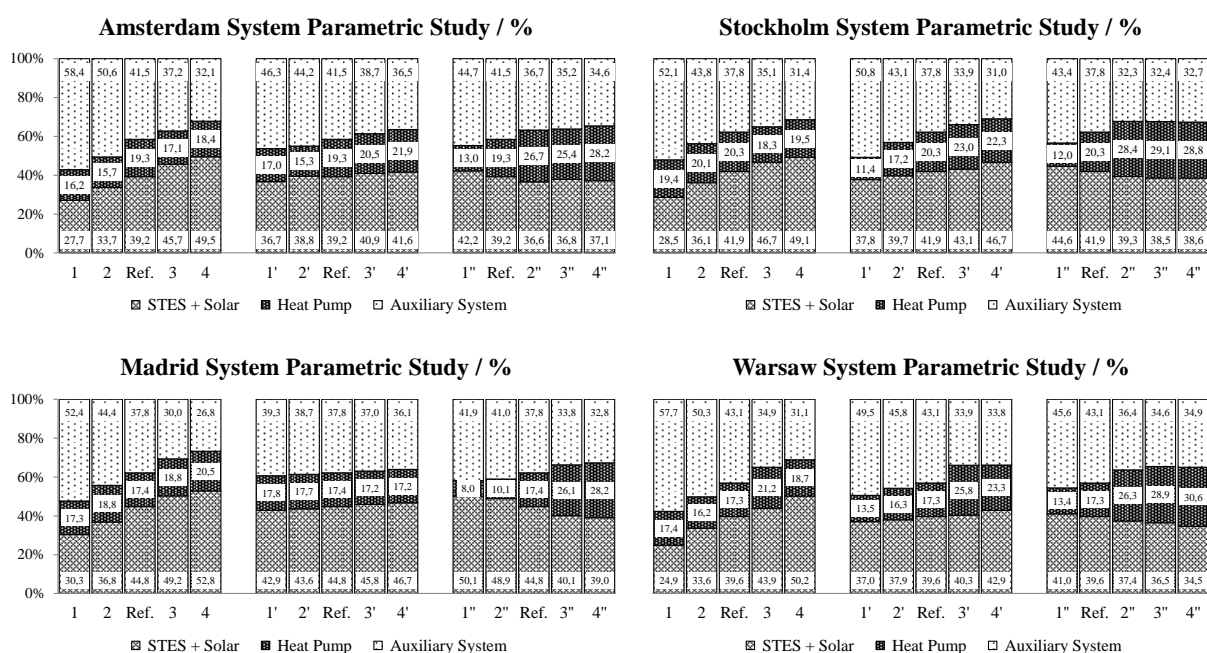

Figure 4: Collector area, STES volume and HP capacity sensitivity analysis. Covered demand distribution depending on location and studied combinations.

All results have been achieved by running simulations in 6 minutes time steps.

F_{saving} depending on Coll. area / %
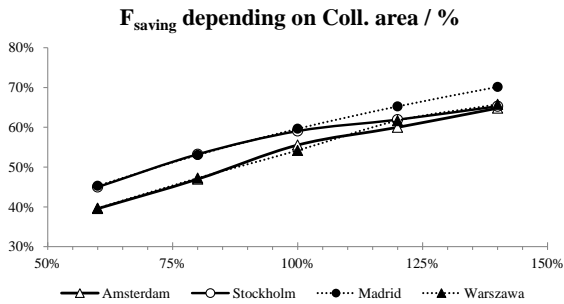
Figure 5: Collector area influence on primary energy savings, %.

F_{saving} depending on STES volume/ %
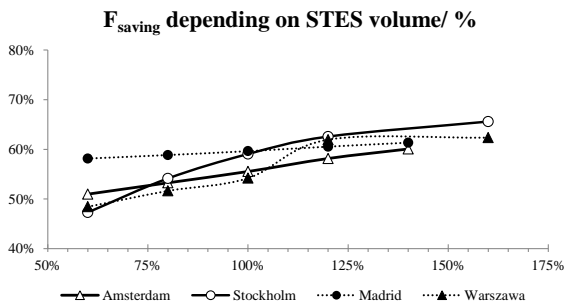
Figure 6: Influence of STES volume on primary energy savings, %.

F_{saving} depending on HP capacity/ %
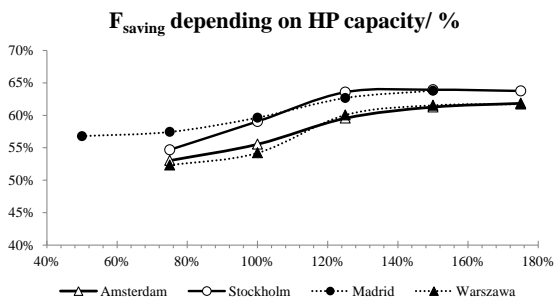
Figure 7: Influence of HP capacity on primary energy savings, %.

6.4   Parameter sensitivity analysis

For the main parameters - collectors area, STES volume and heat pump capacity - a sensitivity analysis was carry out to find the dominating parameter for the economy and efficiency of the system. Table 3 shows both, reference and studied combination of parameters for each location.

Reference systems where designed in order to cover demand by 40% by solar thermal energy, 20% by heat pump and the rest 40% by auxiliary heater.

Figure 4 shows the distribution of covering the demand by the influence of varying the dimension of

System Heat cost, Amsterdam €/MWh
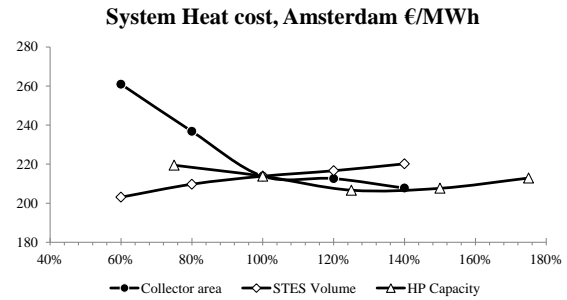
Figure 8: System heat cost depending on collector area, STES volume and HP capacity, Amsterdam.

System Heat cost, Stokholm €/MWh
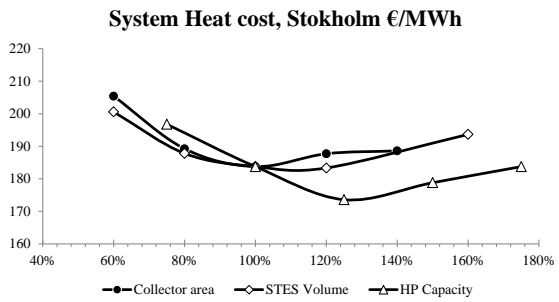
Figure 9: System heat cost depending on collector area, STES volume and HP capacity, Stokholm.

System Heat cost, Madrid €/MWh
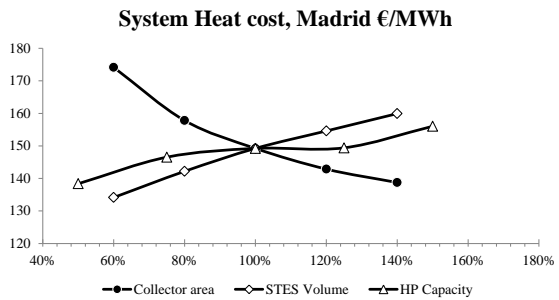
Figure 10: System heat cost depending on collector area, STES volume and HP capacity, Madrid.

System Heat cost, Warsaw €/MWh
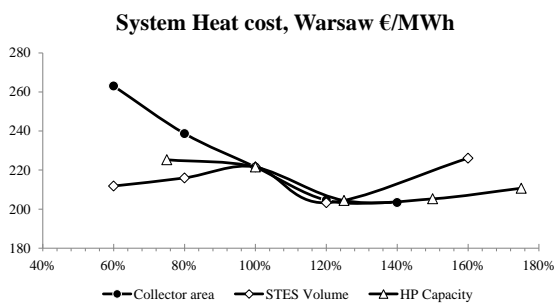
Figure 11: System heat cost depending on collector area, STES volume and HP capacity, Warsaw.

the main parameters on demand covering distribution.

The results show that if larger collector areas are installed less auxiliary energy is needed and primary energy is saved. By analyzing the STES volume , it can be obserbed that larger storage volumes lead to lower auxiliary energy consumption, but the influence is as pronounced as increasing collector's area. Finally, higher heat pump capacity implies the coverage of a larger percentage of the demand by the heat pump, reducing both, energy covered by solar thermal and auxiliary energy. At a certain heat pump capacity practically no more changes are observed.

Figure 5, Figure 6 and Figure 7 show the influence of different parameters on the fractional primary energy saving. The 100% represents the reference system defined above.

The influence of the collector area on the primary energy saving is similar for all locations, in Madrid, Amsterdam and Warsaw the maximum increase respect the reference system is about 25% whereas in the case of Stockholm is about 20% (Figure 5).

The influence of the STES volume is smaller than the influence of the collector area. In the case of Madrid there is only minor improvement when the volume increases whereas in the cases of Stockholm, Amsterdam and Warsaw the primary energy saving increases about 15% (Figure 6).

The heat pump has a maximum influence on primary energy of 9% for all the locations (Figure 7).

Increasing values of the assessed parameters would suppose a reduction of auxiliary energy but simultaniuosly the initial (and operational) costs increase as well. Heat cost is used in order to evaluate increasing collector area, STES volume and HP capacity and at the optimsed dimension economic advantage can be identified.

Figure 8, Figure 9, Figure 10 and Figure 11 show the influence of the above assesed parameters on the system heat cost of STES system at the four different locations.

In general, increasing collector area would suppose a reduction in the system heat cost. For larger collector areas less auxiliary energy is used, but the investment is not entirely justified increasing the collector area. In Amsterdam and Stockholm no improvement can be observed for cases 3 and 4 (see

Table 3) in heat cost. In case of Warsaw increasing the area of 20% (comparing to reference system) would leads to a reduction of heat cost.

Increasing the STES volume results in heat cost increase in cases of Amsterdam and Madrid. The results show that the volume of the reference system is the optimum for Stockholm, and in case of Warsaw, increasing the volume by 20% from the reference one results in a reduction of almost 10% in auxiliary energy use (Table 3) improving the system's heat cost and performance.

In case of the HP capacity an increasing of 25% from reference system is well justified, reducing (or maintaining in case of Madrid) heat cost of the system reducing and also primary energy consumption.

7. CONCLUSIONS

In the presented work, a dynamic simulation of seasonal thermal energy storage system for a small district heating network was conducted under different climate conditions by using TRNSYS. The results of a sensitivity analysis carried out were shown.

The most sensitive parameter for the fractional primary energy saving for all locations is the solar thermal collector area (Figure 5). The heat delivery of the solar thermal collectors dominates the possibility of using the heat pump by utilizing the solar thermal energy.

Not only primary energy savings have to be taken into account, being necessary to also assess system heat cost. The highest primary energy saving with smaller system heat cost for Amsterdam, Madrid and Warsaw is the configuration with largest solar collector area. System with HP pump capacity of 125% from reference is most suitable in Stockholm.

8. ACKNOWLEDGMENT

9. REFERENCES

[1] AERMEC air conditioning: REVERSIBLE CHILLER - Technical manual, IWRL2TI. 1112. 5890989_01.

[2] Weiss, W.: Solar Heating Systems for Houses: A Design Handbook for Solar Combisystems, Earthscan Verlag, Auflage: illustrated edition, 2003.

[3] A: Klein, S.A. et al, 2010, TRNSYS 17: A Transient System Simulation Program, Solar Energy Laboratory, University of Wisconsin, Madison, USA, http://sel.me.wisc.edu/trnsys.

[4] Drück, H.; Pauschinger, T.: MULTPORT Store Model for TRNSYS. User's manual, Institute of Thermodynamics and Thermal Engineering, University of Stuttgart, Stuttgart, 1997.

[5] Winter, W.; Haslauer, T.; Obernberger, I.: Untersuchung der Gleichzeitigkeit in kleinen und mittleren Nahwärmenetzen. Euroheat & Power, Issue 09 & 10/2001, ISSN 0949-166X, 2001.

[6] Mateo Guadalfajara, Miguel A. Lozano, Luis M. Serra. A simple method to calculate Central Solar Heating Plants with Seasonal Storage.SHC 2013, International Conference on Solar Heating and Cooling for Buildings and Industry, September 23-25, 2013, Freiburg, Germany

[7] International Energy Agency.OECD/IEA. Renewables for Heating and Cooling – Untapped Potential. IEA, 2007, Paris. www.iea.org

BUILDING MODELING AND SIMULATION FOR OPERATION TIME ENERGY EFFICIENCY

Borja Tellado[1]
Amaia Castelruiz[2]
Jose Manuel Olaizola[3]
Smart Building and Cities, Construction Unit (ECOIN), TECNALIA
Spain

ABSTRACT

The context for this paper is the meeting point of three different phenomenon that are arising at the very early 21st century society. The spread of IT technologies and worldwide economic and energy scenarios require to take advantage of the synergies of may appear among multiple application domains.

Since the Energy Performance of Buildings Directive was released in 2002 (Directive 2002/91/EC,EPBD) the energy efficiency in building domain has been a pretty big challenge for all EU Member States and specially for the stakeholders involved in the construction industry. This challenge has been faced, in most of the cases, in a monolithic approach.

In the most common scenario, building designers are not aware about the building control strategies that will be applied during the operation time and how the building envelope will perform with them. In parallel, the control engineers do not know about the building thermal inertia and its impact into the control routines. Our work tackles this parading that has been a key factor for unnecessary energy consumptions and users discomfort.

Keywords: energy efficiency, building modeling, optimization

[1]Corresponding author, E-mail:borja.tellado@tecnalia.com
[2]Corresponding author, E-mail:amaia.castelruiz@tecnalia.com
[3]Corresponding author, E-mail: josemanuel.olaizola@tecnalia.com

AEC:Architecture, Engineering and Construction
BacNET: Building Automation and Control Network
BMS: Building Management System
R-Value: Equivalent resistance
gbXML: Green Building XML
g- Value: Solar Factor
HVAC: Heating Ventilation and Air Conditioning
IFC: Industrial Foundation Class
IT: Information Technologies
OBIX: Open Building Information eXchange
OPC: Object Linking and Embedding for Process Control
OSGI: Open Source Gateway Initiative
U- Value: Heat transmittance
XML: eXtensible Marckup Language
W3C: World Wide Web Consortium

INTRODUCTION

In 2010 Tecnalia[4] decided to create a team focused on energy efficiency and urban sustainability composed by building planners, energy management and information technologies experts. **SiMoNa** is the compilation of the experience acquired and the knowledge shared among the members of that multidisciplinary team[1].

SiMoNa is a "smart system for monitoring and actuation" that takes as reference the building model and the forecasted weather to create 24h plans for HVAC systems, electrical loads as well as for indoor comfort set points.

The energy demands dynamic forecasting can be faced in many different ways, from simplified models based in continuous monitoring to complex building models based on statistical data[2][3][4].

---

[4] Tecnalia, located in the Basque Country, is the largest research centre in Spain with more than 1300 employees, organized in 7 research units (Sustainable Construction, Energy & Environment, Innovation Strategies, ICT, Industry & Transport, Health, Technology Services). The team that worked in this study belongs to Sustainable Construction Unit more precisely to the Smart Building and Cities area.

SiMoNa's approach considers a simplified building model feed by real weather and occupancy data. This paper describes **SiMoNa**, the integration of a building domain simulation engine into a building management system to optimize the overall building operation.
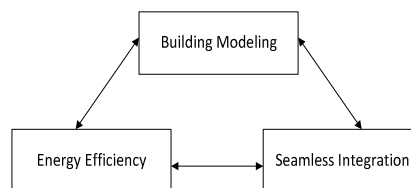
Figure 1: *SiMoNa*'s development pillars

BUILDING MODELING

Integration of design tools in operation domains has been a discussion topic for years. The computing power required running the simulations and the information required to develop proper building models have been issues to solve. The development of powerful IT components and the awareness about the need of efficient workflows for business profitability lead to create the appropriate scenario to integrate design phase knowledge with operation time skills.

This work considers the building modeling from the perspective of the building physics, equipment (HVAC and lighting) and user behavior modeling. [5][6][7]

We suggest three different modeling levels that depend on the existing building design information and available control options. All of the models consider the thermal demand forecast as keystone for the optimization.

Basic Modeling: From the modeling point of view, mainly the building geometry, envelope's isolation level and building usage are considered. In this case the optimization will not cover the production systems optimization.

Advanced Modeling: In addition to the concepts included in the basic modeling approach, HVAC modeling is included. The hot and cool water (or

air) generation and distribution equipment as well as the lighting circuits are modeled. The optimization outcomes include the HVAC equipment's set points and operation periods.

Complete Modeling: The advanced modeling approach is a detailed enhancement of the *advanced* approach. In the *advanced* approach simplifications in the HVAC system modeling are done, mainly in terms of number or cooling and heating circuits, the *complete* approach considers the system whole complexity.

We adopted *EnergyPlus*[8] as simulation engine for forecasting and optimization processes. The optimization target is minimizing the cooling or heating energy consumption to satisfy the users' comfort requirements.

The optimization loop follows the flow described below.
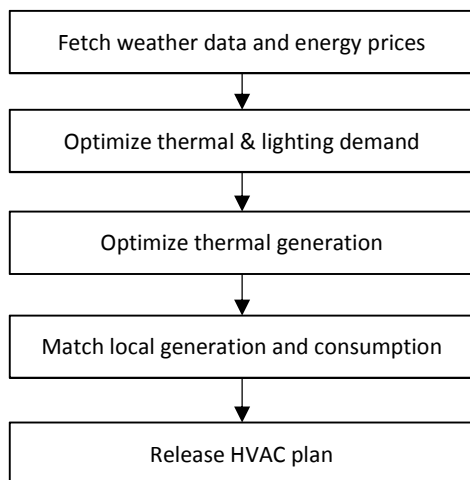
Figure 2: Optimization loop

The optimization processes are indeed divided in sequences of steps:

- *Thermal and lighting demand optimization* relies on a sequence of preconfigured building configurations in order to identify which one is the less energy demanding one.

- *Thermal generation optimization* takes as constraint the targeted comfort level and calculates the operation points (generation and distribution temperatures) for the HVAC system to satisfy the mentioned boundary condition

The *advanced modeling level* has been selected to evaluate the development described in this document. Applied to one of the buildings of University of Mondragon its outcomes are explained in detail in the latter in this document.

The main parameters for the building physics modeling process are:

Description	Symbol	Units
Walls Equivalent resistance	R-Value	m^2K/W
Solar Factor	g- Value	%
Thermal mass	M	kJ
Transmittance	U- Value	W/m^2K
Ground Temperature	Ground T	K
Thermal Bridges	--	W/mK
Air tightness	--	m^3/h
Glass area	--	%
Shadow factor	--	%
Floors	--	Integer
Area	--	m^2

Table 1: Main building physics parameters

The most relevant data for building thermal performance forecast, thus, the weather forecast and building occupancy are dynamically updated and feed to the simulation engine.

The weather forecast is a key input for the simulations; two different weather information sources have been validated. The purpose of the validation is to settle if free weather forecast sources provide accurate enough information.

The validated weather forecast data sources are:
- *Meteomedia* – fee based weather data source
- *NOAA* – Non fee weather data source

The next sequence of figures (3, 4) show the data obtained for outdoor temperature validation.
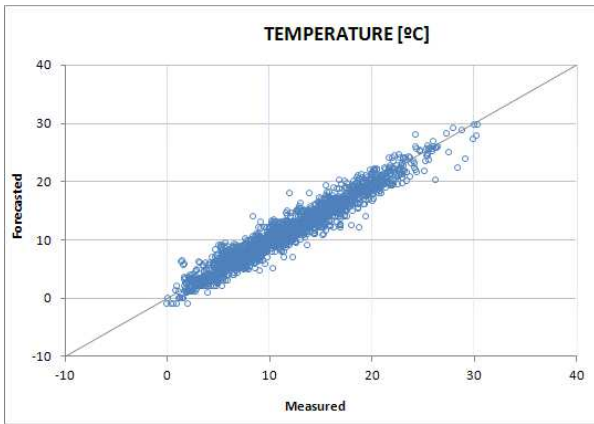
Figure 3: Meteomedia data source
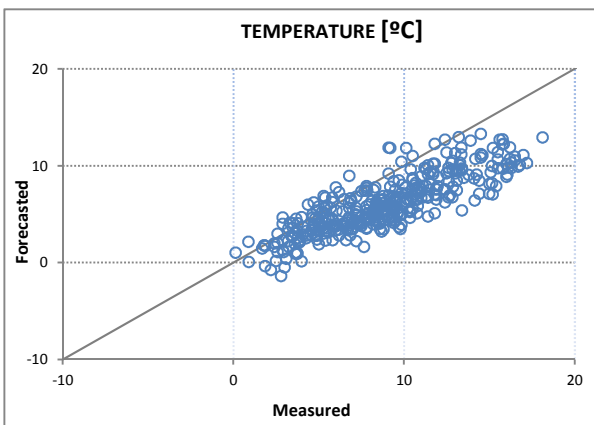
Figure 4: NOAA data source

The values used as inputs for the thermal demand forecasting simulations are:

- Outdoor temperature.
- Wind speed
- Solar radiation
- Cloud coverage

The conclusion of the validation is that available free weather forecast sources are accurate enough

BUILDING MODELS INTEGRATION

The application of design phase building knowledge into operation time lead to more efficient business process, thus, system engineering, and better understanding of buildings' behavior as thermal buffer.

In the context of integration our work relies in open platforms and in communication protocols supported by the W3C.

Building models supported by *gbXML* (Green Building XML) and *OBIX* (Open Building Information eXchange) provide flexibility and scalability to the overall *SiMoNa* platform. Both *gbXML* and *OBIX* are XML based information models.

gbXML provides a seamless data integration platform between CAD models (i.e., REVIT) and simulation software (i.e., Radiance) in this study is used to support design of high performance buildings.

The most relevant data capabilities supported by *gbXML* are:

- 3D and 2D polygon geometry
- Opaque construction and material
- Glazing and shades
- HVAC and Lighting Controls
- Schedules

gbXML together with *IFC* (Industrial Foundation Class) are the two prevalent information infrastructures in the AEC (Architecture, Engineering and Construcction) industry[9].

Next figure (5) shows the information model flow to feed the optimization engine.
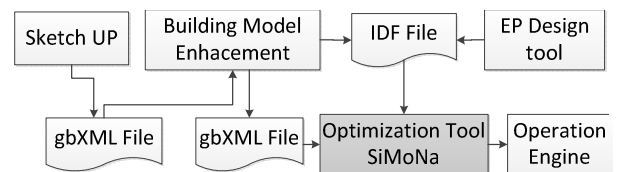
Figure 5 : Building information model flow

OBIX has a complementary role to *gbXML*. While *gbXML* is used to model building design phase information, *OBIX* is used to exchange operation time information between *SiMoNa*'s core and the communication layer or gateway.

ENERGY MANAGEMENT

Third pillar and final target of this study is to achieve an efficient energy management. The implemented energy management policy relies on 24h ahead accurate energy demand and local generation power forecasting in order to minimize the energy demand (thermal and lighting) and maximize self-consumption.

The relationship between lighting and heating/cooling has had a special consideration.

The adopted approach considers the conjunction of thermal gains due to the window area and the heat transfer due to the opaque surfaces.

$$Q_{sr} = S \cdot R \cdot F \qquad (1)$$

$Q_{sr:}$ Solar termal radiation through the window in *Watts*.
$S:$ Window Surface given in m^2.
$R:$ Solar radiation in Windows plane, given in W/m^2
$F:$ Correction factor related to the window type.

$$Q_{str} = K \cdot S \cdot (T_{ec} - T_i) \qquad (2)$$

Q_{str} Solar thermal radiation through the wall in *Watts*
K Thermal transmittance.
S Façade surface
T_{out} Outdoor temperature
T_{in} Indoor temperature

For thermal optimization following parameters have been taken into consideration [10]:
- Outdoor weather conditions
- Thermal gains due indoor loads
- Thermal gains due to solar radiation
- Comfort standards

Second level optimization includes artificial lighting and electrical loads scheduling. Maximize the self-consumption is one of the mayor targets of the designed optimization process.

The total electrical consumption is the addition of the non-controlled loads (including lighting), the shiftable loads and the HVAC consumption.

Then, equation could be rewritten as follows:

$$q1_i + q2_i = q_i^{nc} + q_i^{sh} + q_i^{hvac} \qquad (3)$$
$$i=1,..n$$

Where
$q1_i$: Consumption at time-step i coming from local generation. [kW]
$q2_i$: Consumption at time-step i purchased from market. [kW]
q_i^{nc}: Consumption of non-controlled loads (including lighting) at time-step i. [kW]
q_i^{sh}: Consumption of shiftable loads at time-step i. [kW]
q_i^{hvac}: Consumption of HVAC system at time-step i. [kW]
N: Total number of time-step of the scheduled period [-]

A shiftable is defined as a load that can be started at any of the possible periods within a defined range. This characteristic of the shiftable loads forces to introduce binary variables and convert the optimization into a binary linear programming problem[11]. The binary variables introduced in the problem description are expressed as:

$$q_i^{sh} = \sum_{k=1}^{K} \sum_{j=1}^{Jk} q_i^{sh,kj} \cdot s_{kj} \qquad (4)$$
$$i=1,..,n$$

Where
q_i^{sh}: Consumption of shiftable loads at time-step i. [kW]
K: Total number of shiftable loads.
Jk: Number of strategies of "k" shiftable load.
$q_i^{sh,kj}$: Consumption of "k" shiftable load at time-step i following "j"strategy. [kW]
s_{kj}: Binary variable representing "j" strategy of "k" shiftable load.
N: Total number of time-step of the scheduled period.

In order to ensure that only one strategy per load will be active, the following constrain must be added.

$$\sum_{j=1}^{Jk} s_{kj} = 1 \qquad (6)$$
$$k = 1 \ldots K$$

Where
Jk: Number of strategies of "k" shiftable load.
s_{kj}: Binary variable representing "j" strategy of "k" shiftable load.
K: Total number of shiftable loads.

Around the optimization processes there are auxiliary processes that have a relevant role in the overall framework [12].

- *Day Ahead Forecasting* calculates thermal, electrical demands and local generation.
- *Day Ahead Planning* schedules shiftable loads and usage of local generation power.
- *Energy Dispatcher* executes the calculated schedules.
- *Performance Analysis* evaluates if new forecasting or replanning is required.

The main modules and the information exchanged among them are shown in the figure (6).
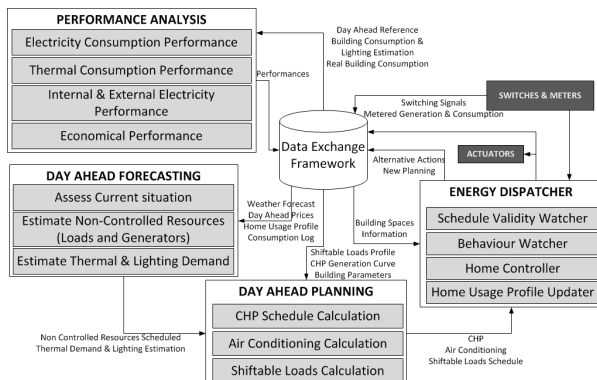
Figure 6: Optimization and auxiliary modules

USE CASE: Mondragon Unibertsitatea

Located in the north of Spain Mondragon Unibertsitatea is a brand new building equipped with laboratories, workshop rooms, study areas, classes and services for 200 students [13].

In terms of HVAC equipment it includes a boiler, a chiller, supported with a heat exchanger, and three primary air handling units.
From the point of view of management policies the main constraints are:

- For all building areas, temperature set-points are fixed for winter and summer periods.
- Windows are not operable and there are fixed external shadowing devices in some of the facades.

In this context the optimization target is "*to optimize the heating and cooling equipment's consumption in order to satisfy established comfort standards*" [14].

Guaranty regulation constraints for indoor spaces and end users comfort standards have had a special follow up. The team has kept close contact with building's maintenance staff in order to early detect unconformities in any of both domains.

The 3D view of the implemented building model is shown in the figure (7).
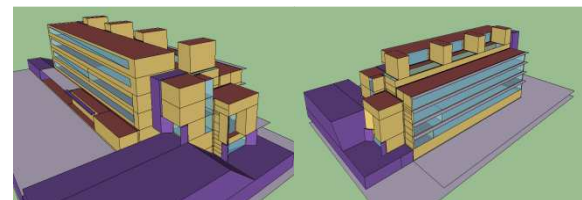
Figure 7: Modeled building 3D view

The platform deployed in Mondragon Unibertsitatea, hereinafter MU, has been integrated with an existing BMS. *SiMoNa* doesn`t replace any of the BMS functionalities but optimizes BMS's set points. The data exchange

between the BMS and *SiMoNa* platform is done using two communication standards

- *BacNET*, to handle HVAC systems
- *OPC*, to handle lighting control network.

Completed 6 months since its deployment (January 2014) the first significant results have been released.

The next sequence of figures (8, 9) describes the chiller's and boiler's set-point evolution.
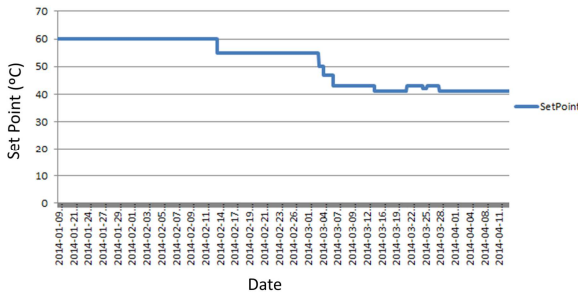
Figure 8 : Boiler's set-point temperature

The optimization process has decreased considerably boiler's operation temperature. The heating thermal demand decreases hugely since mid-March which allows decreasing the circulated hot water temperature from the used 60ºC without risk for the users' comfort. In the month of April the heating demand was almost neglectable and the boiler was disabled.

For the cooling power the opposite behavior is shown.
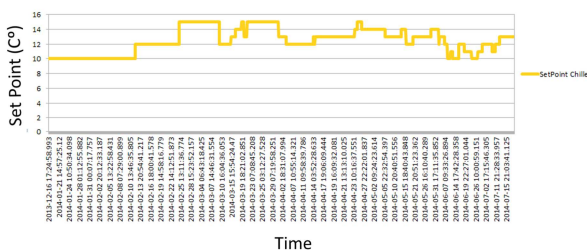
Figure 9: Chiller set point temperature

The standard set point for the chiller was between 7ºC and 9ºC. The chiller optimization was enabled in the month of February, the set point was moved

to 13ºC-15ºC for the months of March/April, in May/June where more cooling power was required, the set-point went again down to 10ºC. It is important to notice that in the end of June and early July the set point raises again due to the low level usage of the building (less students, only office and staff activity) and consequently less cooling power required.

The impact on energy savings due to the optimization processes are summarized below.
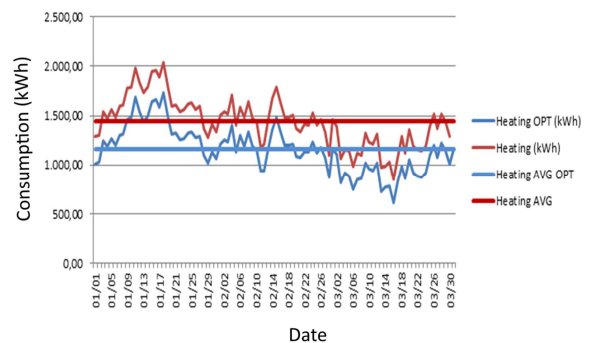
Figure 10: Heating consumption

In figure (10) reddish lines describe the heating, average and daily real, consumption in kWh without any optimization. Blue lines represent the heating consumption, and average, with the *SiMoNa* platform.

For the cooling domain, the chart below shows the values obtained for the cooling consumption. The *SiMoNa* platform's performance for cooling is evaluated against historical data and billing information.

The chart below shows the daily cooling consumption and the average values with the optimization platform (*SiMoNa*) running and without optimization platform.
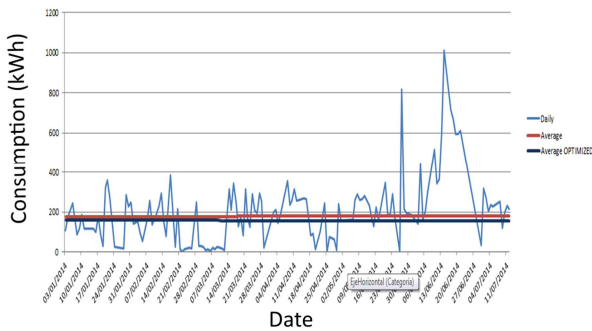
Figure 11: Cooling consumption.

The values for cooling and heating grouped by months are shown in the tables below. The "*standard heating/cooling consumption*" columns values are based on historical values while the "*optimized heating/cooling consumption*" values are released by the installed optimization platform.

Month	Standard Heating Consumption (kWh)	Optimized Heating Consumption (kWh)
Jan.	50.576,13	41.573,66
Febr.	41.145,05	33.206,30
March	37.884,19	29.453,17
April	31.903,78	24.166,39
May	16.744,52	11.502,68
June	9.425,03	5.505,51
July	4.760,54	3.640,54

Table 2: Optimized vs Not Optimize heating consumption

Based on the historical data and the real data the extrapolation for heating consumption values for complete year is shown in the figure (12).
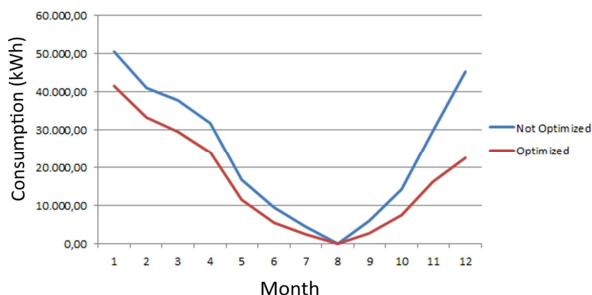
Figure 12: Heating consumption extrapolation consumption is given in kWh.

Month	Standard Cooling Consumption (kWh)	Optimized Cooling Consumption (kWh)
Jan.	2.230,12	2.100,86
Febr.	2.147,55	1.587,69
March	3.773,44	2.845,80
April	4.239,45	2.789,70
May	9.359,73	7.344,39
June	16.776,12	12.966,44
July	6547,89	4640,22

Table 3: Optimized vs Not Optimize cooling consumption

Based on the historical data and the real data the extrapolation for cooling consumption values for complete year is shown in the figure (13).
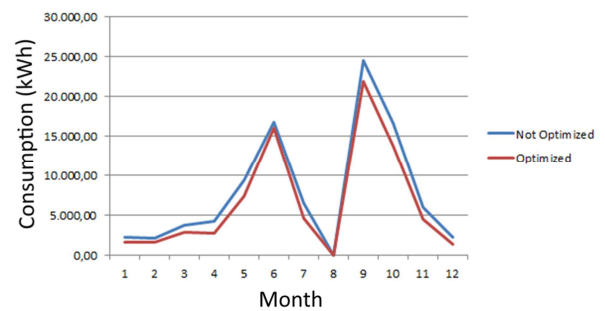
Figure 13: Cooling consumption extrapolation consumption is given in kWh.

Note: The data extrapolation considers that during the summer holidays the building is closed for one month.

CONCLUSIONS

In order to have an accurate evaluation of the deployment we analyzed the work from three different points of view.

From the *technological challenge* point of view, thus, the overall modules integration, the main barriers arise at the *EnergyPlus* integration[15]. *EnergyPlus* is designed to use plain text files as interfaces that makes the information very accessible but on the other hand requires a deep knowledge of the input/output files format.

From the *optimization performance* point of view, the most relevant difficulty is to get an accurate building modeling. It is at this point where a good transfer of the knowledge generated at design phase can help to get proper building models and consequently efficient thermal and lighting demands forecasts[1].

Last but not least the interviewed *end users'* (building owners and maintenance personnel) perception of the platform has to be mentioned. In this context the seamless integration with the existing BMS platforms and the no need of additional refurbishment operations helps to the adoption of the platform.

The end users suggested new features as moving the optimization module to the cloud or upgrading the system to make possible to run optimization on several buildings in parallel.

REFERENCES

[1]Clements-Croome, D. (2004). Intelligent buildings: Design, construction and operation. London: Thomas Telford.
[2] Z. Tian, J. Love, Energy performance ptimization of radiant slab cooling using building simulation and field measurements, Energy and Buildings
[3] M. Wetter, J. Wright, A comparison of deterministic and probabilistic algorithms for non smooth simulation-based optimization, Building and Environment. (2003).
[4] L. Caldas, L. Norford, Genetic algorithms for optimization of building envelopes and the design and control of HVAC systems, Journal of Solar Energy Engineering
[5] EN15251: 2007, Indoor Environmental Input Parameters for Design and Assessment of Energy Performance of Buildings Addressing Indoor Air Quality, Thermal Environment, Lighting and Acoustics, 2007.
[6] S.P. Corgnati, E. Fabrizio, M. Filippi, Costs and comfort: mutual relation between comfort conditions and energy demand in office buildings, in: AICARR International Conference AICARR 2006 HVAC&R: Technology, Rules and Market, Milan, March, 2006.

[7] ANSI/ASHRAE 55-1992, Thermal environmental Conditions for Human Occupancy, American Society of Heating, Refrigerating and Air-conditioning Engineers, Atlanta, GA, 1992.
[8]FumoN,MagoP,LuckR. Methodologyto estimate building energy consumptions ingenergyplus benchmark models. EnergyBuild2010;42(12):2331–7, http://dx.doi.org/10.1016/j.enbuild.2010.07.027
[9] Pohi, J., and Rep, I. 1988. An integrated intelligent CAD environment. *Proceedings, 4ᵗʰ International Conference on Systems Research*, Informatics and Cybernetics, Baden-Baden, Germany
[10] G.S. Brager, R.J. de Dear, Climate, comfort & natural ventilation: a new adaptive comfort standard for ASHRAE Standard 55, in: Proc. Int. Conf. Moving Thermal Comfort Standards into the 21st Century, Oxford Brookes University, Windsor, 2001.
[11]Hu, X., & Eberhart, R. (2002). Solving constrained nonlinear optimization problems with particle swarm optimization. In Proceedings of the sixth world multiconference on systemics, cybernetics and informatics.
[12]Duangsuwan, J., & Kecheng, L. (2008). Multi-agent control of shared zones in intelligent buildings. In International conference on computer science and software engineering.
[13] D.P. Wyon, Indoor environment effects on productivity, in: Proceedings of IAQ 1996 Path to Better Building Environments, ASHRAE, USA, 1996
[14] R.J. de Dear, G.S. Brager, Thermal comfort in naturally ventilated buildings:revisions to SHRAE Standard 55, Energy and Buildings
[15] Bazjanac, V. & T. Maile. 2004. IFC HVAC Interface to EnergyPlus - A Case of Expanded Interoperability for Energy Simulation. Proceedings of the SimBuild 2004 Conference in Boulder, CO, 4-6 August 2004

MODELING AND SIMULATION OF MULTI-ZONE BUILDINGS FOR BETTER CONTROL

Wathsala Perera[*]**and Carlos F. Pfeiffer and Nils-Olav Skeie**
Telemark University College
Department of Electrical, IT and Cybernetics
Porsgrunn, Norway.

ABSTRACT

Buildings are one of the largest energy consumers in most of the countries. Building sector in the European Union (EU) is continuously expanding and currently utilizes 40% of total energy consumption in the union. Out of that, space heating energy demand is the highest. Norway, where a harsh climate predominates, uses 48% of the total energy production for both residential and commercial buildings. Recent investigations carried out in Norway showed that there is a potential of saving 65 TWh both from residential and commercial buildings in 2020.

Nowadays there is a growing trend to use building automation system (BAS) in buildings, ranging from small rooms to multi-zone buildings with diverse architectural designs. BAS helps to make the environment more efficient for occupants with better facility management. Currently, BAS lacks a building model, and the control is based on temperature zones and lowering the temperature only 5^0C when the heaters are unused. A good building model may help to optimally turn the energy on and off and reach the temperature goal of the zones. This will give a better energy performance for the buildings.

This article refers to a multi-zone mechanistic building model which can be used for simulating the thermal behavior of a residential building. It consists of modeling the ventilation, thermal mass of walls, floor, roof and furniture. The model state variables are expressed using a lumped parameter approach. The temperature and relative humidity measurements acquired from a typical residential building in Norway are used to verify the model. Model simulation is carried out in MATLAB environment, and it can be applied for controlling the energy performance of complex building designs reasonably well. Hence the current research project is important as it contributes in achieving the energy saving goals determined in 2020.

Keywords: Mechanistic building model, Multi-zone building, Residential buildings, Ventilation

NOMENCLATURE

Symbols

A	Surface area [m^2]
$\widehat{c}_p$	Specific heat capacity of air [$J/(kgK)$]
E	Enthalpy [J]
$\widehat{h}$	Specific enthalpy [J/kg]
I	Internal energy [J]
M	Molar mass of air [kg/mol]
$\dot{m}$	Air mass flow rate [kg/s]
n	No. of mols [mol]
P	Pressure [Pa]
$\dot{Q}$	Heat flow rate [W]
$\dot{q}$	Heat generation rate [W]
R	Gas constant [$J/(molK)$]
r	Radius of sphere [m]
T	Temperature [K]
t	Thickness [m]
U	Overall heat transfer coeff. [$W/(m^2K)$]
V	Volume [m^3]
α	Thermal diffusivity [m^2/s]
ξ	Furniture temperature [K]
ϕ	Ceiling temperature [K]
ψ	Floor temperature [K]
ρ	Density [kg/m^3]
τ	Time [s]

---
[*]Corresponding author: Phone: +47 3557 5122 E-mail:wathsala.perera@hit.no

θ	Inside air temperature [K]
ω	Wall temperature [K]
Subscripts	
c	ceiling
f	Floor
fur	Furniture
g	Ground
i	Building unit
j	Adjacent room
w	Wall
α	Outside environment
Superscripts	
h	Horizontal opening
s	Surface
v	vertical opening

INTRODUCTION

The total worldwide energy demand is continuously increasing owing to the population growth, economic development and the social development. With the growth of the indicated determinants, building sector has become one of the largest energy consumers and it accounts for nearly 40% of the total global energy consumption [1]. Similarly, the building energy consumption in the EU is continuously expanding and it has also risen to 40% [2]. According to the statistics in 1999, space heating was the key contributor, which accounts for 68% of total household energy consumption in the EU [3]. Among the European nations, Scandinavian countries experience comparatively harsh climate conditions during about one third of the year. Accordingly, in a country like Norway, residential households and commercial buildings consume about 48% of the total energy production [4] mainly for space heating. Recent investigations in Norway, have showed that there is a feasibility of saving 65 TWh both from residential and commercial buildings by 2020 [4], and to achieve this goal Norwegian government authorities have imposed building technical regulations.They encourage the people to save energy using renewable sources and building energy management systems (BEMS).

BEMS are a subset of BAS and they monitor and control the energy of the buildings and building services as energy efficiently as possible while reducing the utility bill without compromising the comfort level of the occupants. These systems are a rapidly expanding field over the last two decades and

they have gained the attention as a standard way of controlling the buildings with regard to the classical techniques such as thermostat control [5]. Currently, the most of the BEMS systems utilize on/off control, PID control or optimum start-stop routines as the control algorithm [5]. PID control is the most used technique in such systems [5]. However the use of classical control algorithms such as PID and on/off may not be the best to be combined with BEMS [6]. In buildings, thermal interaction between different zones and HVAC (Heating, Ventilation and Air-Conditioning) systems lead to multivariable behavior. Classical control techniques have some deficiencies in handling such systems. For example, classical controllers are easy to tune for SISO (Single Input - Single Output) systems and not easy or even impossible to tune for MIMO (Multiple Input - Multiple Output) systems. Advanced control techniques appear with a mathematical model of the building and have the potential to approach these constraints [5]. The required model in advanced control could be multivariable and consequently has a higher probability of delivering improved performance with fewer setpoint deviations and high energy savings when compared with the classical control. Therefore, it is essential to choose a good quality building model to produce a favorable outcome by BAS.

Building heating models can be categorized into three broad categories: (i) mechanistic models (white box or physical models); (ii) empirical or black box models; and (iii) grey box models ([7] - [11]). Mechanistic building models are developed based on the physical principles of mass, energy and momentum transfer. They consist of several equations with numerous coefficients to represent the building geometry and the thermal properties of the building. Large number of numerical software tools are available for solving such systems. However, there are problems associated with mechanistic models regarding the calibration of the physical parameters. Software tools like Energy Plus, TRNSYS, Modelica and Fluent provide comprehensive mechanistic models for building simulation. These models may have a very high accuracy, but they may have a high computational burden when applied to online control. Further, it may not be easy to calibrate these models with respect to the experimental data. Therefore, the selection of a mechanistic

model for a building is a balance between model complexity and the desired accuracy [7]. Application of physical principles to buildings and developing mechanistic type models are available in [12] - [19]. System identification based models, regression models [20], genetic algorithm [21], fuzzy logic models [22], neural network models [23], neuro-fuzzy models [24] and support vector machine [25] are some examples of black box models. These models are generated based on the data measured from a particular building such as inside and outside temperatures, relative humidities, wind speed, solar radiation and air flow rates. Accordingly, these models do not use any physical data of the building and hence the model coefficients do not have a physical meaning. Black box models may perform better than physics based models, but it will only work for a specific building where the data is measured. When the inputs are outside the modeled data range these models may give unrealistic and non-physical results. Grey box models [26] are a combination of both mechanistic and black box models and information about these models is partly known [11]. They are mostly used for parameter estimation and only a limited work has been done on them [11].

The present study focuses on the development of simple but comprehensive mechanistic type building heating model for multi zone buildings, which can also be applied in online control in BAS. The development is based on the single zone building model presented in [19]. There are a number of research articles that explain the modelling of multi-zone buildings using physical principles. [12] presents the development of a multi zone building model for MATLAB/SIMULINK environment implemented into the SIMBAD Building and HVAC Toolbox. Wall thermal mass is considered in the model and it is assumed to have constant thermo physical properties for each layer of the multilayered walls. A window model and solar radiation model are also included in [12]. In [15], a reduced order state space thermodynamic model is developed. Each zone is assumed to be well mixed and inter zone air mixing, air infiltration and solar radiation also modeled. A variety of multi zone building thermal modelling techniques can be found in [27], [17], [16] and [28]. However, the indicated multi zone building models lack either one or several features: (i) zonal mass balance; (ii) thermal mass of walls, floor and roof; (iii) thermal storage capability of building furniture; (iv) solar irradiation; and (v) occupancy. Hence, it is important to develop a reliable multi-zone mechanistic building model that depicts all these effects.

The rest of the paper is organized to present a detailed overview of the multi zone model development, simulation to validate the proposed approach using real experimental data and finally some concluding remarks.

MODELLING APPROACH

In this section, a mechanistic dynamic heating model for a multi zone building unit is developed. The modeled building unit is presented in Figure 1. It is connected to four adjacent rooms, outside environment and ground. Heat is transferred from the main unit to the surroundings via walls, roof and floor. The mechanical ventilation system controls the air flow rate into and out of the building unit. There is a staircase to access the room above the building unit via the horizontal opening in the ceiling. Air is exchanged in between the adjacent rooms owing to the interactions caused by vertical and horizontal openings. A heater is installed inside the building unit to supply the energy for heating. Further, the other electrical appliances discharge their waste energy which can also increase the inside temperature. The furniture inside the unit may behave as a heat sink or heat source depending on the temperature difference between the furniture and the surroundings.
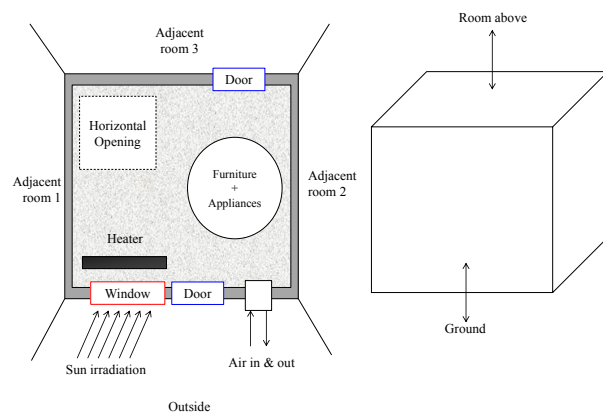

Figure 1: Configuration of the building unit

Application of mass balance for ventilated spaces is vital as ventilation plays a key role in convective mode of heat transfer. The mass balance equation for the indicated multi zone building unit can be expressed as in the equation 1.

$$\frac{d\rho_i}{d\tau} = \frac{1}{V_i}\left[\begin{array}{c}\dot{m}_{\alpha,i} - \dot{m}_{i,\alpha} + \sum \dot{m}^v_{j,i} - \\ \sum \dot{m}^v_{i,j} + \sum \dot{m}^h_{j,i} - \sum \dot{m}^h_{i,j}\end{array}\right] \quad (1)$$

Energy balance for the building unit is derived using the standard energy balance equation, the relation $E = I + PV$, the relation $dE = d(m\widehat{c}_p\theta)$ and the ideal gas law $PV = nR\theta$.

$$\frac{d\theta_i}{d\tau} = \frac{\left[\begin{array}{c}\dot{m}_{\alpha,i}\widehat{h}_\alpha - \dot{m}_{i,\alpha}\widehat{h}_i + \dot{Q}_i \\ + \sum \dot{m}^v_{j,i}\widehat{h}_j - \sum \dot{m}^v_{i,j}\widehat{h}_i \\ + \sum \dot{m}^h_{j,i}\widehat{h}_j - \sum \dot{m}^h_{i,j}\widehat{h}_i\end{array}\right]}{\rho_i V_i(\widehat{c}_{p_i} - R/M_i)} - \frac{\theta_i}{\rho_i}\frac{d\rho_i}{d\tau} \quad (2)$$

Modelling the heat transfer via the building envelope is essential in thermal modelling as its thermal mass has a significant contribution to the temperature fluctuations inside the building. Walls, ceilings, roof and floor usually consist of several layers of dissimilar materials such as wooden panels and insulation materials. In this study, all the layers are recognized as one element of constant thermal properties for simplicity of the model. Transient heat equation $\left(\frac{\partial T}{d\tau} - \alpha \nabla^2 T - \frac{\dot{q}}{\rho \widehat{c}_p} = 0\right)$ is discretized using the finite difference method to obtain the respective energy balance equations for the walls, floor and ceiling of the building unit based on the assumption of one-dimensional heat transfer. The deduced ordinary differential equations for heat transfer through walls, floor and ceiling are given by equations 3, 4 and 5 respectively.

$$\frac{d\omega}{d\tau} = \alpha_w\left[\frac{\omega^s_i - 2\omega - \omega^s_j}{(t_w/2)^2}\right] + \frac{\dot{q}_w}{\rho_w\widehat{c}_{p,w}} \quad (3)$$

$$\frac{d\psi}{d\tau} = \alpha_f\left[\frac{\psi^s_i - 2\psi - \psi^s_g}{(t_f/2)^2}\right] + \frac{\dot{q}_f}{\rho_f\widehat{c}_{p,f}} \quad (4)$$

$$\frac{d\phi}{d\tau} = \alpha_c\left[\frac{\phi^s_i - 2\phi - \phi^s_j}{(t_c/2)^2}\right] + \frac{\dot{q}_c}{\rho_c\widehat{c}_{p,c}} \quad (5)$$

The presence of furniture in a building prolongs the time required to heat a building to a specified temperature. Correspondingly, it takes a longer time to cool down the building as the heat release from the furniture is slow. To simplify the modelling of heat transfer in furniture, all the furniture with different properties are aggregated into a single large spherical object having equivalent average thermal diffusivity. Heat equation in spherical coordinates, $\left(r^2\frac{\partial\xi}{\partial\tau} - \alpha\frac{\partial}{\partial r}\left(r^2\frac{\partial\xi}{\partial r}\right) - r^2\frac{\dot{q}}{\rho\widehat{c}_p} = 0\right)$, is discretized to obtain the representative energy balance equation for the furniture (equation 6).

$$\frac{d\xi}{d\tau} = \frac{\alpha_{fur}}{r}\left[\frac{\xi^s_i - 2\xi - \xi_{centre}}{(r/4)} + \frac{\xi^s_i - \xi_{centre}}{r/2}\right] \quad (6)$$

Equations 1 to 6 presents the ordinary differential equations describing the model for the multi zone building unit. The rest of this section shows the algebraic equations required to obtain the complete model.

It is necessary to evaluate the air mass flow rates via vertical and horizontal openings of the building unit to the neighboring zones. Figure 2 presents the air flow pattern through a vertical and a horizontal opening.

(a) (b)
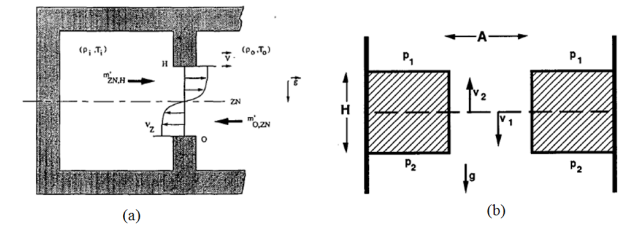
Figure 2: Air flow through (a) Vertical and (b) Horizontal openings [29]

Many authors ([29], [30], [31] and [32]) have developed equations for air flow across a vertical opening considering a constant air density for each zone. Interested readers can refer to the above mentioned references to admit a relation for the mass flow rates ($m^v_{j,i}$, $m^v_{i,j}$) addressed in the equation 1.

The mass flow rate through horizontal openings could be either one way or two way depending on the pressure difference between the zones [29]. Consequently, to determine the direction of the flow, it is necessary to understand the pressures of each zone. Equation 7 is suggested by [33] to determine the air mass flow rate along a staircase. A_o and H_o are the area and thickness of the opening while C_d is the coefficient of discharge.

$$\dot{m}^h = \rho A_o C_d\left[\frac{\Delta\theta g H_o}{\theta}\right]^{0.5} \quad (7)$$

The term $\dot{Q}_i$ in the equation 2 represents the net heat flow to the building unit, and it can be approximated using the equation 8. Heat losses through walls, floor, roof, windows and doors can be estimated using the equation 9 for each component.

$$\dot{Q}_i = \left[\begin{array}{c} \dot{Q}_{heater} + \dot{Q}_{solar} + \dot{Q}_{appliances} - \dot{Q}_w \\ -\dot{Q}_f - \dot{Q}_c - \dot{Q}_{window} - \dot{Q}_{door} - \dot{Q}_{fur}) \end{array} \right] \tag{8}$$

$$\dot{Q} = UA\Delta T \tag{9}$$

THE TEST BUILDING

This section yields a description of the test building which is located in Norway. It is a three storeyed residential building located near Langesund and built in 1987.
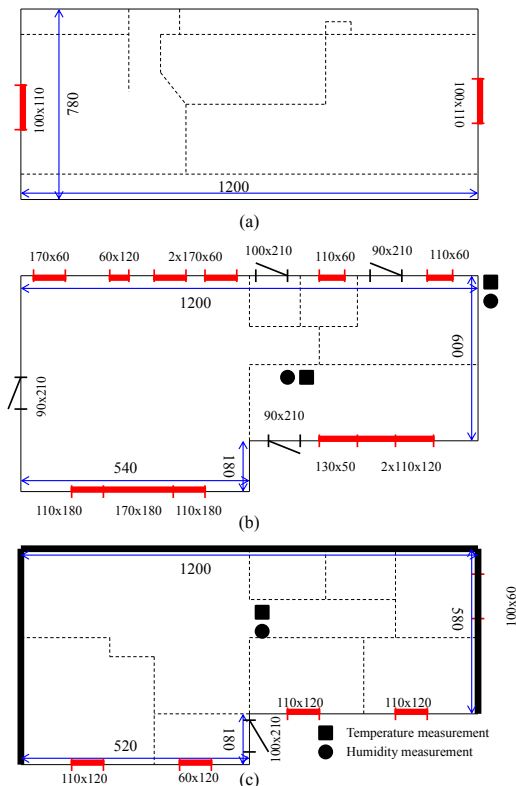
Figure 3: Sketches with the inner dimensions of the test building (a) second floor (attic) (b) first floor (main floor) (c) basement. All the dimensions are in cm.

The building inner dimensions, window and door dimensions are given in Figure 3. The three storeys are accessible via two inner staircases. The main floor and the attic are equipped with a mechanical ventilation system while the basement is not provided with mechanical ventilation. Total average air inflow rate into the building is 230 m^3/h. There is a heat exchanger installed across the ventilation system to heat the incoming air using the outgoing air. This heat recovery system has an efficiency of 90%.

The exterior walls of the attic have a thickness of 30 cm (average) and the roof thickness is 30 cm. It has a volume of 93 m^3. Both attic and main floor are constructed using wood and mineral wool insulation. The furniture volume inside the second floor is estimated to be 3 m^3. There are no heaters fixed in this storey, but four personal computers are running all the time which supply around 700W.

The main floor has the same roof thickness similar to attic with a volume of 196 m^3. It's wall thickness is 15 cm. It is filled up with 25 m^3 of furniture and 3200 W power is supplied for heating purposes. The electrical heaters are controlled by a simple BAS with a set temperature of 20^0C when the building is occupied. In the simulations, the heater is precisely controlled by an On/Off controller having an operating band of $\pm 0.25^0$C, to maintain the temperature at 20^0C. In addition to the electrical heater, wood firing is used to heat the building only during the colder periods, which is not modelled in this article.

The thicker walls of the basement and it's ground floor are built using concrete and the rest is wood. Outer wooden walls of the basement have a thickness of 20 cm and concrete walls have a thickness of 40 cm. The thickness of the ceiling is 30 cm, and the wall height is 235 cm. The total volume of the basement is 185.5 m^3 and the furniture accounts for 40 m^3. There are four heaters installed in the basement. Out of that, two are wall heaters (2x750 W), controlled by the same BAS in the first storey. The others are full time running floor heaters. The floor heaters have switches to turn them OFF or ON(1), ON(2) and ON(3). ON position 1 (160+390 W) is the lowest power usage and ON position 3 is the highest power usage. All the floor heaters are running at position 1 for most of the time. However, in reality, these heaters are manually brought to position 2 depending on the outside temperature.

The experiment of the test building is carried out for 79 days/1897 hours in the period 24 October 2013 - 10 January 2014. The locations where the temperatures and relative humidities are measured, are

Table 1: Model parameters of the test building

Parameter	2nd Storey	1st Storey	Basement
$\alpha_{w,wood}$	9.5×10^{-7}	8.3×10^{-7}	8.3×10^{-7}
$\alpha_{w,concrete}$			4.9×10^{-7}
α_f	-	-	4.9×10^{-7}
α_c	1×10^{-6}	1×10^{-6}	1×10^{-6}
α_{fur}	1.7×10^{-7}	1.7×10^{-7}	1.7×10^{-7}
$U_{w,wood}$	0.01	0.5	1.5
$U_{w,concrete}$			1.15
U_f	-	-	0.01
U_c	0.01	0.27	0.27
U_{fur}	0.5	1	0.1
U_{doors}	-	1.2	-
$U_{windows}$	1.2	1.2	-

symbolized in the sketch (Figure 3). No measurements were collected from the attic of the building during the test period. To eliminate the outliers and the noise present in the data, they are smoothed using 30th order Savitzky-Golay filter.

For the considered period, solar irradiation measurements are not available. Hence, it is roughly estimated using the instant outside temperatures.

A simplified form of the equation 7 has been used to determine the value of the convective air mass flow rates inside the building in between each storey. To define the air movement direction, it is essential to recognize the pressure and density fluctuations of each storey. However, pressure measurements are not logged in this experiment. Therefore, the pressure increment in each zone is calculated by analyzing the volume of air flowing into each storey through the ventilation system.

RESULTS AND DISCUSSION

In this section, the performance of the developed multi-floor building model is analyzed for the selected test building after its implementation in MAT-LAB.

The thermal properties like thermal conductivity, specific heat capacity and density of the building materials are obtained from the literature, and they are used to calculate the thermal diffusivity of the building components. The overall heat transfer coefficients are determined using the experimental data. Parameter identification from test data has revealed that calibrating the parameters presented in the model to normal operating data from a building may lead to grossly inaccurate estimates. The predicted overall heat transfer coefficients, which can admit a favorable solution to the proposed criteria, and the computed thermal diffusivities are given in Table 1. It should be noted that only the thermal parameters observed in the model equations which are acknowledged to be significant are tabulated.

The predicted temperatures of the three storeys of the building are presented in the Figure 4. According to the figure, it can be noticed that the inside temperatures have a close relationship with the outside temperature fluctuations.

In the second storey, only the predicted temperature is shown because of the unavailability of sensor measurements. The temperature is wavering while maintaining 20^0C, which is acceptable according the residents' feedback.

The first storey of the building maintains 20^0C throughout the 79 days, which can be observed by the measured temperature profile. The predictions also produce a consistent 20^0C for more than 90% of the time with the benefit of an ON/OFF temperature controller. Even though the measured temperature is restricted to 20^0C, the predicted temperature is considerably lower close to day 30 and day 45. The low outside temperature predominating over the period is the reason for this scenario. However, in actuality the inside temperature is preserved at the set temperature by wood firing, which is not reflected in the simulation.

The deviations of the basement temperature profiles are proportionately higher compared to the first storey. The maximum divergence between the predicted temperature and the measured temperature approaches 4.5^0C at day 47. The discrepancies could be owing to the action of floor heaters at ON position 2 during the cold periods.

CONCLUSION

Mechanistic building heating models have speeded up the design, construction and operational activities of buildings and succeeded in establishing the new technologies in building operation. Hence, the identification of a proper model of the heat dynamics of a building based on frequent readings will be very useful in defining the energy performance of the building, forecasting the energy consumption and controlling the indoor environment.
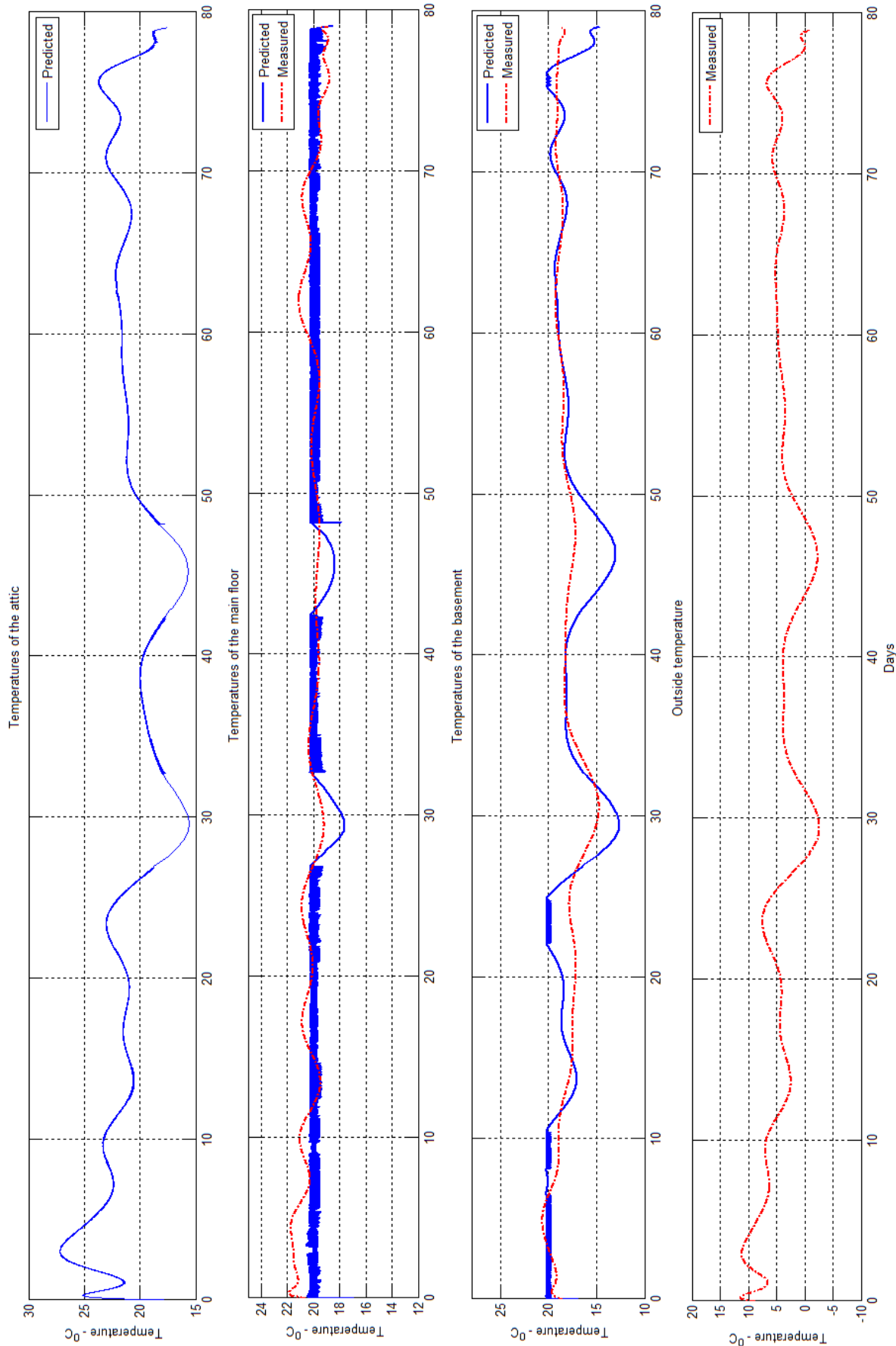
Figure 4: Inside and outside temperature variations of the test building. No temperature measurement data is available for the attic. The main floor and the basement temperature predictions closely follow the measured temperature profiles.

In this paper, a lumped parameter model illustrating the long term heat dynamics of a residential building based on first principles is presented. The model also takes the thermal mass of the building envelope and vertical air mixing into consideration. Hence, it has been shown that the used methodology can provide rather detailed knowledge of the heat dynamics of the building. Moreover, the proposed criteria is simple, computationally attractive and requires limited input information. The developed model accomplishes the application independability and, therefore, the application of this methodology to a broad class of building types is straightforward.

The deficiencies met in the model validation are: requirement for more temperature sensors at representative positions in each floor; solar irradiation measurements; and pressure measurements. These deficiencies can be eliminated, and accurate thermal simulation can be achieved if sufficient and precise input data of the building is available.

Integration of the developed model with a BAS may help to optimize the usage of energy consumption. Further, it will help to achieve the temperature goal of each zone with less energy compared to using a time schedule to control the temperature.

REFERENCES

[1] World Energy Council, World energy resources, 2013.

[2] EBPD, On the energy performance of buildings. Official Journal of the European Union, Directive 2010/31/EU of the European Parliament and of the council, 2010: p. 13-34.

[3] Dounis, A.I. and C. Caraiscos, Advanced control systems engineering for energy and comfort management in a building environment - A review. Renewable and Sustainable Energy Reviews, 2009. 13(6–7): p. 1246-1261.

[4] Valmot, O.R., Enormt potensial for energisparing, in Teknisk Ukeblad 2013. p. 30-31.

[5] Virk, G.S., J.M. Cheung, and D.L. Loveday. Development of adaptive control techniques for BEMs. in International Conference on CONTROL '91. 1991.

[6] Perera, D.W.U., C.F. Pfeiffer, and N.-O. Skeie, Control of temperature and energy consumption in buildings - A review International Journal of Energy and Environment, 2014. 5(4): p. 471-484.

[7] Lu, X., D. Clements-Croome, and M. Viljanen, Past, present and future mathematical models for buildings. Intelligent Buildings International, 2009. 1(1): p. 23-38.

[8] Kramer, R., J. van Schijndel, and H. Schellen, Simplified thermal and hygric building models: A literature review. Frontiers of Architectural Research, 2012. 1(4): p. 318-325.

[9] Foucquier, A., et al., State of the art in building modelling and energy performances prediction: A review. Renewable and Sustainable Energy Reviews, 2013. 23(0): p. 272-288.

[10] Spindler, H.C. and L.K. Norford, Naturally ventilated and mixed-mode buildings—Part I: Thermal modeling. Building and Environment, 2009. 44(4): p. 736-749.

[11] Zhao, H.-X. and F. Magoulès, A review on the prediction of building energy consumption. Renewable and Sustainable Energy Reviews, 2012. 16(6): p. 3586-3592.

[12] Khoury, Z.E., et al., A multizone building model for MATLAB/SIMULINK environment, in Ninth International IBPSA Conference2005: Montreal, Canada.

[13] Fraisse, G., et al., Development of a simplified and accurate building model based on electrical analogy. Energy and Buildings, 2002. 34(10): p. 1017-1031.

[14] Lü, X., Modelling of heat and moisture transfer in buildings: I. Model program. Energy and Buildings, 2002. 34(10): p. 1033-1043.

[15] O'Neill, Z., S. Narayanan, and R. Brahme, Model-based thermal load estimation in buildings, in Fourth National Conference of IBPSA2010: New York, USA.

[16] Yao, Y., et al., A state-space model for dynamic response of indoor air temperature and humidity. Building and Environment, 2013. 64(0): p. 26-37.

[17] Lü, X., et al., A novel dynamic modeling approach for predicting building energy performance. Applied Energy, 2014. 114(0): p. 91-103.

[18] Mendes, N., G.H.C. Oliveira, and H.X.d. Araújo, Building thermal performance analysis by using MATLAB/SIMULINK, in Seventh International IBPSA Conference2001: Rio de Janeiro, Brazil.

[19] Perera, D.W.U., C.F. Pfeiffer, and N.-O. Skeie, Modelling the heat dynamics of a residential building unit: Application to Norwegian buildings. Modeling, Identification and Control, 2014. 35(1): p. 43-57.

[20] Masuda, H. and D.E. Claridge, Statistical modeling of the building energy balance variable for screening of metered energy use in large commercial buildings. Energy and Buildings, 2014. 77(0): p. 292-303.

[21] Xu, X. and S. Wang, Optimal simplified thermal models of building envelope based on frequency domain regression using genetic algorithm. Energy and Buildings, 2007. 39(5): p. 525-536.

[22] Fraisse, G., J. Virgone, and J.J. Roux, Thermal control of a discontinuously occupied building using a classical and a fuzzy logic approach. Energy and Buildings, 1997. 26(3): p. 303-316.

[23] Li, K., H. Su, and J. Chu, Forecasting building energy consumption using neural networks and hybrid neuro-fuzzy system: A comparative study. Energy and Buildings, 2011. 43(10): p. 2893-2899.

[24] Alasha'ary, H., et al., A neuro–fuzzy model for prediction of the indoor temperature in typical Australian residential buildings. Energy and Buildings, 2009. 41(7): p. 703-710.

[25] Zhijian, H. and L. Zhiwei. An Application of Support Vector Machines in Cooling Load Prediction. in Intelligent Systems and Applications, 2009. ISA 2009. International Workshop on. 2009.

[26] Berthou, T., et al., Development and validation of a gray box model to predict thermal behavior of occupied office buildings. Energy and Buildings, 2014. 74(0): p. 91-100.

[27] Hong, T. and Y. Jiang, A new multizone model for the simulation of building thermal performance. Building and Environment, 1997. 32(2): p. 123-128.

[28] Andersen, K.K., H. Madsen, and L.H. Hansen, Modelling the heat dynamics of a building using stochastic differential equations. Energy and Buildings, 2000. 31(1): p. 13-24.

[29] Allard, F., et al., Air flow through large openings in buildings, J.V.D. Maas, Editor 1992, International Energy Agency.

[30] Brown, W.G. and K.R. Solvason, Natural convection through rectangular openings in partitions—1: Vertical partitions. International Journal of Heat and Mass Transfer, 1962. 5(9): p. 859-868.

[31] Allard, F. and Y. Utsumi, Airflow through large openings. Energy and Buildings, 1992. 18(2): p. 133-145.

[32] Riffat, S.B., Algorithms for airflows through large internal and external openings. Applied Energy, 1991. 40(3): p. 171-188.

[33] Peppes, A.A., M. Santamouris, and D.N. Asimakopoulos, Buoyancy-driven flow through a stairwell. Building and Environment, 2001. 36(2): p. 167-180.

MODELING AND SIMULATION OF AN OFFSHORE PIPE HANDLING MACHINE

Witold Pawlus,[*] **Martin Choux, Geir Hovland and Michael Rygaard Hansen**
University of Agder
Faculty of Engineering and Science
Department of Engineering Sciences
PO Box 509, N-4898 Grimstad
Norway

Søren Øydna
MHWirth
Department of Technology and Innovation
PO Box 413, Lundsiden, N-4604 Kristiansand
Norway

ABSTRACT

The objective of modeling the offshore machinery is to allow virtual prototyping and simulation of new designs which in turn makes it possible for engineers to test, redesign, adjust, and optimize a product before it is manufactured. An essential part of the modeling process is validation of the simulation results against real world measurements which in most cases is the limiting factor for achievable accuracy of the modeled system. In this paper we present a case study where a subsystem of an offshore drilling equipment is modeled and benchmarked with a full-scale machinery. Unlike some other works, the current study shows validation of the simulation results and friction identification process. We demonstrate that the model of the vertical pipe handling machine captures the important features of the real world system, and fundamentally improves computational effort of the simulation software as compared to a regular, multi-body model of the same equipment. Hence, the established model could be successfully applied in model based control system design as well as in real-time testing of control systems before commissioning of the equipment.

Keywords: Modeling and simulation, vertical pipe handling machine, electric drivetrain

NOMENCLATURE

c	Wire damping coefficient [N.s/m]
J	Mass moment of inertia [kg.m^2]
k	Wire stiffness coefficient [N/m]
m	Mass [kg]
T	Torque [Nm]
x	Translational displacement [m]
W	Wire force [N]
δ	Wire elongation [m]
$\dot{\delta}$	Wire rate of elongation [m/s]
θ	Rotational displacement [rad]
μ	Friction coefficient [-]

---

[*]Corresponding author: Phone: +47 3723 3281 Fax: +47 3723 3001 E-mail: `witold.p.pawlus@ieee.org`

INTRODUCTION

According to [1], there are strong signs that the hydrocarbon producing industry will tend to develop new fields in the Arctic in the near future. Oil and gas production in the Arctic depends on a complex set of variables. An increased demand for energy, high probability of finding resources and the fact that the Arctic ice is declining have fueled the race for resources. It is important to note, however, that harsh winters with extreme temperatures and year-round ice represent highly challenging conditions for the oil and gas industry. Therefore, it is observed that currently the petroleum enterprises invest in technologies which make exploratory drilling less dif-

ficult, more cost effective and environment friendly.

One of such fields is simulation based engineering. There exists a number of examples showing benefits of using modeling and simulation tools in the design, development, and analysis of offshore processes and machines - see for instance [3]-[7]. The overall tendency is not only to model a given phenomenon but also to utilize the model in either subsequent stages of product development or to gain better understanding of a considered problem. A good example is model predictive control (MPC) used in a closed loop simulation to improve process performance or model based optimization of a machine to provide for enhanced nominal characteristics.

Within the area of modeling and simulation, an increasing amount of research is carried out with particular attention to electrical actuation systems used in offshore conditions. In [8], an induction machine for wind power plants is modeled which enables efficient simulation of multi machine installations like offshore wind parks. In [9]-[11] special attention is given to selected new developments within the field of electric motors. These involve control of an induction generator using direct vector control technique implemented in a virtual simulation environment, application of direct vector control in positioning of servomotors or verification of suitability of linear permanent magnet machine for drilling purposes. Finally, in [12], a set of main design criteria that need to be addressed when choosing components of an electrical drivetrain to operate in offshore environment is specified.

In addition, offshore field work and experimental data gathering is covered in the literature as well - see [13]-[15]. Development and testing of large-scale machinery is presented together with simultaneous faults analysis performed using modeling techniques. Finally, modeling strategies are used in the areas that do not have a direct link with engineering, e.g. optimization techniques applied to lower workload of personnel operating on a drilling rig - see [16]. This wide set of references gives a clear indication that modeling and simulation tools are popular in the offshore drilling industry and find a broad range of applications.

In the current work we use a third party virtual modeling software to create a multi-body model of a subsystem of an offshore pipe handling machine. A mathematical model of the considered mechanism is initially formulated that allows for verification of the simulation results accuracy. Additionally, assumptions and simplification techniques are introduced to facilitate modeling process. Finally, simulation results are benchmarked against full-scale data measured on a real world machine to validate the virtual models.

The present study contributes in three areas. Most importantly, it presents a full process of modeling and simulation of an existing offshore drilling machine, establishment of its multi-body model and formulating its simplified, analytical version. Secondly, it gives an overview on how a complex, rigid multi-body model that is computationally demanding could be optimized for real-time performance. Finally, the accuracy of the simulation results is demonstrated on field data from a full-scale offshore drilling machine by identifying friction phenomenon in the system and comparing simulation results with reference, real world measurements.

OFFSHORE PIPE HANDLING EQUIPMENT
Vertical Pipe Handling Machine

The vertical pipe handling machine shown in Figure 1 is a machine which assembles and delivers stands or pipes to the well center as the drilling process continues. According to [2], it is a column supported at the top and bottom by a track and a rack and pinion system. The lower track is mounted directly on the drill floor, whereas the upper track is connected to the derrick structure. At both ends of the column there are located trolleys which allow for horizontal movement of the machine along the tracks. In total the column includes three arms. Their role is to deliver, handle, and assemble pipes. The upper and lower ones are designed to guide a pipe, i.e. to guide the top and bottom of the pipe being in operation. The middle arm is the so-called gripper arm which is responsible for holding a pipe in a secure grip. It is possible to hoist or lower this arm by using a winch located on top of the column. All three arms are equipped with hydraulic cylinders which allow for their extension / retraction in order to position pipes in the finger boards or well center. The whole machine can rotate about its vertical axis thanks to slew motors mounted at the lower trolley. In the current work, the gripper arm operated by a winch is selected as a case study. Real world torque and

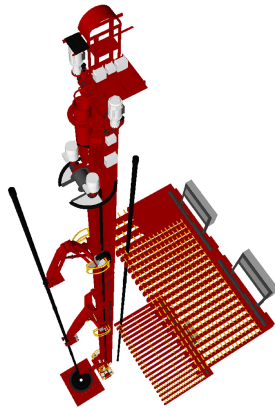velocity profiles are used to validate its simulation model.

Figure 1: *Vertical pipe handling machine (MH VPR^{TM}) - courtesy of MHWirth.*

Figure 2: *The gripper arm structure.*

Gripper Arm - Functional Description

The gripper arm illustrated in Figure 2 is connected to the middle of the column through two dollies that are equipped with trolleys. Trolleys roll up and down on the column within the guide rails allowing, together with the winch mechanism, for vertical motion of the gripper arm. The geometry of the arms ensures that the head moves in a straight horizontal line from the column during extension / retraction cycles that are realized in a separate sequence. The winch drive consists of a motor, a hydraulic brake, a planetary gearbox and a winch drum directly connected to the hoisting wire. The hoisting wire is connected to the dead anchor at the top of the column via the sheave, located on the lower dolly. This arrangement provides for vertical motion of the gripper arm. In addition, there are two hydraulic cylinders installed between the lower and upper dollies that allow for horizontal extension / retraction of the arm by changing their stroke.

Simplified Gripper Arm

In order to create a computationally efficient virtual model of the analyzed gripper arm system, a simplified mechanical structure is considered as shown in Figure 3. Location of joints as well as overall dimensions and masses of particular elements of the

mechanism are kept the same as in the original system. This arrangement is subsequently implemented in SimulationX software and its simulation results are verified with an analytical model introduced in the following Section. SimulationX is a commercially available multi-domain modeling software. It consists of a number of libraries from various physical domains (e.g. rigid body mechanics or hydraulic actuation systems). Applying such predefined components in modeling enhances design and analysis of complex mechatronic systems, as they are typically composed of many integrated sub-systems. In the current work, elements from a multi-body library are used to represent the gripper arm of MH VPR^{TM}.
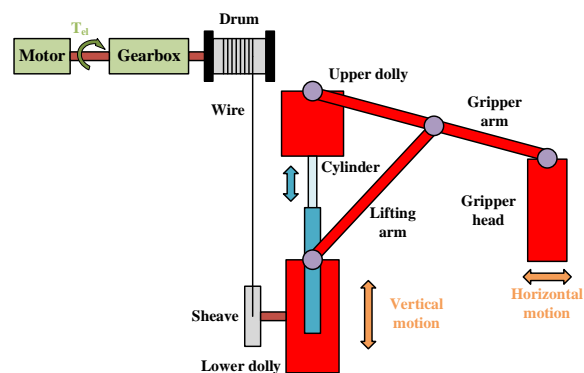
Figure 3: *A simplified gripper arm connected to the winch drivetrain.*

MATHEMATICAL MODELING
Modeling Assumptions

The scope of the current work is to analyze vertical motion of the gripper arm, without the effect of extension / retraction of the hydraulic cylinders. Therefore, it is assumed that the only degree of freedom in the machine is relative motion of the lower dolly (with all its attachments, e.g. upper dolly, gripper arm, etc.) with respect to the winch. In order to formulate a relatively computationally efficient model of such a system, the arrangement shown in Figure 3 is simplified and represented as a mass and drum / winch system, illustrated in Figure 4. Combined mass m_c includes masses of particular components of the gripper arm and mass of the payload (i.e. the pipe being handled). The following assumptions have been made to establish a mathematical model of the analyzed machinery:

1. Drum radius is constant. Normally, there are two layers of wire in use but in the current study we assume that there is no layer shift.

2. Mass of the wire is neglected since it constitutes only a small portion of the system total mass.

3. Inertia and mass of the drum are constant.

4. Wires are modeled as spring-damper systems: stiffness and damping are constant.

5. Gearbox inertia is neglected as it does not contribute significantly to the combined inertia of the modeled system.

6. Heave motion of the platform is neglected.

Wires

The wires are modeled as elastic spring-damper systems. Therefore, the elastic force in each wire is determined to be:

$$W_1 = k \cdot \delta_1 + c \cdot \dot{\delta}_1 \qquad (1)$$

$$W_2 = k \cdot \delta_2 + c \cdot \dot{\delta}_2 \qquad (2)$$

where $\delta_{1,2}$ - elongation of the wire [m], $\dot{\delta}_{1,2}$ - rate of elongation of the wire [m/s], k - stiffness of the
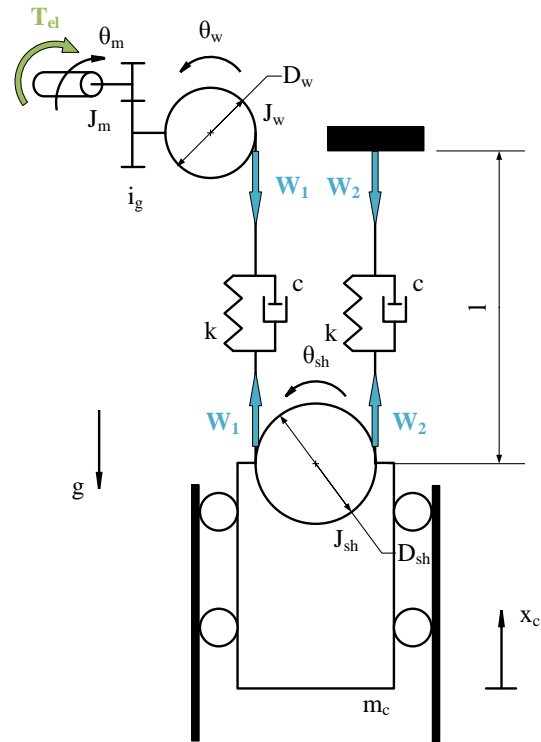
Figure 4: *Simplified representation of the gripper arm as the combined mass system.*

wire [N/m], c - damping of the wire [Ns/m]. The following equations describe wire elongations ($x_c(t)$ - the combined payload displacement [m], θ_w - rotational displacement of a winch [rad], θ_{sh} - rotational displacement of a sheave [rad]):

$$\delta_1 = \theta_w \cdot \frac{D_w}{2} + \theta_{sh} \cdot \frac{D_{sh}}{2} - x_c(t) \qquad (3)$$

$$\delta_2 = -\theta_{sh} \cdot \frac{D_{sh}}{2} - x_c(t) \qquad (4)$$

and wire elongation rates:

$$\dot{\delta}_1 = \dot{\theta}_w \cdot \frac{D_w}{2} + \dot{\theta}_{sh} \cdot \frac{D_{sh}}{2} - \dot{x}_c(t) \qquad (5)$$

$$\dot{\delta}_2 = -\dot{\theta}_{sh} \cdot \frac{D_{sh}}{2} - \dot{x}_c(t). \qquad (6)$$

What is more, since we do not model the wire compression, Equations 3 and 4 are valid only for $\delta_{1,2} \geq 0$. For $\delta_{1,2} < 0$ they become 0. Stiffness of the wire is determined by applying the following relationship (l - length of one wire segment [m], A_{eff} - effective cross-sectional area of the wire [m^2], E - Young's modulus [Pa]):

$$k = \frac{E \cdot A_{eff}}{l}. \tag{7}$$

According to [17], damping of the wire c is assumed to be equal to $c = 0.1 \cdot k$.

Winch and Sheave

Since the winch is fixed to the rig structure, it experiences no acceleration with respect to the overall system. Therefore, the equilibrium equation for the winch becomes:

$$N_w - G_w - W_1 = 0 \tag{8}$$

where N_w - reaction force of winch [N], $G_w = m_w \cdot g$ - gravity force of winch [N]. The sheave is connected to the combined mass, hence it moves together with it having its acceleration $\ddot{x}_c$. Therefore, the equilibrium equation for the sheave is given by:

$$-N_{sh} - G_{sh} + W_1 + W_2 = m_{sh}\ddot{x}_c \tag{9}$$

where: N_{sh} - reaction force of sheave $[N]$, $G_{sh} = m_{sh} \cdot g$ - gravity force of sheave [N]. To model the friction force between the bearing and pin of the sheave / winch, a simple Coulomb friction model is applied according to [17] (F_f - friction force [N], N - normal force [N]):

$$F_f = \mu \cdot N. \tag{10}$$

By substituting Equations 8 and 9 into Equation 10 we obtain the formula for the friction force on the sheave and winch, respectively (μ_{pin} - friction coefficient between bearing and pin):

$$F_{f,sh} = \mu_{pin} |(-G_{sh} + W_1 + W_2 - m_{sh}\ddot{x}_c)| \tag{11}$$

$$F_{f,w} = \mu_{pin} |(G_w + W_1)|. \tag{12}$$

It is assumed that the friction coefficient is the same for both sheave and winch. To mitigate the computational effort of the software during the detection of the change of direction of sheaves rotation, instead of using a typical *signum* function, the following piecewise $S(\dot{\theta})$ function was applied in the friction model:

$$S(\dot{\theta}_{w,sh}) = \begin{cases} -1 & \text{if } \dot{\theta}_{w,sh} < -0.01 \\ \dot{\theta}_{w,sh}/0.01 & \text{if } -0.01 \leq \dot{\theta}_{w,sh} \leq 0.01 \\ 1 & \text{if } \dot{\theta}_{w,sh} > 0.01. \end{cases} \tag{13}$$

Hence, the equation of motion (EOM) for the sheave becomes (D_{sh} - sheave diameter, $D_{pin,sh}$ - pin diameter of sheave):

$$J_{sh} \cdot \ddot{\theta}_{sh} = \frac{D_{sh}}{2} \cdot (W_2 - W_1) - F_{f,sh} \cdot \frac{D_{pin,sh}}{2} \cdot S(\dot{\theta}_{sh}). \tag{14}$$

In order to take into account the external torque (T_{el}) supplied from the electrical system, winch inertia J_w is combined with motor inertia J_m. There is a gearbox between motor and winch (i_g - gear ratio), therefore, the EOM for this system is given by (θ_m - angular position of rotor, D_w - winch diameter, $D_{pin,w}$ - pin diameter of winch):

$$(2J_m + J_w i_g^2)\ddot{\theta}_m = T_{el} + i_g \frac{D_w}{2} W_1 - i_g F_{f,w} \frac{D_{pin,w}}{2} S(\dot{\theta}_w). \tag{15}$$

There are two motors connected to the gearbox shaft in the real system, therefore the rotor inertia is doubled in the above equation and the electric torque is the sum of torques delivered by each motor $T_{el} = T_{m1} + T_{m2}$.

Combined Mass

Combined mass is composed of masses of particular components of the gripper arm structure (including sheave) and the payload being handled (i.e. mass of the pipe). Its EOM is expressed as:

$$W_1 + W_2 - G_c - F_{f,c} = m_c \ddot{x}_c \tag{16}$$

where G_c is the weight of the combined mass and $F_{f,c}$ is the friction force acting on the combined mass along its vertical motion. It is related to the fact that rollers on the upper and lower dollies experience friction while moving inside the guide rails. According to [17], a Coulomb friction model is selected to represent this phenomenon. It was identified that in some cases Equation 13 does not provide for smooth enough detection of combined mass velocity direction switching. Therefore, it was decided to use more sophisticated *atan* function for this purpose. Finally, the vertical friction force acting on the combined mass becomes:

$$F_{f,c} = \begin{cases} F_{C,neg} \cdot \text{atan}(k \cdot \dot{x}_c)/(\pi/2) & \text{if } \dot{x}_c \leq 0 \\ F_{C,pos} \cdot \text{atan}(k \cdot \dot{x}_c)/(\pi/2) & \text{if } \dot{x}_c > 0. \end{cases} \tag{17}$$

Factor *k* adjusts the slope of the *atan* function in the vicinity of zero speed so, in other words, it decides about how fast the friction model responds to changes in velocity direction. A comparative overview of the switching detection functions described by Equations 13 and 17 is illustrated in Figure 5.
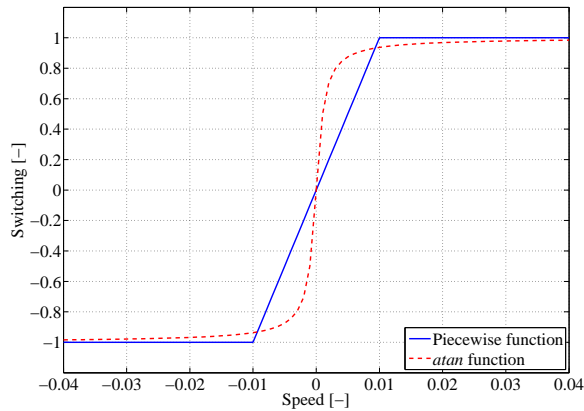

Figure 5: *Velocity switching detection functions.*

SIMULATION RESULTS
Reference Data Acquisition

In the full-scale Vertical Pipe Racker, there are two motors in the gripper arm coupled to one shaft that is actuating the winch through the gearbox (i.e. motors rotate with the same speed). A set of reference electric motors torques measured on a real world machine is illustrated in Figure 6. Both torque and speed profiles shown in this paper are normalized with respect to nominal torque T_n and nominal speed n_n of the motors used in the real machine. They have been recorded during regular machine operation when a pipe has been lowered and hoisted to certain positions. Hydraulic cylinders supporting the upper dolly have been immobilized during this sequence. The analyzed machine is controlled by a closed-loop control system: a reference speed profile is provided as a set point and the resulting torque profiles are recorded. These torque profiles are used in the current work to validate the simulation model of the gripper arm. The modeled system is excited with the real-world electromagnetic torque and the obtained velocity of motors is subsequently compared with the reference velocity recorded on a full-scale machine in order to assess model accuracy.
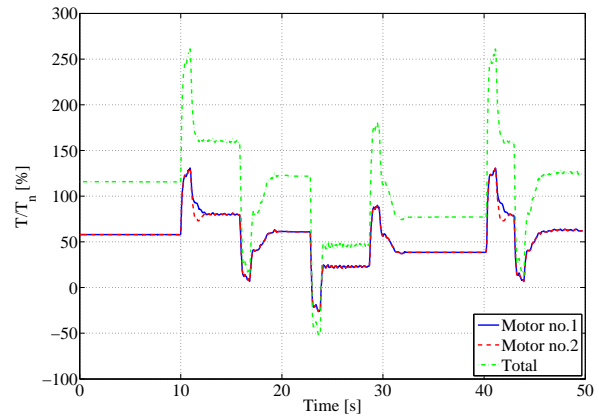
Figure 6: *Reference torque profiles measured on real world gripper arm winch motors.*

Validation of the Gripper Arm Models

Two friction parameters $F_{C,neg}$ and $F_{C,pos}$ are identified in an iterative process. Using Equation 16 it is possible to find the friction force profile $F_{f,c}$ that will fit to the reference electromagnetic torque T_{el} given the total system mass and wire properties. This operation is repeated a few times by adjusting values of $F_{C,neg}$ and $F_{C,pos}$ until the satisfactory system response is achieved. Since the obtained Coulomb friction model is not symmetric, it allows to capture the overall behavior of the gripper arm system depending if it is being hoisted or lowered by the winch. The overall shape of the friction model is depicted in Figure 7. The friction force is normalized with respect to the gravity force acting on the combined mass system.
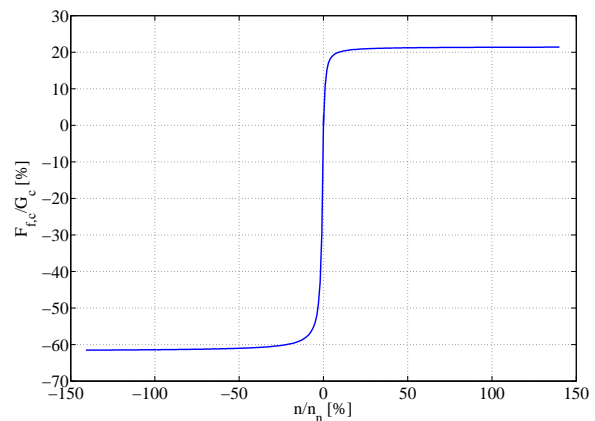
Figure 7: *Modified Coulomb friction model.*

Performed simulations involve validation of both the

multi-body model of the gripper arm composed of a set of rigid bodies and joints as well as the analytical model represented by the combined mass and winch system. The total reference torque acquired from the real world machine is provided to both models as the input electromagnetic torque T_{el}. It is the sum of the torque signals measured on both drives of the drivetrain. The resulting velocity of the motors common shaft is then recorded in both simulations. The simulated velocity is compared with the reference velocity giving the basis to assess models accuracy. Results of this operation are shown in Figure 8.

Figure 8: *Simulation results - velocity profiles.*

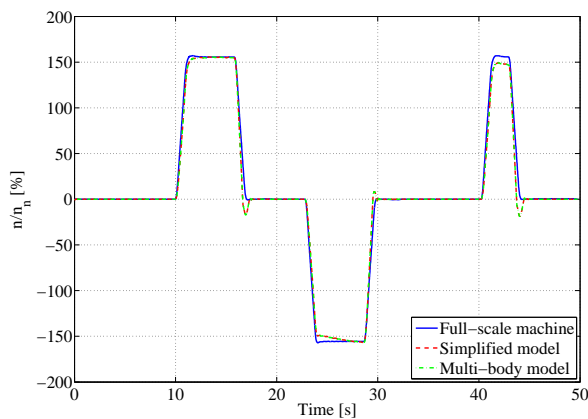Figure 8 shows that both simulated models yield results that closely correspond to the reference velocity profile. Root-mean-squared error (RMSE) for reference and simulated velocities is equal to an acceptable low value of $RMSE = 7.49$ %. The analytical model is also implemented in a virtual simulation software making it possible to compare computational effort needed by a solver to run the simulation. Both multi-body and analytical models are simulated on a commercial PC: Intel® Core™ $i7 - 3770$ CPU @ $3.4GHz$ and $8GB$ RAM. The solver used is BDF (Backward Differentiation Formula) with minimum calculation step size being equal to $dtMin = 1e - 10$ [s]. Time intervals needed by the computer to finish both simulations (each lasting 49.76 [s]) are shown in Table 1.

Multi-body model	Analytical model
91.53 [s]	3.46 [s]

Table 1: Simulation time required by the solver to finalize computations

From Table 1 it follows that the analytical model could be run approximately 26 times faster than the multi-body model. Simultaneously, simulation accuracy remains at the same level as for the multibody (i.e. more detailed) model - see Figure 8.

CONCLUSION

The current paper presents a case study of modeling and simulation of an offshore machine. Contrary to prior works, this study is specifically devoted to vertical pipe handling machine and identification of friction phenomenon appearing in this system. Comparative analysis clearly shows that both analytical and multi-body models of the considered equipment yield simulation results that stay in close accordance with the reference, real world measurements. In addition, it is verified that the simplified, analytical model runs significantly faster on a commercial PC than its more detailed, multi-body equivalent. The difference is so remarkable that the analytical model could easily be used in real-time testing of this equipment allowing to evaluate its control system before commissioning. This has a huge impact on design efficiency and project management, facilitating communication of different teams of engineers at early stages of product development.

It is expected that in the future these types of models could also find different applications. One example is fault detection and diagnostics. Having a validated model of a machine that operates offshore on a full scale drilling rig will allow to detect unexpected deviations in its performance. This will help to identify sources of measurements discrepancies between a reliable model and a real machine and consequently improve maintenance and service tasks. It will be beneficial to extend the current study into additional areas as well. Including a control system in the virtual model will help to improve its performance and robustness by allowing to spend more time on testing different control algorithms. Additionally, it is advisable to use smooth velocity profiles (instead of trapezoidal ones) as reference signals to a controller. It will decrease peaks in torque profiles resulting in a more stable operation of the machine. Finally, testing the established simulation models against different sets or real world measurements (e.g. various payload masses) will result in more robust models being able to yield accurate results under different load conditions.

REFERENCES

[1] Harsem Ø, Eide A, Heen K. *Factors influencing future oil and gas prospects in the Arctic.* Energy Policy 2011;39(12):8037-8045.

[2] Risholt R, Heggland TM, Pimentel L. *Vertical Pipe Racker System - Functional Description.* MHWirth, Tech. Rep. 170859-R-BC75-SA05-0100, 2014.

[3] Stamnes ØN, Kaasa G-O, Aamo OM. *Adaptive estimation of downhole pressure for Managed Pressure Drilling operations.* IEEE International Symposium on Intelligent Control 2011:989-995.

[4] Nikoofard A, Johansen TA, Mahdianfar H, Pavlov A. *Constrained MPC design for heave disturbance attenuation in offshore drilling systems.* MTS/IEEE OCEANS 2013:1-7.

[5] Peng Y, Yancong L, Yongjun S, Guande L. *Optimum Piping Design on Offshore Platform Based on Improved Adaptive Genetic Algorithm.* WASE International Conference on Information Engineering 2010:50-53.

[6] Rahimi M, Rausand M, Wu S. *Reliability prediction of offshore oil and gas equipment for use in an arctic environment.* International Conference on Quality, Reliability, Risk, Maintenance, and Safety Engineering 2011:81-86.

[7] Bak MK, Hansen MR, Nordhammer PA. *Virtual Prototyping - Model of Offshore Knuckle Boom Crane.* 24th International Congress on Condition Monitoring and Diagnostics Engineering Management 2011.

[8] Runge J, Oswald BR. *Modelling of a controlled doubly fed induction machine for the use in offshore wind power plants.* 39th International Universities Power Engineering Conference 2004:1155-1159.

[9] Mahato SN, Singh SP, Sharma MP. *Direct vector control of stand-alone self-excited induction generator.* Joint International Conference on Power Electronics, Drives and Energy Systems 2010:1-6.

[10] Pereira LFA, Haffner JF, Hemerly EM, Grundling HA. *Direct vector control for a servopositioner using an alternative rotor flux estimation algorithm.* IEEE 24th Annual Conference of the Industrial Electronics Society 1988:1603-1608.

[11] Zhang S, Norum L, Nilssen R. *Oscillatory motion application of tubular linear permanent magnet machine.* 35th Annual Conference of IEEE Industrial Electronics 2009:1223-1227.

[12] Gallant TA, Andrews KM. *Large cage induction motors for offshore machinery drive applications.* Petroleum and Chemical Industry Conference, 2006:1155-1159.

[13] Haas D, Painter FD, Wilkinson M. *Root-cause analysis of simultaneous faults on an offshore FPSO vessel.* IEEE Transactions on Industry Applications, 2012;20(2):1543-155.

[14] Corneliu CM, Valentin D, Valentin S. *Optimal location for underwater data collection sensor network nodes creating multi-purpose "Safe-Nets" around offshore exploration areas.* 17th International Conference on System Theory, Control and Computing (ICSTCC) 2013:601-606.

[15] Murrin D, Molloy S, Qiu W, Bose N, Ordonez M. *Large-scale experiments of a marine riser.* Oceans 2008:1-6.

[16] Wongruean M, Lursinsap C, Sanguansintukul S, Sinapiromsaran K. *Mixed Integer Linear Programming model for workload leveling on offshore platform of petroleum company.* International Conference on Intelligent Computation Technology and Automation 2010:683-686.

[17] Walid AA, Gu P, Hansen MR, Hovland G, Iskandarani Y. *Modeling and simulation of an active heave compensated draw-works.* 4th WSEAS International Conference on Manufacturing Engineering, Quality and Production Systems 2011:291-296.

MODELING AND SIMULATION OF SHORT CIRCUIT CURRENT AND TRV TO DEVELOP A SYNTHETIC TEST SYSTEM FOR CIRCUIT BREAKERS

Kourosh Mousavi Takami[1]   **Erik Dahlquist**

Mälardalen University, IST Dep., Box 883, SE 721 23, Vasteras Sweden

 Abstract: A parallel injection of short circuit current and transient voltage to medium and high voltage circuit   breaker (CB) by a synthetic model is studied. Transient recovery voltage is created by a capacitor bank and is applied to CB. Also short circuit current is supplied by a 20/0.765 Kv short circuit transformer. Texas DSP is used as controller and programmed in code composer.

To test of circuit breakers by synthetic test equipments, an accurate control system can satisfy the test criterion. An optical triggered spark gap has been used to interrupt short circuit current and to initialize of transient recovery voltage (TRV) that is applied across the contacts of circuit breaker.

Modeled results are verified by a laboratory based synthetic test system. Test object CB is a 24 Kv, 25 KA with vacuum type chamber.

To find a desired sequence to open/close of backup- test object and auxiliary circuit breakers within appropriate time to inject of recovery voltage is main goal of the presented paper. Modeling and simulation has been done in MATLAB software. Test procedure has been done under IEC 62271-100, 62271-101.

Key words: Synthetic test, Medium voltage circuit breaker, Short circuit current, TRV.

I.   Introduction

The circuit breaker used in the power network is close in the normal situation but it must be opened to protect network if there are abnormal event.

So in short-circuit occurrence, the circuit breaker will clear the high current by interruption and make re-closing duty to other sequences.

---

[1] Coressponding author, k. takami@aol.com

IEC and ANSI/IEEE standards define circuit-breakers short-circuit tests (Isc) [1], [2]. IEEE_ C37 and IEC 62271 electrical standards manage the ratings, performance, features, and testing of circuit breakers.

At the test, short-circuit interrupting current with the full rated voltage is generally not possible in direct tests circuits where one source delivers the required current under the specified voltage.

Synthetic circuits where current and voltage are delivered by separate sources are designed to supply a short circuit current and recovery voltage. It is used for terminal fault interruption and are described in ANSI/IEEE guide C37-081 and IEC guide 427 [3], [4].

Single-phase tests can reveal the interruption of all three phases in a single operation and the method is applied for testing. Although to reproduce the real conditions of a three-phase interruption, it cannot be enough.

Standards oblige that interruption of 100% of Isc be prepared by a symmetrical current as T100s or TD4 and an asymmetrical current as T100a or TD5. Asymmetrical current is summation of an ac and a dc component declining with a time constant of 45 ms (X/R=58 at 50 Hz), dc component is over 20% [5]-[7].

The aim of this article is to present a test procedure for single-phase synthetic testing in a different scenario rather than other models.

Different researchers and organizations studied around the synthetic test. Denis Dufournet and Georges Montillet [8] claimed to present a procedure for three-phase synthetic testing which can properly test the circuit-breaker at a reasonable cost, i.e., a number of tests using a limited number of circuit-breaker specimen for the entire series of type tests. They deal around the theoretical calculations and they didn't suggest a practical laboratory test model.

Jung-Hyeon Ryu et. Al [9] studied on the symmetrical current to give the maximum prearcing energy and asymmetrical current to give the maximum electro-dynamic force. They expressed their circuit used minimum number of voltage circuit, measuring device for current and voltage, plasma making switch and auxiliary breaker. The lack of the job was that it had no special consideration for the test of dead tank GCB intended for GIS (gas insulated switchgear).

L. van der Sluis et al studied on the influence of the arc voltage in system test circuits [9]. different arc voltage waveforms and KEMA arc models are used to study the stress of the direct SLF (short line fault) test circuit and the synthetic SLF test circuit on the

TB (test breaker). For the synthetic test circuit the total arc energy input in the TB is less than the direct test circuit, but just before the current zero the dI /dt and subsequently the arc energy input in the TB is higher. It is demonstrated that the arc-circuit interaction plays an important role for the TB to clear the fault. For SF6 breakers with an arc voltage with a significant extinguishing peak, the voltage injection synthetic test circuit produces an overstress for the TB. The authors studied on the different effects of energy at arcing time in direct and synthetic tests.

Author in the presented paper tried to introduce a model that can be competitive with direct test method, applied energy during short circuit to be high, test system to be low cost- reliable and low time.

II.   Single-phase synthetic test procedure

According to figure 1, a synthetic test circuit has two different sources of current and voltage.

Before the test operation, arcing time, or period between contact separation and arc extinction at current zero, is defined. The arc is made by the high short circuit current source and at the chosen current zero time the recovery voltage is affected by the voltage source.
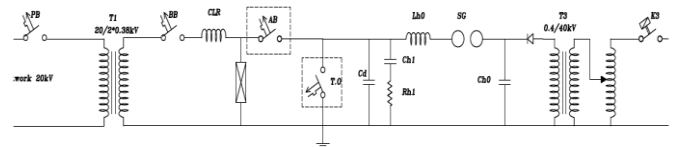
Figure 1. A synthetic test circuit presented by JDEVS.

An important message in the test is related to the implementation of recovery voltage over the arc. At the symmetrical current interruption (T100 or TD4), the characterization is slightly easy. As current zeros are showing every 60 electrical degree. The imposing time for recovery voltage has been defined by IEC standard. It is in final quarter of last half cycle. SABER software is usually used to simulate of short-circuit

III.   Circuit equipments technical specification
A.   Test object CB spec.
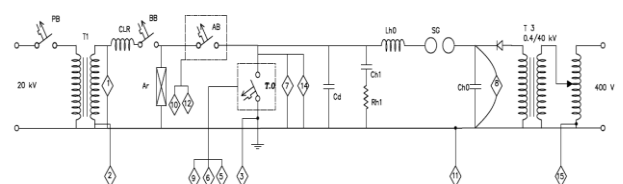
Figure 2. Sampling device position
Table 1. TO CB Spec.

Manufacturer	Parss Switch Co
Type	VD4 P
Nominal Voltage (kV)	24
Nominal Current (A)	2500
Frequency (Hz)	50
RMS Breaking Current (kA)	25
RMS Making Current (kA)	65
Operating Voltage (kV)	20
Operating sequence	O-0.3sec-CO-3min-CO
S.N	230453

B. CB contact separation timing determination

In no load condition timing process has been done, see table 3-4. When current is flowing in test object (TO) CB contacts, DSP controller send an open signal to CB trip coil and the interruption time is distinguished and measured. The time interval between trip signal sending and interruption time declared and calculated as contacts separation time.

Table 2. Contact separation (ms) for TO CB

| Item	Contact Separation (ms)	Opening Coil Voltage (V)
1	44.155	125
2	43.950	125
3	44.110	125
Average	44.070	125

Table 3. Contact separation (ms) for AB CB

| Item	Contact Separation (ms)	Opening Coil Voltage (V)
1	46.410	125
2	46.700	125
3	46.450	125
Average	46.520	125

IV. Simulation

To more investigation and to ensure of calculations in voltage and current of synthetic unit, different simulation has been done. MATLAB, ETAP, CYME,etc is used to modeling and simulation of process. Due to large wide domain of simulations, the following items listed and simulated.

- Simulation for T10, T30, T60 and T100 in order to calculation of parameters cited in IEC 62271 and IEC 62271-101 with a reasonable tolerance.
- Different arcing models simulation.
- Arc combined models Mayer+Casie simulation.
- Simulation of arc voltage effect on the half last cycle of current in vacuum and SF6 CB.
- Close direct asymmetrical (Cdasym) test simulation and synchronous CB fire angle assessment for asymmetrical current.

- Symmetrical (Cssym) test simulation and synchronous CB fire angle assessment for symmetrical current.
- Simulation for T10, T30, T60 and T100 interruption test.
- Simulation to define CLR to perform T10, T30, T60, T100 and closing tests.
- DC components determination simulation (with respect to switching time)
- Charging circuits of capacitors C_{h0} simulation with respect to charge time, charge current and other parameters.
- R_{h1} Resistance simulation with respect to voltage and discharged energy.
- Simulation and evaluation of current and voltage on the all of elements.
- Resistance of L_{h1} reactance simulation with considering to voltage drop regulation.
- 20Kv feeder simulation to choose a proper feeding transformer.
- Short circuit level and X/R of network simulation.
- The effect of number of network parallel transformer simulation.
- The effect of laboratory distance with feeding substation on the test by simulation.
- Effect of short circuit current power of current injection transformer and X/R ratio on the test by simulation.
- Simulation of surge arrester performance when malfunction operation in AB occurs.
- Simulation of test unit and network in order to set of relays and fuses.

A. Transient recovery voltage simulation:

Simulation performed for a 36 Kv, 31.5 KA CB in T100 test. The results for injected current by synthetic circuit and TRV voltage are shown in the figures 3.
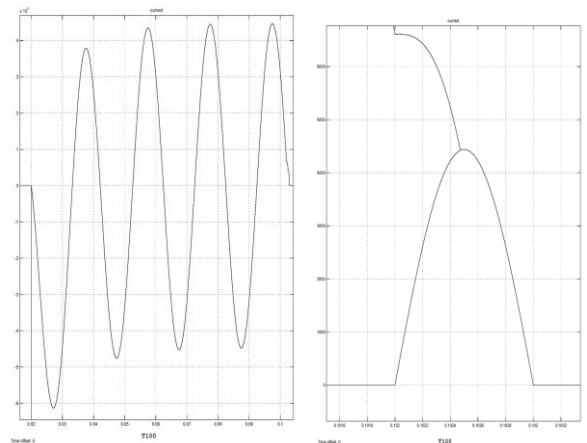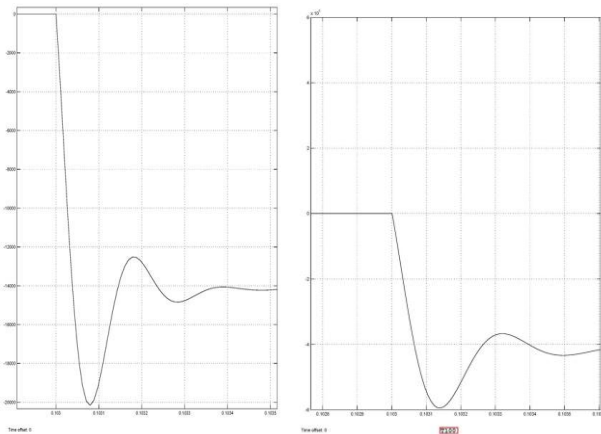
Figure 3. TRV trace by simulation T100 (100% current) results

B. Results and discussion for simulation application

Parameters such as Uc, t_3, td, dU/dt resulted by simulation are shown in table 4, Fig 17. The numen cultures are found in IEC 62271 and are according with IEC 62271-100, 4.102. Table 5 shows the parameters in IEC 62271-100. Table 6 shows a method to regulate of parameters to reach the ranges.

Table 4. Simulation results of parameters according to IEC 62271-100.

Ur kV	Ir kA	Test duty	Uc kV	t3 µs	td µs	dU/dt kV/µs	Uh0 kV	Ch0 µF	Lh1 mH	Rh 1Ω	Ch1 µF	Chd nF
36	31.5	T100	62.3	106.1	15.9	0.59	42.7	32.2	3.15	41	0.857	95.2
36	18.9	T60	66.4	44	6.6	1.51	45	19.3	5.25	171	0.089	9.9
36	9.45	T30	66.1	22.6	3.4	2.93	43.5	9.6	10.5	684	0.012	1.3
36	3.15	T10	66.6	21.4	3.2	3.09	38.5	3.2	31.5	2052	0.003	0.4
24	31.5	T100	41.3	86.4	13	0.48	28.3	48.2	2.1	34	0.832	2.6
24	18.9	T60	44.2	38.7	5.8	1.14	30.5	28.9	3.5	138	0.095	10.6
24	9.45	T30	45.3	19.5	2.9	2.33	30.4	14.5	7	552	0.01	1.1
24	3.15	T10	44.1	16.9	2.5	2.6	26.1	4.8	21	1656	0.003	0.4

Table 5. Parameters values in the IEC62271- 100

Urated kV	Irated kA	Test duty	Uc kV	t3 µs	td µs	dU/dt kV/µs
24	31.5	T100	41	87	13.1	0.47
24	18.9	T60	44	38	5.7	1.16
24	9.45	T30	44	19	2.9	2.32
24	3.15	T10	44	19	2.9	2.32
36	31.5	T100	62	109	16.4	0.57
36	18.9	T60	66	46	6.9	1.43
36	9.45	T30	66	23	3.5	2.87
36	3.15	T10	66	23	3.5	2.87

Table 6. Effect of each element on parameter such as: dU/dt, TRV, t3.

dU/dt		TRV	T3	
Low sensitive	-	+	+	C_{h0}
Low sensitive	-	+	+	L_{h1} ↑
High sensitive	--	-		C_{h1} ↑
	Fix	-	-	R_{h1} ↑
Very low sensitive	+	+	+	C_d ↑↑↑

With considering to the results, the best way to achieve an allowed range of tolerance for t_d, TRV, du/dt are to change capacitance of ch1 and charge voltage of C_{h0}. Other elements rest doesn't change. See table 6.

V. Test
A. Test procedure
- Timing calculation for TO and AB and so spark gap when the current is in a same polarity with current injected by voltage circuit.
- Few cycle delay to eliminate of asymmetrical current
- Zero crossing detection
- Closing pulse to TO and AB according to zero crossing
- Trigger pulse imposing on SG in ±30-50µs
- Closing pulse to BB CB after 200 ms.

The full test procedure is accessable in IEEE C37.013.

B. T60 (60% current) synthetic test
Table 5 shows that the parameters extracted by simulated results have a good fitness with IEC 62271-100, table 8. The values are used to the main model and results are shown in the figures 4.

Table 7. Values of elements for T60 test.

	Ur kV	Test duty	Uh0 kV	Ch0 µF	Lh0 mH	Rh1 Ω	Ch1 µF	Cd nF	CLR µH	Current source voltage
Calculated Values	24	T60	31.4	23	4.41	174	0.076	8.4	60	760
Test (1)	24	T60	30.5	23	4.4	192	0.071	8	60	760
Test (2)	---	---	---	---	---	---	---	---	---	
Test (3)	---	---	---	---	---	---	---	---	---	

Table 8. Results for parameters in T60

Item	Ur kV	Ir kA	Test duty	Isym kArms ±10%	IL^{2}k A(rms) <-10%	TRV kV +10%	t$_3$ µs	td µs ±20%	dU/dt kV/µs +15%	Description	Test Result
IEC 62271-100	24	25	T60	15		44	38	6	1.16		
Test (1)	24	25	T60	15.6	<10%	47.4	40	6.3	1.18	*	passed

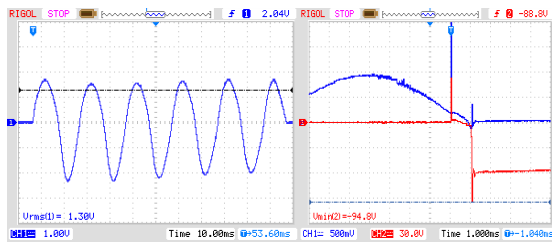| Item	Ur kV	Ir kA	Test duty	Isym kA +5%	Current final loop <-10%	TRV kV +10%	t$_3$ µs	td µs ±20%	dU/dt kV/µs +15%	Description	Test Result
IEC 62271	24	25	T100	25		41	87	13.1	0.47		
Test (1)	24	25	T100	24.7	<-10%	49.2	---	---	---	*	Need tuning
Test (2)	24	25	T100	24.7	<-10%	39	---	---	---	**	Need tuning
Test (3)	24	25	T100	24.7	<-10%	39	---	---	---	***	Need tuning
Test (4)	24	25	T100	24.7	<-10%	49.2	---	---	---	****	Not passed

Fig 4. TRV Voltage and current in TO CB at the last half cycle with sampler no 14 with turn ratio of 500 Fig 6. Current through TO CB, sampling by CT 6000/1.

Short circuit current imposed to the TO CB in 6 cycles. It has a large duration and can damage to the network, in repetitive tests. TRV voltage shows a good trace but current shows a disturbance in the end of cycle. It may relate to the sampling sensors. Totally figures show a successive test for T60.

C. T100 test

The simulation results led to parameters determination. Using the parameters, test performed and the results clustered in the tables 9-10.

Table 9. Values of elements for T100 test.

	Ur kV	Test duty	Uh0 kV	Ch0 µF	Lh0 mH	Rh1 Ω	Ch1 µF	Cd nF	CLR µH	Current source voltage V
Calculated Values	24	T100	29.4	38.3	2.65	42	0.661	73.4	15	760
Test (1)	24	T100	29	38.3	2.6	42	0.638	68	20	760
Test (2)	24	T100	29	38.3	2.6	42	0.638	68	20	760
Test (3)	24	T100	29	38.3	2.6	42	0.638	68	20	760
Test (4)	24	T100	29	38.3	2.6	42	0.638	68	20	760

Table 10. Results for parameters in T100

[2] **Current final loop**

*. AB_Open_time = 46520, SG_Delay_trig_time = 1300,, Dealay_AB_relative_TO=2000, TO_Open_time = 44072

**. Dealay_AB_relative_TO=2000, TO_Open_time = 44072, AB_Open_time = 46520, SG_Delay_trig_time = 2000

***. Dealay_AB_relative_TO=500, TO_Open_time = 44072, AB_Open_time = 46520, SG_Delay_trig_time = 2000

****. Dealay_AB_relative_TO= -500, TO_Open_time = 44072, AB_Open_time = 46520, SG_Delay_trig_time = 2000
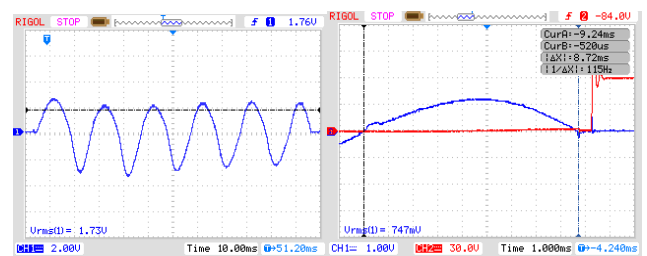

Fig 5. Test 1:TRV Voltage and current in TO CB at the last half cycle Fig 6. Current through TO CB, sampling
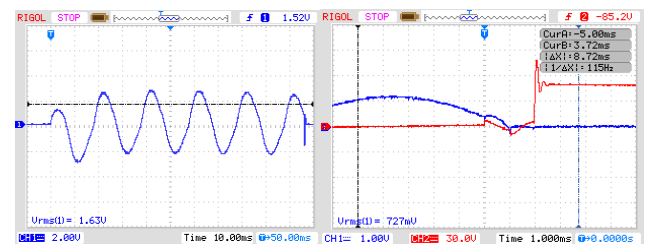

Fig 7. Test 2:TRV Voltage and current in TO CB at the last half cycle Fig 8. Current through TO CB, sampling
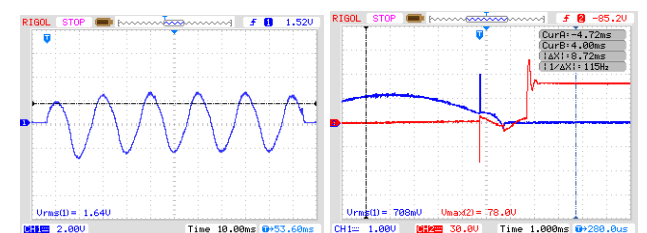

Fig 9. Test 3:TRV Voltage and current in TO CB at the last half cycle Fig 10. Current through TO CB, sampling
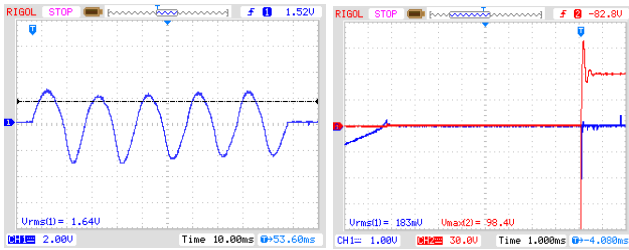
Fig 11. Test 4:TRV Voltage and current in TO CB at the last half
cycle Fig 12. Current through TO CB, sampling

Figures 5-6 for test no 1 show that last half cycle duration decrease from 10 ms to 8.72. Then TRV voltage applied to TO in about 700 ms later. For this reason, delay time for trigger surge gap tuned and test repeated. The results of second test showed in figures 7 and 8. According to the figure, with voltage injection in a correct time, TRV voltage appeared after a full cycle current with 500 Hz. The phenomena can be resulted by a restrike in AB CB that causes to flow current by voltage circuit to AB CB.

Test 3 shows in figures 9-10. Delay time to open AB CB decrease from 2000 μs to 500μs. it can help to make a better condition for AB and TO CB. Because arc time and contacts distances are increased rather than to test 2. Also, restrike in AB can be expected to be cleared.

But achieved results that showed in figures 11-12 demonstrate again a restrike in AB CB. It means AB CB cannot tolerate source TRV voltage.

Delay for opening time of AB CB retuned where AB open sooner than TO CB in Test 4. In this case, AB CB opened sooner than TO with 500 μs. Meanwhile, figures 11-12 show that AB opened again sooner and it is not correct.

Then T100 can be successive if AB CB changes by a 31.5 KA ones. It can resolve restrike problem and can allow the first To be opened and then AB remove the main network connection with test circuit.

A test with more DC component performed and results show in figures 13-14. It seems DC components is more than 20% and the current cab be assumed an asymmetrical current. The change in current have no a significant difference by

symmetrical current in the last quarter of current in the final cycle.
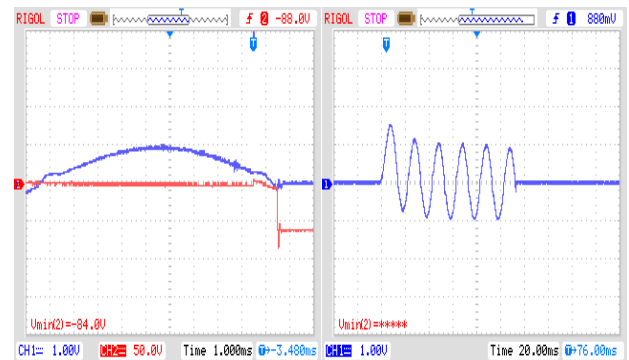

Fig 13. Test 5:TRV Voltage and current in TO CB at the last half
cycle Fig 14. Current through TO CB, sampling

VI.   Conclusion

A synthetic test rearranged and test performed. Results show the voltage and current circuit are correct. The main problem to test by short circuit transformer is related to network. Most of electricity utilities don't allow to test by this type transformer, because of that the repetitive high currents damages to network and can be led to operate of over current relays.

In other hand AB circuit breaker have to be one grade higher than TO. It means to test a 25 KA CB, AB must be 31.5 KA. It may can solve the problem by restrike.

In the presented paper, authors simulated the model and parameters extracted by simulation. The simulated results had a good convergence by IEC values. Also, test has been done by the resulted simulation parameters.

VII.   References

[1] , IEC Standard 56 or 60056 (1987).
[2] , ANSI/IEEE Standard C37-09 (1979).
[3] Guide for Synthetic Fault Testing of AC High-Voltage Circuit-Breakers Rated on a Symmetrical Current Basis, ANSI/IEEE C37-081. [4] , IEC Standard 427 (1989-10).
[5] , IEC Technical Report 1633 (1995).
[6] Supplement to IEEE Guide for Synthetic Fault Testing of AC High-Voltage Circuit-Breakers Rated on a Symmetrical Current Basis, IEEE Standard C37-08la-1997.

[7] High voltage circuit breaker standards—comparative guide, Stephen M. Cary, May 2013, www.eaton.com/

[8] Denis Dufournet et al, Three-Phase Short Circuit Testing of High-Voltage Circuit Breakers Using Synthetic Circuits, IEEE transaction on power delivery, VOL. 15, NO. 1, JANUARY 2000, pp 142/148

[9] Jung-Hyeon Ryu, Ike-Sun Choi and Kern-Joong Kim, Three-phase Making Test Method for Common Type Circuit Breaker, Journal of Electrical Engineering & Technology Vol. 7, No. 5, pp. 778~783, 2012, http://dx.doi.org/10.5370/JEET.2012.7.5.

[10] L. van der Sluis and B.L. Sheng, the influence of the arc voltage in synthetic test circuit, IEEE Transactions on Power Delivery, Vol. 10, No. 1, January 1995. Pp 214-220.

VIII. Acknowledgements

IX. Appendices

The following tables 11-14 and figure 15 show the equipment specifications.

Table 11. Current circuit spec.

No.	Detail	Equipment
1	$S_n = 3.15$ MVA $U_{1n} = 20$ kV $U_{2n}= 2 * 380$ V Uk% = 6 X/R > 10	Short Circuit Transformer (T1)
	$U_{rated} = 850$ V	Surge arrester to protect of Tr.
4	L =60μH $U_n = 1$ kV $I_{SC} = 31.5$ kA	Limiting current reactor LV (CLR)
1	$V_n = 24$ kV $I_n = 2500$ A $I_{sc}=25$ kA Type: VD4 S.N: **230453**	(AB) Auxiliary vacuum CB (Auxiliary Breaker)
1	$V_n = 24$ kV $I_n = 2500$ A $I_{sc}=25$ kA Type: VD4 S.N: **250321**	Vacuum CB (BB) (Back Up Breaker)
1	$V_n = 24$ kV $I_n = 2500$ A $I_{sc}=25$ kA Type: VP4 S.N: **250238**	Vacuum CB (TO) (Test Object)

Table 12. Voltage circuit spec.

Table 13. Control and monitoring equipment spec.

No.	Detail	Equipment	Row
93	4000nF	Main capacitor (Ch$_0$) 12kVAC± 10%	1
3	2000nF		
3	1000nF		
3	500nF		
3	250nF		
3	125nF		
1	40kV/30kVA	High voltage source(T$_3$)	٢
1	140 kV_DC	High voltage diode with resitance	3
1	400V /100 kVA	Auto transformer	٤
3	20 taps from: 0.65 ~ 25 (mH)	Reactor (Lh$_1$)	5
2	One 6 taps and one 5 taps capacitor	Capacitor (Ch1)	6
14	Resistances: 0.5 – 4096 Ω	Resitance (Rh1)	7
2	One 6 taps and one 5 taps capacitor	Capacitor (Ch$_d$)	8
1	In 3 range of voltage	Surge Gap (SG)	9
1	With delay: ±10 μs	Trigger Unit	10
33	20 kVDC	Pneumatic CB 20 kV	11
3	60 kVDC	Pneumatic CB 60 kV	12
---	Vinyl epoxy and ST 38	Structure	13

Table 14. Sampling devices spec

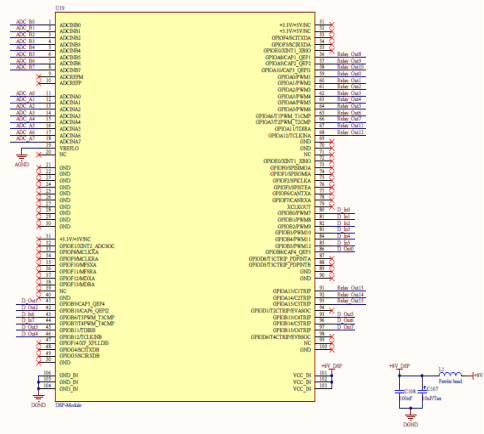| No.	Detail	Equipment
1	Texas Instruments DSP TMS320F2812, 150 MHz 16 ADC, 12 bit, 2 M/s Digital Input: 8 Digital Output:8 Output Relay :16	Microcontroller
1	Analogue Input:16 Analogue Output:16	Signal conditioning board
1	GUI MATLAB	Software
1	Fully shilded	Industrial Case
1	Intel	Computer
1	34 Unit Mazdak type	Control Panel
2	2 Channel, 60 MHz RIGOL	Oscilloscope

Figure 15. DSP model

Ratio	Attenuation ration for conditioning signal board	Attenuation ration for sampler	Sampling Spec.	Description	Signal No.
1200	1200	1	760V	Secondary voltage of T1	1
50000	2	25000	1500 A / 60 mV/ 40µΩ	Secondary current of T1	2
10000	2	5000	300 A / 60 mV / 200 µΩ	TO Current	3
50000	2	25000	1500 A / 60 mV/ 40µΩ		
12000	----	12000	CT 6000/1 / 5 VA & Burden=0.5 Ω		
2	2	-----	Current Shunt resistance 0.5Ω	Opening coil of TO	5
2	2	-----	Current Shunt resistance 0.5Ω	Closing coil of TO	6
120	2	60	2 MΩ	TO voltage (Arc voltage)	7
56000	200	280	280 MΩ	Ch_0 voltage	8
2	2	-----	0-5V Inductive sensor	Traveling TO	9
2	2	-----	Current Shunt resistance 0.5Ω	Closing AB	10
2500	2	1250	75 A / 60 mV / 800 µΩ	Synthetic current	11
2	2	-----	Current Shunt resistance 0.5Ω	Opening coil of AB	12
60000	120	500	100 pF,100kV	TO voltage (TRV)	14
333	2	166.7	10 A / 60 mV / 0.6 mΩ	Primery current of T3	15

Figure. 16. Test set up

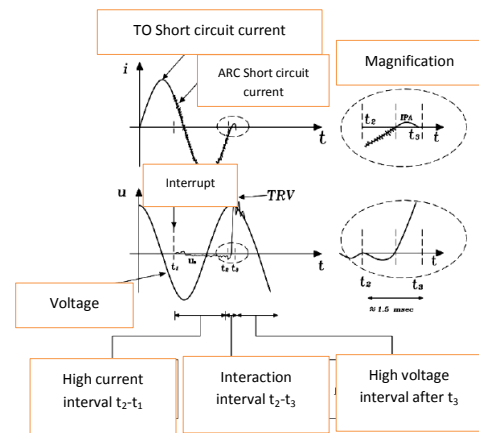

Figure. 17. Interruption sequences.

DC-GRID PHYSICAL MODELING PLATFORM DESIGN AND SIMULATION*

Minxiao Han[1], Xiaoling Su[1], Xiao Chen[1], Wenli Yan[1], Zhengkui Zhao[2]**
[1]State Key Laboratory of Alternate Electrical Power System with Renewable Energy Sources, North China Electric Power University
Beijing, China
[2]State Grid Qinghai Electric Power Maintenance Company,
Qinghai, China

ABSTRACT

This work develops a 6-terminal low voltage DC grid to study DC grid under various scenarios or its interaction with AC system. In order to have the same physical characteristics as the high voltage practical project, this paper presents an equal capacity ratio principle to help the parameter design in low voltage DC grid. All the parameters are selected according to the parameters of the high voltage reference system based on equal capacity ratio principle and optimized by simulation model. Simulation models of original VSC-MTDC and 6-terminal low voltage DC grid are built in PSCAD/EMTDC to validate the equal capacity ratio principle and the simulation results prove the equivalency. Based on the voltage margin control, a coordinated master-slave control method is proposed. The performance of the 6-terminal DC grid is studied under a variety of faults, simulation results proves that the DC bus voltage of the DC grid can be controlled steadily after faults.
Keywords: DC grid, equal capacity ratio principle, voltage coordinating control, simulation model

INTRODUCTION

Features like high reliability, efficiency, electromagnetic compatibility and without phase control requirement or reactive power problems turn DC grid into an interesting and promising technological option. The DC grid has superior characteristics compared with the AC grid. Each power generator connected to the DC grid can easily be operated cooperatively because it controls only the DC bus voltage. With the rapid development of distributed generation, energy storage systems (ESS) and power electronic loads, future power systems will be certainly more and more based on direct current (DC) architectures.

Adoption of a DC grid provide more operational flexibility, such as: increased control over DC and AC side power flow; active power could be exchanged while each ac network maintains its autonomy, hence decreasing the risk of AC fault propagation from one AC network to another; low transmission losses; and could optimize the performance of nearby AC lines in terms of active and reactive power flow [1-3]. Large offshore wind farms located far from their grid connection point will require HVDC to connect to shore to reduce cable losses and decrease reactive power requirements [4-5]. Moreover, a DC grid based on multi-terminal voltage-source converter multi-terminal direct current (DC) technology (VSC-MTDC) might offer significant advantages for the interconnection of the turbines within the wind farm [6-7]. Practical projects of DC grid have been

designed in the European countries to connect offshore wind farms to the AC grids.

Other practical efforts that develop DC grid can be seen in US, Japan, Korea and European countries through the efforts of conceptual design and demonstration projects for DC grid [8]. In order to study DC grid under various scenarios or its interaction with AC system, an acceptable solution is setting up a low voltage, small capacity DC grid in laboratory. Therefore, this paper designs a 6-terminal DC grid. The priority objective of the low voltage DC grid is having the same physical characteristics as the high voltage practical project. According to this requirement, this paper presents an equal capacity ratio principle to help the parameter design in low voltage DC grid. All the parameters are selected according to the parameters of the high voltage reference system based on equal capacity ratio principle and optimized by simulation model.

CONFIGURATION OF THE DC GRID

The low voltage DC grid in laboratory is designed at 500V with 6 terminals which is given in Figure 1. The capacity of each terminal is set at 10kW. Terminal 1, Terminal 2 and Terminal 3 are connected to the AC system. Terminal 4 is connected to energy storage system with bidirectional DC/DC as its interface. Wind power system or a PV system is integrated to the DC grid at Terminal 5. The last terminal is designed to provide electric power to AC load through VSC which using three-phase two-level topology.
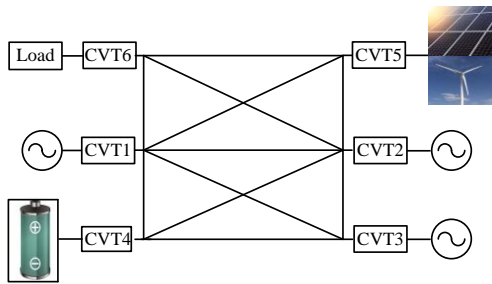

Figure 1:   Configuration of the DC grid

Figure 2 shows the voltage source converter applied in DC grid. u_s is AC power system voltage and u_c is output voltage of the converter at AC side. i is the converter current and i_s is the power system current.

u_{pcc1} is the voltage at PCC. u_{dc} is voltage of the converter at DC side and i_{dc} is the current inject to the DC grid by the converter. $i_{dc\,line}$ is the current flow through the DC line. P_S and Q_S is the power inject to the AC power system by the converter. P_C and Q_C is the power flow to the converter. R and L is the equivalent resistance and inductor between AC power system and the converter, therefore the transformer in figure 2 is ideal.
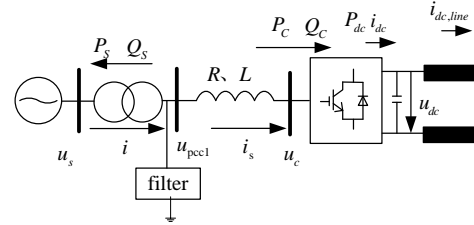

Figure 2:   The voltage source converter in DC grid

EQUAL CAPACITY RATIO PRINCIPLE

Most of the parameter design method is only suitable for high voltage with large capacity VSC-MTDC system. The priority objective of the low voltage DC grid is having the same physical characteristics as the high voltage practical project. Therefore, this paper uses equal capacity ratio principle to help the parameter design in low voltage DC grid. The parameters in low voltage DC grid is selected according to the high voltage reference system at first, and then optimized by simulation model.

$$\frac{\omega_1 C_1 U_{N1}^2}{S_{N1}} = \frac{\omega_2 C_2 U_{N2}^2}{S_{N2}} \tag{1}$$

$$\frac{\omega_1 L_1 I_{N1}^2}{S_{N1}} = \frac{\omega_2 L_2 I_{N2}^2}{S_{N2}} \tag{2}$$

Where S_{N1} and S_{N2} is rated capacity of each system, U_{N1} and U_{N2} is rated voltage of each system, C_1 and C_2 is capacitor in each system, L_1 and L_2 is inductor in each system, ω_1 and ω_2 is angular frequency of each system.

DC CAPACITOR

Parameter design

The reference system is a 10kW DC grid, its DC voltage is set at 800V, and the capacitor at DC side is 1020μF. By following equation (1)

$$\frac{\omega \cdot 1020 \cdot 800^2}{10k} = \frac{\omega C_2 500^2}{10k} \tag{3}$$

Equation (3) gives the DC capacitor is $2611.2\mu F$, and its optimized value is $2400\mu F$. As the convertor is bipolar topology, the grounded capacitor at each polar is $4800\mu F$.

Verification

The DC Capacitor directly impacts transient characteristics of DC grid. When there is a fault in AC system, both the AC and DC system will see large scale power oscillation which may lead to overvoltage. The unbalanced fault cause secondary harmonic oscillation voltage. As the reactance of DC capacitor correspond to the second harmonic power is relevant high, it cause bigger voltage oscillation. Therefore, it is important to consider the inhibition effects when design the DC capacitor.

Reduce DC voltage oscillation

When a system is unbalance, the second order harmonic active power is

$$\Delta P_S = \sqrt{3}kU_N I_N \cos(2\omega t + \varphi_1) = kS_N \cos(2\omega t + \varphi_1) \quad (4)$$

Where k is second order harmonic active power oscillating coefficient, S_N is the rated capacity of the system, φ_1 is initial phase angle of second order harmonic power. If we only consider the DC component and second order voltage harmonic, the voltage of the converter is

$$u_d = U_{DC} + \Delta U_{DC} \sin(2\omega t + \varphi_2) \quad (5)$$

Where U_{DC} is the DC component, φ_2 is initial phase angle of second order harmonic power, $\Delta U_{DC} \sin(2\omega t + \varphi_2)$ is the second order voltage harmonic. Equation (5) gives the second order harmonic power at the DC side as

$$\Delta P_d = 2\omega C_d \Delta U_{DC} U_{DC} \cos(2\omega t + \varphi_2) \\ + 2\omega C_d \Delta U_{DC}^2 \sin(2\omega t + \varphi_2)\cos(2\omega t + \varphi_2) \quad (6)$$

As $2\Delta U_{DC}^2$ in Equation (6) is relevantly small, the second part in Equation (6) can be ignored. Equation (6) is rearranged as

$$\Delta P_d = 2\omega C_d \Delta U_{DC} U_{DC} \cos(2\omega t + \varphi_2) \quad (7)$$

Neglect the switching loss and transmission line loss which gives us $\Delta P_S = \Delta P_d$. We also suggest $\varphi_1 = \varphi_2$, by combination of Equation (5) and Equation (6), we get

$$C_d = \frac{kS_N}{2\omega U_{DC}\Delta U_{DC}} \quad (8)$$

Suppose the max value of voltage fluctuation value as ΔU_{DCmax}, therefore

$$C_d \geq \frac{kS_N}{2\omega U_{DC}\Delta U_{DCmax}} \quad (9)$$

Or

$$C_d \geq \frac{k}{2\omega(\frac{\Delta U_{DCmax}}{U_{DC}})} \cdot \frac{S_N}{U_{DC}^2}(0 < k \leq 1) \quad (10)$$

While $k=1$

$$C_d = \frac{1}{2 \cdot 2 \cdot \pi \cdot 50 \cdot 0.05} \cdot \frac{10000}{500^2} = 127.324\mu F$$

Store electric power

The DC capacitor storage electric power which could last for a certain time to guarantee the system operates at rated power. Assume the time constant related to DC capacitor is τ and it equals to

$$\tau = \frac{C_d U_D^2}{2S_N} \quad (11)$$

If τ is smaller than $5ms$, the capacitor value in equation (11) can inhibit small disturbance or transient overvoltage. Normally τ is $2ms$ in real project, therefore

$$C_d \geq \frac{\tau \cdot 2S_N}{U_D^2} = \frac{2 \cdot 10^{-3} \cdot 2 \cdot 10 \cdot 10^3}{500^2} = 160\mu F(\tau = 2ms)$$

$$C_d \geq \frac{\tau \cdot 2S_N}{U_D^2} = \frac{5 \cdot 10^{-3} \cdot 2 \cdot 10 \cdot 10^3}{500^2} = 400\mu F(\tau = 5ms)$$

All in summary, the DC capacitor value is set at $2400\mu F$.

FILTER PARAMETER DESIGN

Most of the filter in VSC-MTDC is high pass filter, and second order high pass filter is the most widely used. Suppose the filter cutoff frequency is 450Hz and Q_{filter} is 0.08. According to the equal capacity ratio principle, the capacity is 0.25kW (each phase). Figure 3 gives the impedance characteristic of the filter.
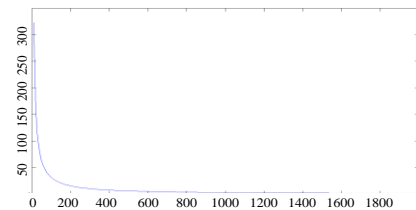

Figure 1:   The impedance characteristic of the filter

DC GRID TRANSMISSION LINE

The transmission line is also chosen according to the equal capacity ratio principle and use T-type equivalent circuit. The reference system is a ±200kV high voltage system with its capacity equals to 200MW. The DC grid in laboratory is designed at ±250V, each terminal capacity is 10kW. Thus the voltage ratio is 800, power ration is 20000 and impedance ratio is 32. We get the T-type equivalent circuit and line parameter as figure 4.
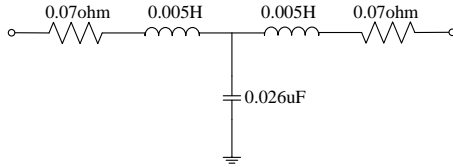

Figure 2: T-type equivalent circuit

REACTOR VALUE DESIGN

The output voltage of converter at AC side u_c is

$$U_C = U_{PCC1} + I \times X_{eq} = (1+X)U_{PCC1} \qquad (12)$$

Where $X = \omega L$.
The relationship between output voltage of converter at AC side and DC side is

$$U_C = \frac{\mu M}{\sqrt{2}} U_{DC} \qquad (12)$$

Where μ is utilization efficiency of DC voltage, M is the modulation ratio. U_{DC} is DC voltage. Because of the control margin and fluctuation of AC and DC voltage, M is set at 0.95. Therefore,

$$U_C = (1+X)U_{PCC1} \le \frac{0.95\mu}{\sqrt{2}} U_{DC} \qquad (14)$$

The nominal voltage value at DC side is 500V and X equals to 0.25. Substituted in equation (14),

$$(1+0.25)U_{PCC1} \le \frac{0.95\frac{\sqrt{3}}{2}}{\sqrt{2}} 500, \quad U_{PCC1} \le 232.7V \qquad (15)$$

The low order harmonics increase along with the U_{pcc1} and M decrease, therefore the transformer secondary voltage (phase to phase) is 230V. Define S_{aB}=10kVA, U_{SB}=230V, thus

$$I_{SB} = \frac{10}{230\sqrt{3}} = 25.1A \qquad (16)$$

Thus

$$Z_{aB} = \frac{230}{25.1\sqrt{3}} = 5.2905\Omega \qquad (17)$$

Therefore the equivalent reactance is

$$L = \frac{0.25Z_{aB}}{\omega} = 4.21mH \qquad (18)$$

Take off the leakage reactance of the transformer which is about 1.4032mH, the reactor value is 2.81mH.

EQUIVALENCY VERIFICATION

All the parameters of the 6-terminal low voltage DC grid is designed based on a 500kV high voltage VSC-MTDC system which has 3 terminals. The voltage source converter uses the three-phase two-level topology. The DC voltage of VSC1 is controlled at constant which is 500kV, while the power flow through VSC2 and VSC3 is controlled constant which are 200MW and -200MW. Simulation models of original VSC-MTDC and 6-terminal low voltage DC grid are built in PSCAD/EMTDC to validate the equal capacity ratio principle. Figure 5 illustrates voltage waveform of VSC-MTDC system. The voltage waveform (Terminal 1, Terminal 2 and Terminal 3) of DC grid is shown in figure 6. The simulation results of low voltage DC grid mainly agree with the VSC-MTDC system DC voltage waveform, which proves the equivalency.

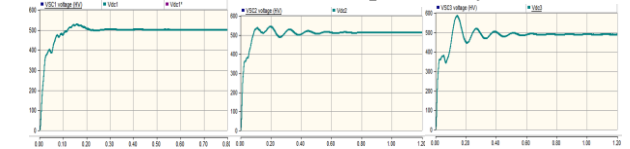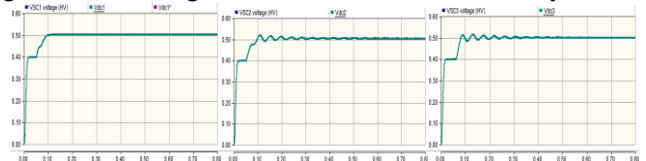**Figure 3:** voltage waveform of VSC-MTDC system

Figure 4: Voltage waveform of DC grid

CONTROL SYSTEM

Master-slave control, voltage margin method and droop control are typical control methods for DC grid. When the master-slave strategy is employed to regulate DC bus voltage in a DC grid, its voltage is determined by the constant DC voltage control converter. At this scenario, the DC voltage will be

unstable when the active power is unbalance or the constant DC voltage control terminal is tripped off against faults. Therefore the DC voltage must be controlled through the coordinating control of the system supervisor layer through communication. Based on the research work above, this paper designs control strategies for DC grid which include control strategy for VSC and bidirectional DC/DC terminal, and coordinated control strategy among multiple terminals.
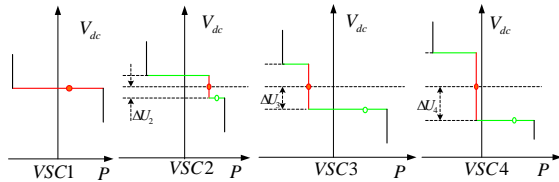

Figure 5:   Operation and control characteristics of the DC grid

Based on the voltage margin control, a coordinated master-slave control method is proposed. Figure shows the operation and control characteristics of the DC grid. Accordance with the laboratory voltage level, the voltage margin value is calculated, where$ΔU_2<ΔU_3<ΔU_4$. Under the steady state, their operational characteristics follow the red line. The DC voltage of VSC1 is controlled at constant, the rest three converters are designed to deliver or inject proper active power. If there is a fault at Terminal 1, the DC voltage at Terminal 2 is controlled at constant, which means its operational characteristics change to the green line and other terminals remain unchanged. The basic principal is the converter with smallest voltage margin will be considered to control DC voltage first. Instead of following the red line, the selected converter will adjust to the green line. The black lines give the operation limit of each converter.

SIMULATION RESULTS

The model of the 6-terminal low voltage DC grid in Fig.1 is tested in PSCAD/EMTDC.The DC voltage at Terminal 1 is controlled at 500V. Terminal 2 delivers 3.5kW active power from AC system to the DC grid, while Terminal 3 delivers 3.5kW active power from DC grid to the DC system. Terminal 2 is connected to energy storage system with bidirectional DC/DC as its interface. A PV system is integrated to the DC grid at Terminal 5. The last terminal provides electric

power to AC load through VSC which using three-phase two-level topology.

Case 1
The output power of Terminal 2 is 3.5kW, it decrease to 2.5kW at 0.8s, at 1.2s it increase to 4kW and Figure 8(a) is its simulation result. The output power of Terminal 3 is -3.5kW, it decreases to -5kW at 0.8s, at 1.2s it increases to -2.5kW. Figure 8 (b) gives the simulation result. The DC voltage waveform of Terminal 1, Terminal 2 and Terminal 3 is shown in Figure 9. Figure 10 illustrates the AC current waveform of Terminal 2 and Terminal 3 during the simulation process.

(a)   (b)
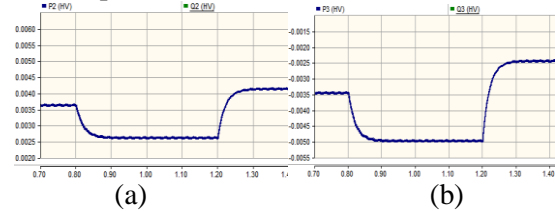
Figure 6:   Simulation result of output power

(a) Terminal 1

(b) Terminal 2
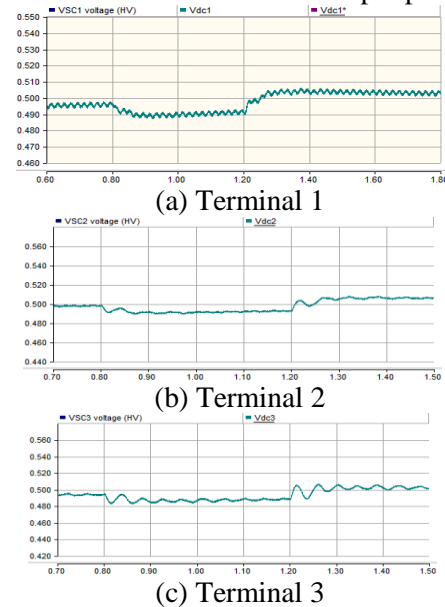
(c) Terminal 3

Figure 7:   The DC voltage waveform
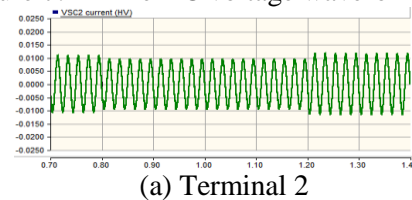
(a) Terminal 2
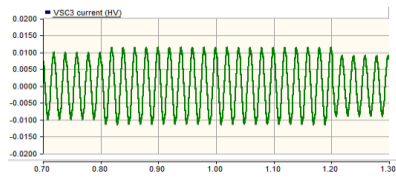
(b) Terminal 3

Figure 8:   The AC current waveform

Case 2

Figure 11 gives the simulation results of DC waveform at each terminal when there is a short circuit fault at the DC side of Terminal 3 at 1*s* and last for 0.05*s*. Figure 12 is the current waveform.
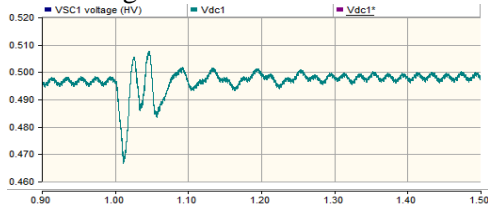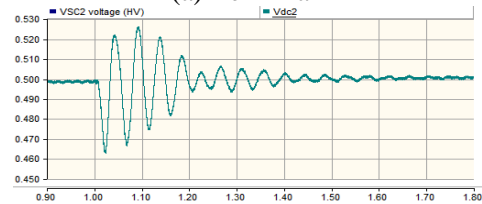
(a) Terminal 1
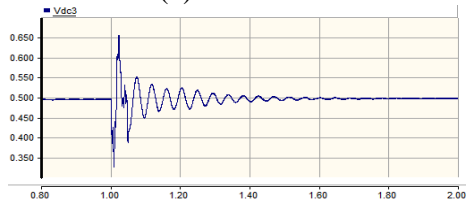
(b) Terminal 2

(c) Terminal 3

Figure 9:   DC waveform at each terminal
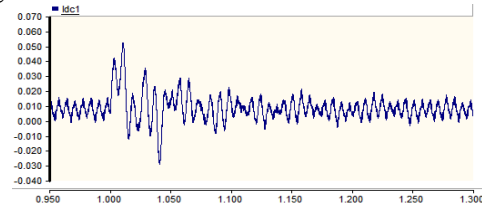
(a) Terminal 1
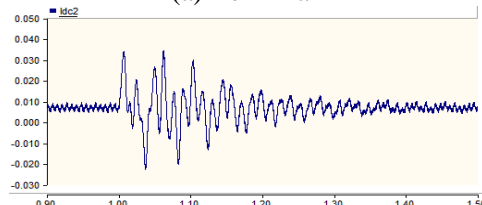
(b) Terminal 2
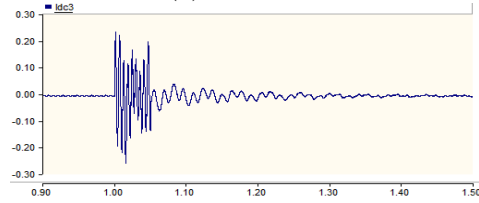
(b) Terminal 2

(c) Terminal 3

Figure 10:   current waveform at each terminal

Figure 13 gives the simulation results of DC waveform at each terminal when there is a three-phase short circuit fault at the AC side of Terminal 3 at 1*s* and last for 0.05*s*. Figure 14 shows the current waveform.

(a) Terminal 1

(b) Terminal 2

(c) Terminal 3

Figure 11:   DC waveform at each terminal
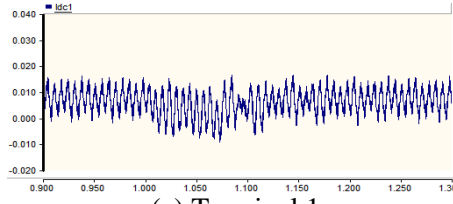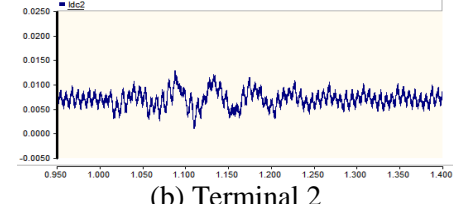
(a) Terminal 1
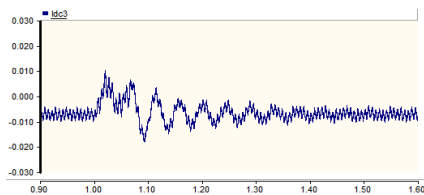
(b) Terminal 2

(c) Terminal 3

Figure 12:   current waveform at each terminal

The simulation results prove that the DC bus voltage of the DC grid can be controlled steadily after a variety of faults which include grounding fault at AC or DC side of the system.

CONCLUSIONS

Developing a low voltage, small capacity DC grid in laboratory to study DC grid under various scenarios or its interaction with AC system is convenient and practical. The equal capacity ratio principle helps the parameter design in low voltage DC grid. All the parameters are selected according to the parameters of the high voltage reference system based on equal capacity ratio principle and optimized by simulation model. The simulation results prove that the low voltage, small capacity DC grid has the same physical characteristics as the high voltage practical project.

Based on the voltage margin control, a coordinated master-slave control method is proposed. Accordance with the laboratory voltage level, the voltage margin value is calculated. With carefully selected margins based on the system strength and converter type, the DC bus voltage of t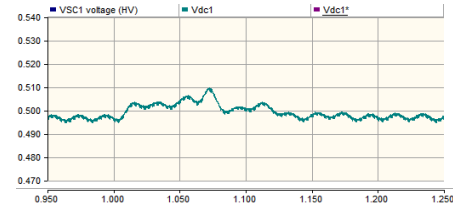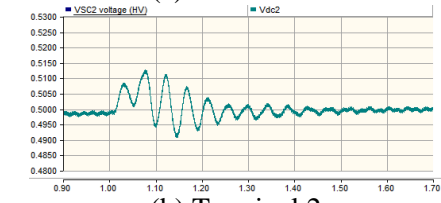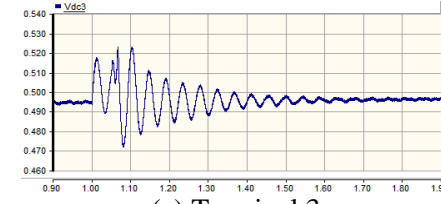he DC grid can be controlled steadily after a variety of faults. A digital simulation model of the 6-terminal low-voltage DC grid in laboratory is built using PSCAD/EMTDC. Simulation results validate the feasibility of the proposed coordinated control strategy. It can maintain the DC bus voltage and against active power unbalance or tripping off converters.

REFERENCES

[1] G. P. Adam, et al. *Network fault tolerant voltage-source-converters for high-voltage applications in AC and DC Power Transmission*, 2010. ACDC. 9th IET International Conference on, 2010, pp. 1-5.

[2] L. Haifeng, et al. *Coordination and optimization of small signal modulators in multi-infeed HVDC systems*, in Transmission and Distribution Conference and Exposition, 2003 IEEE PES, 2003, pp.35-40 Vol.1.

[3] J. Reeve and S. P. Lane-Smith. *Multi-infeed HVDC transient response and recovery strategies*, Power Delivery, IEEE Transactions on, vol. 8, pp. 1995-2001, 1993.

[4] C. Meyer, et al. *Control and Design of DC Grids for Offshore Wind Farms*, IEEE Transactions On Industrial Applications，2007, vol. 43, no. 6, pp. 1475-1482.

[5] W. Lu and B.-T. Ooi, *Optimal acquisition and aggregation of offshore wind power by multi-terminal voltage-source HVDC*, *IEEE* Trans. Power Del., vol. 18, no. 1, pp. 201–206, Jan. 2003.

[6] P. Bresesti, W. Kling, R. Hendriks, and R. Vailati, *HVDC connection of offshore wind farms to the transmission system*, IEEE Trans. Energy Convers., vol. 22, no. 1, pp. 37–43, Mar. 2007.

[7] Gang. Shi, Guoxiang. Wu, Xu. Cai, Zhe. Chen. *Coordinated control of multi-terminal VSC-HVDC transmission for large offshore wind farms*, 2012 IEEE 7th International Power Electronics and Motion Control Conference- Ecce Asia, vol.2, pp. 1278-1282, (2012)

[8] Nilanjan. Ray. Chaudhuri, Rajat. Majumder. *Modeling and stability analysis of MTDC grids for offshore wind farms: A case study on the North Sea benchmark system*, Power and Energy Society General Meeting, 2011 IEEE, pp. 1-7.

AN ALGORITHM FOR OPTIMAL CONTROL OF AN ELECTRIC MULTIPLE UNIT

Nima Ghaviha*, Fredrik Wallin and Erik Dahlquist
Mälardalen University, Sweden
School of Business, Society and Engineering

Markus Bohlin
SICS Swedish ICT AB

ABSTRACT

This paper offers a solution for the optimal EMU train (Electric Multiple Unit) operation with the aim of minimizing the energy consumption. EMU is an electric train with traction motors in more than one carriage. The algorithm is based on dynamic programming and the Hamilton-Jacobi-Bellman equation. To model the train, real data has been used, which was provided by experts from Bombardier Transportation Västerås. To evaluate the model, some experiments have been done on the energy saving in exchange for the increase in the trip time. Moreover a simple accuracy factor is introduced to evaluate the accuracy of the model. The final goal is to use this approach as a base for a driver advisory system, therefore it is important to have the amount of calculations as minimum as possible. The paper also includes the studies done on the calculation time. The solution can be used for driverless trains as well as normal trains. It should be mentioned that this paper is a part of a research which is still in progress and the final model will also be used by Bombardier Transportation Västerås as an evaluation tool for the propulsions systems and trains.
Keywords: Dynamic programming, Hamilton-Jacobi-Bellman equation, DAS, EMU

INTRODUCTION

The rail system is both a big energy consumer and at the same time the most energy efficient means of transportation. The subject of optimization of energy efficient train systems can be divided into two categories: optimization of train units themselves, and optimization of train unit operation, i.e., driving style. The goal in this paper is to work on energy efficient driving style of the train. The main problem is to plan the train movement during a trip with the aim of minimizing the energy consumption. In other words we are looking for an optimal speed profile of a train to minimize the energy consumption for traction force subject to different constraints like travel time, speed limits etc.

Over more than 50 years different approaches have been used to solve this problem. Maximum principle, non-linear programming, dynamic programming and genetic algorithms are among the most widely used approaches. The solution based on Maximum Principle consists of four stages of maximum acceleration, constant speed, coasting

---

* Corresponding author: Phone: +46(0)21 101368,
Email: nima.ghaviha@mdh.se

and maximum deceleration [1]. The problem of optimal train control can also be considered as a nonlinear optimization problem. Sequential quadratic programming is among the nonlinear programming algorithms used to solve this problem [2]. In the dynamic programming approach all the variables are discretized and the best solutions are selected among all possible combinations [1]. Genetic algorithms have also been used to solve this problem [3].

In order to use the solutions on real trains, they are implemented in a form of driver advisory systems (DAS). Currently there are many solutions and DAS's in the market. In [4] a complete study is done on different driver advisory systems and in [5] different solutions are assessed based on different criteria. One of the main obstacles for implementation of different algorithms in a form of DAS is the limitation on the amount of calculation that can be done on a train and during a trip.

In this paper an approach is introduced for the problem of energy efficient driving of a train with the aim of having minimum amount of calculations during the trip. The model should be extendable to handle other constraints such as limitations on the power we can get from the line, maximum acceleration and retardation, regeneration rate etc. The approach is based on a simplified version of the problem which was previously solved in [6].

OBJECTIVE

The objective is to minimize the energy consumption of an EMU (Electrical Multiple Unit) during a specific trip. The distance and trip time are fixed. The aim is to find the optimal speed profile for the train with the minimum energy consumption. The train is equipped with regenerative brakes which can be used in higher speeds. It is not possible to use regenerative brakes at lower speeds, therefore the only available alternative is the mechanical brake. Later on the results shall be used for a driver advisory system to help the driver reach the destination on time and at the same time minimize the energy consumption.

MODEL

The mass of the train is assumed to be concentrated on the gravity center of the train; therefore we treat the train as a single mass point. During the trip there are several forces affecting the train:

- Tractive effort (F_t)
- Running resistance(F_{rr})
- Gradient resistance(F_g)
- Curve resistance(F_c)
- Aerodynamic resistance(F_{ae})

In the current model curve resistance and aerodynamic resistance are assumed to be zero. The summation of the rest of the forces will be the acceleration force.

$$\sum F = m * a \qquad (1)$$

$$m * a = F_t - F_{rr} - F_g - F_c - F_{ae} , \qquad (2)$$

where m is the mass of the train and a is the average acceleration.

Running Resistance

The formula used for the running resistance is as follows:

$$F_{rr} = A + B * v + C * v^2 \qquad (3)$$

A, B and C are the running resistance coefficients that are dependent on the weight of the train and v is the velocity.

Gradient Resistance

The gradient resistance formula used in this model is as follows:

$$F_g = m * g * \frac{s}{1000} \qquad , \qquad (4)$$

where m is the train mass, g is the standard gravity and s is the gradient.

Energy Consumption

The total amount of energy used during a trip is equal to

$$E = \int F_t * x \qquad , \qquad (5)$$

where E is the total energy consumption, F_t is the tractive effort and x is the distance traveled.

APROACH

The approach used in this paper is based on dynamic programming and the Hamilton-Jacobi-Bellman equation and Bellman's backward approach [7]. Using this approach it is possible to find the best solution for all the states of the train during the trip beforehand which makes the amount of calculation needed on the train as minimum as possible. There is a maximum trip time which corresponds to the latest arrival time of the train to its destination. The idea is to have a general solution ready at the start of the trip and find the best solution at each state during the trip. The state of the train is defined with three parameters: time passed, distance traveled and current velocity. Trip time, trip distance and velocity are discretized. Therefore we can represent any state of the train using an array with dimensions of T, X and V, where T is the number of time steps, X is the number of track sections represented and V is the number of admissible train velocities. For each state three outputs are needed and each will be stored in different matrices: the minimum energy needed to reach the final destination (cost-to-go) which is stored in matrix E, the optimum tractive effort which is stored in matrix F_t and the optimum velocity in the next time step which is stored in matrix V_{op}. In the current model it is assumed that at the final time (T), the train will stop at the destination (X). Therefore the final state is ($T, X, 0$) which has a cost-to-go of zero. For the states (T, X, v) where v has any value other than zero a high penalty is assigned. There are also penalties set for the states that represent any position other than final one (X) in the last time step (T).

Cost-to-go calculations

In the following sections the below symbols are used:

E (i, j, k): Minimum energy needed for the train to reach the final state from the state of (i, j, k)

dt: duration of one time step [s]

dx: length of one distance step [m]

dv: one velocity step [km/h]

($T, X, 0$): final state which is the last time step, last distance step and zero velocity

Suppose that we are in a certain state (we call it start point with the parameters of t_s, x_s and v_s) and want to calculate the total energy needed to reach the final state. Suppose that all the states in the next time step (t_s+dt, x, v) are already filled with the minimum energy needed to reach the final state.

$$E(t_s, x_s, v_s) =$$

$$Min\left(de(s,f) + E\left(t_s + dt, x_f, v_f\right)\right)$$

$$\forall \ x_f, v_f \qquad , \qquad (6)$$

where $de(s, f)$ represents the transition cost which is the energy needed for getting the train from the state (t_s, x_s, v_s) to the state ($t+dt, x_f, v_f$).

By backward iteration starting in the final state where $t = T$ and the optimum cost is known, we calculate the optimum cost at time $t-1$ and so forth.

Transition cost

Suppose that the starting state is (t_s, x_s, v_s) and the next state is (t_f, x_f, v_f) with t_f being equal to t_s+dt.

Having v_f and dt we can calculate the x_f and later on de.

$$t_f = t_s + dt \qquad (7)$$

$$v_{avg} = \frac{(v_s + v_f)}{2} \qquad (8)$$

$$x_f = x_s + v_{avg} * dt \qquad (9)$$

$$\Delta x = x_f - x_s \qquad (10)$$

$$F_a = \frac{m*(v_f - v_s)}{dt} \qquad (11)$$

$$F_{rr} = A + B * v_{avg} + C * v_{avg}^2 \qquad (3)$$

As it is mentioned in above equations average velocity in one time step is used for running resistance calculations. For gradient resistance however, the gradient force for all the distance steps in one time step will be checked and the total gradient force will be calculated:

$$F_g = \sum_{x_s}^{x_f} F_{gi} \qquad (13)$$

$$F_t = F_a + F_{rr} + F_g \qquad (14)$$

$$de = F_t * \Delta x \qquad (15)$$

Undesired states

For each state of (t_s, x_s, v_s) there will be $\frac{V}{dv}$ number of states to check in the next time step. Most of them are not feasible and should not be checked.

1. As stated before x_f is calculated based on v_f. States in which the x_f will exceed X won't be checked.
2. The train's traction motor has a certain limit on the available tractive effort based on the velocity (see figure 1). Based on the maximum tractive effort available, the gradient force, the running resistance and the mass of train, the maximum and minimum acceleration rate can be calculated. A limit on acceleration rate will set a limit on the number of different velocities the train can reach from a certain velocity in one time step.
3. There are certain speed limits during the trip. In one time step the train might encounter different speed limits in different distance steps which will reduce the

number of feasible velocities in the next time step.

4. Jerk rate is defined as rate of change of acceleration which can also be represented as rate of change of acceleration force. Having a maximum jerk rate will set another limit on the tractive effort the traction motor can provide and therefore limits the number of states the train can reach in one time step.
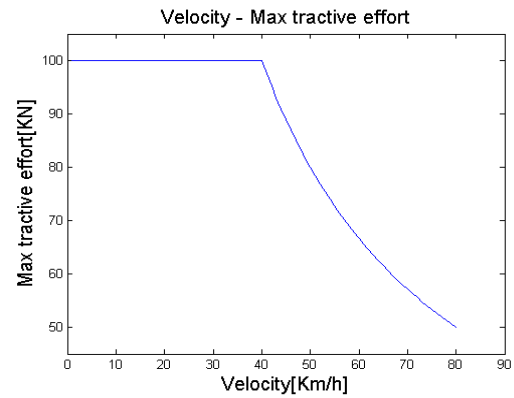
Figure 1 - maximum tractive effort available in different velocities.

The above states will not be checked by the model and the optimum state in the next time step with the minimum $de + E (t_s + dt, x_f, v_f)$ for each (t_s, x_s, v_s) will be chosen among the rest of the states.

Final matrices

Matrices filled at the end of calculations are as follows:

- Next optimum velocity (V_{op})
- Minimum total energy needed to reach the final state (E)
- Optimum tractive effort at each state (F_t)

Finding the Optimum Speed Profile

Filling in the matrices of the general solution takes a long time. However it is needed to be done only once before starting the trip. During the trip the current state of the train can be set as the input and the optimum tractive effort and velocity in the next time step and the minimum total energy needed to reach the final state will be found from the general

solution matrices. The time needed to look up the general solution and find the optimum tractive effort is short enough for the model to be used as an advisory system for the driver. This is discussed further in the next section.

RESULTS AND DISCUSSION

MATLAB is used as the programming tool in this study. Figures 2 to 4 show the speed profile for 3 states (0,0,0), (20, 500, 0) and (20, 500, 60) in the same trip. The trip time is 3.16 minutes and the distance between two stations is 3.02 kilometers. The dotted line is the speed limit in *km/h* and the dashed line represents the gradient.
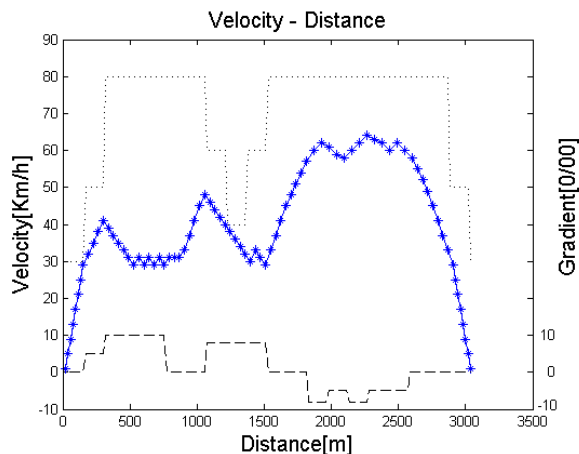
Figure 2-the optimum speed profile for the state (0,0,0) with the speed limits (dotted line) and gradient (dashed line).
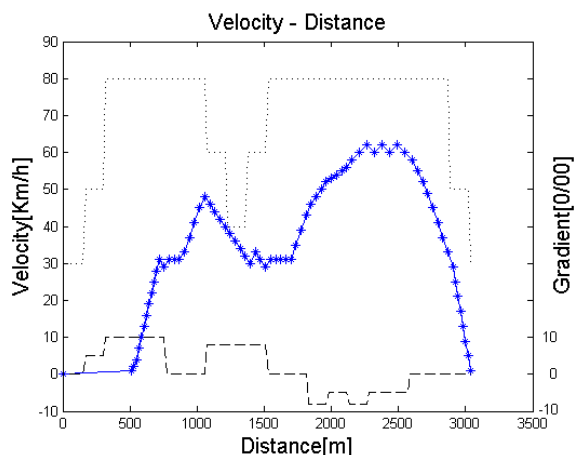
Figure 3- the optimum speed profile for the state (20,500,0) with the speed limits (dotted line) and gradient (dashed line).
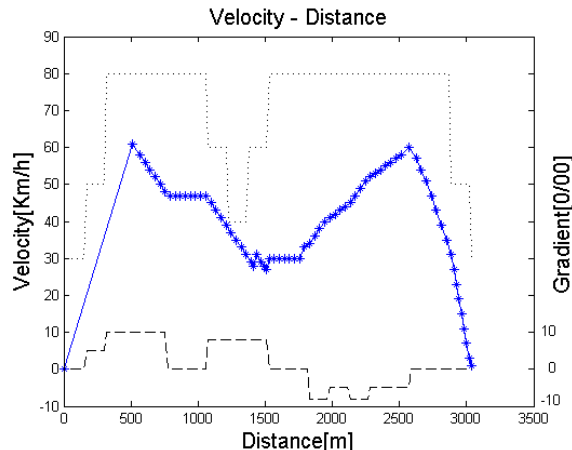
Figure 4- the optimum speed profile for the state (20,500,60) with the speed limits (dotted line) and gradient (dashed line).

Discretization

In this approach time, distance and velocity are discretized. It is obvious that with smaller intervals or steps, there will be smoother curves for speed profiles and more accurate solutions. However with higher number of intervals the calculation time will increase. Moreover the trip time and the trip distance will also affect the calculation time. To study the runtime two trips and four types of discretization have been studied. (See table 1)

	Time	Distance
Trip1	2 min	1.51 Km
Trip2	4 min	3.02 Km

Table 1 – time and distance for each trip

Table 2 shows the number of intervals in each accuracy.

	Number of time steps	Number of distance steps
Accuracy 1	10	20
Accuracy 2	20	40
Accuracy 3	40	80
Accuracy 4	80	160

Table 2 – number of time and distance steps for each accuracy.

Table 3 includes the calculation times for each combination of trip and accuracy in seconds. The calculations are done in MATLAB using a normal PC.

	Accuracy 1	Accuracy 2	Accuracy 3	Accuracy 4
Trip 1	9.9376	21.4295	43.4619	75.6426
Trip 2	15.7453	37.5917	82.8783	174.9483

Table 3 – time required to calculate the general solution in seconds for each trip and accuracy.

As we can see, with increasing the time and the distance and also increasing the number of intervals, the calculation time for the general solution increases. It can be expected that for longer trips the calculation time would increase more. There are still works in progress to decrease the calculation time. The calculation of a general solution shall be done only once and that's before starting the trip. During the trip it is only needed to input the current state of the train (time, distance and velocity) and look up the general solution to find the optimum solution for that specific state. The time needed to look up the general solution and find the optimum tractive effort and the optimum speed profile for trip two and accuracy four is around 0.03 seconds. It is to be mentioned that one time step for trip two and accuracy four is equal to 3 seconds. So it is theoretically possible to take actions when using the system during the trip. The challenges for implementation of the system is discussed under implementation subheading.

Error

To study the effects of the number of intervals for discretization, an accuracy factor is introduced. As mentioned in previous sections to calculate the energy consumption two states are needed. The first state is (t_s, x_s, v_s) and the second state is ($t_s + dt$, x_f, v_f). The second state is chosen according to all possible velocities in the next time step. x_f is estimated based on v_f and dt; it is calculated according to equations of motion and then rounded down to the closest distance step. The estimation is in rounding the real distance step to the integer one.

$$E_i = \left(x_{fR} - x_{fI}\right)^2 \quad error\ in\ time\ step\ i \quad (16)$$

$$E_{average} = Average(E_i) \quad average\ error\ , (17)$$

where x_{fR} is the real distance step and x_{fI} is the integer distance step. $E_{average}$ shows the average of deviations of the estimated distance step from the real distance steps. In order to compare four accuracies with each other, $E_{average}$ is then multiplied by the length of one distance step. The results are shown in table 4.

	Accuracy 1	Accuracy 2	Accuracy 3	Accuracy 4
Trip2	64.0364	35.2121	16.3624	8.9636

Table 4-$E_{average}$ multiplied by the length of one distance step for each accuracy for trip two.

As we can see the more distance and time are discretized the less error we will have.

Energy Calculations

In this model the train is assumed to be a single mass point and the energy calculations are based on the equations of motion. In other words the energy needed for the transition from one state to another one is only the energy needed to move a single mass from one point to another. However in a real train there are other sources of energy consumption like auxiliary systems. Moreover each component in the train has a certain efficiency which will increase the total energy consumption. Including the efficiency in the equations would be quite simple if the efficiencies were constant, but the efficiency of different components will vary in different velocities and different tractive efforts. There are currently not enough data and information on the changes of efficiencies according to velocity and tractive effort. There is work in progress to have more accurate functions ready for this purpose.

Regenerative Brake

The train modeled is equipped with a regenerative brake which works in higher velocities, for low speeds mechanical brake is used (below 7 km/h). Using regenerative brake it is possible to theoretically regenerate all the acceleration force. But in reality there are some losses when braking. Some losses are the same kind of losses as the ones discussed in the previous topic (i.e. losses when transferring energy from the wheels back to the line).

Another kind of loss happens after transferring the energy back to the line. Energy regenerated from braking can be used in different ways. It can be either used by some other train that is accelerating at the same exact moment, saved somewhere for the future use (e.g. in capacitors in certain points in line) or just going to waste. Considering all these three conditions in the model makes it more complex. At the moment we assume that 80 percent of the energy is regenerated from braking. This percentage is a rough estimation used by experts in Bombardier Transportation Västerås. Having the constant coefficient of 0.8 for the regenerated energy, makes it always favorable to brake rather than coast (F_t equals to zero). Therefore the solution will rarely include any coasting.

Validation

Currently there are no real data available to be used for validating the model. There is going to be a test run of a certain train later on during autumn 2014. It is planned that the data from that test run be used for validating the model. However from the test runs of the model the decrease in energy consumption in exchange for increase in time is obvious. The table 6 shows the change in energy consumption in different travel time.

Change in the trip time	+2 sec (1.0%)	+4 sec (2.1%)	+7 sec (3.8%)	+10 sec (5.4%)	+12 sec (6.5%)	+17 sec (9.2%)	+22 sec (12.0%)
Energy saving	9.86 %	16.35 %	33.93 %	40.37 %	47.95 %	60.29 %	60.17 %

Table 4 – Energy saving in exchange for increase in time for trip two and accuracy four.

As it can be seen in the table above in exchange for a small increase in the trip time, the energy consumption will decrease.

Implementation

There are several methods to implement a DAS system [5]. One is to have the optimum speed profile ready and have the driver follow it. The other one is to have a system on the train to give instruction to the driver during the trip. The solution represented in this paper can be used in both ways. However there are some points to be mentioned.

In the current model instructions are given in every time step. Given the fact that the time steps are chosen to be rather short, it is not practically possible to use the current model on a real train. Moreover the instruction given by the model for each state is the optimum tractive effort needed at the moment, which is continuous whereas in the real train, the driver has a possibility to apply a specific amount of tractive effort. In other words the control is discrete.

There are still works to be done on the model to make it ready for a practical use.

CONCLUSION

The problems addressed in this paper was to plan train movement to minimize the energy consumption. The model shall be a base for a Driver Advisory System (DAS) which is currently under development. Since its going to be used later as a DAS, the main challenge was to have the minimum amount of calculations during the trip. The main idea in the model was to have a general solution ready before starting the trip and find the best solution during the trip. There are still new features to be added to the model and it needs to be developed further for it to be used as a DAS. However, no matter the complexities of the new features, the amount of calculations on the train would still be the same or slightly more, because they will all be done before the trip and during the trip the calculations will be limited to just looking up the general solution.

ACKNOWLEDGMENT

REFERENCES

[1] Franke R, Terwiesch P, Meyer M, *an algorithm for the optimal control of the driving of trains*, proceedings of the 39th IEEE conference on Decision and Control, 2000

[2] Miyatake M, Matsuda K. *Energy Saving Speed and Charge/discharge Control of a Railway Vehicle with On-board Energy Storage by Means of an Optimization Model*, IEEJ Transactions on Electrical and Electronic Engineering 2008 4:771 – 778

[3] Chang C.S, Sim S.S, *Optimizing Train Movement through Coast Control Using Genetic Algorithms*. IEE Proceedings – Electrical Power Applications 1997, 144(1):65 – 73

[4] DeltaRail Group, *Driver Advisory Information for Energy Management and Regulation*. In: Stage1 Report, RSSSB Research Program 2009, T724

[5] Panou K, et al. *Railway Driver Advice Systems: Evaluation of Methods, Tools and Systems*. Journal of Rail Transport Planning & Management 2014, http://dx.doi.org/10.1016/j.jrtpm.1013.10.005

[6] Gkortzas P. *Study on Optimal Train Movement for Minimum Energy Consumption*, Master Thesis Work, Mälardalen University 2013

[7] Bertsekas D.P. *Dynamic Programming and Optimal Control, third edition*. Athena Scientific, Belmont, Massachusetts. 2005, ISBN 1-886529-26-4

AN ITERATIVE ALGORITHM FOR TORSION BALANCING DEEP-WATER CABLES AND UMBILICALS

Magnus Komperød[*]
Technological Analyses Centre
Nexans Norway AS
P. O. Box 42, 1751 HALDEN
Norway

ABSTRACT

Direct electrical heating (DEH) is a technology for preventing hydrate formation and wax deposit in oil and gas pipelines. Nexans Norway AS is currently researching and developing deep-water DEH solutions. A Nexans research project which was finished in year 2014 concludes that a deep-water DEH riser cable for 2 300 m water depth is feasible.

This paper presents an iterative algorithm for torsion balancing deep-water cables and umbilicals, using analytical considerations of the armor wires. The main advantage of this algorithm is that it does not depend on analytical expressions of the cable's torsion balance. Hence, the algorithm can be used also on cables which mechanical properties are established using finite element simulations, i.e. not only on cables where there exist analytical models of the mechanical properties.

The algorithm was initially developed for the deep-water DEH riser cable. The algorithm works very well. After two iterations the torsion unbalance was reduced by 98%.

Keywords: Cross Section Analysis; Deep-Water; DEH; Direct Electrical Heating; Offshore Technology; Subsea Cable; Torsion Balancing; Umbilical.

Notation

A_i Cross section area of each armor wire in layer i [m^2].

E_i E-modulus of armor wires in layer i [Pa].

EA_c The cable's axial stiffness [N].

k Iteration number [-].

L_i Pitch length of armor wires in layer i [m].

l_i Length of armor wires over one pitch length in layer i [m].

$M_i(k)$ Change of total cross section area in layer i (all armor wires) from iteration $k-1$ to iteration k [m^2].

$M_{T,c}$ The cable's torsion moment [Nm].

$M_{T,i}$ Contribution to the cable's torsion moment from each armor wire in layer i [Nm].

$N_i(k)$ Number of armor wires in layer i at iteration k [-].

$\bar{N}_i(k)$ Theoretical number of armor wires in layer i at iteration k [-].

$N_i^{\max}$ Maximum allowed number of armor wires in layer i [-].

R_i Pitch radius of armor wires in layer i [m].

$r_i(k)$ Element radius of armor wires in layer i at iteration k [m].

$\bar{r}_i(k)$ Theoretical element radius of armor wires in layer i at iteration k [m].

T_c Axial cable tension [N].

T_i Axial tension of each armor wire in armor layer i [N].

α_i Pitch angle of armor wires in layer i [rad].

$\beta_c(k)$ The cable's torsion moment to axial tension ratio at iteration k [Nm/N].

$\beta_i(k)$ Contribution to the cable's torsion moment to axial tension ratio from all armor wires in layer i at iteration k [Nm/N].

---
[*]Corresponding author: Phone: +47 69 17 35 39 E-mail: magnus.komperod@nexans.com

ε_c Axial strain of the cable [-].

ε_i Axial strain of armor wires in layer i [-].

σ_i Axial stress of armor wires in layer i [Pa].

Values with iteration number $k = 0$ refer to the initial values, i.e. the values before the torsion balancing process begins. For example $N_1(0)$ refers to the initial number of armor wires in layer 1. During general explanations where the armor layer number is not relevant, the layer number sub-script is omitted. Similarly, where the iteration number is irrelevant, the argument k is omitted.

Negative values of L indicate left lay direction, and positive values of L indicate right lay direction. Similarly, negative values of α indicate left lay direction, and positive values of α indicate right lay direction. All other length values are always positive.

INTRODUCTION

The world's increasing energy demand, combined with the exhaustion of many easily accessible oil and gas reserves, drives the petroleum industry into deeper waters. Manufacturers of subsea cables and umbilicals are among those who face the technological challenges of increased water depths.

Another significant challenge of offshore petroleum production is that the pipeline is cooled by the surrounding water. As the pipeline content drops to a certain temperature, hydrates may be formed and wax may start to deposit inside the pipeline wall. Hydrates and wax may partially, or even fully, block the pipeline. Hydrate formation may start at temperature as high as 25°C, while wax deposit may start at 35-40°C [1].

There are several ways to prevent hydrate formation and wax deposition. An intuitive solution is to apply thermal insulation at the outer surface of the pipeline. However, at long pipelines, low flow rates, or production shut downs, this solution may be insufficient.

Depressurizing the pipeline content may be used to prevent hydrate formation. However, at deepwater pipelines, high pressure is required to bring the pipeline content to topside. Plug removal by depressurizing also faces the same problem at deepwater pipelines [2].

When thermal insulation and depressurizing are in-
sufficient, a commonly used approach is to add chemicals to the pipeline in order to reduce the critical temperature for hydrate formation and wax deposition. Methanol or glycol is commonly used [1, 3]. However, as explained in reference [1], adding chemicals has practical as well as environmental disadvantages.

Another approach to prevent hydrate formation and wax deposition is to use power cables inside the thermal insulation of the pipeline. The power cables function as heating elements heating the pipeline. However, embedding the cables inside the thermal insulation may lead to practical difficulties [1].

A technology that has emerged over the last years is direct electrical heating (DEH). The first DEH system was installed at Statoil's Åsgard oil and gas field in the Norwegian Sea in year 2000 [4]. Nexans Norway AS qualified the DEH technology together with Statoil and SINTEF.

In DEH systems, the electrical resistance of the steel in the pipeline wall is used as a heating element. A single phase cable, referred to as piggyback cable (PBC), is strapped to the pipeline. In the far end (the end of the pipeline far away from the topside) the PBC is connected ("short circuited") to the pipeline. In the near end (the end of the pipeline close to the topside), a two-phase DEH riser cable is connected to the PBC and the pipeline; one phase of the riser cable is connected to the PBC, and the other phase of the riser cable is connected to the pipeline. When the riser cable is energized topside, energy is transferred through the PBC into the steel of the pipeline wall.

Nexans Norway AS is currently developing deepwater DEH solutions. A piggyback cable that is reparable, i.e. can carry its own weight, at 1 070 m water depth is already produced by Nexans in a delivery project. When this DEH system is installed outside the coast of Africa, it will be the world's deepest DEH system [4]. A Nexans research project was finished in year 2014, which concludes that a DEH riser cable for 2 300 m is feasible. The cross section of this DEH riser cable is shown in Figure 1. Actually, already in year 2010-2011, Nexans Norway AS predicted the feasibility of such a deepwater DEH riser cable in references [5] and [6].

The deep-water DEH riser cable shown in Figure 1 has four stranded conductors (red color) with electrical insulation systems (dark gray, light gray, and black colors). Outside the conductors are two lay-
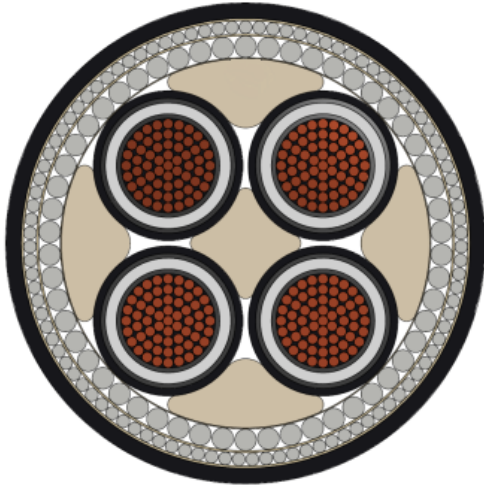
Figure 1: Cross section of the deep-water DEH riser cable, which is feasible for 2 300 m water depth.

ers of armor wires (gray color) and then the outer sheath (the outermost sheath in black color). Empty spaces are occupied with fillers (light brown color), which give better distribution of radial forces. The flexible center profile (light brown color) is patented by Nexans Norway AS. This profile in combination with the accurately developed cable geometry is essential for the cable to be installed and operated at as large water depths as 2 300 m.

For deep-water cables, the submerged weight (i.e. the net force of gravity minus buoyancy) causes large cable tension topside. For such cables, it is desirable that the cable is well torsion balanced. A poorly balanced cable will twist when being axially tensioned. If the cable is fixed in both ends, and thereby prevented from twisting, a poorly balanced cable will set up a torsion moment when being axially tensioned.

The mechanical properties of the deep-water DEH riser cable presented in Figure 1 was analyzed using a finite element method (FEM) software. Hence, there is no *analytical* expression for the cable's torsion balance that can be used for the torsion balancing process. The author then developed the iterative algorithm presented in this paper. The purpose of this algorithm is to torsion balance a cable through analytical considerations of the cable's armor wires. The main advantage of this algorithm is that it can be used even if there is only a FEM model of the cable, i.e. no analytical model. The algorithm proves to be very successful. After two iterations, the DEH riser

cable's unbalance (quantified as the torsion moment to axial tension ratio) was reduced by 98%.

Analytical expressions for a cable's torsion balance are well known in the literature, see for example reference [7]. However, the author is not familiar with any algorithm which has a similar purpose as the algorithm presented in this paper, and that uses the same tuning parameters.

OBJECTIVES OF THE ALGORITHM

In subsea cables and umbilicals, steel armor is commonly used as load carrying element. There are usually two, sometimes four, layers of armor wires of alternating lay directions (left or right). The objective of the algorithm presented in this paper is to torsion balance cables and umbilicals with two armor layers of opposite lay directions. As the cable's torsion moment to axial tension ratio, β_c, is used to quantify the torsion unbalance of the cable, the mathematical formulation of the objective is to achieve $\beta_c = 0$ Nm/N.

Armor wires with circular cross sections are assumed. It is also possible to adapt the algorithm to armor wires of other cross section shapes. However, this is beyond the scope of this paper.

The tuning parameters to achieve torsion balance are the number of armor wires in each armor layer and the armor wires' radii. In other words, the tuning parameters are N_1, N_2, r_1, and r_2. Hence, the algorithm's objective is to tune these four parameters to achieve $\beta_c = 0$ Nm/N.

In Figure 1, N_2 is the number of armor wires in the outer armor layer (i.e. the armor layer right inside the black outer sheath). The parameter r_2 is the radius of each armor wire in this armor layer. Please note the difference between r_2 and R_2: r_2 is the radius of the armor wire itself, while R_2 is the distance from center of the armor wire to center of the cable. Similarly, N_1 is the number of armor wires in the inner armor layer (i.e. the armor layer right inside the outer armor layer), and r_1 is the radius of the armor wires in this layer.

In theory, there is an infinite number of combinations of the four tuning parameters that will achieve $\beta_c = 0$ Nm/N. For a solution to be feasible, two additional constraints must be introduced: (i) The cable's axial stiffness, EA_c, should not change subject to the torsion balancing. This ensures unchanged stress distribution between the armor and the other

cable elements. For realistic cable designs, this also ensures that the cable's capacity (allowed combinations of axial tension and bending curvature) will be almost unchanged. (ii) The fill factors of the armor layers (i.e. the complement of the empty space within each layer) should be unchanged.

In order to limit the complexity of the algorithm, the following simplifications are introduced: (i) Linear elastic materials are assumed. (ii) Radial displacements in the cable, including radial deformations due to the Poisson ratio effect is neglected, because radial displacements require detailed modeling of the non-armor cable elements. (iii) The armor layers' pitch radii, R_1 and R_2, are considered as constants in the algorithm, while they will be subject to small changes in real-life. As will be shown later in this paper, the algorithm gives very good results, despite these simplifications.

THE ITERATION PROCESS

The torsion balancing algorithm is an iteration process. Step 0 is performed once before the first iteration. Step 1 and step 2 are performed once for each iteration.

Step 0: The iteration counter k is set to zero, i.e. $k = 0$.

Compute or simulate the cable's axial stiffness, EA_c, and the cable's initial torsion moment to axial tension ratio, $\beta_c(0)$.

If $\beta_c(0)$ is sufficiently small (absolute value), no torsion balancing is needed.

If $\beta_c(0)$ is too large (absolute value), then go to step 1.

Step 1: Increase the iteration counter k by 1.

Calculate new values of $N_1(k)$, $N_2(k)$, $r_1(k)$, and $r_2(k)$. How to calculate these values will be explained in the next section. Then go to step 2.

Step 2: Compute or simulate the torsion moment to axial tension ratio, $\beta_c(k)$, based on $N_1(k)$, $N_2(k)$, $r_1(k)$, and $r_2(k)$ found in step 1.

If $\beta_c(k)$ is sufficiently small (absolute value), torsion balance is achieved.

If $\beta_c(k)$ is too large (absolute value), then go to step 1.

The computations of step 0 and step 2 must be based on the assumption of no cable twisting, i.e. the cable is prevented from twisting at both cable ends.

Ideally, the cable should be perfectly torsion balanced after one iteration, i.e. $\beta_c(1)$ should be zero. However, due to the simplifications introduced in the previous section, more iterations may be necessary. For the deep-water DEH riser cable presented in Figure 1, two iterations were sufficient. However, the algorithm improved the torsion balance also during the third and forth iterations.

How to compute or simulate EA_c and β_c in step 0, and β_c in step 2, is beyond the scope this paper. Analytical calculations can be used, see for example references [7] and [8]. There are also several commercial available software tools that can be used for this purpose.

The calculations of step 1 can be done using only pen, paper, and a calculator. However, a spreadsheet program or implementing a simple script will ease the work. Nexans Norway AS has implemented step 1 in a spreadsheet.

CALCULATING STEP 1

This section derives the calculations to be performed in step 1 of each iteration.

Inputs to Step 1

At iteration k, the calculation of step 1 takes the following inputs:

- $N_1(k-1)$, $N_2(k-1)$, $r_1(k-1)$, and $r_2(k-1)$. These values were computed in step 1 of iteration $k-1$ (for the first iteration the initial values are to be used). These values will be updated for each iteration.

- $\beta_c(k-1)$. This value was computed in step 2 in iteration $k-1$ (for the first iteration the value was computed in step 0). This value will be updated for each iteration.

- EA_c, E_1, E_2, R_1, R_2, α_1, and α_2. These values are fixed, i.e. they are not updated during the iteration process.

Outputs from Step 1

At iteration k, the calculations in step 1 provide the following outputs:

- $N_1(k)$, $N_2(k)$, $r_1(k)$, and $r_2(k)$. These values will be updated for each iteration. These values are to be used as inputs to step 2 of iteration k, and to step 1 of iteration $k+1$.

An Armor Wire's Contribution to the Cable's Axial Stiffness

All helical cable elements have the same helix center, which is the center of the cable's cross section. While helices are three dimensional geometries, it is common to illustrate these geometries in two dimensions as shown in Figure 2.
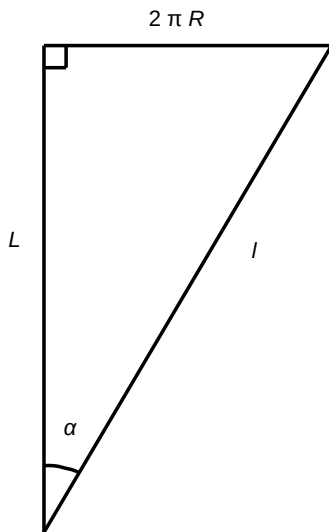

Figure 2: The geometric relationship between l, L, R, and α.

The pitch length, L, is the axial length of the cable corresponding to one revolution of the helix. Elements in the same cable layer always have the same pitch length. The element length, l, is the length of the cable element over one pitch length. The pitch radius, R, is the radius from center of the cable to center of the element. The pitch angle, α, is the angle between the cable's axis (length direction) and the tangent of the helix.

This section derives the individual wire's contribution to the cable's axial stiffness, EA_c. From Figure 2, Pythagoras' theorem gives

$$l^2 = (2\pi R)^2 + L^2. \tag{1}$$

Implicit derivation with respect to L gives

$$2l\frac{\mathrm{d}l}{\mathrm{d}L} = 2L, \tag{2}$$

$$\mathrm{d}l = \frac{L}{l}\mathrm{d}L = \cos(\alpha)\,\mathrm{d}L. \tag{3}$$

Dividing by L, and using $L = l\cos(\alpha)$, gives

$$\frac{\mathrm{d}l}{L} = \frac{\mathrm{d}l}{l\cos(\alpha)} = \cos(\alpha)\frac{\mathrm{d}L}{L}, \tag{4}$$

$$\frac{\mathrm{d}l}{l} = \cos^2(\alpha)\frac{\mathrm{d}L}{L}, \tag{5}$$

$$\varepsilon = \cos^2(\alpha)\varepsilon_c. \tag{6}$$

In Eq. 6 it is used that the cable's axial elongation is $\varepsilon_c \overset{\text{def}}{=} \mathrm{d}L/L$, while the element's elongation is $\varepsilon \overset{\text{def}}{=} \mathrm{d}l/l$. A cable element's axial tension is given as $T = EA\varepsilon$. Hence, Eq. 6 can be rewritten as

$$\varepsilon_c = \frac{\varepsilon}{\cos^2(\alpha)} = \frac{EA\varepsilon}{EA\cos^2(\alpha)} = \frac{T}{EA\cos^2(\alpha)} \tag{7}$$
$$= \frac{T\cos(\alpha)}{EA\cos^3(\alpha)}.$$

Reorganizing Eq. 7 gives

$$\frac{T\cos(\alpha)}{\varepsilon_c} = EA\cos^3(\alpha). \tag{8}$$

$T\cos(\alpha)$ is the component of T along the cable's axial direction, i.e. along edge L of Figure 2. This is the component that carries part of the cable's axial tension. The cable's axial stiffness is defined as $\mathrm{EA}_c \overset{\text{def}}{=} T_c/\varepsilon_c$. Eq. 8 is then the contribution of an individual cable element to the cable's axial stiffness, EA_c. Hence, the contribution to EA_c from all armor wires in armor layer i is

$$N_i E_i A_i \cos^3(\alpha_i). \tag{9}$$

An Armor Wire's Contribution to the Cable's Torsion Balance

This section derives the individual armor wire's contribution to the cable's torsion moment to axial tension ratio. The axial tension of a cable element, T, acts along edge l of Figure 2. The component $T\sin(\alpha)$, i.e. along the edge $2\pi R$ in the figure, acts in the circumferential direction of the cable, i.e normal to the cable's length direction and normal to the

cable's radius. This force component sets up a torsion moment, which lever arm is the cable element's pitch radius, R. Hence, the torsion moment caused by an individual armor wire, M_T, is the lever arm, R, multiplied by the force component, $T\sin(\alpha)$, i.e.

$$M_T = RT\sin(\alpha) = EAR\varepsilon\sin(\alpha) \qquad (10)$$
$$= EAR\varepsilon_c\cos^2(\alpha)\sin(\alpha).$$

In Eq. 10 it is used that $T = EA\varepsilon$, and Eq. 6 is inserted. Inserting the definition of the cable's axial stiffness into Eq. 10 gives

$$M_T = EAR\cos^2(\alpha)\sin(\alpha)\frac{T_c}{\text{EA}_c}, \qquad (11)$$

$$\beta \stackrel{\text{def}}{=} \frac{M_T}{T_c} = \frac{EAR\cos^2(\alpha)\sin(\alpha)}{\text{EA}_c}. \qquad (12)$$

In Eq. 12, β is the cable element's contribution to the cable's torsion moment to axial tension ratio, β_c. Hence, the contribution to β_c from all armor wires in armor layer i is

$$\beta_i = \frac{N_i E_i A_i R_i \cos^2(\alpha_i)\sin(\alpha_i)}{\text{EA}_c}. \qquad (13)$$

Calculating the Number of Armor Wires and the Wire Radii

Eq. 9 expresses an armor layer's contribution to the cable's axial stiffness, EA_c. Hence, for EA_c to be constant from iteration $k-1$ to k, it must be required that

$$N_1(k)E_1 A_1(k)\cos^3(\alpha_1) \qquad (14)$$
$$+ N_2(k)E_2 A_2(k)\cos^3(\alpha_2)$$
$$= N_1(k-1)E_1 A_1(k-1)\cos^3(\alpha_1)$$
$$+ N_2(k-1)E_2 A_2(k-1)\cos^3(\alpha_2).$$

Eq. 14 can be rewritten to

$$M_1(k)E_1\cos^3(\alpha_1) + M_2(k)E_2\cos^3(\alpha_2) = 0, \quad (15)$$

where

$$M_i(k) \stackrel{\text{def}}{=} N_i(k)A_i(k) - N_i(k-1)A_i(k-1). \quad (16)$$

From Eq. 13 the change of armor layer i's contribution to β_c from iteration $k-1$ to k is

$$\beta_i(k) - \beta_i(k-1) \qquad (17)$$
$$= [N_i(k)A_i(k) - N_i(k-1)A_i(k-1)]$$
$$\times \frac{E_i R_i \cos^2(\alpha_i)\sin(\alpha_i)}{\text{EA}_c}$$
$$= \frac{M_i(k)E_i R_i \cos^2(\alpha_i)\sin(\alpha_i)}{\text{EA}_c}.$$

The change of β_c from $k-1$ to k is

$$\beta_c(k) - \beta_c(k-1) \qquad (18)$$
$$= [\beta_1(k) - \beta_1(k-1)] + [\beta_2(k) - \beta_2(k-1)].$$

The objective of the algorithm is to achieve $\beta_c = 0$. Inserting Eq. 17 and $\beta_c(k) = 0$ into Eq. 18 gives

$$-\beta_c(k-1) = \frac{M_1(k)E_1 R_1 \cos^2(\alpha_1)\sin(\alpha_1)}{\text{EA}_c} \qquad (19)$$
$$+ \frac{M_2(k)E_2 R_2 \cos^2(\alpha_2)\sin(\alpha_2)}{\text{EA}_c}.$$

Eq. 15 and Eq. 19 make a set of equations which is linear in $M_1(k)$ and $M_2(k)$. Solving with respect to $M_1(k)$ and $M_2(k)$ gives

$$M_1(k) \qquad (20)$$
$$= \frac{-\beta_c(k-1)\text{EA}_c\cos(\alpha_2)}{E_1\left[R_1\cos^2(\alpha_1)\sin(\alpha_1)\cos(\alpha_2) - R_2\cos^3(\alpha_1)\sin(\alpha_2)\right]},$$

$$M_2(k) \qquad (21)$$
$$= \frac{-\beta_c(k-1)\text{EA}_c\cos(\alpha_1)}{E_2\left[R_2\cos(\alpha_1)\cos^2(\alpha_2)\sin(\alpha_2) - R_1\sin(\alpha_1)\cos^3(\alpha_2)\right]}.$$

Eq. 20 and Eq. 21 express how much the total cross section area of all armor wires in armor layer 1 and 2, respectively, must be changed for the cable to be torsion balanced, while preserving its axial stiffness. However, the equations contain insufficient information to decide $N_i(k)$ and $r_i(k)$. This will be addressed next.

In the derivation to follow, the notation $\bar{N}_i(k)$ and $\bar{r}_i(k)$ will be used instead of $N_i(k)$ and $r_i(k)$, respectively. $\bar{N}_i(k)$ and $\bar{r}_i(k)$ are temporarily theoretical

values that are not constrained to $\bar{N}_i(k)$ being an integer.

Under the assumption of constant pitch radii for both armor layers, the requirement of constant fill factors can be expressed as

$$\bar{N}_i(k)\bar{r}_i(k) = N_i(k-1)r_i(k-1). \qquad (22)$$

Using $A_i = \pi r_i^2$, Eq. 16 can be rewritten to

$$\pi \bar{N}_i(k)\bar{r}_i(k)^2 = \pi N_i(k-1)r_i(k-1)^2 + M_i(k). \qquad (23)$$

Inserting Eq. 22 into Eq. 23 and solving for $\bar{r}_i(k)$ gives

$$\bar{r}_i(k) = r_i(k-1) + \frac{M_i(k)}{\pi N_i(k-1)r_i(k-1)}. \qquad (24)$$

Then inserting Eq. 24 into Eq. 22 and solving for $\bar{N}_i(k)$ obtains

$$\bar{N}_i(k) = \frac{\pi N_i(k-1)^2 r_i(k-1)^2}{\pi N_i(k-1)r_i(k-1)^2 + M_i(k)}. \qquad (25)$$

Eq. 24 and Eq. 25 give values for $\bar{N}_i$ and $\bar{r}_i$ that torsion balance the cable, while preserving the cable's axial stiffness and the layers' fill factors. However, these values are infeasible because $\bar{N}_i$ is not constrained to being an integer. Now the notation N_i and r_i are re-introduced, where N_i is an integer. The true number of armor wires in layer i can be computed as

$$N_i(k) \qquad (26)$$
$$= \min\left(\lfloor \bar{N}_i(k) \rfloor, N_i^{\max}\right)$$
$$= \min\left(\left\lfloor \frac{\pi N_i(k-1)^2 r_i(k-1)^2}{\pi N_i(k-1)r_i(k-1)^2 + M_i(k)} \right\rfloor, N_i^{\max}\right).$$

In Eq. 26, $\min(\cdot)$ is the function that returns the lowest of its arguments. The floor function, $\lfloor \cdot \rfloor$, truncates downward to the nearest integer. Using the floor function, instead of the ceil function, ensures that the fill factors do not increase, which could have resulted in over-filled armor layers. $N_i^{\max}$ is an upper limit of the number of armor wires, which is set based on practical considerations.

Replacing $\bar{N}_i(k)$ and $\bar{r}_i(k)$ with $N_i(k)$ and $r_i(k)$, respectively, in Eq. 23, and solving for $r_i(k)$ gives the true radii of the armor wires in each layer

$$r_i(k) = \sqrt{\frac{\pi N_i(k-1)r_i(k-1)^2 + M_i(k)}{\pi N_i(k)}}. \qquad (27)$$

The calculations to be performed in step 1 of the torsion balancing algorithm can then be summarized as

1. Calculate $M_1(k)$ and $M_2(k)$ from Eq. 20 and Eq. 21, respectively.

2. Calculate $N_1(k)$ and $N_2(k)$ from Eq. 26.

3. Calculate $r_1(k)$ and $r_2(k)$ from Eq. 27.

$M_i(k)$ is a temporary variable that is used for calculating $N_i(k)$ and $r_i(k)$. When $N_i(k)$ and $r_i(k)$ have been calculated, $M_i(k)$ is abandoned.

Eq. 22 ensures constant fill factor only if R_i is constant, which is an approximation. If the true R_i is decreased for one or both armor layers, it is recommended to verify that the fill factor has not become too high. If the fill factor is too high, it can be reduced by setting $N_i^{\max}$ in Eq. 26 to a value lower than $N_i(k)$, and then re-calculate $N_i(k)$ and $r_i(k)$.

TORSION BALANCING THE DEEP-WATER DEH RISER

The torsion balancing algorithm presented in this paper was initially developed for the deep-water DEH riser cable shown in Figure 1.

Initially, the torsion moment to axial tension ratio, β_c, was 1.2×10^{-3} Nm/N. After two iterations of torsion balancing, β_c is reduced by 98% to 2.2×10^{-5} Nm/N. After four iterations, β_c is reduced by more than 99.9% to 8.6×10^{-7} Nm/N.

Although the torsion balance improves significantly over the third and forth iteration, it is believed that this is only of academic interest. In practice, due to tolerances of the armor wires as well as during production of the cable, it seems unlikely that the improvements over the third and forth iterations will be present in the real-life cable.

Figure 3 illustrates how the cable's torsion moment to axial tension ratio, β_c, improves over each iteration of the torsion balancing algorithm. Note that the scale of the figure is logarithmic.
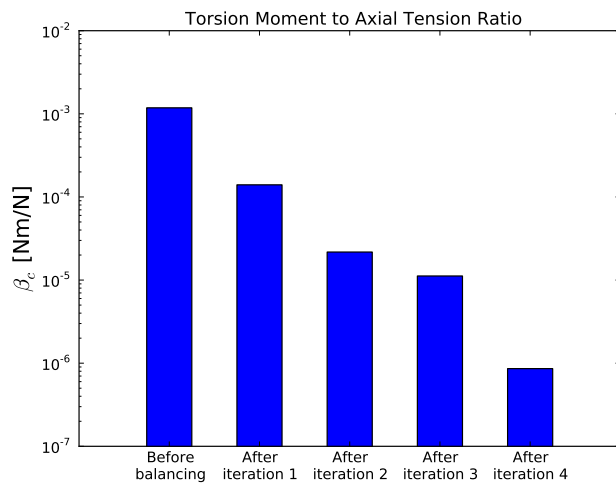
Figure 3: Improvement of β_c for each iteration. Note that the scale is logarithmic.

CONCLUSIONS

This paper derives an iterative algorithm for torsion balancing deep-water cables and umbilicals. The algorithm was developed during a research project where Nexans Norway AS concluded that a deep-water DEH riser cable for 2 300 m water depth is feasible.

The torsion balancing algorithm works very well. After two iterations, the torsion unbalance of the deep-water DEH riser cable (quantified as the cable's torsion moment to axial tension ratio) is reduced by 98%.

REFERENCES

[1] A. Nysveen, H. Kulbotten, J. K. Lervik, A. H. Børnes, M. Høyer-Hansen, and J. J. Bremnes. Direct Electrical Heating of Subsea Pipelines - Technology Development and Operating Experience. *IEEE Transactions on Industry Applications*, 43:118 – 129, 2007.

[2] J. K. Lervik, M. Høyer-Hansen, Ø. Iversen, and S. Nilsson. New Developments of Direct Electrical Heating for Flow Assurance. In *Proceedings of the Twenty-second (2012) International Offshore and Polar Engineering Conference - Rhodes, Greece*, 2012.

[3] S. Dretvik and A. H. Børnes. Direct Heated Flowlines in the Åsgard Field. In *Proceedings of the Eleventh (2001) International Offshore and Polar Engineering Conference - Stavanger, Norway*, 2001.

[4] S. Kvande. Direct Electrical Heating Goes Deeper. *E&P Magazine June 2014*, 2014.

[5] R. Slora, S. Karlsen, S. Lund, P. A. Osborg, and K. Heide. Qualification of Dynamic Deep Water Power Cable. In *Proceedings of the 2010 Offshore Technology Conference - Houston, Texas, USA*, 2010.

[6] R. Slora, S. Karlsen, and P. A. Osborg. Mechanical Qualification of Dynamic Deep Water Power Cable. In *Proceedings of the 30th International Conference on Ocean, Offshore and Arctic Engineering, OMAE 2011 - Rotterdam, the Netherlands*, 2011.

[7] R. H. Knapp. Derivation of a new stiffness matrix for helically armoured cables considering tension and torsion. *International Journal for Numerical Methods in Engineering*, 14:515 – 529, 1979.

[8] E. Kebadze. *Theoretical Modelling of Unbonded Flexible Pipe Cross-Sections*. PhD thesis, South Bank University, 2000.

MODELING THE EFFECT OF TEMPERATURE AND FREQUENCY ON BITUMEN-COATED HELICAL CABLE ELEMENTS

Bjørn Konradsen[1]
Technological Analyses Centre, Hybrid Underwater Cables,
Nexans Norway

Steinar V. Ouren
Material R&D Centre, Submarine High Voltage Division,
Nexans Norway

ABSTRACT

High voltage submarine cables and umbilicals are armored using galvanized steel wires. Polymer modified bitumen (PMB) is used to protect these wires from corrosion. During handling (spooling and bending) of cables at low temperatures the PMB will give rise to high shear forces between the armoring wires which reduce the cable's capacity (allowed combinations of axial tension and bending curvature) and increase the fatigue damage. It is therefore of interest to investigate the relationship of the viscoelastic properties of PMB and temperature. Material testing has included characterization of PMB by a controlled stress rheometer from -15 to +30 ^{O}C. The applied frequency was in the range 0.005 Hz to 0.5 Hz. The tests were done at strain values of 0.01%, 0.1% and 1%. Different parallels were analyzed with respect to variance/precision in the data. The results indicate that high strain and high frequency greatly affect the variance at low temperatures. The average of the parallels was used for making a regression model for the complex shear modulus, G*, as a function of temperature, frequency and softening point. This paper focuses on building a model for prediction of minimum temperature and maximum frequency for cable handling with respect to the viscoelastic behavior of polymer modified bitumen.

Keywords: Rheology, Bitumen, Cables, Umbilicals

NOMENCLATURE

Latin:

A_c	wire cross section area [mm²]
A_w	wire wetted area [mm²]
b_1	displacement of armor wire layer 1 [mm]
b_2	displacement of armor wire layer 2 [mm]
C_w	armor wire circumference [mm]
CoV	coefficient of variation (= stdev/average)
d_R	relative displacement between wires in layers 1 and 2 [mm]
F_y	yield force [N]
G	shear modulus [MPa]
G_{max}	maximum shear modulus [MPa]

$G*$	complex shear modulus [MPa]
i	index for layer 1, 2
$l_{p,i}$	pitch length in armor layer i [mm]
$l_{w,i}$	wetted length of armor wire in layer i [mm]
R	cable bending radius [m]
$r_{p,i}$	pitch radius in armor layer i [mm]
s	arc length [mm]
SP	softening point ("Ring & Ball") [°C]
T	temperature [°C]
V	cable (line) speed [m/min]

---

[1] Corresponding author: Phone +47 69 17 34 39 E-mail:
bjorn.konradsen@nexans.com

Greek:

α_i pitch angle armor layer i [rad]

α_T angle between wires in layers 1 and 2 [rad]

Δy thickness of bitumen coating [mm]

γ shear strain [-]

Θ element angle in the cross section [rad]

Θ_e element end angle [rad]

Θ_s element start angle [rad]

κ cable curvature [m^{-1}]

σ_y yield limit steel wire [MPa]

τ_{max} maximum shear stress [MPa]

ω frequency [rad/s]

INTRODUCTION

To give weight, strength and protection, submarine cables and umbilicals are equipped with several layers of armor steel wires.

Figure 1 shows a picture of an umbilical. The core consists of different elements; high pressure steel tubes, electric cables, fiber optic cables and fillers. The core is protected with several layers of steel wires and an extruded polymer sheath.
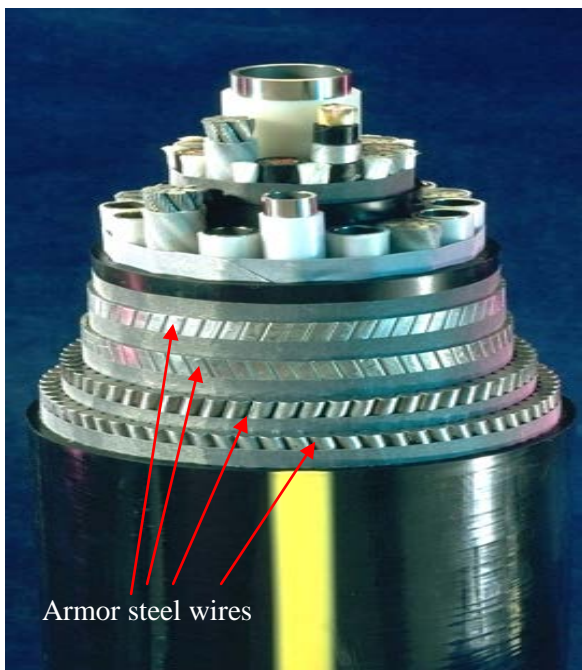
Armor steel wires

Figure 1: Example of a Nexans umbilical

To protect the steel wires from corrosion bitumen is added on to the different armoring layers.

Figure 2: Wires being coated with bitumen

Adding a viscoelastic material like bitumen will give rise to shear forces between the armoring steel wires when the cable is bent. The armor wire movement is due to tensioning and bending of the cable/umbilical. In the case of high temperatures (> 10°C) this is not considered a problem. The challenge with bitumen rises when the surrounding temperature approaches 0°C and below. This is due to the nature of the (polymer modified) bitumen which behaves liquid-like at high temperatures and becomes stiff at low temperatures.

The generation of high shear forces in the armor wires will reduce the capacity (allowed combinations of axial tension and bending curvature) of the cable/umbilical, and increase the fatigue damage. Another serious problem that may arise is "bird-caging". In this case, the armor wires become fixed due to stiff bitumen and the wires are therefore not allowed to move relative to each other. This might result in yielding and/or displacement of the wires, and formation of a "bird-cage" where the wire excess length will bulge out as shown in Figure 3.
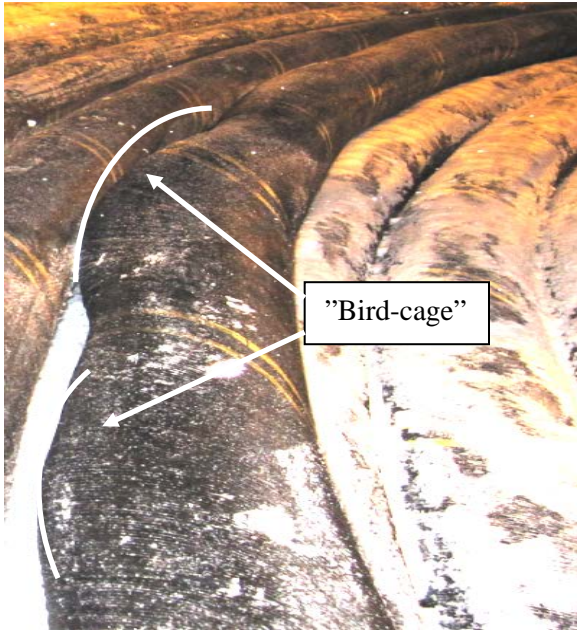
Figure 3: Cable with "bird-cage" [1]

The cross section analysis of cables and umbilicals comprises of calculation of axial-, bending- and torsion stiffnesses, capacity curves and cable/umbilical element stresses. The calculations are based mainly on numerical methods where friction between the different umbilical elements is included. The work presented in this paper aim to improve the computational handling of the effect of bitumen and the shear forces that are generated between the armoring wires while the cable/umbilical is bent.

When doing cable bending tests at Nexans Mechanical Test Centre it can be observed that the temperature has great impact on the measured bending stiffness of the cable. The reason for this is explained by the bitumen behavior.

Although there is a lot of literature to be found on the characterization of bitumen, very little is found on stresses in armor wires due to the use of bitumen in cables. Kebadze [2] and Sødahl [3] have presented work on stresses in armor wires due to friction between the wires. Also, Lutchansky [4] has reported stresses in armor wires using an elastic model (not viscoelastic).

The work presented in this paper is an attempt to combine small scale rheology tests with geometric considerations of real cables.

RHEOLOGICAL TESTING OF BITUMEN

The polymer modified bitumen (PMB) was tested on a Stress Control Rheometer with the following set-up:

Measurement system:
PP15 mm cerrated plates, 2 mm gap
Temperature: ÷ 15°C to + 30°C
Frequency sweep: 0.005 Hz - 0.5 Hz
Strain: 0.01- 0.1- 1%

MODELING STRATEGY

Testing by means of a rheometer is a fast way to characterize bitumen with respect to temperature- and frequency dependency. If the small scale results are valid for real cables, it would be beneficial with respect to both cost and time consumption.

The aim of the modeling is, for a given curvature ($\kappa = 1/R$), to be able to calculate the allowable handling temperature and cable (spooling) speed. This is based on the criterion that the shear forces generated (due to bitumen) in the armoring steel wires should not exceed the yield stress of the wires (τ_{max}).

The modeling comprises of the making of a regression model for the complex shear modulus (G^*) from rheological tests on the rheometer combined with analytical calculation of shear strain in a real cable.

REGRESSION MODEL FOR THE COMPLEX SHEAR MODULUS, G*

A polymer modified bitumen (PMB), which is used for armor steel corrosion protection with 3

different softening points (SP), was investigated in the rheometer. The tests were conducted for temperatures ranging from -15°C to 30°C in 10 steps, frequencies ranging from 0.005Hz to 0.5Hz in 11 steps, and 3 different strains (0.01%, 0.10% and 1.00%).

The runs were repeated two times (3 parallels). The average from the 3 parallels giving the least coefficient of variation (CoV) for the complex modulus (G*) were used in the regression model. As can be seen in Figure 4, the temperature has a big impact on the precision (CoV) for G* for temperatures < -5°C. Also, increasing the strain or frequency tend to increase CoV. To have the most consistent result the strain and frequency should be kept low at low temperatures.
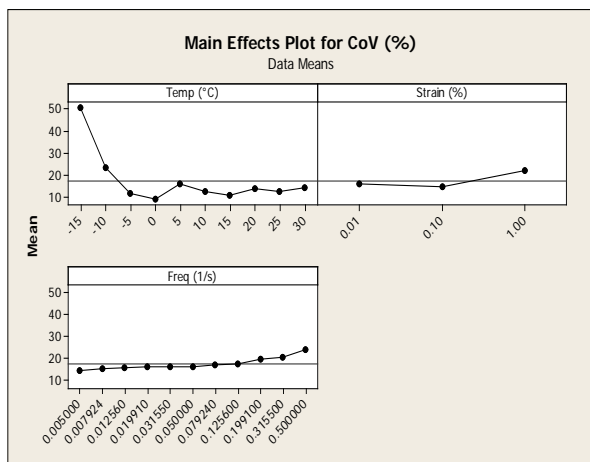
Figure 4: Main effect plot for the CoV for G* (Minitab)

The results from the rheometer tests were arranged in a Minitab Worksheet with one column for each variables; log(G*), T and log(ω). Also, the softening point (SP) was included. The rheology tests were done on 3 samples of the PMB having different softening points; 54°C, 60.5°C and 62.6°C.

"Minitab", which is the statistical software used in the present work, offers different regression model options. A linear mathematical model was chosen for representing the complex shear modulus (G*) because it is simple and gives a

very high degree of statistical significance, and a high value for the coefficient of determination (R^2 = 98.3 %). That is, by this model 98.3 % of the measured variation in log(G*) is explained by the tested levels of the softening points (SP), the temperatures (T) and the frequency (log(ω)).

The following regression equation was found for the complex shear modulus, G*:

$$\log G^* = a + bSP - cT + d\log\omega \qquad (1)$$

where a, b, c and d are regression parameters.

By means of this model the complex shear modulus (G*) can be computed for different values of SP, T and ω.

Cable (line) speed and frequency
To find realistic values for the frequency input to the model the frequency can be expressed as:

$$\omega = \frac{V}{60R} \left[rad/_s \right] \qquad (2)$$

ESTIMATION OF THE SHEAR FORCE IN THE ARMORING WIRE

The yield force (F_y) is calculated as:

$$F_y = \sigma_y A_c \qquad (3)$$

From [4], the arc length of a bent wire helix can be computed as a function of cable bending radius (R) and wire location (Θ) in the cable cross section. When looking into the cross section of the cable, the maximum displacement when the cable is bent, will be for the wire starting at $\Theta_s = 0$ rad and ending at $\Theta_e = \frac{\pi}{2}$ rad. The displacement of the wire is found by calculating the difference in arc length s($\Theta_s = 0$, $\Theta_e = \frac{\pi}{2}$) for bent and non-bent cable.

A good approximation for the bent helix wire arc length s(Θ_s, Θ_e) is given in [4] as:

$$s_i(\theta_s, \theta_e) = a_i(\theta_e - \theta_s) - b_i(\cos \theta_e - \cos \theta_s) \quad (4)$$

The first term, $a_i(\theta_e - \theta_s)$, gives the initial arc length of non-bent helix. The second term, $b_i(\cos \theta_e - \cos \theta_s)$, gives the additional arc length when bending the helix. This term equals $-b_i$ when evaluating it for ($\theta_s = 0$, $\theta_e = \frac{\pi}{2}$). The b_i's are computed and used as a measure for maximum displacement in the different wire layers.

The a_i and b_i in (4) is given as:

$$a_i = \sqrt{\left(\frac{l_{p,i}}{2\pi}\right)^2 + r_{p,i}^2} \quad (5)$$

$$b_i = \frac{\left(\frac{l_{p,i}}{2\pi}\right)^2 r_{p,i}}{R\sqrt{\left(\frac{l_{p,i}}{2\pi}\right)^2 + r_{p,i}^2}} \quad (6)$$

The relative displacement between layer 1 and 2, d_R, is calculated using the cosine rule:

$$d_R = \sqrt{b_1^2 + b_2^2 - 2b_1 b_2 \cos \alpha_T} \quad (7)$$

The pitch angle, α_i, is calculated as:

$$\alpha_i = \tan^{-1}\left(2\pi \frac{r_{p,i}}{l_{p,i}}\right) \quad (8)$$

And the angle between the wires in the first and second layer (α_T) expressed as

$$\alpha_T = \alpha_1 + \alpha_2 \quad (9)$$

The shear strain can now be calculated as

$$\gamma = \frac{d_R}{\Delta y} \quad (10)$$

where Δy (the average bitumen thickness) is given a typical value of 0.5 mm.

As wetted wire length for calculation, $l_{w,i}$, is used as a quarter of the non-bent helical wire length ($\theta_s = 0$, $\theta_e = \frac{\pi}{2}$) which equals the initial wire length that is subjected to displacement. The wetted wire area (A_w) is calculated as

$$A_w = C_w l_{w,2} \quad (11)$$

In (11), $l_{w,2}$ is used since this is the wire that experiences the largest shear force (biggest displacement).

The maximum allowable shear stress in the steel wire is calculated as

$$\tau_{max} = \frac{F_y}{A_w} \quad (12)$$

This leads to the maximum value of the shear modulus

$$G_{max} = \frac{\tau_{max}}{\gamma} \quad (13)$$

The final step is to use G_{max} as the maximum value for G^* in the regression model, and then solve the model with respect to temperature for different values of R, V and SP (for given σ_y, $l_{p,i}$, $r_{p,i}$, and wire geometry).

The model and results will be subject to further validation. (See "FURTHER WORK").

EXAMPLE WITH REAL CABLE DATA

Input:
- yield limit steel wire = σ_y MPa
- armour wire cross section area = A_c mm²
- pitch length in armour layer 1 = $l_{p,1}$ mm
- pitch radius in armour layer 1 = $r_{p,1}$ mm
- pitch length in armour layer 2 = $l_{p,2}$ mm
- pitch radius in armour layer 2 = $r_{p,2}$ mm
- softening point = SP°C

By changing the model input for bending radius and cable spooling speed, a contour plot was

made by means of Excel spreadsheet and Minitab.

The contour plot in Figure 5 shows the acceptable combinations of bending radius and line speed for given temperatures. Calculations shows that increasing the softening point from 54°C to 60°C will affect the acceptable temperature by +0.3°C per 1°C increase in softening point.
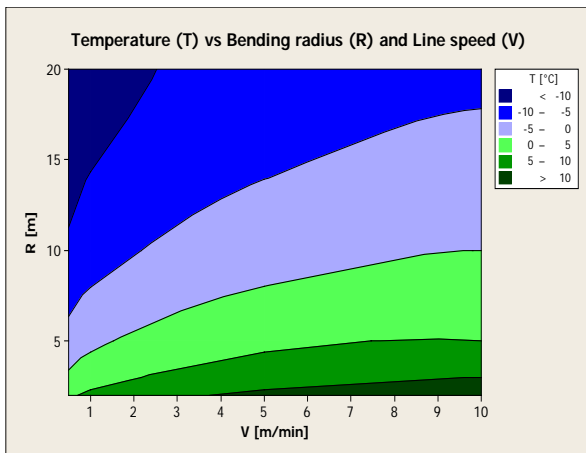
Figure 5: Contour plot of T vs R and V (Minitab)

Example: Using the contour plot

The cable temperature is 0°C.
The cable is subjected to a bending radius of 5 m.
From the contour plot: The cable line speed should be equal to or less than 1.5 m/min.

To increase the cable speed to 5 m/min (still at T = 0°C) the bending radius has to be increased from 5 m to 8 m.

FURTHER WORK

Even though the model presented here seems to function well, giving apparently realistic results, there are a couple of issues that should be discussed: The rheometer analysis is restricted to low strains (< 1 %), while strains up to 500 % have been estimated in real cable armoring. Also, the model is restricted to just one kind of PMB (although with different SP's).

So, prior to further implementation, the model has to be verified through cable spooling and bending tests. Also, the model will be compared to bigger scale tests that will be performed on bitumen samples using larger strains and amplitudes [5].

CONCLUSIONS

From the wire geometry, the maximum shear force on the armoring steel wires is estimated. This serves as a criterion for computation of the acceptable combination of bending radius, cable spooling speed and temperature by the use of the regression model for the complex shear modulus found from analyses of the polymer modified bitumen on the rheometer. An example with real cable data indicates that to increase cable spooling speed from 1.5 m/min to 5 m/min at T = 0°C, the bending radius (R) has to be increased from 5 m to 8 m.

REFERENCES

[1]   Ouren, S. *Viscoelastic Behaviour of Polymer Modified Bitumen at Low Temperatures.* AERC 2014

[2]   Kebadze, E. *Theoretical modelling of unbonded flexible pipe cross-sections*, South bank University, 2000

[3]   Sødahl, N.et al *Efficient fatigue analysis of helix elements in umbilical and flexible risers*, OMAE2010-21012

[4]   Lutchansky, M. *Axial stress in armour wires of bent submarine cables.* Journal of Engineering Industry, 91(3):687-693, 1969

[5]   Olsen, E. *Viscoelastic Behavior of Bitumen in Dynamic Control Umbilicals.* OMAE2014-23178

DERIVING ANALYTICAL AXISYMMETRIC CROSS SECTION ANALYSIS AND COMPARING WITH FEM SIMULATIONS

Magnus Komperød[*]
Technological Analyses Centre
Nexans Norway AS
P. O. Box 42, 1751 HALDEN
Norway

ABSTRACT

Direct electrical heating (DEH) is a technology for preventing hydrate formation and wax deposit inside oil and gas pipelines. Nexans Norway AS is researching and developing deep-water DEH solutions. The company has already produced a deep-water DEH piggyback cable that can carry its own weight at 1 070 m water depth. When this DEH system is installed outside the coast of Africa, it will be the world's deepest DEH system.

This paper derives axisymmetric cross section analysis calculations. The calculations are then applied to the deep-water DEH piggyback cable and compared to finite element method (FEM) simulations of the same cable. There are very good agreements between the analytical calculations and the FEM simulations. For three of five analysis results the differences are 0.6% or less. The largest difference is 4.2%, while the average difference (absolute values) is 1.8%.

Keywords: Axial Stiffness; Axisymmetric Analysis; Cross Section Analysis; DEH; Direct Electrical Heating; Offshore Technology; Subsea Cable; Torsion Stiffness.

NOTATION

A Cross section area of cable element [m^2].

E E-modulus of cable element [Pa].

$\vec{F}_c$ Load vector of the cable.

$\vec{F}_i$ Load vector of cable element i.

G G-modulus (shear modulus) of cable element [Pa].

K_c Stiffness matrix of the cable.

K_i Stiffness matrix of cable element i.

L Pitch length of cable element [m].

l Length of cable element over one pitch length [m].

$M_{T,c}$ The cable's torsion moment [Nm].

$M_{T,i}$ Contribution to the cable's torsion moment from cable element i [Nm].

R Pitch radius of cable element [m].

r Element radius of cable element [m].

r_i Inner element radius of cable element [m].

r_o Outer element radius of cable element [m].

T_c The cable's axial tension [N].

T_i Contribution to the cable's axial tension from cable element i [N].

$\vec{u}_c$ Displacement vector of the cable and all cable elements.

V Volume of cable element [m^3].

α Pitch angle of cable element [rad].

ε_c Axial cable strain [-].

ε_{xx} Axial element strain [-].

$\gamma_{x\theta}$ Shear strain in hoop direction on the surface perpendicular to the cylinder's axis (length direction) [-].

φ_c Cable twist per cable unit length [rad/m].

θ Angular position relative to the center of the cable element [rad].

Π Potential energy of cable element [J].

---

[*]Corresponding author: Phone: +47 69 17 35 39 E-mail: magnus.komperod@nexans.com

Negative values of L indicate left lay direction, and

positive values of L indicate right lay direction. Similarly, negative values of α indicate left lay direction, and positive values of α indicate right lay direction. All other length values are always positive.

INTRODUCTION

The world's increasing energy demand, combined with the exhaustion of many easily accessible oil and gas reserves, drives the petroleum industry into deeper waters. Manufacturers of subsea cables and umbilicals are among those who face the technological challenges of increased water depths.

Another significant challenge of offshore petroleum production is that the pipeline content is cooled by the surrounding water. As the pipeline content drops to a certain temperature, hydrates may be formed and wax may start to deposit inside the pipeline wall. Hydrates and wax may partially, or even fully, block the pipeline. Hydrate formation may start at temperature as high as 25°C, while wax deposit may start at 35-40°C [1].

There are several ways to prevent hydrate formation and wax deposition. An intuitive solution is to apply thermal insulation at the outer surface of the pipeline. However, at long pipelines, low flow rates, or production shut downs, this solution may be insufficient.

Depressurizing the pipeline content may be used to prevent hydrate formation. However, at deepwater pipelines, high pressure is required to bring the pipeline content to topside. Plug removal by depressurizing also faces the same problem at deepwater pipelines [2].

When thermal insulation and depressurizing are insufficient, a commonly used approach is to add chemicals to the pipeline in order to reduce the critical temperature for hydrate formation and wax deposition. Methanol or glycol is commonly used [1, 3]. However, as explained in reference [1], adding chemicals has practical as well as environmental disadvantages.

Another approach to prevent hydrate formation and wax deposition is to use power cables inside the thermal insulation of the pipeline. The power cables function as heating elements heating the pipeline. However, embedding the cables inside the thermal insulation may lead to practical difficulties [1].

A technology that has emerged over the last years is direct electrical heating (DEH). The first DEH system was installed at Statoil's Åsgard oil and gas field in the Norwegian Sea in year 2000 [4]. Nexans Norway AS qualified the DEH technology together with Statoil and SINTEF.

In DEH systems, the electrical resistance of the steel in the pipeline wall is used as a heating element. A single phase cable, referred to as piggyback cable (PBC), is strapped to the pipeline. In the far end (the end of the pipeline far away from the topside) the PBC is connected ("short circuited") to the pipeline. In the near end (the end of the pipeline close to the topside), a two-phase DEH riser cable is connected to the PBC and the pipeline; one phase of the riser cable is connected to the PBC, and the other phase of the riser cable is connected to the pipeline. When the riser cable is energized topside, energy is transferred through the PBC into the steel of the pipeline wall.

Nexans Norway AS is currently developing deepwater DEH solutions. A piggyback cable that is reparable, i.e. can carry its own weight, at 1 070 m water depth is already produced by Nexans in a delivery project. The cross section of this cable is shown in Figure 1. When this DEH system is installed outside the coast of Africa, it will be the world's deepest DEH system [4].
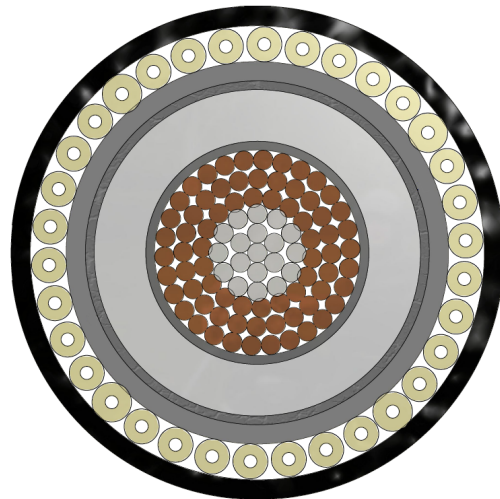

Figure 1: Cross section of the deep-water DEH piggyback cable.

The piggyback cable shown in Figure 1 has 19 (1 + 6 + 12) steel strands in center (gray color in the figure). The purpose of the steel strands is to improve the mechanical capacity of the conductor. This solution is patented by Nexans Norway AS. Outside the steel strands there are 72 (18 + 24 + 30) cop-

per strands (brown color). Outside the stranded conductor there are an electric insulation system (dark gray and light gray colors) and an inner sheath (gray color). Outside the inner sheath there are fillers for mechanical protection (yellow color), and then the outer sheath (black color).

The contribution of this paper is to derive analytical calculations for axisymmetric analysis of the deepwater DEH piggyback cable presented in Figure 1, and compare these analysis results with finite element method (FEM) simulations of the same cable. Analytical calculations increase the analysts' theoretical and practical understanding compared to using FEM tools. Analytical calculations are also very efficient, both in terms of man-hours and CPU time. The analytical derivations presented in this paper are strongly inspired by references [5] and [6].

CROSS SECTION ANALYSIS AND AXISYMMETRIC ANALYSIS

The term cross section analysis refers to a set of analyses on cables, including umbilicals, that describes the cables' mechanical properties. Nexans Norway AS usually includes the following analyses in cross section analyses of DEH cables and umbilicals:

- Axial stiffness when the cable is free to twist [N].

- Axial stiffness when the cable is prevented from twisting [N].

- Bending stiffness [Nm/(m^{-1})].

- Torsion stiffness [Nm/(rad/m)].

- Torsion angle to axial tension ratio when the cable is free to twist [(rad/m)/N].

- Torsion moment to axial tension ratio when the cable is prevented from twisting [Nm/N].

- Capacity during installation.

- Capacity during operation.

The cable's capacity refers to allowed combinations of axial tension [N] and bending curvature [m^{-1}]. Cross section analyses can be done by analytical calculations or by FEM simulations. Reference [5]

gives an excellent introduction to the theoretical fundament for analytical calculations. Several other publications, for example references [6] and [7], also cover parts of this theory.

There also exist commercial available software tools for performing cross section analyses. Both software tools based on analytical calculations and software tools based on FEM simulations are available. The term axisymmetric analysis refers to a subset of those analyses included in the cross section analysis. Axisymmetric analysis includes exactly those analyses where the cable is straight (not bent):

- Axial stiffness when the cable is free to twist [N].

- Axial stiffness when the cable is prevented from twisting [N].

- Torsion stiffness [Nm/(rad/m)].

- Torsion angle to axial tension ratio when the cable is free to twist [(rad/m)/N].

- Torsion moment to axial tension ratio when the cable is prevented from twisting [Nm/N].

As will be shown in this paper, the analyses included in the axisymmetric analysis are mathematically closely related and can be derived from the same stiffness matrix.

DERIVATION OF AXISYMMETRIC ANALYSIS

The derivation presented in this section is strongly inspired by references [5] and [6]. The following assumptions and simplifications apply: (i) Friction is neglected. This is a common assumption in axisymmetric analysis, see for example reference [7]. (Please note that friction is important in the non-axisymmetric part of the cross section analysis.) (ii) Linear elastic materials are assumed. (iii) Radial displacement is neglected. (iv) The Poisson ratio effect is neglected. (v) Helical elements are modeled as tendons. That is, the elements have axial stiffness in tension and compression, while torsion stiffness and bending stiffness are neglected. Please note that the helical elements' influence on the cable's torsion moment and torsion stiffness is included in the model.

From the author's point of view, assumption (i) is probably correct for axisymmetrical analysis in general. The other assumptions must be used with care. In some cases these assumptions have negligible influence on the analysis results, while in other cases they may introduce significant inaccuracy. As shown later in this paper, the analytical calculations give very good agreements with FEM simulations for the deep-water DEH piggyback cable presented in Figure 1. Hence, the applied assumptions do not significantly deteriorate the accuracy of the calculations.

As seen from Figure 1, the cable elements of the PBC can be divided into two types: (i) Non-helical cylinders. Those are the electric isolation system, the inner sheath, and the outer sheath. (ii) Helical elements. Those are the strands of the conductor, as well as the protection fillers. (The center strand of the conductor is modeled as a helical element with zero pitch radius.)

In the axisymmetric case, i.e. when the cable is straight (not bent), the cable has two degrees of freedom: Axial strain, ε_c, and twist per cable unit length, φ_c. These variables are stacked in a vector to form the displacement vector $\vec{u}_c = [\,\varepsilon_c\,,\,\varphi_c\,]^T$. The corresponding loads are: Axial tension, T_c, and torsion moment, $M_{T,c}$. The load vector is then $\vec{F}_c = [\,T_c\,,\,M_{T,c}\,]^T$. The stiffness matrix, K_c, relates the displacement vector and the load vector

$$\vec{F}_c = K_c\,\vec{u}_c \qquad (1)$$

$$\begin{bmatrix} T_c \\ M_{T,c} \end{bmatrix} = \begin{bmatrix} k_{c,11} & k_{c,12} \\ k_{c,21} & k_{c,22} \end{bmatrix} \begin{bmatrix} \varepsilon_c \\ \varphi_c \end{bmatrix}.$$

As will be explained later in this paper, the displacement vector, $\vec{u}_c$, is common for all cable elements, as well as for the cable itself. The load vectors and the stiffness matrices are individual to each cable element. The load vector of cable element i is $\vec{F}_i$, while the load vector of the cable is $\vec{F}_c$. Similarly, the stiffness matrix of cable element i is K_i, and the stiffness matrix of the cable is K_c. The following text derives the stiffness matrices for cylinder cable elements and for helical cable elements.

Stiffness Matrix of a Cylinder Cable Element

Subject to the degrees of freedom presented above, the potential energy, Π, of a non-helical cylinder over an axial length L can be expressed as

$$\Pi(\varepsilon_c, \varphi_c) = \int_V \left(\frac{1}{2} E \varepsilon_{xx}^2 + \frac{1}{2} G \gamma_{x\theta}^2 \right) dV \qquad (2)$$
$$ - T_i L \varepsilon_c - M_{T,i} L \varphi_c.$$

The last two terms of Eq. 2 are the potential energy of the applied loads. The first expression in the integration term of Eq. 2 is the strain energy in the cylinder due to axial tension. As the cylinder is non-helical, the axial strain of the cylinder, ε_{xx}, is equal to the axial strain of the cable, ε_c. Also, the axial strain is equal over the cylinder volume. This simplifies to

$$\int_V \frac{1}{2} E \varepsilon_{xx}^2 \, dV = \frac{1}{2} E \varepsilon_c^2 \int_V dV \qquad (3)$$
$$ = \frac{1}{2} E \varepsilon_c^2 \int_0^L \int_0^{2\pi} \int_{r_i}^{r_o} r \, dr \, d\theta \, dL$$
$$ = \frac{\pi}{2} E L (r_o^2 - r_i^2) \varepsilon_c^2.$$

The second term in the integration term of Eq. 2 is the strain energy in the cylinder due to torsion. A simple geometric consideration shows that the shear strain, $\gamma_{x\theta}$, is given by $\gamma_{x\theta} = r\varphi_c$. As φ_c is constant over the cable volume, it follows that

$$\int_V \frac{1}{2} G \gamma_{x\theta}^2 \, dV = \int_V \frac{1}{2} G r^2 \varphi_c^2 \, dV \qquad (4)$$
$$ = \frac{1}{2} G \varphi_c^2 \int_V r^2 \, dV$$
$$ = \frac{1}{2} G \varphi_c^2 \int_0^L \int_0^{2\pi} \int_{r_i}^{r_o} r^2 \, r \, dr \, d\theta \, dL$$
$$ = \frac{\pi}{4} G L (r_o^4 - r_i^4) \varphi_c^2.$$

Eq. 2 can then be rewritten as

$$\Pi(\varepsilon_c, \varphi_c) = \frac{\pi}{2} E L (r_o^2 - r_i^2) \varepsilon_c^2 \qquad (5)$$
$$ + \frac{\pi}{4} G L (r_o^4 - r_i^4) \varphi_c^2$$
$$ - T_i L \varepsilon_c - M_{T,i} L \varphi_c.$$

The cable is in equilibrium when the potential energy, Π, is at a stationary point. The equilibrium conditions are then

$$\frac{\partial \Pi(\varepsilon_c, \varphi_c)}{\partial \varepsilon_c} = \pi E L(r_o{}^2 - r_i{}^2)\varepsilon_c - T_i L = 0, \qquad (6)$$

$$\frac{\partial \Pi(\varepsilon_c, \varphi_c)}{\partial \varphi_c} = \frac{\pi}{2} G L(r_o{}^4 - r_i{}^4)\varphi_c - M_{T,i} L = 0. \quad (7)$$

Dividing Eq. 6 and Eq. 7 by L gives

$$T_i = \pi E(r_o{}^2 - r_i{}^2)\varepsilon_c, \qquad (8)$$

$$M_{T,i} = \frac{\pi}{2} G(r_o{}^4 - r_i{}^4)\varphi_c. \qquad (9)$$

The stiffness matrix of a cylinder cable element is then given by

$$\vec{F}_i = K_i \vec{u}_c \qquad (10)$$

$$\begin{bmatrix} T_i \\ M_{T,i} \end{bmatrix} = \begin{bmatrix} \pi E(r_o{}^2 - r_i{}^2) & 0 \\ 0 & \frac{\pi}{2} G(r_o{}^4 - r_i{}^4) \end{bmatrix} \begin{bmatrix} \varepsilon_c \\ \varphi_c \end{bmatrix}.$$

Stiffness Matrix of a Helical Cable Element

As stated above, the helical cable elements are modeled as tendons. This means that these elements' bending stiffness and torsion stiffness are neglected. The helical element's potential energy over a pitch length, L, is then

$$\Pi(\varepsilon_c, \varphi_c) = \int_V \frac{1}{2} E \varepsilon_{xx}{}^2 \, dV \qquad (11)$$

$$- T_i L \varepsilon_c - M_{T,i} L \varphi_c.$$

The last two terms of Eq. 11 are the potential energy of the applied loads. The integration term of Eq. 11 is the strain energy in the helical element due to its axial strain. Because bending stiffness and thereby strain from bending are neglected, the axial strain is equal over the element's volume. Hence, the strain energy can be written as

$$\int_V \frac{1}{2} E \varepsilon_{xx}{}^2 \, dV = \frac{1}{2} E \varepsilon_{xx}{}^2 \int_V dV \qquad (12)$$

$$= \frac{1}{2} E \varepsilon_{xx}{}^2 \int_0^l \int_0^{2\pi} \int_0^r r \, dr \, d\theta \, dl$$

$$= \frac{\pi}{2} E l r^2 \varepsilon_{xx}{}^2$$

$$= \frac{1}{2} \frac{EAL}{\cos(\alpha)} \varepsilon_{xx}{}^2$$

In the last line of Eq. 12, it is used that $A = \pi r^2$ and $l = L/\cos(\alpha)$. As for the cylinder case, the helical element is in equilibrium when the potential energy, Π, is at a stationary point. Inserting Eq. 12 into Eq. 11 and differentiating gives

$$\frac{\partial \Pi(\varepsilon_c, \varphi_c)}{\partial \varepsilon_c} = \frac{EAL}{\cos(\alpha)} \varepsilon_{xx} \frac{\partial \varepsilon_{xx}}{\partial \varepsilon_c} - T_i L = 0, \qquad (13)$$

$$\frac{\partial \Pi(\varepsilon_c, \varphi_c)}{\partial \varphi_c} = \frac{EAL}{\cos(\alpha)} \varepsilon_{xx} \frac{\partial \varepsilon_{xx}}{\partial \varphi_c} - M_{T,i} L = 0. \quad (14)$$

The next issue is to derive ε_{xx} as function of ε_c and φ_c. While helical elements are three dimensional geometries, it is common to illustrate these geometries in two dimensions as shown in Figure 2. The pitch length, L, is the axial length of the cable corresponding to one revolution of the helix. Elements in the same cable layer always have the same pitch length. The element length, l, is the length of the cable element over one pitch length. The pitch radius, R, is the radius from center of the cable to center of the element. The pitch angle, α, is the angle between the cable's axis (length direction) and the tangent of the helix. Figure 2 shows the geometric relation between L, R, θ, l, and α. This relation is true for $\theta = 2\pi$ rad.
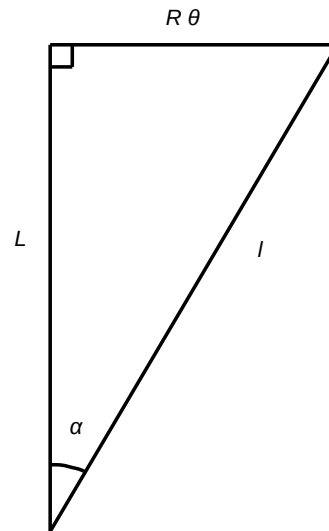

Figure 2: Geometric relation between L, l, R, θ, and α. The relation it true for $\theta = 2\pi$ rad.

Based on Figure 2, Pythagoras' theorem gives

$$l^2 = L^2 + (R\theta)^2. \tag{15}$$

Differentiation of Eq. 15 and division by $2l^2$ gives

$$\frac{\mathrm{d}l}{l} = \frac{L\mathrm{d}L}{l^2} + \frac{R^2\theta\mathrm{d}\theta}{l^2}. \tag{16}$$

In Eq. 16, R is a constant. Inserting $l = L/\cos(\alpha)$, $l = R\theta/\sin(\alpha)$, and $\theta = 2\pi$ rad gives

$$\frac{\mathrm{d}l}{l} = \cos^2(\alpha)\frac{\mathrm{d}L}{L} + \sin^2(\alpha)\frac{\mathrm{d}\theta}{2\pi}, \tag{17}$$

$$\varepsilon_{xx} = \cos^2(\alpha)\varepsilon_c + \sin^2(\alpha)\frac{L}{2\pi}\varphi_c, \tag{18}$$

$$\varepsilon_{xx} = \cos^2(\alpha)\varepsilon_c + R\cos(\alpha)\sin(\alpha)\varphi_c. \tag{19}$$

In Eq. 18 it has been used that $\varepsilon_{xx} \overset{\mathrm{def}}{=} \mathrm{d}l/l$, $\varepsilon_c \overset{\mathrm{def}}{=} \mathrm{d}L/L$, and $\mathrm{d}\theta = L\varphi_c$. In Eq. 19 it has been used that $\tan(\alpha) = 2\pi R/L$. Inserting Eq. 19 and its partial derivatives into Eq. 13 and Eq. 14, and dividing the latter equations with L gives

$$T_i = EA\cos^3(\alpha)\varepsilon_c \tag{20}$$
$$+ EAR\cos^2(\alpha)\sin(\alpha)\varphi_c,$$

$$M_{T,i} = EAR\cos^2(\alpha)\sin(\alpha)\varepsilon_c \tag{21}$$
$$+ EAR^2\cos(\alpha)\sin^2(\alpha)\varphi_c.$$

The stiffness matrix for helical elements is then

$$\vec{F}_i = K_i\vec{u}_c \tag{22}$$

$$\begin{bmatrix} T_i \\ M_{T,i} \end{bmatrix} = \begin{bmatrix} k_{i,11} & k_{i,12} \\ k_{i,21} & k_{i,22} \end{bmatrix} \begin{bmatrix} \varepsilon_c \\ \varphi_c \end{bmatrix},$$

$$k_{i,11} = EA\cos^3(\alpha),$$
$$k_{i,12} = k_{i,21} = EAR\cos^2(\alpha)\sin(\alpha),$$
$$k_{i,22} = EAR^2\cos(\alpha)\sin^2(\alpha).$$

Stiffness Matrix of Cable

The previous sections derive the stiffness matrices of non-helical cylinder elements and helical elements. This section explains how to calculate the stiffness matrix of the cable based on stiffness matrices of the cable elements.

All cable elements, as well as the cable itself, are subject to the same strain along the cable's length direction, ε_c, and the same twist along the cable's axis, φ_c. Hence, they all share the same displacement vector $\vec{u}_c = [\varepsilon_c, \varphi_c]^T$.

The axial tension of the cable, T_c, is equal to the contributions from all cable elements, $\sum_i T_i$. Similarly, the torsion moment of the cable, $M_{T,c}$, is equal to the contributions from all cable elements, $\sum_i M_{T,i}$. Therefore, the cable's load vector is equal to the sum of the load vectors of all cable elements. That is

$$\vec{F}_c = \sum_i \vec{F}_i, \tag{23}$$

$$K_c\vec{u}_c = \sum_i K_i\vec{u}_c = \left(\sum_i K_i\right)\vec{u}_c.$$

Comparison in the second row of Eq. 23 proves that the stiffness matrix of the cable, K_c, is equal to the sum of the stiffness matrices of all cable elements, i.e.

$$K_c = \sum_i K_i. \tag{24}$$

Computing Axisymmetric Analysis Results

The previous section shows how to compute the cable's stiffness matrix. This section explains how to compute the axisymmetric analysis results from the stiffness matrix. The stiffness matrix is on the form

$$\begin{bmatrix} T_c \\ M_{T,c} \end{bmatrix} = \begin{bmatrix} k_{c,11} & k_{c,12} \\ k_{c,21} & k_{c,22} \end{bmatrix} \begin{bmatrix} \varepsilon_c \\ \varphi_c \end{bmatrix}. \tag{25}$$

Note that $k_{c,12} = k_{c,21}$, both for non-helical cylinders, for helical elements, and hence for the cable itself. It is in this context more convenient to write the matrix as a set of linear equations, where it is used that $k_{c,12} = k_{c,21}$. That is

$$T_c = k_{c,11}\varepsilon_c + k_{c,12}\varphi_c, \tag{26}$$
$$M_{T,c} = k_{c,12}\varepsilon_c + k_{c,22}\varphi_c. \tag{27}$$

The following sections derive the axisymmetric results. Please note that the stiffness matrix of the cable must be calculated first, using Eq. 24, and then be

used in the calculations presented below. The opposite, i.e. to first compute the axisymmetric analyses for each cable element, and then sum these analyses to obtain the analysis for the cable will give erroneous results (except for in some special cases).

Axial Stiffness at Free Twist

When the cable is free to twist, it does not set up any torsion moment. Inserting $M_{T,c} = 0$ into Eq. 27, solving for φ_c, and inserting this into Eq. 26 gives

$$T_c = \left(k_{c,11} - \frac{k_{c,12}^2}{k_{c,22}} \right) \varepsilon_c. \tag{28}$$

Hence, the axial stiffness at free twist is $k_{c,11} - \frac{k_{c,12}^2}{k_{c,22}}$.

Axial Stiffness at No Twist

No twist is equivalent to $\varphi_c = 0$. Inserting this into Eq. 26 gives $T_c = k_{c,11}\varepsilon_c$. Hence, the axial stiffness at no twist is $k_{c,11}$.

Torsion Stiffness at Free Elongation

Solving Eq. 26 for ε_c and inserting this into Eq. 27 gives

$$M_{T,c}(T_c, \varphi_c) = \frac{k_{c,12}}{k_{c,11}} T_c + \left(k_{c,22} - \frac{k_{c,12}^2}{k_{c,11}} \right) \varphi_c, \tag{29}$$

$$\frac{\partial M_{T,c}(T_c, \varphi_c)}{\partial \varphi_c} = k_{c,22} - \frac{k_{c,12}^2}{k_{c,11}}. \tag{30}$$

Hence, the torsion stiffness at free elongation is $k_{c,22} - \frac{k_{c,12}^2}{k_{c,11}}$. Please note that in Eq. 29 and Eq. 30, $M_{T,c}$ is a function of T_c and φ_c, not a function of ε_c as in the other cases.

Torsion Angle to Axial Tension Ratio

In this case, the cable is free to twist, i.e. it sets up no torsion moment. Inserting $M_{T,c} = 0$ into Eq. 27, solving for ε_c, and inserting this into Eq. 26 gives

$$T_c = \left(-\frac{k_{c,11}k_{c,22}}{k_{c,12}} + k_{c,12} \right) \varphi_c, \tag{31}$$

$$\frac{\varphi_c}{T_c} = \frac{k_{c,12}}{k_{c,12}^2 - k_{c,11}k_{c,22}}. \tag{32}$$

Hence, the torsion angle to axial tension ratio is $\frac{k_{c,12}}{k_{c,12}^2 - k_{c,11}k_{c,22}}$.

Torsion Moment to Axial Tension Ratio

In this case, the cable is prevented from twisting. Inserting $\varphi_c = 0$ into Eq. 26 and Eq. 27, and solving both equations for ε_c gives

$$\varepsilon_c = \frac{T_c}{k_{c,11}} = \frac{M_{T,c}}{k_{c,12}}, \tag{33}$$

$$\frac{M_{T,c}}{T_c} = \frac{k_{c,12}}{k_{c,11}}. \tag{34}$$

Hence, the torsion moment to axial tension ratio is $\frac{k_{c,12}}{k_{c,11}}$.

UFLEX2D

The UFLEX program system originates from a joint Marintek and Nexans effort kicked off in 1999, resulting in a 2D software module (UFLEX2D) for structural analysis of complex umbilical cross-sections. The first version of the tool was launched in 2001. From 2005 and onwards further development of the 2D module as well as the development of a 3D module (UFLEX3D) has taken place within a Joint Industry Project (JIP). The JIP is still running, and is financed by a group of 10 sponsors covering the following oil and gas industry segments; operators, suppliers, technical service providers.

UFLEX2D is a finite element method (FEM) tool, which can be used to simulate all analysis results that Nexans Norway AS includes in cross section analyses. Figure 3 shows the UFLEX2D FEM model of the deep-water DEH piggyback cable presented in Figure 1.

COMPARING ANALYTICAL CALCULATIONS WITH FEM SIMULATIONS

Table 1 presents the differences of the analytical calculations derived in this paper and the results of the UFLEX2D FEM simulations. The table shows that there are very good agreements between the analytical calculations and the FEM simulations. For three of the five results the differences are 0.6% or less. The largest difference is 4.2%. The average difference (absolute values) is 1.8%.
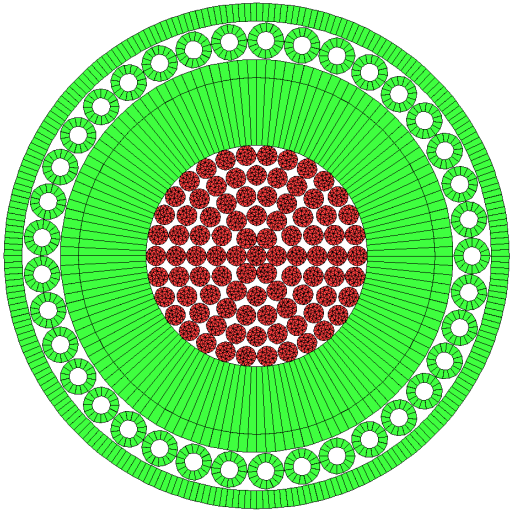
Figure 3: Finite element model of the deep-water DEH piggyback cable. The colors of the figure do not represent any physical values.

Analysis Result	Difference [%]
Axial stiffness (free twist)	0.6
Axial stiffness (no twist)	0.3
Torsion stiffness (free elongation)	−3.8
Torsion angle to axial tension ratio	4.2
Torsion moment to axial tension ratio	0.0

Table 1: Differences between analytical calculations and UFLEX2D FEM simulations.

Based on the good agreements between the analytical calculations and the FEM simulations, it is concluded that the analytical derivations presented in this paper cover the significant physical effects of the deep-water DEH piggyback cable. Further it is concluded that the applied assumptions and simplifications do not significantly deteriorate the accuracy of the calculations.

CONCLUSIONS

This paper derives analytical calculations for axisymmetric analyses. These calculations have been used to compute the axisymmetric analysis results for a deep-water DEH piggyback cable developed by Nexans Norway AS. This piggyback cable is reparable, i.e. can carry its own weight, at 1 070 m water depth. The development of the piggyback cable is part of Nexans' efforts towards deep-water DEH solutions.

The analytical calculations are compared to UFLEX2D FEM simulations. There are very good agreements between the analytical calculations and the FEM simulations. For three of the five analysis results the differences are 0.6% or less. The largest difference is 4.2%, while the average difference (absolute values) is 1.8%.

REFERENCES

[1] A. Nysveen, H. Kulbotten, J. K. Lervik, A. H. Børnes, M. Høyer-Hansen, and J. J. Bremnes. Direct Electrical Heating of Subsea Pipelines - Technology Development and Operating Experience. *IEEE Transactions on Industry Applications*, 43:118 – 129, 2007.

[2] J. K. Lervik, M. Høyer-Hansen, Ø. Iversen, and S. Nilsson. New Developments of Direct Electrical Heating for Flow Assurance. In *Proceedings of the Twenty-second (2012) International Offshore and Polar Engineering Conference - Rhodes, Greece*, 2012.

[3] S. Dretvik and A. H. Børnes. Direct Heated Flowlines in the Åsgard Field. In *Proceedings of the Eleventh (2001) International Offshore and Polar Engineering Conference - Stavanger, Norway*, 2001.

[4] S. Kvande. Direct Electrical Heating Goes Deeper. *E&P Magazine June 2014*, 2014.

[5] E. Kebadze. *Theoretical Modelling of Unbonded Flexible Pipe Cross-Sections*. PhD thesis, South Bank University, 2000.

[6] R. H. Knapp. Derivation of a new stiffness matrix for helically armoured cables considering tension and torsion. *International Journal for Numerical Methods in Engineering*, 14:515 – 529, 1979.

[7] N. Sødahl, G. Skeie, O. Steinkjær, and A. J. Kalleklev. Efficient fatigue analysis of helix elements in umbilicals and flexible risers. In *Proceedings of the ASME 29th International Conference on Ocean, Offshore and Arctic Engineering OMAE 2010*, 2010.

HOW MAXIMUM ALLOWABLE TENSION OF CABLES AND UMBILICALS IS INFLUENCED BY FRICTION

Magnus Komperød[*]
Technological Analyses Centre
Nexans Norway AS
P. O. Box 42, 1751 HALDEN
Norway

ABSTRACT

Direct electrical heating (DEH) is a technology for preventing hydrate formation and wax deposit inside oil and gas pipelines. Nexans Norway AS is researching and developing DEH solutions for deep waters. The company has produced a deep-water DEH piggyback cable that can carry its own weight at 1 070 m water depth. When this DEH system is installed outside the coast of Africa, it will be the world's deepest DEH system.

For deep-water cables, including umbilicals, the maximum allowable tension (MAT) is an important parameter that limits the water depth which the cable can be installed at. As MAT by definition is calculated for straight (non-bent) cables, it can be argued from a theoretical point of view that friction should be disregarded. However, from a practical point of view, one can argue that the cable is rarely perfectly straight, which justifies inclusion of friction.

This paper derives the relation between the cable's axial tension, the axial tensions of the individual cable elements, and friction, with emphasize on how friction influences MAT. Four different approaches for calculating friction's influence on MAT are presented. These approaches range from fully neglecting friction to including the maximum possible friction. Two approaches include friction up to a certain curvature limit, which corresponds to an "almost straight" cable, and neglect the friction for higher curvatures. The most conservative approach gives 19% lower MAT than the least conservative approach for the deep-water DEH piggyback cable.

Keywords: Axisymmetric Analysis; Cable Capacity; Capacity Curve; Cross Section Analysis; Maximum Allowable Tension; Maximum Handling Tension; Offshore Technology; Riser; Subsea Cable; Umbilical.

NOTATION

A_i Cross section area of each cable element in layer i [m^2].

C_i Total radial contact force per unit length of the cable between cable layers $i-1$ and i [N/m].

c_i Radial contact force per unit length of the cable induced by cable layer i [N/m].

E_i E-modulus of cable elements in layer i [Pa].

EA_c The cable's axial stiffness [N].

f_i Maximum possible friction on each element in cable layer i per unit length of the cable [N/m].

L_i Pitch length of cable layer i [m].

l_i Length of cable elements in layer i over one pitch length [m].

MAT   Maximum allowable tension of the cable [N].

N Number of layers of conductor strands [-].

n_i Number of strands in layer i [-].

R_i Pitch radius of cable elements in layer i [m].

r_i Element radius of cable elements in layer i [m].

[*]Corresponding author: Phone: +47 69 17 35 39 E-mail: magnus.komperod@nexans.com

SMYS   Specified minimum yield stress [Pa].

T_c The cable's axial tension [N].

$T_{a,i}$ Axial tension of each cable element in layer i due to axial cable tension [N].

α_i Pitch angle of cable elements in layer i [rad].

ε_c Axial cable strain [-].

ε_i Axial strain of cable elements in layer i [-].

κ_c The cable's bending curvature [m^{-1}].

κ_c^{limit} The upper limit of cable bending curvature for which friction is included in calculations of MAT [m^{-1}].

$\kappa_{c,i}$ The cable's bending curvature where cable elements in layer i slip at angle θ [m^{-1}].

$\kappa_{c,i}^{\text{max}}$ The maximum cable bending curvature for which $\sigma_{f,i}$ is to be calculated for cable elements in layer i [m^{-1}].

θ Angular position of cable element, relative to the center of the cable cross section [rad].

$\sigma_{a,i}$ Contribution to axial stress in cable elements of layer i due to axial tension of the cable [Pa].

$\sigma_{b,i}$ Bending stress in cable elements of layer i due to bending the cable [Pa].

$\sigma_{f,i}$ Contribution to axial stress in cable elements of layer i due to friction when bending the cable [Pa].

$\sigma_{f,i}^{\text{max}}$ Maximum possible contribution to axial stress in cable elements of layer i due to friction when bending the cable [Pa].

$\mu_{i,j}$ Coefficient of friction between elements of layer i and layer j.

Negative values of L_i and α_i indicate left lay direction, and positive values indicate right lay direction.

INTRODUCTION

The world's increasing energy demand, combined with the exhaustion of many easily accessible oil and gas reserves, drives the petroleum industry into deeper waters. Manufacturers of subsea cables and umbilicals are among those who face the technological challenges of increased water depths.

Another significant challenge of offshore petroleum production is that the pipeline content is cooled by the surrounding water. As the pipeline content drops to a certain temperature, hydrates may be formed and wax may start to deposit inside the pipeline wall. Hydrates and wax may partially, or even fully, block the pipeline. Hydrate formation may start at temperature as high as 25°C, while wax deposit may start at 35-40°C [1].

There are several ways to prevent hydrate formation and wax deposition. An intuitive solution is to apply thermal insulation at the outer surface of the pipeline. However, at long pipelines, low flow rates, or production shut downs, this solution may be insufficient.

When thermal insulation is insufficient, a commonly used approach is to add chemicals to the pipeline in order to reduce the critical temperature for hydrate formation and wax deposition. Methanol or glycol is commonly used [1, 2]. However, as explained in reference [1], adding chemicals has practical as well as environmental disadvantages.

A technology that has emerged over the last years is direct electrical heating (DEH). The first DEH system was installed at Statoil's Åsgard oil and gas field in the Norwegian Sea in year 2000 [3]. Nexans Norway AS qualified the DEH technology together with Statoil and SINTEF.

In DEH systems, the electrical resistance of the steel in the pipeline wall is used as a heating element. A single phase cable, referred to as piggyback cable (PBC), is strapped to the pipeline. In the far end (the end of the pipeline far away from the topside) the PBC is connected ("short circuited") to the pipeline. In the near end (the end of the pipeline close to the topside), a two-phase DEH riser cable is connected to the PBC and the pipeline; one phase of the riser cable is connected to the PBC, and the other phase of the riser cable is connected to the pipeline. When the riser cable is energized topside, energy is transferred through the PBC into the steel of the pipeline wall.

Nexans Norway AS is currently developing deepwater DEH solutions. A piggyback cable that is reparable, i.e. can carry its own weight, at 1 070 m water depth is already produced by Nexans in a delivery project. The cross section of this cable is shown in Figure 1. When this DEH system is installed outside the coast of Africa, it will be the world's deepest DEH system [3].

The piggyback cable presented in Figure 1 has 19 (1 + 6 + 12) steel strands in center (gray color in
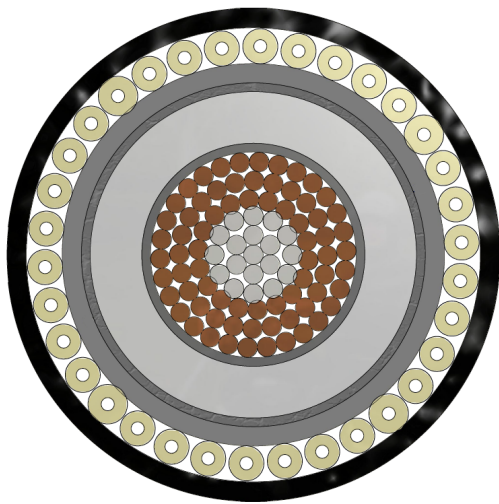
Figure 1: Cross section of the deep-water DEH piggyback cable.

the figure). The purpose of the steel strands is to improve the mechanical capacity of the conductor. This solution is patented by Nexans Norway AS.

Outside the steel strands there are 72 (18 + 24 + 30) copper strands (brown color). Outside the stranded conductor there are an electric insulation system (dark gray and light gray colors) and an inner sheath (gray color). Outside the inner sheath there are fillers for mechanical protection (yellow color), and then the outer sheath (black color).

This paper focuses on how friction influences cables' maximum allowable tension (MAT). This issue is particularly important for deep-water cables and umbilicals. The contributions of the paper are: (i) Derive the relationship between axial cable tension, axial element tension, and friction. This derivation is strongly inspired by references [4], [5], and [6]. (ii) Present four different approaches for how to handle friction when calculating MAT. These four approaches are then compared by applying them to the deep-water DEH piggyback cable and the results are discussed.

The derivations of this paper are based on the following assumptions and simplifications: (i) All materials are assumed to be linear elastic. (ii) Radial displacement and the Poisson ratio effect are neglected. (iii) Helical elements are modeled as tendons. That is, these elements' axial stiffness is modeled, while their bending stiffness and torsion stiffness are neglected. (iv) The cable is prevented from twisting. (v) Only inter-layer contact and friction are

considered, i.e. contact and friction between adjacent cable layers. Intra-layer contact and friction are neglected, i.e. contact and friction within the same cable layer. (vi) When considering radial contact forces, only the steel and copper strands of the piggyback cable is considered, because the radial contact forces caused by the fillers is small compared to those from the strands. (vii) End effects induced in the cable terminations are neglected.

WHY FRICTION INFLUENCES THE MAXIMUM ALLOWABLE TENSION

The technological challenges facing manufacturers of deep-water cables, including umbilicals, are to a large degree caused by the large mechanical forces acting on the cables. The net force of gravity minus buoyancy causes large axial cable tension at hang-off and in the upper part of the cable. The axial cable tension is distributed between the cable elements according to the elements' mechanical properties and the cable geometry.

As many cable elements are helical, large axial cable tension sets up large radial compression forces, which give high friction between the cable elements. When the cable is being bent, the helical elements slide. However, at large axial cable tension, the helical elements stick due to the friction. Then large axial tension and compression forces build up in the elements until the friction is exceeded, and thereby allows the elements to slide. Hence, the axial cable tension gives two contributions to the axial tensions of the cable elements: (i) Distribution of the cable's axial tension to the individual cable elements. (ii) Axial element tensions necessary to exceed the friction.

Large axial cable tension leads to two significant challenges: (i) High axial element tensions may cause the elements to exceed their respective mechanical capacities. (ii) Hanging from topside, the cable is subject to oscillating bending due to waves. Due to high friction, the helical elements partly stick, causing alternating tension and compression. This may lead to fatigue damage of the cable elements. For non-load-carrying elements, both these issues may damage the elements to the extent that they can no longer serve their respective purposes. Even worse is damage to load-carrying elements; this may ultimately break the cable.

This paper focuses on how friction influences the

maximum allowable tension (MAT). MAT is here defined as the maximum axial cable tension, assuming straight (non-bent) cable, where all cable elements are within their respective mechanical capacity criteria. These criteria are typically defined by maximum allowed von Mises stress. If the cable is bent, the cable may be damaged at lower axial tension than MAT.

ELEMENT TENSION VS. CABLE TENSION

In the deep-water DEH piggyback cable of Figure 1, all cable elements are helical, except for the center strand and the sheaths (including the insulation system). All helices have the same center, which is the center of the cable's cross section. While helices are three dimensional geometries, it is common to illustrate these geometries in two dimensions as shown in Figure 2.

The pitch length, L_i, is the axial length of the cable corresponding to one revolution of the helix. Elements in the same cable layer always have the same pitch length. The element length, l_i, is the length of the cable element over one pitch length. The pitch radius, R_i, is the radius from center of the cable to center of the element. The pitch angle, α_i, is the angle between the cable's axis (length direction) and the tangent of the helix. The relation between l_i, L_i, R_i, and α_i is shown in Figure 2.

This section derives the relation between the cable's axial tension, T_c, and the axial tensions of the individual cable elements, $T_{a,i}$. From Figure 2 Pythagoras' theorem gives

$$l_i^2 = (2\pi R_i)^2 + L_i^2. \tag{1}$$

Implicit derivation with respect to L_i

$$2l_i \frac{\mathrm{d}l_i}{\mathrm{d}L_i} = 2L_i, \tag{2}$$

$$\mathrm{d}l_i = \frac{L_i}{l_i}\mathrm{d}L_i = \cos(\alpha_i)\,\mathrm{d}L_i. \tag{3}$$

Dividing Eq. 3 by L_i and using $L_i = l_i \cos(\alpha_i)$ gives

$$\frac{\mathrm{d}l_i}{L_i} = \frac{\mathrm{d}l_i}{l_i \cos(\alpha_i)} = \cos(\alpha_i)\frac{\mathrm{d}L_i}{L_i}, \tag{4}$$

$$\frac{\mathrm{d}l_i}{l_i} = \cos^2(\alpha_i)\frac{\mathrm{d}L_i}{L_i}, \tag{5}$$

$$\varepsilon_i = \cos^2(\alpha_i)\varepsilon_c. \tag{6}$$
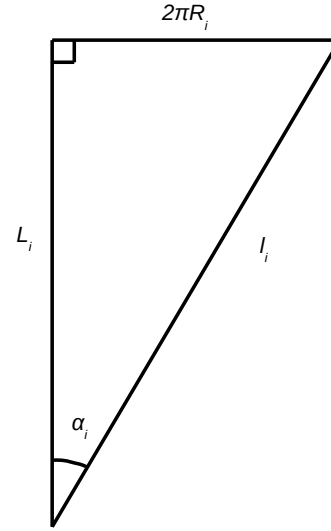

Figure 2: The geometric relation between l_i, L_i, R_i, and α_i.

In Eq. 6 it is used that the cable's axial strain is $\varepsilon_c \overset{\mathrm{def}}{=} \mathrm{d}L_i/L_i$, while the element's axial strain is $\varepsilon_i \overset{\mathrm{def}}{=} \mathrm{d}l_i/l_i$. A cable element's axial tension is given as $T_{a,i} = E_i A_i \varepsilon_i$. Hence, multiplying Eq. 6 with $E_i A_i \cos(\alpha_i)$ leads to

$$T_{a,i} \cos(\alpha_i) = E_i A_i \cos^3(\alpha_i)\varepsilon_c, \tag{7}$$

$$\sum_i T_{a,i} \cos(\alpha_i) = \sum_i E_i A_i \cos^3(\alpha_i)\varepsilon_c \tag{8}$$

$$= \left(\sum_i E_i A_i \cos^3(\alpha_i)\right)\varepsilon_c,$$

$$\frac{\sum_i T_{a,i} \cos(\alpha_i)}{\varepsilon_c} = \frac{T_c}{\varepsilon_c} = \sum_i E_i A_i \cos^3(\alpha_i), \tag{9}$$

$$\mathrm{EA}_c \overset{\mathrm{def}}{=} \frac{T_c}{\varepsilon_c} = \sum_i E_i A_i \cos^3(\alpha_i). \tag{10}$$

In Eq. 8 all cable elements are summed. The strain in the cable's length direction, ε_c, is equal for all cable elements. In Eq. 9 it is used that the cable's axial tension, T_c, is equal to the axial component, $T_{a,i}\cos(\alpha_i)$, of all cable elements. In Eq. 10 it is used the cable's axial stiffness is by definition $\mathrm{EA}_c \overset{\mathrm{def}}{=} T_c/\varepsilon_c$. Note that Eq. 10 is valid also for non-helical elements. For non-helical elements $\alpha_i = 0$.

Multiplying Eq. 6 with $E_i A_i$ and using $\varepsilon_c = T_c/\mathrm{EA}_c$ gives the relation between the cable tension, T_c, and the cable tension's contribution to the elements' ten-

sion, $T_{a,i}$, and axial stress, $\sigma_{a,i}$.

$$E_i A_i \varepsilon_i = E_i A_i \cos^2(\alpha_i) \varepsilon_c, \qquad (11)$$

$$T_{a,i} = \frac{E_i A_i \cos^2(\alpha_i)}{\mathrm{EA}_c} T_c, \qquad (12)$$

$$\sigma_{a,i} = \frac{T_{a,i}}{A_i} = \frac{E_i \cos^2(\alpha_i)}{\mathrm{EA}_c} T_c. \qquad (13)$$

RADIAL CONTACT FORCES

Figure 3 illustrates a tendon being pulled over the circumference of a circle or a circle sector, for example a rope being pulled over a pulley. If the axial tension of the tendon is T [N] and the radius from center of the circle to the center of the tendon is d [m], then the radial contact force, c [N/m], can be shown to be

$$c = \frac{T}{d} = T\kappa, \qquad (14)$$

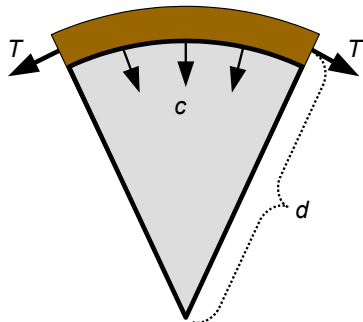where $\kappa = \frac{1}{d}$ is the bending curvature of the tendon.

Figure 3: A tendon (brown color) pulled over the circumference of a circle sector (gray color).

For a helix with pitch radius, R, and pitch angle, α, the helix curvature, κ, can be shown to be

$$\kappa = \frac{\sin^2(\alpha)}{R}. \qquad (15)$$

Hence, when applying axial tension, T, to a helix winded around a cylindrical core, for example a helical cable element on the beneath cable layer, the radial contact force, c, is

$$c = T\kappa = T\frac{\sin^2(\alpha)}{R}. \qquad (16)$$

Eq. 16 expresses the contact force from one cable element per unit length of the element, i.e. along edge

l_i of Figure 2. The contact force per unit length of the cable, i.e. along edge L_i, induced by n_i cable elements is then

$$c_i = \frac{n_i \sin^2(\alpha_i)}{R_i \cos(\alpha_i)} T_{a,i}, \qquad (17)$$

$$c_i = \frac{n_i E_i A_i \cos(\alpha_i) \sin^2(\alpha_i)}{R_i \mathrm{EA}_c} T_c. \qquad (18)$$

Eq. 12 has been inserted into Eq. 17 to give Eq. 18. The contact forces induced by the individual cable layers accumulate, layer by layer, towards the centre of the cable. That is, the contact force between layer N (the outermost layer) and layer $N-1$ is the contact force induced by layer N, i.e. c_N given by Eq. 18. The contact force between layer $N-1$ and layer $N-2$ is the contact force induced by layer $N-1$ and by layer N, i.e. $c_{N-1} + c_N$. Hence, the accumulated contact force acting between layer i and layer $i-1$, C_i, is then

$$C_i = \frac{1}{\mathrm{EA}_c} \left(\sum_{j=i}^{N} \frac{n_j E_j A_j \cos(\alpha_j) \sin^2(\alpha_j)}{R_j} \right) T_c. \quad (19)$$

FRICTION

Assuming Coulomb's friction model, the maximum possible friction force, f [N/m], between two surfaces is $f = \mu c$, where c [N/m] is the normal force and μ [-] is the coefficient of friction.

Except for strands in the the outermost layer and the center strand, all strands are subject to contact forces both from the layer beneath and the layer above. The maximum possible friction force on an element in layer i per length of the element (i.e. along the edge l_i of Figure 2) is then

$$f_i = \frac{\cos(\alpha_i)}{n_i} \left(\mu_{i,i-1} C_i + \mu_{i,i+1} C_{i+1} \right). \qquad (20)$$

In Eq. 20, the term $\cos(\alpha_i)$ is to give the friction per unit length of the element instead of per unit length of the cable. Division by n_i is to give friction per element.

A common assumption in the literature is to assume that friction has no influence on cables subject to only axisymmetric loads, i.e. axial tension and torsion moment only, see for example reference [6]. However, when the cable is being bent, friction may be very significant, depending on the applied axial tension, the cable geometry, and the material properties. When the cable is bent, the cable itself and

the cable elements are tensioned in the outer arc and compressed in the inner arc.

Reference [7] shows that if a helical cable element is prevented from sliding when the cable is bent, the element's elongation in the outer arc is slightly larger than the contraction in the inner arc. If the helical elements can slide freely, the contraction will completely vanish, and only a tiny elongation will remain. This desired effect is actually one of the main reasons why cables are produced with many cable elements being helical.

If friction is present during cable bending, the helical elements will initially stick. Then axial tension and compression forces build up in the helical elements until the friction is exceeded. When the friction is exceeded, the helical elements slip and move. This behavior is explained in references [4] and [6].

The maximum contributions of friction to the axial stresses in cable elements can be approximated by

$$\sigma_{f,i}^{\max}(\theta) = \frac{R_i\theta}{A_i|\sin(\alpha_i)|}f_i, \qquad (21)$$
$$\theta \in \left[-\frac{\pi}{2}, \frac{\pi}{2}\right].$$

In Eq. 21, θ is the helical element's angular position in the cable. For $\theta = 0$ rad the element is at the neutral axis at bending, while for $\theta = \frac{\pi}{2}$ rad the element is at the outer arc at bending, and for $\theta = -\frac{\pi}{2}$ rad the element is at the inner arc. Eq. 21 is derived in references [4] and [6]. The same references also derive an approximation for which cable bending curvature, $\kappa_{c,i}$, the friction is exceeded, i.e. when the helical element starts to slip

$$\kappa_{c,i}(\theta) = \frac{\theta}{E_iA_i\cos^2(\alpha_i)|\sin(\alpha_i)|\sin(\theta)}f_i, \qquad (22)$$
$$\theta \in \left[-\frac{\pi}{2}, \frac{\pi}{2}\right].$$

From Eq. 22 it is seen that the first slip occurs at the neutral axis, $\theta = 0$ rad, and then propagates towards the inner arc, $\theta = -\frac{\pi}{2}$ rad, and the outer arc, $\theta = \frac{\pi}{2}$ rad. Also note that the slip propagation reaches the inner arc and the outer arc at a curvature, $\kappa_{c,i}$, that is $\frac{\pi}{2}$ times as large as the curvature of the first slip. Due to symmetry at the point $\theta = -\frac{\pi}{2}$ rad and at the point $\theta = \frac{\pi}{2}$ rad, the behavior explained here will be repeated for every half pitch length of the helical cable element.

FRICTION'S INFLUENCE ON MAXIMUM ALLOWABLE TENSION

Maximum allowable tension (MAT) is an important parameter for deep-water cables, including umbilicals, because MAT limits the water depths which the cables can be installed and operated. MAT is the maximum axial cable tension, T_c, where all cable elements are within their respective criteria for mechanical capacity. These criteria are typically that the element's von Mises stress should be within a certain percentage of the material's specified minimum yield stress (SMYS). MAT is calculated for straight (non-bent) cables. For bent cables the upper limit of axial tension is usually lower than MAT. It is common practice to use a more conservative MAT value during operation than during cable installation.

The following text presents four approaches, with different degree of conservatism, for how to handle friction when calculating or simulating MAT.

Approach 1

As explained above, it is a common assumption in the literature to assume no influence from friction in the axisymmetric case, i.e. when the cable is not bent. Because MAT by definition is calculated for straight cables, it can be argued from a theoretical point of view that friction should be completely neglected when calculating MAT. That is, evaluation of the elements' mechanical capacities are based only on Eq. 12 or Eq. 13, without considering the contribution from Eq. 21. This is the least conservative approach.

Approach 2

From a practical point of view, one can argue that real-life cables are usually not perfectly straight, i.e. have bending curvatures not exactly equal to zero. Based on this point of view, it may be reasonable to include a contribution from friction. A conservative approach will then be to include the maximum possible friction, as given by Eq. 21.

Using this approach, the total axial stress to be evaluated is $\sigma_{a,i} + \sigma_{f,i}^{\max}\left(\frac{\pi}{2}\right)$, where $\sigma_{a,i}$ is given by Eq. 13 and $\sigma_{f,i}^{\max}$ is given by Eq. 21.

Approach 3

The disadvantage of Approach 1 is that it assumes a perfectly straight cable (exactly zero bending curvature), which may be unrealistic for a real-life cable. Approach 2 includes the maximum possible contribution from friction, regardless of at which cable bending curvature the maximum possible friction is reached. As MAT is defined for non-bent cables, it may be too conservative to include stress from friction occurring at large bending curvatures.

A feasible compromise between Approach 1 and Approach 2 is to include friction up to a certain bending curvature, κ_c^{limit}, which corresponds to an "almost straight" cable, for example $\kappa_c^{\text{limit}} = 1.0 \times 10^{-2}$ m^{-1} (i.e. 1.0×10^2 m bending radius), and neglect friction occurring beyond this curvature.

A cable element is in full slip when Eq. 22 is evaluated for $\theta = \frac{\pi}{2}$ rad. The maximum curvature, $\kappa_{c,i}^{\text{max}}$, for evaluation of $\sigma_{f,i}$ is then the smallest value of Eq. 22 and κ_c^{limit}, i.e.

$$\kappa_{c,i}^{\text{max}} \qquad (23)$$
$$= \min\left(\frac{\pi}{2E_i A_i \cos^2(\alpha_i)|\sin(\alpha_i)|} f_i, \ \kappa_c^{\text{limit}} \right).$$

From reference [6] it follows that until the friction is exceeded, the axial element stress from friction at bending can be approximated by

$$\sigma_{f,i}(\theta) = E_i R_i \cos^2(\alpha_i) \sin(\theta) \kappa_c, \qquad (24)$$
$$\theta \in \left[-\frac{\pi}{2}, \frac{\pi}{2} \right].$$

Eq. 24 is maximized for $\theta = \frac{\pi}{2}$ rad. Then inserting Eq. 23 into Eq. 24 gives the maximum stress due to friction at bending

$$\sigma_{f,i} = E_i R_i \cos^2(\alpha_i) \qquad (25)$$
$$\times \min\left(\frac{\pi}{2E_i A_i \cos^2(\alpha_i)|\sin(\alpha_i)|} f_i, \ \kappa_c^{\text{limit}} \right).$$

If κ_c^{limit} is set to a high value, then $\kappa_{c,i}^{\text{max}}$ is limited by the first term inside the parenthesis of Eq. 23. In this case, Approach 2 and Approach 3 will give the same MAT value. How to decide the value of κ_c^{limit} requires a judgment by the analyst.

The total axial stress to be evaluated is then $\sigma_{a,i} + \sigma_{f,i}$, given by Eq. 13 and Eq. 25, respectively.

Approach 4

The last approach to be discussed in this paper requires a slight re-definition of MAT: Earlier in this paper, MAT was defined as "the maximum axial cable tension, assuming straight (non-bent) cable, where all cable elements are within their respective mechanical capacity criteria". The assumption of straight cable will now be changed to "assuming a small cable bending curvature of κ_c^{limit}".

This approach has the advantage that MAT can be read directly from the capacity curve. The capacity curve illustrates the allowed combinations of axial cable tension, T_c, and bending curvature, κ_c. Hence, once the capacity curve is established, MAT can be found as the value of T_c corresponding to $\kappa_c = \kappa_c^{\text{limit}}$.

Both Approach 3 and Approach 4 use the curvature limit, κ_c^{limit}. The difference between these two approaches is that Approach 4 also takes into account an additional effect: When the cable is bent, the cable elements are also bent. This introduces bending stresses, $\sigma_{b,i}$, in the cable elements, which are also taken into consideration when evaluating the mechanical strength criteria. Hence, Approach 4 is more conservative than Approach 3.

An expression for bending stress is given in reference [6]. For the deep-water DEH piggyback cable presented in Figure 1, $\sigma_{b,i}$ corresponds to 1-2% of SMYS for the curvature $\kappa_c^{\text{limit}} = 1.0 \times 10^{-2}$ m^{-1}. Hence, in this case the difference between Approach 3 and Approach 4 is very small.

Comparison of the Four Approaches

Figure 4 compares MAT values of the deep-water DEH piggyback cable presented in Figure 1, using the four approaches explained above. Figure 4 is scaled so that MAT calculated by Approach 1, i.e. the least conservative approach, corresponds to 100%. For Approach 3 and Approach 4 the curvature limit is set to $\kappa_c^{\text{limit}} = 1.0 \times 10^{-2}$ m^{-1}.

As shown in Figure 4, the most conservative approach (Approach 2) gives 19% lower MAT than the least conservative approach (Approach 1). As expected, there is very good agreement between Approach 3 and Approach 4: Approach 4 is 2% lower than Approach 3.
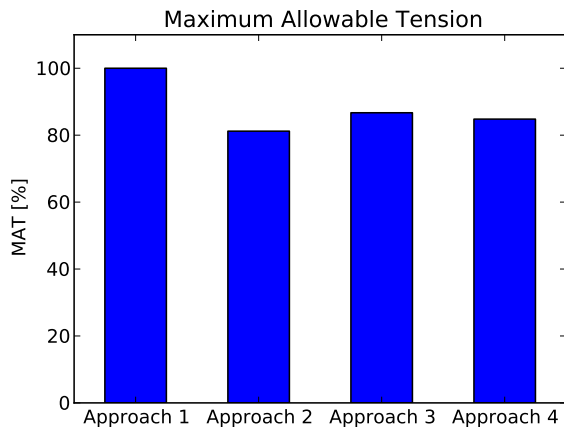
Figure 4: Comparison of approaches 1 through 4 applied to the deep-water DEH piggyback cable presented in Figure 1. The graph is scaled so that MAT calculated by the least conservative approach, i.e. Approach 1, corresponds to 100%.

CONCLUSIONS

This paper derives the relation between a cable's (or umbilical's) axial tension, the cable elements' axial tension, and friction. In particular, it is emphasized how friction influences the maximum allowable tension (MAT).

A common assumption in the literature is to neglect the influence of friction in the axisymmetric case. Hence, from a theoretical point of view, it can be argued that friction should be neglected when calculation MAT, because MAT by definition is calculated for straight (non-bent) cables.

On the other hand, from a practical point of view, one can argue that a real-life cable is rarely perfectly straight (i.e. has exactly zero bending curvature). Therefore, it may be reasonable to include contribution from friction when calculating MAT.

This paper presents four different approaches for how to handle friction when calculating MAT. These approaches range from neglecting friction in Approach 1 to include the maximum possible friction in Approach 2. Approach 3 and Approach 4 are feasible compromises, where friction is included up to a certain cable bending curvature, which corresponds to an "almost straight" cable, while friction above this limit is disregarded. Approach 4 has the advantage that it can be read directly from the cable's capacity curve (i.e. allowed combinations of axial tension and bending curvature).

All four approaches were applied to the deep-water DEH piggyback cable presented in Figure 1. For this cable, the most conservative approach gives 19% lower MAT than the least conservative approach.

REFERENCES

[1] A. Nysveen, H. Kulbotten, J. K. Lervik, A. H. Børnes, M. Høyer-Hansen, and J. J. Bremnes. Direct Electrical Heating of Subsea Pipelines - Technology Development and Operating Experience. *IEEE Transactions on Industry Applications*, 43:118 – 129, 2007.

[2] S. Dretvik and A. H. Børnes. Direct Heated Flowlines in the Åsgard Field. In *Proceedings of the Eleventh (2001) International Offshore and Polar Engineering Conference - Stavanger, Norway*, 2001.

[3] S. Kvande. Direct Electrical Heating Goes Deeper. *E&P Magazine June 2014*, 2014.

[4] E. Kebadze. *Theoretical Modelling of Unbonded Flexible Pipe Cross-Sections*. PhD thesis, South Bank University, 2000.

[5] R. H. Knapp. Derivation of a new stiffness matrix for helically armoured cables considering tension and torsion. *International Journal for Numerical Methods in Engineering*, 14:515 – 529, 1979.

[6] N. Sødahl, G. Skeie, O. Steinkjær, and A. J. Kalleklev. Efficient fatigue analysis of helix elements in umbilicals and flexible risers. In *Proceedings of the ASME 29th International Conference on Ocean, Offshore and Arctic Engineering OMAE 2010*, 2010.

[7] M. Lutchansky. Axial stress in armor wires of bent submarine cables. *Journal of Engineering Industry*, 91(3):687 – 693, 1969.

The Simulation and Optimization of Transposition in Stator Bars of Turbo-Generator

Saeed Yousefi gaskari
Science and Research University Semnan,
Iran
Kourosh Mosavi Takami
PhD, Electric Power engineering

ABSTRACT

In medium voltage high MVA Turbo-generators, generally Roebel bars are used in slot area. To reduce the circulating current in slot area of Turbo-generators, transposed Roebel bars are located in slots. Because of that large turbo-generators trend to offer a top power density, winding strands being as a Roebel transposition form and strands are insulated against each other. Optimized structure of the Roebel bar can remove the circulating currents which have been generated in the stator windings. The structure of the bar causes an increase in volume of copper used in strands of windings. With increasing the copper volume and length of strands, the rugged magnetic field increases in the slot area. Because of this reason, eddy current losses grow in solid winding strands. Thus there must be a balance between eddy current losses and circulating current losses in Turbo-generators. The optimal transposition way based on a finite analysis model is used to create this balance so to optimize the circulating currents desirably. To reduce circulating current, an optimized transposition should be performed in the end area too. Simulations by finite element confirm the desired effect of transpositions.

A 160 MW, 11 KV Turbo-generator has been simulated and the results verified by real data.

Keywords-Turbo-Generator; circulating current losses; eddy current losses; Roebel bars; copper losses; optimization transposition

I. INTRODUCTION

Optimized structure of the Roebel bars has the ability to increment Turbo-generator efficiency, and therefore saving energy. The primary approach was used to optimize the Roebel bar based on the analytical method was founded [1]-[2]. Due to complexity to these methods, today, most of the methods applied to optimizing the winding losses and magnetic fields losses, utilize finite element analysis methods. Because the finite element analysis has a simple grid and the execution time is relatively short. Many technologies offered for elimination of circulating current losses and preventing temperature rise in the Roebel bars [3]-[4]. In traditional transposition was not possible to completely eliminate circulating current. Therefore, remaining losses increases stator winding temperature. This temperature rise in stator windings was considered as an important factor in design constraints on huge Turbo-generator. In traditional technology, stator winding used widely in Turbo-generator and on winding was used for only one rotation. Which issue in addition to the circulating current losses, was increased eddy current losses. Therefore, a new technology offered for optimizing losses in

Slot area.

One of the most complex optimized transpositions which can be done in slot area is transposition with angle of 540 degrees. In this transposition, strands rotate one and half cycle on the tow stator core ends. This transposition has the ability to reduce circulating current in stator slot area to nearly zero. Also, $540°$ transposition can eliminate the induced voltages in the end area. While the $360°$ transposition cannot do this action. However, in the end area circulating current is being still produced. To eliminate these currents, a transposition optimization is done on the end area. Transposition on area and slot area cause increase in the volume of used copper and the length of windings compared to before. Which issue causes increases ragged magnetic field in winding. This leads to the increase of eddy current in the winding. This also makes the copper losses increase. Therefore, main objective of this paper is to compare circulating current and eddy current losses in different designs of winding, to create a balance between the losses. To obtain an optimal transposition, circulating current losses and eddy current losses are estimated as a simplified model in different transposition.

Considering copper loss in the stator winding transposition is one of the most important points that are discussed in this paper. Comparing copper and circulating losses the best transposition is chosen.

II.   STATOR WINDING CONFIGURATION

Stator winding is comprised of two sections; a slot area is located within a groove, and end area that made in the direction of the axis. Stator windings in large Turbo-generators are often double layers half windings, and each of them divided to half similar coil. As shown in fig 1.
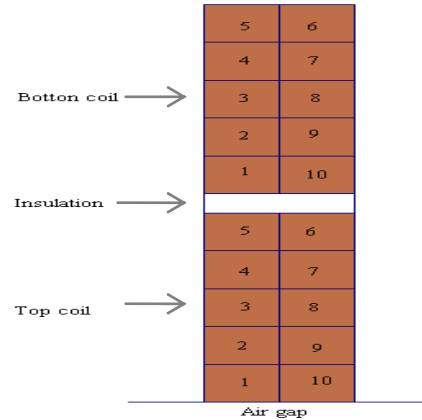

Figure 1. Copper wire order in the simulated model

Conductors used in the windings have appropriate distribution; this appropriate distribution reduces eddy current tremendously. While situation is different in extensive bar. Stator winding in turbo-generators contains number of the string that has a rectangular cross section. These strings are isolated to each other. In order to reduce eddy current losses in this strings. The main problem of such structure is circulating currents that exit however that there are appropriate distribution conductors. The simple structure of Roebel bars is shown in figure 2.
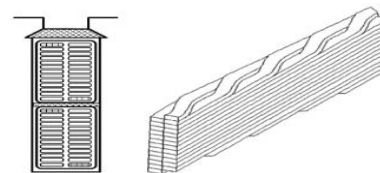

Figure 2. Easy structure of a Roebel bar [5]

III.   TRANSPOSITION IN ROEBEL BARS

Usually in traditional stator windings of turbo-generator circulating current is high in slot area. To reduce circulating currents stator windings in the slot area are transposed. For example the transposition begins from the top to the bottom of the slot and the conductors change their situations choosing available positions in the windings. Amount of circulating currents depends on transposition angle. By transposition angle of 540, this current nearly goes to zero.

This transposition is the best transposition in the slot area. However because of longer core length in comparison with hydro generators the amount of cupper used in slot area increase strikingly and the core becomes longer than the before transposition. This cause rugged magnetic field and eddy currents increase in slot area. Balance between increased eddy currents to circulating currents is one of the most important objectives of this paper that discussed in following sections. In windings that not transposition on the end area, leakage fluxes in the end area major factor of creating circulating currents. To eliminate these currents an optimal transposition in end area usually is used. Transposition angles might be 90 and 180 degree in the end area. 90° Transposition leads to excessive increase in volume of used copper that respect to the transposition of 540 degrees in slot area. This increment volume can be increased remarkably, and eddy currents to be inappropriate. So best transposition to end area is 180 degrees which by using lower volumes of copper, both minimize circulating currents losses and does not increase eddy current losses too much.

According to the above subject, suitable composition for transposition in slot area and end area divided into 4 designs. Which results of simulation by finite element analysis indicates that the most appropriate type of transposition is 180/540/180 transposition. 540° Transposition in slot area as shown in figure 1-2. For example transposition in strand number three is highlighted.
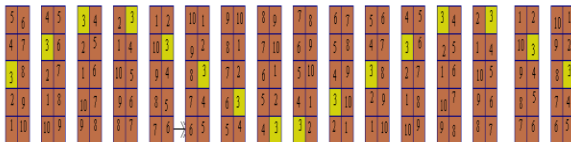

Figure3. 540 degree Transposition in slot area

Circulating current losses and Cupper losses are two major factors in the rise temperature in Roebel bars so these two factors should be considered in the optimization transposition.

IV. ASSESSMENT OF LOSSES IN STATOR BARS

A) Leakage fluxes

Flux difference between the two ends of the wire wrapping is called leakage flux. There is not voltage difference between the fields in this area by 540° transposition in the slot area. Thus there are not flux differences in the slot area. There are leakage fluxes in 360° and 180° transposition, which are the fluxes as follows:

a) Inner coil end leakage flux (figure 4.a)
b) Outer coil end leakage flux (figure 4.b)
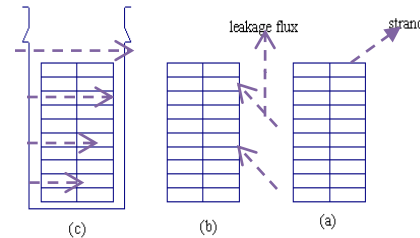c) Slot leakage flux (figure 4.c)

Figure 4. The leakage fluxes that lead to the circulating current.

According to entity leakage flux best for eliminate circulating currents this is that in each strand, currents that generated by leakage flux go toward uniformity. Magnetic reluctance of the leakage flux is very small and its direction is in order transverse flux. This flux has the ability to produce high amounts of circulating currents, especially on strands that are located near the air gap.

(B) Circulating Current losses

Circulating current losses occur by flowing circulating current in strands. Circulating current is different from strand to strand also the total to zero over the cross-section of all strands in one bar.

B-1) Analysis current of strands in slot area at 540°transposition

Strands current calculated as (1):

$[Z]\{I\}=\{V\}$ (1)

Where, [Z] is impedance matrix, including resistance and inductance, and [I] is the strand current vector and [V] is the voltage difference vector.

Assuming, number of strands layers in 540° transposition, is of $N/2$ degree if the strands have two configurations, Roebel transposition become $3n/2$. Dlc is long strands within a distance transposition based on one changing situations. The following equations is used calculate the Z and V in 540° transposition.

$$[Z] = \frac{dl_c}{2}[Zl^0] + dl_c[Zl^1] \dots + \frac{dl_c}{2}\left[Zl^{3n/2}\right]$$
        (2)

$$\{V\} = \frac{dl_c}{2}\{Vl^0\} + dl_c\{Vl^1\} \dots + \frac{dl_c}{2}\{Vl^{3n/2}\}$$

Where, $Zl°$ and $vl°$ are per-unit of Z and V. Superscript indicates the number of transposition.

B-2) strand current

We assume that the number of winding layers of strings is $N/2$, due to the configuration of two rows, the final number of strands is N.

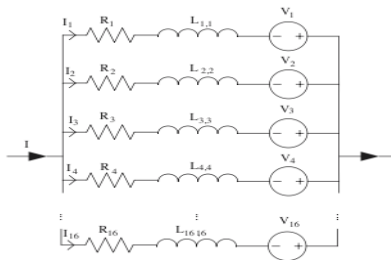Figure 5. Strand current

Resistance R usually is equal at all strings. L_{lk} Is the abbreviation of mutual inductance between l and k. Φ_{exk} is generated magnetic flux in k strand, that produced by rotor currents or other windings. The generated magnetic flux by the current in all strands is as considered internal magnetic flux.

B-3) Current equations

Two types of current equation can consider:

1) Unknown strand current
2) Unknown the circulating current

In this paper, we use of second relationship. A simultaneous equation with unknown circulating current is calculated from the following equation:

$$Ri_n + \text{jw}\sum_{k=1}^{n} L_{n,k}i_k - V$$
$$= -jw(\Phi_{exn} + \Phi_{inn}) - R\frac{I}{n} \ (3)$$

The matrix form of (3) for n equation that has been used in MATLAB in order to compute circulating current is calculated from (4):

$$
\begin{bmatrix} i_1 \\ i_2 \\ \vdots \\ i_{10} \\ V \end{bmatrix} =
\begin{bmatrix} Z_{11} & Z_{12} & \cdots & Z_{110} & -1 \\ Z_{21} & Z_{22} & \cdots & Z_{210} & -1 \\ \vdots & \vdots & \cdots & \vdots & \vdots \\ Z_{101} & Z_{102} & \vdots & Z_{1010} & -1 \\ 1 & 1 & \cdots & 1 & 0 \end{bmatrix}^{-1}
\begin{bmatrix} -jw\lambda_1 - U \\ -jw\lambda_2 - U \\ \vdots \\ -jw\lambda_{10} - U \\ 0 \end{bmatrix}
$$
    (4)

According to the above equation circulating current losses in the winding will be calculated through the following equation:

$$P_c = \sum_{k=1}^{N} I_k{}^2$$
    (5)

In eq. 2, I_k is circulating current in each strand and R is equivalent Resistance.

C) Copper losses

Copper losses are varying in different transposition. Copper losses are calculated by following equation:

$$Q_{cu} = 2.4j_a{}^2$$
    (6)

Where, j_a is current density, and G_{cu} is weigh of copper.

Weigh of copper in Roebel bar is determined by the cross sectional area and length of the string. Cross section is identical in all transposition, thus length of the string plays the main role in copper losses. In figure3 shown a single string in 180/540/180 transposition.
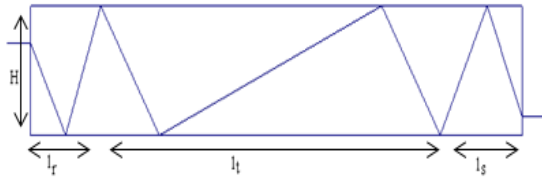

Figure 6. Calculation model of a single model

Based on figure3, length of strands is calculated from the following equation:

$$2\sqrt{L_s^2 + H^2} + 2\sqrt{L_t^2 + 4H^2} + 7L_c \qquad (7)$$

According to the above equation, length of strands in case of 180/180/180 and 180/360/180 transposition can be obtained from the following relations:

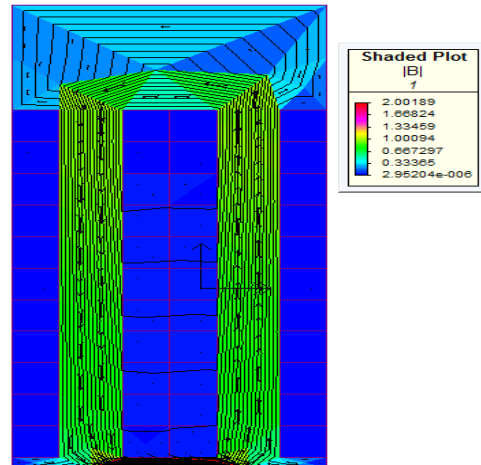$$\sqrt{L_s^2 + H^2} + \sqrt{L_t^2 + 4H^2} + 3L_c \qquad (8)$$

$$2\sqrt{L_s^2 + H^2} + \sqrt{L_t^2 + 4H^2} + 5L_c \qquad (9)$$

V.   RESULT AND DISCUSSION

Magnet software is used to calculate circulating currents in slot and end area. Figure 7 shows the distribution of flux in slot area before the transposition.
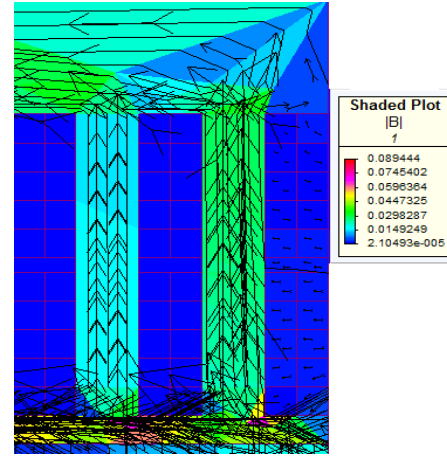
(a)

(b)

Figure7. Distribution of flux in slot area before the transposition. (a) External flux (b) internal flux

According to the figure1, the flux distribution is very high in slot area, this fluxes causes increase circulating currents in slot area, high distribution in slot area causes an increase in circulating currents in the way that existence of transposition in slot area will be essential. In figure 8 shown internal flux distribution in different transpositions.
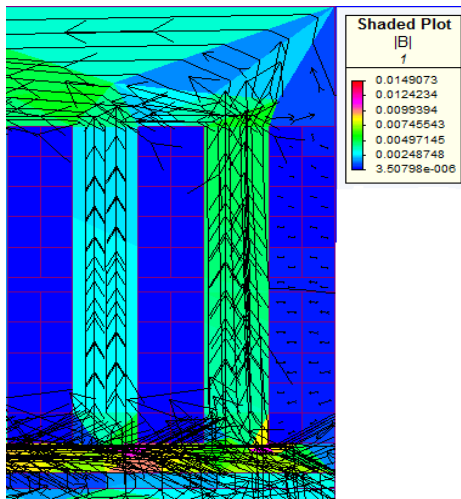
(a)
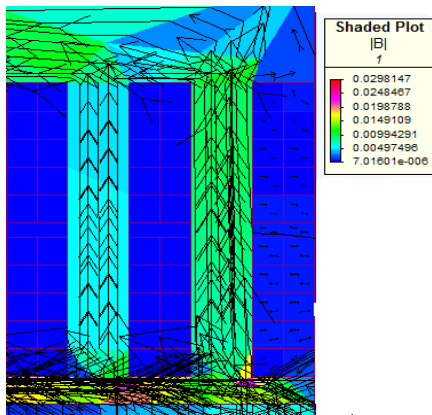
(b)
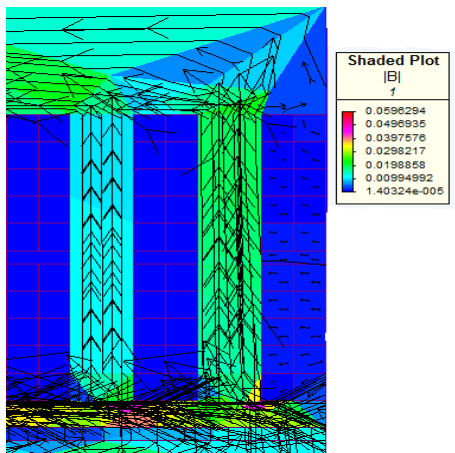
(c)

figure8. Internal flux distribution in different transpositions. (a)540° (b) 360° (c)180°

As clarified in figures, in 540 distribution of internal flux is noticeably reduced this lead to reduce circulating currents. We can calculate circulating currents and circulating currents losses in slot area, by results of the simulations and formulas mentioned in the previous section,

In figure 9 internal and external flux distributions in end area are shown before the transposition.

(a)

(b)

(c)
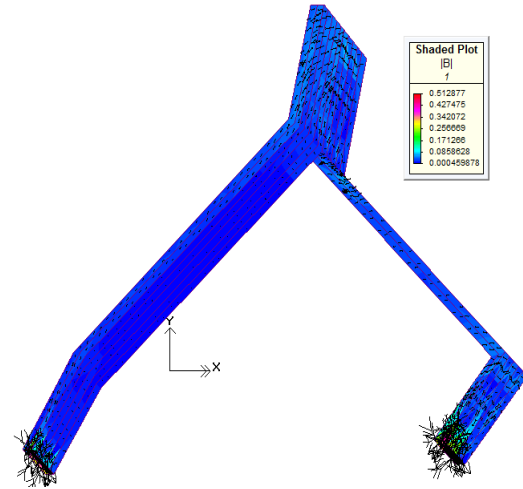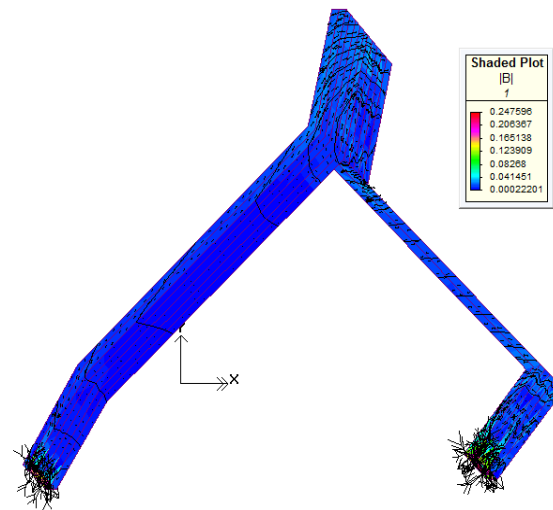
(b)
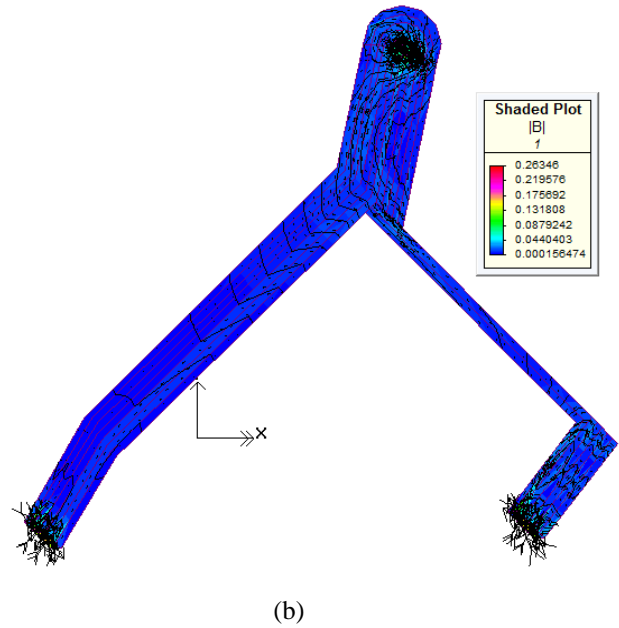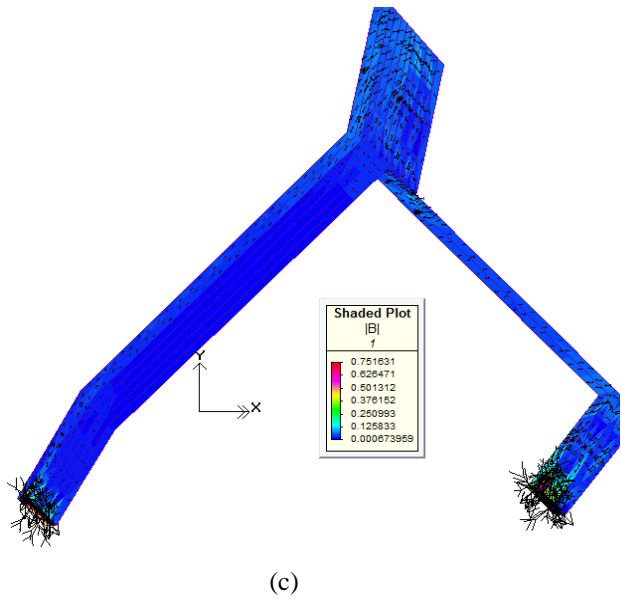
Figure9.flux distributions in end area before of transposition. (a)Circumferential external flux (b) internal flux(c) eternal and external flux

Clarified of the figures and simulation results, flux distribution which leads to an increase in circulating currents is very high. In order to reduce circulating current 180 transpositions is applied at the end area. Simulation results are shown in figure10.

(c)
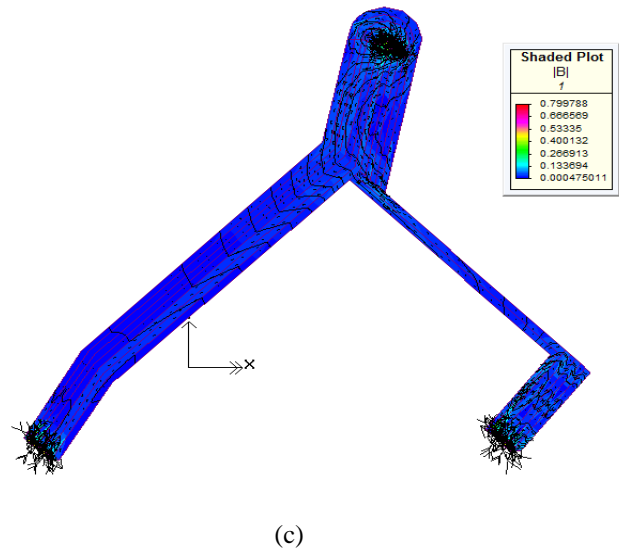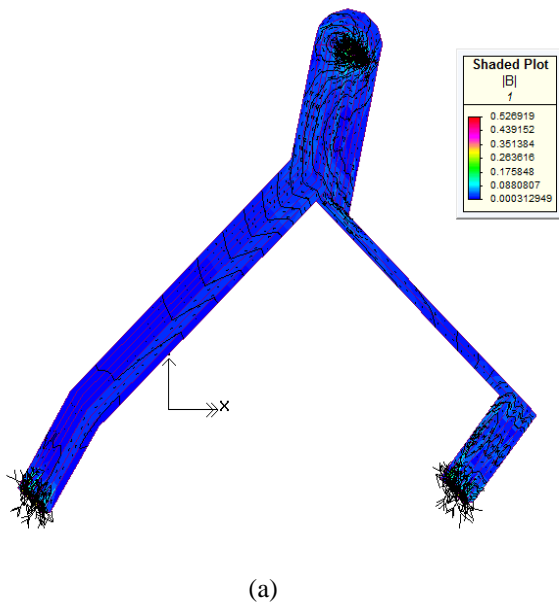
Figure10. Flux distributions in end area whit transposition. (a) Circumferential external flux (b) internal flux(c) eternal and external flux

(a)

Optimal transposition angle depends on slot width, the length of the end winding, the number of strands in Roebel bar, the length of strands in bars, and the leakage flux in the slot and end area. Also circulating current greatly depends on the mentioned circumstances. In figure 11, distribution of circulating current in different transposition in upper coil is shown.
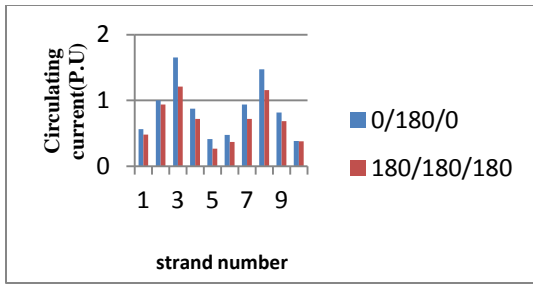
(a)
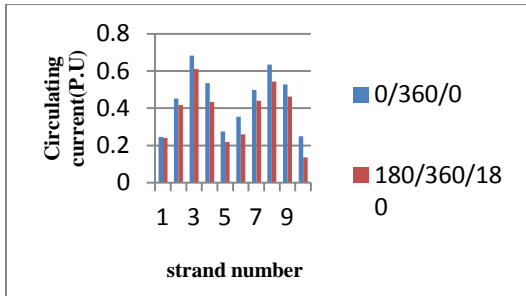
(b)
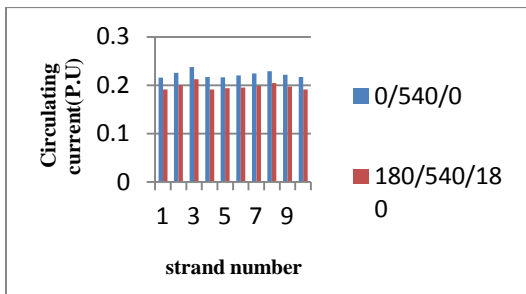
(c)

Figure 11. Calculating currents distribution in top Bar
a) 0/180/0,180/180/180 b) 0/360/0, 180/360/180 c)
0/540/0,180/540/180

In this paper, a 200MW turbo-generator has been selected for review. The table1 shows the main characteristics of this turbo- generator.

Capacity	200 MW
Number of poles	2
Speed	3000 RPM
Stator winding	Y*3
Number of stator slots	60
Kind of transposition	0/180/0
Total losses	595 W

Table1. Main characteristic of turbo- generator

In the previous section calculation methods of circulating currents and copper losses have been presented. Calculation results of circulating current in the upper and lower coil of 0/540/0 transposition is approved by [7]. 0/180/0 transposition has the maximum circulating current losses that owns the value of 140.32W. With knowing that the circulating current in the stator bars can lead to excessive temperature, the 180/540/180 transposition is the best case which reduces circulating current losses with the valve of 0.79W. Though the copper losses in this type of transposition is more than mentioned types. On the other hand total losses as lower than previous transposition. Circulating current, copper and total losses in different transpositions are shown in table2.

| Transposition	Circulating current losses	Copper losses	Total losses
0/180/0	140.32	449.34	589.66
180/180/180	103.54	458.29	561.83
0/360/0	57.24	465.47	522.71
180/360/180	24.87	479.25	504.12
0/540/0	18.57	485.36	503.93
180/540/180	0.79	498.25	499.04

Table2. Theoretical losses in the top Bar (in watts)

VI.   CONCLUSION

There are high circulating current losses and eddy current losses, in stator winding of huge Turbo-generator. These losses decrease machine efficiency, due to the heat generated. By optimizing the transposition of stator winding, the losses are reduced drastically. Based on the tests that performed, best transposition in stator winding is 180/540/180.

Since, end area is long, transposition with more angles become possible, e.g. 180° transposition. This transposition increases the volume of coppers which is used in windings. Simultaneously, eddy current losses increase. However, this increscent in eddy current losses are more less than the reduction in circulating current losses. Hence, the total losses are reduced by using this transposition.

REFERENCES

[1] J.Hadermann. "Transposition in stator bars of large turbo generator" IEEE Transaction on Energy conversion, vol.19, 2004, pp.553-560

[2] Toma Dordea, Valentin Muller, Leana Jorac, Ghrorge Madescue, Martian Mot, Lucian Ocolisian. "Analytical method for the optimization of Roebel bars compose of full elementary conductors" Romanian Academy, 300223 Timisoara, bd, viteazul nv24,2006.

[3] M.fujita, Y.Kabata, T.Tokumasu, M.Kakiuchi, H.shiomi, S.Nagano. "Air cooled large turbine generator with multiple pitched ventilation ducts" IEEE International conference, 9054152, 2005, pp.910-917.

[4] Chen Shu-xin; Fan Ming-Qing. "Optimization of hydrogen cooled turbo-generator rotor wedge cooling method" IEEE Conference Publications" vol.12242752, 2011, pp.497-500

[5] Jibin Zou; Bo Zao; Yongxiang Xu; Jing Shang; Weiyan Liang. "A New End Windings Transposition to Reduce Windings Eddy Loss for 2 MW Direct Drive Multi-Unit PMSM" IEEE Journals & Magazines, vol13056910, 2012, pp.3323-3326

[6] K. Takahashi, M. Takahashi, M. Sato, "Calculation method for strand current distributions in armature windings of a turbine generator", Electrical Engineering in Japan, Vol. 143, pp. 50–58, 2003

[7] Sheng Xia, Yingying Yao, "Optimization of Transposition in Stator Bars of Hydro-generators" School of Electrical Engineering Zhejiang University Hangzhou, China, IEEE Conference Publications, vol. 13034920,2012,pp.1-4

To promote electricity smart grid performances by numerical modeling applications

Hassan Gholinejad[*]   Kourosh Mousavi Takami   Amin Mousavi Takami Erik Dahlquist
hassan.gholinejad@mdh.se   k.takami@aol.com   aminamt19@gmail.com   erik.dahlquist@mdh.se
IST DEp., Malardalen University, Box 883, SE 721 23, Vasteras, Sweden

Abstract:

Wide world's utilities are generating, transmitting and distributing of electricity throughout the country and are responsible to its quality.

Distributed automated distribution system has been proposed for planning to reduce losses, optimize capacity and load balancing in electricity networks. The world electricity average loss is about 8% and outage per customer time is about 10 min/ year. The indices are needed to optimize in developing countries.

This paper deals on a modeled distribution system in Sari distribution region and evaluates three mentioned parameters on network quality. Restoration, maneuvers to achieve the minimum loss, reactive power controlling, load balancing etc are investigated.

Modeling performs by MATLAB software, EMTP for transient modeling and Digsilent with real data by Sari Distribution Company. In this paper, a new approach by rearrangement aimed at reducing losses and improving of load balancing in distribution networks was presented.

Keywords: Modelling, smart grid, electricity network

---

[*] Corresponding author, Malardalen University, PhD Student. Vasteras, Sweden, www.mdh.se.

I. Introduction:

The smart grid is an intelligent and advanced power grid that utilizes electric and information communications technology to provide high quality power services by maximizing energy usage efficiency, indexed by KEPCO. Utilities have to supply world-class electricity to its customers and try to improve the efficiency of its power supply, transmission and distribution facilities to the world-best level.

European, North America and South Asia utilities are more developed rather than to Middle East and African companies. Tavanir in Iran is doing this task as a mother company. In Iran, more than 264000 million Kwh electricity generated in 2013through the more than 70000 MW installed power stations. Peak load occurred in August 2014 with about 48500 MW. Losses in Iran are averagely 15%, Tavanir reported. While South Korea's installed capacity in 2013 was 81,806 MW and the peak load reached to 75,987 MW. It means Iranian electricity strategy have to be aligned in the field of clean energy with smart grid. Authors focus on Iran's network as developing countries that need to improve distribution networks indices.

Due to extend of network in Iran, it is needed to study around micro grid networks. Smart grid can handle a grid in island operation, manage generation and load balancing, manage separation and parallel with other grids, improve grid access, increase grid availability, allow production dispatchment , allow demand response and demand side management, promote the development of an energy market, allow energy network integration (Gas and electricity), allow grid services exchange etc. Those abilities of smart grid help to utilities to deliver stable, continuous and low outage electricity to customers.

A microgrid network helps to more reliability. In this way a good understanding about network behaviors is necessity. Also, advanced modeling and analytical techniques are developed to help better maneuvering-restoration, understand and design widespread distribution grids. This is performed by scenarios according to technology and policy changes, probabilistic modeling loads, using of learning mechanism, smart scanning tools for system properties such as stability and multi-objective stochastic optimization on networks for planning.

Because of that grids must become more adaptive to maneuver; demand, unwanted faults and expansions, a model of network to pre evaluate of conditions help to operator. Mindless maneuver cause significant damage to the network energy distribution. It needs an effective algorithm for optimizing distribution system operation in a smart grid, from cost and system stability points of view. It should be proposed an algorithm with the least possible cost while giving the highest priority to loads and DG. Then a recovery algorithm can be used to provide decision support to mitigate undesired effects and present a well plan. A simulated condition can help to understand forward actions.

An algorithm which is mainly dependent on forecasted data of the power available from different sources as well as the load demand, a full attention has been paid to the forecasting process.

Hence, a non-linear regression technique has to be applied to build accurate forecasting models for different sources and for the load. These models help in monitoring and predicting the total power generation and demand online. Furthermore, a controller such as fuzzy based should be utilized to make use of the forecasted data of the coming peak period then decide dynamically the amount of power that should be taken out of energy storage.

Different case studies must be investigated to verify the validity of the proposed algorithm and define the system behavior under several conditions.

II. Modeling and simulation investigation

General objectives of modeling and simulation are to define the project vision, the fundamental concepts and the system architecture. Also to develop the necessary tools to support all project phases through numerical simulations.

 The chosen reference network is a typical distribution LV and MV grid, working in radial mode with the possibility of connections. It includes feeders departing from one LV/MV substation.

Adopted Software Platforms are Dig Silent for the steady-state phenomena analysis and EMTP-RV for the transient analysis.

Developed models in the modeling can be Gas turbine and wind generator, Static VAR compensator, Dynamic loads, Lines, protections and substations. Developed DMS and EMS functions are including of Generation curtailment, Load shedding and Voltage and power control strategies with coordinated behavior of generation units.

At the most recent years, MATLAB used for calculation and AutoCAD has been used for drawing a designed network. It took several times to calculating, drawing and editing. A well experienced engineer with a good capability in software was used to do this hard job.

Today, to simulate of super distribution grids (Smart network) occurs several Challenges that should study more and more.

Data and data portability between power system applications, Visualization and analysis of huge systems, Parallel computations, Real-time computations, online analysis, Unification of simulation methods and environments are the main concerns.

Multi-domain simulations are a majority in modeling and have to be paid attention.

It is best to model the network in Dig Silent. If transient analysis is needed, ETAP is a well option. In LV system transient phenomena is not considered. Using MATLAB can model the active load and dynamics are investigated.

EMTP is used to simulation and analysis of electromagnetic transients, ddetailed simulation and analysis of large scale electrical systems, Network analysis including of network separation, power quality, geomagnetic storm, interaction between compensation and control components, wind generation, synchronous machines: SSR, auto-excitation, control, Power electronics, short-circuit conditions, network interaction, distribution line systems insulation coordination, switching, design, wideband line and cable models. Switchgear side molding like TRV, shunt compensation, current chopping, delayed-current zero conditions can be performed as well.

Modern grids require advanced study and analysis methods: for power system design, operation and post-mortem analysis.

Numerical models and solution methods now play a dominant role and contribute to all research and development levels. The needs for grid simulations increase significantly faster than the capability of researchers to deliver models and faster simulations methods. Simulation and modeling are essential for the evolution and operation of modern power systems.

> Can we build an electronic copy of the operated system?
> Can we merge real-time and off-line simulation tools?
> Can we replicate analog simulator style with numerical simulators?
> What is the highest computational speed?
> How far: wideband and size
> Can we unify simulation environments to work with unique data sets and various analysis methods?
> Can we create portable models and data?
> Use Concurrent and multi-domain simulation methods

New trends: Cloud computing
> Applications for power systems
• Generation scheduling, unit commitment
– Complex optimization problems
• Load-flow
– Probabilistic methods
• Transient stability and electromagnetic transients
– Acceleration of simulations
– Sensitivity analysis
   – Contingency analysis
> Dispatching of computing jobs into a resource pool
> Simulation services with centralized and shared data
> Increased utilization of available computing services
> Higher automation levels
• Reduced human intervention
• Private cloud systems
• Public cloud systems
• Community cloud: organizations working together

Parallel computing

Availability of increasing calculation capabilities through multicore computers make the engineers to faster calculations. Power system simulations involve the solution of linear sparse systems. Traditional methods are generally sequential and use only one CPU. The matrices are very sparse, moderate size, coupled and unsymmetrical and the machine need to a parallel computing to reduce the processing time. For Load flow and steady-state studies the matrices are coupled but the solution is performed once. For time domain it is possible to use the natural delay of the lines to decouple the system. Not always feasible!. It is essential to explore new ways to increase the speed of calculations while maintaining accuracy. Most of researchers are trying to increase the speed of calculations using the possibilities offered by new technologies and by parallel computing. Several simulation tools addressing different aspects, telecom, control, electromechanical and electromagnetic transients, collaborate together to simulate the same power system. Collaborative software environment can be implemented through a co-simulation channel in an indirect interaction (FMI). Use Federated simulation systems run-time infrastructure (RTI) to support interoperability (HLA) is investigated here. Scalable performance via parallel and distributed simulation techniques is discussed.

Experimental issues:

Management of balance including independent thermal and electric loads is the first challenges. Operation in intentional islanding and connected to public network must be considered. Study and development of control and interface systems are needed to understand the model description and analyzing. Study of storage and compensation systems with power and quality functions need to model of system in computer. Study and development of protection systems for low short circuit power systems are needed to verify the results by coordination and protection abilities. Development of grid operation and control systems change the model for every step of modeling and should considered.

Low Voltage Generation Systems: Micro Grid test facility, Wide spectrum of market available technologies: Photovoltaic Panels, Mini Wind Generators, Small Domestic cogeneration systems and Fuel Cells. Generator size in microgrid system is **10 – 100** kW.

Electrical and Thermal Load Emulators

The research activity has to afford themes related to load estimation, modelling techniques and load control policies. As it will be necessary to reply different load trends, according to network power level, an emulation load system will be employed. Through a proper controlled inverter system it will be possible to reproduce active and reactive load power profiles for an amount of about 2MW.

The availability of thermal emulation system is essential to dissipate the thermal power produced by co/tri-generative systems, in an independent way of real available thermal users. This system will allow the modulation of the cold/warm load request in order to control generators in different ways (thermal or electrical load follow modes). Thermal load profiles will be reproduced to simulate the real behaviour of this type of systems when they are connected to a real heating/conditioning network.

In order to test a variable topology network some devices could vary total impedance of MV electrical lines or of the upstream network. Through the network emulator the feeding condition of the experimental network could be varied respect to the upstream primary station. The dispatching panel, together with the protection and lines emulation system, will set up a MV feeder, emulating over-head and underground lines for an amount of about 30 km.

Input for modeling are including of: Consumption and generation programs, Real-time Power Request Adjustment and Measurements from nodes are needed.

Outputs can be as: Operation Set Point for MV generators and loads and Operation Set Point for LV micro-grid controller.

Optimization can be studied around: Power flows on the MV and LV network, Exploitation of

distributed energy resources and Power Quality at each network node.

To have a good smart grid is needed to the communication system will ensure: Efficiency by ability to exchange data in real-time mode, Reliability by possibility of retaining data exchange in situations of difficulty of communication (distance, meteorological agents, presence of foreign sources and noises) and to restore the link once interrupted; Security that it will be essential to secure the secrecy and integration of the information. It should be low-cost; it allows widespread installation which distribution network

With consider to the wanted requirements in the introduction section, authors proposed a combined simulation - computation method to upgrade the present smart grid control, monitoring and protection system.
The following sections are showing the methods and a typical modeling to restoration by a reconfiguration of distribution medium voltage network.

III. Modeling a typical network with economical evaluation

A Simulated model with the following design studied and results are discussed. This section includes 18 feeders including of adjacent feeders of this network. The network has 8 opened CBS. Nominal voltage is 20 kV and the maximum allowable voltage drop in the network is equal to 5 percent.
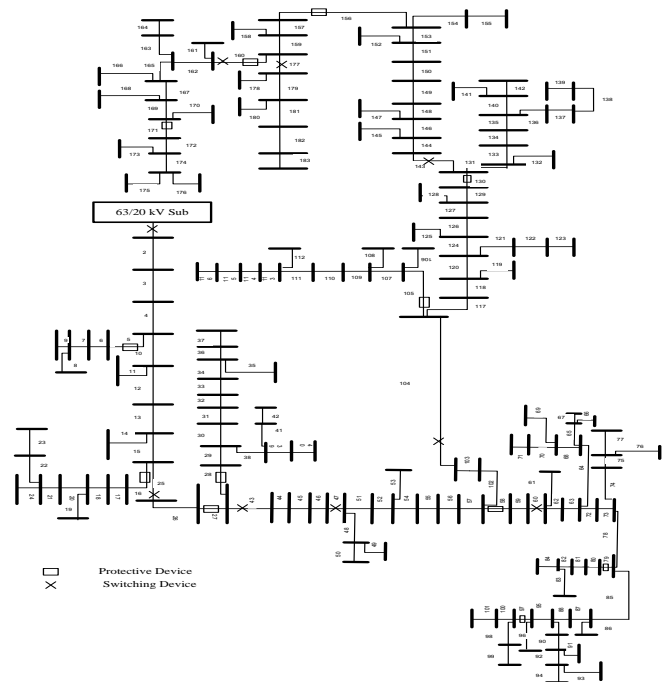
Fig. : Studied network, modeled in Digsilent environment.

Method of performing load flow backward - forward, before performing optimizing aimed at reducing losses is shown in Table 1.

Table 1: Important parameters of the network before reconfiguration done (at maximum load conditions).

Open indexes	Losses (kW)	Load balancing index	Maximum voltage drop in branch
372-31.1 375-378 369-368 340.2-385 333-332 320-309 318.1-319 315-325	63/9436	0.68975	1.048%

As can be seen, the loss before performing system reconfiguration, based on the maximum amount of load buses, is 63 9636kW.

To consider a load balancing index for the whole system, the appropriate parameters must be defined as a measure of load balance in i branch. This index is indicative of how the branches are pregnant. For

this purpose, a parameter is defined as follow:

$$Line\, Usage\, Index = \frac{S_i}{S_i^{\max}}$$

Where: S_i is Apparent power at the sending bus of branch I and $S_i^{\max}$ is definging its maximum capacity (MVA). The index measures the load balancing problem can be presented as follows.

$$X = \begin{bmatrix} \dfrac{S_1}{S_1^{\max}} & \dfrac{S_2}{S_2^{\max}} & . & . & \dfrac{S_i}{S_i^{\max}} & . & . & . & \dfrac{S_n}{S_n^{\max}} \end{bmatrix} \quad (1)$$

$$LBI = Var(X) \qquad (2)$$

Also according to equations (1) and (2), load balancing index is 0.74 and maximum system voltage drop is 1.04 percent.

Load flow results after reconfiguration with aim to improvement of load balancing and loss reduction and to define the limits a typical feeder in a forward backward approach has been done. Also voltage profile of the network after optimization is shown in Fig 13 and results of computation are shown in the table 2. These calculations are based on full load time of the network has been done.

Table 2: Profile network after reconfiguration.

Open indexes	Losses	Losses reduction	Load balancing index	Improving load balancing	Maximum voltage drop	Improving the maximum voltage drop
373-31.1 366-376 368-369 334-333 332-333 320-323 318-319 340-380	58/258	11/258 %	0.756 %	%6	%0/52	%56/73

As shown in Table 2, to perform reconfiguration, with reducing 11.89% network losses, from the 63/965 kW to 57/82 it has.

Maximum voltage drop with a 56% recovery rate, from 1.04 reach to 0.59. Also, the feeder load balancing in different branches has been associated with an improvement of 4 percent.
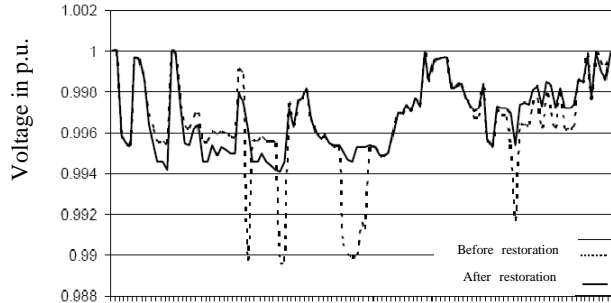

Figure 3: Diagram of the voltage profile after optimization.

In order to implement the algorithm with the system restoration, at the first it is needed to introduce a fault point in the distribution network.

The opening and closing of the CBs in order to restore the system at sample points in the system has been shown in the table (3). Improving the reliability of the distribution network algorithm is used to perform the modeling.

In order to implement the algorithm with system recovery, the need to introduce the fault occurrence point in distribution network is desired.

The opening and closing process of circuit breakers at the sample points, in order to system restoration, that applied by algorithm of improving the reliability of the distribution network on a sample feeder is shown in the table (3).

Table (3): The opening and closing process on several sample faults

291-292	344-345/2	Feeder No 4	337-380		
428/8	2954/8	3658/8	2395	Not feeding the load due to fault (kW)	
-	295-308	302-318	312-320	Closing the CB in order to feed the Isolated maximum load	Step 1
-	٠/٠	٠/٠	٠/٠	Not fed load (kW)	
-	106/85	222/08	75/96	Network losses (kW)	
-	2/58	2/08	1/42	Maximum voltage drop (percent)	
-	301-325	-	309-320	Closing the CB(create loop)	Step 2
-	313-324	-	320-323	Opening the CB (radial network)	
-	٠/٠	-	٠/٠	Not fed load (kW)	
-	69/8	-	73/98	Network losses (kW)	
-	1/82	-	1/28	Maximum voltage drop (percent)	
-	304-316	-	333-352	Closing the CB(create loop)	Step 3

The first header row of Table 3 also has: "291-292 | 344-345/2 | Feeder No 4 | 337-380 | opening the CB to being isolated from the network"

-	302-323	-	315-345	Opening the CB (radial network)	
-	٠/٠	-	٠/٠	Not fed load (kW)	
-	72/68	-	65/78	Network losses (kW)	
-	1/82	-	0/74	Maximum voltage drop (percent)	
-	306-309	-	-	Closing the CB(create loop)	
-	320-322	-	-	Opening the CB (radial network)	Step 4
-	٠/٠	-	-	Not fed load (kW)	
-	75/25	-	-	Network losses (kW)	
-	1/52	-	-	Maximum voltage drop (percent)	

In this table, the lost loads per four different faults in different parts of the network are displayed.

In all these cases, if there is another path to system restoration, with passing the first stage, all lost loads are restored.

Later, in order to optimizing the network structure switching is done when the fault occurred.

Thus, as can be seen in the later stage, switching is led to improve the network losses and the maximum allowable voltage drop of the networks.

This improvement is due to transfer and distribution of no fed feeder loads at the network level and in the most efficient and possible way.

IV. Economic analysis results

At the studied networks, the losses rate in the low-load seasons is equal to 41/8664 kW and in full load seasons is 63/9536kW.

The value of the losses in a given day, with the official rate of electricity 2.45 cent$ per kWh for low load season is equivalent of 24.66 $. For full load season is 38.6 $. Then average annual value of losses is equal to 11573 $.

Table 4: Calculation of savings due to reduced losses

Average annual ($)	The dissipated energy in a day ($)	The dissipated energy per year ($)	The dissipated energy in a month (USD)	Description	
17006	9172	764	24.7	low load seasons	Losses before reconfiguration
	14362	1197	38.6	Full load seasons.	
7230	7965	664	21.8	low load seasons	Loss after reconfiguration
	12463	1039	34	Full load seasons.	
1478	1207	100	2.9	low load seasons	Savings due to rearrangement
	1899	158	4.6	Full load seasons.	

As can be seen, annually average value of not dissipated energy is equal to 1478 $.

It is noteworthy that the achieved numbers just do rearrangements result on one of the city distribution network feeders (feeder section 8).

Obviously, applying this method on the rest of the network, as well as its economic value will increase.

In this paper, a new approach aimed at reducing losses and improving the rearrangement of load balancing in distribution networks was presented.

In this regard, the ant colony algorithm was used to make a wide search space.

The used optimization function is a multivariate function with fuzzy variables.

Simulation results show that the performance of the proposed method on two networks, a new structure for CB state found, that not only the losses optimally reduced but also the balance of load improved in a well shape.

The voltage drop is reduced to its minimum. These results indicate the ability of proposed algorithm in solving of distribution network rearrangement.

Due to system restoration, table (7) shows the total savings at the end of each stage of the process, including switching in the last stage, has been calculated.

During the operation, the improvement of the network, it will be possible to operators that with knowledge of the technical and economic status of the network at fault, the best choice is made.

Finally, this method consider to shortening of the electrical network outages due to faults. The factor is considered as one of the most important parameters of the reliability of the network.

Table 7: Economic Evaluation of power losses in the recovery operation.

				Description	Stage
65/556				Net loss in normal operation mode (kW)	
344-345/2	Feeder No 4	337-380	227-250	Opening the CB to being isolated from the network.	
2954/8	3658/8	2395	2395	Not fed the load due to fault (kW)	
-	295-308	302-318	312-320	Closing the CB to feed the Isolated maximum load	Stage 1
-	126/7	201/9	74/56	Network losses (kW)	
-	61.1	136/3	9/78	Added losses (kW)	
-	7.5	16.7	1.287	Added losses costs ($)	
·	219.3	292	185/7	Savings due to restoring (USD)	
-	212	275	184	Total savings (USD)	
-	312-321	-	309-320	Closing the CB(create loop)	Stage 2
-	330-331	-	320-323	Opening the CB (radial network)	
-	79/2	-	73/96	Net losses (kW)	
-	13/52	-	8/41	Added losses (kW)	
-	2.25	-	1.057	Added losses costs (USD)	
-	219	-	185	Savings due to restoring ($)	
-	217	-	184	Total savings ($)	
-	310-322	-	333-334	Closing the CB(create loop)	Stage 3
-	325-327	-	315-317	Opening the CB (radial network)	
-	75.68	-	67.1	Network losses (kW)	
-	11.01	-	-0.65	Added losses (kW)	
-	2	-	-0.166	Added losses costs ($)	
-	219.3	-	185	Savings due to restoring ($)	
-	217.3	-	185	Total savings (RLS)	
-	317-319	-	-	Closing the CB(create loop)	Stage 4
-	319-320	-	-	Opening the CB (radial network)	
-	76.42	-	-	Net losses (kW)	
-	10.91	-	-	Added losses (kW)	
-	1.99	-	-	Added losses costs ($)	
-	219.3	-	-	Savings due to restoring ($)	
-	217.3	-	-	Total savings ($)	

V. Conclusions

Research on power system simulation and analysis tools is now facing new and major challenges: Simulation of extremely large networks, ery complex networks, penetration of renewable energy and Smart Grids.

New trends and means for solving increasingly complex problems are performed by Parallel computations, Cloud computing, Collaborative computing, Advanced visualization methods and Data portability with CIM.

To combine a simulation method with numerical and computational technique help to have a more string smart grid. Robust algorithm is needed to analysis of several reconfigurations of networks. CBs maneuver help to get better restorations. To merge the methods a powerful algorithm with most strong software is needed. Authors tried to combine the simulation and computational methods to introduce a new face for smart grid system configuration.

In this paper, a new approach by rearrangement aimed at reducing losses and improving of load balancing in distribution networks was presented.

Simulation results show that the performance of the proposed method on two networks, a new structure for CB state was found, that optimal reduction of

losses and load balancing in the lines has been improved in a desired shape.

Economical, reliability index and technical tools are used to get a full and complete analysis.

VI. Refrences

[1] Enrico Carpaneto and Gianfranco Chicco, "Ant-Colony Search-Based Minimum Losses Reconfiguration of Distribution Systems", *IEEE MELECON Dubrovnik. Croatia*, pp. 971-974, May 2004.

[2] T.Q.D.Khoa and B.T.T.Phan, "Ant Colony Search - based Loss Minimum for Reconfiguration of Distribution Systems", *IEEE Power India Conference*, pp. 1-6, 10-12 April 2006.

[3] Chun Wang and H. Z. Cheng, "Optimization of Network Configuration in Large Distribution Systems Using Plant Growth Simulation Algorithm", *IEEE, Trans. On Power Systems*, Vol. 23, No. 1 pp. 119-126, Feb 2008.

[4] Chiang-Tzong Su, Chung-Fu Chang, Ji-Pyng Chiou, "Distribution Network Reconfiguration for Loss Reduction by Ant Colony Search Algorithm", *Electric Power Systems Research*, Vol. 75, pp. 190-199, 2005.

[5] Hsiao-Dong Chiang, Rene Jean-Jumeau, "Optimal Network Reconfiguration in Distribution Systems: Part 2: Solution Algorithms and Numerical Results", *IEEE, Trans. On Power Delivery*, Vol. 5, No. 3, pp. 1568-1574, July 1990.

[6] Isamu Watanabe, "An ACO Algorithm for Service Restoration in Power Distribution Systems", *IEEE Congress on Evolutionary Computation*, Vol. 3, pp. 2864- 2871, 2-5 Sept, 2005.

[7] R. Hooshmand and E. mashhoor, "Application of Fuzzy Algorithm in Optimal Reconfiguration of Distributed Networks for Loss Reduction and Load Balancing", *Eng Int Syst*, Vol. 14, No. 1, pp. 15-23, March 2006.